Transactions of the ASME®

Journal of Engineering for Gas Turbines and Power

Published Quarterly by The American Society of Mechanical Engineers

VOLUME 117 • NUMBER 3 • JULY 1995

Technical Editor
H. L. JULIEN (1998)

Associate Technical Editors
Advanced Energy Systems
M. J. MORAN (1996)
Gas Turbine
C. J. RUSSO (1995)
R. KIELB (1996)
S. SAMUELSEN (1996)
L. RIEKERT (1997)
Internal Combustion Engine
W. CHENG (1996)
Nuclear Engineering
H. H. CHUNG (1996)
Power
P. H. GILSON (1996)
D. LU (1998)

BOARD ON COMMUNICATIONS
Chairman and Vice President
R. MATES

Members-at-Large
T. BARLOW, N. H. CHAO, A. ERDMAN,
G. JOHNSON, L. KEER,
E. M. PATTON, S. PATULSKI,
S. ROHDE, R. SHAH, F. WHITE,
J. WHITEHEAD, K. T. YANG

OFFICERS OF THE ASME
President, **D. T. KOENIG**
Exec. Director
D. L. BELDEN
Treasurer
R. A. BENNETT

PUBLISHING STAFF
Managing Director, Engineering
CHARLES W. BEARDSLEY
Director, Technical Publishing
JANET M. WEINRIB
Managing Editor, Technical Publishing
CYNTHIA B. CLARK
Managing Editor, Transactions
CORNELIA MONAHAN
Senior Production Editor,
VALERIE WINTERS
Production Assistant,
MARISOL ANDINO

TECHNICAL PAPERS

Gas Turbines: Aircraft

Gas Turbines: Ceramics

Gas Turbines: Coal Utilization

Gas Turbines: Combustion and Fuels

Gas Turbines: Controls and Diagnostics

Gas Turbines: Electric Utilities and Cogeneration

(Contents continued on page 416)

Transactions of the ASME, Journal of Engineering for Gas Turbines and Power (ISSN 0742-4795) is published quarterly (Jan., April, July, Oct.) for $150.00 per year by The American Society of Mechanical Engineers, 345 East 47th Street, New York, NY 10017. Second class postage paid at New York, NY and additional mailing offices. POSTMASTER: Send address changes to Transactions of the ASME, Journal of Engineering for Gas Turbines and Power, c/o THE AMERICAN SOCIETY OF MECHANICAL ENGINEERS, 22 Law Drive, Box 2300, Fairfield, NJ 07007-2300.

CHANGES OF ADDRESS must be received at Society headquarters seven weeks before they are to be effective. Please send old label and new address.

PRICES: To members, $40.00, annually; to nonmembers, $150.00. Add $30.00 for postage to countries outside the United States and Canada.

STATEMENT from By-Laws. The Society shall not be responsible for statements or opinions advanced in papers or ... printed in its publications (B7.1, par. 3).

COPYRIGHT © **1995** by The American Society of Mechanical Engineers. Authorization to photocopy material for internal or personal use under circumstances not falling within the fair use provisions of the Copyright Act is granted by ASME to libraries and other users registered with the Copyright Clearance Center (CCC) Transactional Reporting Service provided that the base fee of $3.00 per article is paid directly to CCC, Inc., 222 Rosewood Dr., Danvers, MA 01923. Request for special permission or bulk copying should be addressed to Reprints/Permission Department.

INDEXED by Applied Mechanics Reviews and Engineering Information, Inc. Canadian Goods & Services Tax Registration #126148048

Downloaded 03 Jun 2010 to 171.66.16.159. Redistribution subject to ASME license or copyright; see http://www.asme.org/terms/Terms_Use.cfm

(Contents continued)

Gas Turbines: Industrial and Cogeneration

Gas Turbines: Manufacturing and Materials

Gas Turbines: Marine

Gas Turbines: Pipelines and Applications

Gas Turbines: Structures and Dynamics

ANNOUNCEMENTS

T. Esch
Lehrstuhl für Flugantriebe,
Technische Universität München,
Munich, Federal Republic of Germany

M. Giehrl
Department ETWW,
MTU-München GmbH,
Munich, Federal Republic of Germany

Numerical Analysis of Nozzle and Afterbody Flow of Hypersonic Transport Systems

Using an implicit Finite-Volume Navier–Stokes code, the flow field in a Single Expansion Ramp Nozzle (SERN) for a hypersonic aircraft is studied. Comparisons between experimental data and CFD calculations for certain components of the integrated exhaust system (cold two-dimensional nozzle flow, high temperature reacting three-dimensional combustion chamber flow, and two-dimensional nozzle flow with external flow) are presented. To show the sensitivity of the considered components to off-design operating conditions, comprehensive numerical studies have been carried out. For the determination of nozzle performance a detailed two-dimensional analysis from transonic to hypersonic flight Mach numbers has been performed. A direct optimization method has been used to investigate the influence of the lower nozzle flap shape on the thrust vector.

Introduction

The exhaust nozzle for hypersonic aircraft is an important part of the propulsion system. Throughout a flight mission from low subsonic ($M \approx 0$) to hypersonic speeds ($M \approx 7$) the nozzle system has to work over a wide range of different operating conditions. The nozzle pressure ratio for example varies from 3 at take-off to about 800 at the maximum flight Mach number. To achieve high installed performance over this range of pressure ratios, a geometric highly flexible, yet highly integrated exhaust nozzle system is required. The two-dimensional Single Expansion Ramp Nozzle (SERN) is considered to be most suitable for hypersonic application and was the chosen baseline exhaust system within the German Hypersonic Technology Program. It is characteristic for this type of nozzle that the rear part of the aircraft acts as a nozzle wall (see Fig. 1).

At higher flight Mach numbers the nozzle performance becomes more and more important as a 1 percent reduction in nozzle thrust coefficient will result in a loss of net installed thrust of about 4 percent (Lederer and Hertel, 1993).

In the transonic flight range the situation is different. Large changes in thrust vector are associated with the concept of asymmetric thrust nozzles, which were designed for high Mach number operation. As an example, Fig. 2 shows the typical variation of the axial thrust coefficient $c_{fg,x}$ over the flight Mach number. This considerably influences the flyability and stability of the whole aircraft in the transonic flight Mach number region (Herrmann and Rick, 1991; Lederer and Hertel, 1993; Bauer et al., 1993).

To predict the performance and the behavior of the SERN nozzle accurately throughout the whole flight range, the internal high-temperature reacting nozzle flow and the complex interaction between nozzle flow and external flow field (see Fig. 3) have to be described properly by CFD methods. Since most of the phenomena shown in Fig. 3 are still difficult to describe numerically, the way chosen here was to subdivide the nozzle/afterbody configuration into separate components: (1) nozzle, (2) combustion chamber, and (3) nozzle, flap and external flow. These components were experimentally investigated in great detail and serve as "benchmark experiments" for the CFD methods. The advantage of this approach is that the experimental and numerical analysis can be carried out under well-defined (boundary) conditions, enabling the validation of the numerical methods and the model assumptions (e.g., turbulence, combustion) in the CFD code. Besides this, it is possible to study the influence of changes in operating conditions on the performance parameters of the engine components.

Numerical Method

The Navier–Stokes equations, describing three-dimensional, steady, and compressible flows in conservation form, are solved by means of a finite volume approach using a fully implicit time-stepping method with multigrid acceleration (TASCflow/ASC, 1992).

The discretization of the convective terms is based on a skew upwind evaluation of the cell face fluxes together with a physically based correction term (Physical Advection Correction), which makes the method second-order accurate. The transient terms are approximated by first-order backward differences.

To facilitate the computation and to guarantee that the solution method is strongly conservative, a single-cell colocated grid with Cartesian velocity components is used. To prevent odd-even decoupling it is ensured that the velocities depend on the local pressure differences. The method used is similar to the methods of Chi and Hsu and is based on a similarity to the local finite volume momentum equations (TASCflow/ASC, 1992).

To account for intervariable coupling (e.g., pressure/velocity, pressure/density) a fully coupled solution algorithm is used for mass and momentum equations. The coupled algebraic linear system of equations is solved by a multigrid method running a W-cycle. As base solver coupled vectorized Incomplete Lower Upper (ILU) factorization is used.

Two turbulence models are available in the code. The first model is the standard two-equation $k-\epsilon$ turbulence model with log-law wall functions. The second model is a two-layer turbulence model, which combines the high Reynolds $k-\epsilon$ model in the fully turbulent outer region with a low-Reynolds one-equation model in the viscous region near the wall.

Two-Dimensional Nozzle Flow, Cold

The main component of the investigated exhaust system is formed by a plane asymmetric nozzle.

Contributed by the International Gas Turbine Institute and presented at the 39th International Gas Turbine and Aeroengine Congress and Exposition, The Hague, The Netherlands, June 13–16, 1994. Manuscript received by the International Gas Turbine Institute March 9, 1994. Paper No. 94-GT-391. Associate Technical Editor: E. M. Greitzer.

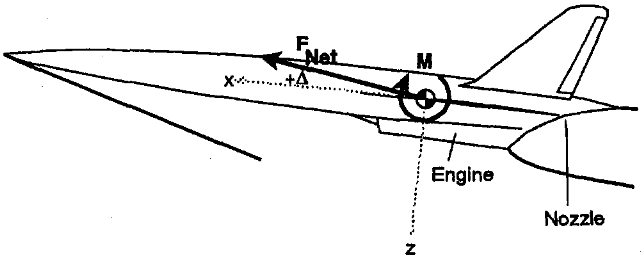

Fig. 1 Hypersonic aircraft (scheme)

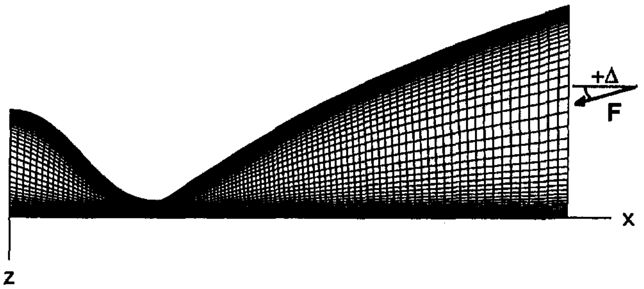

Fig. 4 Grid (112 × 51 control volumes)

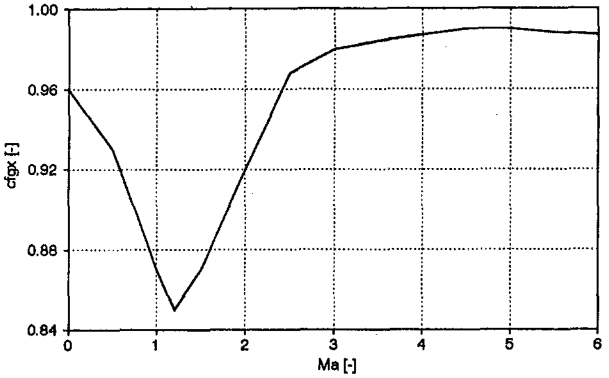

Fig. 2 Axial thrust coefficient

Tests on a subscale model of this nozzle were performed at the DLR/SMAT (Cologne/Germany) for cold ($T_0 = 293$ K) and hot ($T_0 = 800$ K) flows (Stursberg, 1993). Parallel to the experiment comprehensive numerical studies were carried out (Esch, 1992). Figure 4 shows an example of one of the grids used for the computation. Clearly visible are the lower flat wall and the upper curved wall, where the grid is refined to resolve the large gradients of velocity and temperature within the boundary layer.

Besides the comparison between experimental and numerical data, grid dependence and various other sensitivity studies were carried out (Esch, 1992). As an example for a comparison between experiment and calculation Fig. 5 shows the local pressure ratio p_0/p_w along the lower and upper nozzle walls. The agreement is good except for a small region along the lower wall, where the weak shock, which emanates from the change in curvature right after the nozzle throat, hits the lower flat wall and influences the flow field more than predicted by CFD.

In addition to local flow field values integral nozzle performance parameters were also compared, such as mass flow ratio μ, thrust coefficient c_f, and the thrust vector angle Δ.

In Table 1 the performance parameters predicted by theory and those based on experimental data are shown. For the considered operating point the agreement is good.

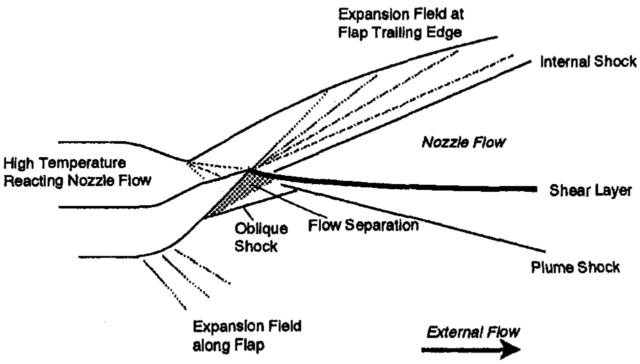

Fig. 3 Scheme of flow field structures in the nozzle/afterbody region

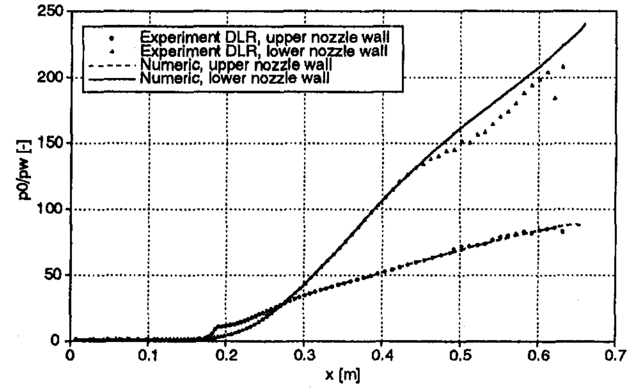

Fig. 5 Comparison between experimental and numerical p_0/p_w distributions in the nozzle at design conditions (Table 1)

Nomenclature

A = area, m^2
F = thrust vector, N
M = Mach number
T = temperature, K
V = speed, m/s
c_p = pressure coefficient = $(p - p_\infty)/q_\infty$
c_f = thrust coefficient = $F/(p_0A^*)$
c_{fg} = gross thrust efficiency = F_g/F_{id}
p = pressure, Pa
q = dynamic pressure, Pa
x, y, z = Cartesian coordinates (aircraft/model fixed), m
Δ = thrust vector angle = arctan (F_z/F_x), deg
Π = pressure ratio = p_0/p_∞
α = angle of attack, deg
μ = mass flow ratio = $\dot{m}_n/\dot{m}_{id,n}$

Subscripts

e = exit
n = nozzle
g = gross
id = ideal
w = wall
x, y, z = direction of Cartesian coordinates
0 = stagnation conditions
∞ = free stream
$*$ = nozzle throat

Table 1 Integral performance parameters, comparison experiment—CFD

		Experiment	Numerics
c_{fx}	[-]	1.56	1.55
Δ	[°]	9.5	10.76
μ	[-]	0.991	0.993
Reservoir: $T_0 = 293K$, p_0=10bar; $\Pi = 198$ Experimental data: Detsch, 1993			

One advantage of theoretical calculation is that changes in geometry and internal/external flow field parameters can often be done more easily than in the experiment. CFD can therefore be used to simulate distinct off-design conditions and to give important information about the sensitivity of a system to deviation from the design point. As an example, Fig. 6 shows the dependence of the thrust vector angle Δ on the pressure ratio $\Pi = p_0/p_e$. For pressure ratios Π larger than approximately 70 nearly no influence of changes in the exit pressure p_e is visible. Between $\Pi \approx 20$ and $\Pi \approx 70$ the thrust vector is turned downward by more than 140 percent. The reason for this behavior is that the first shocks inside the nozzle are located at the lower side, because of the different pressure levels between lower and upper nozzle wall. Across the oblique shock the flow Mach number decreases whereas the static pressure increases, which leads to a downward acting force. The increase in thrust vector angle is stopped, when the first shocks appear at the upper nozzle wall ($\Pi \lesssim 20$).

Three-Dimensional Combustion Chamber Flow

In order to analyze the flow in a hydrogen combustion chamber for a hypersonic ramjet engine, the flow code used for the nozzle configurations is now applied in three dimensions together with an Eddy-Break-Up model for the chemical reactions.

The cylindrical combustion chamber has an injection device with 6 arms equally spaced on the circumference. Each of these arms injects hydrogen through a number of small holes in the axial direction of the combustion chamber. Further downstream the cross section changes from circular to rectangular and the combustion chamber is followed by a SERN nozzle, Fig. 7.

This configuration meets the basic features of a proposed hypersonic propulsion system and is extensively tested, with different laser methods, at the DLR ramjet test facility in Cologne (Schodl, 1993).

Modeling the complete combustion chamber, at a resolution fine enough to resolve the local flow phenomena in the injection zone, would have resulted in a computer model far too large for the computers available. So the combustion chamber was split into two models: one for the injection zone and one for the transition duct.

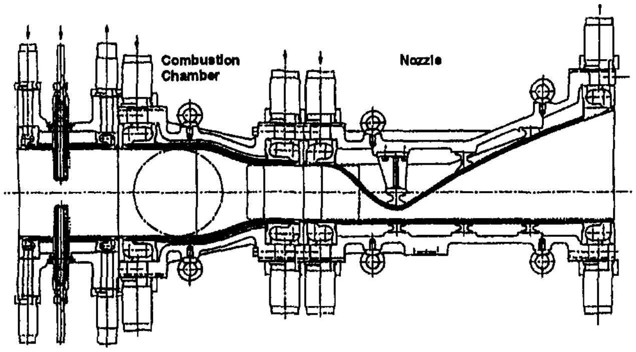

Fig. 7 Scheme of combustion chamber and nozzle

In order to exploit the high degree of symmetry of the injection device, a 30 deg sector model, around one half of one of the injection rods, was generated, containing about 60,000 computational cells, Fig. 8. The model for the transition duct assumes a symmetry plane in the middle of the duct and therefore only half of the cross section is discretized with about 80,000 cells.

The results from the injection zone are mapped to the inlet of the transition duct and the results at the end of the duct are compared to the measurements.

Because of the alignment of the injection holes with the main flow direction, the combustion process takes place in stratified zones, which extend down to the rectangular exit plane of the transition duct.

Up to now only velocity measurements (L2F) were available for comparison. Figure 9 shows the calculated and measured velocity profiles at the exit plane. The absolute speed corresponds within about 10 percent and the form of the profiles also agrees fairly well.

Because the flow field depends strongly on the chemical reactions in the combustion chamber, the agreement found is quite encouraging.

The next steps, besides the comparison with further experimental results, will be the extension of the computational model, including the nozzle flow, in order to validate the reaction model in an accelerating flow, and to gain insight into the performance of the complete propulsion system, including chemical reactions.

Two-Dimensional Nozzle/Afterbody Model

The performance of the exhaust system of a hypersonic aircraft is described by the thrust nozzle performance and also

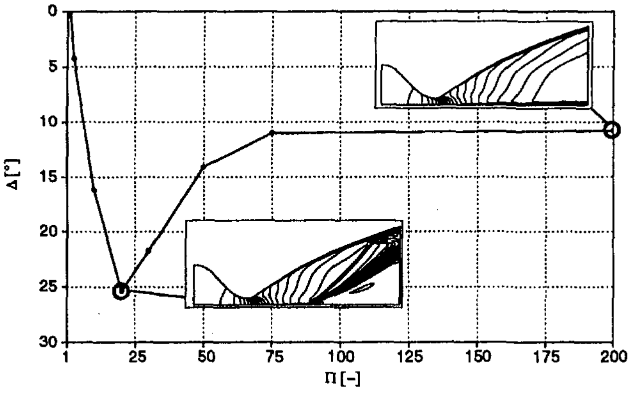

Fig. 6 Thrust vector angle as function of pressure ratio Π

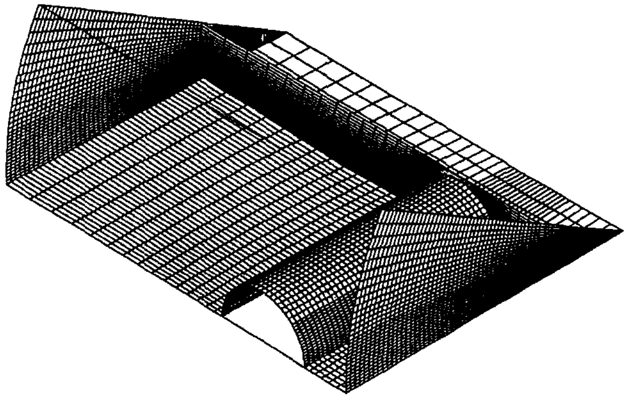

Fig. 8 Computational grid

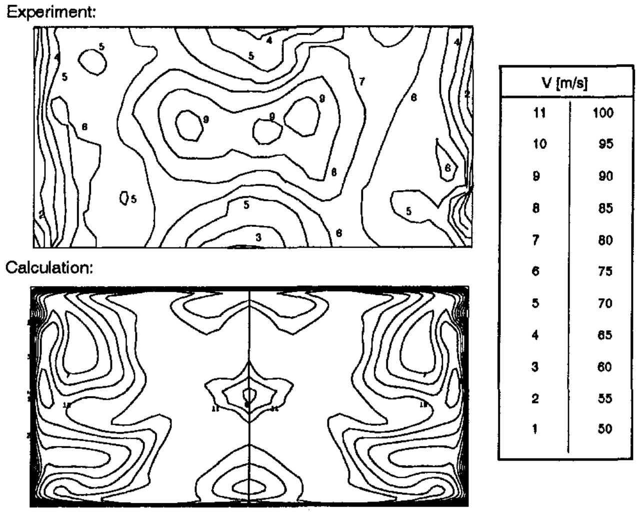

Fig. 9 Velocity profiles at the combustion chamber exit plane

strongly influenced by the integration of the nozzle into the airframe.

The nozzle/afterbody configuration can be thought of as being a combination of the components: nozzle and airframe (i.e., expansion ramp and lower flap). Both components strongly influence each other:

- over-/underexpanded nozzle flow may change the flow fields along the lower flap and the expansion ramp (flow separation, shocks)
- the pressure distributions along flap and ramp (especially for the transonic flight Mach numbers) may lead to significant changes in size and direction of the thrust vector (see Fig. 11).

To study the interference between the main nozzle flow and the ambient flow a generic windtunnel model (Fig. 10) was built and tested in the Trisonic Windtunnel (TMK) and the Hypersonic Windtunnel (H2K) at the DLR in Cologne (Niezgodka, 1993). Figures 12 and 13 show comparisons between calculated and measured wall pressure distributions along the upper nozzle wall plus expansion ramp (Fig. 12) and along the lower flap (Fig. 13) for different flight Mach numbers, angles of attack, and pressure ratios (Esch, 1993a). To simplify the calculations only cold main nozzle flows were considered. The agreement among the data is fairly good, except for the pressure distribution along the nozzle flap at low Mach numbers. The flow separation along the flap, as predicted by CFD, cannot be seen in the experimental data, though Schlieren photographs show its existence and suggest that the region with separated flow is slightly larger than calculated. The discrepancies along the lower side of the windtunnel model ($x > 0.12$ m) are mainly due to disturbances of the flow field by the nose shock of the model, which is reflected at the windtunnel walls and the model itself. To avoid those undesired influences on the measurement in the transonic flight range, further experiments will be carried

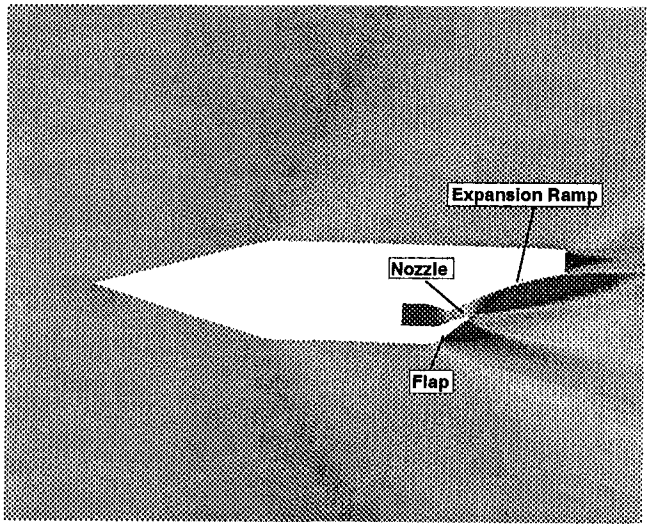

Fig. 10 CFD/windtunnel model

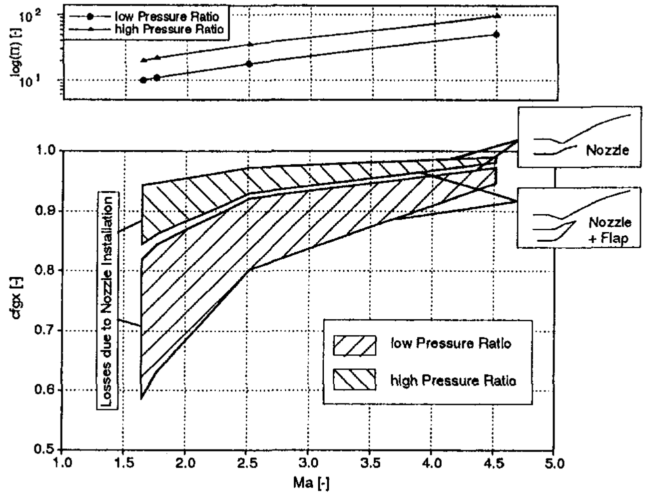

Fig. 11 Gross thrust coefficient as function of flight Mach number and pressure ratio

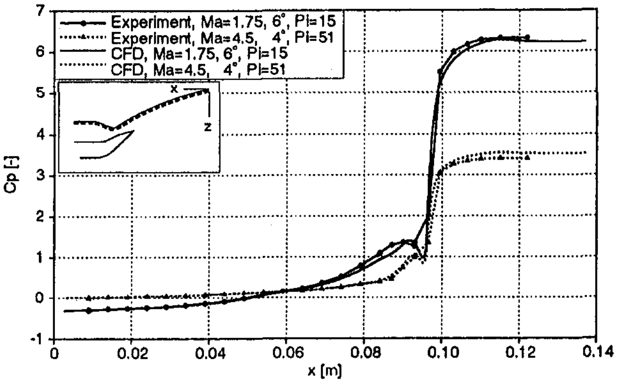

Fig. 12 Local pressure coefficient c_{pl} along expansion ramp

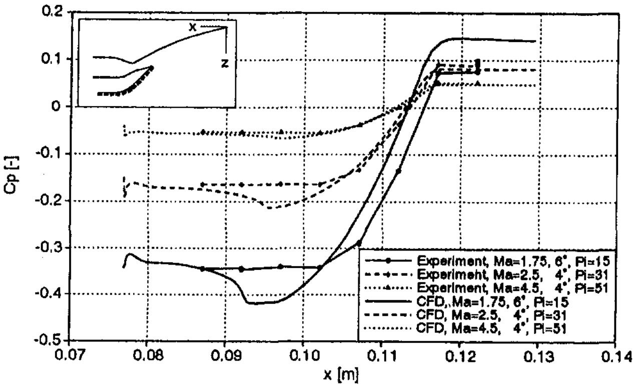

Fig. 13 Local pressure coefficient c_{pl} along flap

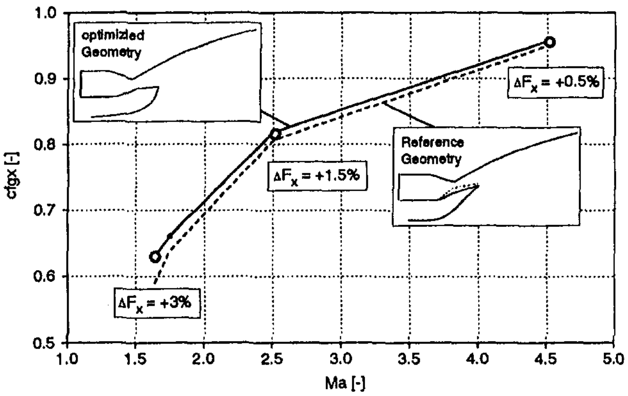

Fig. 14 Optimization of lower nozzle flap

out in the near future at larger test facilities (TWG, DLR Göttingen).

To study the effects of different parameters on the performance of the exhaust system and to describe the gross thrust vector behavior realistically over a flight mission from transonic to hypersonic Mach numbers, the numerical flow field analysis was carried out over a wide range of different operating conditions: Mach: 1.6–6.0, Π = 3–800, and α = 0–8 deg.

As an example, Fig. 11 shows the change in thrust coefficient $c_{fg,x}$ as a function of flight Mach number and pressure ratio $\Pi = p_0/p_\infty$ for the windtunnel model. Associated with the concept of single expansion ramp nozzles are large thrust vector variations (magnitude and direction) at transonic Mach numbers, which are caused by expansion losses of the nozzle and increasing external drag of the nozzle flap. This behavior is independent of the chosen pressure ratio Π, though increasing Π compensates, up to a certain amount, the losses caused by the low local pressure distribution along the flap. For high flight Mach numbers the influence of the flap on the installed performance gradually vanishes.

Optimizing the Lower Nozzle Flap. Splitting the thrust coefficient c_{fg} into a component provided by the nozzle and a component provided by the flap shows that the losses due to the nozzle integration are mainly caused by the lower flap, Fig. 11. The same holds true for the changes in the thrust vector angle.

The question that arises is: Can the thrust vector be influenced by modifying the lower flap? If so, how would a flap look, which for a given flap overall size produces minimum drag or minimum changes in thrust vector angle?

To answer this question an optimization method was coupled with the CFD code and was used to find the required flap contours (Esch, 1993b). The nozzle/afterbody configuration used for the windtunnel test was chosen as reference geometry for all optimization calculations.

Figure 14 shows the results of optimization runs using the thrust coefficient $c_{fg,x}$ as "target function." The upper solid line represents the results for the optimized geometry, the dashed line shows the data for the reference geometry.

In the region of transonic flight Mach numbers, improvements in the x component of gross thrust of around +3 percent (compared to the reference geometry) were possible, whereas for higher Mach numbers only small changes in $c_{fg,x}$ could be achieved (+0.5 percent at M = 4.5). First calculations have shown that much larger changes in the thrust vector angle will be possible ($\approx$ +18 percent at M = 1.64, Π = 14), however, at the price of increased base drag.

The resultant flap shape and the data given in Fig. 14 strongly dependent on the used target function (x component of thrust, thrust vector angle, or any combination of both), the basic geometry, the operating conditions, and of course the (geometric) boundary conditions chosen for the optimization.

Nevertheless it can be seen that optimization, even in early stages of development, is a useful tool, which gives a lot of information on possible performance improvements or sensitivities of the nozzle/afterbody configuration.

Conclusions

Within this study CFD methods have been successfully used to calculate the flow fields in (1) an asymmetric nozzle, (2) a combustion chamber, and (3) a nozzle/afterbody configuration of an integrated hypersonic aircraft engine.

The main interest of the analysis was to describe properly the performance of the propulsion system throughout the whole flight mission range from M = 1.6 to M $\approx$ 7.

Validation of the numerical methods and the physical models was performed by recalculating a set of well-defined experiments (Stursberg, 1993; Niezgodka, 1993) and, whenever possible, comparing local and global experimental and numerical results.

The agreement between measurements and calculations was quite good in nearly all the test cases. For sensitivity studies CFD calculations were carried out not only at the design point but also for off-design conditions.

The application of an optimization routine together with CFD calculations can give useful information on possible performance improvements. This was shown at the example of the nozzle/afterbody configuration used for the windtunnel tests.

Acknowledgments

This study was carried out within the frame of the German Hypersonic Technology Program funded by the BMFT and within the Special Research Program 255 (SFB 255, Project B1, Prof. Dr.-Ing. H. Rick) funded by the DFG. The authors are thankful for the support given by the MTU Munich, the DLR Cologne, the Technical University Dresden, and the Technical University Munich, Lehrstuhl für Flugantriebe, Prof. Dr.-Ing. G. Kappler M. Sc.

References

Advanced Scientific Computing Ltd., 1992, "Theory Documentation," Waterloo, Ontario, Canada.

Bauer, A., Ludäscher, M., and Rick, H., 1993, "Leistungsrechnung und Simulation des Betriebsverhaltens von Antriebssystemen für Hyperschallflugzeuge," *DGLR-Jahrestagung*, Göttingen, 28.9.–1.10.1993, 93-03-09.

Detsch, F., 1993, "Untersuchungen an Düsenmodellen, Bestimmung der Wanddruckverteilung und der Schubbeiwerte für eine Rechteckdüse," Institut für Strömungsmechanik Laboratorium Hochgeschwindigkeitswindkanal, TU-Dresden, Bad-Salzungen.

Esch, Th., 1992, "Untersuchung des Strömungsfeldes in einer Rechteckdüse," Interner Institutsbericht LFA-ES-10/92, Lehrstuhl für Flugantriebe, TU-München.

Esch, Th., 1993a, "NS-Rechnungen zur Triebwerksstrahl Interferenz beim MTU-Heckmodell, Vergleich Experiment–Rechnung," Interner Institutsbericht LFA-Es-2/93, LFA, TU-München.

Esch, Th., 1993b, "Berechnung schuboptimaler SERN-Düsenkonturen mit Hilfe direkter Optimierungsverfahren," Interner Institutsbericht LFA-Es-12/93, LFA, TU-München.

Herrmann, O., and Rick, H., 1991, "Propulsion Aspects of Hypersonic Turbo-Ramjet-Engines With Special Emphasis on Nozzle/Aftbody Integration," ASME Paper No. 91-GT-395.

Lederer, R., and Hertel, J., 1993, "Exhaust System Technology," SPACE COURSE 1993, TU-München.

Niezgodka, J., 1993, "Druckverteilungsmessungen zur Simulation der Interferenz des Triebwerksstrahles auf das Heck der Sänger-Unterstufe (MTU-Heckmodell)," Technical Report IB-39113-93C15, DLR-WT-WK, Köln.

Schodl, R., 1993, DLR-SMAT, Köln, private communication.

Stursberg, K., 1993, DLR-SMAT, Köln, private communication.

Y. Kinoshita

J. Kitajima

Y. Seki

Akashi Technical Institute.

A. Tatara

Jet Engine Division.

Kawasaki Heavy Industries, Limited,
Akashi, Japan

Experimental Studies on Methane-Fuel Laboratory Scale Ram Combustor

The laboratory scale ram combustor test program has been investigating fundamental combustion characteristics of a ram combustor, which operates from Mach 2.5 to 5 for the super/hypersonic transport propulsion system. In our previous study, combustion efficiency had been found poor, less than 70 percent, due to a low inlet air temperature and a high velocity at Mach 3 condition. To improve the low combustion efficiency, a fuel zoning combustion concept was investigated by using a subscale combustor model first. Combustion efficiency more than 90 percent was achieved and the concept was found very effective. Then a laboratory scale ram combustor was fabricated and combustion tests were carried out mainly at the simulated condition of Mach 5. A vitiation technique was used to simulate a high temperature of 1263 K. The test results indicate that ignition, flame stability, and combustion efficiency were not significant, but the NO_x emissions are a critical problem for the ram combustor at Mach 5 condition.

Introduction

The Super/Hypersonic Transport Propulsion System Research Project (HYPR Project) has been under way since 1989 in Japan. The propulsion system is a combined-cycle engine (CCE), which consists of a turbojet engine for the lower speed range from take-off to Mach 3 and a ramjet engine for the higher speed range from Mach 2.5 to 5. The liquid methane or liquid natural gas containing high-purity methane was selected as its fuel. Although it is a challenge to use the novel fuel, it has many advantages. The fuel is superior to help deal with the high temperatures created by high-speed flight and it is available in large quantities. Also, it offers the possibility of reducing fuel costs.

The ramjet engine for a commercial hypersonic transport will need to achieve low fuel consumption for superior economy and low emissions for environmental quality. However, there are many technical problems that must be overcome to develop the ram combustor. The operating conditions of the ram combustor, such as inlet air temperature, pressure, and velocity, change significantly during a flight mission (Watanabe et al., 1993). For example, when relatively low-temperature air, $T_6 = 603$ K, flows into the combustor at a high speed, $U_6 = 98$ m/s, at Mach 3 condition, it is difficult to obtain reliable ignition, stable flame, high combustion efficiency, and low pressure loss. On the other hand, extremely high-temperature air, $T_6 = 1263$ K, flows into the combustor at a relatively low speed, $U_6 = 40$ m/s, at Mach 5 condition. Therefore, it becomes important to establish technologies on efficient cooling for the combustor liner and flameholder, and also on the reduction of NO_x emissions. The objective of this study is to establish the combustion technology mentioned above and to obtain design data for the development of the ramjet engine combustor.

Mullen and Fenn (1951) conducted experimental research on a ramjet combustor by using a small-scale V-gutter flameholder. Longwell et al. (1953) investigated fundamental flame stabilization characteristics on a V-gutter flameholder system. Gregory et al. (1971) examined the effects of inlet air temperature on the flame stabilization, and also on combustion efficiency up to 920 K on the afterburner system, and Branstetter and Reck (1973) examined the effect up to 1255 K. However, this research was carried out using JP fuel and there is little on a ram combustor that used methane as a fuel.

Authors have been investigating combustion characteristics on the laboratory scale ram combustor (LSC) using natural gas as a fuel. In the early stage of our work, fundamental flame stabilization and combustion characteristic tests were conducted at the simulated conditions of flight Mach number 3. The results indicated that there were some difficulties on flame stabilization, but an acute problem was poor combustion efficiency about 70 percent (Kinoshita et al., 1992). To settle this significant problem a series of fundamental combustion tests on a fuel zoning combustion concept was conducted with a subscale ram combustor. A fuel zoning combustion concept means an idea of making active chemical reactions by creating a locally stoichiometric premixture around the flameholder. The test results proved it to be valid for improving combustion efficiency. As a next step, a Laboratory Scale Ram Combustor (LSC) test was conducted with a rectangular ram combustor. The combustor was a subscale part model but its dimensions were near those of an actual ram combustor. A series of combustion tests was carried out at the simulated conditions of Mach 3 and 5. Useful data for the design of the Mach 5 ram combustor were obtained.

This paper presents, first, the experiment and test results of the fundamental combustion test on a fuel zoning combustion concept, then the laboratory scale ram combustor test results.

Experimental Apparatus and Measurements

Fuel Zoning Combustion Tests. A subscale ram combustor was used to examine whether the fuel zoning combustion method was effective for improvement of combustion efficiency. A subscale ram combustor was much smaller than an actual combustor and it may be difficult to predict the actual combustor performance from its test results. However, it is considered proper to assess the feasibility and potential of the fuel zoning combustion concept.

Combustor Description. A schematic of the subscale combustor is illustrated in Fig. 1. The combustor was 155 mm in diameter and 1500 mm in length. The combustor consisted of

---

Contributed by the International Gas Turbine Institute and presented at the 39th International Gas Turbine and Aeroengine Congress and Exposition, The Hague, The Netherlands, June 13–16, 1994. Manuscript received by the International Gas Turbine Institute March 4, 1994. Paper No. 94-GT-369. Associate Technical Editor: E. M. Greitzer.

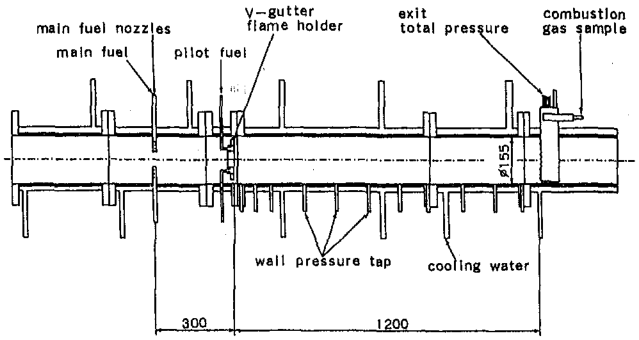

Fig. 1 A schematic of a subscale combustor for a fuel zoning combustion concept

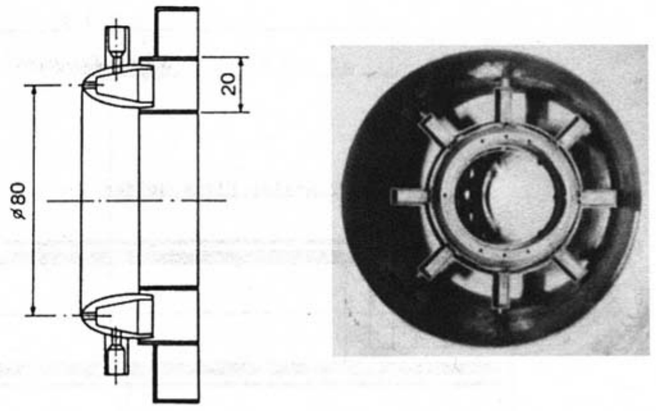

Fig. 3 A schematic of the flameholder of the subscale combustor

three major parts: main fuel injection system, a flameholder, and a heat pipe. The combustor was cooled by water.

The main fuel injection system was located 300 mm upstream of the flameholder. Sixteen fuel injectors were spaced circumferentially around the injection plane. Two types of fuel nozzle, shown in Fig. 2, were used in this test. One was a premixing fuel nozzle and the other was a zoning fuel one. The premixing fuel nozzle placed twelve injection holes of 0.6 mm diameter at relatively long intervals on the body and was expected to achieve better mixing performance. On the other hand, the zoning fuel nozzle placed eight injection holes of 1 mm diameter at short intervals and this fuel nozzle was expected to make a locally fuel-rich mixture around the flameholder. To make the fuel zoning effective, the zoning fuel nozzle with a flow separator was also investigated. Fuel was delivered perpendicularly to the air flow for both fuel injectors.

The flameholder employed the configuration of an annular V-gutter with eight radial segment gutters as shown in Fig. 3. A pilot fuel nozzle was installed inside the gutter to perform reliable ignition and to sustain stable combustion. Eight injection holes of 3 mm diameter were equispaced inside the annulus V-gutter. The blockage ratio of the flameholder was 35 percent and the dimensions of the annulus gutter were 20 mm in width, 90 mm in center diameter, and 45 deg in gutter angle.

Measurements. Combustion tests were conducted at the simulated conditions of Mach 3, namely $T_6 = 600$ K, $P_6 = 0.14$ MPa, and $U_6 = 98$ m/s. Combustion gas was sampled by a water-cooled gas sampling probe mounted on the exit plane of the ram combustor and was cooled rapidly by the water. Therefore it is considered that proper quenching of the reaction occurred within the probe. Products of combustion were analyzed by a flame ionization detector for total unburned hydrocarbon (THC), nondispersive infrared instruments for CO and CO_2, a paramagnetic analyzer for O_2, and a chemiluminescence analyzer for NO_x. Combustion efficiency was calculated from measured exhaust gas compositions.

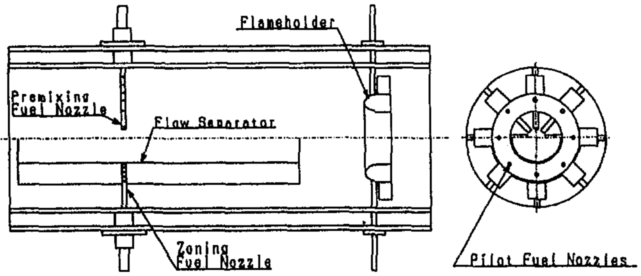

Fig. 2 Main fuel injection system and a flameholder of the subscale combustor

A flame stability test was carried out at the inlet temperature of 600 K, varying the inlet air velocity. The equivalence ratio of lean blowout was measured when the pilot flame was extinguished by reducing the pilot fuel flow rate. The equivalence ratio of rich blowout was also measured when the main flame blowout by increasing the main fuel flow rate and the pilot fuel flow rate was kept constant, $\phi_p = 0.085$, in this test.

Laboratory Scale Ram Combustor Test. The laboratory scale ram combustor (LSC) used in this study was a rectangular model and a part of a practical scale ram combustor. The configurations of the flameholder and fuel injection system were originally drafted by SNECMA and designed by KHI. The purposes of this LSC test were to obtain combustor performance, especially combustion efficiency and NO_x emissions, at Mach 3 and 5 conditions and to make problems clear for the ram combustor of the combined-cycle engine.

Combustor Description. A schematic drawing of the LSC is illustrated in Fig. 4. The dimensions of the combustor were 130 mm in width, 180 mm in height, and 1279 mm in length. The inner wall of the combustor was made of refractory cement and there was a water jacket outside the wall.

Two types of main fuel nozzle were designed and fabricated. One was a premixing fuel nozzle and the other was a zoning fuel nozzle just the same as the subscale combustor. The main fuel injection system, which is shown in Fig. 5, was located 79 mm upstream of the flameholder. Pairs of the premixing fuel nozzle were mounted 30 mm on both sides of a vertical centerline of the injection plane. Fuel was delivered perpendicularly to the air flow through ten equispaced holes of 1 mm diameter on the body of injectors. This premixing fuel nozzle was expected to show better mixing ability by the result of CFD analysis that was carried out by SNECMA. The zoning fuel nozzle

Nomenclature

B.R. = blockage ratio, percent
E.I. = emission index, g/kg fuel
M = inlet air Mach number
P = total pressure, MPa
PLR = total pressure loss ratio, percent

T = total temperature, K
U = inlet air velocity, m/s
ηb = combustion efficiency, percent
ϕ = equivalence ratio

Subscripts

p = pilot
6 = ram combustor inlet
7 = ram combustor exit

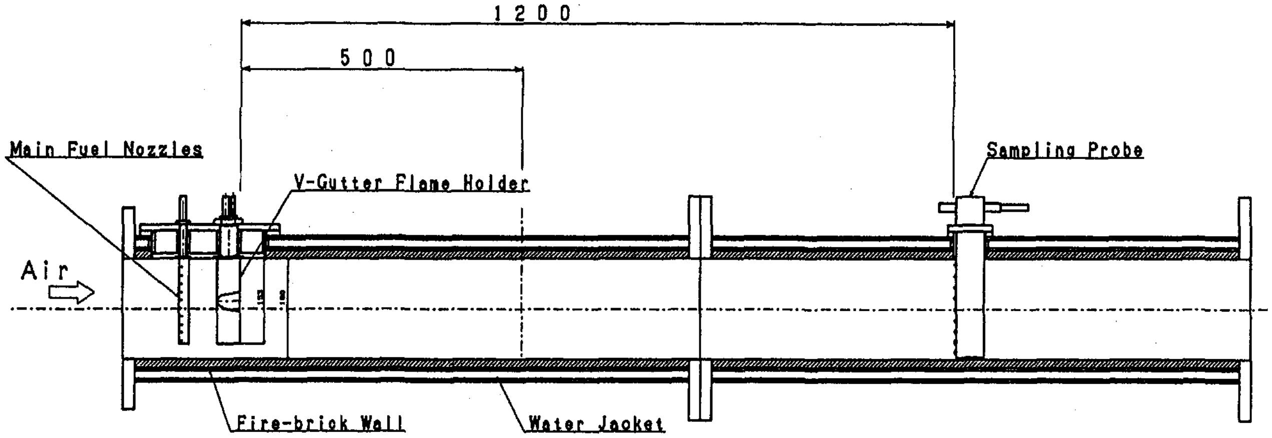

Fig. 4 A schematic of a laboratory scale ram combustor

was a single injector, which was mounted between the two premixing fuel nozzles and had 30 injection holes of 1 mm diameter on its body, and also on the trailing edge.

The flameholder, Fig. 6, consisted of a vertical main V-gutter and two horizontal arm V-gutters. The height and the width of the flameholder were respectively 153 mm and 32 mm for the main V-gutter and 90 mm and 36 mm for the arm V-gutters. The blockage ratio of the flameholder was 30 percent. This flameholder was cooled by auxiliary air (shop air). A tube was inserted inside the flameholder and cooling air was supplied into it. The cooling air was injected to the inner surface of the flameholder through small holes on the tube. The cooling air was exhausted to the atmosphere so as not to affect combustion phenomena in the combustor. A pilot fuel nozzle was also put inside the V-gutter as shown in Fig. 6.

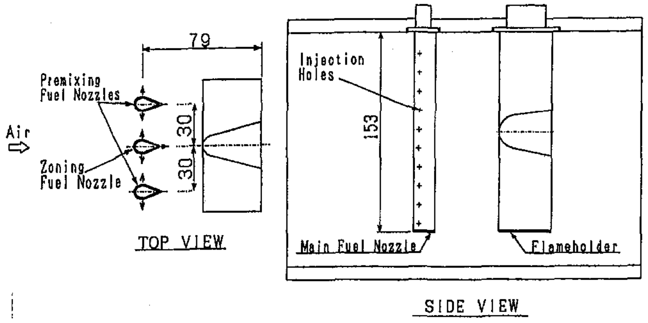

Fig. 5 Main fuel injection system and a flameholder of the LSC

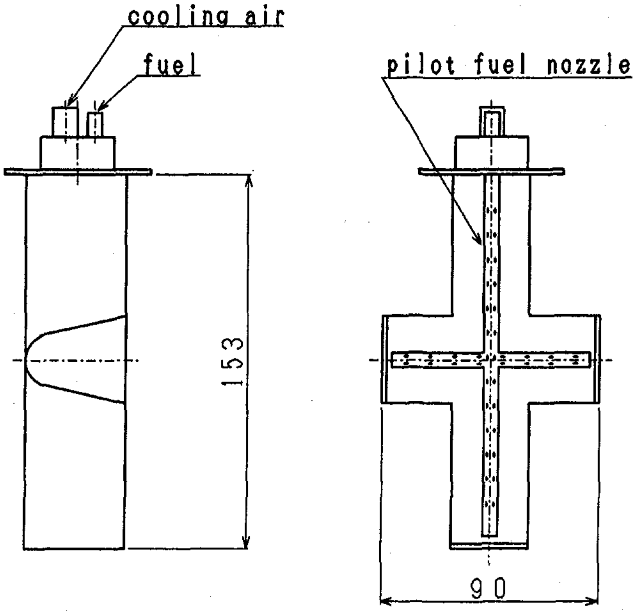

Fig. 6 Schematic of the flameholder of the LSC

Measurements. Combustion tests were carried out at the simulated conditions of Mach 3 and 5. These are the representative operating conditions of the combined cycle engine: Mach 3 is a starting point of ramjet single mode and Mach 5 is a high-speed cruise condition. Test conditions at Mach 3 were these: $T_6 = 600$ K, $P_6 = 0.14$ MPa, $U_6 = 98$ m/s, $\phi_p = 0.085$, and $\phi = 0.3$. At Mach 5 they were $T_6 = 1263$ K, $P_6 = 0.2$ MPa, $U_6 = 40$ m/s, $\phi = 0.43$ and 0.35. To simulate such a high temperature at Mach 5 condition a vitiation technique was used in this study.

A water-cooled gas sampling probe with 9 holes of 2 mm diameter like the one used in the fuel zoning combustion test was installed at the exit plane of the combustor. The probe was moved to three locations on the plane and the locations of sampling point are shown in Fig. 7. Measuring the average performance of the combustor, e.g., average combustion efficiency and average emission index of NO_x, combustion gas was sampled through all holes of the probe, then gathered and

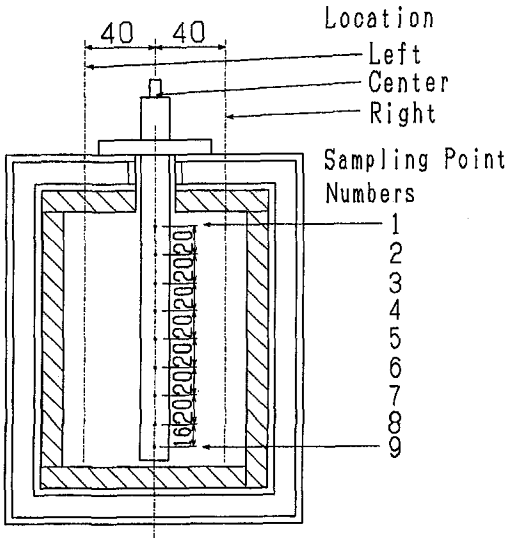

Fig. 7 Schematic of sampling points at exit plane

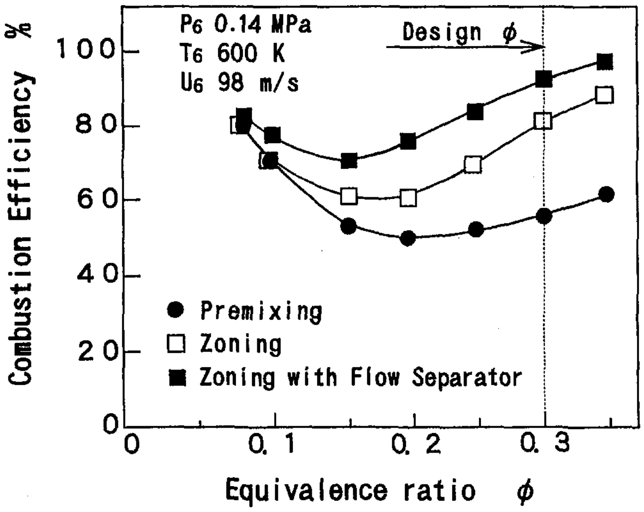

Fig. 8 Effect of main fuel nozzle configurations on combustion efficiency

analyzed. Moreover the spatial measurement was also carried out by individual sampling of the gas through each hole.

Test Facility. Combustion air was pressurized by a compressor and was heated up to 750 K maximally by a heat exchanger, then was supplied to the test rig. In the case of the Mach 5 combustion test, a vitiation heater that was located 1500 mm upstream of the ram combustor was used to simulate such a high temperature. Although oxygen concentration of vitiated air was reduced by vitiation, oxygen was not added to make a test procedure easy. Fuels used in this study were natural gas containing 98.5 percent methane for the ram burner and kerosene for the vitiated heater, respectively.

Results and Discussion

Fuel Zoning Combustion Test. Figure 8 shows the combustion efficiency obtained by the premixing fuel nozzle and the zoning fuel nozzle with and without flow separator as a function of overall equivalence ratio. The equivalence ratio of the pilot fuel was kept constant, $\phi_p = 0.085$, for each case. The result indicates that the premixing fuel nozzle gave the combustion efficiency no more than 55 percent at the design equivalence ratio of Mach 3, $\phi = 0.3$. The reasons for poor combustion efficiency are not only the combustor inlet conditions such as low temperature and high velocity mentioned above, but also the low overall equivalence ratio. The equivalence ratio of 0.3 is much lower than that of ramjet engines that have been studied for the space plane.

To improve the low combustion efficiency, a fuel zoning combustion concept was tried in this ram combustor study. This concept was expected to achieve high combustion efficiency by making a locally stoichiometric mixture around the flameholder. Square plots show the test results obtained by the zoning fuel nozzle without the flow separator. Combustion efficiency was improved largely for all the equivalence ratios as compared with the premixing fuel nozzle. About 80 percent combustion efficiency was obtained at the design equivalence ratio. Blackened square plots in the figure show the results of the zoning fuel nozzle with the flow separator. The flow separator was used to control an amount of air for mixing with fuel and was expected to enhance the zoning effect further. The result shows the highest efficiency is more than 90 percent at the equivalence ratio of 0.3. Consequently this fuel zoning combustion concept was found very effective for improving the low combustion efficiency at such a low overall equivalence ratio.

The fuel zoning combustion concept, however, had faults regarding flame stability and the pressure loss of the combustor. Figure 9 shows the stability loops for the premixing fuel nozzle and the zoning fuel nozzle. The lean blowout was the same with the two fuel nozzles, because it occurred by an extinction of the pilot flame and it had nothing to do with main fuel. The equivalence ratios of lean blowout were very low for the wide range of inlet air velocity. The upper side of the stability loop means rich blowout that is of primary interest. A continuous line of rich blowout was obtained by using the zoning fuel nozzle. Rich blowout of the premixing fuel nozzle could not be measured owing to limitation of the supplying pressure of main fuel. A dotted line in the figure shows the maximum equivalence ratios tested and it indicates that the equivalence ratios of rich blowout were higher than those. Rich blowout using the zoning fuel nozzle occurred at the lower equivalence ratio as compared with the premixing fuel nozzle over the entire range of the inlet air velocity shown in the figure. The local equivalence ratio around the flameholder caused by the zoning fuel nozzle was supposed to be much higher than that caused by the premixing fuel nozzle if the overall equivalence ratio was the same. Therefore the pilot flame that was anchored in the wake of the flameholder was extinguished at a lower equivalence ratio to the zoning fuel nozzle. Fortunately, the equivalence ratio was about 0.4 at the inlet air velocity of 100 m/s, that is design velocity of Mach 3, and it exceeded the design equivalence ratio at Mach 3 condition, even though the zoning fuel nozzle was selected. Combustion oscillation was observed for both fuel nozzles, and the equivalence ratios associated with the oscillation were shown in the figure. The results show that the oscillation occurred at almost the same equivalence ratios over 0.4 for both fuel nozzles.

A total pressure loss ratio is defined as

$$\mathrm{PLR} = \frac{P_6 - P_7}{P_6} \times 100 \qquad (1)$$

The total pressure loss ratios measured by using the three nozzles, namely premixing fuel nozzle, zoning fuel nozzle with and without the flow separator, are shown in Fig. 10 as a function of the equivalence ratio. The ratios at no-combustion condition were 3 and 5 percent for the premixing fuel nozzle and the zoning fuel nozzle with the flow separator, respectively. This discordance was caused by a difference of the total blockage ratio between the two nozzles. The total pressure loss ratio was increased in proportion to an increase of the equivalence ratio. A value of 8 percent was obtained at the design equivalence

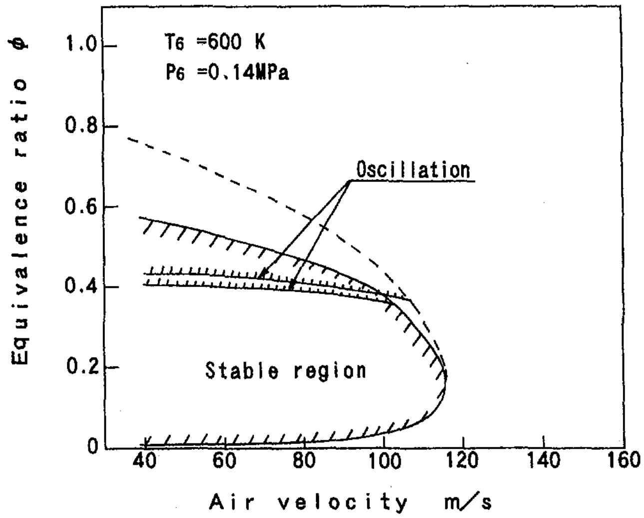

Fig. 9 Effect of main fuel nozzle configurations on stability loops

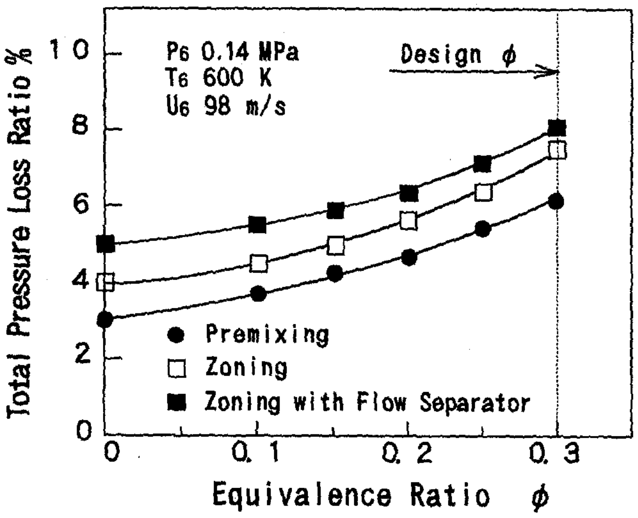

Fig. 10 Effect of main fuel nozzle configuration on the total pressure loss ratio

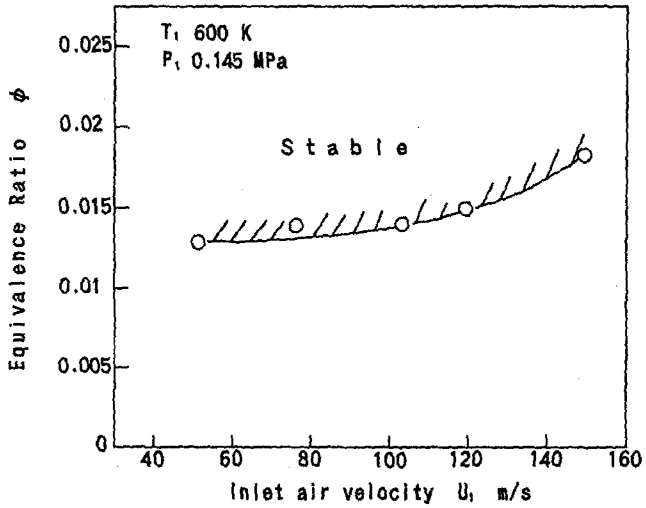

Fig. 12 Weak extinction of the LSC at Mach 3 condition

ratio, $\phi = 0.3$, by the latter nozzle. It was certainly higher than the ratio obtained by the premixing fuel nozzle; however, 8 percent met the requirement value.

Moreover, emissions of nitrogen oxides are another prime interest from the environmental point of view. Figure 11 illustrates the emission index of nitrogen oxides obtained with the three fuel nozzles. As the equivalence ratio increased, the emission index of NO_x decreased slightly first, then increased steeply for all the fuel nozzles. The zoning fuel nozzle gave the highest NO_x emissions, since it achieved the highest combustion efficiency among the three fuel nozzles. The emission index of 1 g/kg fuel was measured at the design equivalence ratio of 0.3. However, it is much lower than the NO_x emissions of currently operating subsonic turbofan engines. The test result indicates that the level of NO_x emissions is not significant at Mach 3 flight condition.

Laboratory Scale Ram Combustor Test

Basic Performance at Mach 3. Combustion must be sustained stable over the entire range of operating conditions. Figure 12 shows the weak extinction of this combustor. The flame was stable for a wide range of inlet air velocity and the equivalence ratio of lean blowout was 0.013 at the design inlet air velocity of Mach 3, $U_6 = 98$ m/s. The rich extinction could not be measured for just the same reason as the fuel zoning combustion test. Ignition was accomplished reliably at low equivalence ratios over the wide range of inlet air velocity by injecting pilot fuel and minimum ignition equivalence ratios were very close to those of the lean blowout. Large pressure rises and instability at ignition were not observed. A hydrogen–air torch ignitor system was used for ignition.

Pressure loss is one of the significant parameters for an engine performance and the total pressure loss ratio less than 8 percent (no combustion condition) is required for the ram combustor of the combined cycle engine. The total pressure loss ratios of 3.5 and 8 percent were respectively measured at no combustion condition and at the design condition of Mach 3. Therefore the results met the requirement sufficiently and were almost the same as the total pressure loss ratios obtained with the subscale combustor.

The fuel zoning combustion technique, which was found to be very effective to achieve high combustion efficiency in the previous test, was applied to this laboratory scale ram combustor. Combustion efficiency is shown in Fig. 13 as a function of the equivalence ratio, when the zoning fuel nozzle was used. The result of using the premixing fuel nozzle is also illustrated

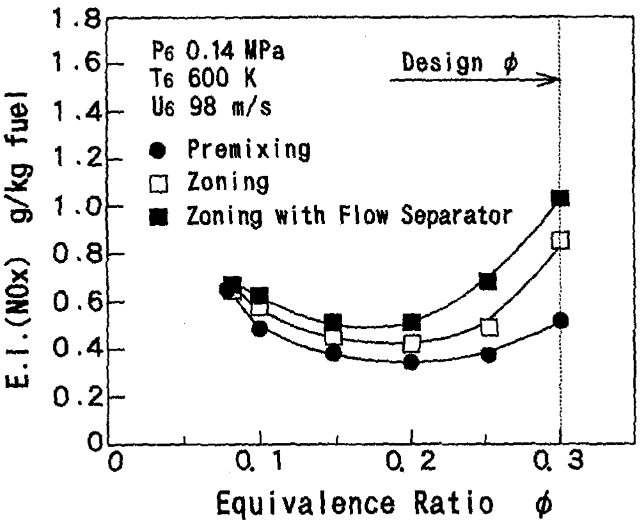

Fig. 11 Effect of main fuel nozzle configuration on emissions of nitrogen oxides

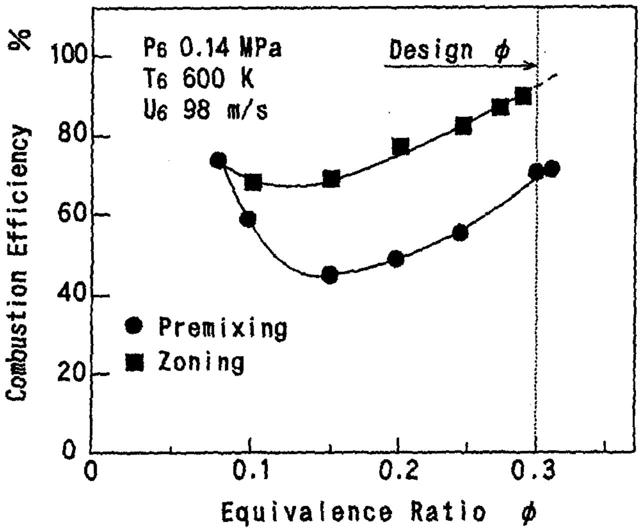

Fig. 13 Combustion efficiency of the LSC at Mach 3 condition

in the figure for comparison. The zoning fuel nozzle improved combustion efficiency and increased the value from 66 percent, obtained with the premixing fuel nozzle, to more than 90 percent. These results indicate that this application was successful but they also indicate that more efforts are needed to attain the same higher combustion efficiency as the currently used turbojet combustor.

The characteristic of NO_x emissions of the laboratory scale ram combustor was similar to that of the subscale combustor and the NO_x emission index of 1.7 g/kg fuel was obtained with the zoning fuel nozzle at the design condition of Mach 3.

Basic Performance at Mach 5. Combustor inlet conditions at Mach 5 are quite different from those at Mach 3; they are: T_6 = 1263 K, P_6 = 0.4 MPa, and U_6 = 40 m/s. It can be supposed from the conditions that the major problem on combustion is emissions of nitrogen oxides and that ignition, flame stability, and pressure loss are not serious owing to its high inlet air temperature and low velocity. For the main purpose of reducing emissions of nitrogen oxides, the premixing fuel nozzle was chosen in this Mach 5 combustion test.

Ignition and flame stability performances were excellent and they have already been reported by the authors (1993). The total pressure loss ratios were very low and were measured less than 1 percent owing to the low inlet air velocity at this condition.

Combustion efficiency at Mach 5, that is a cruising speed of the combined cycle engine, is also one of the concerns, because it influences directly not only the operating cost but also the environmental quality. A vitiation technique was used to simulate such a high temperature at Mach 5. Typical constituents of vitiated air are:

O_2	15.5 percent	(volume)
CO_2	4.0 percent	(volume)
CO	10.0 ppm	(volume)
UHC	0 ppm	(volume)
NO_x	150 ppm	(volume)

The vitiated air contained little carbon monoxide and unburned hydrocarbons; therefore it can be considered that these concentrations measured in the ram combustor were formed in the ram combustor itself. Figure 14 shows the local combustion efficiency distribution at the exit plane of the ram combustor. The test result indicates that the sphere, showing combustion efficiency more than 99.5 percent, extended for the most part to the exit plane. The result also indicates that much higher combustion efficiency will be expected to be achieved in the practical combustor, because it will use fresh air.

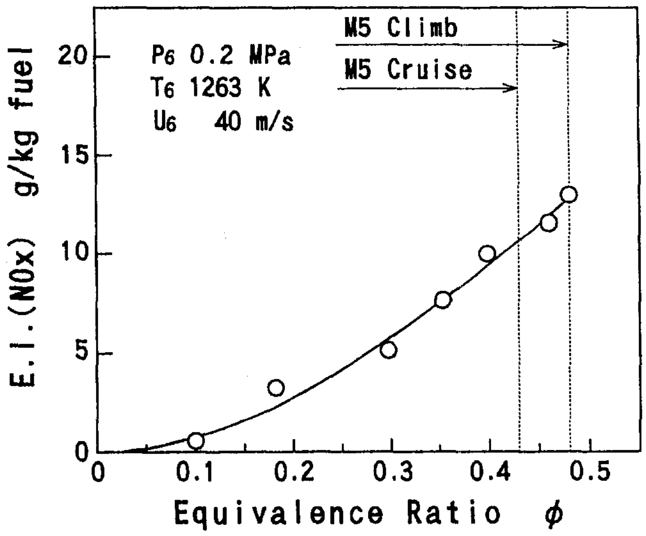

Fig. 15 Emissions of nitrogen oxides of the LSC at Mach 5 condition

The fuel zoning combustion concept cannot be applied at such a high inlet temperature condition. It will increase flame temperature more than premixed combustion. An increase in flame temperature generates the CO emissions due to an increase of CO equilibrium concentration and it results in a fall in combustion efficiency. Moreover it also stimulates the NO_x emissions greatly.

It is difficult to predict the emissions of nitrogen oxides quantitatively from the results. This is because the vitiated air contained a large amount of nitrogen oxides already before it en-

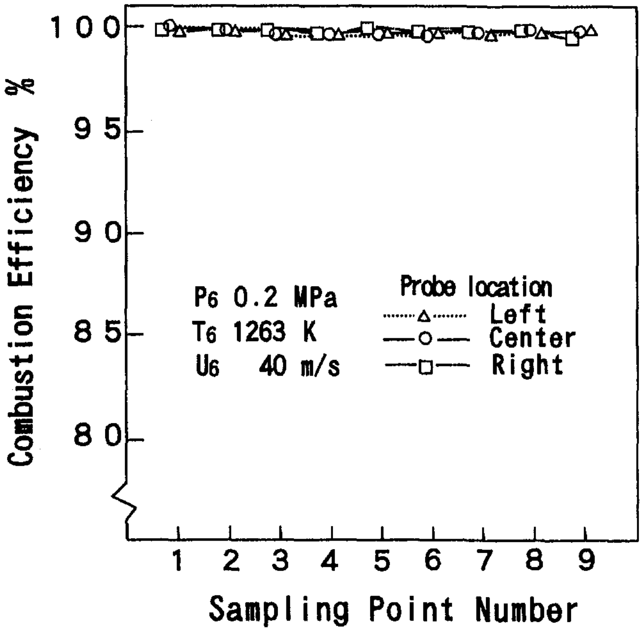

Fig. 14 Combustion efficiency at exit plane of the LSC at Mach 5 condition

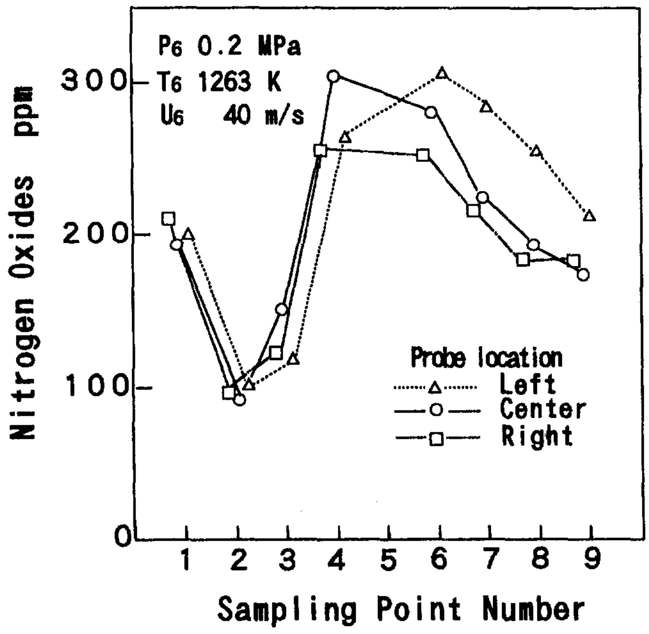

Fig. 16 Emission distributions of nitrogen oxides at exit plane

tered the ram combustor. However, it is very important to know the emissions level of the ram combustor even in a qualitative sense. Figure 15 shows the emission index of nitrogen oxides as a function of the equivalence ratio. The emission index was calculated by subtracting the NO_x value of vitiated air from that of the exhaust gas measured at the combustor exit. An increase in equivalence ratio increased the emission index of nitrogen oxides greatly and the index of 12.5 g/kg fuel for the climb equivalence ratio and the index of 11 g/kg fuel for the cruise equivalence ratio were obtained. These data were obtained at the inlet pressure of 0.2 MPa and with vitiated air. Therefore, it is supposed that the emission level of an actual combustor of the combined cycle engine will be extremely high.

Figure 16 illustrates the NO_x concentration distribution at the exit plane. Distribution figures were almost the same for each probe location and maximum concentrations were measured near the middle part of the ram combustor. The local equivalence ratios at the same exit plane were measured and are shown in Fig. 17. The local equivalence ratio was calculated by subtracting the average equivalence ratio of the vitiation heater from the individual equivalence ratios at the ram combustor exit. A fuel-rich zone was observed near the middle of sampling points for each horizontal location of the sampling probe. It is the place that showed the highest NO_x concentration. The results indicate that making the local equivalence ratio even, that is, improving the premixing quality, is needed to reduce the emissions of nitrogen oxides.

Conclusions

The laboratory scale ram combustor (LSC) test program has been conducted to obtain the fundamental combustion characteristics of the ramjet engine combustor that operates from Mach 2.5 to 5 for the hypersonic transport.

Prior to the LSC test a fundamental combustion test on a fuel zoning combustion concept was investigated for the purpose of improving combustion efficiency at Mach 3 condition.

1 Greater than 80 percent combustion efficiency was obtained by applying a fuel zoning combustion concept and it was found very effective for improving low combustion efficiency at Mach 3 condition.
2 The faults regarding flame stability and pressure loss were made clear on the fuel zoning combustion concept but the degrees were not so serious.

A laboratory scale ram combustor was fabricated and combustion tests were carried out at the simulated condition of Mach 3 and 5.

3 Combustion efficiency of 90 percent was successfully achieved at Mach 3 condition by applying the same concept as the fundamental combustion test. Combustion efficiency of more than 99.95 percent was measured for most of the combustor exit plane at Mach 5.
4 NO_x emission index of 11 g/kg fuel was obtained for the cruise equivalence ratio; therefore, it is supposed that a large amount of NO_x emissions will be generated at an actual combustor. It will be necessary to improve the premixing quality to reduce nitrogen oxide emissions.

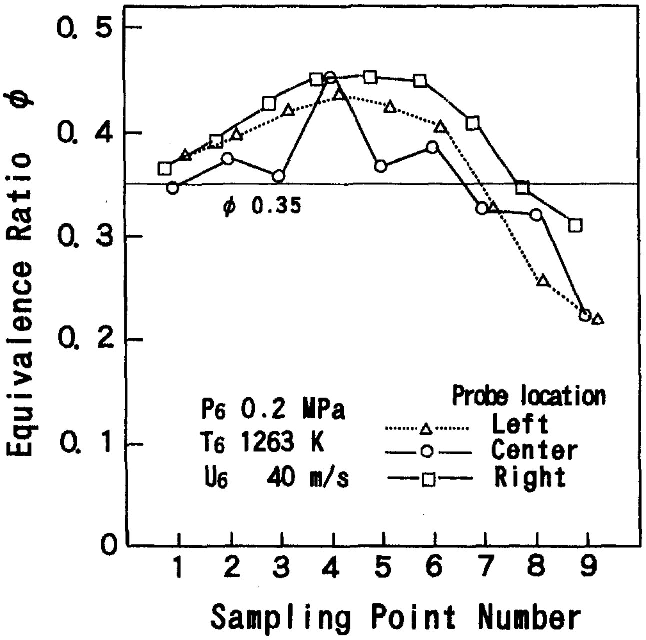

Fig. 17 Equivalence ratio distributions at exit plane

Acknowledgments

This experimental study was conducted under the entrustment contract with NEDO (New Energy and Industrial Technology Development Organization) as a part of the National Research and Development program (Industrial Science and Technology Frontier Program) of the Agency of Industrial Science and Technology, Ministry of Industrial Trade and Industry.

References

Branstetter, J. R., and Reck, G. M., 1973, "Afterburner Performance of Circular V-Gutters and a Sector of Parallel V-Gutters for a Range of Inlet Temperatures to 1255 K (1800°F)," NASA TN D-7212.

Gregory, M. R., Robert, B., and Larry, A. D., 1971, "Preliminary Sector Tests at 920 K (1200°F) of Three Afterburner Concepts Applicable for Higher Inlet Temperatures," NASA TN D-6437.

Kinoshita, Y., Kitajima, J., Shiraha, M., and Tatara, A., 1992, "Combustion Study on Methane-Fuel Laboratory Scale Ram Combustor," ASME Paper No. 92-GT-413.

Kinoshita, Y., Kitajima, J., and Seki, Y., 1993, "Studies on Methane-Fuel Ram Combustor for HST Combined Cycle Engines," Paper No. ISABE 93-7080.

Longwell, J. P., 1953, "Flame Stabilization by Bluff Bodies and Turbulent Flames in Ducts," *Forth Symposium (International) on Combustion,* The Williams and Wilkins Company, Baltimore, MD, pp. 90–97.

Longwell, J. P., Frost, E. E., and Weiss, M. A., 1953, "Flame Stability in Bluff Body Recirculation Zones," *Industrial and Engineering Chemistry,* Vol. 45, No. 8, pp. 1629–1633.

Mullen, J. W., and Fenn, J. B., 1951, "Burners for Supersonic Ram-jets: Factors Controlling Over-all Burner Performance," *Engineering and Process Development,* Vol. 43, No. 1, pp. 195–211.

Watanabe, Y., Miyagi, H., Sekido, T., Miyagawa, H., Tanaka, F., Aoki, T., Morita, M., and Yanagi, R., 1983, "Conceptual Design Study on Combined-Cycle Engine for Hypersonic Transport," Paper No. ISABE 93-7018.

Technology Demonstration Nozzle for Mach 7 Turboramjets

K. Pirker

U. Knott

MTU Motoren- und Turbinen-Union,
Munich, Federal Republic of Germany

Under the German Hypersonic Technology Program, future-oriented designs and technologies for reusable space vehicles, such as SÄNGER, are being developed. Pioneering the way in a new field of technology, MTU constructed and tested, with success from the very beginning, an actively cooled, asymmetric rectangular nozzle (SERN—single expansion ramp nozzle) of advanced design, characterized by the following innovative features:

- *rectangular, flap-controlled variable flow cross section;*
- *liquid-hydrogen-cooled structures;*
- *high-temperature-resistant sealing system for variable nozzle flaps; and*
- *uncooled expansion ramp in carbon/carbon composite with anti-oxidation coating.*

Development of the nozzle called for the mastery of new manufacturing techniques; proof of concept was provided in the successful performance of initial tests of 300 second duration.

Introduction

In studies into the German SÄNGER hypersonic reusable space vehicle, MTU has elaborated a lead concept for the propulsion system (Fig. 1) (Heitmeir et al., 1992; Krammer et al., 1992). The nozzle is a vital component of any air-breathing engine, hence the aim of the work was to develop the appropriate technologies, and to manufacture and test suitable nozzle components. The nozzle has to be designed for high temperatures in the region of 2750 K, accompanied by pressures of 8 bar, as well as for high degree of variation of the nozzle throat area and high nozzle divergence angle. The throat area of the nozzle is actively cooled with liquid hydrogen, but cooling of the expansion ramp is not necessary thanks to the use of a carbon/carbon composite material (Figs. 2, 3, 10).

Design

In view of the high thermal and mechanical stresses to be withstood by the nozzle, it has been designed strictly in accordance with the principle of separation of functions.

The cooling structure forms the aerodynamically active surface, which absorbs the thermal stresses. The pressure is absorbed by the four-walled casing, which carries the cooling structure supported on spacers. The cooling structure is composed of two (C263 Ni-base alloy) plates welded together and shaped after machining of the ducts for the hydrogen coolant (Fig. 4). The rear surface of the cooling structure is provided with an electroplated copper coating 0.5 mm thick to increase the heat exchange effect between adjacent ducts (hot/cold) and decrease the temperature gradients.

Coolant, flowing in two parallel, unequal streams, is conducted simultaneously through the upper nozzle wall and to flaps 1 and 2. The flow is then combined in a mixer (for temperature equalization), is again split into two parallel, but equal streams to pass to the side walls, before being conducted to a collector and finally to a flare for the hydrogen to be burned off.

The gas-path surface is provided with a low-pressure plasma-spray (LPPS) zirconium oxide thermal barrier coating, which helps reduce the thermal stress to which the cooling structure is subjected.

As the coolant collectors on the cooling plate are rigidly connected with the casing structure, a thermo-elastic link must be provided that is capable of compensating for the relative movements between the nozzle walls and the supporting structure as a result of thermal expansion. This is accomplished by the use of inlet and outlet pipes for each duct, whose elasticity enables them to act as expansion sleeves and thus to compensate for differences in thermal expansion (Fig. 5).

The nozzle-supporting structure absorbs the pressure, and is protected from the effects of the hot gas by the cooling structure. The pressure in the supporting structure rises briefly to as much as 13 bar when the flow reaches the diffuser on startup, and the rectangular cross section of the nozzle calls for a very stiff structure. In order to minimize leakage of the sealing gas (nitrogen), the side-wall deformation is limited to 0.5 mm.

The most important factors to be borne in mind concerning the design were the pressures to be withstood, acceptable deformation of the structure, and low weight, as well as the need to comply with constraints with regard to time and costs. In view

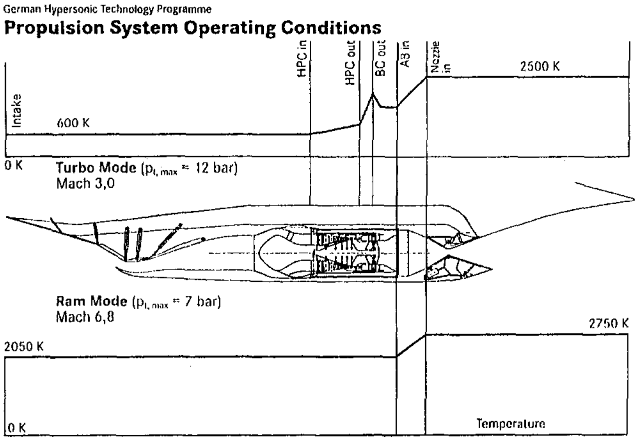

Fig. 1 Lead concept for the propulsion system

Contributed by the International Gas Turbine Institue and presented at the 39th International Gas Turbine and Aeroengine Congress and Exposition, The Hague, The Netherlands, June 13–16, 1994. Manuscript received by the International Gas Turbine Institute March 9, 1994. Paper No. 94-GT-392. Associate Technical Editor: E. M. Greitzer.

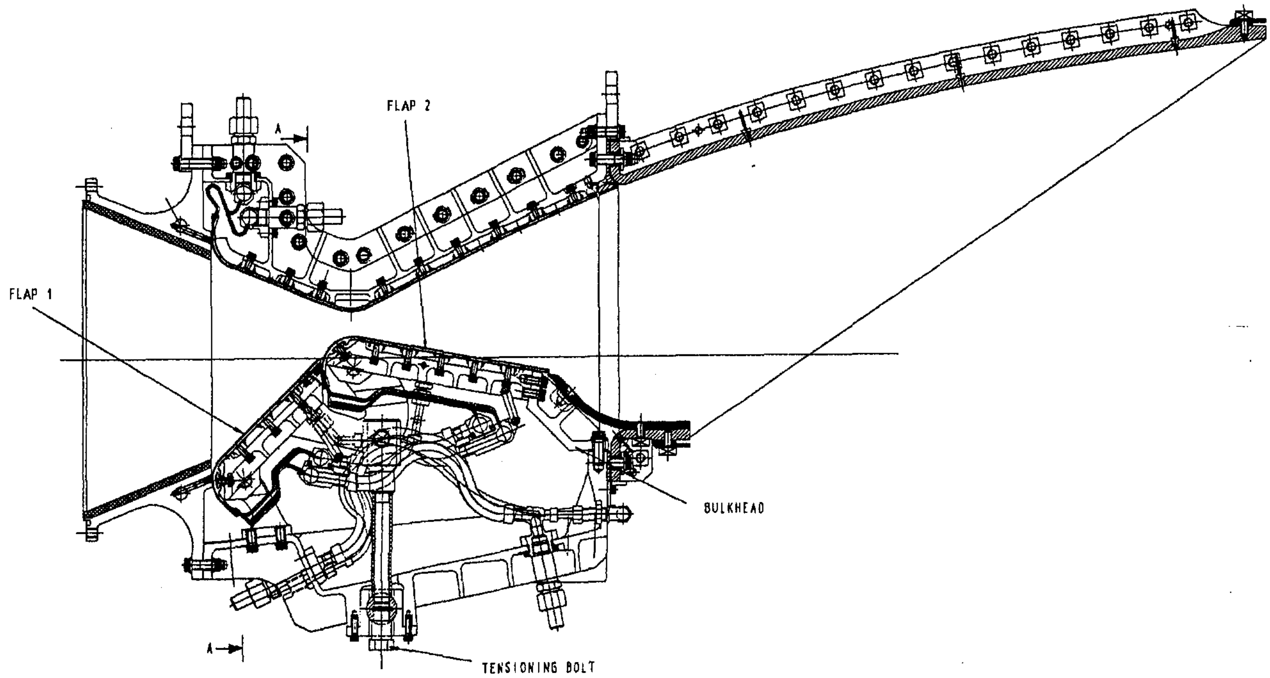

Fig. 2 Cross section of the technology demonstration nozzle

of these demands, a milled structure consisting of four walls and reinforcing struts with flaps and adjustment mechanism was chosen.

The supporting structure is provided with grooves for the SiC sealing strips and the clamping cylinders (Fig. 6). To prevent the ingress of hot gas, the space beneath the flaps is pressurized with nitrogen. The two flaps serve for setting the nozzle throat area and the nozzle opening angle depending on the flight Mach number. The throat area adjustment is effected via spacer sleeves and tensioning bolts. The nozzle opening angle is determined by bulkheads, which are interchangeable.

The nozzle-flap adjustment, connections for the sealing gas and the sealing gas pressure regulator, and the accompanying pressure-relief valve are mounted on the bottom wall of the casing.

The gas expands to the ambient pressure at the expansion ramp, where the temperature is low enough to render active cooling unnecessary.

The expansion ramp is connected to the supporting structure via ZrO_2 bushes, metallic disks, and Inconel 718 bolts, where the bushes serve to insulate the metallic bolts. A C/C material is unsuitable for the bolts for this application because it would be overloaded.

Before being operated for the first time, the nozzle was subjected to an exhaustive series of inspections and tests. For example, each cooling duct was flow tested by thermography.

The tests, aimed primarily at proof of concept, were carried out on DASA's ramjet test facility in Ottobrunn. In addition to pressure and temperature measurements, the outside wall temperature was determined by infrared measurement.

Manufacture

Material and process investigations were carried out concerning the components:

- Cooling structure
- Supporting structure
- Sealing system, and
- Expansion ramp

Cooling Structure. Attention in the development work was directed primarily at the cooling structure, consisting of two shaped plates welded together. Several versions, differing with regard to method of manufacture and design, were considered, Fig. 7, namely:

1 *LPPS Version With Circular Ducts.* Nimonic 80/Inconel 718 tubes of circular cross section are embedded in a Nimonic 80/Inconel 718 matrix by low-pressure plasma spraying. The gas-path surface is provided with a ZrO_2 thermal barrier coating, and the rear side is electroplated with copper to improve temperature equalization.

2 *Plate Version With Circular Ducts With Nickel-Plated Seal Coating.* The cooling ducts are machined into a Nimonic 80/Inconel 718 plate by milling or electrical discharge machining and sealed by electroplating with nickel. For this, the ducts are filled with a low-melting SnBi alloy, which is removed after the ducts have been plated. As with the first version, the gas-

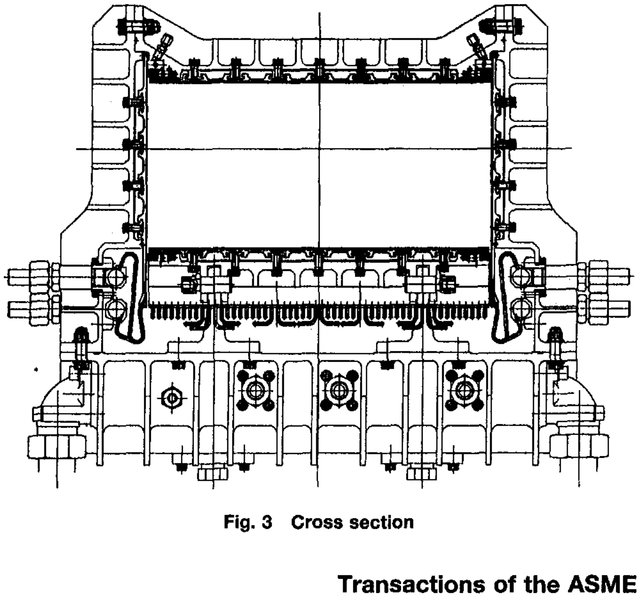

Fig. 3 Cross section

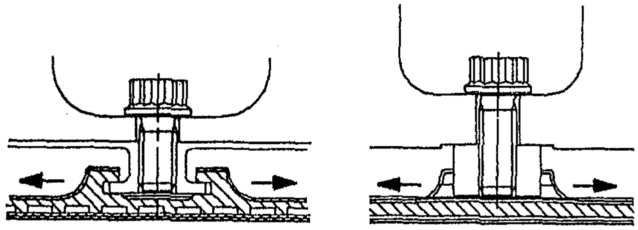

Fig. 4 Cooling structure on casing

path surface is provided with a thermal barrier coating, and the rear side is copper plated.

3 Twin-Plate Version With Circular Ducts. The cooling ducts are machined into two plates, which are then joined by brazing, diffusion welding, or EB welding. In this version also, the gas path surface has a ZrO_2 thermal barrier coating with copper plating at the rear side.

4 Plate Version With Rectangular Ducts With Nickel-Plated Seal Coating. Similar to version number 2, but with rectangular rather than circular ducts.

5 Twin-Plate Version With Rectangular Ducts. Similar to version number 3, but with rectangular rather than circular ducts (Fig. 7).

Choice finally fell upon version 5 (Figs. 8*a* and 8*b*), and corresponding manufacturing trials were carried out. Brazing as well as EB welding was investigated for version 5.

Brazing. Brazing was carried out in a furnace in high vacuum (10^{-6} mbar) with integrated hot press. As braze material, the nickel-base alloy MBF80 (composition 15Cr, 4B, remainder Ni) in foil form was used. Both the braze and the brazing temperature were adapted to the C263 base material, meaning that the base material is solution annealed simultaneously with brazing. The structural strength of the overall system is not seriously affected by the diffusion of braze particles (mainly boron) at the grain boundaries. The formation of braze "menisci" gives unbroken, smooth transitions between the fins and cover plate, which is highly desirable with regard to strength.

The strength of the joints was verified by brazing a plate with closed ducts, and subjecting it to a thermal shock test consisting of repeated variation of the temperature between −170 and +150°C, and hydraulic pressure at 25, 50, 100, 200, and 400 bar. Bursting did not occur until a pressure of 460 bar was reached.

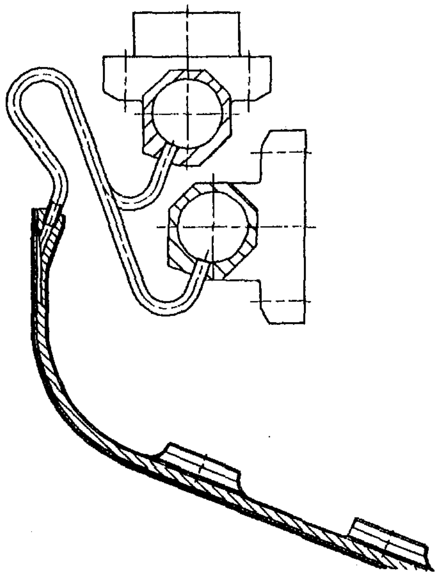

Fig. 5 Thermoelastic link

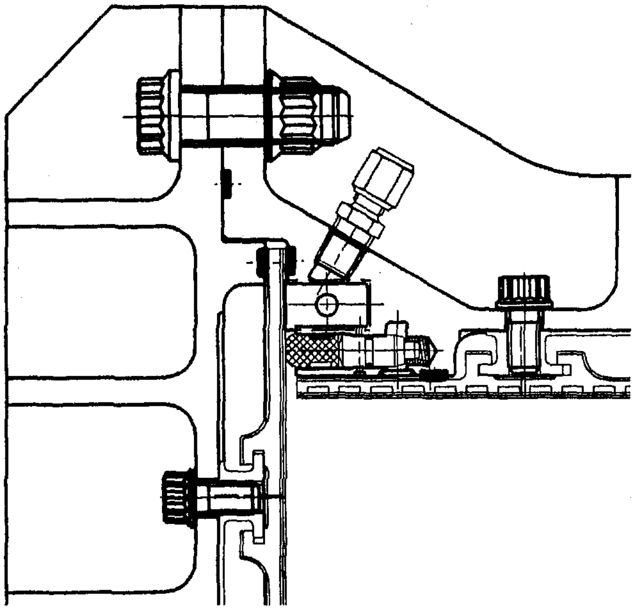

Fig. 6 SiC sealing strips

EB Welding. Welding was carried out at the struts (Fig. 8*b*). The heat developed during welding causes the cover plate to sink slightly (by about 2–3/100ths mm). The area of contact is smaller than with the brazed version, and the exposed area is unfavorable with regard to strength (notch effect) and corrosion. Despite this it was decided to pursue the EB-welded version because of the lower manufacturing risk compared with the brazed version, and especially because the results appeared to be more easily transferable to larger nozzles. At present it is possible to braze plates measuring only up to 400 × 400 mm.

Critical aspects with regard to the feasibility of the project were the cold-forming characteristics of the base material and the characteristics of the joints. Cold-forming tests were carried out using the die shown in version 5, Fig. 7, on the same material as that of the component. Examination of critical areas did not reveal any signs of damage, such as cracks or rupture, on either brazed or welded plates.

As the coolant collectors on the cooling plate are rigidly connected with the casing structure, a thermo-elastic link must be provided that is capable of compensating for the relative movements between the nozzle walls and the supporting structure as a result of thermal expansion. This is accomplished by brazing inlet and outlet pipes in the alloy X10CrNiTi 18 9 into each duct. Both the low-melting silver-base braze (VH720 and VH780) and the nickel-base braze AMS 4777 were investigated. Bearing in mind the copper plating at the rear side of the plates (melting point of copper = 1080°C), the brazing temperature must be restricted to a certain limit. The lower-melting silver-base braze materials give satisfactory results if both the inlet and outlet pipes and the holes in the plates are nickel-plated. As the copper electroplating is capable of withstanding the high brazing temperature, it was decided to braze in the pipes with the AMS 4777 nickel-base braze (since nickel plating is not required).

Supporting Structure. The nozzle-supporting structure has to absorb the pressures, and is protected against the effects of the hot gas by the cooling structure. Because of its good machining properties and high strength in heat-treated condition ($r = 930\ N/mm^2$), the easily obtainable heat treatable steel

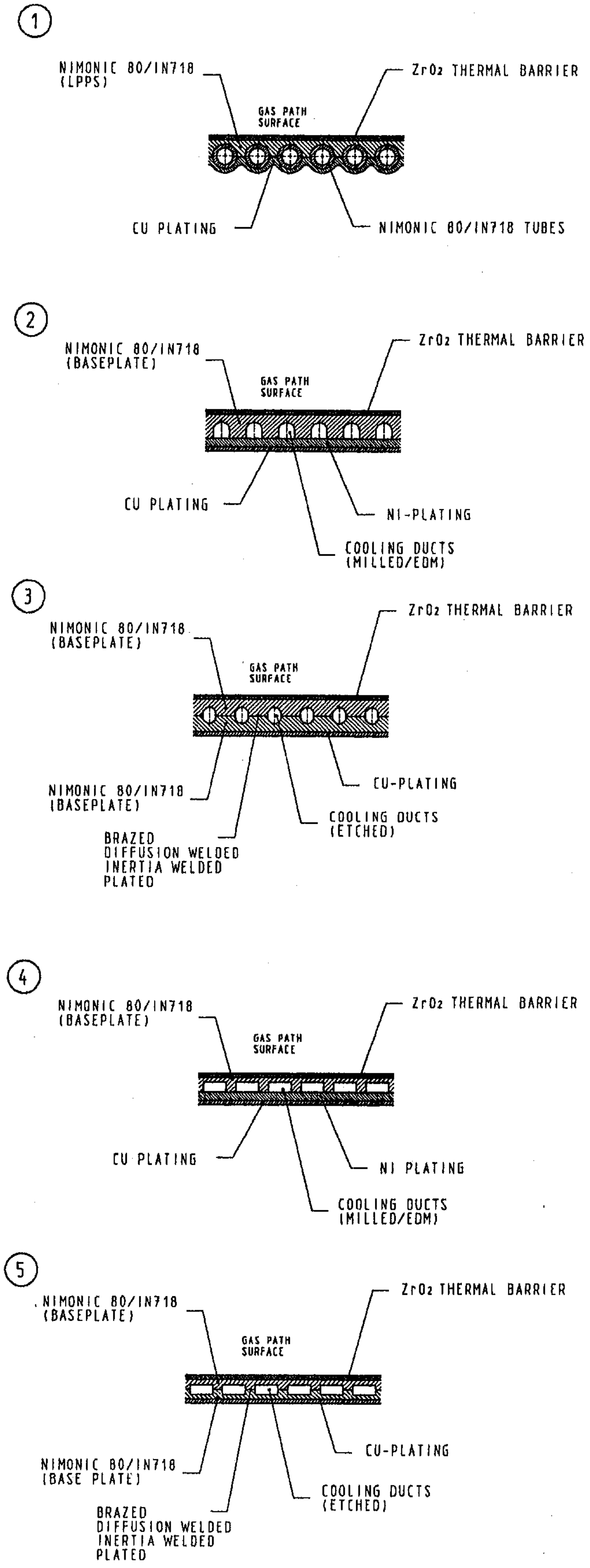

Fig. 7 Cooling structure versions

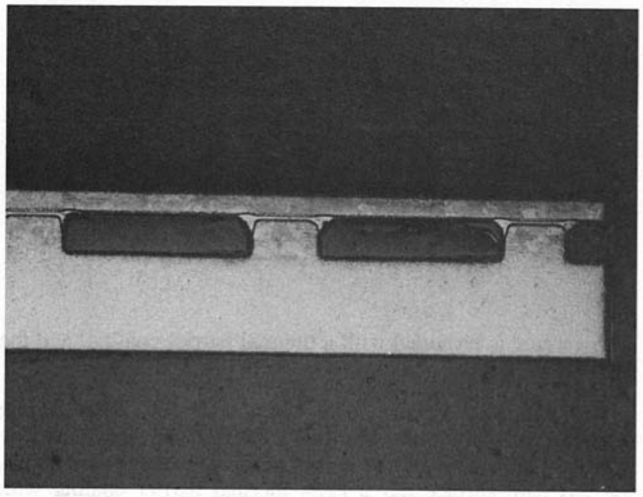

Fig. 8(*a*) Section through cooling plate version 5

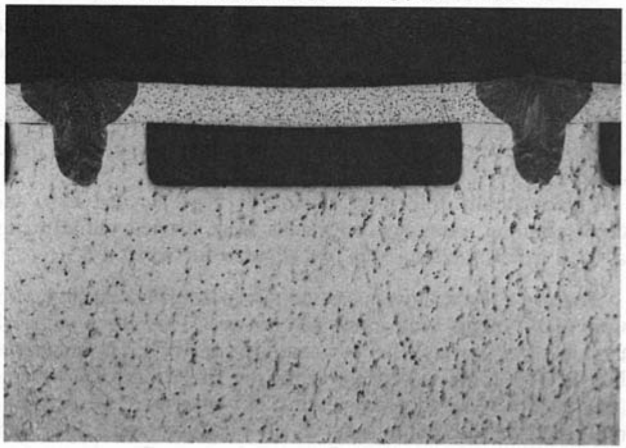

Fig. 8(*b*) Section through EB-welded cooling plate

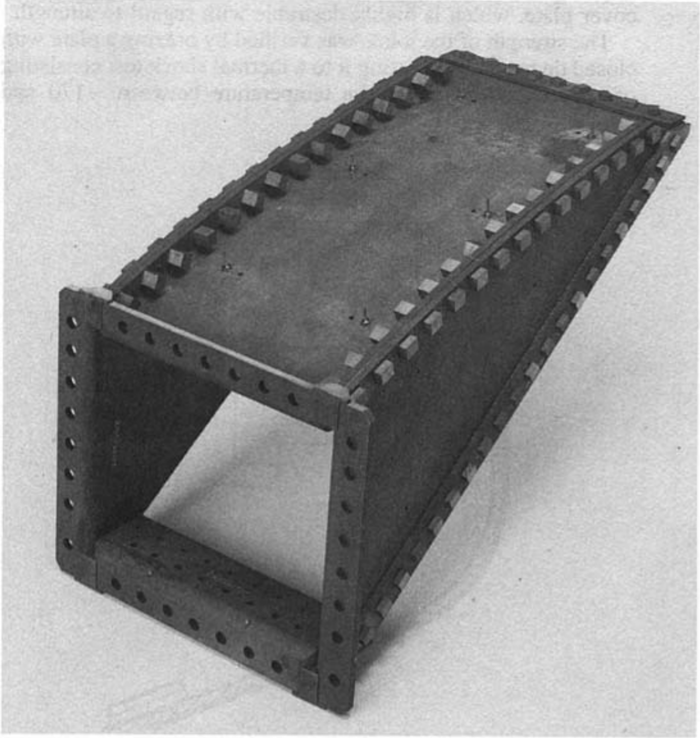

Fig. 9 C/C expansion ramp

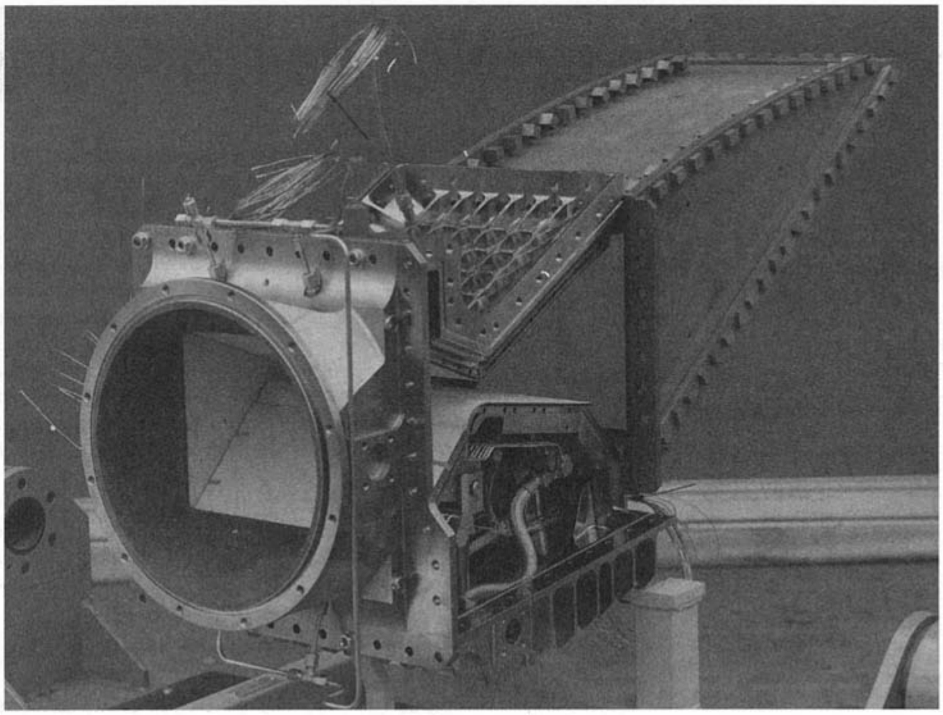

Fig. 10 Technology demonstration nozzle

1.7734 (15CrMoVG) was chosen as the material for the supporting structure. The resistance to corrosion was increased by electrodeless nickel plating.

Sealing System. The material monolithic SiC, which is capable of withstanding very high temperatures (1600°C in this application), was used for the sealing strips, where the strips were produced by pressing (SiC powder plus binder), machining, sintering, and finally grinding to size. As the bulkheads are protected behind the C/C heat shields, the seals do not have to withstand such high temperatures, allowing shaped seals 0.1 mm thick in the alloy X10CrNiTi 18 9 to be used.

Expansion Ramp. Bearing in mind the requirements:

- temperature resistance up to 1600 K
- oxidation resistance for a test period of 10 times 60 seconds
- low weight
- 0.8 bar underpressure in operation with diffuser
- gas flow velocity of Ma 3.69

a carbon/carbon composite material with anti-oxidation coating was chosen for the expansion ramp.

The material consists of phenolic resin-impregnated mats reinforced with longitudinal and transverse fibers, where the parts are carbonized after manufacture of the CFRP. The volatile constituents of the CFRP are burned away, leaving a porous C/C material as the intermediate product. The porosity is then reduced to 10–15 percent by repeated impregnation with phenolic resin and carbonization. Afterward, the C/C components are graphitized, and machined to obtain the required dimensions. The components are then treated with silicon by chemical vapor deposition (CVD) in the furnace. The silicon reacts with the carbon in the matrix to form SiC, and the resulting thin film of SiC forms the protection against oxidation. The ramp was designed and manufactured with SGL (Sigri Greate Lakes, Meitingen) (Strobel et al., 1993).

Summary

The nozzle with rectangular flow cross section is designed for a flow rate of approximately 20 kg/s (combustor diameter 330 mm), a pressure of 8 bar, and a temperature of 2800 K.

The twin-shell nozzle is complete with cooling and supporting structures, and expansion ramp. The cooling structure consists of two EB-welded plates with a ZrO_2 thermal barrier LPPS coating at the gas-path (surface) side, and a copper electroplating at the rear side. It is mounted on the supporting structure in such a way as to ensure freedom of movement due to thermal expansion. The liquid hydrogen coolant flows into the cooling structure from the collectors via individual elastic tubes. The supporting structure consists of four walls reinforced with struts, and serves as the pressure vessel. The nozzle throat area and the nozzle flap position are set via spacer-sleeves and tensioning bolts. The nozzle flaps are sealed in relation to the side walls by SiC strips. The space below the flaps is pressurized with nitrogen to prevent the ingress of hot gas. The expansion ramp is made in a carbon–carbon material with anti-oxidation coating, and is uncooled.

Initial testing was carried out with a combustor temperature of 2400 K, and a pressure of 4.4 bar; with a thrust of greater than 9 kN and expansion ramp temperature greater than 1500 K being attained. Testing at higher pressures and temperatures is now to be carried out (Lederer and Kruger, 1993).

Acknowledgments

The authors would like to express their gratitude for the support received from their colleagues at MTU and their contributions to this paper. The work is being carried out with funding provided by the German Ministry of Research and Technology.

References

Heitmeir, F., Lederer, R., and Herrmann, O., 1992, "German Hypersonic Technology Programme: Air-Breathing Propulsion Activities," AIAA Paper No. 92-5057.

Krammer, P., et al., 1992, "German Hypersonic Technology Programme Status: Air-Breathing Propulsion," AIAA Paper No. 93-5094.

Lederer, R., and Krüger, W., 1993, "Nozzle Development as a Key Element for Hypersonics," AIAA Paper No. 93-xxxx.

Strobel, X. X., et al., 1993, "Light-Weight Structures for Hypersonic Propulsion Systems," AIAA Paper No. 93-5037.

Turbine Engine Icing Spray Bar Design Issues

C. S. Bartlett
Department of Propulsion Testing Technology,
AEDC Group,
Arnold Engineering Development Center,
Sverdrup Technology, Inc.,
Arnold AFB, TN 37389

Techniques have been developed at the Engine Test Facility (ETF) of the Arnold Engineering Development Center (AEDC) to simulate flight through atmospheric icing conditions of supercooled liquid water droplets. Ice formed on aircraft and propulsion system surfaces during flight through icing conditions can, even in small amounts, be extremely hazardous. The effects of ice are dependent on many variables and are still unpredictable. Often, experiments are conducted to determine the characteristics of the aircraft and its propulsion system in an icing environment. Facilities at the ETF provide the capability to conduct icing testing in either the direct-connect (connected pipe) or the free-jet mode. The requirements of a spray system for turbine engine icing testing are described, as are the techniques used at the AEDC ETF to simulate flight in icing conditions. Some of the key issues facing the designer of a spray system for use in an altitude facility are identified and discussed, and validation testing of the design of a new spray system for the AEDC ETF is detailed. This spray system enables testing of the newest generation of high-thrust turbofan engines in simulated icing conditions.

Introduction

Icing tests are conducted to gather data on the performance of an aircraft and its propulsion system in icing conditions. The data are gathered either in flight or ground testing. Flight testing can be conducted in natural or simulated icing conditions. Simulated conditions are typically generated with the aid of an icing spray tanker, as discussed by Ashendon (1993) and by Belte and Woratschek (1986). Ground testing is typically conducted using simulated icing conditions in either sea level or altitude test facilities. This paper addresses the techniques used to simulate icing conditions in altitude test facilities.

Altitude icing simulation facilities and techniques have been in development and use at the ETF since the early 1970s. The simulation capabilities have been implemented in several of the propulsion development test cells at the AEDC ETF. The facilities have been used to conduct icing testing for military and commercial, domestic, and international customers. The icing test capabilities have been documented by Gall and Floyd (1971), Hunt (1978), and Bartlett et al. (1990). A detailed accounting of the test of a large propulsion system inlet is given by Bartlett and Phares (1993).

The facilities at the AEDC provide the capability of simulating icing in either the direct-connect or free-jet test modes as illustrated in Fig. 1. The direct-connect test mode is most often used for turbine engine testing. In the direct-connect test mode, the engine air mass flow rate and thrust can be measured most accurately. The free-jet test mode is most useful for testing of inlets or external surfaces such as wings, empanages, and probes. This paper addresses direct-connect testing of turbine engines.

Icing Simulation

Requirements. Requirements of an icing simulation system are determined from the natural icing conditions to be simulated. The natural icing conditions are generally documented by specific aviation regulatory authorities. Examples are shown in Fig. 2 and documented in the Air-worthiness Standards (1984). The envelopes relate ambient temperature and altitude pressure in icing conditions. Further, they relate the cloud liquid water content to the mass median diameter of the droplets in the cloud. Clouds are typically grouped as moderate or severe, depending on the level of the liquid water content.

The flight simulation must satisfy the conditions a turbine engine encounters in flight, specifically the stagnation pressure and temperature corresponding to a specific flight Mach number at a prescribed ambient temperature and altitude pressure. In the ground test simulation, the required stagnation pressure and temperature are delivered to the engine. The flight altitude pressure is maintained in the test cell by the ETF exhaust plant. The ability to deliver the stagnation pressure and temperature to the test cell plenum and the ability to simulate the specified test cell pressure are a function of the air supply and exhaust capacity of the test facility, and are beyond the scope of this paper.

Icing conditions are generally characterized by the amount of liquid water in the cloud, termed the liquid water content, LWC. In nature, clouds exist with a distribution of droplet diameters generally characterized by the mass median diameter, MMD. The MMD is the diameter for which half of the cumulative mass of all droplets is below and half is above. Most icing encounters occur at MMD ranging from 15 to 40 μm. For ground icing simulation, an "icing spray" system is used to deliver a continuous stream of finely atomized water droplets into the airstream before the airstream enters the test engine. The requirements of the spray system are to deliver the proper amount of liquid water to the engine with the cloud of droplets being at the proper mass median droplet diameter and with the water uniformly distributed across the engine face.

Techniques. The approach taken at the AEDC ETF to inject the continuous stream of water is to mount water-atomizing spray nozzles into a series of spray bars and to place the spray bars upstream of the test engine. An in-depth study of the requirements for the simulation of icing conditions at the AEDC was reported by Willbanks and Schulz (1973). A parametric study was performed to determine the effects of the test cell inlet and the water spray conditions upon the thermodynamic state of the droplet-laden flow in the engine test section. The study indicated it is necessary to consider the effects of the engine inlet or cowling on the flow conditions at the turbine engine compressor face. Specifically, the icing conditions at the

---

Contributed by the International Gas Turbine Institute and presented at the 39th International Gas Turbine and Aeroengine Congress and Exposition, The Hague, The Netherlands, June 13–16, 1994. Manuscript received by the International Gas Turbine Institute March 17, 1994. Paper No. 94-GT-340. Associate Technical Editor: E. M. Greitzer.

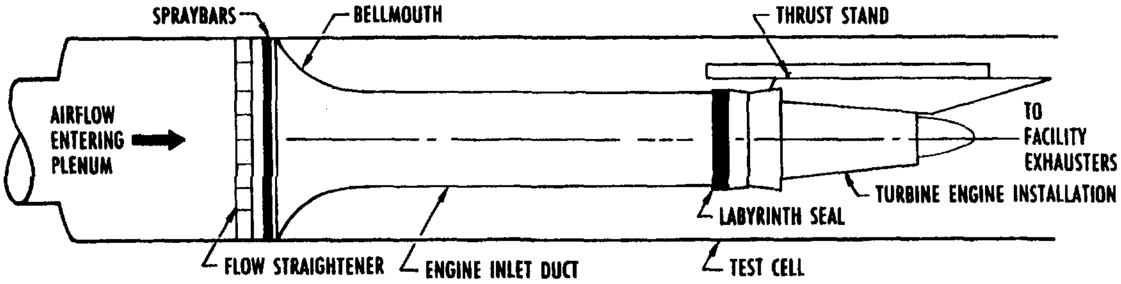

a. A direct-connect propulsion engine test cell configuration

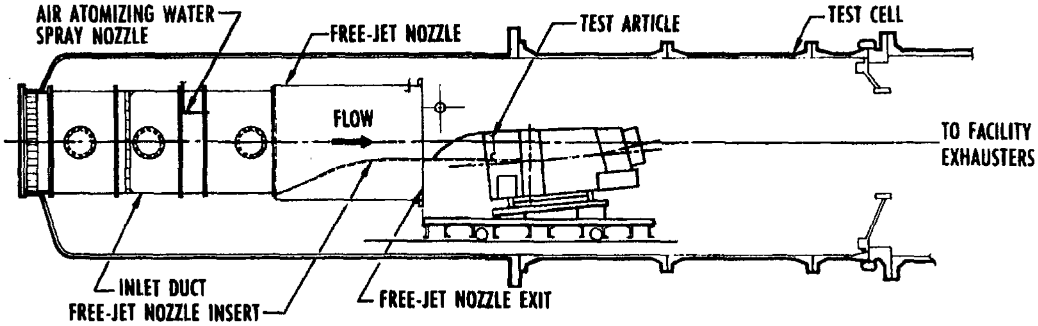

b. A free-jet propulsion engine test cell configuration

Fig. 1 Simulated icing test modes

compressor face are seldom identical to those existing at free stream. Regulatory icing envelopes address free-stream conditions, and hence must be adjusted for specific engine and aircraft configurations. One effect that must be considered is the ratio of liquid water that must be delivered into the compressor face relative to the free-stream liquid water content through which the aircraft is flying. The airflow entering the engine is often either accelerated or decelerated from the free-stream conditions as depicted in Fig. 3. The water droplets have a finite mass and typically do not follow airflow streamlines as they are ingested by the engine. The droplets are selectively captured according to the ratio of inlet to free-stream velocities and droplet mass. The injection efficiency is discussed by Gelder (1958), Pheifer and Maier (1977), and Bartlett (1988). The ratio of compressor face LWC to free-stream LWC can be estimated and is shown in Fig. 4 for a droplet of MMD equal to 20 μm. The plot in Fig. 4 shows the ratio of compressor face to free-stream LWC as the flight Mach number ranges from approximately 0.2 to 0.9. The two curves in Fig. 4 represent engine operation corresponding to compressor face Mach numbers of 0.25 and 0.50. Typically, during ground icing testing the LWC delivered to the compressor face is greater than free-stream LWC by a factor of 1.1 to 1.15 for simulation of cruise or hold conditions and as high as 1.3 to 1.4 for idle descents. The LWC factors must be taken into account to ensure the spray delivery system can accommodate the total water flow required for the engine icing test.

Design Issues

The key design issues facing the water spray injection system designer are discussed below. The determination of the water flow rate requirements of the spray system is explained and the spacing of spray nozzles in the spray bars is reviewed. The shape of the spray bar and the freeze protection of the spray bar fluid passages are discussed.

Water Injection. The essential issue that must be decided during the design of an icing spray system is the water flow rate that must be delivered into the airstream passing through the compressor. The water flow rate can be determined from the mass conservation equation expressed in terms of the ratio of injected water mass flow rate to engine air mass flow rate by

$$W_w/W_a = \mathrm{LWC}/\rho_a$$

The LWC term represents the mass of liquid water per volume of air entering at the compressor face. W_w is the injected water mass flow rate, W_a is the mass flow rate of air entering the compressor, and ρ_a is the density of the air at the compressor face. The equation can be expanded, assuming perfect gas, and rearranged to yield the mass flow rate of water as

$$W_w = K(\mathrm{LWC})(W_a)(T)(R)/P$$

where K is a unit conversion factor, P is the static pressure at the compressor face, W_a is the air mass flow rate entering the compressor face, T is the static temperature at the compressor face, and R is the gas constant for air.

The ratio of maximum to minimum water flow rate required of the water spray system (dynamic range for the injected water flow rate) can be found once knowledge of the extremes of LWC, W_a, T, and P are known for a particular test. The dynamic range can often be on the order of 35 to 1.

The injected water must be uniformly distributed across the compressor face to ensure a proper icing simulation. This uniformity is obtained by proper spacing of individual spray nozzles within the spray bar array and by dispersion of the droplets downstream of the spray bar.

Spray Nozzles. Once the injected water flow rate requirements have been determined, the water must be injected in the form of finely atomized droplets. Natural clouds exist with a distribution of droplet diameters generally characterized by a droplet mass median diameter, MMD. Icing testing is conducted for droplet MMD ranging from 15 to 40 μm, with the majority of testing being conducted at 20 μm MMD. Typical icing spray nozzles use pressurized air to assist in the breakup of a water jet into droplets. There are several different nozzle types used throughout the world in the production of spray for icing simulation. Each different nozzle has a characteristic performance relating MMD to water mass flow rate. Figure 5 illustrates the

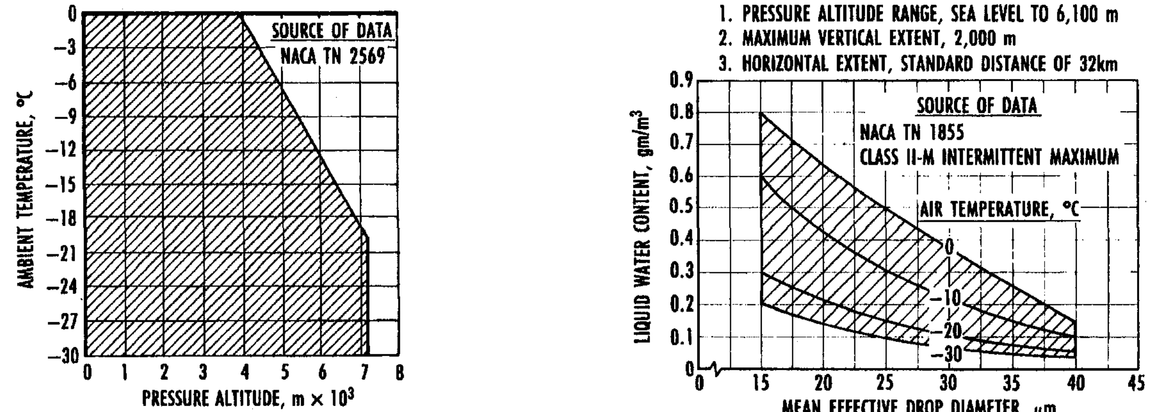

a. Ambient temperature versus ambient pressure, stratiform clouds

b. Liquid water content versus mass median droplet diameter, stratiform clouds

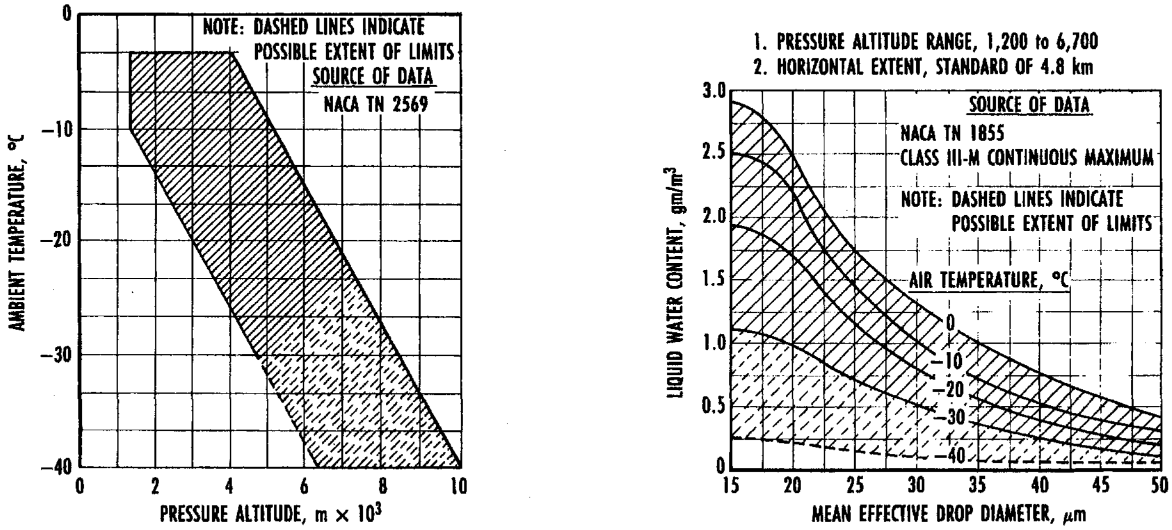

c. Ambient temperature versus ambient pressure, cumuliform clouds

d. Liquid water content versus mass median droplet diameter, cumuliform clouds

Fig. 2 Cloud icing conditions

performance characteristics of three different nozzles used at the AEDC ETF during icing simulation testing. The MMD and water flow rate values are referred to nominal operation points arbitrarily chosen for illustration. The spray nozzles are placed in ports in an array of spray bars placed upstream of the test engine.

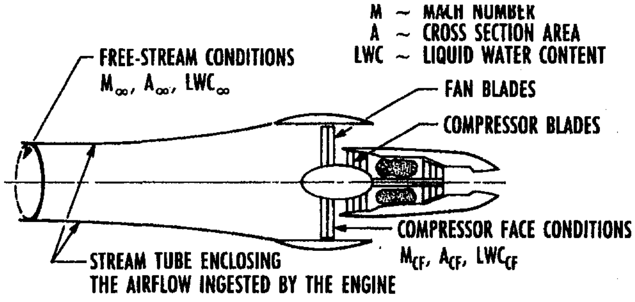

a. Inlet Mach number less than flight Mach number

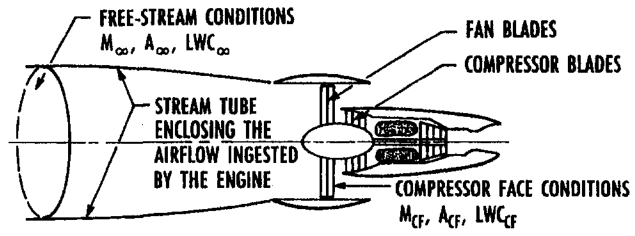

b. Inlet Mach number greater than flight Mach number

Fig. 3 Schematic showing possible stream tubes for turbofan icing testing

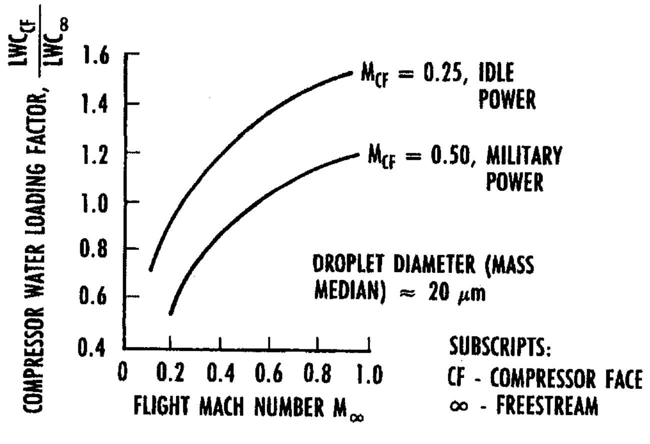

Fig. 4 Compressor face liquid water loading factor for two compressor face Mach number

Spray Bar. Spray nozzles are mounted in rigid spray bars containing the water and atomizing air supplies to the individual spray nozzle ports. Both the water flow rate and the MMD produced by an individual spray nozzle in a spray bar are sensitive to the water and atomizing air pressure at the nozzle. Spray bar water and atomizing airflow passages must be designed for uniform pressure to avoid unacceptable variations in either water flow rate or droplet size production along the bar. The allowable pressure variations can be determined from knowledge of the nozzle characteristics. The partial derivatives of the water flow rate and the MMD production with respect to water supply and atomizing air supply pressure can be determined from nozzle operation curves. These partial derivatives can be used to determine maximum pressure variations (losses) along the spray bar fluid passages.

The cross-sectional areas of the water and atomizing air passages influence the cross-sectional area of the spray bar. The thickness of the spray bar must be balanced with the chord length of the bar. The length and shape of the bar should be less than that which would cause the bar to act as an uncharacterized turning vane, and the bar thickness and spacing must be selected to prevent the speed of the flow between the bars from becoming higher than desired.

Another aspect of the spray bar design concerns spray bar internal water passage freezing. To conduct icing tests, the engine and the test facility are brought to the required operating condition and held there until the facility and the engine reach a specified thermally stable state. The stabilization process can take on the order of 30 minutes. As this stabilization process takes place, the icing system spray bars are exposed to the cold airstream temperatures, often approaching −30°C. The design of the spray bar should allow initiation of water spray from the ''cold soak'' without any freezing in the water passages. Experience has shown a significant problem can exist if enough heat is not supplied into the spray bar. Water can freeze in the passage, often in the nozzle itself, preventing proper operation of the nozzle, and resulting in unknown LWC and MMD delivery to the compressor face. The amount of heat input required is a function of the rate of heat loss to the cold airstream.

Spray Bar and Nozzle Spacing. The total water flow injected through the spray nozzles must be delivered uniformly to the engine face. The spray nozzle ports along the spray bars and the distance between adjacent bars place the nozzles approximately 18 to 20 cm on center, as depicted in Fig. 6. The spray bars are approximately 5 cm thick and approximately 20 cm long. During testing, not all nozzle ports are used, some being intentionally plugged. This allows variation of the total number and spacing of the nozzles, provides flexibility for the total water flow rate delivered through the spray bars, and permits some control of the uniformity of the spray delivered to the compressor face.

ASTF Icing System (AIS)

Since the first icing testing conducted at AEDC ETF, demands on icing systems have expanded to larger free-jet nozzles and to test engines with increasing air mass flow rates. Hence the icing test facilities are run at conditions that increase the speed of the flows in the region of the spray bar array. Concerns surfaced regarding the mixing and spreading of the droplet spray in the flow downstream of the spray bars. Further, higher speeds have increased the convective heat loss from the warm bars to the cold airstream, making the water passages within the spray bar more susceptible to freezing.

An icing spray system has been designed for the Aeropropulsion Systems Test Facility, ASTF, at the AEDC. This facility is used for the testing of the largest turbofan engines, those in the 450,000 N-thrust class. The design of the spray bar system specifically addresses the concerns of hydraulic head, spray mixing, and spreading, and the heat loss from the spray bar. The spray system is designated the ASTF Icing System, AIS.

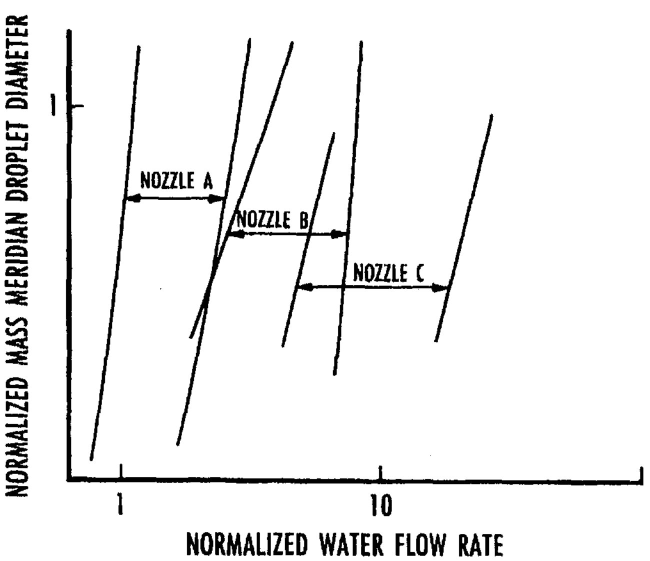

Fig. 5 Performance envelopes for typical icing spray nozzles

Hydraulic Head. The spray bar mounting for the AIS is designed to minimize the influence that hydraulic head differences could have on water flow delivery from the spray nozzles. Without allowing for hydraulic head, the water pressure delivered to the spray nozzle can vary by as much as 40 percent from the top to the bottom spray bars. This is an unacceptable variation and would lead to unacceptable uniformity of LWC at the compressor face. In the AIS there are 17 horizontally mounted spray bars. The spray nozzle water is delivered to eight groupings of two bars, and the center bar, as shown in Fig. 6. Each grouping and the central bar are independently controlled for water flow rate with a flow trim valve placed in series with a water flow rate meter. This arrangement allows each spray bar grouping to deliver the specified water flow rate and avoids adverse hydraulic head effects across the 3.2-m-dia spray array.

Spray Mixing and Spreading. The spray issuing from the spray bars must mix with the airstream. The liquid water is delivered uniformly to the compressor face. The extent to which the droplets mix is a function of the spacing of individual spray nozzles and the wake from the spray bars. Since AEDC ETF has considerable experience with the approximately 18- to 20-cm spacing between nozzles, this spacing was selected as a baseline design for the AIS. The thickness of the spray bars was selected to yield the maximum Mach number between adjacent bars to be less than 0.7. One requirement of the spray bar design was that no water from the spray nozzle could wash back onto the bar. Water that washes back onto the bar could freeze and pose an intolerable foreign object damage hazard to the test engine. Heating the bar to prevent freezing of the wash would only permit the wash back to collect and shed in an uncontrollable and unknown manner, affecting both compressor face LWC and MMD.

Spray Bar Heat Loss. The internal water passages of the spray bar are prone to freezing since they are exposed to airstream below the freezing temperature of water. The AIS spray bars are designed with features to prevent the temperature in the water passages from reaching the freezing point of water during all planned operations of the spray system.

Spray Bar Design Validation

There were no known spray mixing and heat loss data upon which to base a design, so prototype designs were evaluated

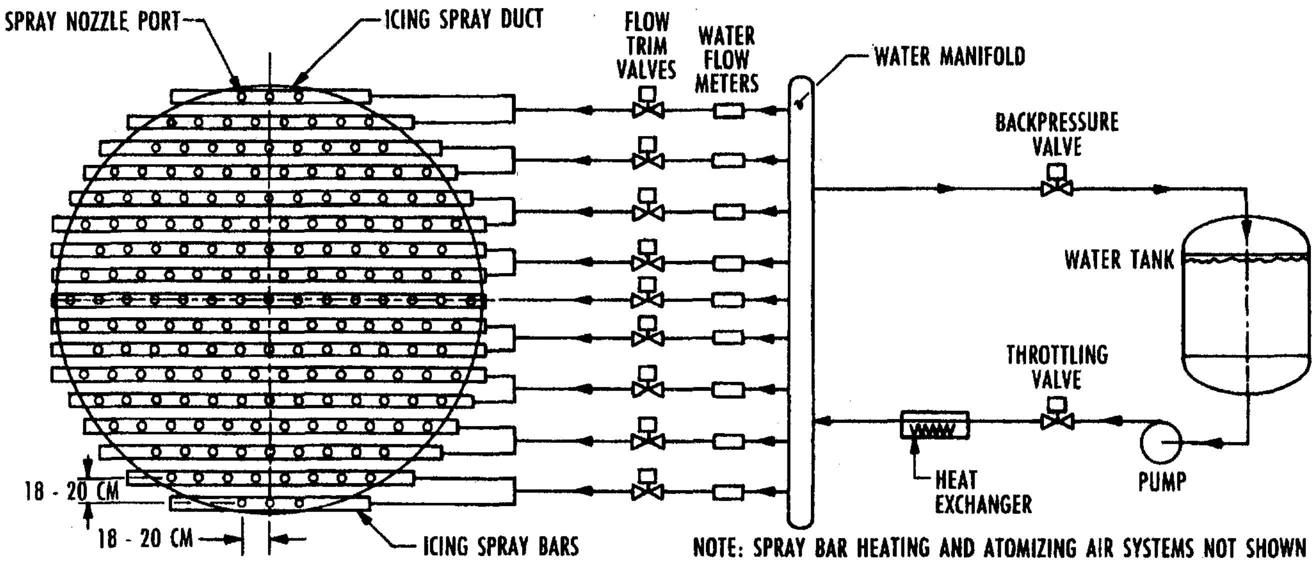

Fig. 6 Icing spray bar configuration and spray bar grouping for the ASTF test cell icing spray system

experimentally. The design validation effort had as its primary goal the collection of data to provide a basis for the spray bar shape. The secondary objective was to evaluate proposed designs that would prevent the freezing of the spray bar internal water passages during extended exposure to the cold airstream.

Spray Bar Shape. Two prototype spray bar shapes, a bluff body and an aerodynamic shape, were selected for evaluation. The procedure was to evaluate both shapes and iterate upon the spray bar geometry, if required, to promote mixing and prevent back wash of water onto the spray bar. The evaluation baseline adopted to determine proper mixing was based on the mixing obtained with a spray bar shape used in ETF for the past 20 years. Other requirements included the provision the spray bar and nozzle configuration must prevent back wash of liquid water onto the bar at approaching air flow speeds equivalent to Mach 0.5. The prototype bars are shown in Fig. 7 for the bluff body, and in Fig. 8 for the aerodynamic streamlined body. A spray nozzle extension was used to place the spray nozzle further downstream, as shown in Fig. 7(*c*). The original hexagonal head retainer nut for the spray nozzle was replaced with a streamlined retainer nut, faired smoothly into the spray nozzle extension.

Test Apparatus. The test apparatus consisted of the prototype spray bars, ice collection bars, and test cell as shown in Fig. 9. The testing was conducted in the R-1D research test cell, an cylindrical free-jet test cell with a plenum chamber upstream of a bellmouth contraction section, which connects to the free-jet duct. The free-jet duct exits into the test chamber. A test bar was installed with the spray bar leading edge posi-

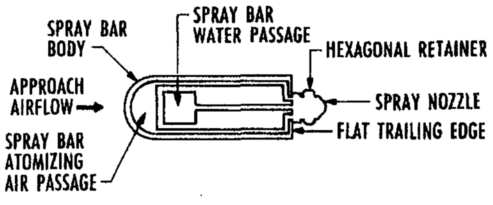

a. Baseline spray bar shape

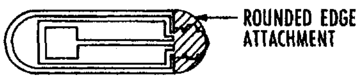

b.Baseline shape with rounded trailing edge

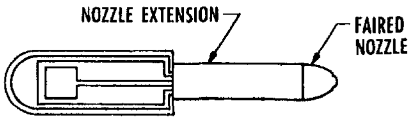

c. Baseline shape with nozzle extension and faired retainer cap

Fig. 7 Cross-sectional profiles of the bluff body spray bars

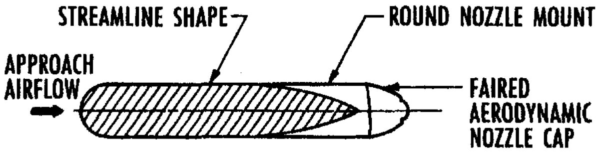

a. Aerodynamic shape

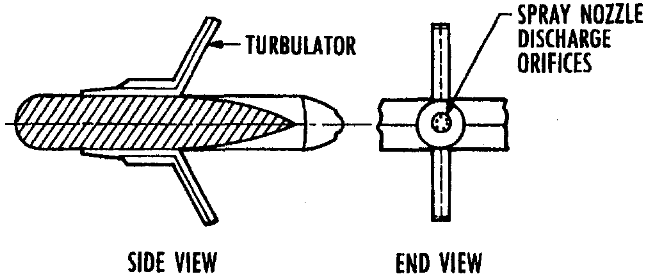

b.Aerodynamic shape with turbulator

Fig. 8 Cross-sectional profile of aerodynamic spray bars

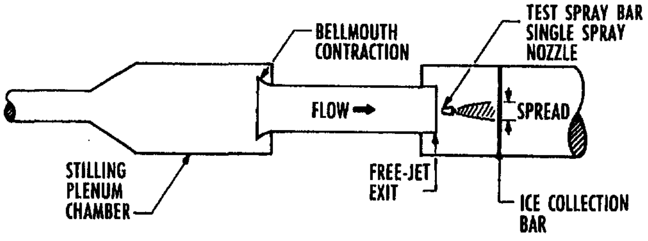

Fig. 9 Spray bar shape and mixing validation test apparatus

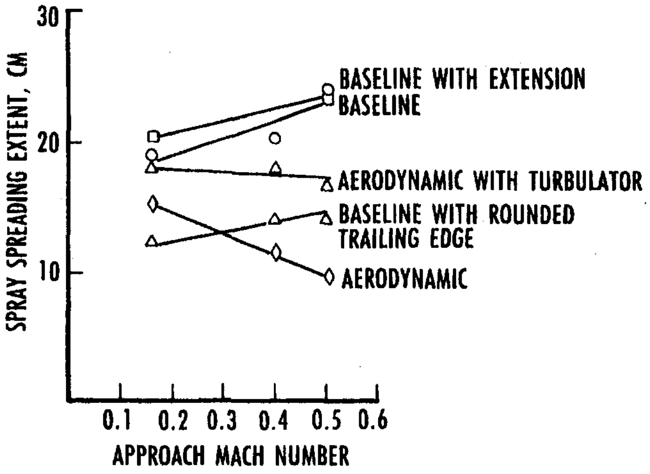

Fig. 10 Results of the spray spreading tests

tioned 5 cm downstream of the free-jet exit plane. Each bar tested was supplied with one water atomizing spray nozzle. The bar was positioned horizontal and centered in the free-jet exit flow with the spray nozzle placed along the free-jet centerline. Spreading of the droplets behind the bars was determined by the extent of accumulation of ice on horizontal and vertical bars placed 0.6 m downstream of the trailing edge of the spray nozzle exit. The 0.6 m distance was selected based on studies indicating the mixing at this distance downstream of the spray bar was significantly influenced by the flow behind the spray bar. The Mach number at the free-jet exit plane was varied from 0.16 to 0.50, representing the range of conditions expected during operation of the installed spray system.

Test Procedure. The testing was conducted in the following manner. The test spray bar configuration was installed in the test cell. Water and atomizing air were supplied to the spray nozzle to simulate a typical icing spray nozzle operating condition. The water and atomizing air supply pressures were set to 170 KPa, with a resulting water flow rate of approximately 0.08 L/min. The desired Mach number was set and determined by the ratio of stagnation to static pressure at the free-jet duct exit. The spray was initiated, and the aft edge of the spray bar was observed for signs of wetting caused by wash back of spray onto the spray bar surface. Backlighting of the spray enhanced the ability to detect any recirculation of the water back onto the bar. The water spray was maintained for approximately 2 min to allow ice to collect on the vertical and horizontal rods positioned to collect spray spreading data.

The following spray bar configurations were evaluated (extension was fixed length):

1 bluff body flat trailing edge, rounded leading edge (without extension of the spray nozzle),
2 bluff body with rounded trailing and leading edges (with extension of the spray nozzle),
3 bluff body flat trailing edge, round leading edge (with extension of the spray nozzle),
4 aerodynamic shape (without nozzle extension) and,
5 aerodynamic shape with turbulator (without nozzle extension).

Test Results. There was evidence of unacceptable recirculation of water onto the spray bar for all bluff body configurations tested unless the spray nozzle was placed 10 cm downstream from the aft edge of the spray bar with a nozzle extension. The spray spreading date for the spray bar configurations tested are shown in Fig. 10. The figure relates the extent of spray spreading in the vertical direction, perpendicular to the horizontally mounted spray bar. Linear fits of the spreading data are plotted versus the Mach number of the flow approaching the spray bar. The test results indicate that spreading increases as the spray bar approach Mach number increases for the bluff body bar while the spreading from the streamlined bar decreases. Some mixing augmentation was evaluated for the aerodynamic bar, including the use of turbulators near the spray nozzle. The turbulators did improve mixing but failed to yield the mixing equal to that of the bluff body. Investigators decided to continue design of the AIS spray bars using bluff body shapes with extension to place the nozzle aft of the bluff body trailing edge.

Spray Bar Heating. The required operations of the AIS spray bar are:

1 purge of the water passages and maintenance of the fluid passage temperature during no water flow operation,
2 initiation of spray,
3 steady water spray operation, and
4 termination of spray.

The most difficult of the operations to accomplish is prevention of freezing in the fluid passages during the no-water-flow operation. The spray bars are operated in this manner each time a new engine test condition is being set with the engine and test facility approaching thermally stable operation. This exposes the spray bar to the cold airstream with no water flowing through the spray nozzles for as long as 30 min.

A prototype bluff body spray bar design was fabricated and evaluated for freeze prevention adequacy. The prototype spray bar was installed in the R-1D test cell described above. The objective of the test was to demonstrate that the water spray could be initiated from the spray nozzle after allowing the spray bar to cold soak with no water spray. The approach to prevent water passage freezing was to maintain a continual flow of heated water through a spray bar heating water passage and to maintain a heated air purge on the spray nozzle operation. At spray initiation, the purge would be terminated and water would be supplied to the spray nozzle. Electrical heating elements were added to the bar in case the heated purge method did not prevent freezing in the water passage.

Spray Bar Design. The prototype spray bar consists of three integral fluid passages. The passages carry the spray bar heating water, water to supply the spray nozzle, and atomizing air for the spray nozzle. The fluid passage assembly is wrapped in a thin stainless-steel shell with an air gap between the shell and the fluid passages. The outer skin acts as a stiffener for the assembly, and the air gap acts as an insulating layer to reduce heat loss from the fluid passages to the airstream. The nozzle extension is surrounded by a plastic insulating material to reduce heat loss to the cold airstream. A cross section of the prototype spray bar with the spray nozzle extension is shown in Fig. 11. Thermocouples were placed inside the water passage at the entrance to the water tube and at the tip of the water tube in the spray nozzle to measure the temperatures within the fluid passages during purge and spray operations.

Test Procedure. Water at 60°C was circulated through the heating water passage, Fig. 11, at all times to simulate planned AIS spray system operation. The spray nozzle water, heated to 40°C, was supplied to the bar through a three-way valve that could be shuttled to divert water from the water passage into a drain line and simultaneously purge the water passage with air heated to 55°C, from the atomizing air supply. The purge air flow rate, 0.57 kg/min, and pressure, 690 kPa, supplied to the water passage during purge were selected to correspond to the worst-case flows expected at any nozzle across the spray array during planned AIS operation.

The spray bar was to be exposed to a −30°C airstream at approach Mach number of 0.5 until temperatures within the water passages were steady. After the steady-state conditions

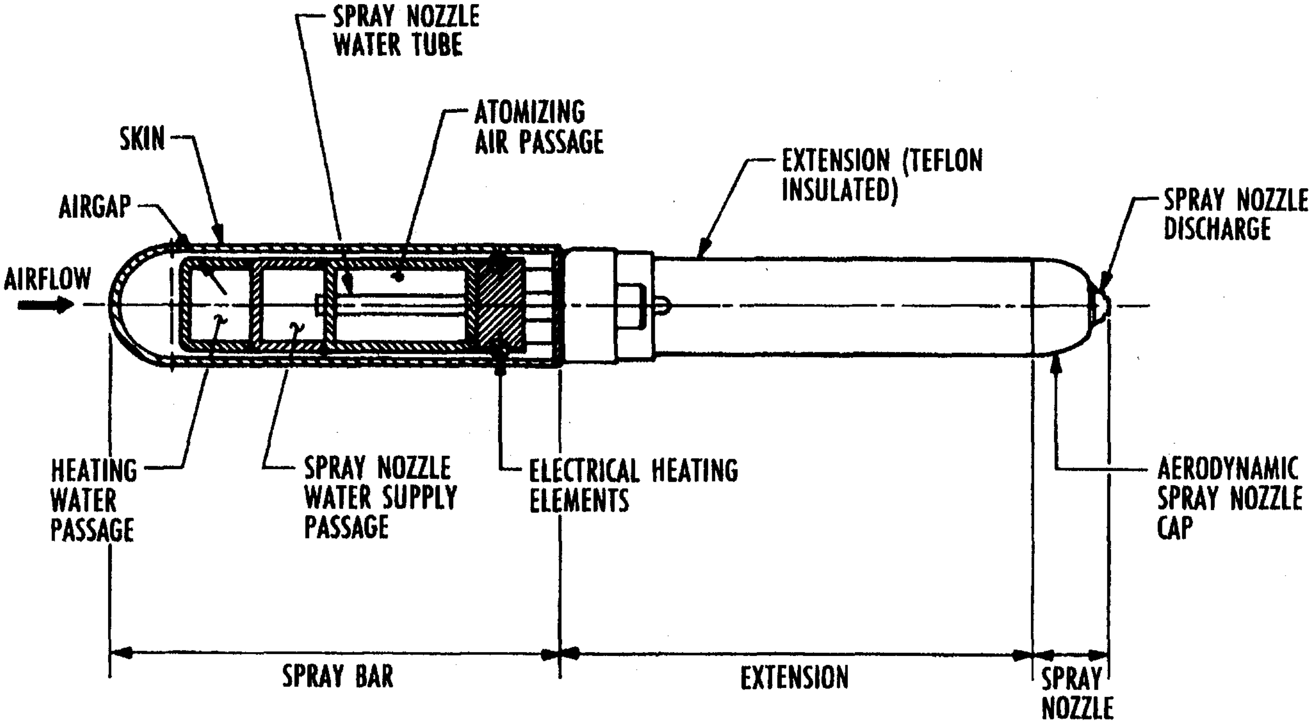

Fig. 11 Cross-sectional view of the prototype icing spray bar

were obtained, transient data collection was started. The three-way shuttle valve then diverted the water from the overboard drain back to the water passage and simultaneously terminated the purge air flow. The atomizing air pressure was reset from an elevated "purge" level to the normal spray nozzle operating level. A drain valve in the water passage downstream of the spray nozzle was opened for 10 s to allow the passage to fill quickly. The drain valve was then closed, and a stable spray condition was attained.

Test Results. The results of the evaluation indicated the heated air purge would be adequate to prevent freezing in the water passages. The temperature at the entrance to the water tube to the spray nozzle went from approximately 64°C during the purge to a steady 51°C during steady spraying. The temperature in the spray nozzle water passage went from 20°C during purge to 28°C during spray, comfortably above freezing. Stable temperatures during the spray were obtained within 140 s of purge termination.

The use of the electrical heating elements was demonstrated to determine their effectiveness. Repeating the operation described above with the heating elements activated indicated that the minimum temperature in the water passage was greater than 38°C with the heaters operating at nominal heat input. The electrical heating system provides additional margin for freeze prevention.

Summary

Ground simulation of flight through icing conditions has been discussed. The key issues have been reviewed, including the simulation of stagnation temperature and pressure and altitude pressure for a turbine engine. The simulation of the liquid water content and droplet size associated with icing encounters has been reviewed. The design of a new spray system at the Arnold Engineering Development Center Engine Test Facility has been described. The basis for the spray system spray bar shape and freeze prevention has been presented. Validation testing of the designs has been discussed. Bluff body spray bars were selected for their ability to mix the droplets into the airstream. The design included provisions to prevent freezing of water within the spray bar water passages. Electrical heating elements were added to the design to provide added margin against freezing in the water passages.

Acknowledgments

The research reported in this paper was performed by the Arnold Engineering Development Center (AEDC), Air Force Materiel Command. Work and analysis for this research were done by personnel of Sverdrup Technology, Inc., AEDC Group, technical services contractor for the AEDC propulsion test facilities. Further reproduction is authorized to satisfy needs of the U. S. Government.

References

Ashendon, R. A., 1993, "The Air Force Flight Test Center Artificial Icing and Rain Testing Capability Upgrade Program," AIAA Paper No. 93-0295.

Bartlett, C. S., 1988, "Icing Scaling Considerations for Aircraft Engine Testing," AIAA Paper No. 88-0202.

Bartlett, C. S., et al., 1990, "Icing Test Capabilities for Propulsion Systems at the Arnold Engineering Development Center," AGARD-CP-480.

Bartlett, C. S., and Phares, W. J., 1993, "Icing Testing of a Large Full Scale Inlet at the Arnold Engineering Development Center," AIAA Paper No. 93-0299.

Belte, D., and Woratschek, R., 1986, "Helicopter Icing Spray System Evaluation and Improvements," USAAEFA 82-05-3.

Federal Aviation Administration, Federal Aviation Regulation, Part 25, 1984, "Airworthiness Standards: Transport Category Airplanes: Appendix C."

Gall, E. S., and Floyd, F. X., 1971, "Icing Test Capability of the Engine Test Facility Propulsion Development Test Cell (J-1)," AEDC-TR-71-94 (AD-729205).

Gelder, T. F., 1958, "Droplet Impingement and Ingestion by Supersonic Nose Inlet in Subsonic Tunnel Conditions," NACA TN 4268.

Hunt, J. D., 1978, "Engine Icing Measurement Capabilities at the AEDC," AGARD-CP-236.

Pheifer, G. D., and Maier, G. P., 1977, "Engineering Summary of Powerplant Icing Technical Data," FAA-RD-77-76.

Willbanks, C. E., and Schulz, R. J., 1973, "Analytical Study of Icing Simulation for Turbine Engines in Altitude Test Cells," AEDC-TR-73-144 (AD-770069).

A. Brückner-Foit

A. Heger

D. Munz

Institute for Reliability and Failure Analysis,
University of Karlsruhe,
Karlsruhe, Federal Republic of Germany

Assessment of Notches in Ceramic Components

The failure probability of notched tensile bars is calculated using the multi-axial Weibull theory. The influence exerted by the stress concentration factor, the stress gradient in the notch root, and the Weibull exponent is analyzed.

1 Introduction

Common design practice for metallic components compares the maximum stress at the most critical point to the strength. Frequently this maximum stress can be determined even if a stress analysis of the component under consideration has not been made. A well-known example is notches for which analytical and approximate values of the stress concentration factor in the notch root have been determined for a large number of notch geometries [1].

The aim of this study is to investigate the influence of notches on the reliability of ceramic components in order to provide a database from which appropriate design rules can be derived. For this purpose, simple tensile bars containing notches of various geometries are analysed in this paper using the finite-element method to determine the stress field and using the multiaxial Weibull theory. The dependence of the reliability on the stress concentration factor, on the stress gradient in the notch root, and on the material parameters of the ceramic material is determined.

2 Weibull Theory for Multiaxial Loading

The failure behavior of ceramic components subjected to a multiaxial stress state can be assessed using the multiaxial Weibull theory as developed by Batdorf et al. [2, 3], Evans [4], and Matsuo [5]. It is assumed that failure is caused by unstable extension of natural flaws of random size, of random location, and of random orientation with respect to the principal stress axes. The worst flaw, i.e., the flaw for which the most unfavorable combination of size, location, and orientation is obtained, will propagate unstably and will cause catastrophic failure.

The critical crack size can be determined using fracture mechanics, if the natural flaws can be approximated by planar cracks. Within the framework of this model, a multi-axial stress state gives rise to a mixed mode loading of a crack, and the critical size is a function of the mode I–mode III stress intensity factors $K_{\rm I}$, $K_{\rm II}$, $K_{\rm III}$:

$$a_c = a_c(K_{\rm I}, K_{\rm II}, K_{\rm III}) \tag{1}$$

with

$$\begin{aligned} K_{\rm I} &= \sigma_n \sqrt{a \cdot Y_{\rm I}} \\ K_{\rm II} &= \tau_n \sqrt{a \cdot Y_{\rm II}} \\ K_{\rm III} &= \tau_n \sqrt{a \cdot Y_{\rm III}} \end{aligned} \tag{2}$$

and the correction factors $Y_{\rm I}$, $Y_{\rm II}$, and $Y_{\rm III}$. The stress σ_n normal to the crack plane and the shear stress τ can be calculated by an appropriate transformation of the stress tensor [5].

An equivalent mode I stress intensity factor $K_{\rm Ieq}$ can be introduced with

$$K_{\rm Ieq} = \sigma_{eq} \cdot \sqrt{a} \cdot Y_{\rm I}, \tag{3}$$

where the equivalent stress σ_{eq} depends on σ_n, τ, and on $Y_{\rm I}$, $Y_{\rm II}$, and $Y_{\rm III}$. The critical crack size is then given by:

$$a_c = \left(\frac{K_{\rm Ic}}{\sigma_{eq} \cdot Y_{\rm I}}\right)^2 \tag{4}$$

where $K_{\rm Ic}$ denotes the fracture toughness.

A variety of multi-axiality criteria are given in the literature leading to different expressions for σ_{eq}. A summary can be found in [6]. An example of one of these criteria is [7]:

$$\sigma_{eq} = \sqrt{\sigma_n^2 + \left(\frac{2}{2-\nu}\right)^2 \cdot \tau^2} \tag{5}$$

which is derived using the assumption that the value of the energy release rate in the crack plane determines the onset of unstable crack propagation, and a penny-shaped crack is a suitable model for the natural flaws. ν denotes Poisson's ratio.

In Weibull theory the following expression is used for the probability that a given flaw exceeds its critical crack size [6]:

$$Q_1 = \frac{1}{V}\int_V \frac{1}{4\pi}\int_\Omega \left(\frac{\sigma_{eq}}{\tau_0}\right)^m d\Omega dx \tag{6}$$

where Eq. (4) was used for the critical crack size. In Eq. (6), V denotes the volume of the component, Ω is the unit sphere, and x is the vector of coordinates. The parameters m, τ_0 in Eq. (6) depend on the toughness of the flaw-free material and on the statistical properties of the flaw size distribution. Equation (6) implies that all locations of flaws and all orientations occur with equal probability, i.e., that the material is homogeneous and isotropic.

The number n of cracks in the volume V is also a random variable and can be described by Poisson's distribution. The probability of having exactly n cracks in V is given by:

$$p_n = \frac{M^n \cdot e^{-M}}{n!}, \tag{7}$$

where M is the average number of cracks in V. The following relation for the failure probability P_f is obtained from Eqs. (6), (7) [6] using the weakest-link model:

$$P_f = 1 - \exp(-M \cdot Q_1). \tag{8}$$

With the definition of a new material parameter b:

$$b = \frac{\tau_0}{H} \cdot \left(\frac{V}{V_0 \cdot M}\right)^{1/m} \tag{9}$$

where V_0 is a reference or unit volume, and H is the normalized stress integral given by:

Contributed by the International Gas Turbine Institute and presented at the 39th International Gas Turbine and Aeroengine Congress and Exposition, The Hague, The Netherlands, June 13–16, 1994. Manuscript received by the International Gas Turbine Institute March 10, 1994. Paper No. 94-GT-484. Associate Technical Editor: E. M. Greitzer.

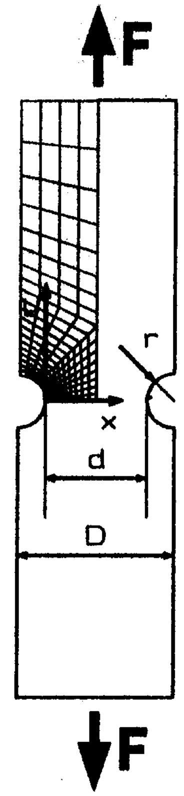

Fig. 1 Geometry of notched tensile bar with typical finite-element mesh

$$H = \left(\frac{1}{V_0}\int_V \frac{1}{4\pi}\int_\Omega \left(\frac{\sigma_{eq}}{\sigma^*}\right)^m d\Omega dx\right)^{1/m}, \tag{10}$$

Eq. (8) can be rewritten as:

$$P_f = 1 - \exp\left(-\left(\frac{\sigma^*}{b}\right)^m\right) \tag{11}$$

where σ^* is a reference stress characterizing the loading of the component. Equation (11) implies that the stress at fracture is a Weibull distributed random variable.

The normalized stress integral H is independent of the applied load level and is hence a convenient tool to characterize the effect of the spatial stress distribution on the failure probability, particularly if two components with different geometries are compared. In this case the corresponding Weibull parameters $b^{(1)}$, $b^{(2)}$ (Eq. (11)) are related by:

$$\frac{b^{(1)}}{b^{(2)}} = \frac{H^{(2)}}{H^{(1)}} \tag{12}$$

The allowable stress levels $\sigma^{(1)*}$, $\sigma^{(2)*}$ for two different designs of a component are related by:

$$\frac{\sigma^{(1)*}}{\sigma^{(2)*}} = \frac{H^{(2)}}{H^{(1)}} \tag{13}$$

at a given level of reliability, which is characterized by a specific value of P_f. From Eqs. (9)–(12) it is clear that the information needed for the design of ceramic components is contained in the normalized stress integral, which will be used in the subsequent investigations. However, it should be kept in mind that the numerical value of H depends on the choice of the normalization volume V_0. The ratio of H values, on the other hand, is independent of V_0.

The five-dimensional integral Eq. (10) has to be evaluated in order to determine the failure probability or the normalized stress integral H. Several postprocessors [8, 9] are available that perform the numerical integration using the stress field given in the output file of a commercial finite element code.

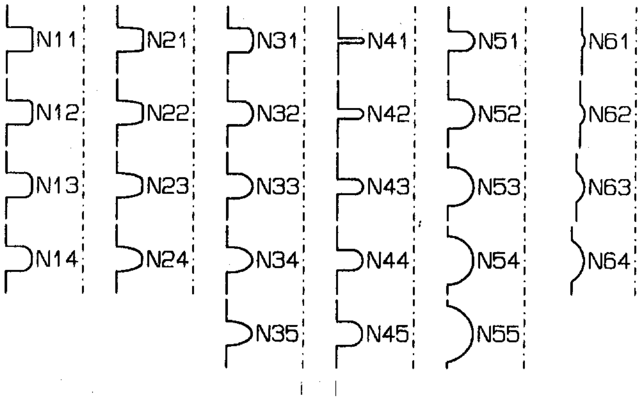

Fig. 2 Notch geometries

3 Notches in Ceramic Components

The stress field of a notched tensile bar for various notch geometries was calculated using a linear elastic finite-element analysis. Figure 1 shows the geometry of the bar with a typical finite-element mesh. The stress field in the notched cross section is characterized by the stress-concentration factor:

$$\alpha_k = \frac{\sigma_{1,\max}}{\sigma_{\mathrm{nom}}} \tag{14}$$

and the normalized stress gradient

$$\chi^* = -\frac{1}{\sigma_{1,\max}} \cdot \frac{d\sigma_1}{dx}\bigg|_{x=0} \tag{15}$$

where $\sigma_{1,\max}$ is the maximum stress in the notch root ($x = 0$) and σ_{nom} is the nominal stress.

The geometries of the notches considered are shown in Fig. 2. The width of the notched cross section d was kept constant in all cases. With these geometries a wide range of $\alpha_k - \chi^*$ values has been covered (see Table 1, $1.9 < \alpha_k < 5$ and $0.3 < \chi^* < 2$). The normalized stress gradient χ^* could be evaluated with sufficient accuracy for those notches only for which the notch roots were situated on the symmetry line of the structure because of the limitations imposed by the finite-element mesh.

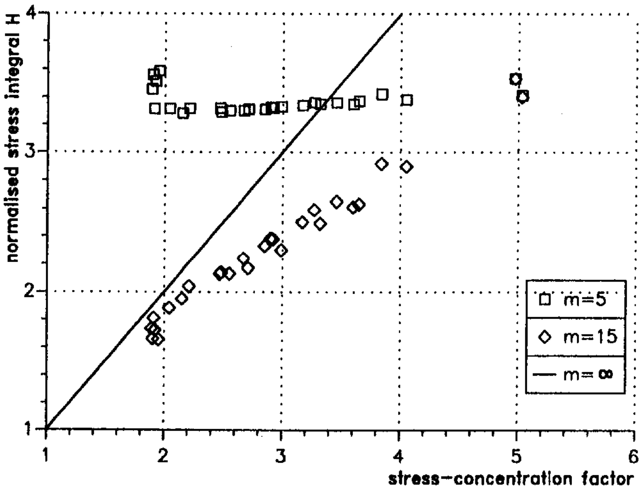

Fig. 3 Dependence of the normalized stress integral H on the stress concentration factor α_k; $m = \infty$: deterministic limit with $H = \alpha_k$

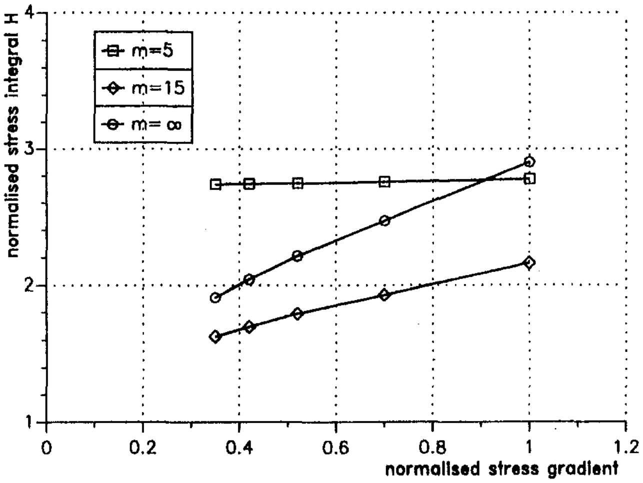

Fig. 4 Dependence of the normalized stress integral H on the normalized stress gradient X^*; notches with $\alpha_k \sim X^*$(N51–N55)

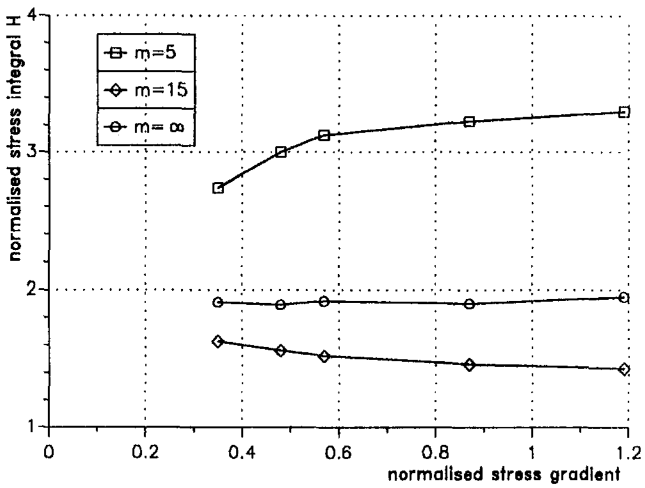

Fig. 5 Dependence of the normalized stress integral H on the normalized stress gradient X^*; notches with $\alpha_k \approx 1.9$(N55 and N61–N64)

The normalized stress integral H, Eq. (10), was calculated for these notched tensile bars using the finite-element code ABAQUS and the post-processor STAU [8]. The reference stress σ^* in Eq. (11) was set equal to the nominal stress. The equivalent stress was determined using Eq. (5).

All dimensions including the unit volume V_0 were given in mm. The thickness of the bars was assumed to be equal to 1, the nominal width d was 40, and the length was 90.

Figure 3 shows the variation of the normalized stress integral H with the stress concentration factor α_k. For low values of the Weibull exponent m, the value of H depends only weakly on the stress concentration factor, whereas H approaches α_k for high values of m, i.e,, low scatter of the material strength. In the deterministic limit ($m \to \infty$), only the maximum stress $\sigma_{1,\max}$ contributes to the failure probability and H is equal to α_k. The influence of the shape of the notch is small compared to the influence of the stress-concentration factor for realistic values of m, as notches of very different shapes such as N21 and N41 yield H values $H_{21} = 3.53$ and $H_{41} = 3.40$, respectively, for $m = 15$, which are much closer to each other than the values obtained from notches of similar shapes and different values of α_k (e.g., N11 and N21: $H_{11} = 2.63$ and $H_{21} = 3.40$).

Table 1 Dimension of notches defined in Fig. 2 in notched tensile bars with length 90 mm and nominal width d = 40 mm

notch number	α_k,eqn.(14)	χ^*, mm^{-1}, eqn.(15)	$\frac{D}{d}$, see Fig.1
N11	3.65	-	1.250
N12	2.99	-	1.250
N13	2.71	-	1.250
N14	2.55	-	1.250
N21	5.03	-	1.250
N22	4.05	-	1.250
N23	3.60	-	1.250
N24	3.32	-	1.250
N31	2.15	-	1.250
N32	2.48	-	1.250
N33	2.85	-	1.250
N34	3.17	-	1.250
N35	3.46	0.63	1.250
N41	4.97	1.21	1.250
N42	3.84	0.75	1.250
N43	3.27	0.55	1.250
N44	2.92	0.47	1.250
N45	2.67	0.38	1.250
N51	2.90	1.00	1.250
N52	2.47	0.70	1.250
N53	2.21	0.52	1.250
N54	2.04	0.42	1.250
N55	1.91	0.35	1.250
N61	1.95	1.19	1.030
N62	1.90	0.82	1.045
N63	1.92	0.57	1.075
N64	1.89	0.49	1.115

Because of the strong correlation between α_k and χ^* for most of the examples studied here a special class of notches was selected with almost constant $\alpha_k = 1.9$ and $0.35 < \chi^* < 1.2$ (N55, N61–N64 in Fig. 2). These notches are compared to notches with $\alpha_k \sim \chi^*$ in the same order of magnitude (N51–N55 in Fig. 2). Figures 4 and 5 show the normalized stress integral H as a function of χ^* in both cases.

A reduced nominal width of $d = 20$ was used in this case in order to obtain more accurate values for the stress gradients. The effect of the nominal width on the normalized stress integral H is quite important, especially for low values of m, as can be seen by comparing Fig. 3 with Fig. 4.

The relationship between H and χ^* (Fig. 4) looks very similar to that between H and α_k for N51–N55 (Fig. 3), i.e., the effect of the stress gradient cannot be separated from the effect of the effect of the peak stress in the notch root. The increase in H with χ^* (i.e., a steeper gradient of the stress in the notch root) observed for $m = 5$ in the case of N55 and N61–N64 (see Fig. 5) is due to the fact that the stress gradient χ^* increases with increasing total width D (see Table 1). The nominal width and the nominal stress were kept constant and hence a larger value of D implies that the stress in the remainder of the bar outside the notched cross section decreases. H decreases with increasing χ^* for $m = 15$, because the width effect is suppressed and the change of the stressed volume in the notched cross section becomes dominant.

4 Conclusion

The influence of notches on the reliability of ceramic components can be assessed using a normalized stress integral. The stress-concentration factor α_k in the notch root is the most important influencing factor, which implies that notches of different shapes but similar values of α_k yield similar values of the stress integral.

References

1 Peterson, R. E., *Stress Concentration Factors,* Wiley, New York, 1974.

2 Batdorf, S. B., and Crose, J. G., "A Statistical Theory for the Fracture of Brittle Structures Subjected to Nonuniform Stress," ASME *Journal of Applied Mechanics,* Vol. 41, 1974, pp. 459–461.

3 Batdorf, S. B., and Heinisch, H. L., "Weakest Link Theory Reformulated for Arbitrary Fracture Criterion," *J. Amer. Ceram. Soc.,* Vol. 61, 1978, pp. 355–358.

4 Evans, A. G., "A General Approach for the Statistical Analysis of Multiaxial Fracture," *J. Am. Ceram. Soc.,* Vol. 61, 1978, pp. 302–308.

5 Matsuo, Y., "A Probabilistic Analysis of Fracture Loci Under Bi-axial Stress State," *Bull. JSME*, Vol. 24, 1981, pp. 290–294.

6 Thiemeier, T., Brückner-Foit, A., and Kölker, H., "Influence of the Fracture Criterion on the Failure Probability of Ceramic Components," *J. Am. Ceram. Soc.*, Vol. 74, 1991, pp. 48–52.

7 Paris, P. C., and Sih, G. C., "Stress Analysis of Cracks," in: *Fracture Toughness Testing and Its Applications*, ASTM STP 381, American Society of Testing of Materials, Philadelphia, PA, 1965, pp. 30–83.

8 Heger, A., Brückner-Foit, A., and Munz, D., "STAU—ein Programm zur Berechnung der Ausfallwahrscheinlichkeiten mehrachsig beanspruchter keramischer Komponenten als Post-Prozessor für Finite-Elemente-Programme," Internal Report, Institute for Reliability and Failure Analysis, University of Karlsruhe, Germany, 1991.

9 Nemeth, N. N., Manderscheid, J. M., and Gyekenyesi, J. P., "Ceramic Analysis and Reliability Evaluation of Structures (CARES)," User's and Programmer's Manual, NASA TP-2916, Washington, DC, 1989.

Assessment of Damage in Ceramics and Ceramic Matrix Composites Using Ultrasonic Techniques

S. I. Rokhlin

Y. C. Chu

Department of Welding Engineering,
Ohio State University,
Columbus, OH 43210

G. Y. Baaklini

NASA Lewis Research Center,
Cleveland, OH 44135

This paper addresses the application of ultrasonic methods to damage assessment in ceramics and ceramic matrix composites. It focuses on damage caused by thermal shock and oxidation at elevated temperatures. The damage-induced changes in elastic constants and elastic anisotropy are determined by measuring the velocities of ultrasonic waves in different propagation directions within the sample. Thermal shock damage measurement is performed in ceramic samples of reaction bonded silicon nitride (RBSN) and aluminum oxide. Thermal shock treatment from different temperatures up to 1000°C is applied to produce the microcracks. Both surface and bulk ultrasonic wave methods are used to correlate the change of elastic constants to microstructural degradation and to determine the change in elastic anisotropy induced by microcrack damage. Oxidation damage is studied in silicon carbide fiber/reaction bonded silicon nitride matrix (SCS-6/RBSN) composites. The oxidation is done by exposing the samples in a flowing oxygen environment at elevated temperatures, up to 1400°C, for 100 hours. Significant changes of ultrasonic velocities were observed for composites before and after oxidation. The elastic constants of the composites were determined from the measured velocity data. The Young's modulus in the fiber direction as obtained from ultrasonic measurements decreases significantly at 600°C but retains its original value at temperatures above 1200°C. This agrees well with the results of destructive tests by other authors. The transverse longitudinal and shear moduli obtained from ultrasonic measurements decrease continually until 1200°C. The results of this work show that the damage-induced anisotropy in both ceramics and ceramic matrix composites can be determined successfully by ultrasonic methods. This suggests the possibility of assessing damage severity using ultrasonic techniques.

1 Introduction

The inherent brittleness of ceramic materials often results in catastrophic failure due to microcrack damage caused by thermal treatment or mechanical loading. The thermal shock microcracking appears because of thermally induced stresses and as a result, permanent loss of stiffness and strength occur. A simple model describing the strength behavior of ceramic materials as a function of thermal shock temperature difference was proposed by Hasselman (1969, 1970). However, as shown experimentally, the actual behavior depends on the composition and the microstructure of the material (Gupta, 1972; Lutz et al., 1991); in some cases the behavior is very similar to the model, but in other cases the predicted behavior hardly appears.

When the crack size is greater than the ultrasonic wavelength, one may consider the crack as a material discontinuity and get information on the crack size by measuring waves reflected from the crack. On the other hand, when there are multiple cracks within one ultrasonic wavelength, the damage is considered as distributed microcrack damage. The appearance of microcracks in the material is similar to the appearance of a second phase, which leads to mechanical property (elastic moduli and strength) changes. The effective elastic modulus of a cracked medium depends on crack shape, density and crack preferred orientation (Budiansky and O'Connell, 1976; Laws and Brockenbrough, 1987). To measure the effective elastic properties of a cracked medium, the ultrasonic wavelength used in measurement must be greater than the crack size and spacing. The measured effective elastic properties of the damaged material represent the effect of microcracks (Hefetz and Rokhlin, 1992) and can be related to material damage via damage mechanics.

The fracture resistance of ceramic materials can be improved by reinforcing them with continuous fibers. It is known (Evans and Marshall, 1988; Prewo, 1988) that the properties of ceramic materials reinforced by continuous fibers are dominated by the interfaces. However, in a high-temperature environment fiber-matrix interfaces in ceramic matrix composites often suffer from oxidation reactions caused by diffusion of oxygen through the matrix. The damage is greater if the matrix contains interconnected pores allowing easy oxygen transport to the interface. For this reason ceramic matrix composites subjected to thermal oxidation treatments may not retain the desired strength and toughness (Bhatt, 1989).

In this study we have applied ultrasonic techniques to assess thermal shock damage in ceramics and oxidation damage in ceramic matrix composites. By measuring damage-induced elastic anisotropy, we aimed to correlate ultrasonic measurements with the degradation in mechanical properties of ceramics and ceramic matrix composites.

2 Experimental Approach

2.1 Samples

(a) Monolithic Ceramic Samples. The monolithic ceramics used in this study were commercial alumina and Si_3N_4 reac-

---

Contributed by the International Gas Turbine Institute and presented at the 39th International Gas Turbine and Aeroengine Congress and Exposition, The Hague, The Netherlands, June 13–16, 1994. Manuscript received by the International Gas Turbine Institute February 25, 1994. Paper No. 94-GT-228. Associate Technical Editor: E. M. Greitzer.

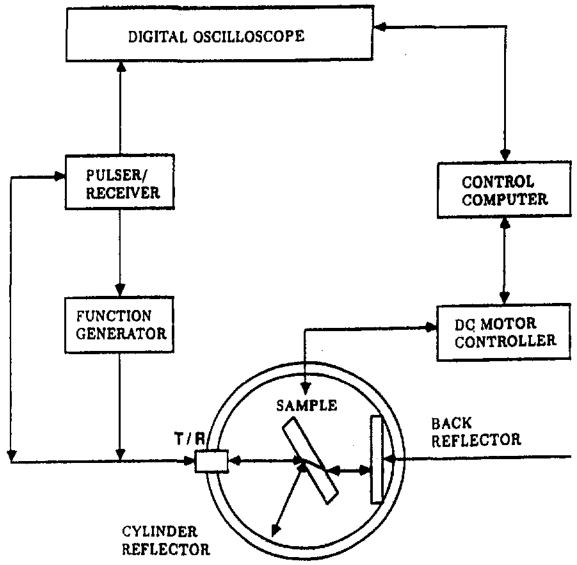

Fig. 1 Schematic diagram of the experimental apparatus for ultrasonic determination of elastic constants

tion bonded silicon nitride (RBSN). The 24 × 24 mm alumina samples were 4.7 mm thick and cut from 7.5-cm-dia disks supplied by Coors Ceramics. The RBSN ceramic samples were 6.15 mm thick and approximately 12.8 by 28 mm in size with 22 percent porosity.

(b) Ceramic Composite Samples. The SiC/RBSN ceramic matrix composite used in this study was a 28-ply unidirectional panel with 30 percent fiber volume and 30 percent matrix porosity. The sample was approximately 127 by 12.5 mm and 6.22 mm thick.

(c) Thermal Shock, and Oxidation Process. Thermal shock was applied to the monolithic ceramic samples by first slowly heating them to a predetermined elevated temperature, then holding at stabilized temperature for at least 15 minutes, followed by quenching into ice water.

The ceramic composite panel was cut into three samples for thermal oxidation experiments after the initial ultrasonic evaluation had been done. The thermal oxidation treatment is applied to the samples by directly heating the samples in flowing oxygen for 100 hours at different temperatures. The effect of damage due to thermal oxidation was then ultrasonically evaluated and results compared with those obtained prior to oxidation.

2.2 Experimental Apparatus. Ultrasonic measurements were made in the computer-controlled goniometer shown in Fig. 1. Angle resolution and repeatability were better than 0.01 deg. The water temperature inside the goniometer was stabilized at 29.8 ± 0.01°C. The advantage of this experimental system is that both transmitted and reflected ultrasonic signals can be measured at oblique incidence using only one transducer. The received signal is digitized and averaged by a LeCroy 9400 125 Mhz digital oscilloscope. The reflected signal was used for surface wave velocity measurements. The time delay of the transmitted (through the sample) signal is measured as a function of incident angle and is used to calculate wave propagation velocities at different refraction angles.

2.3 Surface Wave Measurements. Due to thermal shock numerous microcracks initiate from ceramic sample surfaces. Thus a technique for assessment of thermal shock damage initiation should be sensitive to property changes in the near surface region. For this reason, measurement of the velocity of the Rayleigh wave (surface wave with near-surface energy localization) is used (Hefetz and Rokhlin, 1992). Using Snell's law, the Rayleigh wave velocity can be determined by

$$V_R = \frac{V_o}{\sin \theta_R} \qquad (1)$$

where V_o is the wave velocity in the immersion fluid, V_R is the Rayleigh wave velocity, and θ_R is the Rayleigh critical angle, which can be measured by finding the incident angle corresponding to the dip in the reflection coefficient curve.

2.4 Bulk Ultrasonic Measurements. For the bulk properties, a self-referenced bulk wave method (Chu and Rokhlin, 1992) is utilized. The basic idea of this method is illustrated schematically in Fig. 2. The phase velocity at normal incidence is measured with high precision by overlapping multiple reflected signals from the front and back surfaces of the sample. The phase velocities in the samples at refraction angle θ_r (corresponding to the incident angle θ_i shown in Fig. 2) are calculated using the phase velocity in the normal direction V_n and the time delay change for the rotated sample (due to the acoustic path length and material velocity changes in the sample at angle θ_r relative to those at normal incidence):

$$V_{\theta_i}(\theta_r) = \left[\frac{1}{V_n^2} + \frac{\Delta t_o - (\Delta t_o + \Delta t_{\theta_i})\cos\theta_i}{hV_o} + \frac{\Delta t_{\theta_i}(2\Delta t_o + \Delta t_{\theta_i})}{4h^2}\right]^{-1/2} \qquad (2)$$

with

$$\theta_r = \sin^{-1}\frac{V_{\theta_i}\sin\theta_i}{V_o} \qquad (3)$$

Here V_n is the phase velocity at normal incidence, V_o is the sound speed in water, h is the thickness of the sample, $\Delta t_o = 2h(1/V_o - 1/V_n)$, and Δt_θ is the difference in the time-of-flight measurements between normal incidence and arbitrary oblique incidence at incident angle θ. Short pulses (1 to 1.5 periods)

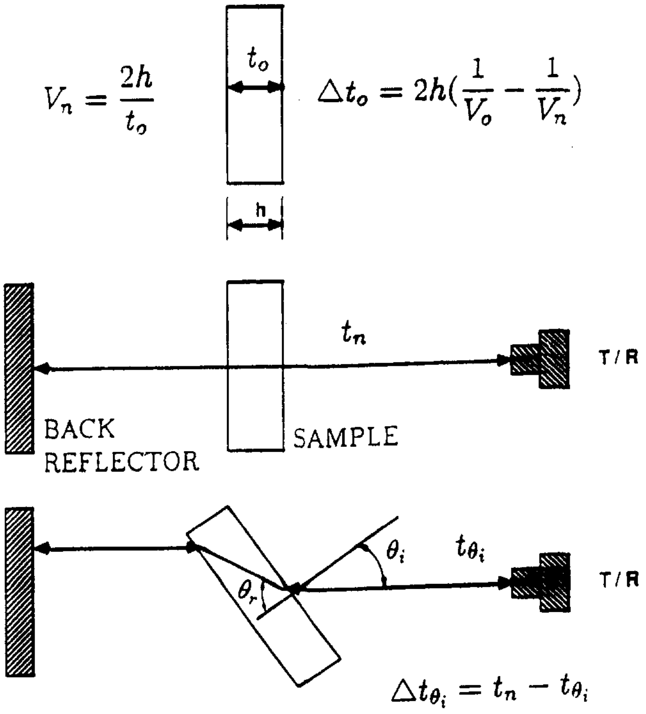

Fig. 2 Schematic diagram of the self-reference bulk wave method

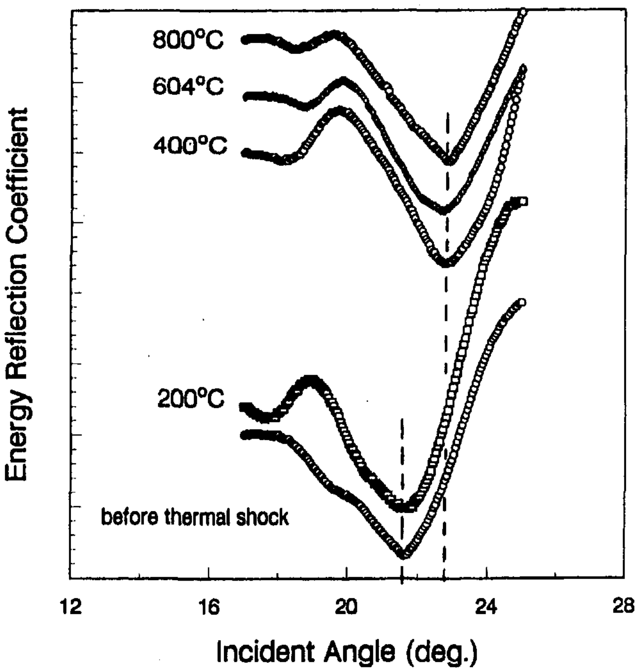

Fig. 3 Change of Rayleigh critical angle due to thermal shock for RBSN (2.25 MHz)

with central frequencies 2.25 or 5 MHz were used in the self-reference measurements.

3 Assessment of Thermal Shock Damage

3.1 Rayleigh Critical Angle Measurements in RBSN Ceramics. Thermal shock damage in monolithic RBSN samples was measured for different temperatures using the Rayleigh critical angle method at different frequencies. A low-frequency 2.25 MHz transducer was found to give better results because of the longer wavelength. As discussed in the introduction, the wavelength should be greater than the crack size and spacing in order to obtain the effective elastic properties of the damaged material. The actual microcrack density in RBSN is difficult to measure due to material porosity and inapplicability of the liquid penetrant method. Figure 3 shows the measured energy reflection coefficient versus incident angle for different thermal shock conditions. The coefficient is defined as ratio of the reflected energy flow to the incident wave energy flow. The dips in these curves represent the Rayleigh critical angles. From the results shown in Fig. 3, one can see that the change in the Rayleigh critical angle for thermal shock temperatures above 400°C is more than 1 deg (5 percent). At the system resolution (0.01 deg), the surface wave method provides sufficient sensitivity for determination of early-stage thermal shock microcrack damage.

We also found that the reduction of the Rayleigh wave velocity due to thermal shock correlates with the ultimate bending strength, as shown in Fig. 4, where the Rayleigh wave velocity and ultimate bending strength are plotted in the same graph. Data for strength are from Bhatt (1988). Although the data for strength may vary for materials made in different batches, the critical temperature for thermal shock is less affected by the manufacturing process. Thus the correlation shown in Fig. 4 indicates that the Rayleigh critical angle method is useful for determining the thermal shock critical temperature corresponding to damage initiation. For RBSN ceramics the critical temperature for thermal shock is about 400°C.

3.2 Bulk Ultrasonic Wave Measurements in Alumina Ceramics. The surface wave method is suited for surface and subsurface damage determination. Previous studies on thermal shock damage in alumina (Hasselman, 1970; Gupta, 1972; Hefetz and Rokhlin, 1992) have shown that its thermal shock critical temperature is about 200 to 300°C and substantial growth in crack density and length begins for thermal shock temperatures above 500°C. To measure samples with well-developed microcracks the ultrasonic bulk wave application is appropriate (Hefetz and Rokhlin, 1992). Bulk ultrasonic phase velocity measurement can be applied to determine the change of macroscopic elastic properties. Results from ultrasonic measurements can be used to determine the microcrack density using damage models or to investigate the applicability of damage theories by comparison with their predictions.

Damaged ceramic samples can be considered as layered media with damaged layers in the surface regions and undamaged layers in the center. With increase of thermal shock temperature the thickness of the damaged layers increases and finally the crack lengths become comparable to the sample thickness. In this case, the sample with distributed damage can be considered as a *homogeneous material with uniformly distributed microcracks*. To produce a uniform distribution of microcracks in the alumina sample, thermal shock temperatures were set at 600, 700, and 800°C. Samples were evaluated after thermal shock treatment using the bulk ultrasonic wave method described in section 2. The microcracks in alumina samples can be visualized by liquid penetrants. For the temperatures used, there are three to five cracks within one wavelength. The longitudinal wave velocity measurements versus refraction angle (angle of deviation from the sample surface normal) are shown in Fig. 5. The data are given for different thermal shock temperatures and for the sample without thermal shock. As one can see, the material shows increasing elastic anisotropy as the thermal shock temperature increases.

The preferred orientation of damage, as shown schematically in Fig. 6, leads to the appearance of strong elastic anisotropy. Strong dependence of velocity on angle of propagation can be observed in the thermal shock temperature range tested. The ultrasonic velocity in the direction along the crack orientation (normal to the sample surface) is weakly dependent on the damage. The velocities of waves propagating in directions perpendicular to the microcracks (higher refraction angle) are much more sensitive to the damage.

The elastic constants of the material have been calculated from the experimentally measured velocity using nonlinear least-square optimization (Rokhlin and Wang, 1992) to obtain

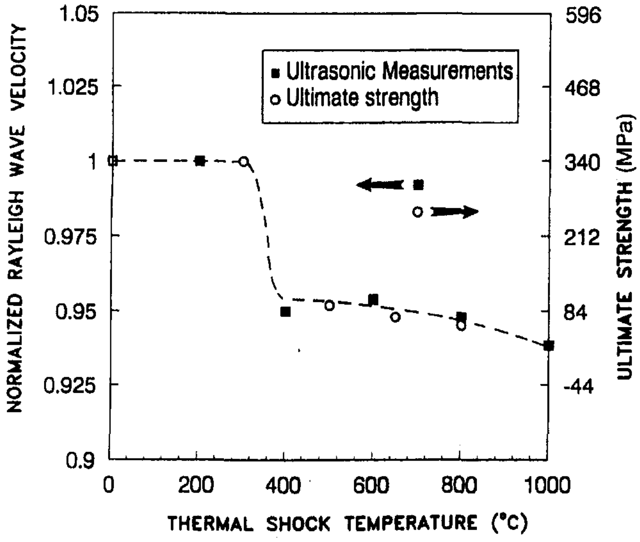

Fig. 4 Effect of thermal shock on Rayleigh wave velocities and ultimate bending strength of RBSN ceramics. The bending strength data are from Bhatt (1988).

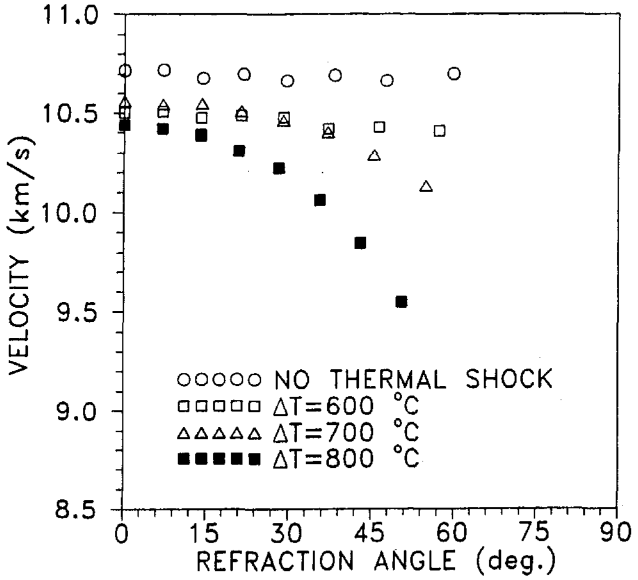

Fig. 5 Longitudinal wave velocities versus refraction angle for different thermal shock temperatures

the best fit to the solution of the Christoffel equation. The data are summarized in Table 1 for normal and shear moduli. One can see that for damaged materials the modulus C_{33}, where the 3 axis is perpendicular to the sample surface, has only a small change, while the moduli in the plane parallel to the surface (C_{11} and C_{22}) change significantly. Based on these results it can be concluded that the cracks from thermal shock are nearly normal to the sample surface. It is important that one can infer nondestructively the preferred microdamage orientation from ultrasonic data.

4 Damage Modeling and Determination of Microcrack Density

As discussed in the previous section, the thermal shock induced microcracks in ceramics are aligned along the sample surface normal. It is reasonable to model such cracks as two-dimensionally oriented slit cracks. To characterize the elastic properties of the cracked solid Laws and Brockenbrough (1987) introduced the compliance matrix S

$$\epsilon_i = S_{ij}\sigma_j \tag{4}$$

whose elements can be expressed in terms of the dimensionless crack density ξ and the compliance S_o of the nondamaged material:

$$S = S_o + \frac{\xi\pi^2}{4}\{\Lambda\} \tag{5}$$

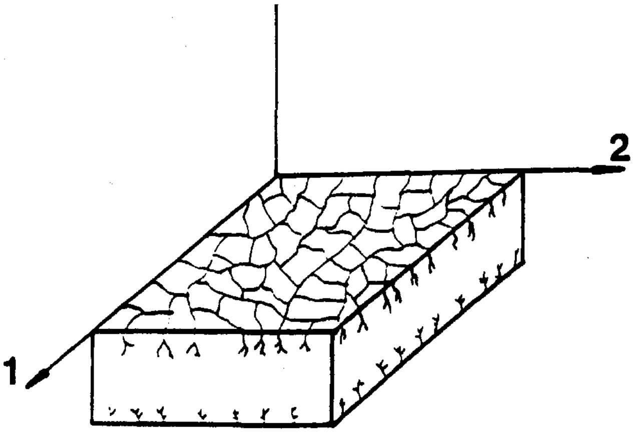

Fig. 6 Schematic illustration of thermal shock damage

The dimensionless crack density ξ for slit cracks with width $2a$ and length l is given by

$$\xi = Na^2l \tag{6}$$

where N is the number of cracks per unit volume. The 6 × 6 matrix $\{\Lambda\}$ is defined by the average crack energy $\{\Psi\}$ under the averaged loading $\bar{\sigma}$:

$$\{\Psi\} = \frac{\xi\pi^2}{8N}\bar{\sigma}\cdot\{\Lambda\}\cdot\bar{\sigma} \tag{7}$$

For samples with microcracks caused by thermal shock, it is reasonable to assume that the cracks are arbitrarily oriented in the 1–2 plane (Fig. 6). Assuming the nondamaged material is isotropic with Young's modulus E_o, Poisson's ratio ν_o, and shear modulus G_o, the nonvanishing components of the $\{\Lambda\}$ matrix are given by (Laws and Brockenbrough, 1987)

$$\{\Lambda\}_{11} = \{\Lambda\}_{22} = \frac{1}{E_t} - \frac{\nu_o^2}{E_o}; \tag{8}$$

$$\{\Lambda\}_{44} = \{\Lambda\}_{55} = \frac{1}{2G_a}; \tag{9}$$

$$\{\Lambda\}_{66} = 2\left(\frac{1}{E_t} - \frac{\nu_o^2}{E_o}\right) \tag{10}$$

where E_t and G_a are the transverse Young's modulus and axial shear modulus of the damaged material, respectively. Substituting $\{\Lambda\}$ into Eq. (5) the dimensionless crack density can be expressed in terms of the elastic properties of the damaged and nondamaged materials:

$$\xi = \frac{4(1 - E_t/E_o)}{\pi^2(1 - E_t\nu_o^2/E_o)} \tag{11}$$

Thus, we can determine the dimensionless crack density ξ from the Eq. (11) by measuring the elastic properties with and without thermal shock. It is clear from Eq. (11) that E_t vanishes (sample disintegrates) when $\xi = 4/\pi^2$. We expect that the experimentally determined crack density will not exceed this theoretical limit.

Here we apply the given formulas to determine the crack density in alumina samples after thermal shock treatment. The elastic properties of the nondamaged sample can be determined from the ultrasonic velocities (longitudinal wave velocity V_L = 10.7 km/s and transverse wave velocity V_T = 6.2 km/s) and the density (3.96 g/cm^3). The elastic moduli calculated from the ultrasonic velocities and material density are

$$E_o = 372 \text{ GPa}, \; G_o = 152 \text{ GPa, and } \nu_o = 0.25.$$

Using the elastic properties of alumina samples after thermal shock from different temperatures in Table 1, we can calculate the dimensionless crack density corresponding to different ther-

Table 1 Effect of thermal shock damage on elastic properties of alumina samples

Elastic properties	Without thermal shock	Thermal shock at 600 °C	Thermal shock at 700 °C	Thermal shock at 800 °C
C_{11}, GPa	453	450	427	355
C_{22}, GPa	453	450	427	355
C_{33}, GPa	453	439	446	436
C_{44}, GPa	152	136	133	127
C_{55}, GPa	152	136	133	127

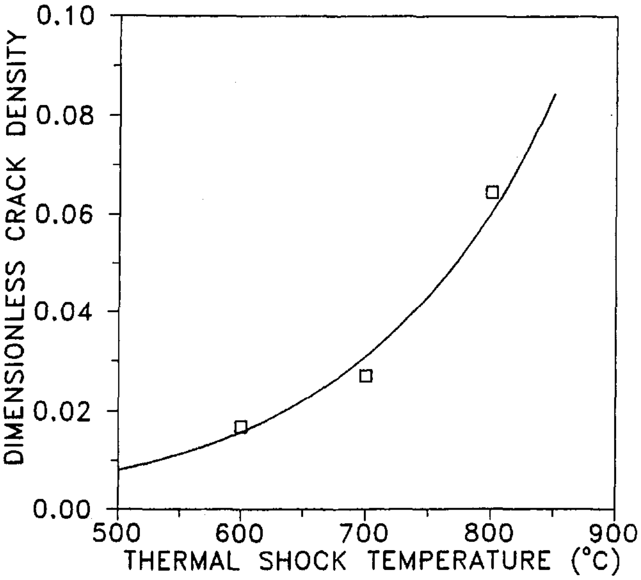

Fig. 7 The dimensionless crack density determined from ultrasonic data versus the thermal shock temperature

mal shock temperatures. Results of this calculation are shown in Fig. 7 where the dimensionless crack density is plotted as a function of thermal shock temperature. As can be seen, the crack density increases rapidly as the thermal shock temperature increases. Since the dimensionless crack density is defined in terms of the number of cracks per unit volume and the crack size, it is clear that its increase may be due either to increase in the number of cracks or to crack growth.

The ultrasonically measured elastic properties of cracked samples and those calculated using the damage model are shown in Fig. 8(*a, b*) for the transverse Young's modulus E_t and axial shear modulus G_a, respectively. In both figures the results are normalized to the moduli of the nondamaged material. The solid line is the calculated elastic modulus of the damaged material as a function of the dimensionless crack density ξ used in the damage model. The square points correspond to experimentally determined transverse (to the crack surfaces) moduli of the damaged samples. The good fit in Fig. 8(*a*) for the transverse Young's modulus is not surprising since the crack density has been found from experiment using the same model.

The results for the axial shear modulus are shown in Fig. 8(*b*). Two independent measurements using Rayleigh critical angle measurements (triangles; Hefetz and Rokhlin, 1992) and bulk wave velocity measurements (squares) are shown. As one can see the experimental results obtained from the two different measurements (bulk and Rayleigh angle methods) agree well. The ultrasonically determined axial shear moduli agree with those calculated using the damage theory but there is a systematic shift between these two at different crack densities. The reason for this difference may be due to microcrack branching, whereas the model assumes plane cracks vertically oriented. The crack branching effect also appears in the reduction of the elastic constant in the crack preferred direction, C_{33} (see Table 1), of the damaged samples, which is not expected for vertical cracks. Thus, the difference is primarily due to the simplified crack geometry in our model.

5 Ultrasonic Assessment of Thermal Oxidation Damage

SCS-6/RBSN composites are composed of CVD SiC fibers (SCS-6 from Textron), porous RBSN (Si_3N_4) matrix, and a carbon-rich coating as the interface between fiber and matrix. The CVD SiC fiber has a complex microstructure with a graphite-coated carbon core in the center surrounded by a transition zone and then a layer of β-SiC. The carbon-rich coating on the fiber surface is basically a mixture of graphite carbon and fine SiC particles. The RBSN matrix (Si_3N_4) has 20 to 40 percent porosity and a small amount of unreacted silicon. Most pores in the matrix are interconnected, which allows the oxygen to reach the fiber-matrix interface. Apparently high-temperature oxidation of the carbon coating may occur, leading to debonding of the fiber/matrix interfaces. Bhatt (1989) demonstrated that the strength and stiffness of SCS-6/RBSN composites are severely reduced after oxidation at different temperatures due to this phenomenon. We will demonstrate below that ultrasonic waves can be a powerful tool for assessing oxidation damage.

The as-received composite sample was evaluated prior to the oxidation study. The ultrasonic velocities in the as-received composite are shown by squares in Fig. 9. The elastic constants obtained from the measured velocity data are given in Table 2. After the initial ultrasonic measurement, the sample was cut into three pieces for thermal oxidation at different temperatures. The temperatures for thermal oxidation of these samples were 600, 1200, and 1400°C, respectively. The samples after heat

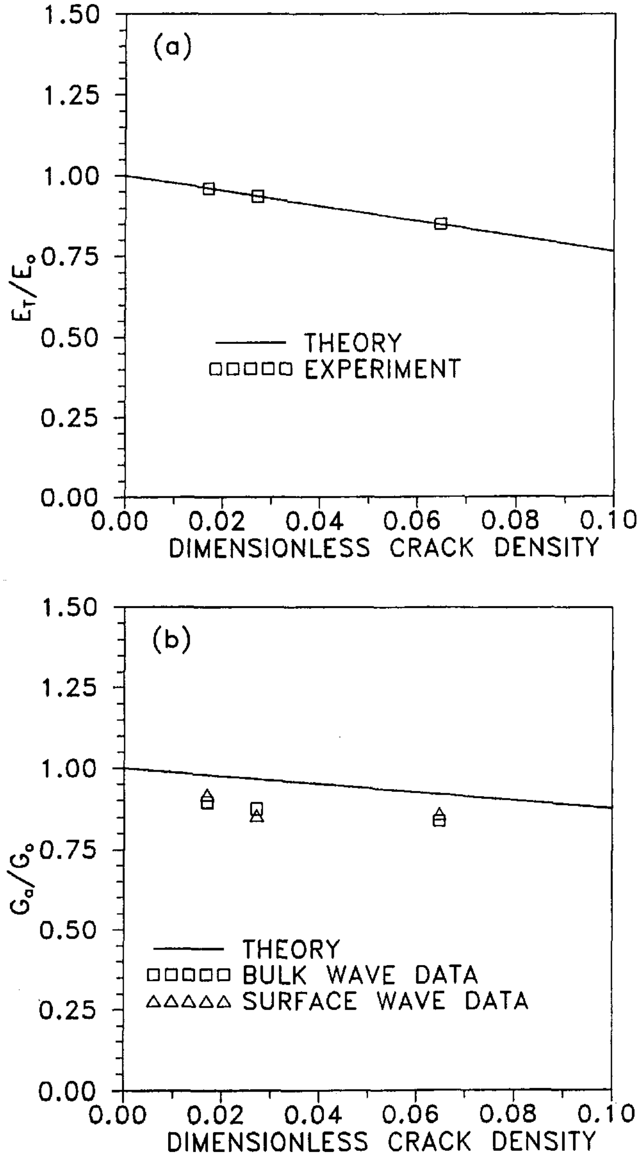

Fig. 8 Elastic moduli of a damaged material versus crack density: (*a*) transverse Young's modulus and (*b*) shear modulus along the crack direction. Solid line is theory and points are experiment.

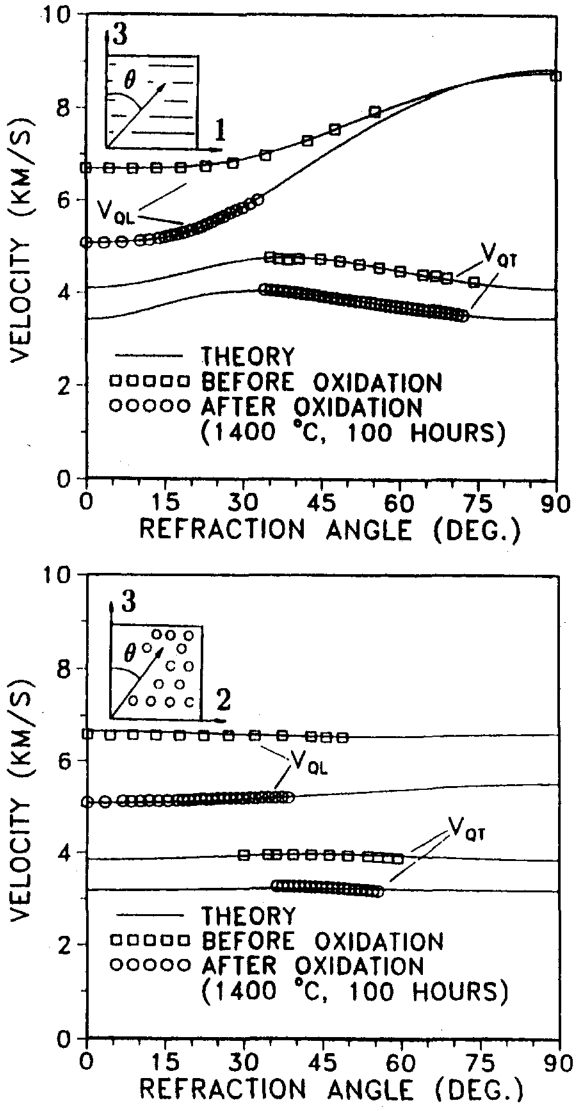

Fig. 9 The angular dependence of the phase velocities in the 1–3 and 2–3 planes for composite samples before and after 100 hour oxidation at 1400°C. The measured data are shown as discrete points and the solid lines are theoretical values calculated from the reconstructed elastic constants.

treatment in flowing oxygen for 100 hours were evaluated using the bulk ultrasonic wave method. A 2.25 MHz transducer was used for all the samples. The low frequency was selected to reduce ultrasonic attenuation.

As an example, Fig. 9 shows the comparison between the ultrasonic measurements of phase velocities for both quasi-longitudinal and quasi-shear waves before and after oxidation at 1400°C. Significant changes in phase velocities and angular dependence occur for both waves due to oxidation damage.

The elastic properties of samples oxidized at different temperatures were obtained from velocity data. The elastic constants and the density determined before and after oxidation are given in Table 2. Bhatt (1989) showed that at higher oxidation temperatures a layer of oxide diffusion barrier is formed on the surfaces of the samples. This minimizes the diffusion of oxygen through the pores. This is also supported by our density data indicating that impregnation of pores by water in the immersion test is significantly reduced after oxidation at temperature above 1200°C. Using elastic constants for samples oxidized at different temperatures, one can calculate the axial Young's modulus E_1 given in the last row of Table 2. The effect of thermal oxidation on the Young's modulus in the fiber direction is shown in Fig. 10 where the circular points are results of tensile tests reported by Bhatt (1989) and the rectangular points are results of ultrasonic measurements. As one can see, the agreement between these two results is good.

Two possible mechanisms for changes of the elastic moduli are suggested by Bhatt (1989). One is oxidation of the fiber surface coating and the other is oxidation of the carbon core. According to Bhatt, the oxidation of the carbon core at temperatures beyond 400°C extends at least 20 mm from the sample ends. Oxidation of the fiber coating was found at 600 and 1000°C in the cross section 25 mm from the sample ends. The stiffness of the fiber-matrix interface affects mostly the composite transverse and shear stiffnesses, and has very little effect on the composite longitudinal stiffness. Thus the ultrasonic results suggest that the dominant effect on the reduction of the transverse moduli C_{22} and C_{33} listed in Table 2 should be the oxidation of the fiber coating.

It has been shown (Chu and Rokhlin, 1992) that stiffnesses of the carbon core and the fiber coating are much lower than the stiffnesses of the RBSN matrix and the SiC fiber shell. Thus even though their volume fraction is about 5 to 6 percent of the composite, their contribution to the composite longitudinal stiffness is minor. The observed composite longitudinal stiffness reduction may be caused by fiber degradation due to oxidation. This degradation was observed by Bhatt (1989) for the reduction in the fiber tensile strength under the same oxidation conditions. If the fiber modulus has a similar reduction as the strength, it would explain the composite longitudinal stiffness reduction. In this case the SiC fibers in our experiment were degraded at 600°C by oxidation, while this degradation was prevented at higher temperature due to formation of an oxide layer on the sample surfaces.

Another possible explanation of the reduction of the composite longitudinal stiffness (Fig. 10) in the intermediate temperature range of oxidation is the loss of interfacial bonding due to oxidation of the interphasial layer and thus elastic coupling between fibers and matrix. The retention composite longitudinal stiffness at higher temperatures of oxidation (above 1200°C) may be caused by the formation of bridging interlocks between fibers and matrix due to the reaction product SiO_2. Gravitometry study on oxidation of SiC/RBSN composites (Bhatt, 1989) showed that substantial weight gain was found for composites oxidized at temperatures above 1000°C while no weight gain was found for composites oxidized at intermediate temperatures. Also recent studies (Kooner et al., 1993; Tortorelli et al., 1993) have shown experimental evidence for the formation of such interphasial oxide bridges in Si-based ceramic composites after oxidation. Partial fiber to matrix bonding by bridges leads to transfer of longitudinal loading from matrix to fibers, thus maintaining longitudinal stiffness. This is analogous to small sensitivity to cracks of the longitudinal waves (Fig. 5) propagating along the crack direction (0° in Fig. 5). On the other hand,

Table 2 Properties of SCS-6/RBSN composites before and after 100 hour oxidation at different temperatures

Conditions/ properties	Before oxidation	Oxidized at 600 °C	Oxidized at 1200 °C	Oxidized at 1400 °C
Density (dry) g/cc	2.51	2.48	2.55	2.50
Density (wet) g/cc	2.70	2.68	2.58	2.59
C_{11} (GPa)	207	161	203	203
C_{22} (GPa)	118	87.7	67.5	78.6
C_{33} (GPa)	120	79.4	55.4	66.6
C_{12} (GPa)	32.3	N/A	N/A	20.1
C_{13} (GPa)	32.0	28.9	15.9	20.1
C_{23} (GPa)	33.4	N/A	N/A	17.9
C_{44} (GPa)	40.1	N/A	N/A	26.3
C_{55} (GPa)	45.2	24.0	24.4	30.6
C_{66} (GPa)	43.4	N/A	N/A	31.2
E_1 (GPa)	193	145	194	193

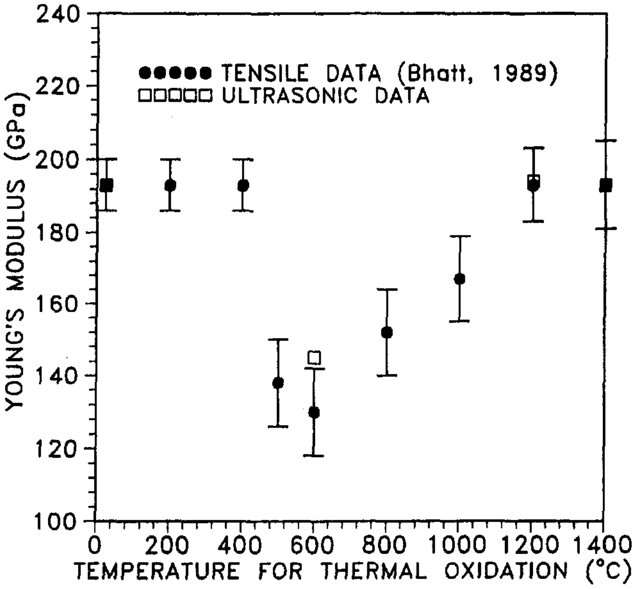

Fig. 10 The reduction of composite longitudinal Young's modulus as a function of oxidation temperatures

the ultrasonic waves are very sensitive to fiber/matrix debonding in the transverse direction, which is reflected in a significant reduction of transverse and shear moduli at all oxidation temperatures.

6 Summary

This study focuses on ultrasonic assessment of the effects of thermally induced damage on ceramics and ceramic matrix composites. Ultrasonic bulk and surface wave methods were used to assess thermal shock damage in ceramics and thermal oxidation damage in ceramic matrix composites. The assessment of microcrack damage in ceramics is based on measurements of damage-induced elastic property changes. In the initial stages of the damage when microcracks initiate from the sample surface, the ultrasonic surface waves are used. These measurements can estimate the thermal shock critical temperature and correlate the stiffness reduction to the ultimate strength of the sample. For severely damaged materials, bulk waves are used to measure the damage-induced elastic anisotropy, which relates to microcrack density and orientation.

For ceramic matrix composites oxidized at elevated temperatures for 100 hours, significant changes in both shear and longitudinal velocities are observed. Variation of elastic constants obtained by ultrasonic measurements suggests that the dominant mechanism for the reduction of the transverse and shear properties is oxidation of the fiber-matrix interface. The reduction of the longitudinal stiffness appears to be influenced by degradation of SiC fibers. It was demonstrated that ultrasonic measurements show good correlation with the results of destructive methods in thermal shock and oxidation damage assessment.

Acknowledgments

This work was sponsored by NASA Lewis Research Center under grant #NAG3-1220. The authors would like to thank Mr. Meir Hefetz for his help with experiments and Dr. R. T. Bhatt for providing SiC/RBSN composite samples.

References

Bhatt, R. T., 1988, "Properties of Silicon Carbide Fiber-Reinforced Silicon Nitride Matrix Composites," NASA TM-101356.

Bhatt, R. T., 1989, "Oxidation Effect on the Mechanical Properties of SiC Fiber-Reinforced Reaction-Bonded Silicon Nitride Matrix Composites," NASA TM-102360.

Budiansky, B., and O'Connell, R. J., 1976, "Elastic Moduli of a Cracked Solid," *Int. J. Solids Structures*, Vol. 12, pp. 81–97.

Chu, Y. C., and Rokhlin, S. I., 1992, "Determination of Macro and Micromechanical and Interfacial Elastic Properties of Ceramic Matrix Composites From Ultrasonic Data," *J. Acoust. Soc. Am.*, Vol. 92, pp. 920–931.

Evans, A. G., and Marshall, D. B., 1988, "The Mechanical Properties of Fiber Reinforced Ceramic Matrix Composites," *Mat. Res. Soc. Symp. Proc.*, Vol. 120, pp. 213–246.

Gupta, T. K., 1972, "Strength Degradation and Crack Propagation in Thermally Shocked Al_2O_3," *J. Am. Ceram. Soc.*, Vol. 55, pp. 249–253.

Hasselman, D. P. H., 1969, "Unified Theory of Thermal Shock Fracture Initiation and Crack Propagation in Brittle Ceramics," *J. Am. Ceram. Soc.*, Vol. 52, pp. 600–604.

Hasselman, D. P. H., 1970, "Strength Behavior of Polycrystalline Alumina Subjected to Thermal Shock," *J. Am. Ceram. Soc.*, Vol. 53, pp. 490–495.

Hefetz, M., and Rokhlin, S. I., 1992, "Thermal Shock Damage Assessment in Ceramics Using Ultrasonic Waves," *J. Am. Ceram. Soc.*, Vol. 75, pp. 1839–1845.

Kooner, S., Lawrence, C. W., and Derby, B., 1993, "High Temperature Interfacial Shear Strength Testing of Ceramic Matrix Composites," *Ceram. Eng. Sci. Proc.*, Vol. 14, No. 7–8, pp. 229–236.

Laws, N., and Brockenbrough, J. R., 1987, "The Effect of Micro-Crack Systems on the Loss of Stiffness of Brittle Solids," *Int. J. Solids Structures*, Vol. 23, pp. 1247–1268.

Lutz, E. H., Swain, M. V., and Claussen, N., 1991, "Thermal Shock Behavior of Duplex Ceramics," *J. Am. Ceram. Soc.*, Vol. 74, pp. 19–24.

Prewo, K. M., 1988, "Glass and Ceramic Matrix Composites Present and Future," *Mat. Res. Soc. Symp. Proc.*, Vol. 120, pp. 145–156.

Rokhlin, S. I., and Wang, W., 1992, "Double Through-Transmission Bulk Wave Method for Ultrasonic Phase Velocity Measurement and Determination of Elastic Constants of Composite Materials," *J. Acoust. Soc. Am.*, Vol. 91, pp. 3303–3312.

Tortorelli, P. F., Nijhawan, S., Riester, L., and Lowden, R. A., 1993, "Influence of Fiber Coatings on the Oxidation of Fiber-Reinforced SiC Composites," *Ceram. Eng. Sci. Proc.*, Vol. 14, No. 7-8, pp. 358–366.

A. Saith
Sundstrand Power Systems,
San Diego, CA 92123

P. F. Norton

V. M. Parthasarathy

Solar Turbines Inc.
San Diego, CA 92101

Application of SPSLIFE to Preliminary Design Evaluation and Life Assessment of CSGT Components

The Ceramic Stationary Gas Turbine (CSGT) Program has utilized the SPSLIFE computer code to evaluate the preliminary design of ceramic components. The CSGT program is being performed under the sponsorship of the United States Department of Energy, Office of Industrial Technology, to improve the performance of stationary gas turbines in cogeneration through the selective replacement of hot section components with ceramic parts. Preliminary design evaluation and life assessment results are presented here for the following components: (1) Stage 1 turbine blade, (2) Stage 1 turbine nozzle, and (3) combustor inner liner. From the results of the analysis, recommendations are made for improving the life and reliability of the components. All designs were developed in Phase I (preliminary design) of the CSGT program and will be optimized in Phase II (detail design) of the program.

Introduction

The widespread use of ceramics has been limited by concerns about reliability and life. Several strategies have been employed to address these issues. Clean room environments during processing have reduced the presence of inclusions. Hot isostatic pressing has reduced the size of internal voids. Sophisticated in-process inspection procedures and component proof testing have helped to eliminate defective components. Despite considerable progress in these areas, however, the relatively low fracture toughness of ceramics results in critical flaw sizes that are generally too small to be detected reliably, and it becomes necessary to resort to statistical analysis to evaluate the interaction of the stress distribution in the component with the postulated flaw distribution.

The gas turbine design engineer with conventional metallic component design experience is accustomed to working with fixed, deterministic design criteria: a set of rules evolved over time to ensure that operation under all loading conditions is safe, given the prescribed service design life required for a competitive offering in the marketplace. Acceptable maximum design stresses are identified, and the designer uses these limits for conceptualizing a safe metallic component. With ceramics, however, the design criteria for fast fracture and slow crack growth failure modes are statistical in nature, requiring the analytical assessment of component life and reliability. The optimum design of highly stressed ceramic components thus becomes an iterative process, where the mechanical designer initially conceptualizes a preliminary design, which will require modifications based on the results of the stress, life, and reliability analyses.

Ceramic component survival probabilities should be specified by the turbine designer prior to component design. The issue of what constitutes an acceptable survival probability will be addressed by selecting survival probability levels that are consistent with data taken from current production metallic field engines.

SPSLIFE Computer Code

To improve the process of preliminary design evaluation and life assessment, the Ceramic Stationary Gas Turbine (CSGT) program (Van Roode et al., 1994) has utilized the proprietary "SPSLIFE" computer code developed by Sundstrand Power Systems. SPSLIFE is a user-friendly, interactive program for the evaluation of ceramic turbine engine components (Bomemisza and Saith, 1994). The program is used for materials selection, design evaluation, and life assessment.

Figure 1 shows how the SPSLIFE program links structural analysis (finite element) files and materials data files with life assessment modules for different modes of failure to provide quantitative estimates of component life and survival probability. Stress, temperature, and geometry data are extracted from the structural analysis files. Temperature-dependent material parameters such as characteristic strength and Weibull modulus, slow crack growth constants, creep and oxidation data are extracted from the materials files. The analysis produces presentation quality Design Assessment Maps (DAM) depicting stress and temperature distributions for the components together with design envelopes for fast fracture, slow crack growth, creep and oxidation. Cyclic fatigue, proof testing, and wear modules are also planned.

SPSLIFE Design Assessment Maps are component-specific, and provide a graphic overview of the design evaluation results. The maps are based on the "fracture map" concept discussed in the ceramics literature (Quinn and Wiederhom, 1993), and follow the general layout previously published (Soma et al., 1987). The stress/temperature distributions plotted on the SPSLIFE DAMs are derived from finite element nodal values, as distinct from other element locations such as integration points. The results presented in this report use an oxidation analysis model based on previous work in this area (Soma et al., 1987), and a creep model published in the literature (Wiederhom et al., 1991). The fast fracture model uses enhanced uniaxial Weibull methodology (Weibull, 1951) distinguishing between three different categories of flaws: internal or "volume" flaws, as-fired surface flaws, and machined surface flaws. The slow crack growth or static fatigue model uses Evans–Wiederhom methodology (Wiederhom, 1974) again distinguishing between internal flaws, as-fired surface flaws, and machined surface flaws. The program requests separate materi-

---

Contributed by the International Gas Turbine Institute and presented at the 39th International Gas Turbine and Aeroengine Congress and Exposition, The Hague, The Netherlands, June 13–16, 1994. Manuscript received by the International Gas Turbine Institute February 26, 1994. Paper No. 94-GT-420. Associate Technical Editor: E. M. Greitzer.

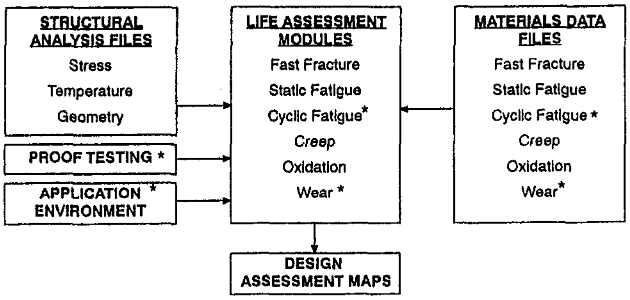

*** Not implemented to date.**

Fig. 1 SPSLIFE design concept

als data file entries for each category of flaws to ensure that proper attention is given to surface properties.

For fast fracture and for slow crack growth, three design envelopes are shown on the Design Assessment Map corresponding to three different survival probabilities; any nodes above and to the right of these contours show that the design goal is not being met. For reference, independently derived component fast fracture and slow crack growth survival probabilities using the NASA CARES and CARES/LIFE codes are shown in the top right hand corner of SPSLIFE Design Assessment Maps. Further information on the NASA programs can be obtained in other NASA publications (Nemeth, 1993).

Application to CSGT Program

Results for three CSGT components are presented in this paper:

- Stage 1 turbine blade
- Stage 1 turbine nozzle
- Inner combustor liner

Two scenarios are evaluated for the turbine blade, four scenarios for the turbine nozzle, and three designs for the inner combustor liner. The analyses are based on component finite element models that were created in Phase I of the CSGT program, and should be considered preliminary in nature. The preliminary finite element models are relatively coarse, for the purpose of rapidly obtaining "first-cut" results. It should also be noted that the analysis results have not been adequately calibrated against test data at the time of writing. Stress data from the finite element analyses, as well as the temperature ranges used, are listed in Table 1. All stress results are linear elastic, representative of engine steady-state conditions at 1121°C (2050°F) turbine rotor inlet temperature and 14,950 rpm.

Blade Design Evaluation and Life Assessment

The leading candidate for the root attachment of the turbine blade has evolved as a conventional "dovetail" design, such as that used on several other external ceramic programs. The airfoil is the same as the current production engine, but solid and uncooled, instead of using internal cooling passages. Two scenarios were evaluated for this design, and are presented below. In the first scenario, the blade root is machined, and the airfoil is in the as-fired condition. This is referred to as Condition 1. In the second scenario, the entire surface of the blade is machined, designated as Condition 2. For both scenarios, the blade material evaluated is a commercial silicon nitride material, designated as Material A. Separate material properties are entered for as-fired and machined surfaces.

The temperature map and the stress map of the dovetail blade are shown in Figs. 2(*a*) and 2(*b*) respectively. The Design Assessment Map for Material A, Condition 1, is shown in Fig. 3.

Interpretation of SPSLIFE Design Assessment Maps. Design envelopes for the primary failure modes, fast fracture, slow crack growth, creep, and oxidation can be identified in the map legend, and are represented by solid, dash, dash-dot, and dot line types, respectively. The vertical location of these lines is dependent upon both a user-defined reliability required by program goals, and the stress distribution within the component. (It should be emphasized that the solid lines and dashed lines bear no relationship to the vertical stress scale; the designer is simply interested in the proximity of the stress/temperature points with the failure envelope). For this reason the lines, or failure envelope, can be described as "component specific," and cannot be set without a detailed knowledge of the stress spectrum within the part.

The three solid lines represent fast fracture failure contours for three preselected component survival probabilities derived from program design objectives. The fast fracture failure equation is satisfied *only* for the contour that passes through the highest stress node point. It may be that the highest stress node point does not pass through one of the three lines. In that case, the user can estimate the survival probability by examining the relative location of the highest stress node point with respect to the three contours.

For a single reliability, the probabilistic summation of effective volume, effective machined surface area, and effective as-processed surface area of the component is calculated, using the respective material characteristic strength and Weibull moduli of all three flaw conditions in the calculations. The fast fracture survival probability of the component, for example, is estimated by visually examining the location of the highest stress points with respect to the solid lines. The diamonds and circles on the map represent the maximum nodal principal stress and temperature values throughout the component based on the ANSYS finite element stress analysis. The diamonds represent surface nodes, and are superimposed on the circles, which represent volume nodes. The fast fracture survival probability predicted by the NASA CARES program is also shown for reference on the top right-hand corner of the map. NASA CARES results are frequently used for quantitative work. A value of 0.8 was used for the Shetty constant in the CARES analysis.

Similarly, the three dashed lines represent the slow crack growth failure contours. Again, these are based upon the probabilistic summation of effective volume, effective machined surface area, and effective as-processed surface area of the component, as for the solid lines. The slow crack growth survival probability of the component is estimated by visually examining the location of the highest stress points with respect to the dashed lines. Again, it should be emphasized that the vertical scale does not apply to the dashed lines representing the slow crack growth envelopes. The slow crack growth survival probability predicted by the NASA CARES/LIFE program is also shown for reference on the top right-hand corner of the map. CARES/LIFE results have been used for quantitative assessments. A value of 0.8 was used for the Shetty constant in the CARES/LIFE analysis.

The creep line represents the stress–temperature envelope for a 30,000 hour creep life, which is the current design "life" for the CSGT program. When all the diamonds and circles are to the left of and below this line, the component is assessed to have adequate reliability in the creep mode. Predicted creep life for the component can be seen on the right-hand side of the map.

Similarly, the oxidation line represents the stress–temperature limit for a 30,000 hour oxidation life. When all the diamonds and circles are to the left of and below this line, the component is assessed to be safe in the oxidation mode. Predicted oxidation life for the component is shown on the right-hand side of the map.

Table 1 General component descriptions

Component	Material	FE Model: Number of Brick Elements (Shell Surface Elements)	Temperature Range	Surface Stress MPa (ksi)	Internal Stress MPa (ksi)
Turbine Blade	Silicon Nitride (A)	2042 (1849)	650 °C - 1090 °C (1200 °F - 2000 °F)	173 (25.6)	186 (27)
Turbine Nozzle	Silicon Nitride (A) Silicon Carbide (B)	3522 (5475)	834 °C - 1291 °C (1534 °F - 2356 °F)	234 (34) 317 (46)	241 (35) 324 (47)
Axial Tile	Silicon Carbide (B)	392 (560)	1010 °C - 1365 °C (1850 °F - 2490 °F)	189 (27.4)	191 (27.7)
Integral Inner Liner	Silicon Carbide (B)	4480 (5120)	1010 °C - 1365 °C (1850 °F - 2490 °F)	198 (28.7)	197 (28.6)
4-Ring Inner Liner	Silicon Carbide (B)	4480 (4160)	1010 °C - 1365 °C (1850 °F - 2490 °F)	75 (10.9)	78 (11.3)

DAM for Turbine Blade, Material A, Condition 1. This scenario represents the dovetail blade in the standard condition, with machined blade root and the airfoil in the as-fired condition. The Design Assessment Map for this scenario is shown in Fig. 3. The map is plotted for a design life of 30,000 hours, and assumes that the blade is made from a commercial silicon nitride material designated as Material A.

The creep line represents the boundary for a 30,000 hour creep life. Since all the diamonds and circles are to the left of and below this line, the component is assessed to be safe in the creep mode. Creep life for the component is assessed to be greater than one billion hours. The oxidation line represents the boundary for a 30,000 hour oxidation life. Since all the diamonds and circles are to the left of and below this line, the component is assessed to be safe in the oxidation mode. Oxidation life for the component is assessed to be greater than one billion hours. However, it should be noted that the oxidation life numbers are based on generic silicon nitride data as suitable oxidation data for Material A were not available.

The solid lines correspond to cumulative fast fracture survival probabilities of 99.0, 99.5, and 99.9 percent, respectively. The SPSLIFE estimate for the fast fracture survival probability of the blade is 99.8 percent. The fast fracture survival probability predicted by the NASA CARES program for the blade is 99.73 percent. The dashed lines correspond to cumulative slow crack growth survival probabilities of 99.0, 99.5, and 99.9 percent, respectively, for each blade. The SPSLIFE estimate for the slow crack growth survival probability is 99.0 percent. The slow

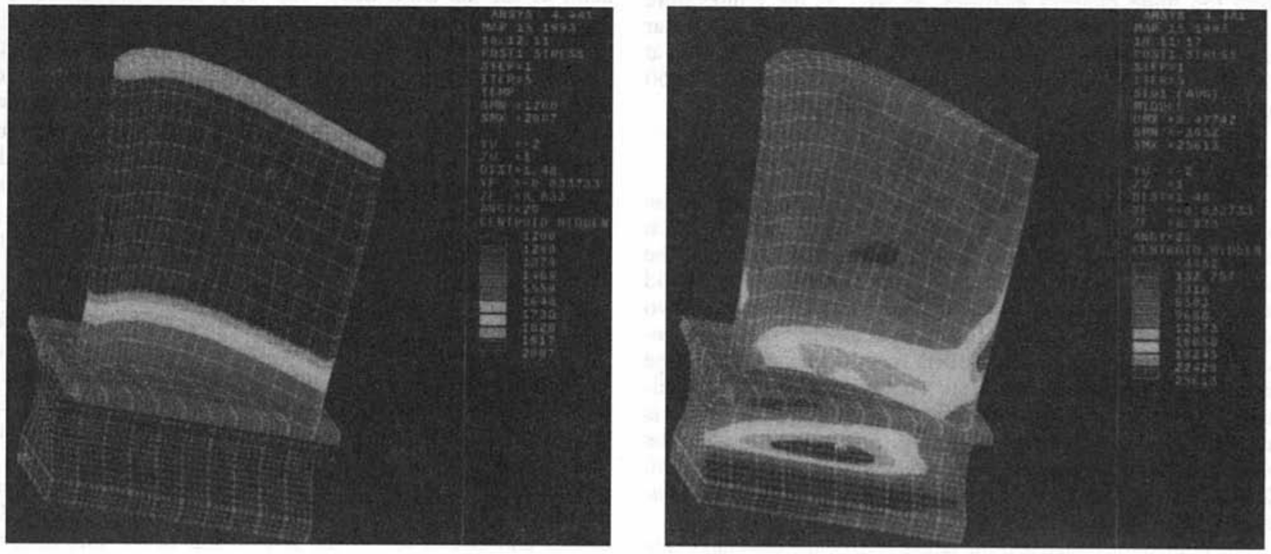

(A) Temperature Map

(B) Stress Map

Fig. 2 Finite element maps of the ceramic dovetail blade

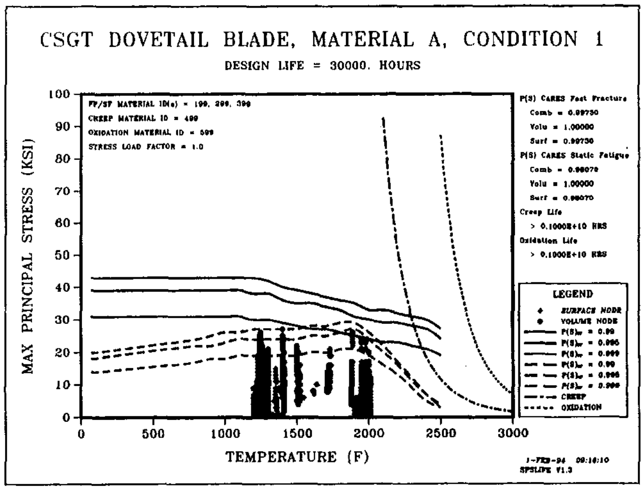

Fig. 3 Design assessment map for ceramic dovetail blade: Material A, condition 1

crack growth survival probability predicted by CARES/LIFE is 98.07 percent. CARES/LIFE results have been used for quantitative assessment.

Due to lack of more specific data for different flaw populations, the analysis uses the same temperature-dependent slow crack growth parameter values for the three flaw populations defined above. The eventual effect of engine environment on slow crack growth parameters is not represented by the materials data. These conditions apply to all the designs described in this paper.

DAM for Turbine Blade, Material A, Condition 2. Figure 4 shows the Design Assessment Map for the fully machined dovetail blade. This is an analysis that assumes all as-processed surfaces on the blade have been machined to obtain typical ''as-machined'' properties. This map is drawn with preselected probabilities of survival of 99, 99.9, and 99.99 percent. Results represent the upper bound survival probabilities achievable by grinding or by abrasive flow machining. SPSLIFE survival probabilities for each blade are greater than 99.99 percent in fast fracture and in slow crack growth. The CARES/LIFE survival probability is higher than in Condition 1, increasing to nearly 100 percent in fast fracture, and to 99.99 percent in slow crack growth.

Blade Summary. The dovetail blade with machined root and as-fired airfoil surfaces looks marginal in slow crack growth. This weakness is eliminated by fully machining the blade. However, a more practical alternative may be to select a blade material that has better surface strength and/or better slow crack growth properties. Alternative silicon nitride materials are being examined to meet these requirements. Also, attempts are under way to reduce the stresses in the airfoil to acceptable limits.

Nozzle Design Evaluation and Life Assessment

The preliminary temperature and stress maps of the turbine nozzle are shown in Figs. 5(*a*) and 5(*b*), respectively. Attempts to lower the stress levels at the airfoil trailing edge centered on cutbacks at the trailing edge. From a preliminary design perspective, removal of a few elements at the trailing edge was a quick method of investigating this approach. The resulting stress map is shown in Fig. 5(*c*).

The turbine nozzle was evaluated for two materials: a commercial silicon nitride material previously designated as Material A, and a commercial silicon carbide material designated as Material B. In addition, several scenarios were run to study the impact of successfully lowering the maximum nozzle stress to 138 MPa (20 ksi).

DAM for Turbine Nozzle, Material A. The Design Assessment Map for the nozzle using Material A is shown in Fig. 6. The map is plotted for a design life of 30,000 hours. Several diamonds and circles are above the creep envelope, indicating that the component has unacceptable reliability in the creep mode. Creep life for the component is assessed to be 4100 hours. The solid lines correspond to SPSLIFE cumulative fast fracture survival probabilities of 90.0, 95.0, and 99.0 percent, respectively, for each nozzle segment. The SPSLIFE Design Assessment Map shows that the nozzle is assessed to be safe at these probability levels. The fast fracture survival probability predicted by the NASA CARES program for each nozzle segment is 99.97 percent. The dashed lines show that the nozzle has unacceptable reliability in slow crack growth. CARES/LIFE shows slow crack growth survival probability of 1.76 percent.

DAM for Turbine Nozzle, Material A at 138 MPa (20 ksi). An analysis was performed to determine the impact of successfully lowering the maximum stress in the nozzle to 20 ksi. A load factor of 0.57 was applied to the stress spectrum in the above model. The Design Assessment Map for this analysis is shown in Fig. 7. The map is plotted for a design life of 30,000 hours. For the peak stress of 138 MPa (20 ksi), the component is safe in the creep and oxidation modes. Creep life for the component is assessed to be 378,000 hours, and oxidation life is assessed to be greater than one billion hours. Fast fracture is also not a problem. The fast fracture survival probability for each nozzle segment approaches 100 percent. However, the nozzle segment is marginal in slow crack growth. The slow crack growth survival probability predicted by the CARES/LIFE program for each nozzle segment is 98.24 percent.

DAM for Turbine Nozzle, Material B. The Design Assessment Map for the silicon carbide pinned nozzle is shown in Fig. 8. The map is plotted for a design life of 30,000 hours. The stresses are higher than for the silicon nitride nozzle, as shown in Table 1. However, this material is more resistant to creep. Creep life for the component is assessed to be 1,193,000 hours. An oxidation analysis was not performed due to lack of adequate data. However, the component is expected to be safe in this failure mode. The solid lines show that the nozzle segment has slightly less than 90 percent probability of survival in fast fracture, which is assessed to be unsafe. The fast fracture survival probability predicted by the NASA CARES program

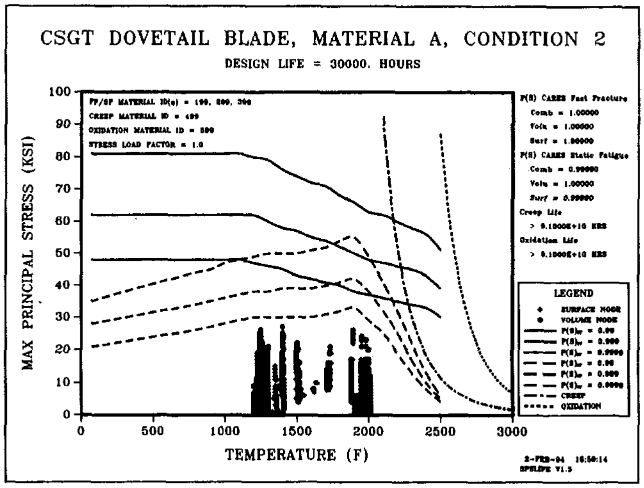

Fig. 4 Design assessment map for ceramic dovetail blade: Material 1, condition 2

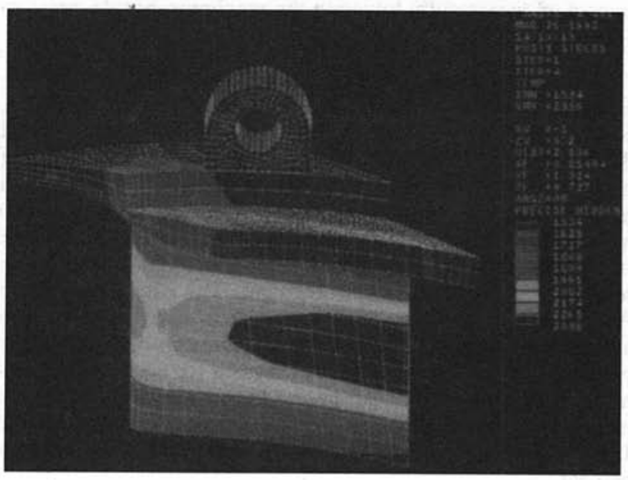

(A) Temperature Map

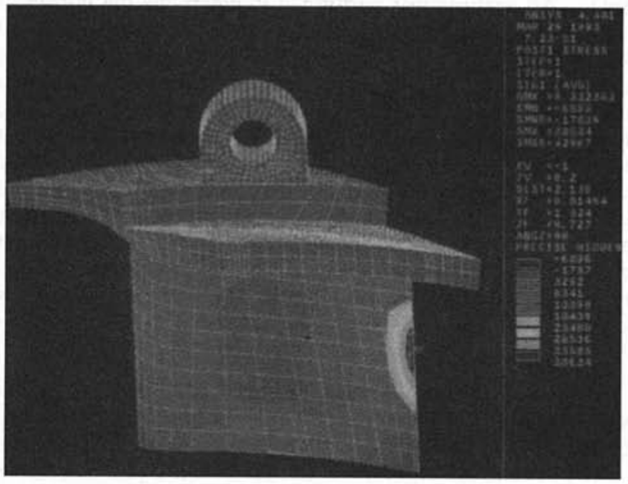

(B) Stress Map

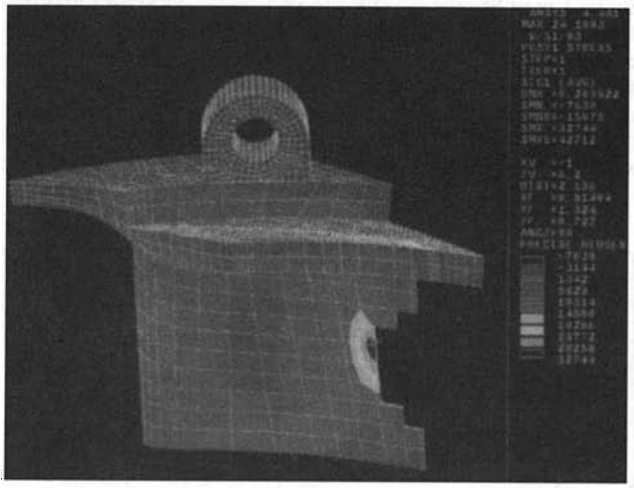

(C) Stress Map (Nozzle With Cutbacks)

Fig. 5 Finite element maps of the ceramic nozzle

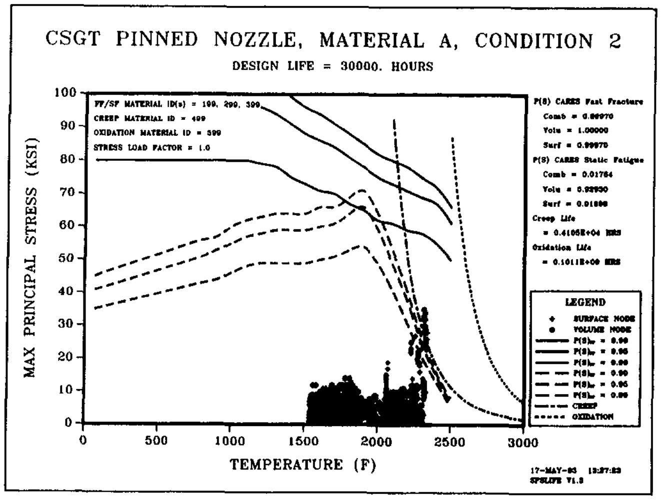

Fig. 6 Design assessment map for ceramic nozzle: Material A

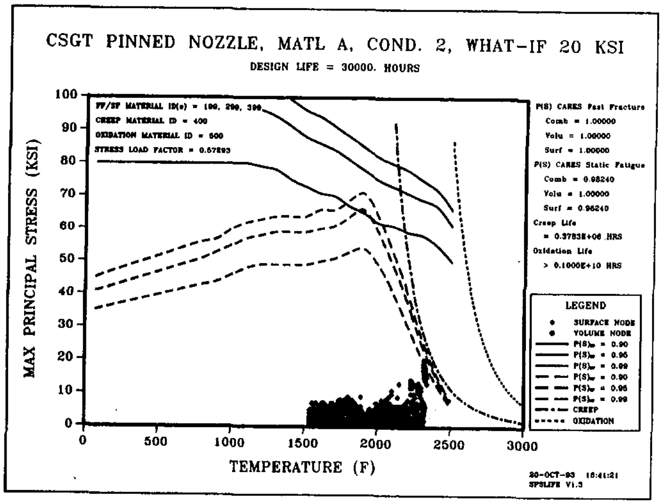

Fig. 7 Design assessment map for ceramic nozzle: Material A, maximum stress reduced to 20 ksi

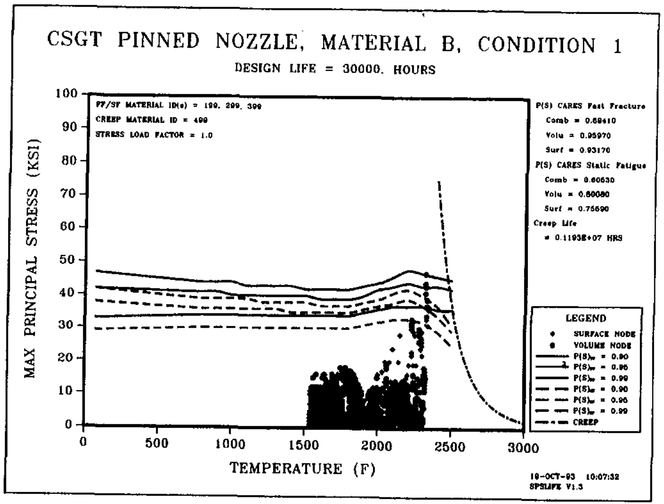

Fig. 8 Design assessment map for ceramic nozzle: Material B

for each nozzle segment is 89.41 percent. The dashed lines show that the nozzle is not safe in slow crack growth. The slow crack growth survival probability predicted by the NASA CARES/LIFE program for each nozzle segment is 60.53 percent.

DAM for Turbine Nozzle, Material B at 138 MPa (20 ksi). As with Material A an analysis was performed to determine the impact of successfully lowering the maximum stress in the noz-

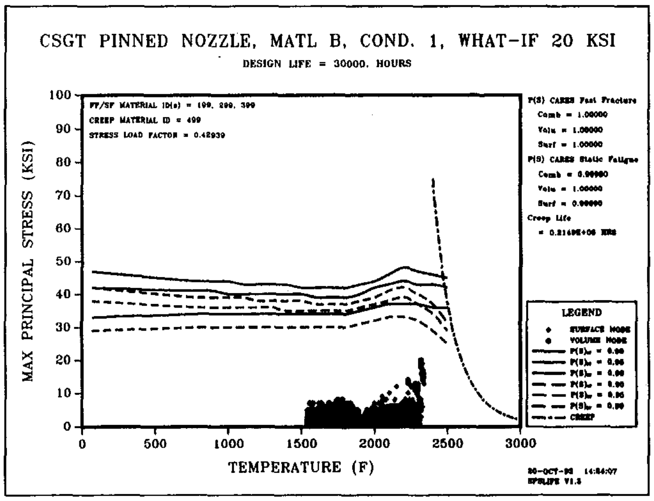

Fig. 9 Design assessment map for ceramic nozzle: Material B, maximum stress reduced to 20 ksi

zle to 20 ksi. A load factor of 0.43 was applied to all the stresses in the above model. The Design Assessment Map for the analysis is shown in Fig. 9. The map is plotted for a design life of 30,000 hours.

Creep life for the component increases to 21,486,000 hours. The solid lines show that fast fracture is no longer a problem. The fast fracture survival probability predicted by the NASA CARES program for each nozzle segment approaches 100 percent. The dashed lines show that the nozzle is also safe in slow crack growth. The slow crack growth survival probability predicted by the NASA CARES/LIFE program for each nozzle segment is 99.98 percent.

Nozzle Summary. The turbine nozzle encounters high stresses at high temperatures, and is a challenging component to design. The silicon nitride version of the nozzle is marginal in creep and unsafe in slow crack growth. The silicon carbide version, on the other hand, is unsafe in fast fracture and in slow crack growth. The 138 MPa (20 ksi) analyses show that if the maximum stress is lowered to 20 ksi, the silicon nitride nozzle would still be marginal in slow crack growth. The silicon carbide nozzle would be safe at 20 ksi; however, it is harder to reduce the maximum stress to 20 ksi for silicon carbide than for silicon nitride due to the higher elastic modulus of silicon carbide.

Two recommendations emerge from these results: (*i*) select a material that has a better combination of fast fracture, slow crack growth, and creep properties, and (*ii*) investigate design improvements to lower the stresses and/or temperatures while minimizing effect on performance. Both directions are being pursued in Phase II of the CSGT program.

Combustor Liner Design Evaluation and Life Assessment

The CSGT combustor has been developed to fit the production Centaur 60 SoloNOx gas turbine and incorporates three ceramic liner designs, which represent the hot cylindrical wall surfaces of the combustor. The uncooled 1200°C (2200°F) ceramic liner walls will enable the combustion system to demonstrate operation in a stable lean firing condition sufficient to produce NO_x emissions less than 10 ppmc while maintaining less than 50 ppmc carbon monoxide (CO). Designing with ceramic materials combines the application of two major advantages in combustor technology: (*i*) more efficient air flow management, and (*ii*) lower emissions. The ceramic portion of the liner uses less cooling air, leaving relatively more available for exit profile and pattern factor trimming while the ceramic liner itself runs much hotter. The hot ceramic wall will reduce the formation of CO and unburned hydrocarbons, which are caused by local film cooling flows admitted through conventionally cooled liner walls.

There are three ceramic insert designs for the CSGT combustor, all utilizing a "rolling friction" interface system at the endwalls of the subassembly inserts to accommodate the thermal expansion mismatch between the metal support structure and the ceramic liner. One of the three designs uses monolithic ceramic inserts with the outer and inner liner surfaces divided into tiles which extend axially between each end wall. The current design utilizes 24 tiles circumferentially for the outer liner and 12 tiles for the inner liner. The SPSLIFE analysis has used an earlier inner liner model utilizing only 10 tiles. It should be noted that the analysis results for the tile option are for *one* tile only. As such, the survival probability will reflect the smaller area and volume of the individual tile. The tiles are interlocked by features ground into the edges of the tiles. At the end walls the tiles are retained as with the ring design where the ceramic ball bearings load directly to the monolithic part.

The second of the three designs utilizes a simple continuous (integral) tube concept for both the inner and outer liner. The third design approach uses monolithic ceramic ring segments, which can be represented by cutting the inner integral tube in the second design, into four separate axial rings each 2 in. long. The rings are configured to accept rolling elements directly at the endwalls and have a shiplap edge design for piloting adjacent segments.

The three liner designs offer a necessary degree of flexibility and variation necessary at this time, since it is unclear which will prove to be the most successful. The system that exhibits superior performance and satisfies the design intent will be selected for the 4000 hour field test.

DAM for Axial Combustor Tile, Material B. The temperature and stress map of an axial tile is shown in Fig. 10. The axial tile was evaluated using a silicon carbide material designated as Material B. The two large surfaces of the tile were assumed to be in the as-fired condition; the four sides and mating surfaces were assumed to be in the machined condition.

The Design Assessment Map for this scenario is shown in Fig. 11. The map is plotted for a design life of 30,000 hours. The component is safe in the creep mode. Creep life for the component is assessed to be 1,872,000 hours. An oxidation analysis was not performed due to lack of adequate data. The solid lines show that the tile has approximately 99 percent probability of survival in fast fracture. The fast fracture survival probability predicted by the NASA CARES program for each tile is 99.13 percent. The dashed lines show approximately 96 percent probability of survival per tile in slow crack growth. The slow crack growth survival probability predicted by the NASA CARES/LIFE program for each tile is 97.59 percent.

DAM for Integral Inner Combustor Liner, Material B. The stress map of the integral inner combustor liner is shown in Fig. 12. The two large surfaces of the liner were assumed to be in the as-fired condition, and the two ends were assumed to be in the machined condition. The Design Assessment Map for this scenario is shown in Fig. 13. The map is plotted for a design life of 30,000 hours. The creep line shows that the component is safe in the creep mode. Creep life for the component is assessed to be 315,000 hours. An oxidation analysis was not performed due to lack of adequate data. The solid lines show that the liner is unsafe in fast fracture. The fast fracture survival probability predicted by the NASA CARES program for the liner is 46.85 percent. The dashed lines show that the liner is also unsafe in slow crack growth. The slow crack growth survival probability predicted by the NASA CARES/LIFE program for the liner is 7.19 percent.

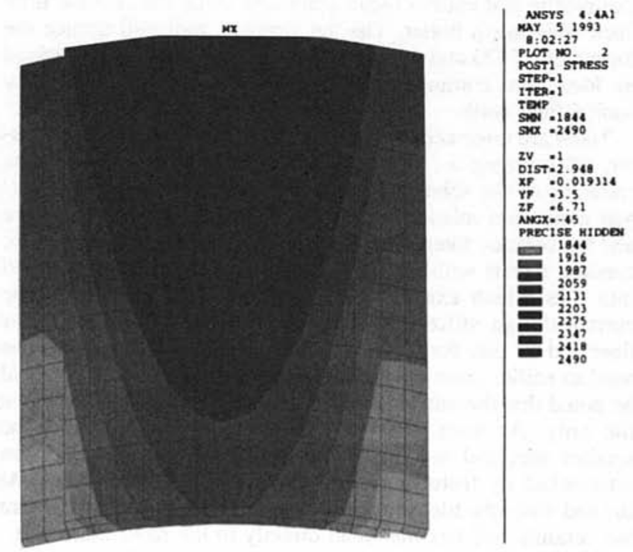

(A) Temperature Map

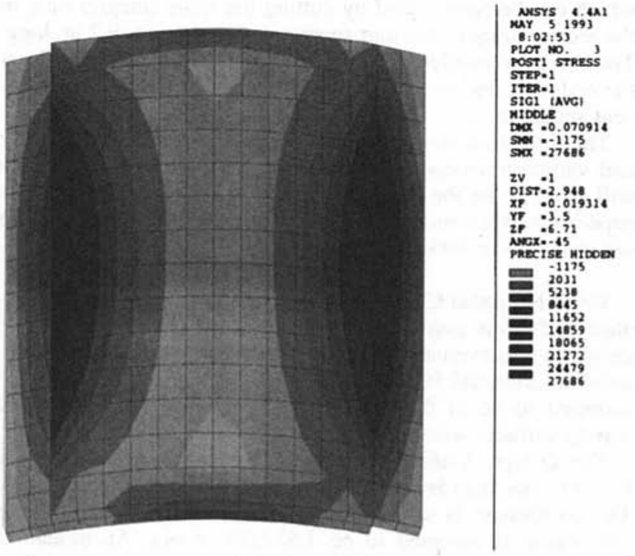

(B) Stress Map

Fig. 10 Finite element map of a ceramic axial combustor tile: Material B

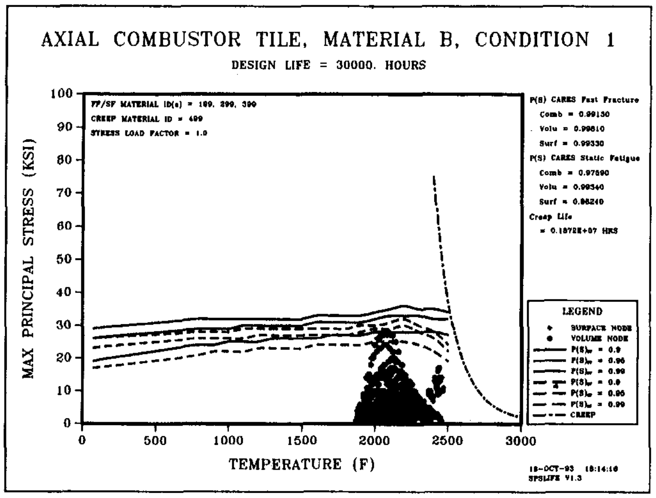

Fig. 11 Design assessment map for a ceramic axial combustor tile: Material B

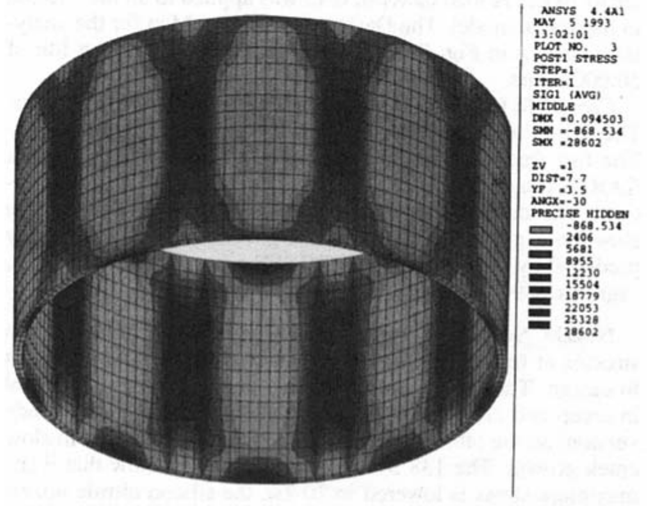

Fig. 12 Finite element stress map of an integral ceramic combustor liner: Material B

DAM for Four-Ring Inner Combustor Liner, Material B. The stress map of the four-ring inner combustor liner is shown in Fig. 14. The two large surfaces of the liner were assumed to be in the as-fired condition, and the two ends were assumed to be in the machined condition. The Design Assessment Map for this scenario is shown in Fig. 15. The map is plotted for a design life of 30,000 hours. The creep line shows that the component is very safe in the creep mode. Creep life for the component is assessed to be 11,220,000 hours. An oxidation analysis was not performed due to lack of adequate data. The solid lines show that the liner is very safe in fast fracture. The fast fracture survival probability predicted by the NASA CARES program for the liner approaches 100 percent. The dashed lines show that the liner is also very safe in slow crack growth. The slow crack growth survival probability predicted by the CARES/LIFE program for the liner also approaches 100 percent.

Combustor Summary. The four-ring inner combustor liner design has lower stress levels than the axial tile design and the integral inner liner design. As a result, this design has

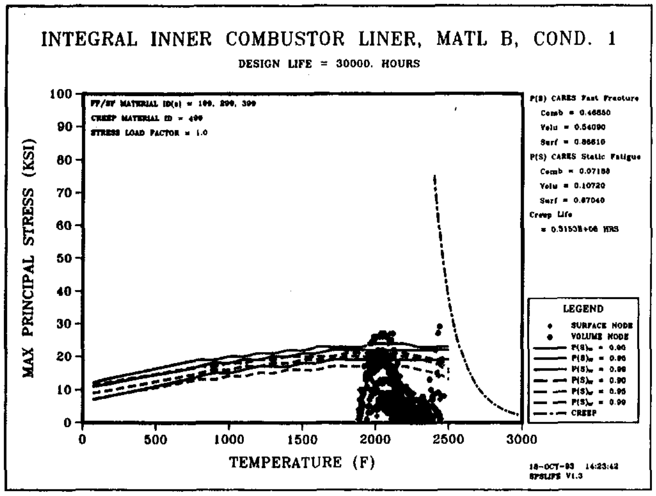

Fig. 13 Design assessment map for an integral ceramic combustor liner: Material B

a higher calculated reliability. The probability of survival in slow crack growth is nearly 100 percent, and creep life is also not perceived as a problem. However, the feasibility of making such a large ring out of a commercial silicon carbide material needs to be examined. Reaction-bonded Si-SiC material should also be evaluated for this design. The axial tile design is marginal in slow crack growth, due primarily to the low characteristic strength and Weibull modulus of material B. The integral inner combustor liner has low probability of survival in slow crack growth. This design is not recommended for monolithic ceramics.

Summary

The dovetail blade design appears to satisfy the design objectives. However, material A is marginal in slow crack growth for this application. Data on slow crack growth are limited at the present time, especially for low-stress, high-time regimes. As more test data are accumulated, a more accurate assessment of the slow crack growth phenomenon will be made.

The turbine nozzle experiences high stresses at the trailing edge due to the severe combustor "hot spot" radial profile, resulting in high-temperature gradients. Both Material A and Material B do not meet the life requirements of the current design. At the time of writing, design improvements are being investigated as a result of the DAM results, to lower the airfoil stresses to a level that achieves the design reliability goals.

The multiple ring inner combustor liner design has a higher probability of survival than the axial tile design and the integral liner design. The feasibility of making such a large ring out of a commercial silicon nitride material is being examined. Reaction-bonded Si–SiC material is being evaluated for this design. A lower temperature version of the axial tile design may also meet requirements, provided the lower temperature does not unduly compromise engine performance. An SPSLIFE analysis needs to be carried out on such a design. The integral liner design has lower probability of survival, and will not be suitable for monolithic ceramics given the predicted temperature gradients.

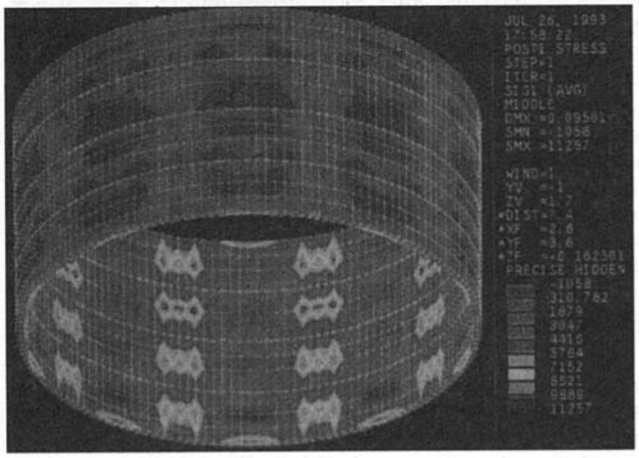

Fig. 14 Finite element stress map of a four-ring ceramic combustor liner: Material B

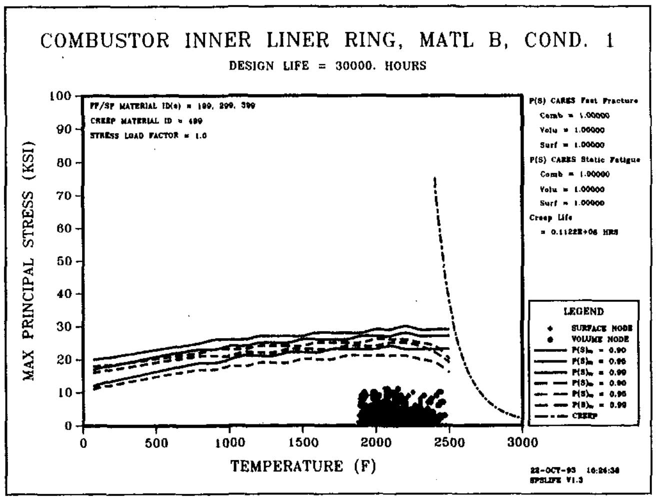

Fig. 15 Design assessment map for integral inner combustor liner: Material B

The probability of survival of components evaluated in this report can be improved by proof testing. Analyses of truncated probabilities will be performed in the detailed design phase. However, proof testing will be viewed strictly as a quality control measure, and should not become a means to test for the acceptability of a particular design.

Acknowledgments

The work presented in this paper was performed on DOE contract DE-AC02-92CE40960, under the guidance of Dr. Mark van Roode, CSGT Program Manager at Solar Turbines Incorporated, and Mr. Tibor Bomemisza, subcontract Program Manager at Sundstrand Power Systems.

Advice and assistance received from Dr. John Gyekenyesi, Noel Nemeth, and Lynn Powers of NASA-Lewis related to CARES, CARES/LIFE, and ANSYS codes are gratefully acknowledged.

References

Bomemisza, T., and Saith, A., 1994, "SPSLIFE: A User-Friendly Approach to the Structural Design and Life Assessment of Ceramic Components," ASME Paper No. 94-GT-486; accepted for publication in the *Transactions of the ASME.*

Nemeth, N. N., et al., 1993, "Time-Dependent Reliability Analysis of Monolithic Ceramic Components Using the CARES/LIFE Integrated Design Program," presented at the ASTM Symposium on Life Prediction Methodologies for Ceramic Materials in Advanced Applications—A Basis for Standards, Cocoa Beach, FL.

Quinn, G. D., and Wiederhom, S. M., 1993, "Structural Reliability of Ceramics at Elevated Temperatures," presented at the ASTM Symposium on Life Prediction Methodologies for Ceramic Materials in Advanced Applications—A Basis for Standards, Cocoa Beach, FL.

Soma, T., Ishida, Y., et al., 1987, "Ceramic Component Design for Assuring Long-Term Durability," *Advanced Ceramic Materials,* Vol. 2, No. 4.

Van Roode, M., Brentnall, W. D., Norton, P. F., and Boyd, G. L., 1994, "Ceramic Stationary Gas Turbine Development Program, First Annual Summary," ASME Paper No. 94-GT-313.

Weibull, W., 1951, "A Statistical Distribution Function of Wide Applicability," ASME *Journal of Applied Mechanics,* Vol. 18, No. 3.

Wiederhom, S. M., 1974, "Subcritical Crack Growth in Ceramics," *Fracture Mechanics of Ceramics,* R. C. Bradt et al., eds., Plenum, New York.

Wiederhom, S. M., et al., 1991, "Tensile Creep Testing of Structural Ceramics," *Proc., Annual Automotive Technology Development Contractors' Coordination Meeting,* Dearborn, MI.

A. Hamed

T. P. Kuhn

Department of Aerospace Engineering and
Engineering Mechanics,
University of Cincinnati,
Cincinnati, OH 45221

Effects of Variational Particle Restitution Characteristics on Turbomachinery Erosion

This paper presents the results of an investigation to determine the effects of variational particle rebounding models on surface impacts and blade erosion patterns in gas turbines. The variance in the particle velocities after the surface impacts are modeled based on the experimental measurements using Laser-Doppler Velocimetry (LDV) under varying flow conditions. The probabilistic particle trajectory computations simulate the experimental variance in the particle restitution characteristics using cumulative distribution functions and random sampling techniques. The results are presented for the particle dynamics through a gas turbine flow field and are compared to those obtained with deterministic rebound models based on experimental mean values.

Introduction

When gas turbines operate in environments with suspended solid particles, it is very difficult to remove the solid particles from the gas stream without taxing the performance with losses. Even small particles of one to thirty micron size have been known to be very damaging to the exposed components of coal burning turbines (McCay, 1973). Surface erosion by particle impacts increases tip clearances and blade surface roughness and produces changes in the blade shape, especially in the leading and trailing edges. All these combined effects lead to a permanent deterioration in turbine performance and increased repair and maintenance costs. Blade erosion in turbomachines is affected by many factors, such as the blade geometry, blade row location, rotational speed, flow conditions, blade material, and particle characteristics. A clear understanding of the nature of the particle trajectories, and the factors affecting the particle impact conditions with the blade surfaces, is essential to predicting blade surface erosion intensity and pattern.

The erosion of metals by solid particle laden flow have been investigated experimentally under different particulate flow conditions (Hamed et al., 1988; Tabakoff et al., 1980). Empirical erosion equations (Hamed et al., 1988) have been derived from the erosion measurements given a particle target material combination. They include the effects of parameters known to affect the surface erosion such as the particle impacting velocity and impingement angle, and the metal and gas temperature. These equations have been employed in calculating the blade erosion based on the predicted particle impact data in the particle trajectory simulations (Hamed et al., 1988).

The simulation of particulate flow dynamics in turbomachines requires separate models to determine the particle rebound conditions after surface impacts. These particle surface interactions occur as a consequence of the particle trajectory deviations from the flow streamlines due to their higher inertia. In addition to causing surface erosion, these impacts also influence the rest of the particle trajectories and the particle redistribution through the flow field, and the subsequent particle surface impacts. It is particularly important to model the particle surface interactions accurately in turbomachines because of the drastic changes in the magnitude and direction of the particle velocity after impacting the rotor blades and the effect this has on the subsequent blade rows. Up until now, deterministic models have mostly been used in modeling particulate flows in turbomachines. The equations governing the particle motion are integrated numerically in the flow field and the particle characteristics are determined using empirical equations that represent the mean values of the experimentally measured particle rebound conditions. Consequently, the exhibited variance in the LDV measurements of the particle rebounding conditions (Hamed and Tabakoff, 1991) is not represented in the computational procedures upon surface impacts.

In the present investigation, a new modeling methodology for the particle dynamics that reproduces the experimentally measured variance in the particle restitution conditions is proposed and validated. The method is based on randomly sampling the experimentally measured rebounding conditions at the different impact angles and using the generated samples in the particle trajectory computations to determine the particle rebounding conditions after each surface impact. A study was first conducted to determine the appropriate sample size that reproduces with fidelity the experimentally measured variance in the particle rebound characteristics, which was then implemented in the particle trajectory simulations at the surface interactions. The results of the computations in a turbine flow field are presented and compared with the predicted blade impact data based on correlations of the mean values of the restitution parameters at the test conditions. The results demonstrate the influence of the variance in the rebound characteristics on the impact conditions and the associated blade erosion.

Experimental Particle Restitution Characteristics

A 5 W argon-ion Laser-Doppler Velocimeter was used to obtain experimental measurements of the particle rebound velocities after impacting a target sample of the blade material placed under varying impact conditions in an especially designed particulate flow tunnel (Tabakoff and Wakeman, 1979). Experimental measurements were obtained for the rebounding velocities of 150 μm mean diameter sand particles with an incoming velocity, V_1, of 98 m/s (320 ft/sec) impacting Rene 41 target samples at an impact angle, β_1 = 10, 15, 30, 45, 60, and 80 deg. Two perpendicular velocity components were obtained in the synchronized LDV measurements of the particle rebound conditions. These measurements were used to determine the magnitude and direction of the rebounding velocity relative to the sample. Referring to Fig. 1, the particle rebounding conditions are normalized by the incoming values to define the total velocity and directional restitution coefficients

---

Contributed by the International Gas Turbine Institute and presented at the 38th International Gas Turbine and Aeroengine Congress and Exposition, Cincinnati, Ohio, May 24–27, 1993. Manuscript received at ASME Headquarters March 1, 1993. Paper No. 93-GT-124. Associate Technical Editor: H. Lukas.

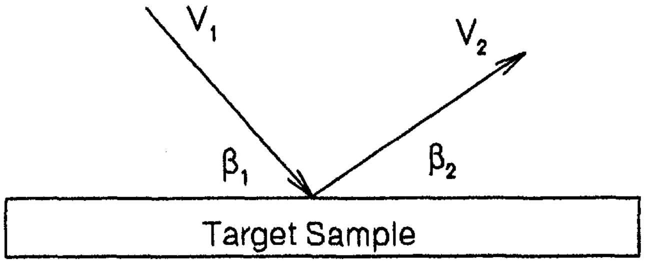

Fig. 1 Definition of impact/rebound geometry

$e_v = V_2/V_1$ and $e_\beta = \beta_2/\beta_1$. The details of the experimental study are omitted here but a complete description of the tunnel, LDV, and data acquisition systems used can be found in the paper by Hamed and Tabakoff (1991).

Tables 1(*a*) and 1(*b*) list the statistical means and standard deviations of the experimentally measured e_β and e_v distributions at the tested impingement angles. Typical histograms obtained from the experimental measurements at the 15 deg impact angle are shown in Figs. 2(*a*) and 2(*b*). Attempts to characterize these distributions by a variety of theoretical distributions known in literature (e.g., normal, log-normal, etc.) were unsuccessful based on the failure of goodness-of-fit tests such as the chi-square test for density functions and the Kolmogorov–Smirnov test for cumulative distributions (Soong, 1981). Fitting of empirical distributions was not attempted because of the variety of observed experimental distribution shapes.

Table 1 Statistics of experimentally measured particle rebound distributions (sand/Rene 41)

a) e_β Particle Restitution Ratio

Impact Angle (degrees)	Mean	Standard Deviation	Std Dev/Mean * 100%
15	1.356	0.723	53.32
30	0.861	0.313	36.35
45	1.115	0.294	26.37
60	0.855	0.166	19.42
80	0.750	0.132	17.60

b) e_v Particle Restitution Ratio

Impact Angle (degrees)	Mean	Standard Deviation	Std Dev/Mean *100%
15	0.463	0.142	30.67
30	0.439	0.083	18.91
45	0.397	0.129	32.49
60	0.373	0.095	25.47
80	0.303	0.064	21.12

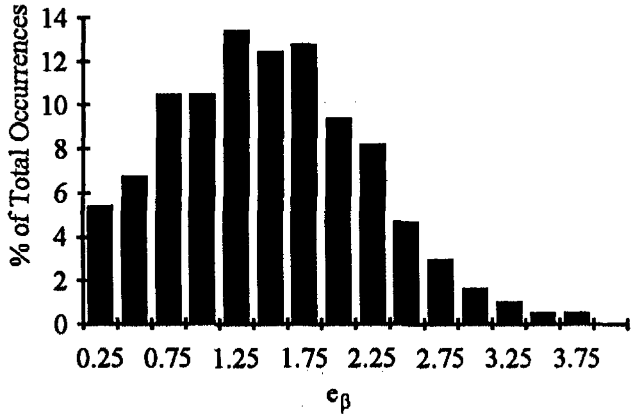

(a) Directional Restitution Ratio

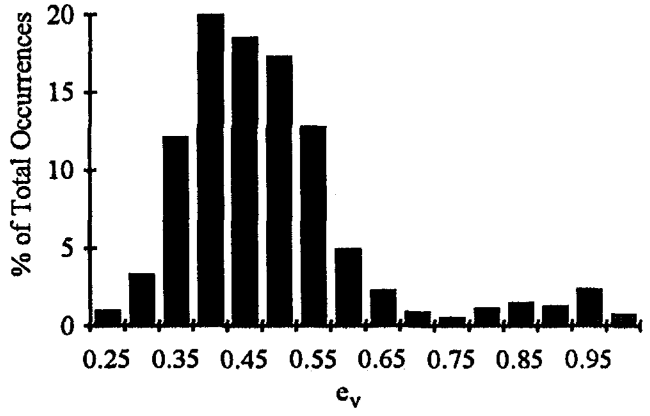

(b) Total Velocity Restitution Ratio

Fig. 2 Experimentally measured particle restitution ratios at 15 deg (sand/Rene 41)

Nomenclature

A = erosion equation constant = 0.8296E-6 mg/g
B = erosion equation constant = 0.2
C_D = particle drag coefficient
d = particle mean diameter, m
e = particle restitution ratio (rebound condition/impact condition)
$\bar{e}$ = unit vector
$\bar{F}$ = force vector of interaction between particle and gas, N/kg
K_0 = velocity nondimensionalizing constant = 100 ft/s
m = erosion equation constant = 2.38
n = erosion equation constant = 3.2
r = radial distance, m
V = velocity magnitude, ft/s
$\bar{w}$ = relative velocity vector, m/s
$\bar{x}$ = location vector, m
β = angle relative to surface, deg
δ = erosion parameter, mg/g
Δ = simulation differential (probabilistic solution-deterministic solution)
ρ = density, kg/m^3
τ = time, s
ω = blade angular velocity, rad/s

Subscripts

g = gas phase
n = surface normal velocity component
p = particle phase
t = surface tangent velocity component
v = total velocity
β = directional angle
θ = circumferential direction
1 = impact condition
2 = rebound condition

Probabilistic Simulation Methodology

Advanced probabilistic methods developed over the past decade include First/Second-Order Reliability Methods and the Advanced Mean Value Method, among others (Millwater et al., 1992). These methods involve approximate analytical techniques to model the response to uncertainties in the random variables, which are described in terms of probability density functions (PDFs) or cumulative density functions (CDFs). These methods, which are generally accurate, flexible, and efficient, require accurate characterization of the random variables. Choosing an improper distribution to describe the random variables in these methods can produce very misleading results (Fox and Safie, 1992). The Monte Carlo method, on the other hand, may require a large number of simulations to describe accurately the response of the model in the tail regions of the response distribution function (Millwater et al., 1992). However, the method does not require analytical representation of the random variables and is exact in the limit as the number of simulations grows very large.

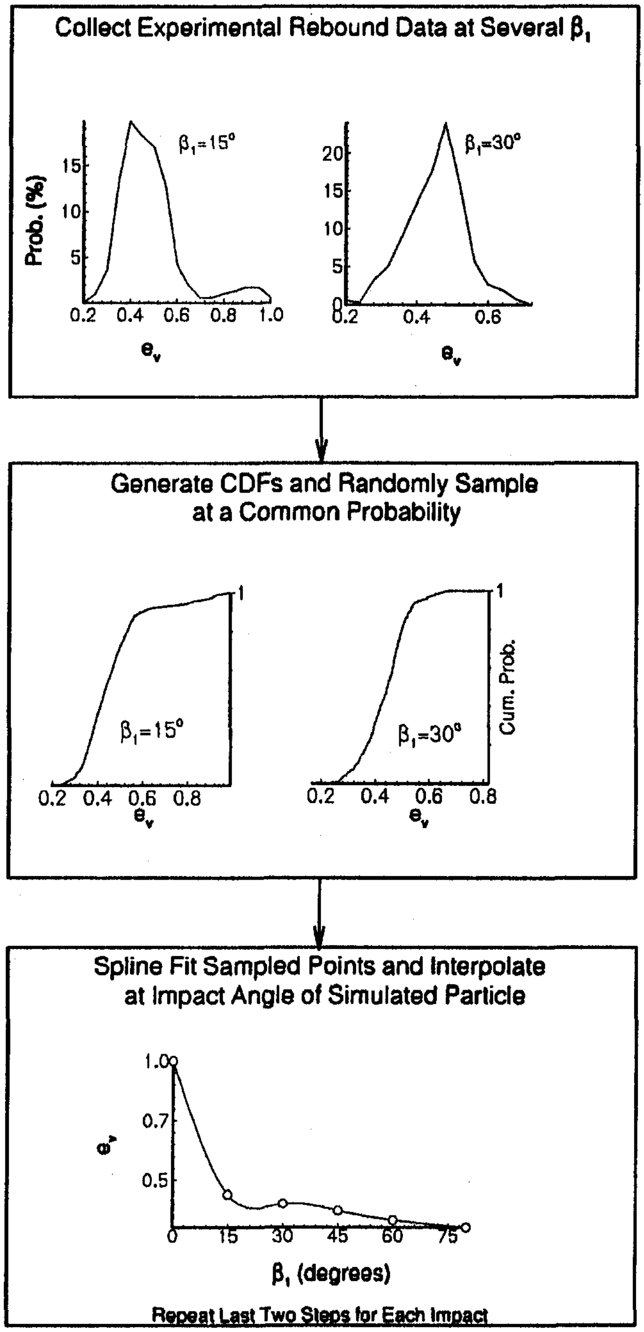

Fig. 3 Schematic of sampling process

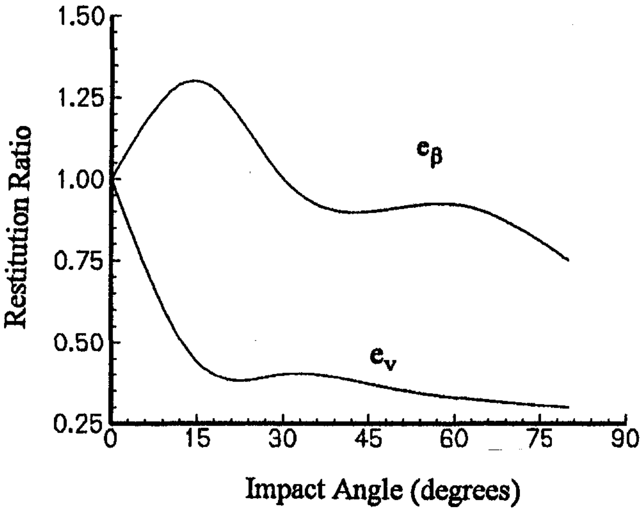

Fig. 4 Particle restitution ratio mean value polynomials for sand/Rene 41

In the present study, a probabilistic approach is adopted in the trajectory calculations to simulate the effects of the experimentally measured variance accurately in the particle restitution ratios. The Monte Carlo method was adopted in modeling particle rebound characteristics based on sampling the experimentally measured e_β and e_v distributions as shown schematically in Fig. 3 for e_v. Referring to Fig. 3, the experimental rebound data for e_β and e_v at each impingement angle were first sorted to generate discrete point CDFs. When a particle impacts a surface in the particle dynamics simulation, the inverses of the CDFs are determined at all impingement angles at a randomly selected common probability. Cubic splines are then constructed for e_β and e_v as a function of the impingement angle β_1 from the points sampled in this manner with the restriction that e_β and e_v have a value of unity at $\beta_1 = 0$ deg. These splines are used to interpolate values of e_β and e_v at the impingement angle of the simulated particle in the trajectory calculations. For each subsequent impact, the process is repeated with new sampling

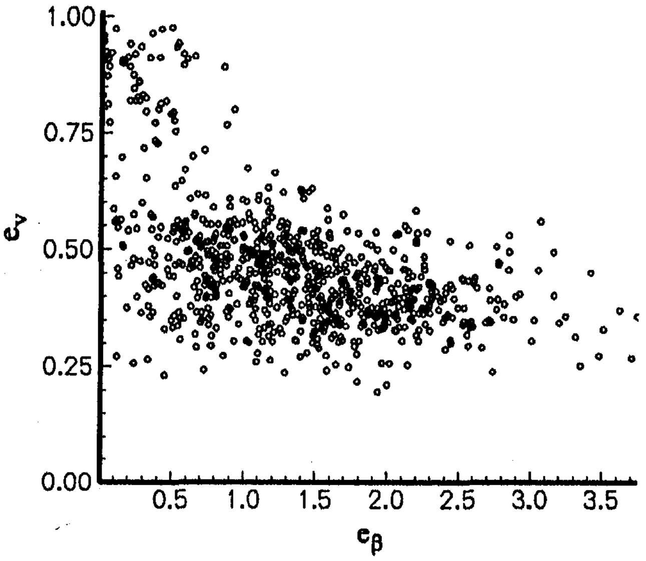

Fig. 5 Correlation between directional and total velocity restitution ratios at 15 deg (sand/Rene 41)

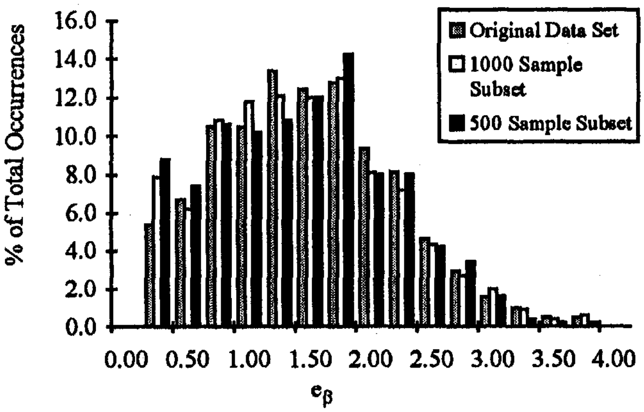

(a) Directional Restitution Ratio

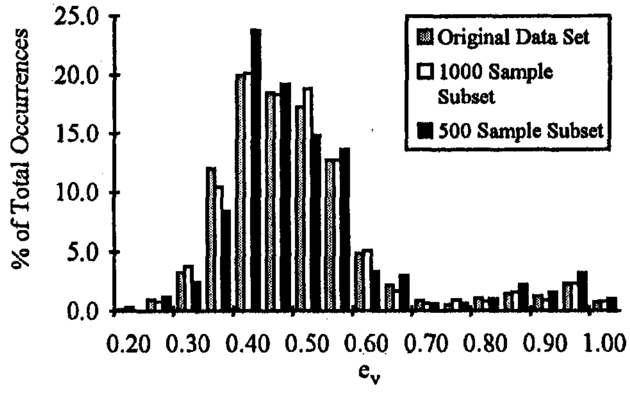

(b) Total Velocity Restitution Ratio

Fig. 6 Variation of restitution ratio distribution with sample size at 15 deg (sand/Rene 41)

probabilities for the two restitution parameters, which are controlled by two independent seeds.

In this modeling structure, the sample values of e_β and e_v in the particle trajectory simulations are dependent on the particle impact angle as well as the sampling probability. Simply put, two particles with identical impact angles and velocities may rebound from a surface impact with different velocity magnitudes and directions because of the different probabilities used in sampling the CDFs. This fact illustrates the probabilistic quality of this modeling approach. Experimentally observed variance in e_β and e_v can be reproduced with fidelity this way, provided enough impacts occur for thorough sampling of the CDFs.

In contrast, the deterministic approach does not model the experimentally measured variance in the particle rebound characteristics. The statistical means of the e_β and e_v distributions are estimated and used to create two least-squares polynomials $e_\beta(\beta_1)$ and $e_v(\beta_1)$ as shown in Fig. 4, which are used in the deterministic particle trajectory calculations to interpolate values of e_β and e_v at each surface impact. In this approach, particles with identical impact conditions will rebound from the surface with identical velocity magnitudes and directions.

Validation and Assessment of Experimentally Based Restitution Model. Sampling e_β and e_v independently requires that the variables be statistically independent, otherwise a correlation coefficient is used to indicate the amount of linear dependence between variables. Statistical independence frees the model from conforming to the laws of joint probability and simplifies the structure of the model. Accounting for any correlation could be included in the probabilistic methodology to increase the overall accuracy at the expense of increasing the complexity (Law and Kelton, 1991). Although correlation coefficients are easily computed, they are not tests for independence. Tests for statistical independence, however, are generally impractical so correlation coefficients are used to indicate the likelihood of independence (Soong, 1981). Before the simulation of particle dynamics was performed, a preliminary study was conducted to determine the status of statistical dependence between e_β and e_v and to evaluate sample size effects.

The correlation coefficient between e_β and e_v was calculated for the data collected in the sand/Rene 41 particle rebound experiments. Sets of data collected at each impingement angle were analyzed and the correlation coefficient determined. Figure 5 shows typical correlation between e_β and e_v for the 15 deg impingement angle test results. Correlations were positive for some impact angles and negative for others with no consistent pattern over the range of impingement angles. Since the correlation test was not conclusive and in order to take advantage of the consequence of independent variables, e_β and e_v were modeled independently.

Sample size tests were performed on the experimental rebound data to determine the minimum number of sample points

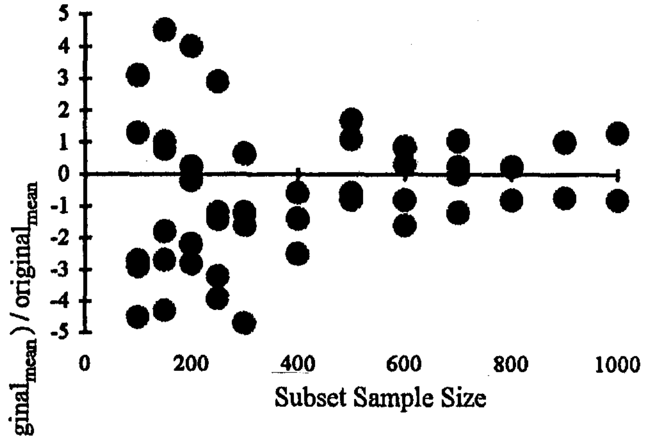

(a) Directional Restitution Ratio

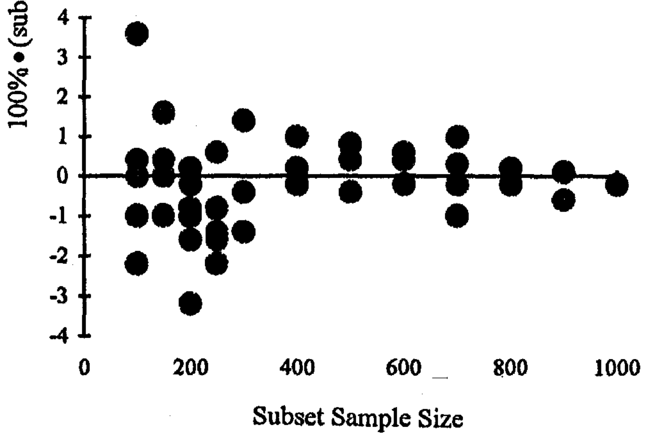

(b) Total Velocity Restitution Ratio

Fig. 7 Effect of sample size on restitution ratio distribution mean value

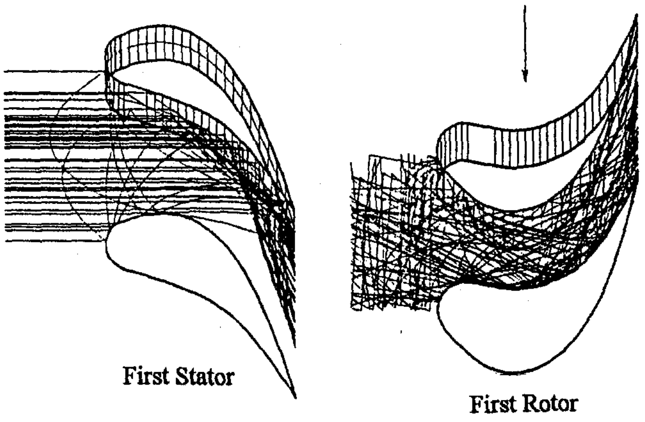

(a) Deterministic Model

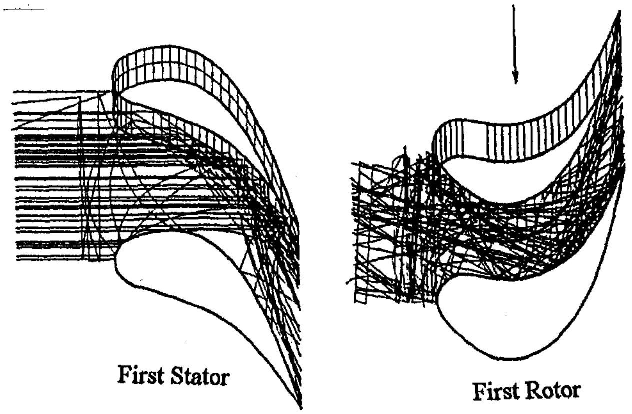

(b) Probabilistic Model

Fig. 8 Projected sand particle trajectories

required to obtain a data subset with a similar statistical distribution. This knowledge is useful both in conducting experiments as well as analysis involving particle rebounding. Sample size tests are important in determining the proper size of a simulation (i.e., number of particles) required for adequate reproduction of variance in the random variables e_β and e_v. It can also be used to minimize the experimental efforts and consequently the consumption of expendables such as compressed air, sand, and target materials and laser use.

Data subsets of e_β and e_v of varying sizes were created from the experimental data sets at each impingement angle, using a sampling procedure as outlined in the previous section. The subsets were compared to the original data sets using the two-sample test. The two-sample tests showed that subsets containing as little as 50 percent of the amount of data found in the original distributions were statistically similar to the original distributions. Figures 6(a) and 6(b) illustrate the variation in e_β and e_v distribution shape with the sample size for the 15 deg impingement angle test case. Figures 7(a) and 7(b) show the growth in uncertainty of the e_β and e_v subset distribution means relative to the original set distribution mean for the 15 deg test case.

Particle Trajectory and Blade Erosion Computation. The equations governing the particle motion, in the turbomachinery flow field are expressed in a coordinate system relative to a frame of reference fixed with respect to the blades (Hamed et al., 1988). The following equations are given for a rotating blade row:

$$\frac{d}{d\tau}\left(\frac{d\bar{x}_p}{d\tau} + \omega r_p \bar{e}_\theta\right) = \bar{F} \qquad (1)$$

Under particulate flow conditions in turbomachines, the effect of the forces due to gravity and interparticle interactions are negligible compared to those due to aerodynamic and centrifugal forces. In addition, the force of interaction between the two phases is dominated by the drag due to the difference in velocity between the solid particles and the flow field. Therefore, the force of interaction is dependent on the relative velocity between the particles and the gas flow, as well as the particle size and shape, and is given by:

$$\bar{F} = \frac{3}{4}\frac{\rho}{\rho_p}\frac{C_D}{d}\left[\left(\bar{w}_g - \frac{d\bar{x}_p}{d\tau}\right)\cdot\left|\bar{w}_g - \frac{d\bar{x}_p}{d\tau}\right|\right] \qquad (2)$$

The drag coefficient C_D is dependent on the Reynolds number, which is based on the relative velocity between the particle and the gas. Empirical relations are used to fit the drag curve over a wide range of Reynolds numbers. The same equations can be used in the stator by setting ω equal to zero and replacing the relative gas velocity by the absolute gas velocity.

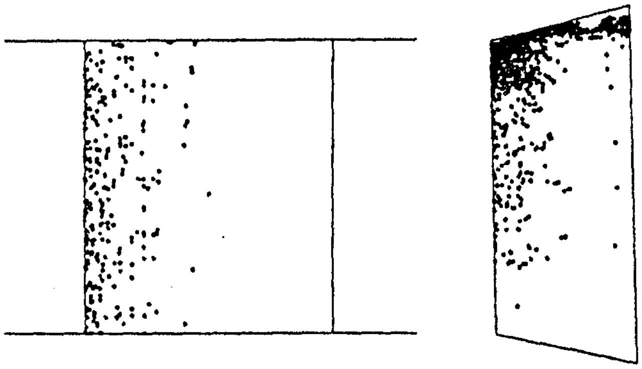

(a) Deterministic Model

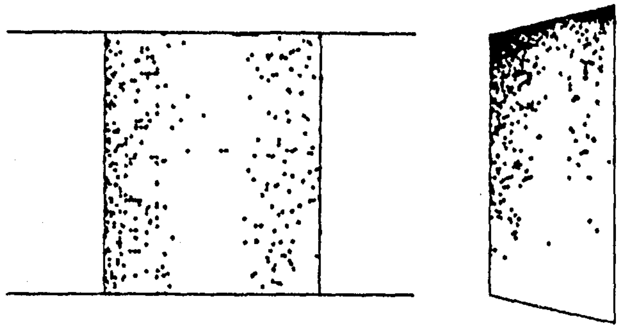

(b) Probabilistic Model

Fig. 9 Blade suction surface impact locations

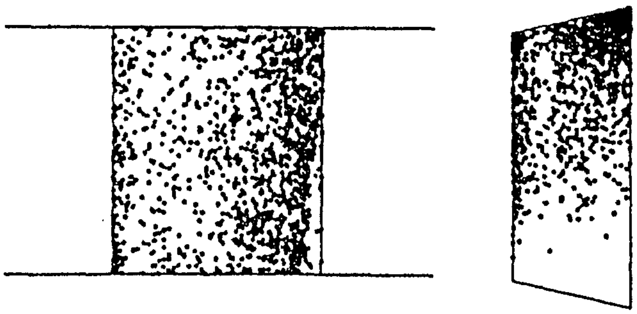

(a) Deterministic Model

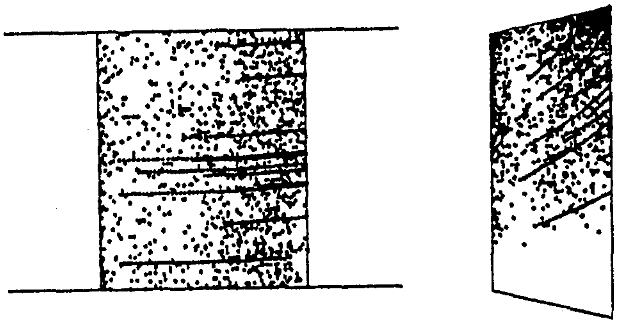

(b) Probabilistic Model

Fig. 10 Blade pressure surface impact locations

The particle trajectory calculations consist of the numerical integration of Eqs. (1)–(2) using a second-order Runge–Kutta scheme. The flow field is synthesized from a number of blade-to-blade stream surface solutions (Katsanis, 1965). Each flow field solution on a blade-to-blade stream surface provides the pitchwise and streamwise variation in the flow properties.

The stream surface shapes and stream filament thickness as determined from a midchannel hub-to-tip stream surface solution (Katsanis and McNally, 1977) model the influence of the hub and tip contouring and the radial variation in the blade shapes. The particle trajectories are computed in the flow field, up to the point of blade, hub, or tip impact. The magnitude and direction of particle impact velocity relative to the surface are determined by the local trajectory and the blade surface geometry at the impact point. Restitution ratios e_β and e_v sampled in the manner described earlier are used to determine the magnitude and direction of the particle velocity after impacting a surface.

The blade surface impact data are used to predict the erosion rates from empirical correlations derived from experimental erosion test results. The erosion rate according to these equations is a function of the impact velocity and impingement angle relative to the surface (Tabakoff and Hamed, 1977). The erosion mass parameter, δ, is defined as the ratio of the eroded mass of target material to the mass of impinging particles. The general expression for δ under cold flow conditions is given by:

$$\delta = A \cdot \left[\left(\frac{V_1}{K_0} \right)^n \cos^n \beta_1 (1 - e_t^2) + B \left(\frac{V_1}{K_0} \right)^m \sin^m \beta_1 (1 - e_n^2) \right] \quad (3)$$

The empirical constants A, B, m, and n are found experimentally by measuring the erosion of samples of the blade material in an erosion tunnel. The parameters e_t and e_n are particle restitution ratios for the tangential and normal velocity components of the impacting particles. Values of e_t and e_n are acquired from mean value polynomials constructed from experimental rebound data, similar to those in Fig. 4.

Results and Discussion

The numerical simulation for 150 μm sand particle dynamics were carried out through the first stage of a 0.45 scale model two-stage axial flow pump drive turbine (Roelke et al., 1966) for the standard inlet air equivalent conditions of 1893 rpm and 3.207 kg/s mass flow. Particle trajectories were computed using the deterministic and probabilistic particle rebound models based on experimental data collected in the sand/Rene 41 particle rebound tests. Simulations were performed for 1000 particles whose particle distribution at the stator inlet was statistically specified according to mass flux. The particles were given an initial velocity lag of 50 percent relative to the flow (Hamed, 1988). Twenty-five independent probabilistic simulations were performed to determine the variability of blade impact and erosion patterns using the probabilistic model. The same particle initial conditions were used in the different simulations, but the seeds for the control of sampling CDFs of e_β and e_v were varied. Computed particle trajectories and blade impact erosion patterns based on the deterministic model solutions are presented and compared to a representative solution based on the probabilistic model. Erosion ratios and impact frequencies predicted by both models at a given location are compared. Additionally, the estimated variations of erosion and impact frequency based on the probabilistic model are presented.

Figures 8(a) and 8(b) show representative trajectory projections for 90 sand particles through the first stage of the turbine based on the deterministic solution and a probabilistic solution respectively. The primary differences between solutions in the stator are observed after the blade pressure surface impacts. The

Table 2 Comparison of deterministic and probabilistic simulation results

a) Calculated Erosion Rates

Blade/Surface	Location of Deterministic Maximum Erosion.		Erosion Rates	
	% Axial Chord	% Radius	Determ.	Prob. Min / Max
			(mgm/gm/cm^2) x10^5	
Stator: Suction	4.244	86.49	1.396	1.391/1.435
Stator: Pressure	90.24	13.42	2.770	1.860/2.657
Rotor: Suction	1.570	92.02	1.695	1.260/2.363
Rotor: Pressure	96.34	94.72	1.261	0.781/1.112

b) Calculated Impact Frequencies

Blade/Surface	Location of Deterministic Max. Imp. Freq.		Impact Frequencies	
	% Axial Chord	% Radius	Determ.	Prob. Min / Max
			(imp/gm/cm^2) x10^{-3}	
Stator: Suction	4.244	86.49	0.855	0.808/0.950
Stator: Pressure	4.897	52.53	1.110	0.723/1.141
Rotor: Suction	1.570	92.02	3.526	2.536/4.084
Rotor: Pressure	88.55	94.53	1.395	1.073/1.438

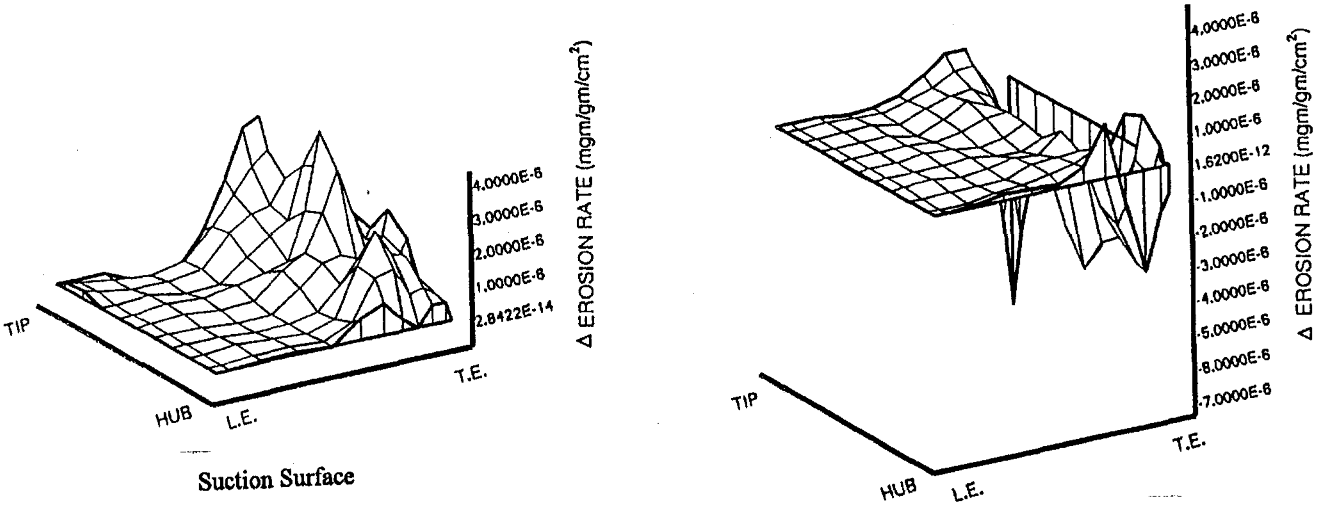

Suction Surface

Pressure Surface

Fig. 11 Stator erosion rate differential map

probabilistic solution predicts that some of the particles impact the aft portion of the suction surface before exiting the blade passage. The deterministic solution, however, shows the particles leaving the blade passage without impacting the aft portion of the suction surface. Comparison of the solutions in the rotor passage does not reveal any obvious differences.

Figures 9(*a*) and 9(*b*) present the locations of suction surface impacts for 1000 sand particles based on the deterministic solution and a representative probabilistic solution, respectively. Figures 10(*a*) and 10(*b*) similarly present the impact locations on the pressure surfaces. Figure 9(*b*) shows a significant number of impacts as predicted in the probabilistic solution on the aft portion of the stator suction surface. The deterministic solution shows no impact on the stator blade suction surface past the 50 percent axial chord. Similarly, more rotor suction surface impacts are predicted by the probabilistic solution near the trailing edge than by the deterministic solution. On the stator pressure and suction surfaces (Figs. 10*a*,*b*) no noticeable difference can be observed in the predicted impact patterns of the deterministic and probabilistic solutions. The streaks on the stator pressure surface in the probabilistic solution represent particles impacting the surface at low velocities and shallow angles and remaining close to the blade surface after rebounding, resulting in higher impact frequencies for these particles.

The magnitude and location of maximum local blade surface erosion rates and impact frequencies, calculated by the deterministic model, are listed in Tables 2(*a*) and 2(*b*). The minimum and maximum values of erosion rate and impact frequency calculated at these locations by the 25 independent probabilistic simulations are also shown and presented in the table for comparison.

According to Table 2(*a*), the stator suction surface shows that the deterministic solution predicts a maximum calculated erosion rate near the smallest of all probabilistic simulations.

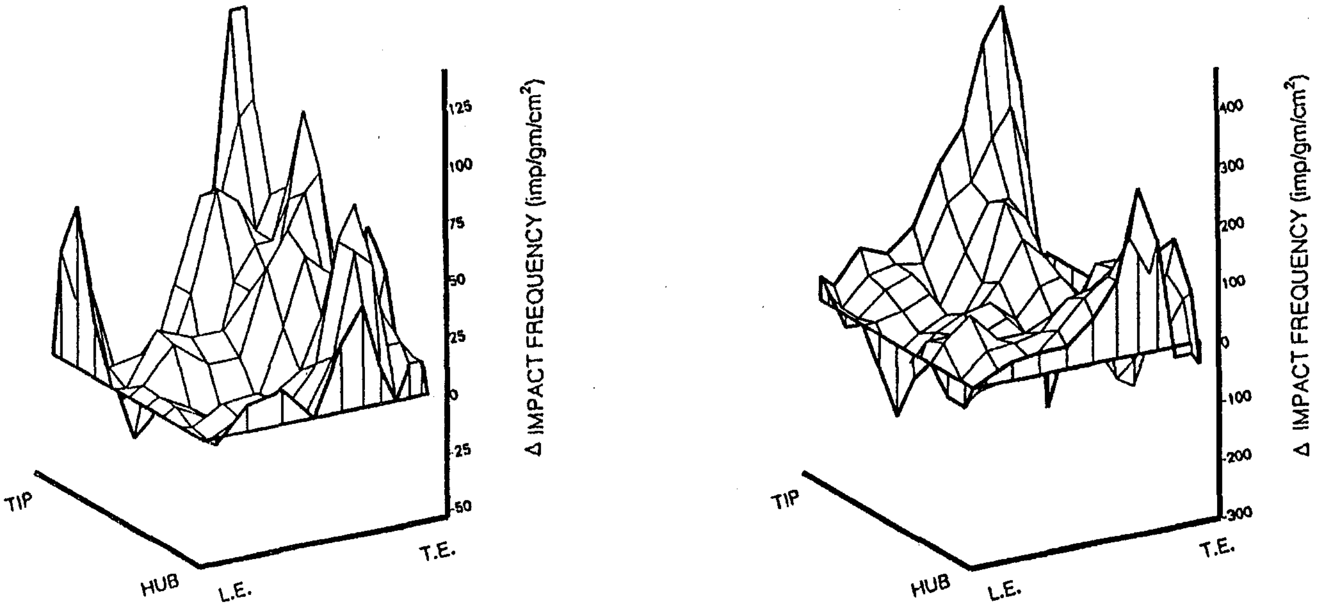

Suction Surface

Pressure Surface

Fig. 12 Stator impact frequency differential map

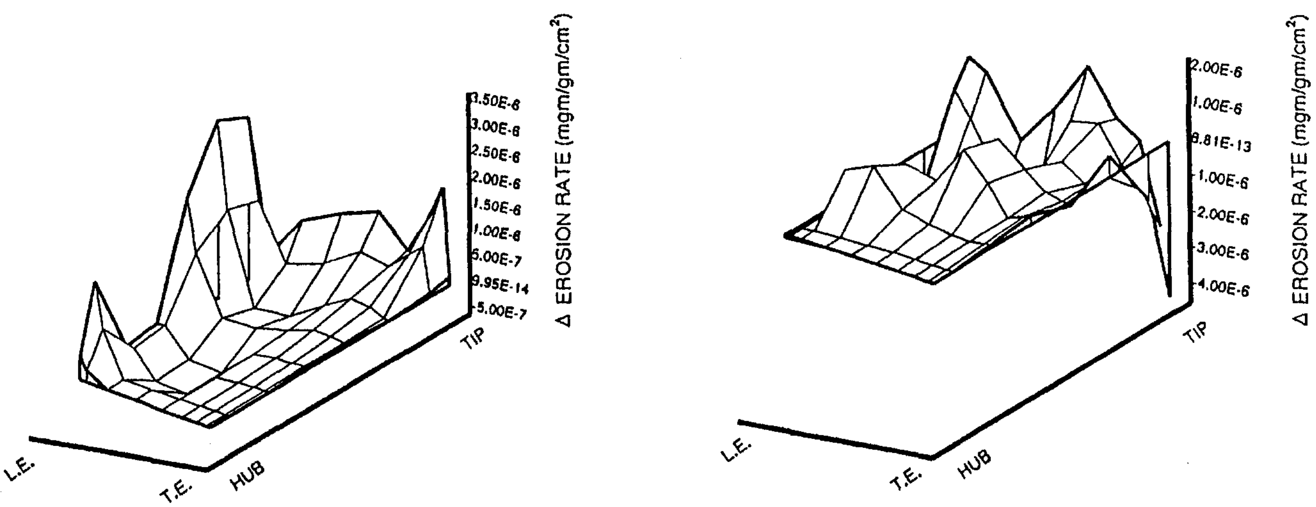

Suction Surface

Pressure Surface

Fig. 13 Rotor erosion rate differential map

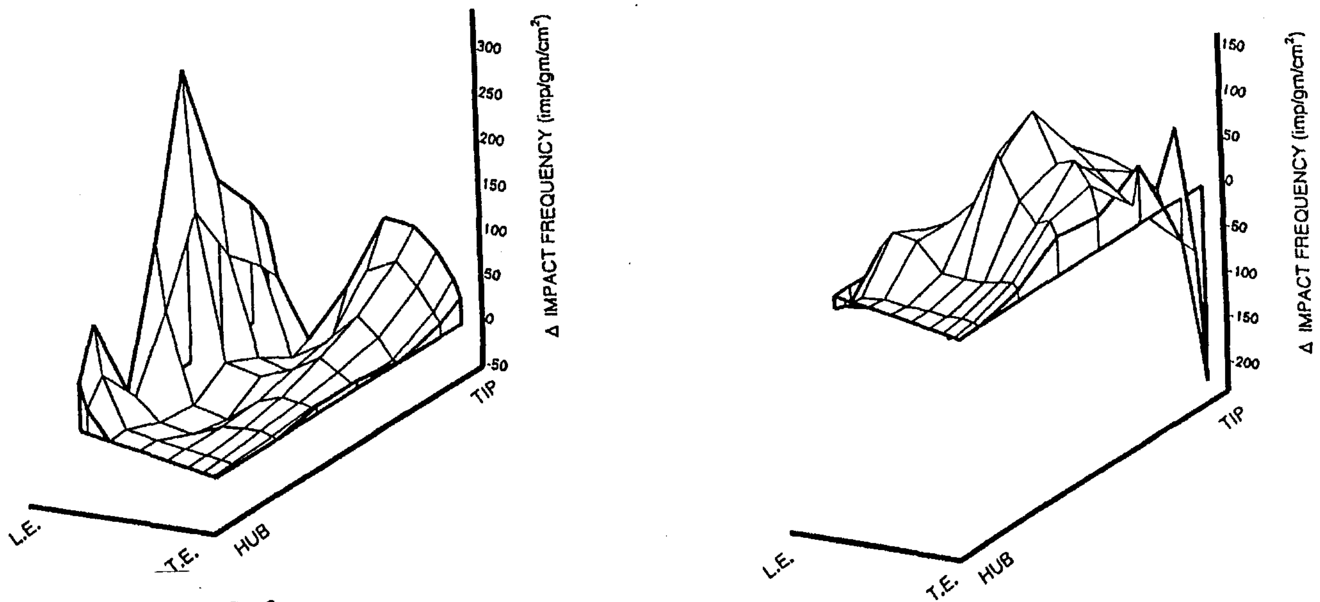

Suction Surface

Pressure Surface

Fig. 14 Rotor impact frequency differential map

On the pressure surface, Table 2(*a*) indicates that the maximum erosion rate from the deterministic solution near the trailing edge is slightly greater than the largest value calculated at that location by the probabilistic simulations. Therefore the deterministic model's maximum local stator blade erosion predictions are generally more conservative on the pressure surface. Similar conclusions can be made for the predicted rotor blade maximum local erosion. The corresponding results for the calculated impact frequencies are presented in Table 2(*b*). These results also indicate that the deterministic model provides conservative predictions of the maximum impact frequency on the rotor blade pressure surface. The predictions on the suction surfaces, however, may be significantly underestimating the possible damage to the blade surfaces.

Maps of differences between the deterministic and probabilistic erosion rates and impact frequencies are presented in Figs. 11–14. In those figures, the blade surface contours of erosion rate and impact frequency based on the deterministic solution are subtracted from the contours of the probabilistic simulation with the highest calculated local erosion rate. Maps with negative values therefore indicate a conservative deterministic solution, while positive values indicate an underestimation by the deterministic model.

Figures 11 and 12 indicate that stator suction surface erosion rate and impact frequencies near the trailing edge are underestimated by the deterministic model. This results from the significant number of impacts predicted by the probabilistic model on the aft portion of the blade. The pressure surface generally shows little difference in the predicted erosion and impact patterns, but the deterministic solution is slightly conservative near the trailing edge. According to Figs. 13 and 14, the deterministic solution underestimates the erosion rate and impact frequency on the rotor blade surfaces with the largest discrepancies near the suction surface leading edge.

Conclusions

A probabilistic approach to the simulation of particle dynamics has been proposed and validated. Results obtained for particle dynamics in the first stage of an axial flow turbine show significant differences between the deterministic and probabilistic simulations. In general, the results indicate that the deterministic modeling approach yields conservative predictions of surface erosion on blade pressure surfaces yet underestimates the erosion on the suction surfaces. The most important difference was observed near the trailing edge of the stator suction surface where the probabilistic particle impacts were not predicted by the deterministic model.

Acknowledgments

This research was supported by NSF Grant No. CTS-9012309. The second author wishes to acknowledge the support of the Ohio Aerospace Grant Consortium through the NASA Space Grant/OAI Graduate Fellowship.

References

Fox, E. P., and Safie, F., 1992, "Statistical Characterization of Life Drivers for a Probabilistic Design Analysis," AIAA Paper No. 92-3414.

Hamed, A., Tabakoff, W., and Mansour, M., 1986, "Turbine Erosion Exposed to Particulate Flow," ASME Paper No. 86-GT-258.

Hamed, A., 1988, "Effect of Particle Characteristics on Trajectories and Blade Impact Patterns," ASME *Journal of Fluids Engineering,* Vol. 110, pp. 33–37.

Hamed, A., Tabakoff, W., and Wenglarz, R., 1988, "Particulate Flow and Blade Erosion," von Karman Institute for Fluid Dynamics Lecture Series.

Hamed, A., and Tabakoff, W., 1991, "Experimental Investigation of Particle Surface Interactions for Turbomachinery Applications," *Laser Anemometry Advances and Applications,* Vol. 2, Proceedings of the Fourth International Conference on Laser Anemometry, Advances and Applications, Cleveland, OH, ASME, pp. 775–780.

Katsanis, T., 1965, "Fortran Program for Calculating Transonic Velocities on a Blade-to-Blade Stream Surface of a Turbomachine," NASA TND 2809.

Katsanis, T., and McNally, W. D., 1977, "Revised Fortran Program for Calculating Velocities and Streamlines on the Hub-Shroud Mid-channel Stream Surface of an Axial, Radial, or Mixed Flow Turbomachine or Annular Duct, Vols. 1 and 2," NASA TND 8430 and NASA TND 8431.

Law, A. M., and Kelton, W. D., 1991, *Simulation Modeling and Analysis,* McGraw-Hill, Inc., New York.

McCay, L., 1973, "The Coal Burning Gas Turbine Project," Report of the Interdepartmental Gas Turbine Steering Committee, Australian Government Publishing Service.

Millwater, H. R., Smalley, A. J., Wu, Y.-T., Torng, T. Y., and Evans, B. F., 1992, "Computational Techniques for Probabilistic Analysis of Turbomachinery," ASME Paper No. 92-GT-167.

Roelke, R. J., Stabe, R. G., and Evans, D. G., 1966, "Cold-Air Performance Evaluation of Scale Model Oxidizer Pump-Drive Turbine for the M-1 Hydrogen-Oxygen Rocket Engine—II. Overall Stage Performance," NASA TND-3368.

Soong, T. T., 1981, *Probabilistic Modeling and Analysis in Science and Engineering,* Wiley, New York.

Tabakoff, W., and Hamed, A., 1977, "Aerodynamic Effects on Erosion in Turbomachinery," JSME & ASME Paper No. 70, presented at the Joint Gas Turbine Congress, Tokyo, Japan.

Tabakoff, W., and Wakeman, T., 1979, "Test Facility for Material Erosion at High Temperature," *Erosion, Prevention and Applications,* ASTM STP 664, pp. 123–135.

Tabakoff, W., Hamed, A., and Ramachandran, J., 1980, "Study of Material Erosion in High Temperature Coal Gas Streams," ASME JOURNAL OF ENGINEERING FOR POWER, Vol. 102, No. 2, pp. 265–270.

P. O. Hedman
Department of Chemical Engineering,
Advanced Combustion,
Engineering Research Center,
Brigham Young University,
Provo, UT 84602

G. J. Sturgess
Pratt & Whitney,
East Hartford, CT 06108

D. L. Warren
Department of Mechanical Engineering,
Advanced Combustion,
Engineering Research Center,
Brigham Young University,
Provo, UT 84602

L. P. Goss
Systems Research Laboratories, Inc.,
A Division of Arvin/Calspan,
Dayton, OH 45440

D. T. Shouse
Wright Laboratory,
Wright-Patterson AFB, OH 45433

Observations of Flame Behavior From a Practical Fuel Injector Using Gaseous Fuel in a Technology Combustor

This paper presents results from an Air Force program being conducted by researchers at Brigham Young University (BYU) Wright-Patterson Air Force Base (WPAFB), and Pratt and Whitney (P&W). This study is part of a comprehensive effort being supported by the Aero Propulsion and Power Laboratory at Wright-Patterson Air Force Base, and Pratt and Whitney in which simple and complex diffusion flames are being studied to understand better the fundamentals of gas turbine combustion near lean blowout. The program's long-term goal is to improve the design methodology of gas turbine combustors. This paper focuses on four areas of investigation: (1) digitized images from still film photographs to document the observed flame structures as fuel equivalence ratio was varied, (2) sets of LDA data to quantify the velocity flow fields existing in the burner (3) CARS measurements of gas temperature to determine the temperature field in the combustion zone, and to evaluate the magnitude of peak temperature, and (4) two-dimensional images of OH radical concentrations using PLIF to document the instantaneous location of the flame reaction zones.

Introduction

As part of a comprehensive Air Force program, three different combustors have been utilized to investigate lean blowout in aircraft gas turbine engines. These vehicles consist of a simplified research combustor (Task 100), a technology combustor (Task 150), and a simplified, generic gas turbine combustor (Task 200). The technology combustor (Task 150) incorporates the practical fuel injectors used in the generic gas turbine combustor (Task 200) into the simpler research combustor (Task 100), to permit study of injector characteristics in isolation. The work presented concerns work with the Task 150 technology combustor. While many detailed studies exist in the literature concerning jet flames, both free and enclosed, almost nothing is available on the flame characteristics produced by practical ways of introducing the reactants into an engine combustor. This work goes some way toward remedying this situation.

The Task 150 technology combustor uses a practical liquid fuel injector with a classic gas turbine engine air blast atomizing configuration, involving coswirling airsheets on either side of a coswirling annular (normally liquid) fuel sheet, with the outer air passage and the fuel passage both converging on the central air passage. For this study, the burner was fueled by gaseous propane. Two injectors of this same configuration have been used, high-swirl (HS) and low-swirl (LS) injectors. Only data from the high-swirl configuration are reported in this paper. The technology combustor has been configured so that the geometry around the injector is nearly axisymmetric with a diameter of about 150 mm. However, the combustor incorporates flat quartz windows about 60 mm in width on each of four sides so that laser-based optical diagnostic instruments can be used. This unique configuration allows complex diagnostic measurements to be made in a simpler geometry than the Task 200 generic gas turbine combustor, but which embodies most of the features of an actual jet engine combustor in a near axisymmetric configuration that is easier to model mathematically. Four methods of measurement have been used to characterize the flame. These include still film photographs, LDA measurements of velocity, CARS measurements of gas temperature, and images from PLIF measurements of the OH radical.

Experimental tests have been conducted on the research combustor at both BYU and WPAFB locations. These tests included operational characteristics, flow partitioning in various injector passages, visual flame structure, planner laser induced fluorescence (PLIF) imaging of OH radicals in the flame boundary, laser-Doppler anemometry (LDA) velocity information, and coherent anti-Stokes Raman spectroscopy (CARS) temperature data. The effects of various parameters on the fuel equivalence ratio at lean blowout (LBO), an important operational characteristic, have also been investigated but are not reported in this paper.

Intriguing flame structures have been visually observed, and captured in video images, digitized still photographs, and PLIF images of the OH radical with the Task 150 configuration. The digitized images from still photographs have characterized the flame shapes observed visually. The instantaneous two-dimensional PLIF images have frozen flame structures missed with the visual observations. The partitioning of air flows through the dome and insert jets, and the primary and the secondary air swirlers was also determined. Preliminary analysis of PLIF images of the OH radical, combined with air flow split information, have helped describe the basic mixing patterns observed as the fuel equivalence ratio is changed. The flame attaches to the burner or lifts from the burner as the fuel equivalence ratio is changed.

LDA measurements have quantified the axial, radial, and tangential velocity components in the combustor for two op-

---

Contributed by the International Gas Turbine Institute and presented at the 39th International Gas Turbine and Aeroengine Congress and Exposition, The Hague, The Netherlands, June 13–16, 1994. Manuscript received by the International Gas Turbine Institute March 4, 1994. Paper No. 94-GT-389. Associate Technical Editor: E. M. Greitzer.

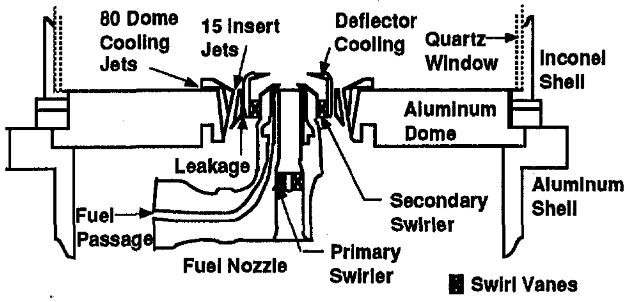

Fig. 1 Schematic of the T150 high-swirl injector

erating conditions (ϕ = 0.72 and ϕ = 1.49) at an air flow rate of 500 slpm. This information has yielded local velocity and turbulence data and preliminary analysis of zero axial velocity contours has been used to identify the major recirculation zones. Data from both isothermal flows and combusting hot flows have been collected. Mean axial, tangential, and radial velocity LDA data for combusting hot flow data are presented in the paper. These data are also useful for model validation.

CARS gas temperature data have also been collected for the Task 150 technology combustor with the high swirl injector at an air flow rate of 500 slpm and at fuel equivalence ratios (ϕ) of 0.75, 1.00, 1.25, and 1.50. This unique set of data shows the corresponding geometric changes in the structure of the mean gas temperature distribution as fuel equivalence ratio is changed, and quantifies the change in the magnitude of the peak temperature as the fuel equivalence ratio changes from lean, to stoichiometric, to fuel rich. Mean gas temperature data for ϕ = 0.75, 1.00, and 1.50 are presented in the paper.

Combustor Test Facility

Three burners are being utilized as part of a comprehensive Air Force program to investigate lean blowout in the combustors of aircraft gas turbine engines (Sturgess et al., 1991b). These vehicles consist of the simplified Task 100 research combustor, the Task 150 technology combustor, and the Task 200 simplified, generic gas turbine combustor. This work provides a bridge between the combustion characteristics of confined, co-annular fuel and air jets discharged into a sudden expansion (Task 100 research combustor) and the characteristics of a linear array of four swirling fuel injectors installed in a rectangular combustion chamber that simulates a segment of a real jet engine combustor (Task 200 simplified, generic gas turbine combustor). The Task 150 technology combustor incorporates one of the practical fuel injectors used in the Task 200 generic gas turbine combustor into the simpler Task 100 research combustor, to permit study of its characteristics in isolation. The use of the Task 150 technology combustor allows the combustion characteristics of a real injector to be investigated in a simple geometry where various diagnostic measurements (primarily laser-based optical measurements) can be more easily made.

In an actual engine combustor, additional combustion and cooling air is added to the combustor downstream of the actual fuel injector. This adds an additional complexity to the flow and combustion characteristics, which is being investigated in a subsequent study. Only the characteristics in the zone near the injector are presented in this paper.

The work reported herein was accomplished in identical burners available in the Combustion Laboratories at BYU and WPAFB, respectively. The burners were designed by researchers at P&W (Sturgess et al., 1992) and fabricated at WPAFB. The features of the dome and injector can be seen in Fig. 1. The type injector used in this study is a classic gas turbine engine air blast atomizing configuration, involving coswirling airsheets on either side of a coswirling annular (normally liquid) fuel sheet, with the outer air passage and the fuel passage both converging on the central air passage.

Two injectors of this same configuration were used. The high-swirl (HS) injector has a nominal swirl number (based on vane angle) of 1.41, and the low-swirl (LS) injector has a nominal swirl number of 1.05. The total air passage effective areas were 0.176 $in.^2$ for the HS injector and 0.266 $in.^2$ for the LS injector, with outer to inner flow splits of 2.8 and 2.2, respectively. The outer swirler vane angle was 55 deg for both injectors, while the inner swirler vane angle was 70 deg for the HS injector and 45 deg for the LS injector. The injectors were mounted in a plain bulkhead dome containing insert jets angled at 12.5 deg into the flame, and radially outward flowing film cooling jets. This arrangement closely simulates that of an engine combustor. The total effective air flow area of the dome, excluding the fuel injector, was 0.160 in^2.

The combustion chamber, shown in Fig. 2, has been designed to be nearly axisymmetric and incorporate quartz windows to allow optical diagnostics (primarily laser-based optical measurements) to be made. The combustor cross section is square with generously filleted corners to minimize secondary flow development. The hydraulic diameter is 150 mm. This box-section combustor with corner fillets allows reasonable optical access while providing a cross section that approximates a two-dimensional axisymmetric cross section. The bluff body provides a recirculation region that can stabilize the flame. Optical windows of fused quartz are provided on the four flat sides for a downstream length of 490 mm. The combustor overall length to hydraulic diameter ratio is 4.9, and the exit blockage is 45 percent by means of an orifice plate. The only air addition in this configuration is through the dome.

The combustor is mounted on a 240 mm long spool piece containing a mounting pad for the fuel injector flange. The combustor and spool piece are situated on an inlet air conditioning section, also shown in Fig. 2. Reactants are supplied at ambient temperature and pressure. Ignition is by means of a removable torch ignitor. This combustion chamber allows the combustion characteristics of a practical injector to be investi-

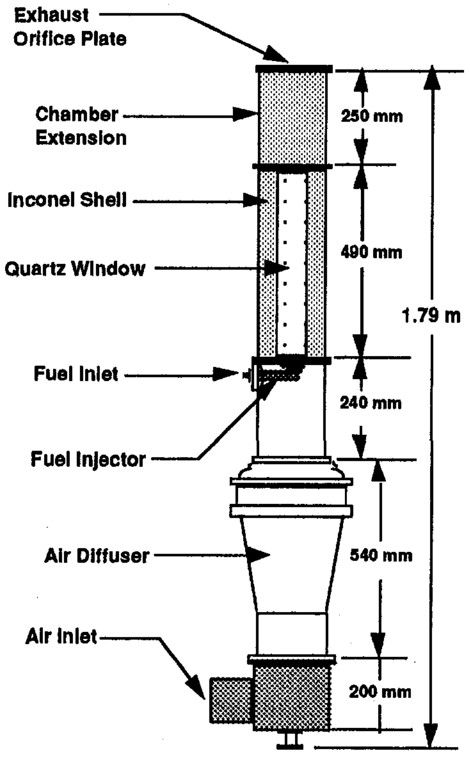

Fig. 2 Laboratory-scale gas turbine combustor

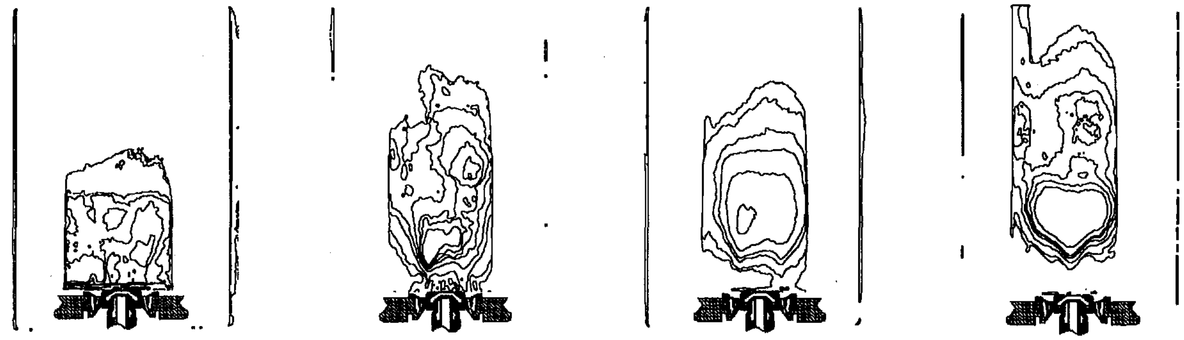

Very Rich Attached
$\phi = 2.38$

Rich Attached
$\phi = 1.72$

Rich Lifted
$\phi = 1.42$

Funnel Cloud
$\phi = 1.09$

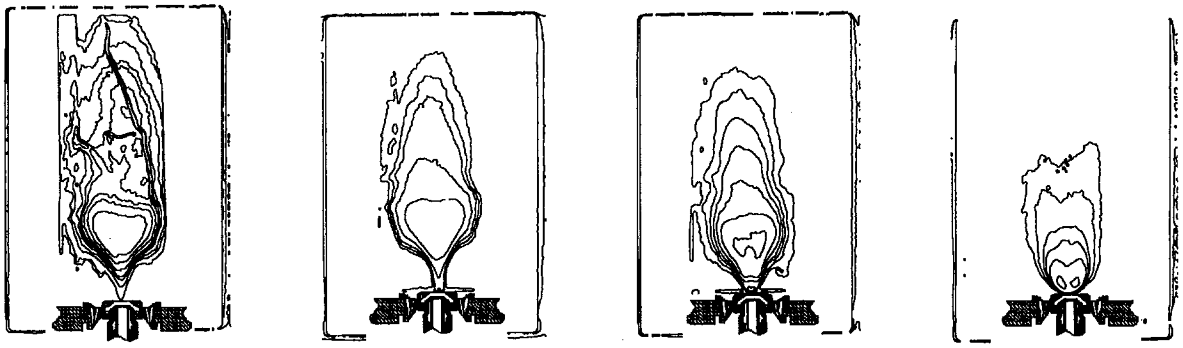

Attached Vortex
$\phi = 0.93$

Debris Cloud
$\phi = 0.85$

Fully Developed
$\phi = 0.78$

Near LBO
$\phi = 0.46$

Fig. 3 Characteristic flame shapes from digitized still photographs (T150-HS nozzle, 310 slpm air)

gated in a simple geometry where various diagnostic measurements can be made.

In order to separate the effects of liquid fuel atomization and spray droplet evaporation from the effects associated with fuel/air mixing and aerodynamic flow pattern, these first evaluations involved the use of a gaseous propane fuel. Planned subsequent evaluations will use liquid ethanol. Liquid ethanol is expected to simulate closely the combustion characteristics of the liquid jet fuels, but without significant soot formation. Extensive sooting could cloud the quartz windows precluding easy optical access. The present paper deals exclusively with propane results with the HS injector.

The results presented concern work with the Task 150 technology combustor using the high-swirl injector and gaseous propane fuel. While many detailed studies exist in the literature concerning jet flames, both free and enclosed, almost nothing is available on the flame characteristics produced by practical ways of introducing the reactants into an engine combustor. This work goes some way toward remedying this situation.

Photographic Flame Characterization

A complex series of intricate flame structures have been observed in the Task 150 technology combustor according to the operating conditions and fuel injector used. Some of the flame behavior could be related to that seen in the Task 100 research combustor (Sturgess et al., 1991a, 1993), and some of the structures to those seen in the Task 200 generic combustor (Sturgess and Shouse, 1993). These flame structures were studied directly with use of visual observations, video recordings, and still photography. The still film photographs have been digitized and filtered using computer techniques to produce isochromatic contour plots, Fig. 3, for quantitative purposes.

One of the traits of the Task 150 technology combustor is the wide variety of flame structures observed. Each flame shape indicates a different mode of operation, which differs from the others in the location of the flame fronts, or by some structure such as thickness or intensity. The different structures observed arise from changes in the flow fields, mixing patterns, or fuel equivalence ratio as operating conditions are varied. The differences and similarities of the flame structures for the swirling injectors together with the results from the co-axial jet diffusion flame (Task 100 combustor) provide significant insights to the combustion processes. The shape of the flame, at the minimum, provides qualitative information on the mixing process and location of flame fronts. Such information can yield insights into the processes present. Flames fronts exist because fuel and oxidizer have been transported to a point where combustion can be supported. The location of these fronts relative to the outlet orifices of fuel and air are of obvious interest.

The fuel equivalence ratios where the transitions from one flame structure to another were determined are a function of fuel flow rate. The flames for both Task 150 injectors were attached to the outside of the insert air jets when the burner was operated very fuel rich. The flame would then lift, reattach, and lift again as the fuel equivalence ratio was progressively reduced depending on the injector (high swirl versus low swirl) and the air flow rate. During the reattachment phase, the flame would take on many of the characteristics of a strong vortex, and shared many features associated with a tornado. Consequently, the terminology of funnel cloud, tornado, and debris cloud were adopted to differentiate some of the observed flame structure from the general description of a vortex flow. The characterization of the flame structure was carried out by visual observations. Still film photographs were taken of the different

Table 1 Summary of experimental conditions for LDA measurements

Injector	Flow	Air slpm (70 F)	C3H8 slpm (0 C)	N2 slpm (0 C)	ϕ
T150HS	Cold	500		14	0.72
T150HS	Hot	500	14		0.72
T150HS	Cold	500		29	1.49
T150HS	Hot	500	29		1.49
T100	Cold	1000		23	0.59

structures. These images were digitized and manipulated using various computer programs into the isochromatic contour plots found in Fig. 3 for the high swirl injector. The major factor affecting flame structure was the overall fuel equivalence ratio in the burner determined from total air and fuel flow rates, and to a much lesser extent the air flow rate. At a given air flow rate, the fuel would be reduced until a transition in flame structure was judged to have been reached. These observations were not easily made. With the high swirl nozzle, the flame structures flowed smoothly from one mode to another. These smooth transitions left no sharp break point in flame behavior. Consequently, the images presented in Fig. 3 are only representative of the types of flame structures observed.

At very fuel-rich conditions ($\phi = 2.38$ and $\phi = 1.72$), the flame was attached to the insert jets, in a manner similar to that observed with the Task 100 technology combustor at rich conditions. Unlike the Task 100, however, these flames were very short, presumably because of the much faster mixing due to the swirling motion of the gases. As the amount of fuel was further reduced (decreasing fuel equivalence ratio at a constant air flow rate), the still rich flame lifted and stabilized on a downstream recirculation zone that appeared to be associated with the injector ($\phi = 1.42$). The primary combustion zone continued to lengthen as relatively less fuel entered the combustion chamber ($\phi = 1.42$ to $\phi = 1.09$).

After the rich lifted condition, further reductions in fuel equivalence ratio caused the flame to stabilize in the rapidly swirling vortex at the center of the combustor, with flame structures that resembled the development of a tornado. As seen in Fig. 3, a structure that resembled a funnel cloud formed within the rich lifted flame ($\phi = 1.09$) and gradually descended as the fuel flow was continually decreased ($\phi = 1.09$ to $\phi = 0.93$) forming a tornado-like flame structure. Further reductions in ϕ caused the tornadolike flame to enter the primary swirler passage in the injector ($\phi = 0.93$). Continued reduction in fuel equivalence ratio caused a flame in the shape of a bowl, which looked much like the debris cloud of a tornado, to attach to the nozzle on the outside of the tornadolike structure ($\phi = 0.85$). The minute detail of the debris cloud was lost in the process of converting from the still photograph to the image presented in Fig. 3. Continued reduction of the fuel flow resulted in the growth in size and intensity of the debris cloud-like flame structure while the funnel cloud-like structure was simultaneously decreasing. The total disappearance of the funnel cloud structure marked a transition to a fully developed flame that was strongly attached to the center of the injector ($\phi = 0.78$). At lower air flow rates (less than ca 500 slpm), this strongly attached flame would weaken until the lean blowout limit ($\phi = 0.46$) was reached (blowout occurred from an attached flame). At high air flow rates (greater than ca 500 slpm), the flame would once again lift, attach to a downstream recirculation zone, and eventually blowout from the separated flame structure ($\phi = 0.42$), much like that observed in the Task 100 research combustor.

Gas Velocity Measurements

A laser-Doppler anemometer (LDA) was used to make extensive measurements of gas velocity in the burner at five separate experimental conditions. The experimental conditions used are summarized in Table 1.

The LDA measurements reported in this paper are for the Task 150 burner with the high-swirl injector installed. Measurements were made for lean conditions ($\phi = 0.72$) where the flame was well attached to the central part of the injector, and also at fuel-rich conditions ($\phi = 1.49$) where the flame was attached to the dome and insert jets. LDA measurements were also obtained in isothermal, nonreactive flows where nitrogen was substituted for the propane fuel. This has allowed the effect of the flame temperature on the flow field and gas velocities to be determined for at least two of the test conditions used. However, only the data from the combusting flow experiments are reported in this paper.

A schematic of the LDA experimental setup is presented in Fig. 4. The beam from the argon-ion laser was split into two beams, frequency shifted (40 and 34 MHz), polarized, and focused into a diagnostic volume in the test section. The forward-scattered LDA signals for the radial (or tangential) and axial velocity components were focused into fiber optic cables and passed to a photomultiplier tube to be amplified and converted to electrical signals. These electrical signals were collected with TSI, Inc., counters and analyzed with a Macintosh IIfx computer. A Le Croy 9314L Quad 300 MHz oscilloscope was used to monitor the Doppler bursts to help in the alignment of the LDA system and to insure quality data were being collected. Even with careful alignment, there was still some noise, which was filtered using a data analysis program.

A brief investigation was made to evaluate the effect of the number of points taken at a given test location on the accuracy of the gas velocity measurement. Three different sets of data were collected, a set with 5000 points, a set with 2000 points, and a set with 1000 points. In general, there was little difference observed in the mean axial and tangential velocities determined from the different number of points in the data sets. However, the fluctuating velocity components (i.e., rms velocities) were better described by the data sets containing the largest number of points. Nevertheless, for this study, 1000 data points were collected at each test location. This allowed a greater number of experimental conditions and geometries to be evaluated, albeit at slightly reduced data accuracy.

The two component velocity data (either axial and radial, or axial and tangential) were obtained for each of the test conditions described above (Table 1). The burner was translated with respect to the laser diagnostic volume in an X, Y, and Z coordinate system. Translation in the Z coordinate direction allowed different axial locations to be sampled. Translation in the X or Y axis allowed different radial locations to be sampled. For these tests, the X or Y translations were done along a coordinate centerline. Translation in the X coordinate direction along the Y coordinate centerline allowed axial and radial velocity data to be obtained. The edge of the windows limited transla-

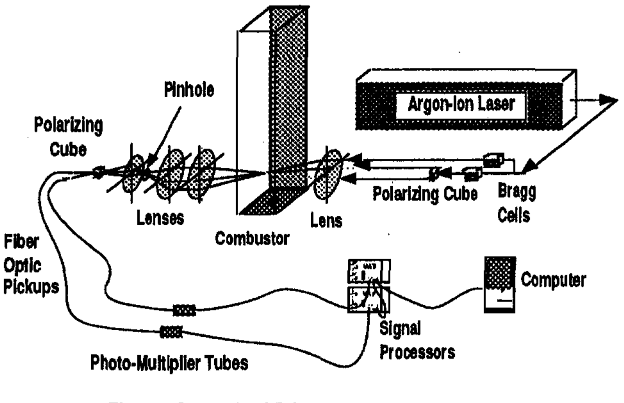

Fig. 4 Setup for LDA velocity measurements

tion in this coordinate direction to about ±30 mm. Translation in the Y coordinate direction along the X coordinate centerline allowed axial and tangential velocity data to be obtained. As the diagnostic volume was brought near the quartz windows, significant optical noise was added to the Doppler signals. The quartz windows were approximately ±75 mm from the center of the reactor. The optical noise from the windows generally limited data collection to ±65 mm, although with especially clean windows, it was sometimes possible to get good data at ±70 mm.

Typically, data were collected at 0.5 or 1.0 mm radial increments where the velocity gradients were large. Data were collected at up to 10 mm increments where velocity profiles were relatively flat. A typical set of data was taken at axial locations of 10, 15, 20, 25, 50, 75, 100, 125, 150, 200, and 240 mm above the dome of the reactor. Occasionally, other intermediate locations were examined where large velocity gradients or other interesting behavior were found.

The basic flow field in the combustor was derived by interpolation of the velocity data obtained. The field is dominated by multiple regions of flow recirculation. The axial velocity from both the X and Y coordinate traverses has been combined for one of the Task 150-HS cold flow cases (14 slpm N_2, 500 slpm air), interpolated, and the zero axial velocity contours plotted in Fig. 5. Each zero axial velocity contour bisects a recirculation zone. While the data have not been analyzed in the detail needed to quantify the recirculation patterns totally, estimates of the recirculation zones are indicated. Eventually, flow streamlines will be plotted to identify the various flow fields better. However, for this paper, only axial, tangential, or radial data have been used.

Figure 5 identifies several important recirculation zones. Although the near field is similar to that in a real gas turbine combustor, the downstream region in not due to the absence of air addition by means of transverse jets, as is usual practice. Since current interest is concentrated on the near field, this deviation is not of great significance. It is interesting to note that there is a zone of flow reversal on the centerline of the burner very near the discharge of the injector. This flow reversal is undoubtedly caused by the highly swirling flow, and is consistent with the strong vortex structures observed earlier (Fig. 3). A recirculation zone is also apparent in the lower corners of the combustion chamber. This zone appears to be driven by the dome cooling jets, and is consistent with the observed horizontal flow in the radial direction that emanates from these cooling jets.

Another major recirculation zone is centered on the zero axial contour that angles from the face of the injector outward till it reaches the wall of the combustor at a down stream location at about 140 mm. This large recirculation zone seems to have a major impact in stabilizing the flame under certain operating conditions. The last observed recirculation zone surrounds the zero isovelocity contours that exist between the 100 mm and 240 mm axial locations. This recirculation pattern was very weak as judged by the magnitude of the velocities measured, and was only observed in the isothermal case. It was not seen in the combusting cases. The influence of the combustion was sufficient to eliminate this pattern from the flow field. Combustion also altered the shape and location of the other recirculation zones, but each of the other zones remained in the combustion cases.

Figures 6(*A*), 6(*B*), and 6(*C*) present the isocontour plots for the mean axial, mean tangential, and mean radial velocity measurements respectively for the fuel lean case ($\phi = 0.72$). In each figure, the velocity contour plot from the centerline to the maximum measurement radius was created using commercial computer software, duplicated, and reversed. The reversed image was combined with the original image and superimposed on a schematic of the burner to provide an indication of the flow characteristics with respect to the burner. The data presented in Figs. 6(*A*) and 6(*B*) were collected along the Y coordinate direction out to about 60 mm. The data in Fig. 6(*C*) are limited to a radial location of about 30 mm because of the width constraints of the windows. The flow fields and recirculation patterns presented here are generally consistent with those observed in Fig. 5.

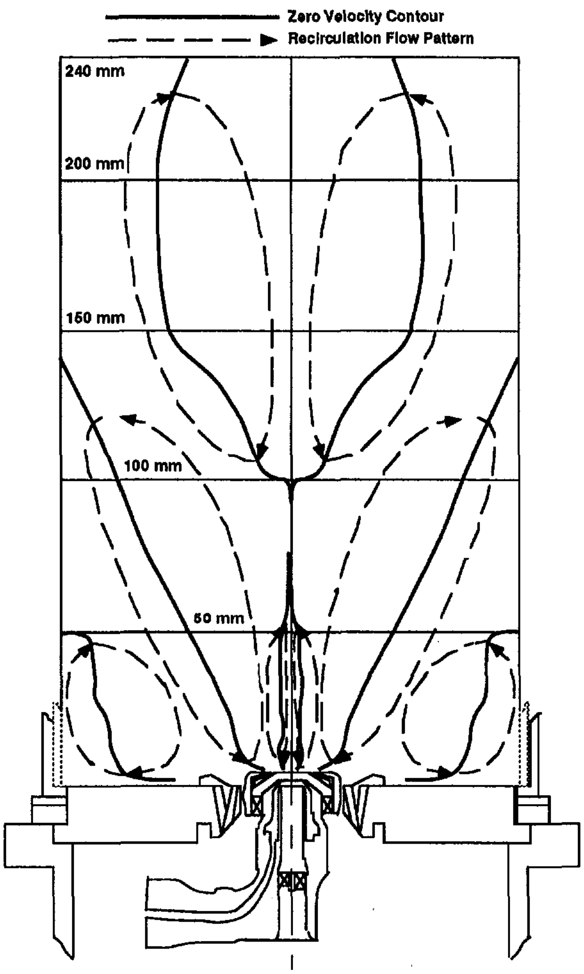

Fig. 5 Recirculation patterns with the high-swirl fuel injector

The flame at the operating condition was well attached to the center of the injector, and was considered to be fully developed, as was shown earlier in the discussion of Fig. 3. Mass balance calculations based on isothermal axial velocity measurements have been used to determine the overall accuracy of the LDA measurements. It was found that the mass flow rate was strongly influenced by the gradient assumed near the wall, but reasonable velocity interpolations gave reasonable mass balance closure.

The sharp peak in axial velocity component shown in Fig. 6(*A*) near the injector is clearly evident. The rapid decay of the high-velocity region near the injector as one moves downstream is also apparent. The recirculation zone directly over the injector is dramatic, and clearly shows a significant region of flow reversal. The tangential velocity in this zone is very high as seen in Fig. 6(*B*). The other major recirculation pattern in the combustor is of a somewhat different shape and in a somewhat different location than observed in the isothermal case (Fig. 5). The recirculation patterns caused by the dome jets are notably absent. Visual observations confirmed that the corner recirculation still existed in the combustion flow cases, but it was not possible to collect LDA data close to the window near the bottom of the reactor because of excess optical noise.

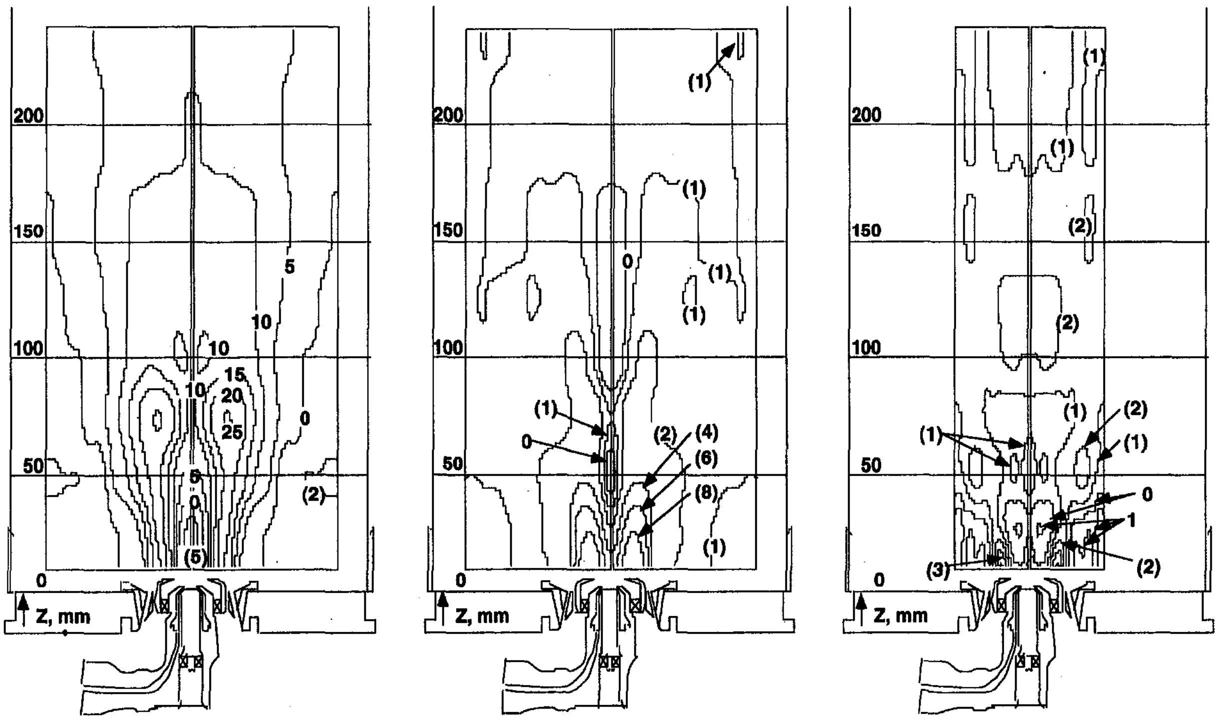

Note: (N) denotes negative number

A) Mean Axial Velocity, m/s B) Mean Tangential Velocity, m/s C) Mean Radial Velocity, m/s

Fig. 6 Isovelocity contours for the T150-HS burner at ϕ = 0.72 and 500 slpm air flow rate

The radial velocity data are presented in Fig. 6(*C*). These data are limited to a radial location of about 30 mm. The radial flow velocities are all very low in magnitude, but do show some interesting structures. The low magnitudes of these velocities are close to the resolution of the LDA instrument. A similar set of gas velocity data for the Task 150-HS combustor operating at a fuel equivalence ratio of 1.49 is presented in Figs. 7(*A*), 7(*B*), and 7(*C*) for the mean axial, mean tangential, and mean radial velocity measurements, respectively. The flame at this operating condition was attached to the insert and dome jets as was shown earlier in the discussion of Fig. 3. As above, the radial data in Fig. 7(*C*) are limited to a radial location of about 30 mm, but the axial and tangential data in Figs. 7(*A*) and 7(*B*) were collected out to about 60 mm. The flow fields and recirculation patterns presented here are also generally consistent with those observed in Figs. 5 and 6.

As for the ϕ = 0.72 case, the sharp peaks in mean axial velocity component associated with the injector are still clearly evident, but seem to decay more rapidly than in the ϕ = 0.72 case. The recirculation zone directly over the injector is still dramatic, and shows little difference in the magnitude of the reversed velocity or in the size and shape of the recirculation pattern when compared to the ϕ = 0.72 case. The other major recirculation pattern in the combustor is of a similar shape to that observed with the ϕ = 0.72 case, but seems to be much stronger (i.e., has much larger reversed flow velocity components). The recirculation patterns caused by the dome jets are still absent. As in the ϕ = 0.72 case, visual observations confirmed that the corner recirculation still existed in this combustion flow case, but it was not possible to collect LDA close to the window near the bottom of the reactor because of optical noise near the quartz windows.

The radial velocity data are presented in Fig. 7(*C*). Again, the radial flow velocities are all very low in magnitude, but do show some interesting structures, that are quite different than seen with the lean flame. The low magnitudes of these velocities are also close to the resolution of the LDA instrument.

The differences in velocities between the lean flame and the rich flame show that there is a strong influence of the location of the flame zone on the flow fields as characterized by the measured velocity fields.

Gas Temperature Measurements

Coherent anti-Stokes Raman spectroscopy (CARS) was used to obtain a set of gas temperature measurements in the Task 150-HS combustor at fuel equivalence ratios of 0.75, 1.00, 1.25, and 1.50; and at an air flow rate of 500 slpm. The details of the CARS facility have been well documented in previous publications (Boyack and Hedman, 1990; Hancock et al., 1991, 1992). The CARS setup used for this study, as shown in Fig. 8, is very similar to the folded box-CARS phase matching scheme employed by Boyack (Boyack and Hedman, 1990). Boyack located his combustor directly on the CARS optical table, and was able to focus the laser beams easily directly into his combustor. In this experimental setup, the combustor was remotely located. Consequently, the laser beams were directed off the optics table over a distance of about 10 m onto a set of optical bread boards located on either side of the Task 150-HS combustor. The optical components needed to create the box-CARS phase matching were located on these remote optical breadboards. As with Boyack's work, the CARS signal was focused into the end of the fiber optic used to transfer the signal back to the spectrometer. The CARS lasers and spectrometer were keep in an optics room distant from the combustion facilities in an effort to keep the optical components relatively clean.

Like the gas velocity measurements, the CARS temperature measurements were taken at closely spaced radial increments where large gradients in temperature were found and in a coarser grid where the temperature gradients were found to be relatively

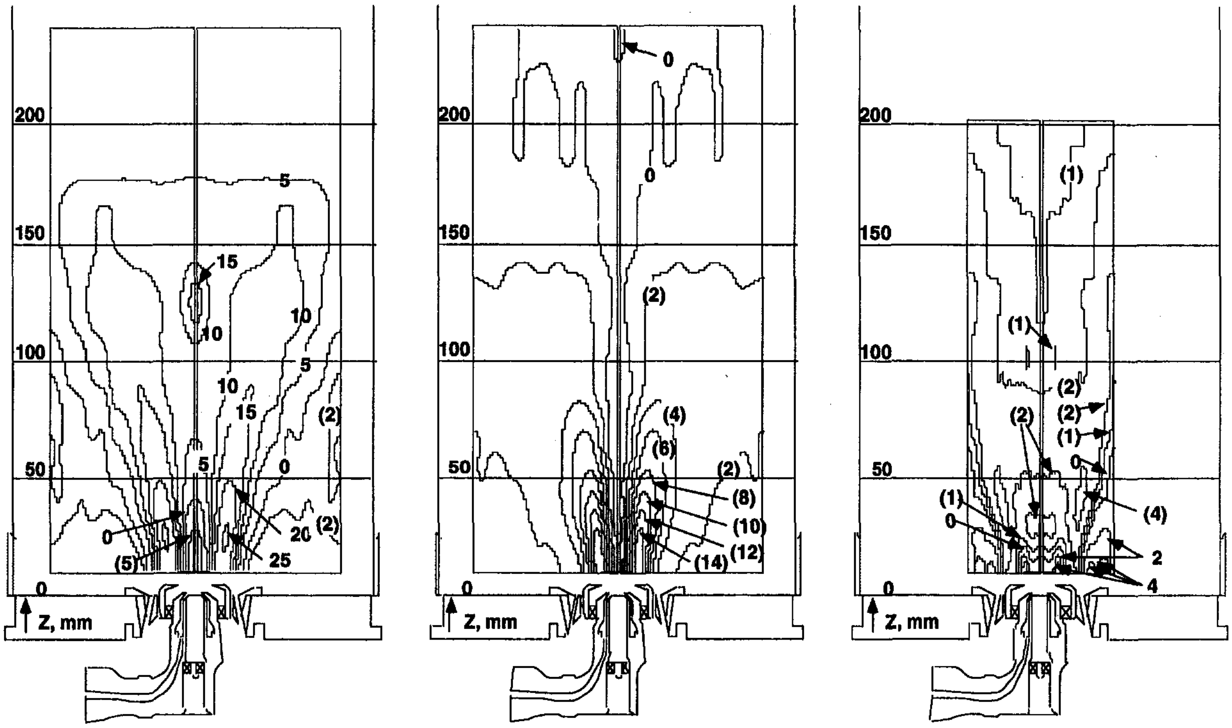

Note: (N) denotes negative number

A) Mean Axial Velocity, m/s B) Mean Tangential Velocity, m/s C) Mean Radial Velocity, m/s

Fig. 7 Isovelocity contours for the T150-HS burner at ϕ = 1.49 and 500 slpm air flow rate

shallow. Temperature data were taken at similar axial locations as well. The temperature data were taken along the X coordinate, and consequently are available only out to a radius of about 30 mm, but were taken to an axial location of about 300 mm. Attempts at obtaining data along the Y axis to radial locations near the quartz window resulted in laser damage to the quartz window. Nevertheless, the CARS temperature data obtained have provided adequate temperature measurements to well quantify the temperatures in the region of most interest near the injector.

Figure 9 presents isocontour plots of temperature data for the Task 150-HS combustor operating with an air flow rate of 500 slpm and at fuel equivalence ratios of 0.75, 1.00, and 1.50. The data at ϕ = 1.25 have been excluded from the paper because of space considerations. Two hundred discrete temperature data points were taken at each of 92 separate diagnostic locations from the centerline to a 30 mm radial location, and from 10 mm to 300 mm axial location. These sets of data were used to determine the mean temperatures used to create the isothermal contour plots shown. In order to show the symmetry of the flame, the contour plot was duplicated, and computer software was used to flip the image and add it to the opposite side of the combustor. The flow fields are very symmetric about the centerline in this highly swirled flame. The doubled image gives a better representation of the temperature field in the vicinity of the injector.

The relatively cold region (600 K to 1000 K) directly above the injector in all three cases generally corresponds to the central recirculation zone seen in the gas velocity plots (Figs. 6 and 7). Surrounding the cold central zone is an intermediate temperature region that seems to be associated with the penetration of the very high axial velocity into the combustor. Higher temperatures exist on either side of this penetration zone. It is unfortunate that temperature data could not be obtained in the lower corners of the combustor where the recirculation zones near the dome are located. The data do suggest that this region is relatively cool for the ϕ = 0.75 case, but seem to indicate a relatively hot region in this corner recirculation zone for the ϕ = 1.5 case. This observation seems to be consistent with the observed relocation of the flame zone from the central core of the vortex when operating fuel lean to the outer recirculation zone when operating fuel rich, as noted in the digitized film images and in the PLIF images of OH radical discussed in the last section of this paper.

Temperatures in excess of the ϕ = 0.75 adiabatic flame temperature (1963 K) are seen in a zone near the centerline at an axial location of about 100 mm for the fuel lean case. Since this is a non-premixed flame, this suggests that this diffusion zone may be operating with near-stoichiometric (ϕ = 1.00) mixtures of fuel and air. The peak temperature that was measured was 2085 K which is about 178 K below the theoretical stoichiometric adiabatic flame temperature of 2263 K.

In the stoichiometric case (ϕ = 1.00), the peak measured temperature is 67 K below the theoretical stoichiometric adiabatic flame temperature of 2263 K. The zone of near-peak temperature extends from an axial location of about 100 mm to about 170 mm and forms a toroidal shaped ring around the centerline. Beyond the high-temperature region, the temperatures decrease, dropping to about 1800 K at the combustor exit (not shown).

Isocontour plots of gas temperature measurements for the ϕ = 1.50 case are shown in Fig. 9(*C*). It is interesting to note that the peak temperature (1875 K) in the fuel-rich case, like the stoichiometric case, is just below the predicted (ϕ = 1.50) adiabatic flame temperature of 1974 K. It seems reasonable that the peak measured temperature in this case would be close to the adiabatic flame temperature, since all of the oxygen would be consumed early in the flame, preventing a zone near stoichiometric from ever existing.

The variation in temperature field as the fuel equivalence ratio changes from fuel lean to fuel rich seems to be consistent with the observations made from the still photographs. At ϕ =

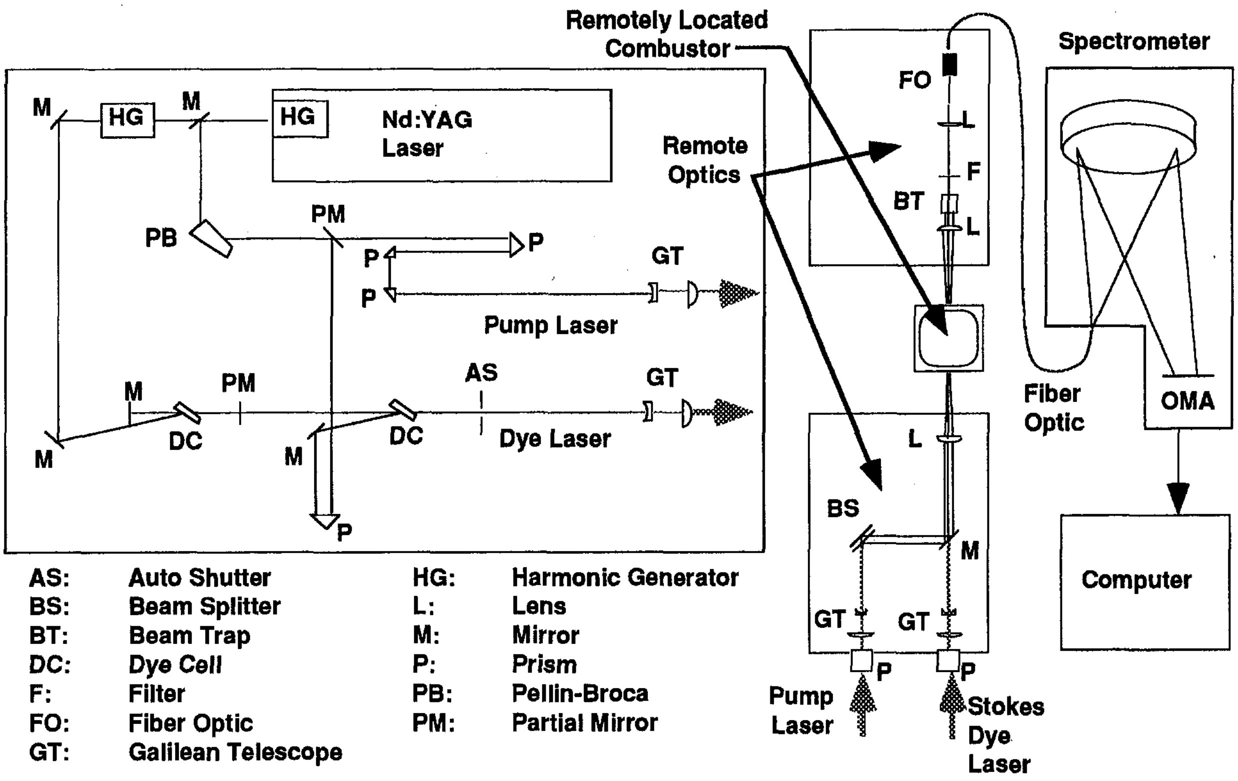

Fig. 8 Schematic of CARS system installation on the combustor

0.75, the flame is well attached to the burner, with a narrow vortex penetrating into the injector and a fully developed flame structure attached to the injector. The temperature distributions at $\phi = 1.0$ and $\phi = 1.25$ (not shown) were very similar, and seemed to agree with the flame structures described in Fig. 3 as a rich lifted flame and a funnel shaped flame. At $\phi = 1.50$ (Fig. 9*C*), the center cold zone has been reduced in size, and there are higher temperatures at the outer edge of the measurement region that support the visual observation that the flame is attached to the insert jets. These results also suggest that a fairly high temperature exists in the corner recirculation zone when the combustor is operating in a fuel rich mode. In general, the temperature measurements are consistent with the visual flame conditions, the PLIF images of the OH radical, and the velocity measurements for this particular test condition.

PLIF Imaging of OH Radical

In PLIF (planner laser induced fluorescence) imaging, a dye laser is tuned to a resonant frequency, which causes the particular combustion radical or molecule to fluoresce at a different resonant frequency. This fluorescence is then recorded and the two-dimensional image preserved with an electronic camera. In these experiments, OH radicals were excited with an ultraviolet (ca 283 nm) light sheet produced by a tunable dye laser pumped with a 10 ns pulse from a Nd:Yag laser. This sheet of laser light was passed through centerline of the reactor. An intensified CCD camera, located normal to the laser sheet, captured the 75 mm high two-dimensional UV (ca 308 nm) image (Fig. 10). This nearly instantaneous map of OH radical concentration in the flame zone was then stored by a Macintosh computer. The images have been analyzed and enhanced using conventional computer software.

OH radicals are commonly chosen for PLIF because they are important markers in hydrocarbon flames. These radicals are produced in large quantities during the combustion process, and are a good indicator of flame fronts. However, in some circumstances, these radicals may persist for long distances downstream of the actual flame front, limiting their usefulness. Also, as in any laser diagnostic technique, there is a concentration level below which the OH radical will not be detected. With these limitations in mind, conclusions based solely on PLIF images of the OH radical must be carefully drawn.

Many PLIF images of the OH radicals were obtained in the Task 150-HS combustor at 500 slpm air flow and at fuel equivalence ratios that ranged from 0.62 to 1.75. Images were taken at values of fuel equivalence ratio that roughly correspond to the changes in flame structure that had been observed visually and documented with still photographs (Fig. 3). Comparison of the two types of flame image, and the relation of these images to the time-mean flow field and bulk equivalence ratios, explains much about the flame structures. However, comparison of a sequence of instantaneous OH images at fixed operating conditions, e.g., Fig. 11, also reveals the highly nonstationary character of the flame zone. This behavior is similar to that observed previously in the Task 100 research combustor (Roquemore et al., 1991).

The experimental behavior of the Task 100 research combustor is quite different from the predictions by computational fluid dynamics (CFD) programs. These computer codes predict the flame to be anchored in the jet shear layer for all fuel equivalence ratios. However, the flame has been experimentally observed (Roquemore et al., 1991) to attach to the backward-facing step just outside the air tube at fuel equivalence ratios (ϕ) in excess of 1.08. In these operating conditions, a small "coke bottle" shaped flame pilots a thicker flame sheet, which is much lower in the combustor than the CFD programs predict. A waisting in the flow field is predicted by the CFD code, but the mixture is predicted to be too lean to burn. Roquemore postulates that a discrete and intermittent process is responsible for the entrainment of the fuel into the step recirculation zone. This type of transport would require passageways in the flame in order to deliver the unburned fuel from the fuel tube to the

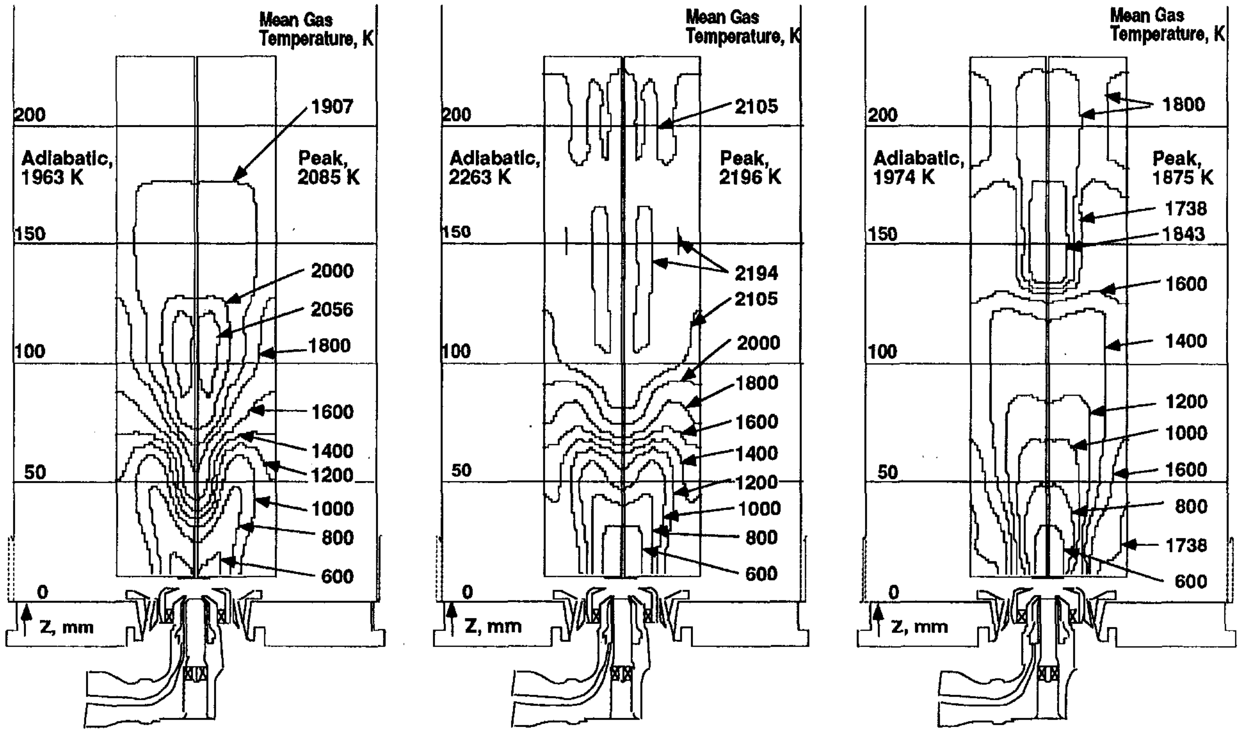

A) Fuel Equivalence Ratio = 0.75 B) Fuel Equivalence Ratio = 1.00 C) Fuel Equivalence Ratio = 1.50

Fig. 9 Mean gas temperature isocontours for the T150-HS burner at 500 slpm air flow rate

step recirculation zone. These passageways would appear as a region with little to no OH radical present.

Much of what Roquemore postulated has been found in PLIF images of the OH radical collected in the Task 100 research combustor. In the well-attached flame ($\phi = 1.56$), the OH radicals appear in vortex structures being shed off the backward step. These structures were very clear in the images collected. In the lean condition, OH radicals were not observed below 150 mm in the reactor, with relatively small amounts between 150–200 mm and very large amounts beyond. Similar observations have been made in the PLIF images of the OH radical for the Task 150 technology combustor (e.g., Fig. 11 and Fig. 12*A*, 12*B*, and 12*C*). Figure 11 shows four separate instantaneous images at two different axial locations at $\phi = 1.29$. Figure 12 shows composites of several single PLIF images of OH radical grouped as a collage in the appropriate locations within the combustor at a fuel lean condition ($\phi = 0.62$), near-stoichiometric ($\phi = 1.08$), and at a fuel-rich condition ($\phi = 1.49$). These images dramatically illustrate the characteristics of swirling flames and the highly variable nature of the instantaneous flame shape. Therefore, it seems likely that the conclusion reached for the co-axial jet system of the Task 100 research combustor (Roquemore et al., 1991; Sturgess et al., 1992, 1991b), that mass transport in axisymmetric, turbulent, recirculating flames is dominated by nonstationary flow phenomena, and not by gradient transport is confirmed, even in a practical injection system. The implication of this finding for accurate mathematical modeling of practical turbulent combustion systems is very important.

It is informative to correlate these OH images with the information known about the partitioning of the air flow rates through the various air passageways through the nozzle. The local fuel equivalence ratios shown in Table 2 were calculated from the air flow through each of the different passageways and the total fuel flow. Implicit in these calculations are two assumptions. First, the fuel is assumed to mix uniformly within each combination of partitions before mixing with remaining air. Second, any fuel blockage effects (which would change the partitioning as a function of fuel flow) are assumed to be negligible. At this air flow rate (500 slpm), LBO occurs at a fuel equivalence ratio of about 0.42.

With these assumptions in mind, and knowing the flammability limits (ϕ) of propane are roughly 0.5 to 2.5, some conclusions can be cautiously applied to these images. In every case, the air in the primary swirler alone does not provide sufficient oxidizer to permit combustion. Thus, the fuel must mix with at least the secondary swirled air before combustion is possible. As shown in Fig. 12 (*A*), with a fuel equivalence ratio of 0.62, the funnel structure expected in a swirl stabilized flame is clearly evident. The local fuel equivalence ratio with the air from the two swirled jets is 1.11, indicating little air from the insert jets is needed to complete the combustion. Although Fig. 12(*A*) shows high concentrations of OH radical extending above the funnellike structure, visual observations reveal the visible flame region is apparently only a thin sheet, much like a horn, or funnel, with a rounded cusp.

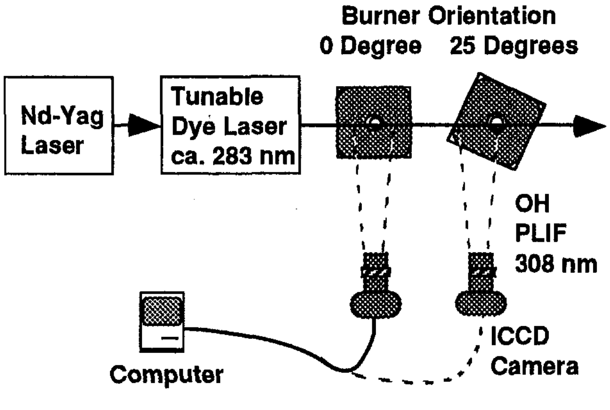

Fig. 10 Instrumentation for PLIF imaging of OH radical

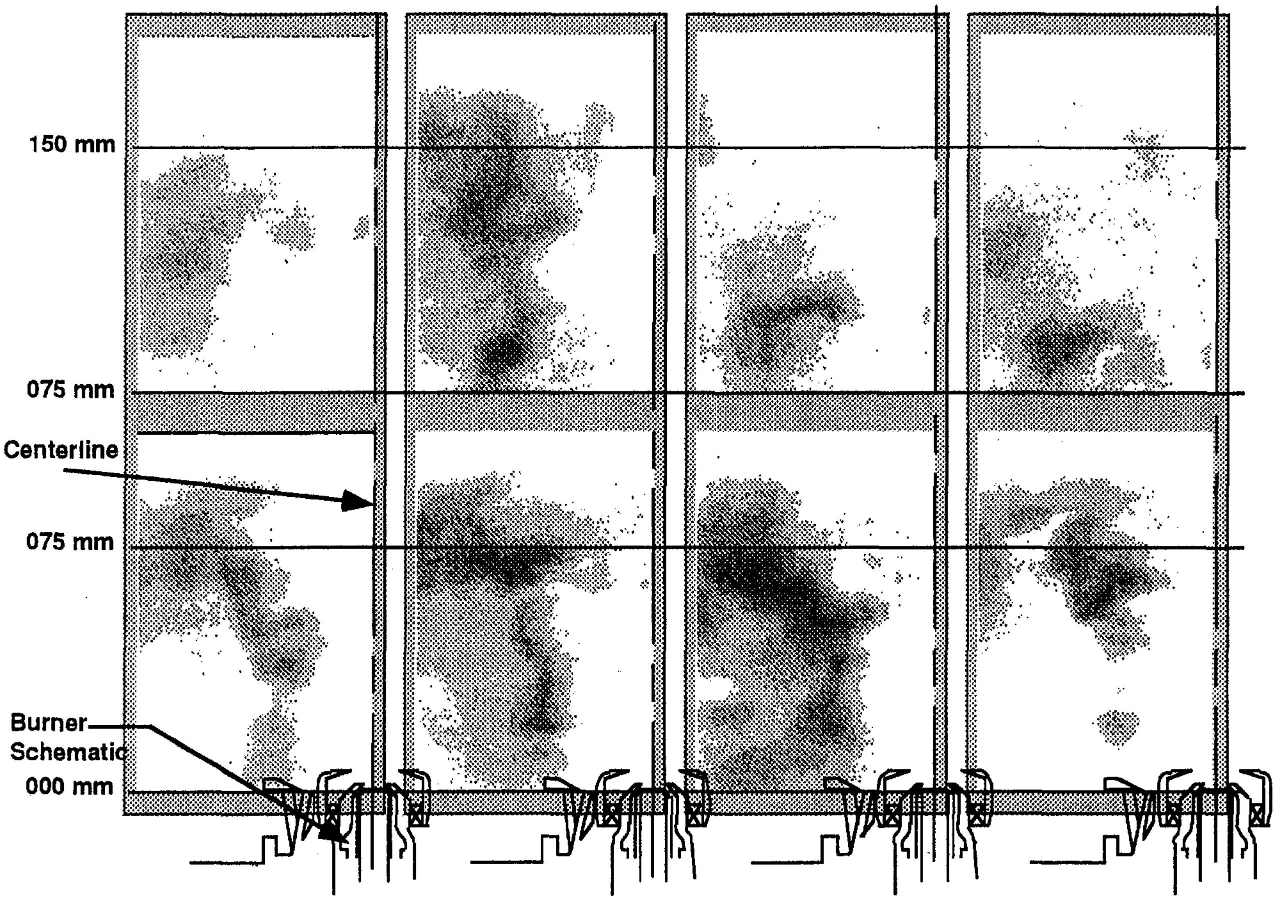

Fig. 11 Instantaneous flame images by PLIF of the OH radical (T150-HS nozzle, 500 slpm air, ϕ = 1.29)

As the overall fuel equivalence ratio is increased to 1.08 (Fig. 12*B*), the swirled air/fuel mixture was still within flammability limits. What changed was the extra fuel left to mix with the insert jets. This additional fuel, as shown in Fig. 12 (*B*), apparently burned on the shoulders of the funnel like structure. Finally, as the overall fuel equivalence ratio is increased to 1.49 (Fig. 12*C*), the very fuel-rich swirled air directly over the injector can no longer support combustion. The estimated fuel equivalence ratio in this central zone is estimated to be about 2.67, which exceeds the rich flammability limits for propane and air. The characteristic funnel of a swirl stabilized flame is no longer visible in Fig. 12(*C*). The combustion is only taking place where air from the insert and dome jets has reduced the local fuel equivalence ratio to within the flammability limits of propane and air. This can be illustrated by comparing Fig. 12(*A*) with Fig. 12(*C*). These two images appear to be negatives of each other—where one is black the other is white. This tends to support an assumption of the fuel mixing with each air passageway in turn from the inside out.

Observations and Conclusions

There have been considerable insights into the operational characteristics of a practical injector gained from this study. However, there is much to be done before a full understanding of the combustion characteristics of a practical gas turbine combustor is achieved.

A complex series of intricate flame shapes have been observed in the Task 150 technology combustor. Each flame shape indicates a different mode of operation, which differ from one another in the location of the flame fronts, or by some structure such as thickness or intensity. The different structures observed arise from changes in the flow fields, mixing patterns, or fuel equivalence ratio as operating conditions are varied. The fuel equivalence ratio where the flame transitions from one structure to another is the major operating variable affecting flame structure. The flames were attached to the insert air jets when the burner was operated very fuel rich. The flame would then lift, reattach, and lift again as the fuel equivalence ratio was progressively reduced. During the reattachment phase, the flame would take on many of the characteristics of a strong vortex and showed characteristics much like a tornado. Consequently, the terminology of funnel cloud, tornado, and debris cloud were adopted to describe some of the observed flame structure.

Gas velocity measurements were made where the flame is well attached to the injector (ϕ = 0.72), at fuel-rich conditions (ϕ = 1.49) where the flame is attached to the dome and insert jets, and in isothermal, nonreactive flows where nitrogen was substituted for the propane fuel. These velocity data have allowed the effect of the flame temperature on the flow field and gas velocities to be determined.

Gas velocity data near the injector have shown sharp peaks in mean axial velocity near the outlet of the injector, and a corresponding strong tangential component in this same location. The insert jets had a marked influence on the axial and radial components, but seemed to have little effect on the tangential velocity components. The sharp gradients in axial velocity component were observed to decay quite rapidly with increasing downstream position. The strong tangential velocities associated with the injector decayed rapidly and diffused to the outer edges of the reactor becoming nearly uniform (ca −1 m/s across the duct by the 150 mm axial location. Mass balance calculations based on isothermal axial velocity measurements have been used to determine the accuracy of the LDA measurements, and to assist in the extrapolation of the velocity to the

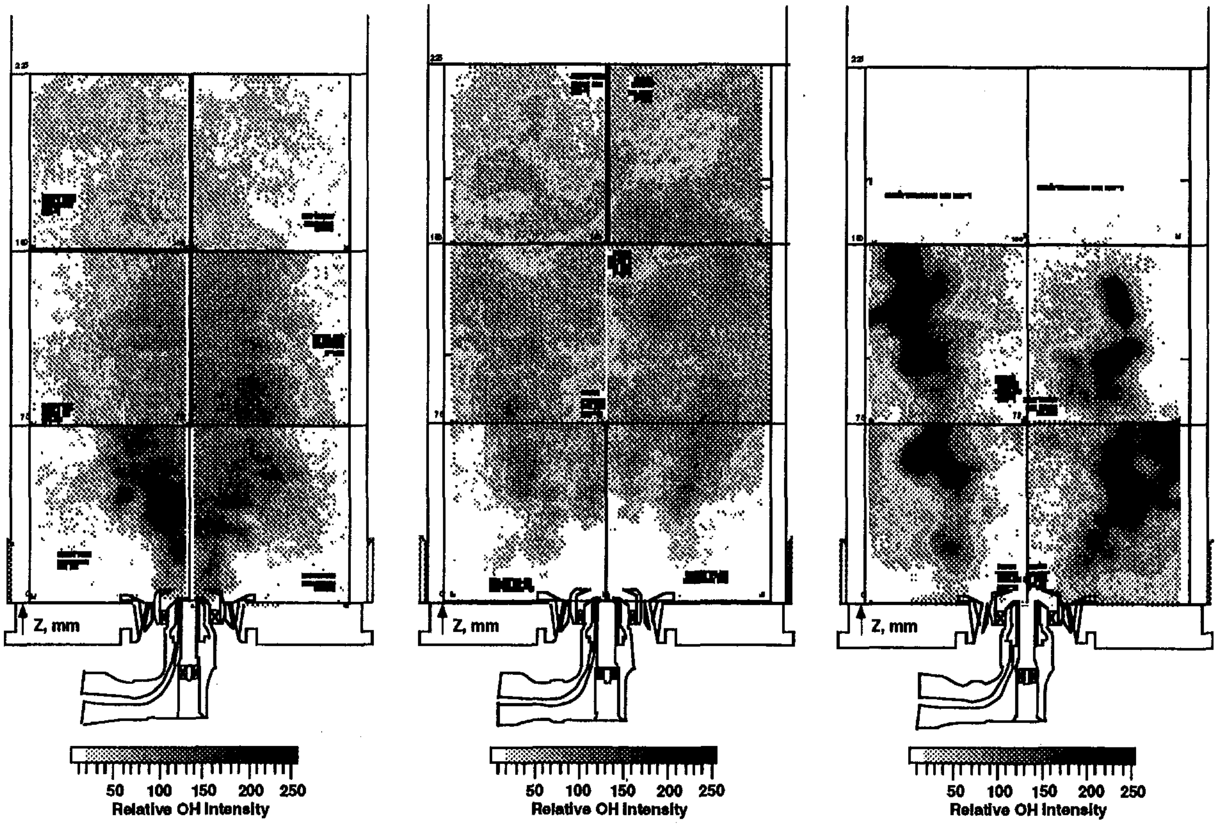

a) Fuel Equivalence Ratio = 0.62 **b) Fuel Equivalence Ratio = 1.08** **c) Fuel Equivalence Ratio = 1.49**

Fig. 12 Instantaneous PLIF contours of OH radical (T150-HS burner, 500 slpm air)

wall. The mass flow rate is strongly influenced by the gradient assumed near the wall, but reasonable velocity interpolations gave reasonable mass balance closure.

Images from still photographs and angular velocity data deduced from the tangential velocity measurements have shown that the flow in the region behaves much like that observed in a strong vortex, with the rotational speed in rpm increasing toward infinity as the zero radius position is approached. The high rotational speeds are consistent with visual observations of the flames. The steep gradients in angular velocity suggest the shear stresses in the swirling eddies are very high.

An analysis of the zero axial velocity contours for one of the isothermal flow cases (14 slpm N_2, and 500 slpm air) has been used to show the complex flow structure that includes four recirculation zones: one at the bottom edge of the reactor driven by the dome jets, a second small but intense recirculation zone associated with the injector swirlers directly over the injector, a third major recirculation zone that begins at the edge of the injector and angles upward to the wall of the reactor, and a weak fourth recirculation zone high up in the combustor. The weak fourth zone was not seen in the combusting flows. The recirculation zones are consistent with the visual observations and video images taken of the reactor.

Table 2 Local ϕ from total fuel flow and air for each flow passage combination

Overall ϕ	ϕ with air from primary swirler	ϕ with air from primary + secondary swirlers	ϕ with air from primary + secondary swirlers + insert jets
0.62	4.17	1.11	0.80
1.08	7.26	1.94	1.39
1.49	10.02	2.67	1.92

CARS gas temperature measurements have been successfully made in the Task 150 technology combustor. The measured peak temperatures were slightly below the predicted adiabatic flame temperature for the stoichiometric and fuel rich cases. The peak temperature was slightly higher than the adiabatic flame temperature for the lean case, which suggests a local diffusion zone within the flame that is close to a stoichiometric fuel equivalence ratio.

The variation in temperature field as the fuel equivalence ratio changes from fuel lean to fuel rich seemed to be consistent with the observations made from the still photographs. In general, the temperature measurements are consistent with the visual flame conditions, the PLIF images of the OH radical, and the velocity measurements for this particular test condition.

The PLIF images of the OH radical taken with the Task 150-HS technology burner dramatically illustrate the characteristics of swirling flames and the highly variable nature of the flame shape. The air from the insert jets significantly affects the flame structure, and the different modes of operation observed. Correlation of these OH images with the partitioning of the air flow rates through the various air passageways of the injector showed a consistent correlation between the local fuel equivalence ratio and the location of the flame structure. The images at low overall fuel equivalence ratio where the flame is well attached to the burner, and the images at high overall fuel equivalence ratio where the flame is attached to the insert jets are negatives of each other—where one is black the other is white. This supports the assumption of the fuel mixing with each passageway in turn from the inside out.

Acknowledgments

This paper presents results from an Air Force Office of Scientific Research (AFOSR) program being conducted at Brigham Young University (BYU), Provo, Utah, and at Wright-Patterson Air Force Base (WPAFB). This study is part of an extensive research effort being carried out by the Fuels Combustion Group of the Aero Propulsion and Power Laboratory at Wright-Patterson Air Force Base (APPL, WPAFB), Dayton, Ohio, in which simple and complex diffusion flames are being studied to understand better the fundamentals of gas turbine combustion. The program's long-term goal is to improve the design methodology of gas turbine combustors.

References

Boyack, K. W., and Hedman, P. O., 1990, "Dual-Stokes CARS System for Simultaneous Measurement of Temperature and Multiple Species in Turbulent Flames," *Twenty-Third Symposium (International) on Combustion,* The Combustion Institute, Pittsburgh, PA.

Hancock, R. D., Hedman, P. O., and Kramer, S. K., 1991, "Coherent Anti-Stokes Raman Spectroscopy (CARS) Temperature and Species Concentration Measurements in Coal-Seeded Flames," *Combustion and Flame,* Vol. 71, pp. 593–604.

Hancock, R. D., Boyack, K. W., and Hedman, P. O., 1992, "Coherent Anti-Stokes Raman Spectroscopy (CARS) in Pulverized Coal Flames," *Advances in Coal Spectroscopy,* Henk L. C. Meuzelaar, ed., Plenum Publishing Company, pp. 373–407.

Roquemore, W. M., Reddy, V. K., Hedman, P. O., Post, M. E., Chen, T. H., Goss, L. P., Trump, D., Vilimpoc, V., and Sturgess, G. J., 1991, "Experimental and Theoretical Studies in a Gas-Fueled Research Combustor," Paper No. AIAA 91-0639.

Sturgess, G. J., Heneghan, S. P., Vangsness, M. D., Ballal, D. R., and Lesmerises, A. L., 1991a, "Lean Blowout in a Research Combustor at Simulated Low Pressures," ASME Paper No. 91-GT-359.

Sturgess, G. J., Sloan, D. G., Roquemore, W. M., Reddy, V. K., A. L. Shouse, D., Lesmerises, A. L., Ballal, D. R., Heneghan, S. P., Vangsness, M. D., and Hedman, P. O., 1991b, "Flame Stability and Lean Blowout—A Research Program Progress Report," *Proceedings of the 10th ISABE Conference,* Nottingham, United Kingdom, pp. 372–384.

Sturgess, G. J., Sloan, D. G., Lesmerises, A. L., Heneghan, S. P., and Ballal, D. R., 1992, "Design and Development of a Research Combustor for Lean Blowout Studies," ASME JOURNAL OF ENGINEERING FOR GAS TUBRINES AND POWER, Vol. 114, pp. 13–19.

Sturgess, G. J., Heneghan, S. P., Vangsness, M. D., Ballal, D. R., Lesmerises, A. L., and Shouse, D., 1993, "Effects of Back-Pressure in a Lean Blowout Research Combustor," ASME JOURNAL OF ENGINEERING FOR GAS TURBINES AND POWER, Vol. 115, pp. 486–498.

Sturgess, G. J., and Shouse, D., 1993, "Lean Blowout Research in a Generic Gas Turbine Combustor With High Optical Access," ASME Paper No. 93-GT-332.

A Review of Droplet Dynamics and Vaporization Modeling for Engineering Calculations

S. K. Aggarwal

F. Peng

Department of Mechanical Engineering,
University of Illinois, Chicago,
Chicago, IL 60607

The present paper reviews the methodologies for representing the droplet motion and vaporization history in two-phase flow computations. The focus is on the use of droplet models that are realistic in terms of their efficient implementation in comprehensive spray simulations, representation of important physical processes, and applicability under a broad range of conditions. The methodologies available at present to simulate droplet motion in complex two-phase flows may be broadly classified into two categories. First one is based on the modified BBO equation. This approach is more comprehensive, but requires modifications and/or correlations at higher droplet Reynolds number. The second approach aims at developing correlations, using detailed numerical simulations or laboratory experiments, for the effects of flow nonuniformity and droplet relative acceleration on the instantaneous drag and lift coefficients. Recent advances made in the droplet vaporization models are also discussed. The advanced vaporization models include the effects of transient liquid heating, gas-phase convection, and variable thermophysical properties. All of these models are discussed, and recommendations are made for their inclusion in comprehensive two-phase computations.

Introduction

Modeling of droplet dynamics and vaporization history in a turbulent, two-phase flow is a challenging problem. First of all, it requires an accurate representation of droplet motion in an unsteady, turbulent flow field. Important considerations here include the description of instantaneous turbulent velocity field for the carrier fluid, and the effects arising from flow nonuniformity and droplet relative acceleration, mass transfer, curvilinear trajectory, and shear-generated lift forces. Droplet vaporization adds another level of complexity to the modeling problem, due to the effects of transient liquid heating, gas-phase convection, and variable thermophysical properties. The problem is further compounded in situations involving nondilute sprays and high pressures, especially those approaching supercritical values.

In this paper, we review the methodologies available at present to represent the droplet dynamics and vaporization history in turbulent, two-phase flows. The review is not intended to be a comprehensive study of the extensive literature that already exists on the subject, rather to focus on those droplet models that have a realistic representation of relevant physical processes, and can be implemented efficiently in comprehensive spray simulations. Many excellent reviews already exists on the various phenomena related to droplet motion and vaporization. The work on droplet motion is reviewed by Clift and Gauvin (1971), Clift et al. (1978), and Leal (1980). The spray modeling work is reviewed by Williams (1973) and Faeth (1977), and the droplet vaporization models by Law (1982), Sirignano (1983), and Aggarwal et al. (1984). The present review considers both the droplet dynamics and the vaporization aspects, and may be viewed as a supplement to the cited reviews. It should also be mentioned that many other important issues, such as droplet–turbulence interactions, droplet–droplet interactions, and high-pressure phenomena, are not covered in this review. In the following, the droplet dynamics models are reviewed first, followed by a review of vaporization models. Conclusions and recommendations for additional work are presented in the last section.

1 Droplet Dynamics Models for (Low-Pressure) Subcritical Conditions

The study of droplet motion has developed in many different directions due to the varied contexts in which they appear. For sufficiently small droplets, the Reynolds number is in the Stokesian regime and the droplet motion can be estimated in terms of an unsteady Stokes flow theory. Originally Basset (1888), Boussinesq (1885), and Oseen (1927) developed a force expression for a slowly moving, accelerating, rigid sphere in a still fluid:

$$m_d \frac{du_{di}}{dt} = 3\pi\mu_g D_d (u_{gi} - u_{di}) + \frac{1}{2}\cdot\frac{\pi}{6}\cdot D_d^3 \rho_g \frac{d}{dt}(u_{gi} - u_{di}) + 6\cdot\frac{D_d^2}{4}\cdot\sqrt{\pi\rho_g\mu_g}\cdot\int_{t_0}^{t} \frac{\frac{d}{dt}(u_{gi} - u_{di})}{\sqrt{t - t'}}\cdot dt' \quad (1)$$

where the terms on the right-hand side are, respectively, the Stokes drag, added-mass term, and Basset history term. Later, Tchen (1947) extended the BBO equation to incorporate the effects of a temporally varying flow field on particle transport. Corrsin and Lumley (1956) modified Tchen's equation to account for spatial nonuniformity of the flow field. Riley (1971) revised Corrsin and Lumley's equation to account properly for the effect of undisturbed flow on the particle motion. Maxey and Riley (1983) pointed out some inconsistencies in the modifications suggested by Tchen (1947) and Corrsin and Lumley (1956), and obtained the modified BBO equation in the following form:

Contributed by the International Gas Turbine Institute and presented at the 39th International Gas Turbine and Aeroengine Congress and Exposition, The Hague, The Netherlands, June 13–16, 1994. Manuscript received by the International Gas Turbine Institute February 19, 1994. Paper No. 94-GT-215. Associate Technical Editor: E. M. Greitzer.

$$\frac{du_{di}}{dt} = \frac{3}{4}\cdot\frac{\rho_g}{\rho_d}\cdot\frac{C_{Ds}}{D_d} V_r\cdot\left(u_{gi} - u_{di} + \frac{1}{24} D_d^2 \nabla^2 u_{gi}\right)$$
$$+ \frac{\rho_g}{\rho_d}\frac{Du_{gi}}{Dt} + \frac{1}{2}\frac{\rho_g}{\rho_d}\frac{d}{dt}\left(u_{gi} - u_{di} + \frac{1}{40} D_d^2 \nabla^2 u_{gi}\right)$$
$$+ \frac{\rho_g}{\rho_d}\sqrt{\frac{81\nu_g}{\pi D_d^2}} \int_{t_0}^{t} \frac{1}{\sqrt{t - t'}} \frac{d}{dt}\left(u_{gi} - u_{di} + \frac{D_d^2}{24} \nabla^2 u_{gi}\right) dt'$$
$$+ \left(1 - \frac{\rho_g}{\rho_d}\right) g_i \quad (2)$$

The derivative d/dt denotes a time derivative following the moving sphere, and D/Dt the time derivative following a fluid element. The terms on the right-hand side correspond in turn to the effects of viscous Stokes drag, pressure gradient of the undisturbed flow, added mass, Basset history term, and buoyancy.

Equations (1) and (2) have several limitations when they are employed in the computations of turbulent sprays. First of all, they are limited to low Reynolds number flows (Re < 1). In addition, the effects of heat and mass transfer (Stefan flow) on the drag coefficient, and the presence of lift force due to shear, are not accounted for. Also, the consideration of turbulence and the proximity of other droplets require further modifications to the droplet drag equation. Different approaches used to account for some of these effects are discussed in the following.

1.1 Corrections for Higher Reynolds Number. A substantial amount of research (Clift et al., 1978) has found that the effects of flow nonuniformity and droplet relative acceleration on the droplet drag and lift forces can significantly alter the droplet motion. A review of the effects of acceleration is given by Clift et al. (1978) and Clift and Gauvin (1971), and of flow nonuniformity by Clift et al. (1978) and Leal (1980). Hughes and Gililand (1952) and Hjelmfelt and Mockros (1967) predicted that a sphere that falls freely experiences drag higher than that given by the Stokes coefficient as it accelerates to its terminal velocity. Odar and Hamilton (1964) used an experimental study and obtained separate correlations for the effects of added mass term and Basset history term at Reynolds number values up to 62. Tsuji et al. (1990) investigated experimentally the drag on a sphere in a periodically pulsating flow for Reynolds number in the range 8000 $<$ Re $<$ 16,000. Their results show that the drag increases in the accelerating flow and decreases in the decelerating flow. Odar (1968) provided data on the drag of a sphere along a circular path in the Reynolds number range from 6 to 185, which shows that the effects of added mass and history of motion increase for this case, whereas the contribution from steady-state drag remains the same as that in a rectilinear motion. Rivero (1991) and Chang (1992) investigated numerically the time-dependent, axisymmetric flow past a sphere at Re varying between 0 and 100, including both oscillatory flows with zero mean and constantly accelerating or decelerating flows. Their results support the idea of an added-mass effect even when there is flow separation. The added-mass term is attributable to the pressure distribution and the coefficient appears to be $\frac{1}{2}$ under a wide range of conditions. The results of these studies indicate that the drag at intermediate or high Reynolds number increases due to droplet relative acceleration. Contrary to the above, Temkin and Kim (1980) and Temkin and Mehta (1982) obtained the drag by observing the motion of a sphere in a shock tube, and reported the opposite results. Ingebo (1956) reported results showing the same trend.

As is evident from the literature, droplet motion in multiphase flows is not completely understood at moderately high Reynolds number. In particular, there is significant uncertainty about the role of flow nonuniformity and droplet acceleration on droplet motion. The previous studies also indicate that the efforts to represent these effects in the droplet dynamics equation have proceeded along two different directions. One approach has employed further modifications (Odar and Hamilton, 1964) to the BBO equation to represent the effects of higher Reynolds number. In the second approach, different correlations have been proposed to modify the standard drag coefficient for including the effects of flow nonuniformity and droplet acceleration.

Approach 1. This approach employs the modified BBO equation, and incorporates the effect of convective acceleration of the gas surrounding the droplet at higher droplet Reynolds number and accounts for shear lift force.

(a) The modified BBO equation. Odar and Hamilton (1964) used an experimental study and obtained separate correlations for the effects of added mass term and Basset history term at Reynolds number values up to 62. They expressed the total drag force by the use of empirical coefficients C_{Ds}, C_A, and C_H.

$$m_d \frac{du_{di}}{dt} = C_{Ds}\cdot\frac{\pi}{4} D_d^2 \cdot\frac{1}{2}\cdot \rho_g V_r (u_{gi} - u_{di})$$
$$+ C_A\cdot\frac{\pi}{6}\cdot D_d^3 \rho_g \frac{d}{dt}(u_{gi} - u_{di})$$
$$+ C_H\cdot\frac{D_d^2}{4}\cdot\sqrt{\pi \rho_g \mu_g}\cdot\int_{t_0}^{t} \frac{\frac{d}{dt}(u_{gi} - u_{di})}{\sqrt{t - t'}}\cdot dt'$$
$$+ \frac{\pi}{6} D_d^3 \rho_g \frac{Du_{gi}}{Dt} \quad (3)$$

Nomenclature

A_c = acceleration factor
m = mass
B_M = mass transfer number
$\dot{m}$ = droplet vaporization rate
B_T = heat transfer number
Nu = Nusselt number
C_A = added-mass drag coefficient
R_d = droplet radius
C_D = drag coefficient
Re = droplet Reynolds number = $D_d V_r / \upsilon_g$
C_{Do} = steady-state drag coefficient
Sc = Schmidt number
C_H = Basset history drag coefficient
T = temperature
C_L = lift coefficient
u_i = velocity component in i direction
C_p = specific heat
V_r = magnitude of relative velocity
D = mass diffusivity
x_i = displacement in i direction
D_d = droplet diameter
Y_F = mass fraction of fuel vapor
d_{ij} = deformation rate tensor
ρ = density
g = gravity
μ = viscosity
K = coefficient of Saffman's lift force
ν = kinematics viscosity
κ = nonuniformity parameter
L = latent heat
L' = effective latent heat

Subscripts

g = gas
$i = 1$ = radial direction
$i = 2$ = axial direction
d = droplet
s = droplet surface
∞ = value at infinity

where C_{Ds}, C_A, and C_H are, respectively, the steady-state, added-mass, and history drag coefficients used to represent the effect of higher Reynolds number. C_{Ds} is defined later in Eq. (27). Based on their measurements, Odar (1966) suggested the following empirical formulas for C_A and C_H:

$$C_A = 1.05 - \frac{0.066}{A_C^2 + 0.12} \tag{4}$$

$$C_H = 2.88 + \frac{3.12}{(1 + A_C)^3} \tag{5}$$

A_C is the acceleration factor defined by

$$A_C = \frac{V_r^2}{D_d} \bigg/ \frac{dV_r}{dt} \tag{6}$$

and the droplet mass

$$m_d = \tfrac{1}{6}\pi \cdot D_d^3 \rho_d \tag{7}$$

Odar (1966) confirmed that Eqs. (4) and (5), derived for a simple harmonic motion, are valid for the free fall of a sphere in a viscous fluid.

(b) Shear lift force. Saffman (1965, 1968) studied theoretically the lift on a small sphere in a steady, uniform shear flow and gave the following expression for the shear lift force:

$$F_L = 6.46 \rho \nu^{1/2} R_d^2 (u_{g1} - u_{d1}) \left| \frac{du_{g1}}{dx_2} \right|^{1/2} \operatorname{sign}\left(\frac{du_{g1}}{dx_2} \right) \tag{8}$$

where u_{g1} and u_{d1} are the velocities of the fluid and the particle in the x direction, and du_{g1}/dx_2 is the shear rate of the mean flow. In the derivation, it was assumed that

$$\mathrm{Re}_s = \frac{V_s D_d}{\nu} \ll 1, \quad (V_s = |u_{g1} - u_{d1}|) \tag{9}$$

$$\mathrm{Re}_G = \frac{G D_d^2}{\nu} \ll 1, \quad \left(G = \left| \frac{du_{g1}}{dx_2} \right| \right) \tag{10}$$

$$\mathrm{Re}_G = \frac{\Omega D_d^2}{\nu} \ll 1 \tag{11}$$

and

$$\epsilon = \frac{\mathrm{Re}_G^{1/2}}{\mathrm{Re}_s} \gg 1 \tag{12}$$

where Ω is the rotational speed of the sphere. Equation (8) can be used with confidence only when these conditions are met. However, practical situations arise during the study of droplet motion in turbulent flow that require an expression for the shear lift force at larger droplet Reynolds number, Re_s, when conditions (9)–(12) are no longer met.

McLaughlin (1991) extended Saffman's analysis to find shear lift force for $\mathrm{Re}_s \ll 1$, but arbitrary ϵ, and expressed the lift force coefficient as

$$\frac{C_L}{C_{LSa}} = 0.443 J(\epsilon) \tag{13}$$

Saffman's (1965) result was recovered as $J \rightarrow 2.255$ for large $J(\epsilon)$. McLaughlin found that $J(\epsilon)$ decreases to zero rapidly as ϵ decreases, which means that Saffman's expression would overpredict the shear lift force. From the table given in McLaughlin (1991), a curve fit for $J(\epsilon)$ is constructed by Mei (1992) for $1 \le \epsilon \le 20$,

$$J(\epsilon) \approx 0.6765[1 + \tanh(2.5 \log_{10} \epsilon + 0.191)] \times [0.667 + \tanh(6(\epsilon - 0.32))] \tag{14}$$

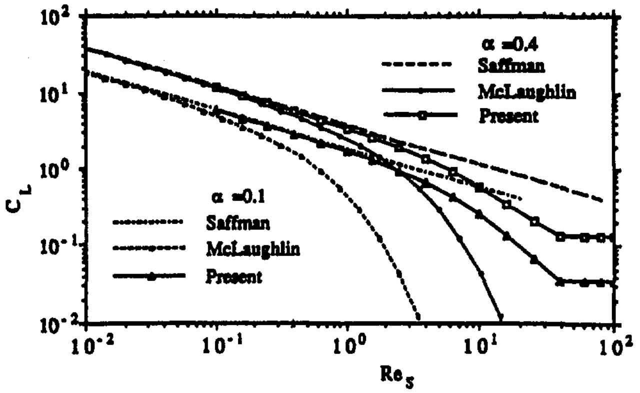

Fig. 1 Shear lift coefficient based on the present approximate expression of Mei (1992) and the analyses of Saffman's (1965) and McLaughlin (1991) (from Mei, 1992)

Dandy and Dwyer (1990) reported computational results for the shear lift force at finite $\mathrm{Re}_s (0.1 \le \mathrm{Re}_s \le 100)$ and finite shear rate,

$$\alpha = \frac{G R_d}{V_r} = \frac{1}{2} \mathrm{Re}_s \epsilon^2, \quad (0.005 \le \alpha \le 0.4) \tag{15}$$

After careful examination of the numerical results of Dandy and Dwyer (1990), Mei (1992) proposed the following approximation for C_L:

$$\begin{aligned} \frac{C_L}{C_{LSa}} = \frac{F_L}{F_{LSa}} &= (1 - 0.3314\alpha^{1/2}) \exp\left(-\frac{\mathrm{Re}_s}{10} \right) \\ &\quad + 0.3314\alpha^{1/2}, \quad \mathrm{Re}_s \le 40 \\ &= 0.0524(\alpha\, \mathrm{Re}_s)^{1/2}, \quad \mathrm{Re}_s > 40 \end{aligned} \tag{16}$$

which combines the analytical result of Saffman (1965) at small Re_s and α and the numerical result of Dandy and Dwyer (1990). In the above, the subscript *Sa* denotes the corresponding result obtained by Saffman (1968). Figure 1 shows the comparison of the results of Saffman (1965), Dandy and Dwyer (1990) (Eq. (16)), and McLaughlin (1991) (Eqs. (13) and (14)). It can be seen that at low Re_s all three forms agree well with each other for $\alpha = 0.4$. At low shear rate, $\alpha = 0.1$, McLaughlin's result deviates quickly from the numerical result of Dandy and Dwyer as Re_s increases. This is expected because the asymptotic result of McLaughlin is valid only at low Re_s, while a decrease in ϵ means an increase in Re_s for a fixed α. Thus, one cannot expect the result to be accurate for a fixed shear rate α with decreasing ϵ. On the other hand, for a fixed Re_s (say $\mathrm{Re}_s = 0.1$), McLaughlin's analysis indicates that the lift force decreases rapidly as ϵ or α decreases and deviates from Saffman's prediction, while the numerical result of Dandy and Dwyer at $\mathrm{Re}_s = 0.1$ differs only slightly from Saffman's prediction even at $\alpha = 0.005$ and 0.01. It is not clear whether the discrepancy at $\mathrm{Re}_s = 0.1$ and $\alpha \ll 1$ is due to the nonlinear inertia effect neglected in the analysis or to the numerical uncertainties, such as the size of the computational domain and grid resolution, in dealing with three distinctive regions of the flow field defined by Re_s and α.

It should also be mentioned that the analysis of Saffman (1965) and that of McLaughlin (1991) are based on the assumption that $\mathrm{Re}_\Omega \ll 1$. In the low Re regime, the rotation has little effect on the shear lift. The numerical result of Dandy and Dwyer is for $\mathrm{Re}_\Omega = 0$. The effect of rotation on the shear lift force at finite Re_Ω is not clear at present.

Approach 2. The second approach, instead of using the modified BBO equation, employs different correlations to represent the effects of flow nonuniformity and droplet relative acceleration on drag and lift forces operative on a droplet. The effect of flow nonuniformity is represented in terms of a nondimensional parameter κ and the droplet Reynolds number (Puri and Libby, 1990), and the effect of acceleration in terms of a nondimensional parameter A_c (Temkin and Kim, 1980). The correlations are expressed in the following form:

$$C_D = C_{Ds}(1 + f(\kappa, \mathrm{Re})) - C_{AD} \cdot A_C \tag{17}$$

$$C_L = C_{KL} \cdot f(\kappa, \mathrm{Re}) - C_{AL} \cdot A_C \tag{18}$$

where $f(\kappa, \mathrm{Re})$ is a function involving both the flow nonuniformity and Reynolds number.

Then, the droplet acceleration components may be expressed in the radial and axial directions as:

$$\frac{du_{d1}}{dt} = \frac{3}{4} \cdot \frac{\rho_g}{\rho_d} \cdot \frac{V_r}{D_d} [-C_L(u_{g2} - u_{d2}) + C_D(u_{g1} - u_{d1})] \tag{19}$$

$$\frac{du_{d1}}{dt} = \frac{3}{4} \cdot \frac{\rho_g}{\rho_d} \cdot \frac{V_r}{D_d} [C_L(u_{g2} - u_{d2}) + C_D(u_{g1} - u_{d1})] \tag{20}$$

Based on the experimental data, different correlations have been proposed. Temkin and Kim (1980) and Temkin and Mehta (1982) gave the following expression for the drag coefficient:

(*a*) For water droplets, having diameters in the range 87–575 μm, in uniform flow behind a weak shock wave and the Reynolds number range $3.2 < \mathrm{Re} < 77$:

$$C_D = C_{Ds} - K \cdot A_C \quad \text{for} \quad \frac{dU_r}{dt} < 0 \tag{21}$$

where K is a constant of order 1.

(*b*) For water droplets, having diameters in the range of 115–187 μm, in propagating N waves, and the Reynolds number range $9 < \mathrm{Re} < 115$:

$$C_D = C_{Ds} - 0.048 \cdot A_C \quad (-45 < A_C < -3) \tag{22}$$

$$C_D = C_{Ds} - \frac{3.829}{A_C} - 0.204 \quad (5.9 < A_C < 25) \tag{23}$$

The parameter A_C is defined as

$$A_C = \left(\frac{\rho_d}{\rho_g} - 1\right) \cdot \frac{D_d}{V_r^2} \cdot \frac{dV_r}{dt} \tag{24}$$

These relations indicate that acceleration decreases and deceleration increases droplet drag.

Puri and Libby (1990) conducted experiments on droplets moving in a Poiseuille flow in the Reynolds number range of 0.7 to 27 and κ in the range of 10^{-3} to 6×10^{-3} and determined that the droplets experience drag larger than that given by the standard drag. They suggested the following correlation for the drag coefficient:

$$C_D = C_{Ds} \cdot \left(1 + 575\left(\frac{\kappa^2}{\mathrm{Re}}\right)^{3/4}\right) \tag{25}$$

They also determine the presence of lift due to flow nonuniformity. Following the relations of Saffman (1965) and Drew (1978) and considering their own data and those of Eichhorn and Small (1964), they present an empirical formula for the coefficient C_L as

$$C_L = 20C_{Ds}\left(\frac{\kappa^2}{\mathrm{Re}}\right)^{3/4} \tag{26}$$

For low Reynolds numbers, C_{Ds} is given by the Stokes drag, whereas for high Reynolds number, it involves Stokes drag and a correction such as proposed by Putnam (1961), i.e.,

$$C_{Ds} = \frac{24}{\mathrm{Re}} \cdot \left(1 + \frac{\mathrm{Re}^{2/3}}{6}\right) \tag{27}$$

Peng and Aggarwal (1993) studied the droplet motion in Poiseuille flow and counterflow, and proposed the modified correlations for the effects of flow nonuniformity and relative acceleration at moderately high Reynolds number.

$$C_D = C_{Ds}\left(1 + C_{KD}\left(\frac{\kappa^2}{\mathrm{Re}}\right)^{3/4}\right) - C_{AD} \cdot A_C \tag{28}$$

$$C_L = C_{KL} \cdot C_{Ds}\left(\frac{\kappa^2}{\mathrm{Re}}\right)^{3/4} - C_{AL} \cdot A_C \tag{29}$$

where C_{KD}, C_{AD}, C_{KL} and C_{AL} are constant.

In Poiseuille Flow:

$$C_{AD} = 0.42, \quad C_{AL} = 5 \times 10^{-3} \quad \text{when} \quad A_C < 0.0$$

$$C_{KD} = 575.0, \quad C_{KL} = 50.0$$

In Counterflow:

$$C_{AD} = 0.52, \quad C_{AL} = 0.15 \quad \text{when} \quad A_c < 0.0$$

$$C_{AD} = 0.2, \quad C_{AL} = 0.15 \quad \text{when} \quad A_c > 0.0$$

$$C_{KD} = 725.0, \quad C_{KL} = 400.0$$

Equation (24) is used to calculate A_c.

Figures 2(*a*) and 2(*b*) show the time history of standard drag force, pressure gradient force, added-mass force, Basset history force, and Saffman lift force predicted by using Approach 1 for a droplet moving in Poiseuille flow (taken from Peng and Aggarwal, 1993). The important observation is that the Saffman lift force is significant compared to the standard drag force, and influences the droplet trajectory in the radial direction. However, the other forces such as pressure gradient force, added-mass force, and Basset history force are negligible compared with the standard drag force. Figure 3 shows the comparison of droplet trajectories predicted by Approaches 1 and 2 with experimental data. It is observed that the application of Approach 1 does not give good predictions for this case. For the case of droplet moving in counterflow, the comparison of droplet trajectories predicted by Approaches 1 and 2 is shown

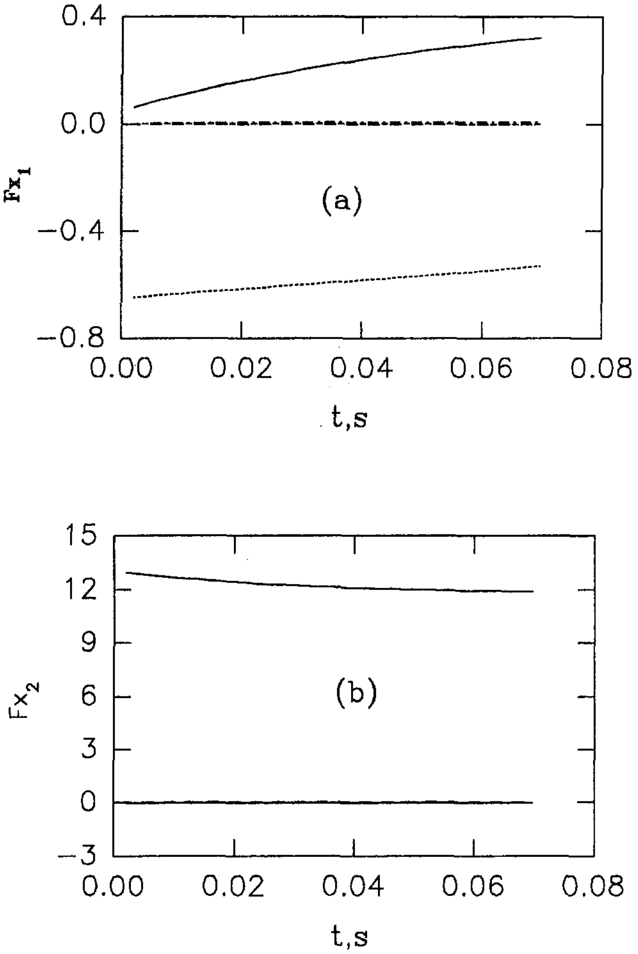

Fig. 2 Time history of individual forces in radial and axial directions for droplet in Poiseuille flow using Approach 1

in Fig. 4. It is indicated that Approach 1 yields trajectory that is significantly different from that obtained experimentally. In order to understand these differences, the time history of various forces represented in Approach 1 is given in Fig. 5. Important observation is that with Approach 1, all the secondary forces are negligible compared to the standard drag force. Consequently, the predictions of Approach 1 are similar to those obtained by considering only the standard drag.

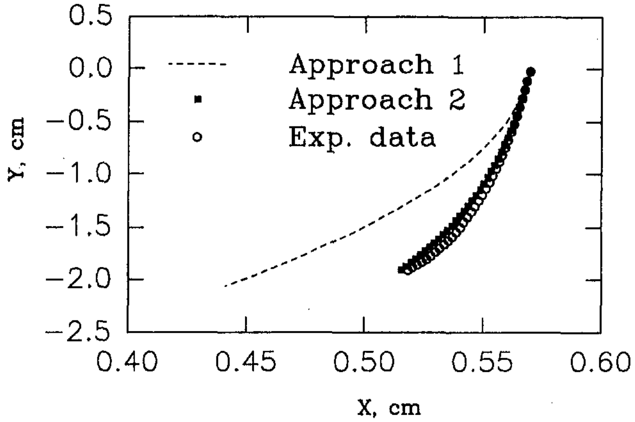

Fig. 3 Comparison of computed and experimental droplet trajectories in Poiseuille flow

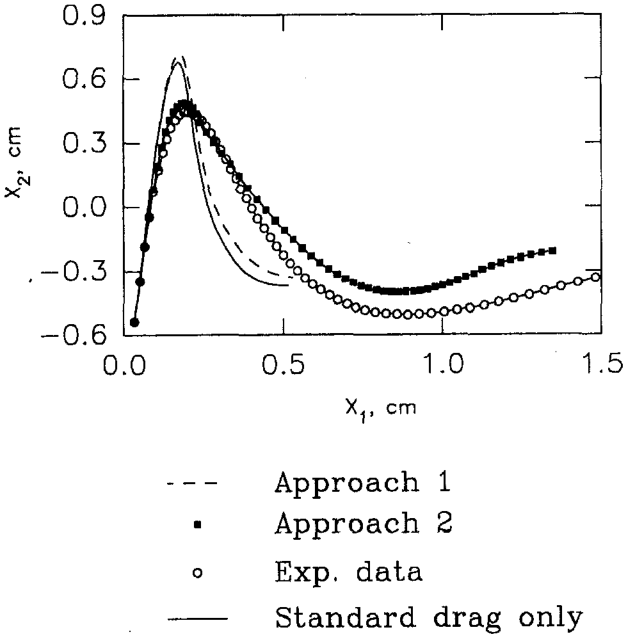

Fig. 4 Comparison of computed and measured droplet trajectories in counterflow

1.2 Correction for Vaporization. Many spray applications involve elevated temperatures where the effects of heat and mass transfer on droplet drag must be considered. Yuen and Chen (1976) found that vaporization affects drag in two ways. First, the temperature and concentration gradients between the droplet surface and the ambient cause substantial reduction in the absolute viscosity of the gas, which decreases friction drag. Second, vaporization affects the boundary layer surrounding the droplet; this blowing effect reduces friction drag and increases form drag. Yuen and Chen argue that the decrease in viscous drag due to blowing is accompanied by an increase in the pressure drag of similar magnitude. In order to account for both variable properties and blowing, a large number of steady-state correlations for drag and heat and mass transfer have been proposed.

Yuen and Chen (1976) showed experimentally that for low to moderate vaporization rates ($B_T = C_p(T_\infty - T_s)/L \leqslant 3$), the drag coefficient of an evaporating droplet may be approximated by the standard drag curve, provided the gas viscosity μ is evaluated at reference temperature and concentration obtained by using the $\frac{1}{3}$ rule:

$$T_{\text{ref}} = T_s + \tfrac{1}{3}(T_\infty - T_s),$$

$$Y_{F,\text{ref}} = Y_{Fs} + \tfrac{1}{3}(Y_{F\infty} - Y_{Fs}) \qquad (30)$$

Renksizbulut and Yuen (1983a) conducted numerical experiments with droplets in air streams up to 1059 K, and comparing their results with the experimental data of Yuen and Chen (1976) and Eisenklam et al. (1967), proposed the following correlation for the drag coefficient of a droplet evaporating in air:

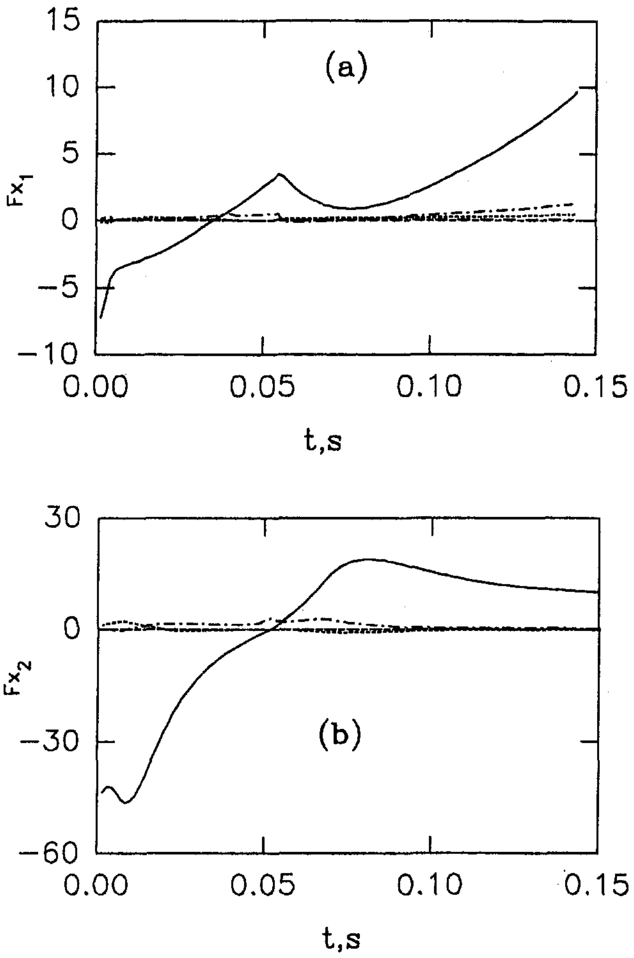

Fig. 5 Time history of individual forces in radial and axial directions for droplet in counterflow using Approach 1

$$C_{Ds} = \frac{24}{\text{Re}} (1 + 0.2 \text{ Re}^{0.63})(1 + B_T)^{-0.2} \tag{31}$$

where the $\frac{1}{2}$ rule is used to evaluate the thermophysical properties, except for the density in Re, which is the free-stream density. Their correlations are valid for $10 < \text{Re} < 300$. The $(1 + B_T)^{0.2}$ factor accounts for the reduction in drag due to the blowing effect of evaporation.

Chiang et al. (1991) proposed the following drag correlation, which agrees within 4 percent with results from their variable-property Navier–Stokes numerical calculation:

$$C_{Ds} = \frac{24}{\text{Re}} (1 + 0.325 \text{ Re}^{0.474})(1 + B_T)^{-0.32} \tag{32}$$

for $0.4 \leq B_T \leq 13$); $30 \leq \text{Re} \leq 200$). The thermophysical properties are evaluated as in the Renksizbulut–Yuen correlation. This correlation indicates a larger reduction in drag due to blowing than does the Renksizbulut–Yuen correlation.

2 Droplet Vaporization Models

The basic droplet vaporization model for an isolated single-component droplet in a stagnant environment was formulated by Godsave (1953), Spalding (1953), Goldsmith and Penner (1954), and Wise et al. (1955). The model has been termed the d^2 law because it predicts that the square of the droplet diameter decreases linearly with time. Since then this model has been studied extensively both experimentally and theoretically. These studies, reviewed by Williams (1973), Faeth (1977), Law (1982), Sirignano (1983), and Aggarwal et al. (1984), consider the effects of relaxing many of the assumptions employed in the basic model. Basically, the existing literature on single-droplet vaporization can be classified into two major categories. In the first category, the basic model is still spherically symmetric but the extensions are proposed to account for the effects of gas-phase convection and transient liquid-phase processes. These include the Ranz–Marshall correlation (1952), infinite conductivity model (Law, 1976), conduction limit model (Law and Sirignano, 1977), the vortex model (Tong and Sirignano, 1983), and the effective-conductivity model (Abramzon and Sirignano, 1989). In the second category, the investigations are based on an axisymmetric model. These include the Prakash–Sirignano model (1978, 1980) and Tong–Sirignano (1983). The present paper aims to complement the extensive reviews by Law (1982), Sirignano (1983), and Aggarwal et al. (1984) and discusses some recent advances that can be easily implemented in turbulent, two-phase flow computations.

(*a*) *Renksizbulut-Yuen Model.* Based on experiments, Renksizbulut and Yuen (1983a) provided a correlation for the Nusselt number of a droplet evaporating in air:

$$\text{Nu} = (2 + 0.57 \text{ Re}^{0.5} \text{ Pr}^{0.333})(1 + B_T)^{-0.7} \tag{33}$$

where the $\frac{1}{2}$ rule is used to evaluate the thermophysical properties, except for the density in the Re, which is the free-stream value. Their correlations are valid for $10 < \text{Re} < 300$. Renksizbulut and Haywood (1988) provided an expression for the vaporization rate as

$$\dot{m} = 2\pi R_d \text{ Nu} \cdot k_f \frac{(T_s - T_\infty)}{L} \tag{34}$$

where Nu is given by Eq. (37), and k_f and L are thermal conductivity and latent heat of vaporization at T_s, respectively. Equation (38) is obtained by assuming that the droplet is at its wet bulb temperature.

(*b*) *Abramzon–Sirignano Model.* Abramzon and Sirignano (1989) provided a new vaporization model of a moving fuel droplet, which represents the extension of the classical droplet vaporization model and includes such important effects as variable physical properties and nonunitary Lewis number in the gas phase, the influence of Stefan flow (blowing) on heat and mass transfer, and the effect of transient liquid heating. In their extended film model, the instantaneous vaporization rate is expressed as:

$$\dot{m} = 2\pi \rho D R_d \text{ Sh}^* \ln (1 + B_M) \tag{35}$$

and

$$\dot{m} = 2\pi \frac{\kappa}{C_p} R_d \text{ Nu}^* \ln (1 + B_T) \tag{36}$$

$$H = \frac{C_p(T_\infty - T_s)}{B_T} \tag{37}$$

where Sh* and Nu* are written as:

$$\text{Sh}^* = 2 + (\text{Sh}_0 - 2)/F_M \tag{38}$$

$$\text{Nu}^* = 2 + (\text{Nu}_0 - 2)/F_T \tag{39}$$

The values B_m and B_T are calculated as

$$B_M = \frac{Y_{Fs} - Y_{F\infty}}{1 - Y_{Fs}} \tag{40}$$

$$B_T = (1 - B_M)^{\Phi} - 1 \tag{41}$$

$$\Phi = \frac{C_{pl}}{C_p} \frac{\mathrm{Sh}^*}{\mathrm{Nu}^*} \frac{1}{\mathrm{Le}} \tag{42}$$

The correction factors F_M and F_T are approximated by the function $F(B)$ as

$$F(B) = (1 + B)^{0.7} \frac{\ln (1 + B)}{B} \tag{43}$$

Nu_0 and Sh_0 are the Nusselt and Sherwood numbers employed in the classical model. Two commonly used correlations for Nu_o and Sh_o are Frossling correlations:

$$\mathrm{Nu}_0 = 2 + 0.552\, \mathrm{Re}^{1/2}\, \mathrm{Pr}^{1/3} \tag{44}$$

$$\mathrm{Sh}_0 = 2 + 0.552\, \mathrm{Re}^{1/2}\, \mathrm{Sc}^{1/3} \tag{45}$$

and the Clift et al. (1978) correlation,

$$\mathrm{Nu}_0 = [1 + (1 + \mathrm{Re}\,\mathrm{Pr})^{0.333} f(\mathrm{Re})] \tag{46}$$

$$\mathrm{Sh}_0 = [1 + (1 + \mathrm{Re}\,\mathrm{Sc})^{0.333} f(\mathrm{Re})] \tag{47}$$

where $f(\mathrm{Re}) = 1$ for $\mathrm{Re} \leq 1$ and $f(\mathrm{Re}) = \mathrm{Re}^{0.077}$ for $1 < \mathrm{Re} < 400$ and $0.25 < \mathrm{Sc} < 100$.

All thermophysical properties are evaluated with the $\frac{1}{3}$ rule, except for the density appearing in Re, which is evaluated at the free-stream value. The model agrees with the classical theory in the limit of small Reynolds number, and with the experimental data of Renksizbulut and Yuen (1983b) at high Reynolds numbers.

(c) Chiang–Sirignano Model. From numerical calculations, Chiang et al. (1991) reported Sherwood and Nusselt number correlations similar to those of Renksizbulut and Yuen. They do not provide an expression for the vaporization rate. However, by analogy with the Abramzon–Sirignano model, the vaporization rate is

$$\dot{m} = 4\pi R_d D \frac{\mathrm{Sh}}{2} B_M \tag{48}$$

where the Sherwood number is

$$\mathrm{Sh} = (2 + 0.46\, \mathrm{Re}^{0.6}\, \mathrm{Sc}^{0.333})(1 + B_M)^{-0.7} \tag{49}$$

valid for $0.3 < B_M < 4.5$ and $30 < \mathrm{Re} < 250$.

3 Discussion and Conclusions

(a) Droplet Dynamics Models. Literature review indicates that both flow nonuniformity and acceleration effects influence the forces on droplets, and there is considerable uncertainty regarding their quantitative contribution to the total drag and lift forces. The effects of curvilinear motion and droplet rotation are also not adequately represented in the droplet dynamics equation. Regarding the quantitative effect of heat and mass transfer on drag, some correlations (Eqs. (30), (31) and (32)) have been proposed, but differences exist in representing the effect of transfer numbers B_M and B_T, and calculating the average properties of gas film surrounding a droplet.

The modified BBO equation (Eq. (2)) is regarded as a more comprehensive approach to model the droplet motion in two-phase flow simulations. The equation is, however, limited to small droplet Reynolds number, $\mathrm{Re} < 1$. Some modifications (Eqs. (4) and (5)) have been proposed, where the effect of higher Reynolds number is represented in terms of correction factors. Following a careful examination of the literature, we write the modified BBO equation in the following form:

$$\begin{aligned}\frac{du_{di}}{dt} = {} & \frac{3}{4} \cdot \frac{\rho_g}{\rho_d} \cdot \frac{C_{Ds}}{D_d} V_r \cdot (u_{gi} - u_{di}) + \frac{\rho}{\rho_d} \frac{Du_{gi}}{Dt} \\ & + C_A \frac{1}{2} \frac{\rho_g}{\rho_d} \frac{d}{dt} (u_{gi} - u_{di}) \\ & + C_H \frac{\rho_g}{\rho_d} \sqrt{\frac{81\nu_g}{\pi D_d^2}} \int_{t_0}^{t} \frac{1}{\sqrt{t - t'}} \frac{d}{dt} (u_{gi} - u_{di}) dt' \\ & + \frac{\rho_g}{\rho_d} \cdot \frac{2K\nu_g^{1/2} d_{ij}}{D_d (d_{lk} d_{kl})^{1/4}} (u_{gj} - u_{dj}) + \left(1 - \frac{\rho_g}{\rho_d}\right) g \end{aligned} \tag{50}$$

where the effect of higher Reynolds number on the unsteady terms is included by using the empirical coefficients C_A and C_H, and on steady-state drag term by using C_{Ds} (see Eq. (27)). In addition, the shear lift force is included, using a generalization of the expression provided by Saffman (1965) for three-dimensional shear fields, with $K = 2.594$ and d_{ij}, the deformation rate tensor, defined as

$$d_{ij} = \tfrac{1}{2}(u_{gij} + u_{gji}) \tag{51}$$

where

$$u_{g_{ij}} = \frac{\partial u_{gi}}{\partial x_j} \tag{52}$$

The generalized lift expressions is restricted to small Reynolds number (Re_s). In addition, it requires that Re_s be smaller than the square root of the Reynolds number based on the velocity gradient, Eq. (12). The modifications such as Eq. (16) could be used when these conditions are not satisfied. Equations (4)–(6) may be used to calculate C_A and C_H. It is clear, however, that more theoretical and experimental investigations are needed in order to develop reliable correction factors that are applicable to a variety of flows. Another important consideration is the relative magnitude of terms in the modified BBO equation representing the flow nonuniformity and acceleration effects. Results from scale analysis and numerical simulations indicate that at high density ratios (ρ_d/ρ_g), representative of liquid fuel sprays at atmospheric pressures, these terms are negligible compared to the steady-state drag term. However, several experimental studies (Temkin and Kim, 1980; Temkin and Mehta, 1982; Puri and Libby, 1989, 1990; Tsuji et al., 1990) find these effects to be significant even at high density ratios, with the implication that the effects are negligible for $\mathrm{Re}_s < 1$, but become important as Re_s increases. At higher pressures, the terms representing these effects in the modified BBO equation become important, but are restricted to $\mathrm{Re}_s < 1$. Moreover, the effects of curvilinear motion and skewness of acceleration vector from velocity vectors on drag and lift are not included. Thus, there exists a need to study the flow nonuniformity and acceleration effects on droplet motion at higher Reynolds number and pressures.

An alternative approach to incorporate the effects of flow nonuniformity and relative acceleration is to use suitable correlations such as Eqs. (28) and (29), with C_{Ds} given by Eq. (27) for nonevaporating droplets, and Eqs. (31) or (32) for evaporating droplet. These correlations are not general, however. They would also be modified by other effects such as the radius of curvature of droplet trajectory and the skewness of acceleration vector from velocity vector. More experimental studies employing simplified configurations, where the relative magnitudes of flow nonuniformity, relative acceleration, and droplet Reynolds number can be independently controlled, are needed in order to develop better correlations.

(b) Vaporization Models. Following the classical d^2 law model, many significant advances in the modeling of droplet vaporization history have been reported. The advances have aimed at relaxing the assumptions employed in the classical treatment. For example, the advanced models now include the effect of variable thermophysical properties, nonunity Lewis number in the gas film outside the droplet, and the effects of transient liquid heating and gas-phase convection. In spite of the availability of such detailed vaporization models, only the simplest ones, based on the d^2 law formulation, have been employed in comprehensive spray computations: only in some recent studies (Aggarwal and Chitre, 1992; Shuen and Chen, 1993) dealing with the computation of turbulent sprays, have more advanced models been introduced. We believe that the computational capabilities are now sufficiently advanced to include the more detailed models in turbulent, two-phase simulations. The simulations should include an algorithm for calculating the variable thermophysical properties, an effective-conductivity model for the effect of transient liquid heating, and the "extended-film" model (Abramzon and Sirignano, 1989) for the effect of gas-phase convection.

Acknowledgments

This work has been supported by NASA through Grant No. 3-796 under the technical direction of Dr. D. L. Bulzan. The authors would also like to thank Hitesh Patadia in preparing the final version of this paper.

References

Abramzon, B., and Sirignano, W. A., 1989, "Droplet Vaporization Model for Spray Combustion Calculations," *Int. J. Heat Mass Transfer,* Vol. 32, p. 1605.

Aggarwal, S. K., Tong, A. Y., and Sirignano, W. A., 1984, "A Comparison of Vaporization Models in Spray Calculations," *AIAA J.,* Vol. 22 (10), pp. 1448–1457.

Aggarwal, S. K., and Chitre, S., 1992, "On the Structure of Unconfined Spray Flames," *Combust. Sci. Technol.,* Vol. 81, p. 97.

Basset, A. B., 1888, *A Treatise on Hydrodynamics,* Deighton, Bell and Co., Cambridge; Vol. 2, Ch. 21.

Boussinesq, J. V., 1885, "Sur La Resistance . . . d'une Sphere Solide," *C. R. des Seances de l'Academie,* Vol. 100, p. 935.

Chang, E., 1992, "Accelerated Motion of Rigid Spheres in Unsteady Flow at Low to Moderate Reynolds Numbers," Ph.D. Thesis, Brown University, Rhode Island.

Chen, Z. H., Liu, G. E., and Sohrab, S. H., 1987, "Premixed Flames in Counterflow Jets Under Rigid Body Rotation," *Combust. Sci. Tech.,* Vol. 51, pp. 39–50.

Chiang, G. H., Raju, M. S., and Sirignano, W. A., 1991, "Numerical Analysis of Convecting, Vaporizing fuel Droplets With Variable Properties," *Int. J. Heat Mass Transfer,* Vol. XX, pp. XX–XX.

Clift, R., and Grauvin, W. H., 1971, "Motion of Entrained Particles in Gas Stream," *Can. J. Chem. Eng.,* Vol. 49, p. 439.

Clift, R., Grace, J. R., and Weber, M. E., 1978, *Bubbles, Drops and Particles,* Academic Press, New York.

Corrsin, S., and Lumley, J., 1956, "On the Equation of Motion for a Particle in Turbulent Fluid," *Appl. Sci. Res. A,* Vol. 6, pp. 114–116.

Dandy, D. A., and Dwyer, H. A., 1990, "A Sphere in Shear Flow at Finite Reynolds Number: Effect of Shear on Particle Lift, Drag and Heat Transfer," *J. Fluid Mech.,* Vol. 216, pp. 318–410.

Drew, D. A., 1978, "The Force on a Small Sphere in Slow Viscous Flow," *J. Fluid Mech.,* Vol. 88, pp. 393–400.

Dwyer, H. A., and Sanders, B. R., 1986, "A Detailed Study of Burning Droplets," *Twenty-First Symposium (International) on Combustion,* The Combustion Institute, Pittsburgh, PA, p. 633.

Dwyer, H. A., and Sanders, B. R., 1988, "Calculations of Unsteady Reacting Droplet Flows," *Twenty-Second Symposium (International) on Combustion,* The Combustion Institute, Pittsburgh, PA, p. 1923.

Eichhorn, R., and Small, S., 1964, "Experiments on the Lift and Drag of Spheres Suspended in a Poiseuille Flow," *J. Fluid Mech.,* Vol. 20, pp. 513–527.

Eisenklam, P., Arunachalam, S. A., and Weston, J. A., 1967, "Evaporation Rates and Drag Resistance of Burning Drops," *Proc. 11th Symp. (Int.) Symp. on Combustion,* Butterworths, London, pp. 715–728.

Faeth, G. M., 1977, "Current Status of Droplet and Liquid Combustion," *Prog. Energy Combust. Sci.,* Vol. 3, pp. 191–224.

Flatbush, E. K., "Computer Simulation of the Burning of a Multicomponent Droplet," M. S. Thesis, University of California, Davis, 1987.

Godsave, G. A. E., 1953, "Studies of the Combustion of Drops in a Fuel Spray: The Burning of Single Drops of Fuel," *Fourth Symposium (International) on Combustion,* Williams and Wilkins, Baltimore, pp. 818–830.

Goldsmith, M., and Penner, S. S., 1954, "On the Burning of Single Drops of Fuel in an Oxidizing Atmosphere," *Jet Propul.,* Vol. 24, pp. 245–251.

Haywood, R. J., Nafziger, R., and Renksizbulut, M., 1989, "A Detailed Examination of Gas and Liquid Phase Transient Processes in Convective Droplet Evaporation," ASME *Journal of Heat Transfer,* Vol. 111, p. 495.

Hjelmfelt, A. T., Jr., and Mockros, L. F., 1967, "Stokes Flow Behavior of an Accelerating Sphere," *J. Engng. Mech. Div. (Proc. ASCE),* Vol. 93, No. EM687.

Hughes, R. R., and Gilliand, E. R., 1952, "The Mechanics of Drops," *Chem. Engng. Prog.,* Vol. 48, p. 497.

Ingebo, R. D., 1956, "Drag Coefficients for Droplets and Solid Spheres in Clouds Accelerating in Air Streams," NACA Technical Note, TN 3762.

Jarosinski, J., 1986, "A Survey of Recent Studies on Flame Extinction," *Prog. Energy Combust. Sci.,* Vol. 12, p. 81.

Law, C. K., 1976, "Unsteady Droplet Vaporization With Droplet Heating," *Combustion and Flame,* Vol. 26, pp. 17–22.

Law, C. K., and Sirignano, W. A., 1977, "Unsteady Droplet Combustion With Droplet Heating. II, Conduction Limit," *Combustion and Flame,* Vol. 29, pp. 175–186.

Law, C. K., 1982, "Recent Advances in Droplet Vaporization and Combustion," *Prog. Energy Combust. Sci.,* Vol. 8, pp. 171–201.

Leal, L. G., 1980, "Particle Motions in a Viscous Fluid," *Ann. Rev. Fluid Mech.,* Vol. 12, pp. 435–476.

Maxey, R. M., and Riley, J. J., 1983, "Equation of Motion for a Small Rigid Sphere in a Nonuniform Flow," *Phys. Fluids,* Vol. 26, pp. 883–889.

McLaughlin, J. B. 1991, "Inertial Migration of a Small Sphere in Linear Shear Flows," *J. Fluid Mech.,* Vol. 224, pp. 261–274.

Mei, R., 1992, "An Approximate Expression for the Shear Lift Force on a Spherical Particle at Finite Reynolds Number," *Int. J. Multiphase Flow,* Vol. 18, No. 1, pp. 145–147.

Odar, F., and Hamilton, W. S., 1964, "Forces on a Sphere Accelerating in a Viscous Fluid," *J. Fluid Mech.,* Vol. 18, pp. 302–314.

Odar, F., 1966, "Verification on the Proposed Equation for Calculation of the Forces on a Sphere Accelerating in a Viscous Fluid," *J. Fluid Mech.,* Vol. 25, pp. 591–592.

Odar, F., 1968, "Unsteady Motion of a Sphere Along a Circular Path in a Viscous Fluid," ASME *Journal of Applied Mechanics,* Vol. 35, pp. 652–654.

Oseen, C. W., 1927, *Hydrodynamik,* Akademische Verlagsgesellschaft, Leipzig.

Peng, F., and Aggarwal, S. K., 1993, "Droplet Motion Under the Influence of Flow Nonuniformity and Relative Acceleration," presented at the 206th ACS National Meeting.

Prakash, S., and Sirignano, W. A., 1978, "Liquid Fuel Droplet Heating With Internal Circulation," *International Journal of Heat and Mass Transfer,* Vol. 21, pp. 885–895.

Prakash, S., and Sirignano, W. A., 1980, "Theory of Convective Droplet Vaporization With Unsteady Heat Transfer in the Circulating Liquid Phase," *International Journal of Heat and Mass Transfer,* Vol. 23, No. 3, 1980, pp. 253–268.

Putnam, A., 1961, "Integratable Form of Droplet Drag Coefficient," *ARS J.,* Vol. 31, pp. 1467–68.

Puri, I. K., and Libby, P. A., 1989, "Droplet Behavior in Counterflowing Streams," *Combust. Sci. and Tech.,* Vol. 66, pp. 267–292.

Puri, I. K., and Libby, P. A., 1990, "On the Forces of Droplets in Poiseuille Flow," *Phys. Fluids A,* Vol. 2, No. 7, pp. 1281–1284.

Ranz, W. E., and Marshall, W. R., 1952, "Evaporation From Drops," *Chem. Engng. Prog.,* Vol. 48, pp. 141–173.

Renksizbulut, M., and Haywood, R. J., 1988, "Transient Droplet Evaporation With Variable Properties and Internal Circulation at Intermediate Reynolds Numbers," *Int. J. Multiphase Flow,* Vol. 14, pp. 189–202.

Renksizbulut, M., and Yuen, M. C., 1983a, "Experimental Study of Droplet Evaporation With Variable Properties and Internal Circulation at Intermediate Reynolds Numbers," *Int. J. Multiphase Flow,* Vol. 14, p. 189.

Renksizbulut, M., and Yuen, M. C., 1983b, "Numerical Study of Droplet Evaporation in a Viscous Fluid," ASME *Journal of Heat Transfer,* Vol. 105, p. 389.

Riley, J. J., 1971, Ph.D. Thesis, The Johns Hopkins University, Baltimore, MD.

Rivero, M., 1991, "Etude Par Simulation Numérique des Forces Exercés Sur Une Inclusion Sphérique Par un Écoulement Accéléré," Thése de Doctorat, I.N.P.T.

Saffman, P. G., 1965, "The Life on a Small Sphere in a Slow Shear Flow," *J. Fluid Mech.,* Vol. 22, pp. 385–400.

Shuen, J.-S., and Chen, K.-H., 1993, "A Multi-block 2-D Computer Code for Chemically Reacting Flows With Sprays at All Speeds," User's Manual, NASA Lewis Research Center, Cleveland, OH.

Shuen, J. S., Chen, K. H., and Choi, Y., 1993, "A Time-Accurate Algorithm for Chemical Non-equilibrium Viscous Flow at All Speeds," AIAA Paper No. 92-3639; also to appear in *J. Comput. Phys.*

Sirignano, W. A., 1983, "Fuel Vaporization and Spray Combustion Theory," *Prog. in Energy and Comb. Sci.*, Vol. 9, p. 291.

Spalding, D. B., 1953, "The Combustion of Liquid Fuels," in: *Proc. 4th Symp. (Int.) on Combustion*, Williams and Wilkins, Baltimore, MD, pp. 847–864.

Tchen, C. M., 1947, "Mean Value and Correlation Problems Connected With the Motion of Small Particles Suspended in a Turbulent Fluid," Ph.D. Thesis, Delft, The Netherlands.

Temkin, S., and Kim, S. S., 1980, "Droplet Motion Induced by Weak Shock Waves," *J. Fluid Mech.*, Vol. 96, pp. 133–157.

Temkin, S., and Mehta, H. K., 1982, "Droplet Drag in an Accelerating and Decelerating Flow," *J. Fluid Mech.*, Vol. 116, pp. 297–313.

Tong, A. Y., and Sirignano, W. A., 1983, "Analysis of Vaporizing Droplet With Slip, Internal Circulation and Unsteady Liquid Phase Heat Transfer," JSME–ASME Thermal Engineering Joint Conference, Honolulu, HI, Mar.

Tong, A. Y., and Sirignano, W. A., 1984, "Multicomponent Droplet Vaporization in a High Temperature Gas," ASME Winter Annual Meeting, Paper No. 84-WA/HT-17.

Tsuji, Y., Kato, N., and Tanaka, T., 1990, "Experiments on the Unsteady Drag and Wake of a Sphere at High Reynolds Number," *J. Multiphase Flow*, Vol. 17, No. 3, pp. 343–354.

Williams, A., 1973, "Combustion of Droplets of Liquid Fuels: A Review," *Combust. Flame*, Vol. 21, pp. 1–31.

Wise, H., Lorell, J., and Wood, B. J., 1955, "The Effects of Chemical and Physical Parameters on the Burning Rate of a Liquid Droplet," Fifth Symposium (International) on Combustion, Reinhold, NY, pp. 132–141.

Yuen, M. C., and Chen, L. W., 1976, "On Drag of Evaporating Droplets," *Combust. Sci. Tech.*, Vol. 14, p. 147.

Thermal Stability and Heat Transfer Characteristics of Methane and Natural Gas Fuels

D. Chin

J. C. Hermanson

L. J. Spadaccini

United Technologies Research Center,
East Hartford, CT 06108

The thermal decomposition and heat transfer characteristics of gaseous, high-purity methane, several methane–hydrocarbon mixtures, and a typical natural gas fuel were evaluated using an electrically heated, stainless-steel tube test apparatus. Of several candidate heat transfer correlations, the Dittus–Boelter heat transfer correlation provided the best fit of the methane heat transfer data over the range of Reynolds numbers 10,000 to 215,000. The thermal stability (i.e., deposit formation) characteristics of the methane–hydrocarbon mixtures and the natural gas fuel were established and compared with the deposition characteristics of high-purity methane. Testing was conducted at wall temperatures up to 900 K (fuel temperatures to 835 K) for durations of up to 60 hours. Measurements of deposit mass indicated that there was essentially no deposit buildup for wall temperatures below 650 K. Deposit began to form at wall temperatures between 650 K and 775 K. Above 775 K, there was a rapid monotonic increase in deposition. The data suggest that the use of high-purity methane instead of natural gas at temperatures above 775 K could reduce the deposit thickness under similar operating conditions by as much as a factor of three, or permit operation at correspondingly higher temperatures.

Introduction

Advanced engine programs that seek to increase engine thrust-to-weight ratios by burning fuel at conditions near stoichiometric will require corresponding increases in the ability to cool engine components. In current engines, compressor bleed or inlet ram air is the primary medium for cooling the vehicle and its propulsion systems. A large amount of ram air may be required for these cooling applications, significantly impacting the engine inlet cross section and associated inlet ram drag. Moreover, the ram air undergoes a very rapid rise in temperature with increasing flight Mach number. For example, at Mach 4, the inlet air reaches stagnation temperatures of about 910 K; at Mach 6, approximately 1670 K (Mechanical Engineering Staff, 1986). Consequently, air cannot be used for cooling at high Mach No. because the air stagnation temperatures exceed material limits. In this case, the fuel is the only coolant available.

Liquid methane is an attractive candidate fuel for supersonic and hypersonic aircraft because of its high heat of combustion, high density, and high heat sink capacity. Studies have shown that methane fuel for advanced turboramjet-powered aircraft can provide substantial increases in range, payload, power-to-weight ratio, and speed, while reducing gross weight and fuel costs relative to jet fuel (Joslin, 1968). Regenerative cooling with hydrocarbon fuels is feasible up to a point where the coolant temperature reaches a limit defined by a thermal decomposition or ''coking'' temperature. Above this temperature, carbon deposit formation on the inside surfaces of cooling passages can lead to clogging. In addition, the increased thermal resistance due to the deposit can lead to a progressively increasing surface temperature and, possibly, structural failure. Compared to kerosene fuels, which break down at elevated temperatures to form gum and coke, thermal decomposition of pure methane is expected to be much less severe. The greater stability of methane compared with larger hydrocarbon molecules stems from the fact that methane contains only primary carbon–hydrogen bonds, which have greater bond dissociation energies than secondary and tertiary carbon–hydrogen and carbon–carbon bonds. Although pure methane may be the fuel of choice, natural gas may be a more practical alternative from economic considerations. Since natural gas is a mixture of methane with other hydrocarbon species in varying amounts (depending on the source), the small concentrations of hydrocarbon impurities normally present can greatly affect the thermal stability and promote deposit formation.

Only a limited amount of heat transfer and thermal stability information has been published on methane and natural gas. Some studies (Back and Back, 1983; Nishiyama and Tamai, 1980) have focused on static methane cells at low pressure. Additional data are required to extend available correlations over a range of anticipated turboramjet operating conditions. The objective of this research was to develop a heat transfer and thermal stability database to guide the specification of a methane fuel for turboramjets.

Experimental Approach

Fuel thermal stability and heat transfer data were collected by exposing methane fuel to a thermal environment that simulated anticipated engine operating conditions. Of the various possible experimental arrangements for conducting simulation tests, an electrically heated tube, which provides a simple and direct approach, was adopted for this study. In this method fuel flows through a length of thin-walled metal tubing that is heated by the energy generated by an electric current passing through the tube wall. Insulating the outside of the tube virtually eliminates external heat loss, resulting in essentially all of the generated heat being transferred to the fuel.

Since the electrical resistance of the tube material does not vary significantly with temperature, the local heat flux remains essentially constant along the tube, and the fuel and wall temperatures increase from inlet to outlet. Thus, experiments may be run to simulate a constant heat load applied to the tube, and in a single test, yield quantitative data over a range of flow and temperature conditions. This is in contrast to an isothermal tube test configuration, wherein the wall temperature is held constant

---

Contributed by the International Gas Turbine Institute and presented at the 39th International Gas Turbine and Aeroengine Congress and Exposition, The Hague, The Netherlands, June 13–16, 1994. Manuscript received by the International Gas Turbine Institute March 4, 1994. Paper No. 94-GT-390. Associate Technical Editor: E. M. Greitzer.

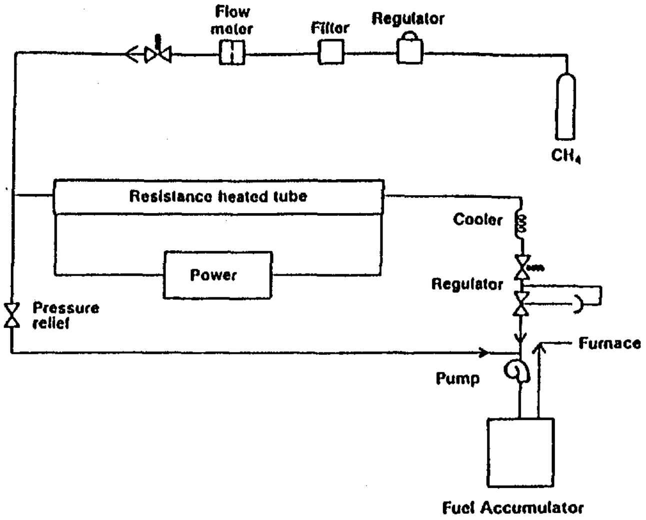

Fig. 1 Test apparatus

and all data are acquired at a single condition. In this configuration, the heat flux may change to maintain isothermal conditions.

Measurement of the thermal parameters (e.g., power input, wall temperature, and fuel temperature) during the test, and subsequent determination of the resulting deposit mass, allowed determination of the heat transfer and rate of deposition. Direct measurements of the temperature at the external tube surface were provided by thermocouples welded to the tube. From measurements of the inlet and outlet fuel temperatures, the electrical power dissipated in the tube (the heat generation), and the fuel flow rate and pressure, it was possible to calculate the heat transfer characteristics at any environmental condition being simulated. The thermal stability of a fuel was evaluated by measuring the mass of the accumulated deposit.

Test Apparatus. The heat transfer and deposit formation experiments were conducted in a heated tube apparatus capable of continuous operation. The apparatus, shown schematically in Fig. 1, consisted of the following major components: (1) a resistance-heated tube that was insulated from the surroundings, (2) a proportional temperature controller to maintain a constant fuel exit temperature by regulating the input electrical power, (3) a metering orifice to determine and regulate the flow rate, (4) a back-pressure regulator to maintain a selected fuel pressure, (5) a nitrogen purge system, (6) a stressed-fuel storage accumulator and exit gas pumping system, and (7) a gas-fired furnace for disposal of the methane fuel downstream of the heated test tube.

The test tubes were fabricated from 347 stainless steel with a standard test section length of 1.8 m. Tests were conducted with tubes 3.2 mm in outer diameter with a nominal wall thickness of 0.51 mm. Prior to installation, the tubing was soaked in acetone, rinsed and blown dry with clean, filtered nitrogen.

Each 1.8-m test tube was instrumented with 16 chromel-alumel thermocouples welded to the outer surface of the test tube with a nominal spacing of 11.5 cm. Isolation amplifiers were connected to each thermocouple to protect the data analysis equipment from voltage spikes and to eliminate the background voltage applied across the tube by the DC power supply. The inner wall temperatures were determined from the outer wall temperature data and the thermal conductivity of the tube material. The calculated difference between the inner and outer wall temperatures was small, generally amounting to less than 6 K. In addition, fuel temperatures were measured at the tube inlet and the tube outlet; the fuel pressure was measured at the tube inlet. All test data were recorded using a microprocessor-controlled data logger. The data system was capable of scanning up to 70 input channels at a scan rate of 35 channels per second.

Quantitative measurements of the amount of deposit formed on the inner surface of each test tube were performed using a LECO Model RC-412 carbon determinator. Prior to analysis, each test tube was sectioned into 24 segments of approximately equal length. Each segment was then vacuum dried for several hours at a temperature of 373 K to remove any remaining fuel. The carbon determinator removed the carbonaceous deposit by heating the sample in an oven to a temperature of 873 K in a pure oxygen atmosphere. Measurement of the concentrations of carbon dioxide and carbon monoxide using infrared spectroscopy, coupled with knowledge of the gas sample pressure and volume, allowed determination of the mass of carbon burned off from each tube segment with an accuracy of ±3 percent.

Test Conditions. Heat transfer tests were conducted with ultrahigh purity (99.97 percent) methane. Thermal stability tests were conducted with ultrahigh-purity methane, mixtures of methane with various hydrocarbon contaminants, and a typical commercial-grade methane (natural gas). The mixtures consisted of methane in combination with 7 percent ethane, or 3.5 percent ethane and 3.5 percent ethylene. The nominal compositions of the test gases and the flow conditions for each test are given in Table 1. The commercial-grade methane employed in these tests had a typical composition as listed in Table 2.

The test mixtures were supplied to each test tube at a nominal flow rate of 0.002 kg/s at a pressure of 10.4 atm. The corresponding Reynolds numbers, based on tube inside diameter, typically ranged from 50,000 at the entrance to the heated tube to 100,000 at the tube exit. The test tube outer surface temperatures ranged from as low as 410 K at the entrance to as high as 930 K at the end of the tube. The bulk temperature of the gas mixtures at the entrance of the heated tube was nominally 300 K.

Results and Discussion

Heat Transfer. Turbulent heat transfer coefficients were determined for methane gas in a heated tube over a range of temperatures and velocities. The convective heat transfer coefficient, h, is defined by the relation:

$$Q/A = h(T_{wi} - T_b) \qquad (1)$$

where Q is the total heat input (determined from the electrical power dissipation), A is the wetted surface area, T_{wi} is the inner wall temperature, and T_b is the bulk fuel temperature at the point of interest.

Determination of the inner wall temperature distribution is readily made by calculating the thermal conduction through the wall, considering the effects of internal heat generation due to electrical power dissipation. The relation between inner and outer wall temperatures is:

$$T_{wi} = T_{wo} - (q'/16k_w)[2d_o^2 \ln (d_o/d) - d_o^2 + d^2] \qquad (2)$$

where T_{wi} and T_{wo} are the inner and outer temperatures, d and d_o are the inner and outer diameters, q' is the heat generation per unit volume, and k_w is the thermal conductivity of the tube material.

Fuel temperatures were measured with thermocouples positioned at the inlet and outlet of the test tube. However, the distribution of temperature over the length of the heated tube was not necessarily linear, depending on the variation of fuel specific heat. The fuel bulk temperature profile was determined by integration of the energy equation:

$$dT_b/dx = \pi dq\dot{m}c_p/A \qquad (3)$$

where d is the inner diameter of the heated tube section, $\dot{m}$ is the mass flow rate of the fuel, and c_p is the local heat capacity of the fuel.

Table 1 Parameters for thermal stability tests

Gas Composition	T_{wall} [K]	P [atm]	Reynolds No.	$\dot{m}$ [kg/s]	Time [hr]
Commercial Grade Methane	410-910	10.6	72100-97500	0.00267	26.3
Methane/7% Ethane	430-930	10.7	66400-90900	0.00243	39.9
Commercial Grade Methane	461-930	10.5	59200-80900	0.00215	48.4
Methane/ 3.5% Ethane/ 3.5% Ethylene	410-920	10.1	50500-74900	0.00193	59.5
Ultra-High Purity Methane	480-890	10.6	54200-81000	0.00210	33.8

This equation was numerically integrated, starting with the measured inlet fuel temperature, to provide the entire fuel temperature profile. The exit temperature calculated from this equation was compared with the measured exit temperature. This procedure yielded a fuel temperature profile of high accuracy, as good as the knowledge of the fuel specific heat. Specific heats and other thermodynamic properties of the fuel mixtures were calculated using the NIST Thermophysical Properties of Hydrocarbon Mixtures Database (SUPERTRAPP) (Ely and Huber, 1990).

Heat transfer tests were conducted over a broad range of Reynolds numbers (10,000 to 215,000) to facilitate comparison of the experimental heat transfer coefficients with the standard Dittus–Boelter, Sieder–Tate, and Petukhov correlating equations (Holman, 1981). In all cases, the experimental Nusselt numbers obtained agreed closely with these correlations. Of the three correlations, the Dittus–Boelter correlation

$$Nu_{DB} = 0.023\, Re^{0.8} Pr^{0.4} \quad (4)$$

is the simplest to use and appeared to provide a very close fit to the data obtained (see Fig. 2).

Calculated inner wall temperatures and calculated fuel temperatures for a representative case (methane/7 percent ethane) are plotted versus the length from the test tube inlet in Fig. 3. The inner wall temperatures at a given downstream location are essentially those of the measured temperature of the outer wall, differing by typically less than 6 K. The data points shown correspond to different times, ranging from 2 to 40 hours after the start of the test. The curves shown are least-squares quadratic polynomial fits to the wall and fuel temperature data shown in the figure. Both the wall and fuel temperatures in the stainless tubes increased monotonically from the tube entrance to the tube exit with the difference between wall and bulk fuel temperature remaining fairly constant at about 65 K. For the test conditions and gas mixtures employed in these tests, none of the wall temperatures were observed to exhibit a significant or systematic increase with time, as might be expected for constant input power if there was a significant change in thermal resistance due to buildup of deposit on the inner wall.

Table 2 Composition of commercial natural gas

Elemental Composition	Volume %
Methane	96.62
Ethane	2.32
Propane	0.54
n-Butane	0.10
i-Butane	0.12
Nitrogen	0.30

Deposit Formation. The measured carbon deposition rates for various methane–hydrocarbon mixtures are shown in Figs. 4–6. In each figure, the deposition rates, normalized by the internal surface area of the samples and the test durations, are shown plotted against the wall temperatures. Unused stainless-steel tube sections of identical cross section were analyzed for carbon deposit to furnish tare values, which were subtracted from the carbon burn-off results. The average value of these

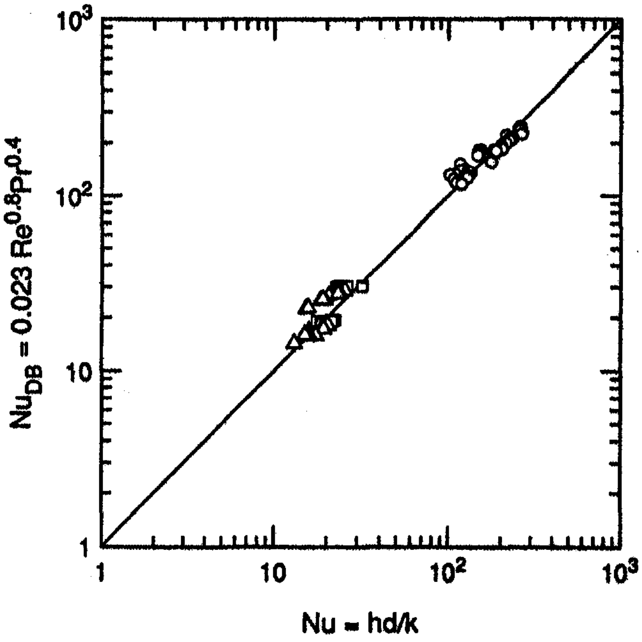

Fig. 2 Nusselt numbers—experimental heat transfer data and Dittus–Boelter correlation

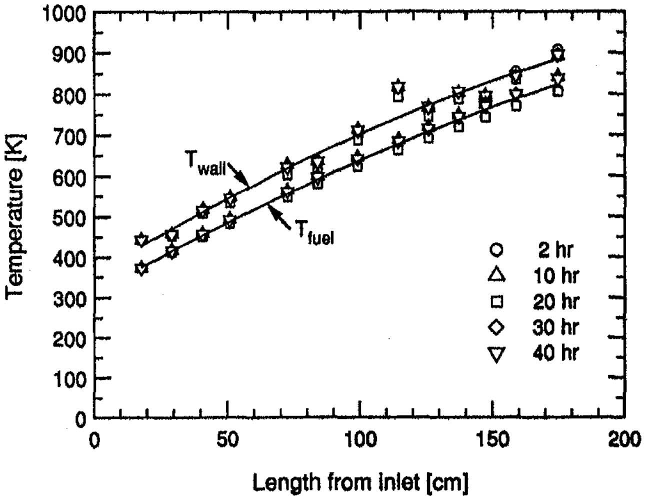

Fig. 3 Wall and fuel temperature profiles for methane/7 percent ethane

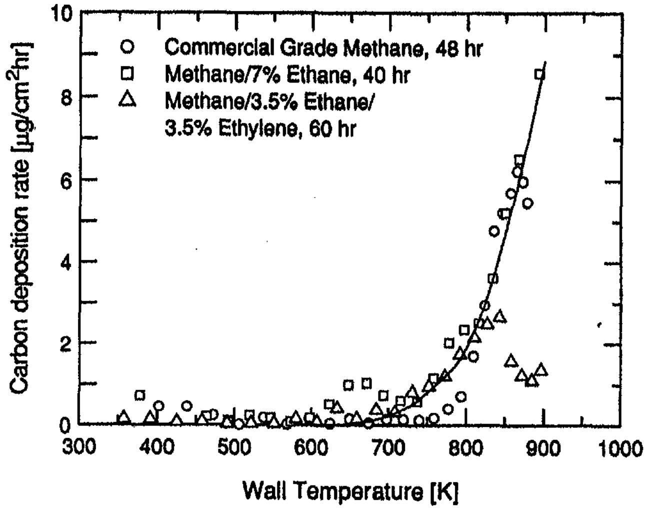

Fig. 5 Deposition rates for methane–hydrocarbon mixtures

tares amounted to a deposition rate of roughly 0.2 μg/cm^{2}h based on a 40-h test.

Representative deposition rate data for tests with commercial methane are shown in Fig. 4. The symbols correspond to two different tests, with the time indicated corresponding to the total time of each test. In both cases, there was essentially no deposit buildup for wall temperatures below approximately 650 K. Between roughly 650 K and 775 K, there was a rapid increase in deposition rate, leading to deposition rates of as much as 9 μg/cm^2-h at the maximum wall temperature of approximately 900 K. At intermediate temperatures (650 K to 800 K), a somewhat higher rate of deposit formation was measured for the test of shorter duration. This may reflect an influence of the wall material or surface condition during the early stages of the test. In any case, the two data sets appear to converge for wall temperatures greater than 850 K.

The deposition data for commercial grade methane are compared with the corresponding data for mixtures of methane with 7 percent ethane and methane with 3.5 percent ethane/3.5 percent ethylene in Fig. 5. The total test times in all cases shown were at least 40 h. While there is some scatter in the data, the deposition characteristics of the methane–hydrocarbon mixtures shown are consistent with the trends exhibited for the commercial methane. The scatter in the data reflects measurement uncertainties that preclude accurate determination of deposition rates below the threshold temperature of approximately 650 K. The deviation apparent in the methane/3.5 percent ethane/3.5 percent ethylene case at high temperature (greater than 850 K) is likely due to a change in flow characteristics at the end of the tube rather than inhibition caused by ethylene chemistry. (The lower bond dissociation energy of ethylene compared to methane or ethane would be expected to reduce the thermal stability of the mixture.)

Deposition rate data for ultrahigh-purity methane are shown in Fig. 6. As in the previous cases, there was very little deposition below a threshold temperature of approximately 650 K. Although there is scatter in the data, the results for temperatures above 650 K are consistent with an increase in deposition rate with temperature that is somewhat less (roughly a factor of two or three) than for commercial methane or the methane–hydrocarbon mixtures (cf. Figs. 5 and 6). This observation is consistent with the expectation that the presence of hydrocarbon impurities should result in an increase in carbon deposition rate relative to that of pure methane. The results of these tests suggest that hydrocarbon contaminant species typically found in natural gas can lower the maximum allowable operating temperature by approximately 100 K, relative to pure methane.

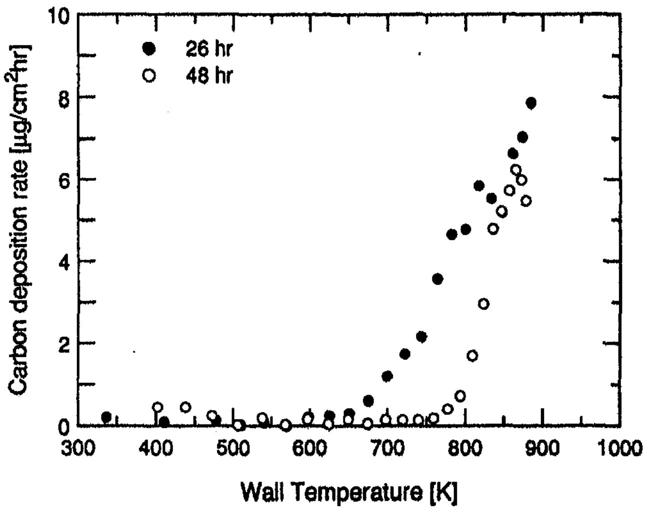

Fig. 4 Deposition rates for commercial methane

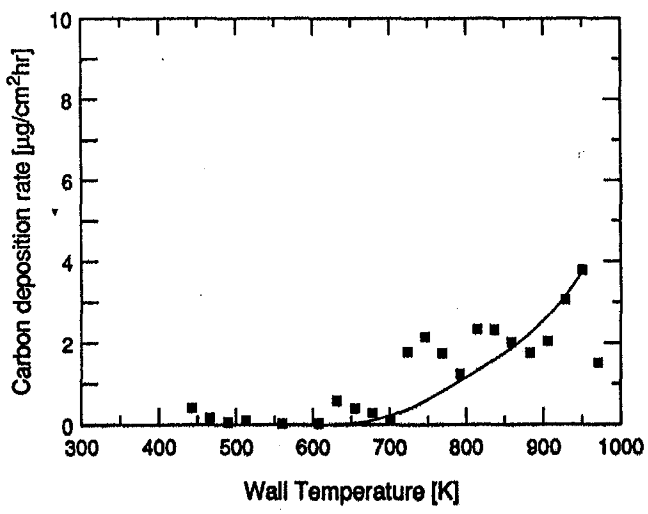

Fig. 6 Deposition rate for ultrahigh-purity methane

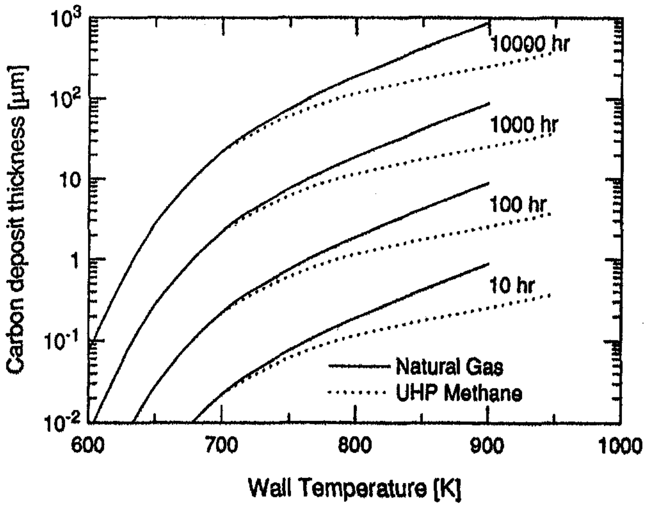

Fig. 7 Estimated deposit buildup for methane and natural gas

The maximum measured deposition rate for the mixtures, approximately 9 μg/cm^{2}h at a wall temperature of 900 K, corresponds to a deposit thickness of approximately 4 μm for a test duration of 40 h. This estimate assumes an average density of the deposit of 1 g/cm^3. Estimates for other times (10, 100, 1000, and 10000 h) are presented in Fig. 7. The curves representing natural gas are based on all the methane gas mixture data given in Fig. 5; the curves for ultrahigh-purity methane, on the data shown in Fig. 6. Implicit in this analysis are the assumptions that the deposition rate and deposit density are constant, and that the deposition rate can be defined by the local wall temperature. The curves shown in Fig. 7 provide an estimate of the thickness of deposits that might be formed on fuel system component surfaces over reasonable engine operating times. For example, after 1000 h of service at a wall temperature of 900 K, use of methane–hydrocarbon mixtures similar to those considered in this study would lead to a potential deposit thickness of 0.09 mm. This deposit thickness would amount to a blockage of roughly 0.2 percent for a tube of similar inside diameter to those in these tests (2.2 mm). The use of high-purity methane could limit the deposit buildup under similar operating conditions to approximately one-third that of natural gas, leading to roughly an order of magnitude decrease in blockage due to deposition. For both high-purity methane and methane–hydrocarbon mixtures, the deposit thickness decreased rapidly with decreasing temperature and was essentially negligible at temperatures below 700 K.

In all the cases considered, significantly less deposit was formed than would be the case for liquid fuels under similar conditions. This is illustrated in Fig. 8, where the deposition data for the gaseous methane–hydrocarbon mixtures are compared with that of a liquid-phase jet fuel, JP-5 (Marteney and Spadaccini, 1986), over a similar range of temperature. The maximum deposition rate of the JP-5 at a temperature of 645 K is nearly two orders of magnitude higher than the maximum rate observed for the gaseous methane fuels of this study.

Thermal decomposition of liquid hydrocarbon fuels is governed by three distinct reaction mechanisms depending upon fuel temperature. Below fuel temperatures of 570 K, liquid-phase autoxidation reactions produce deposit formation at a rate increasing with increasing temperature. Between 570 K and 770 K, there is a competition between autoxidative and pyrolytic reactions in the deposit formation process (Edwards, 1992). The dominant mechanism for deposit formation shifts from the autoxidation to the pyrolysis in this region (Taylor, 1974). Deposit rates peak around 640 K to 700 K and then decrease with increase in temperature due to depletion of oxygen dissolved in the fuel (Heneghan et al., 1993). Above about 770 K, direct pyrolysis of the fuel gives rise to the deposits. At these temperatures, deposition rate again increases with increasing temperature.

These mechanisms are reflected in the JP-5 thermal stability deposition rates shown in Fig. 8. Not all mechanisms are evident, however, for the gaseous methane deposition rates, primarily owing to the absence of oxygen. In addition, the methane gas mixtures were not characterized by the presence of sulfur, aromatics, or other minor species known to promote deposit formation in liquid fuels. Above 900 K, though, an increase in deposition rate occurs for both the JP-5 and the methane as pyrolysis is the dominant deposit formation mechanism.

Summary and Conclusions

The thermal stability and deposit formation characteristics of several methane–hydrocarbon mixtures and a typical natural gas were established using heated tube tests and compared with the deposition characteristics of high-purity methane. Quantitative measurements of deposit mass indicate there was essentially no deposit buildup for wall temperatures below 650 K. Between approximately 650 K and 775 K, there was a rapid increase in deposition rate, leading to deposition rates of up to 9 μg/cm^2-h at the maximum wall temperature of approximately 900 K for natural gas and the methane–hydrocarbon mixtures. The corresponding rate for the high-purity methane was lower by roughly a factor of three. Wall temperature profiles did not exhibit any systematic increase in time (even at the highest temperatures) that would indicate a change in heat transfer brought about by significant deposit formation. In all cases the deposit thickness was much lower (up to two orders of magnitude) than that reported for liquid fuels.

Estimates of deposit thicknesses that might form in fuel system components utilizing gas-phase methane or natural gas indicate a very small deposit buildup after 1000 hrs of operation at a wall temperature of 900 K. The use of high-purity methane could reduce the deposit thickness under similar operating conditions by as much as a factor of three, or permit operation at even higher temperatures. Below a temperature of 700 K, there appears to be essentially no difference in deposition rate between high-purity methane and methane–hydrocarbon mixtures containing up to 7 percent hydrocarbon impurities.

The data suggest that the presence of hydrocarbon impurities typically found in natural gas could impose a requirement that the maximum allowable operating temperature be decreased by 100 K, relative to high-purity methane. These results indicate that the use of high-purity methane instead of natural gas would

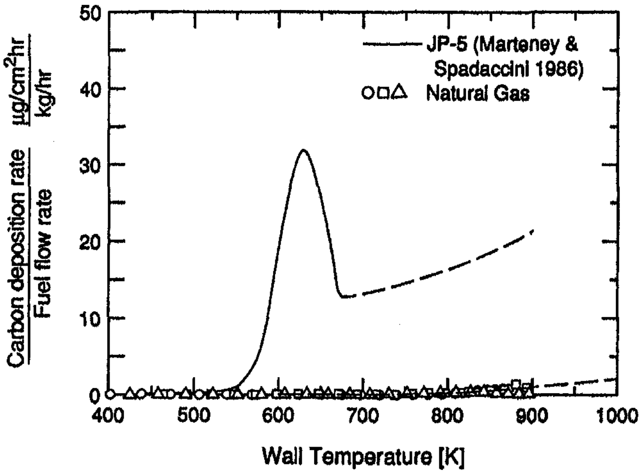

Fig. 8 Comparison of deposition rates for natural gas and JP-5

result in significantly lower deposit formation under similar operating conditions, or permit operation at higher temperatures.

Acknowledgments

This paper is based on work performed for the New Energy and Industrial Technology Development Organization (NEDO), as part of the Japanese National Project on Super/Hypersonic Transport Propulsion Systems (HYPR) of the Ministry of International Trade and Industry (MITI) in Japan. The authors gratefully acknowledge the technical contributions of Ken Beemer (UTRC) for heated tube testing and William H. Edwards (P&W) for carbon burn-off measurements.

References

Back, M. H., and Back, R. A., 1983, "Thermal Decomposition and Reactions of Methane," in: *Pyrolysis—Theory and Industrial Practice,* Academic Press, New York.

Edwards, T., 1992, "Deposition During Vaporization of Jet Fuel in a Heated Tube," *30th AIAA Aerospace Sciences Meeting,* Reno, NV, Jan. 6–9.

Ely, J. F., and Huber, M. L., 1990, "NIST Standard Reference Database 4—NIST Thermophysical Properties of Hydrocarbon Mixtures Database," Version 1.0.

Heneghan, S. P., Martel, C. R., Williams, T. F., and Ballal, D. R., 1993, "Studies of Jet Fuel Thermal Stability in a Flowing System," ASME JOURNAL OF ENGINEERING FOR GAS TURBINES AND POWER, Vol. 115, pp. 480–485.

Holman, J. P., 1981, *Heat Transfer,* 5th ed., McGraw-Hill, New York.

Joslin, C. L., 1968, "The Potential of Methane as a Fuel for Advanced Aircraft," presented at the ASME Aviation and Space Conference, June.

Marteney, P. J., and Spadaccini, L. J., 1986, "Thermal Decomposition of Aircraft Fuels," ASME JOURNAL OF ENGINEERING FOR GAS TURBINES AND POWER, Vol. 108, pp. 648–653.

Mechanical Engineering Staff, 1986, "Propelling the Aerospace Plane," *Mechanical Engineering,* Vol. 108, No. 6, pp. 32–36.

Nishiyama, Y., and Tamai, Y., 1980, "Wall Effects During Thermal Reactions," *CHEMTECH,* Vol. 10, No. 11, pp. 680–684.

Taylor, W. F., 1974, "Deposit Formation From Deoxygenated Hydrocarbons, Part I—General Features," *Ind. & Eng. Chem., Prod. Res. & Devel.,* Vol. 13, No. 2, pp. 133–138.

D. L. Daggett

A. Veninger

Rolls-Royce Inc., Engineering,
Atlanta, GA 30339

C. Lewis

S. Bullock

Rolls-Royce PLC, Engineering,
Derby, United Kingdom

R. Kamin

Aircraft Division,
Naval Air Warfare Center,
Trenton, NJ 08628

The Development of an Aviation Fuel Thermal Stability Test Unit

A test unit has been developed by Rolls-Royce for the U.S. Navy to use in evaluating fuel thermal deposition typically found in various aircraft engine components. Although the current Jet Fuel Thermal Oxidation Tester (JFTOT) provides a qualitative thermal stability evaluation, it may not be able to predict in-service problems. Conditioning and testing of the fuel under realistic conditions is crucial if one is to predict deposit formations accurately. Engine fuel deposit evaluations and evidence from unpublished Rolls-Royce laboratory rig tests were used to help design a test unit that would address fuel stability problems in current or future aircraft. The Aviation Fuel Thermal Stability (AFTS) test unit embodies test modules that were selected with extensive fuel systems experience to enable the evaluation of thermal deposition in various fuel components using properly conditioned fuel. The test modules are controlled and results are recorded by a computer. This paper includes a review of the AFTS test unit design and preliminary test results thereof.

Background

Kerosene grade gas turbine fuels are subject to thermal stress in the flow path between the aircraft fuel tanks and the combustion chamber. Advances in aircraft technology continue to increase the heat loads, and therefore the thermal stress, placed on the fuel. The additional heat loads increase the potential for fuel to undergo thermal oxidation deposition. This deposition can adversely affect the performance and durability of the aircraft in a number of areas. Insoluble deposits can block fine mesh screens or filters such as those found in fuel management units or nozzles. Gums or lacquers can form on and cause stiction of lightly loaded, close tolerance, sliding components. Carbonaceous deposits can form on fuel injectors and cause degraded atomization, flow rate, and fuel distribution characteristics.

The U.S. Navy has particular concern about the potential for thermal degradation in its aircraft due to the nature of its shipboard aviation fuel distribution system. The shipboard distribution system is made up predominantly of copper–nickel piping. Surveys have shown that concentrations of up to 800 ppb of copper have been found in aviation fuel aboard ship. Previous work has shown that copper in concentrations above 50 ppb can be extremely deleterious to a fuel's thermal oxidation stability.

Current specification testing of a fuel's thermal oxidation stability is performed using the Jet Fuel Thermal Oxidation Tester (JFTOT). Although the JFTOT has been a satisfactory go-no-go quality control test, its capabilities as a quantitative research tool are extremely limited. Oxidation stability in the JFTOT is rated according to the visual appearance of the deposits that form on a heated tube as well as the pressure drop across a 17 μm filter. In order to quantify the effect of fuel thermal stability and aircraft operating parameters on hardware performance and durability, a wide variety of rig, component, and engine tests have been conducted. However, these tests usually have limited flexibility and require an extensive amount of fuel, manpower, and cost to conduct.

Internal, unpublished research conducted by Rolls-Royce, as well as other published data (Hazlett, 1991; Kirklin and David, 1992; Goodyear and Vere, 1985), show that fuel type, bulk fuel temperature, fuel residence time, metal wall temperature, recirculation paths, degree of initial filtration, fuel wetted metallurgy, surface roughness, and fluid flow characteristics all affect the degree of fuel thermal degradation and ultimate deposition. These deposits manifest themselves according to fuel conditioning, component characteristics, and fluid dynamics. The AFTS test unit strives to enable the test operator to simulate most of these conditions as they may be encountered in the aircraft/engine environment. Test specimens may then be evaluated for the amount of deposits formed from the system operating conditions, or the fuel may simply be evaluated for its quality by gaging the various deposits formed on all the test specimens.

System Description

The AFTS test unit comprises test modules representing critical aircraft fuel components that have been found to develop in-service deposits. The fuel has been conditioned prior to each of these test modules to represent typical aircraft fuel system operating conditions.

Typical Aircraft Fuel System. Three major thermal regimes have been identified in aircraft, as shown in Fig. 1, that are known to contribute to fuel deposits: low (ambient—350 K), intermediate (350–450 K), and high temperature (470–570 K).

Low Temperature Regime. This area is characterized as that leading from the fuel tanks up to the engine high-pressure (HP) pump and is operated at low pressure. The types of deposit in this section generally tend to be particulate. Deposit precursors can also form in this regime that result in further deposition downstream. The rates of buildup are highly dependent on temperature, flow regime (residence time), and fuel type/composition including dissolved gases, water, etc.

Intermediate Temperature Regime. This regime usually is found within the aircraft engine after the HP pump and engine oil cooler but before the fuel nozzles. Deposits in this section tend to be gums, fuel borne, and surface particulate. The rates of deposit are again influenced by the fuel temperature, flow regime, and fuel type. Fuel wetted component material composition becomes important in this section.

Contributed by the International Gas Turbine Institute and presented at the 39th International Gas Turbine and Aeroengine Congress and Exposition, The Hague, The Netherlands, June 13–16, 1994. Manuscript received by the International Gas Turbine Institute March 8, 1994. Paper No. 94-GT-217. Associate Technical Editor: E. M. Greitzer.

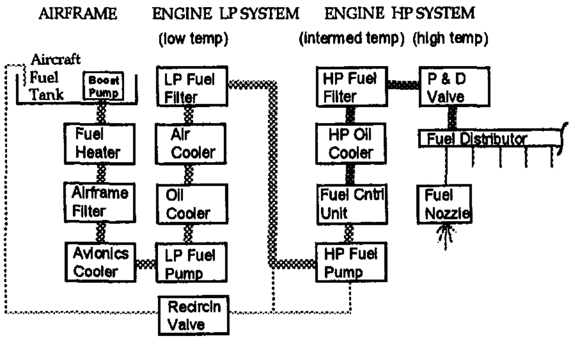

Fig. 1 Aircraft fuel system components

High Temperature Regime. This section is generally isolated to the fuel distribution system and/or fuel nozzles. It is characterized by the hot walls found within these parts. Deposits tend to be carbonaceous in nature and are fuel borne as well as surface deposited. The rates of deposit are influenced by the fuel temperature, flow regime, fuel type, component surface material, surface roughness, fluid dynamics, and most importantly, surface temperature and previous thermal stressing.

AFTS Test Unit Fuel System. Within the three thermal regimes, various test modules (Fig. 2) are included to represent aircraft components that have been shown to exhibit or affect deposition problems: conditioning (fuel delivery) filter, LP fibrous filters, HP filter screens, lightly loaded fuel management unit (FMU) sliding control valves, and fuel nozzle or injector passages.

In designing the support system that drives the test modules, care was used in selecting equipment that had similar metallurgy to engine components. Haphazard use of parts with unknown material composition may lead to false indications of deposits in the test specimens.

Enough flexibility has been built into the unit to cater for simulation of present day, or future, aircraft fuel system conditions. Table 1 shows the system operating range along with the present specifications of the test modules. The test unit may be run in a single flow pass mode that is the most common testing method, partial recirculation to simulate spill from the aircraft HP fuel pump, or full recirculation for leak checking and maintenance. Further detail of the major components is presented.

Inlet Filter. Rolls-Royce tests have shown that the degree of initial filtration can have an impact on deposit formation. The inlet filter can condition the fuel prior to reaching the fuel heating section and test specimens. A 10 μm aircraft filter is used to simulate an airframe filter (if installed) or ground service vehicle filter. The inlet filter also serves to remove any debris that may be generated by the LP fuel pump. As this filter operates at ambient temperatures, no thermal-related deposits are expected to be found, but instead the filter serves to condition the fuel prior to thermal testing.

LP Filter Module. To address the possible blockage problem of aircraft engine LP filters from fuel additives, and locate low-temperature fuel-borne particulate, this module characterizes the powerplant main LP filter that operates in the low-temperature regime (ambient—350 K). A 10 μm aircraft LP filter is modified (Fig. 3) to reflect closely the conditions and deposit characteristics found in service. Table 2 shows typical aircraft turbine engine filtration ratings.

Table 1 AFTS test unit operating parameters

Parameter	Specification
Fuel Flow	5.7-22.7 LPH (9.5 normal)
Flow Path	Single Pass, Recirculation, Partial Recirculation
LP Pressure	138 to 690 kPa
LP Temperature	Ambient to 370 K
HP Pressure	690 to 9660 kPa
HP Temperature	Ambient to 500 K
LP Filter Module	Scaled 10 µm, resin-impregnated, LP aircraft filter
HP Filter Module	Scaled 70 µm, 304 stainless steel, HP aircraft filter
Stiction Module	Similar to aircraft spool valve
Nozzle Module	Instrumented, reusable, scaled EDM 316 stainless steel tube

Most filters are sized for a specific dirt holding capacity. However, a rule of thumb is to provide 0.85 to 1.70 cm^2 of filter area per 1 LPH fuel flow. Since it is important to keep a pleated configuration on the test filter to mimic the type and location of aircraft fuel deposits, the excess filter area is blocked with an epoxy material similar to that used on production filters.

Stiction Module. To simulate the problems of hysteresis or sticking in close tolerance (down to 0.00254 mm) spool valves within the engine FMU, a 35 kPa hydraulic differential pressure sensing spool valve is used. Very small fuel deposit accumulations can be measured by this module.

Actual fuel dynamic similitude with engine components was difficult to achieve in this module due to availability of valve sizes; however, metallurgy is sufficiently similar. A survey of fuel management manufacturers showed the most common types of materials used in manufacture to be 440C stainless steel, 6061-T6 aluminum, and 5144C steels. The test valve uses 12L14.

The valve operates for approximately 12 hours, full open, while deposits are being formed on the valve barrel wall. The valve then slowly closes over a 30 second interval by rerouting the fuel flow around the valve. This causes an internal spring to push the spool down into the closed position, trapping fuel deposits between the spool and the barrel wall. Fuel is then again gradually routed back through the valve, pushing the spool back into its full open position. By simultaneously measuring the differential pressure across and the flow through the valve, one is able to record a qualitative measure of the degree of stiction by noting the hysteresis of the valve. Figure 4 illustrates the stiction module operating characteristics through one cycle.

Nomenclature

abs = absolute filtration (complete retention)
AFTS = Aviation Fuel Thermal Stability
EDM = Electro-Discharge Machining
FMU = Fuel Management Unit
JFTOT = Jet Fuel Thermal Oxidation Tester
kPa = kilopascal
K/s = degrees Kelvin per second
HP = High Pressure
LP = Low Pressure
LPH = Liters Per Hour
m/s = meters per second
nom = nominal filtration (95–98 percent retention rate)
μm = micron

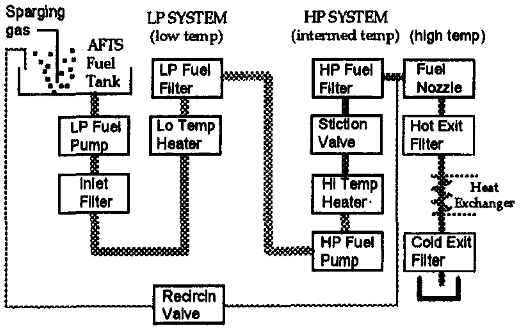

Fig. 2 AFTS major components

HP Filter Module. Aircraft intermediate-temperature fuel screens and HP filters have been found to develop deposits by catching fuel-borne particulate as well as generating surface deposits. This module can simulate either and currently uses a 70 μm, 304 stainless steel woven mesh screen as shown in Fig. 5. The screen is sized to simulate a small last chance filter and allows for 51.5 m/min fuel velocity in the mesh open area. These filters are prepared and weighed prior to the test and reweighed after the test. Discrete test data are gathered from deposit weight while real-time data are obtained from recording the differential pressure across the filter.

Heated Nozzle Module. Engine fuel nozzles are especially susceptible to internal passage wall deposits and fuel-borne particulate blockage due to the hot environment the nozzle operates in.

The heated nozzle module can simulate hot parts of the fuel system, such as fuel nozzle feed arms, that operate with high metal wall temperatures, turbulent flow, rough walls, and high inlet bulk fuel temperatures, all of which contribute to increased deposition. The nozzle module also represents factors that act to decrease deposition, such as high wall shear stresses, low fuel residence time, and 316 stainless steel metal construction (one of the lowest deposition steels).

If one is to predict engine deposit rates, it is also important to re-create the same heating mechanism as found in aircraft engines. Some laboratory testing methods suggest using a heated tube while holding a constant wall temperature throughout the duration of the test (Chin and Lefebvre, 1992). However, in a turbine engine, the fuel nozzle wall temperature is not constant but varies in direct proportion to the amount of fuel deposition. A constant heat flux is available to the fuel nozzle walls by the hot compressor discharge air flowing around the outside of the nozzle as shown in Fig. 6. Cooler fuel flowing through the inside of the nozzle carries away some of this heat, lowering the nozzle wall temperature from its surroundings. As carbon deposits gather on the nozzle wall, an insulation is formed and the wall temperature rises to approach that of the compressor discharge air.

Table 2 Sample of aircraft filtration ratings (Straus, 1991)

Engine	Component	Material	Rating (μm)
A	main filter servo screens	cellulose/cotton in phenolic resin steel	40 (80 abs) 40 (nom)
B	main filter servo screens	polyester/fiber glass steel	40 (80 abs) 40
C	main filter servo screens nozzle screens	fiberglass steel stainless steel	10 (35 abs) 100 to 300 40 to 400
D	low press. filter high press filter servo screens	paper steel wire stainless steel wire	10 (40 abs) 250 40 to 100
E	engine filter servo screens	- steel	- -

Actual engine and fuel nozzle test data, along with laboratory test results and CFD modeling, were used to design the nozzle tube test section to match closely typical aircraft internal nozzle thermal and fluid dynamics. The tube test section can simulate a Rolls-Royce RB211-535 fuel nozzle feed arm. However, during testing, increased wall temperatures are normally used to ensure sufficient deposit accumulations in a reasonable amount of time. The nozzle tube consists of three sections, a middle heated test section and two end attaching pieces as shown in Fig. 7. The center tube test section was EDM manufactured from 316 stainless steel to match surface finish and metallurgy.

The AFTS test unit uses an HP system pressure sufficiently high to assure the fuel is kept above its vapor pressure to avoid two-phase flow. A constant available heater power is used to drive the nozzle module. As a test commences, a rise in the tube wall temperature is observed over time that indicates deposition is taking place. A good correlation has been shown by Rolls-Royce, Goodman and Bradley (1970), and AFTS test results, between this rise in wall temperature and the total amount of carbon deposits (Fig. 8). This approach enables the continuous measurement of carbon buildup throughout the duration of the test and provides a temporal record of results. After testing, the entire tube is subjected to carbon burn-off analysis to verify the temperature rise versus carbon deposit test results.

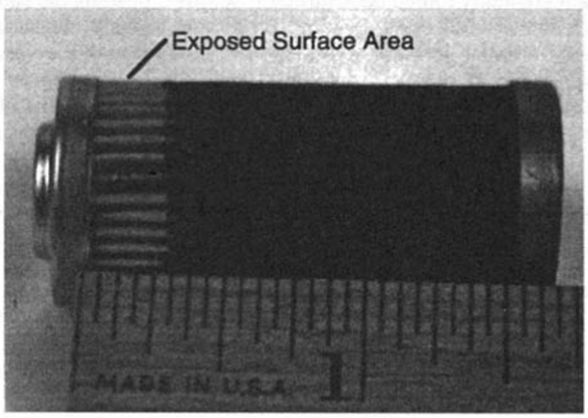

Fig. 3 Modified LP filter

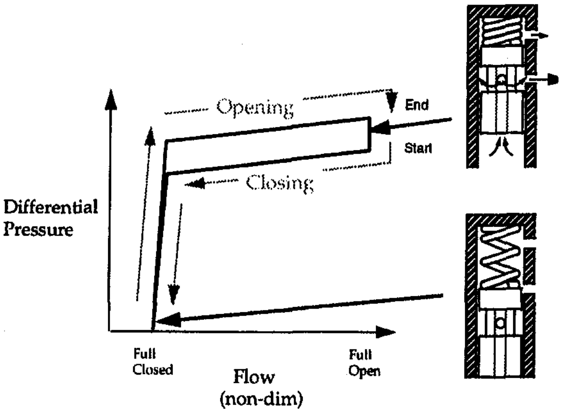

Fig. 4 Stiction module operation

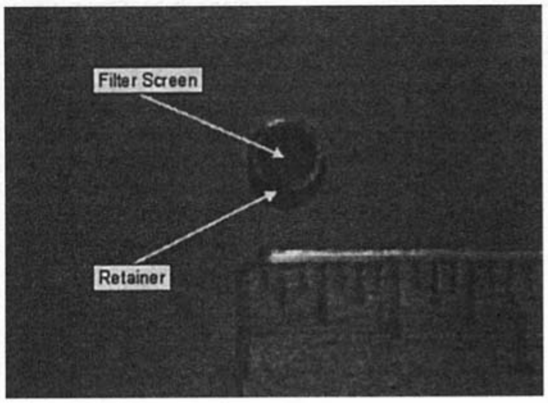

Fig. 5 HP filter screen

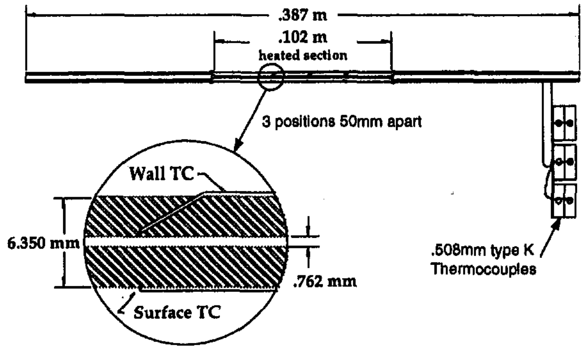

Fig. 7 Heated nozzle tube assembly

Hot and Cold Exit Filter Modules. Two filters were included downstream of the heated nozzle: one aft of the nozzle (hot exit filter) and another after the water-cooled heat exchanger (cold exit filter). Although there is no aircraft equivalent of the cold exit filter, the hot exit filter may be used to evaluate the blockage potential of small nozzle exit slot passages. An analysis can also be made of the cooling effect on fuel during low heat stress tests. In addition, the filters also serve to protect the unit's flow metering valve. Both filters use a stock housing with a 830 mm^2 area element. A new 60 μm sintered 316 stainless steel element is carefully prepared and weighed before and after each test.

Test Unit Assembly. The test unit is comprised of a cabinet containing all the mechanical test modules (Fig. 9) and another two cabinets containing the control/data acquisition computer along with the supporting relay and electronic hardware (Fig. 10). The mechanical cabinet is located inside a test cell while the computer and relay cabinets are located in a control room.

The computer controls all the mechanical systems and records test data to disk as well as displaying real-time results. Testing may be conducted in a semiautomatic–automatic mode by issuing commands from a keyboard, or the test sequence may be fully automated. System parameters are monitored for unsafe conditions, and if found, the test will be automatically aborted with a controlled shutdown.

Preliminary Results

Prior to installation at the Navy facility in Trenton, NJ, the test unit was shipped to the Rolls-Royce laboratories in Derby England for component functional checks, integrated system testing, and validation of test data.

A sequence of tests were conducted to evaluate the sensitivity of the test unit as well as to determine its ability to discriminate between fuels of differing thermal stability. The tests were run in a single flow pass mode (no recirculation), fixed low temperature (300 K), low pressure (483 kPa), LP system condition with a varied high temperature (433–455 K), fixed high pressure (4831 kPa) HP system condition. The nozzle was run at numerous constant available power settings. Jet-A1 was used as the baseline fuel for all temperature comparison tests. These conditions encompass the upper temperature regimes of many actual engine fuel systems.

LP Filter. The LP filter showed no signs of thermal related deposits because the LP system was operated at a low temperature (300 K) with relatively short test periods (25 hours).

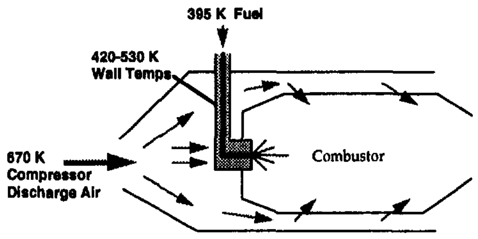

Engine Combustor Nozzle

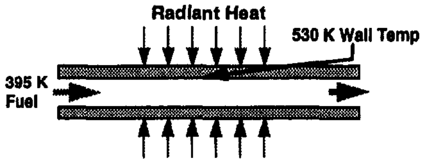

Test Start

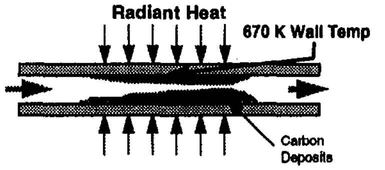

Test End

Fig. 6 Engine and AFTS nozzle heating

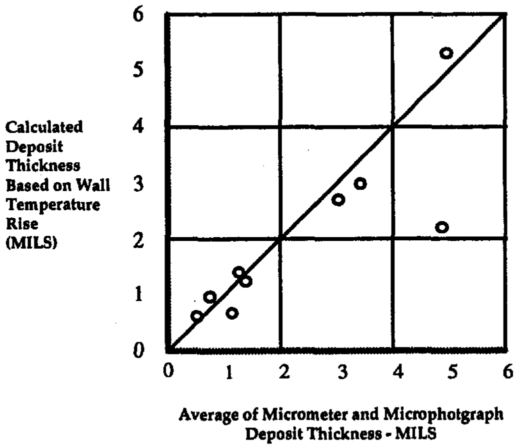

Fig. 8 Temperature rise versus deposition thickness (extrapolated from Goodman and Bradley, 1970)

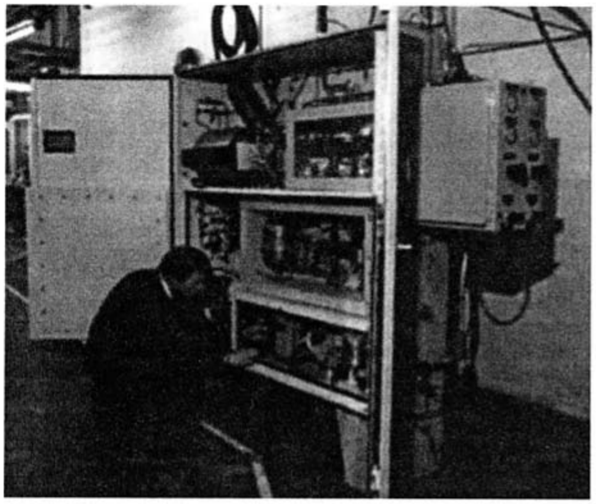

Fig. 9 AFTS mechanical cabinet

Stiction Module. The most significant result obtained for the stiction module was from a low-stability fuel (JFTOT breakpoint of 493 K) that was operated at a bulk fuel temperature of 433 K. Significant hysteresis was observed in as little as 14 hours as shown in Fig. 11. Tests conducted with higher stability fuels (538 K breakpoint) at the same temperature showed little indication of deposits after more than 50 hours.

HP Filter. The HP filter was operated with three different bulk fuel temperatures; 433, 444, and 455K. As the fuel-borne, thermal related, carbonaceous deposits build on the filter screen, the differential pressure across the filter increases. A relief valve opens at approximately 25 kPa to bypass the filter and allow continued testing. Figure 12 illustrates the filter blockage over time for the three differing bulk fuel temperatures using Jet-A1 fuel with a JFTOT breakpoint of 538 K.

A sharp increase in deposits was seen for small increases in bulk fuel temperatures. At 455 K, the test was terminated early due to rapid filter blockage. Most integrated testing was conducted with bulk fuel temperatures of 433 K to allow sufficient time for other fuel components to gather deposits before the HP filter became blocked. The slow heating rate of the fuel at 0.58 degrees Kelvin per second results in a long residence time that increases the deposit rate. Faster, and more realistic, heating rates are to be evaluated in the future.

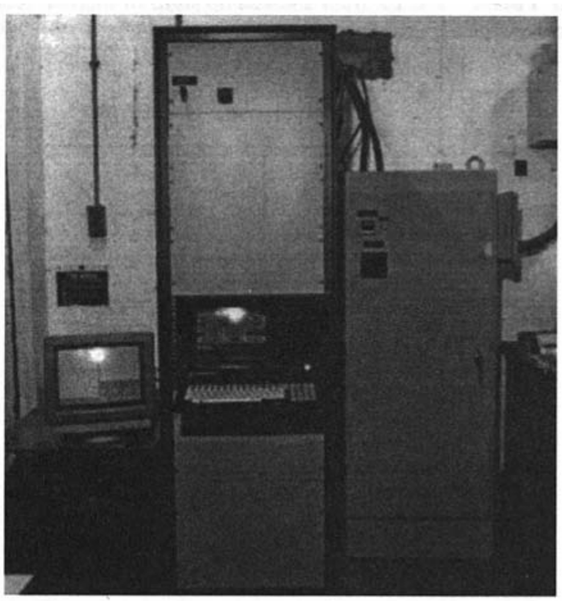

Fig. 10 AFTS computer and relay cabinets

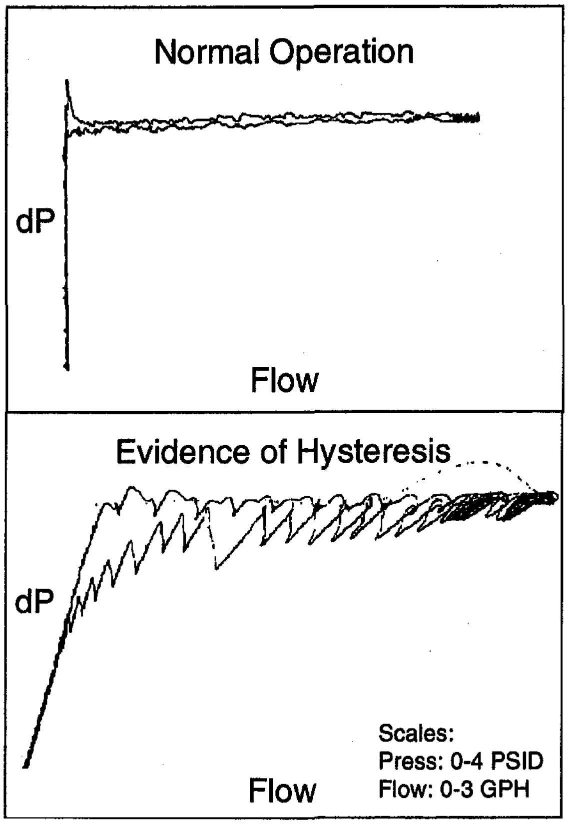

Fig. 11 Stiction module result comparison between low and high-stability fuels

Heated Nozzle Module. The nozzle module is able to gather real-time data of carbonaceous wall deposits. Figure 13 shows the results of two tests with differing initial nozzle wall temperatures. A deposit hold-off period is observed initially, as shown in other Rolls-Royce tests, after which the deposit rate increases. The increase in wall temperature, while at a constant heating power, is due to the insulating qualities of the carbon deposit. Both the initial and final wall temperatures were driven

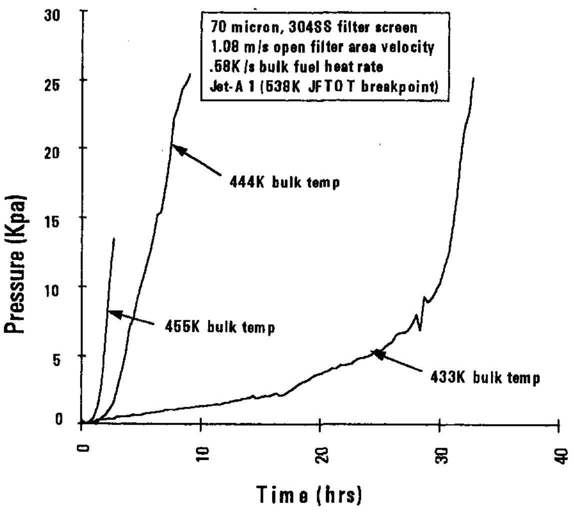

Fig. 12 HP filter blockage versus bulk fuel temperature

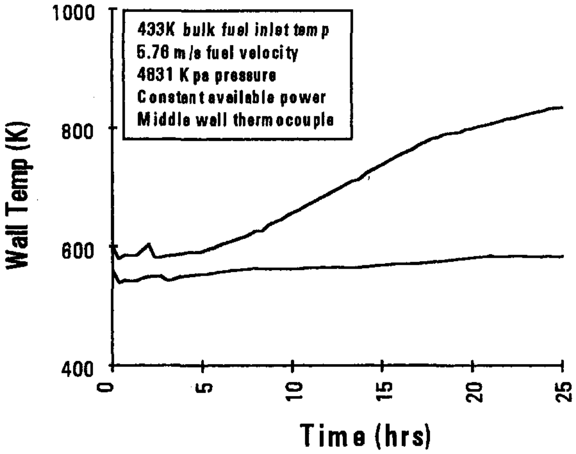

Fig. 13 Heated nozzle tube deposits over time for two differing initial wall temperatures

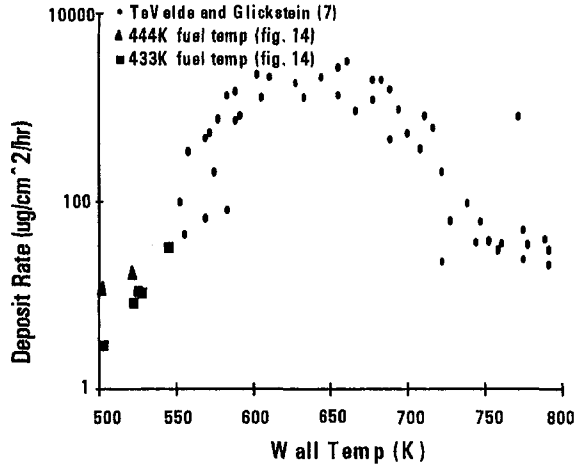

Fig. 15 Comparison of AFTS nozzle data with that of TeVelde and Glickstein (1983)

to higher levels than might be found in current aircraft nozzles to ensure sufficient carbon accumulations within the test period.

At the end of each test, the nozzle tube was removed and subjected to a carbon burn-off test to verify the results of the tube temperature rise. Figure 14 illustrates the deposit buildup for various heater power (initial inner wall temperature) settings using two different inlet fuel temperatures. The trends seem to indicate a higher level of wall deposits with increasing fuel inlet temperatures and increasing initial wall temperatures.

The AFTS test unit was designed to mimic turbine engine fuel conditions, and as such, provides an opportunity to compare nozzle deposit data with previous work done on heated tubes. Data from Fig. 14 are superimposed on test results presented by TeVelde and Glickstein (1983) at United Technologies Research Center (UTRC) and are shown in Fig. 15. Although the UTRC tests utilized an 8 foot long, resistance heated stainless steel tube, with ambient JP-5 fuel inlet temperatures, the AFTS test data appear to follow the UTRC data trend. The decrease in deposit rate above 650 K as shown by the UTRC data is believed to be caused from fuel-entrained oxygen depletion and a change in the deposit mechanism from autooxidation to pyrolysis.

Hot and Cold Exit Filter Modules. Initial tests show that the nozzle inlet bulk fuel temperature as well as the nozzle power have an impact on deposits arrested by the hot and cold exit filters. Figure 16 shows that increasing bulk fuel temperature results in increased deposits. Increasing the nozzle power (initial wall temperature) has the same effect. The hot exit filter always developed more deposits than the cold exit filter.

Interestingly enough, an Air-Force test rig using a similar test setup showed differing results. In addition, the cold exit filter developed more deposits than the hot at comparable bulk fuel temperatures and test duration to the AFTS unit. Figure 17 shows the comparison between those data (Heneghan et al., 1995) and those of the AFTS test unit. Variables that may contribute to this discrepancy are: the use of 2 μm filters versus 60 μm in the AFTS unit, and a much faster bulk fuel heating rate as well as a much lower filter velocity than the AFTS unit. The effect of these variables merits further testing.

Conclusion

A test unit was developed that showed its ability to quantify fuel thermal stability in those areas typically found in aviation turbine engines sensitive to deposition. The fuel is conditioned to represent realistic conditions while the test specimens closely reflect the dynamic, thermal, and material properties of actual aircraft fuel system components. Real-time data are obtained that provides good discrimination of changing test conditions and fuel quality. The AFTS test unit is now a viable test vehicle

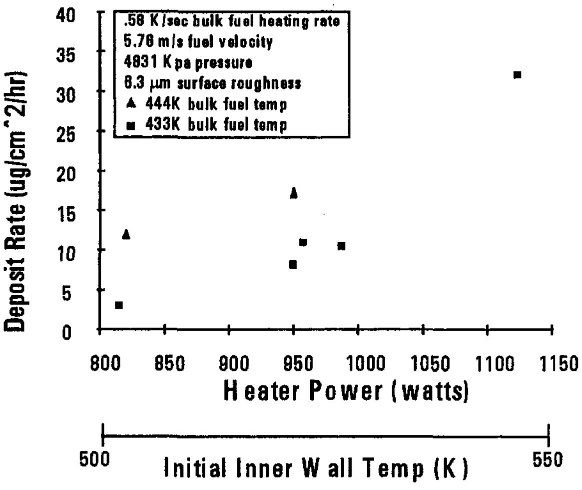

Fig. 14 Heated nozzle tube deposits for differing fuel inlet and initial wall temperatures

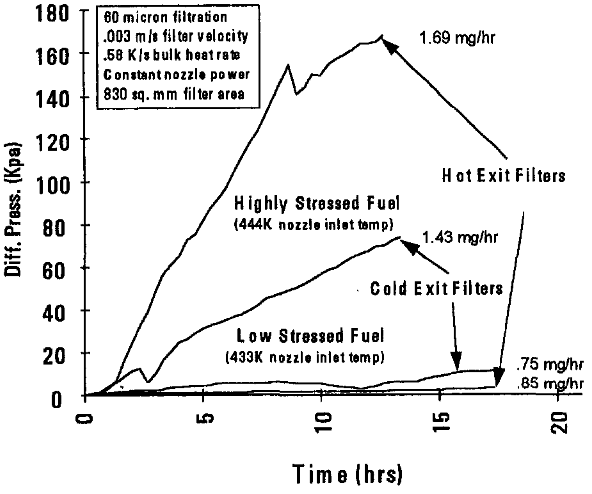

Fig. 16 Hot and cold exit filter blockage over time for two differing prestressed fuels

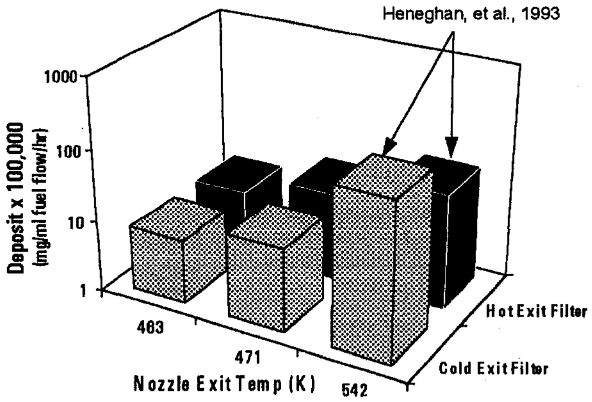

Fig. 17 Comparison of AFTS hot and cold exit filter results with those of Heneghan et al. (1995)

for investigating the causes and results of thermal degradation of aviation fuels.

Acknowledgments

This work was supported by the US Naval Air Warfare Center, Trenton, NJ, under contract No. N00140-90-C-0781.

References

Chin, J., and Lefebvre, A., 1992, "Experimental Techniques for the Assessment of Fuel Thermal Stability," *Journal of Propulsion and Power,* Vol. 8, No. 6, pp. 3–4.

Goodman, H., and Bradley, R., 1970, "High Temperature Hydrocarbon Fuels Research in an Advanced Aircraft Fuel System Simulator," Technical Report AFAPL-TR-70-13, WPAFB, OH, p. 109, Fig. 3.

Goodyear, E., and Vere, R., 1985, *Aviation Fuels Technology,* Macmillan Publishers LTD, London, United Kingdom.

Hazlett, R., 1991, "Thermal Oxidation Stability of Aviation Turbine Fuels," ASTM Publication 31-001092-12, Philadelphia, PA.

Heneghan, S. P., Martel, C. R., Williams, T. F., and Ballal, D. R., 1995, "Effects of Oxygen and Additives on the Thermal Stability of Jet Fuels," ASME JOURNAL OF ENGINEERING FOR GAS TURBINES AND POWER, Vol. 117, 1995, pp. 120–124.

Kirklin, P., and David, P., 1992, "Aviation Fuel: Thermal Stability Requirements," ASTM Publication STP 1138, Philadelphia, PA.

Straus, K., 1991, "Survey of Current Aircraft Engine Conditions," CRC Report No. 573, Atlanta, GA, p. 8.

TeVelde, J. A., and Glickstein, M. R., 1983, "Heat Transfer and Thermal Stability of Alternative Aircraft Fuels," Report AD/A137404, p. 20.

Part-Load Operation of Combined Cycle Plants With and Without Supplementary Firing

P. J. Dechamps

N. Pirard

Ph. Mathieu

Department of Nuclear Engineering and
Power Plants,
University of Liège,
Liège, Belgium

The design point performance of combined cycle power plants has been steadily increasing, because of improvements both in the gas turbine technology and in the heat recovery technology, with multiple pressure heat recovery steam generators. The concern remains, however, that combined cycle power plants, like all installations based on gas turbines, have a rapid performance degradation when the load is reduced. In particular, it is well known that the efficiency degradation of a combined cycle is more rapid than that of a classical steam plant. This paper describes a methodology that can be used to evaluate the part-load performances of combined cycle units. Some examples are presented and discussed, covering multiple pressure arrangements, incorporating supplemental firing and possibly reheat. Some emphasis is put on the additional flexibility offered by the use of supplemental firing, in conjunction with schemes comprising more than one gas turbine per steam turbine. The influence of the gas turbine controls, like the use of variable inlet guide vanes in the compressor control, is also discussed.

Introduction

This paper presents a method that can be used to evaluate the off-design performance of combined cycle units. In particular, the interest in looking at this off-design performance is to know about the reduced load efficiency of these plants. It is well known that combined cycles, like all equipment based on industrial gas turbines, experience a rather rapid performance degradation when the load is reduced, even if the design point performance is attractive (Dechamps et al., 1993).

In many countries experiencing a very rapid load growth, combined cycles are being installed because of their very short construction time, but will be replaced later by classical steam plants. In other countries like Belgium, the base-load duty is entirely covered by nuclear power plants. As a result of these situations, combined cycles are quite often required to cover the intermediate load range or to provide the load following capability of the generation mix. Hence, their reduced load performance is of great importance (Harmel, 1989).

The method presented can be implemented on microcomputers, and the required performance can be evaluated in a few seconds. Some emphasis is put on the devices and control systems usually used to improve the off-design performance, like a sliding steam pressure. The advantages of using supplemental firing as an additional control parameter are also discussed.

Most of the numerical method presented deals with the calculation of the heat exchange in the heat recovery steam generator, assuming that the off-design performance of the gas turbine and of the steam turbine can be determined by well-known techniques.

Modeling of One Pressure Level

Introduction. Although most of the heat recovery steam generators currently installed and in service comprise more than one pressure level, they can usually be broken into several modules, each composed of the three heat exchangers that build up a pressure level, i.e., an economizer, a vaporizer, and a superheater.

It is therefore worth looking at the model of a single-pressure-level HRSG, because more complex arrangements can be built by connecting together several such models.

Assumptions. Figure 1 presents the required notations corresponding to the heat exchange diagram for one pressure level comprising the three above-mentioned heat exchangers.

The Heat Exchange Coefficient Off-Design. A method must be used to evaluate the heat transfer coefficient in each of these heat exchangers when going off design. In order to avoid the computational burden of using detailed methods, it can be assumed that the heat transfer coefficient varies according to the following formula:

$$h = h_D \cdot \left(\frac{\dot{m}}{\dot{m}_D}\right)^{\alpha} \cdot \left(\frac{T}{T_D}\right)^{\beta} \text{ (gas side properties)} \qquad (1)$$

which only requires the detailed calculation of the heat transfer coefficient at the design point and suitable values of the exponents α and β. This is based on the assumption that the gas-side resistance to heat transfer is controlling.

A theoretical analysis provides values of 0.6 for α and 0.6 for β assuming that the flow over the heat exchanger tubes is fully turbulent and that the gas is a perfect gas. A fitting of Eq. (1) with results from a detailed heat transfer coefficient calculation procedure gives values of 0.52 and 0.31 for α and β, respectively. These values have been selected for the examples discussed in this paper.

System of Equations. The energy balances for the superheater can be written as:

$$Q_{su} = S_{su} \cdot h_{su} \cdot \Delta T_{\ln su} \qquad (2)$$

$$Q_{su} = \dot{m}_g \cdot (h_1 - h_2) \qquad (3)$$

$$Q_{su} = \dot{m}_v \cdot (h_a - h_b) \qquad (4)$$

The same equations apply for the vaporizer, taking into account the fact that the approach temperature difference (the

---

Contributed by the International Gas Turbine Institute and presented at ASME Cogen Turbo Power '94, Portland, Oregon, October 25–27, 1994. Manuscript received by the International Gas Turbine Institute July 23, 1994. Associate Technical Editor: E. M. Greitzer.

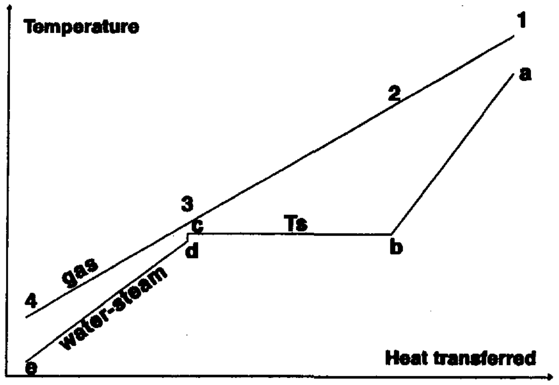

Fig. 1 Heat transfer diagram and notations for one pressure level

economizer does not provide a saturated liquid) must be considered here:

$$Q_{va} = S_{va} \cdot h_{va} \cdot \Delta T_{\ln va} \quad (5)$$

$$Q_{va} = \dot{m}_g \cdot (h_2 - h_3) \quad (6)$$

$$Q_{va} = \dot{m}_v \cdot (h_b - h_d) \quad (7)$$

The economizer takes over the remaining heat load:

$$Q_{ec} = S_{ec} \cdot h_{ec} \cdot \Delta T_{\ln ec} \quad (8)$$

$$Q_{ec} = \dot{m}_g \cdot (h_3 - h_4) \quad (9)$$

$$Q_{ec} = \dot{m}_v \cdot (h_d - h_e) \quad (10)$$

These heat balance equations must be complemented by the saturation relation:

$$Ts = \text{saturation temperature}(p) \quad (11)$$

and by an appropriate Stodola-like choking relation at the steam turbine inlet:

$$\frac{\dot{m}_v \cdot \sqrt{T_a}}{p} = \text{constant} * \text{steam turbine inlet area} \quad (12)$$

Equations (2) to (12) are a system of 11 nonlinear equations with the same number of unknowns (namely p, Ts, T_d, T_a, T_2, T_3, T_4, $\dot{m}_v$, Q_{su}, Q_{va}, Q_{ec}), which can be solved if the inlet conditions for the gas and the feedwater are known. The heat transfer coefficient in Eqs. (2), (5), and (8) can be appraised with Eq. (1).

Solving the Equations. Two main routes can be followed to solve the system composed of Eqs. (2) to (12):

- All the equations can be solved simultaneously with a global method based on a matrix formulation, or,
- The equations can be solved sequentially with a small number of guesses and checks when an equation has more than one unknown variable at the time it has to be solved. The best strategy can be determined by applying Mottard's rule, for example, although the explicit or implicit nature of the equations has to be taken into account as well (Kehlhofer, 1979).

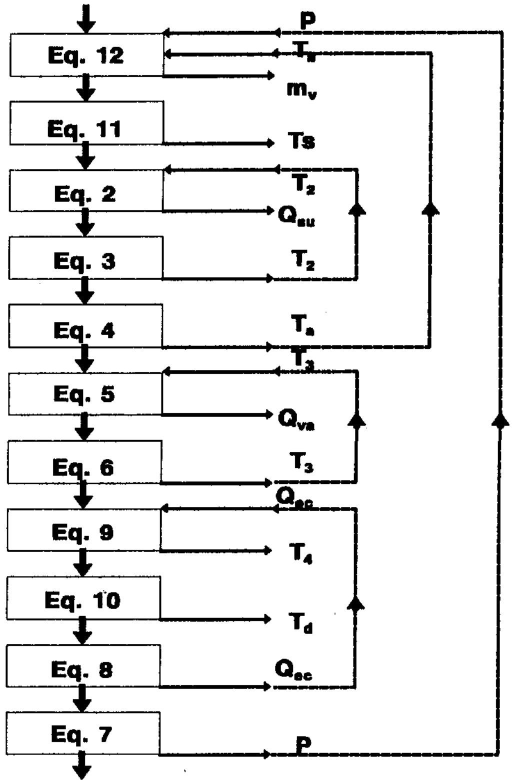

Fig. 2 Solving the equations for one pressure level

The sequential approach was thought to be better for this kind of problem, especially when considering the number of equations that should be solved simultaneously with the first method in the case of multiple pressure systems. This approach was implemented in our home-made combined cycle code CCCALC (Dechamps, 1993). Figure 2 represents the order of application of the equations. The variables to be guessed and checked later on are P, T_a, T_2, T_3, and Q_{ec}. The maximum number of imbricated loops is 3, although it is 2 most of the time. The equations involving a logarithmic mean temperature difference (2), (5), and (8) are all taken in their explicit form, thus avoiding the extraction of a temperature out of the logarithmic expression.

Modeling Multiple Pressure Level Systems

A system comprising more than one pressure level can be connected in two ways:

Nomenclature

CC = combined cycle
h = heat exchange coefficient, W/m^2 K
HP = high pressure, bar
HRSG = heat recovery steam generator
IP = intermediate pressure, bar
LHV = low heating value, MJ/kg
LP = low pressure, bar
$\dot{m}$ = mass flow rate, kg/s
p = pressure, bar

Q = heat exchanger load, kW
S = heat exchanger transfer surface, m^2
$\bar{T}$ = average gas temperature, K
TET$_{\text{iso}}$ = turbine entry temperature, K
Ts = saturation temperature, K
VIGV = Variable Inlet Guide Vane
α, β = exponents in evaluating h off-design
$\Delta T_{\ln}$ = logarithmic mean temperature difference

Subscripts

D = design point
ec = economizer
g = gas
s = steam
su = superheater
va = vaporizer
w = water

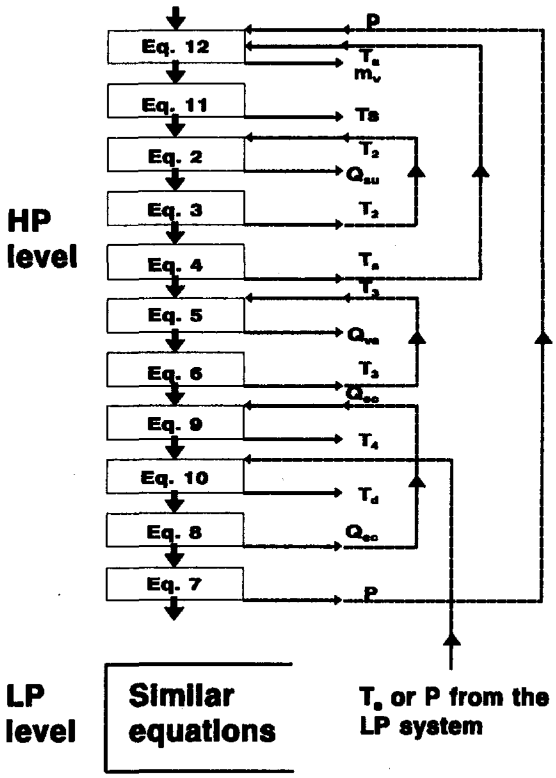

Fig. 3 Solving the equations for multiple pressure systems

- The pressure levels are independent one from another, all pressure levels are fed from the same deaerator. In this case, the system of equations just need to be solved for each pressure level.
- A given HP pressure level is fed from the drum of the IP or LP pressure level. This is sometimes referred to as a cascade arrangement. In this case, the feedwater temperature for the HP level is the saturation temperature of the LP drum. Therefore, there exists a link between the various pressure levels. In the equations, this introduces an additional loop between the equations for the two considered pressure levels. However, this additional loop does not really require an additional guessed parameter, because this temperature is directly linked to the saturation pressure of the LP drum, which has to be guessed anyway when solving this level.

Figure 3 illustrates this point. The feedwater temperature is required for the application of Eqs. (8) and (10). As Eq. (10) comes first in the order of calculation, the value of the feedwater temperature T_e (or of the corresponding pressure for the LP drum) has to be guessed before applying Eq. (10) as indicated by Fig. 3.

Unfired Single Pressure Combined Cycle Plant

Introduction. The above-presented technique is first applied to the simplest possible system, in order to point out some general conclusions about the off-design performance of combined cycle plants.

Assumptions and Design Point Performances. Table 1 summarizes most of the design assumptions of the system whose off-design behavior will be studied. Table 2 presents the main design point performance figures of this combined cycle plant.

Performance Analysis

Part-Load Efficiency. The very first criterion when analyzing the off-design performance of a power generation system is its part-load efficiency. As far as the considered system is concerned, two strategies can be used to reduce the output:

1. Reduce the gas turbine TET first, then close the gas turbine compressor VIGVs afterwards.
2. Close the VIGVs first, until the mass flow is reduced to 75 percent of the design value in this case, then eventually further reduce the gas turbine fuel flow with the VIGVs fully closed, i.e., with the air mass flow at 75 percent of its design value.

Figure 4 shows the combined cycle part-load efficiency (relative to the design point efficiency) against the ratio of the output over the design output for the two previously mentioned strategies. It clearly appears that the best way to reduce the output is to close the VIGVs first (Gyarmathy, 1989; Gyarmathy and Ortmann, 1991; Facchini, 1993; Desideri and Fibbi, 1993). This is essentially because the gas turbine exhaust temperature is better maintained when closing the VIGVs than when reducing the TET.

Indeed, two regulations can be used when closing the VIGVs:

Table 1 Unfired single pressure combined cycle plant—assumptions

Gas turbine

all characteristics taken form a typical E-technology machine of the 150 MW-class
inlet pressure loss : 10 mbar
HRSG back-pressure : 25 mbar
ambient temperature : 15°C
fuel : natural gas - LHV = 47.5 MJ/kg

HRSG

pinch point temperature difference : 10°C
approach point temperature difference : 2°C
drum pressure : 50 bar
superheater outlet temperature : 520°C
total transfer surface : 55000 m²
econo steaming off design counteracted by recirculation

Steam Cycle - General

steam turbine isentropic effectiveness : 85%
condenser pressure : 50 mbar
generators efficiency : 99%
auxiliary power consumption : 1 % of the gross output

Table 2 Unfired single pressure combined cycle design performance

Gas Turbine

net power output / efficiency : 144.95 MWe / 32.5 %
exhaust temperature : 551.37 °C
exhaust mass flow : 506.9 kg/s

HRSG

steam production : 66.6 kg/s
stack temperature : 149.8 °C
overall effectiveness : 74.9 %

Steam Cycle

net power output : 73.63 MWe
outlet quality : 91.09 %
Rankine cycle efficiency : 32.6 %

Overall

net plant power output : 218.58 MWe
net plant efficiency : 49 %

1 The gas turbine TET is kept constant, therefore producing a rise in gas turbine exhaust temperature.
2 The gas turbine exhaust temperature is kept constant.

Even if both strategies exist, the second one was used in this study, because keeping the TET constant produces a rise in gas turbine exhaust temperature, which was thought to be unacceptable both for the HRSG and for the resulting superheated steam temperature (reaching 580°C in this case). If the VIGVs were fully closed with a constant TET, the superheated steam temperature would exceed its design value by more than 30°C, which would require an important desuperheating injection rate. It should be noted that the difference in efficiency that appears on Fig. 4, i.e., of the order of 2% pt. is significant in terms of combined cycle efficiency, considering that it is of the same magnitude as that between simple and dual pressure combined cycle at design. Therefore, it can be said that choosing the right strategy at reduced load is almost as important as choosing the right combined cycle design.

LP Steam Turbine Outlet Quality. The LP steam turbine outlet quality is a factor that may limit the operation of the steam turbine at very low loads. The steam quality should stay above the value recommended by the steam turbine manufacturer in order to avoid erosion problems on the last stage blades. Such a limiting value is commonly within the range 0.86–0.89.

Figure 5 illustrates this in the case when the TET is used first to reduce the load, and in the case when the VIGVs are used first. From this point of view as well, the use of VIGVs in the first place produces a more acceptable steam turbine outlet quality at very reduced loads.

Economizer Steaming. The economizer approach temperature difference is usually reduced when the output of the steam cycle is reduced. It may happen that this temperature difference becomes nil, meaning that some vaporization takes place in the economizer. To avoid the stability and control problems associated with this phenomenon, a recirculation of the economizer flow back to its inlet may be used.

Figure 6 illustrates this, in the case when the VIGVs are used first to reduce the output, showing that the recirculation is required only when the TET is reduced, after the VIGVs are fully closed. Indeed, the approach temperature difference is even increased when closing the VIGVs, giving one more reason for their use.

If only the TET were used to control the plant output, the recirculation would be required not below 70 percent of the design output, but below nearly 100 percent.

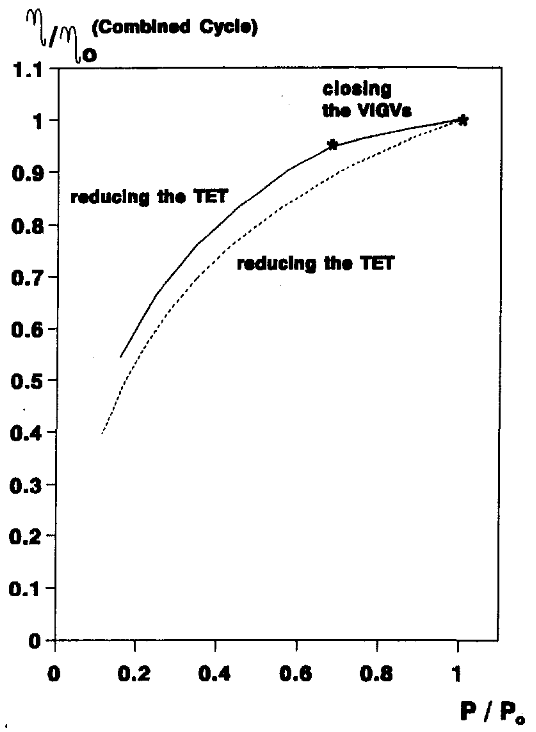

Fig. 4 Unfired single pressure level system combined cycle part-load efficiencies

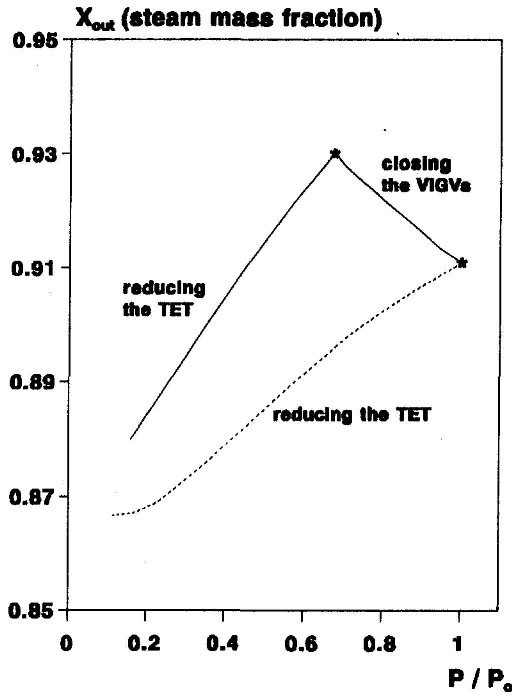

Fig. 5 Unfired single pressure level system steam turbine outlet quality

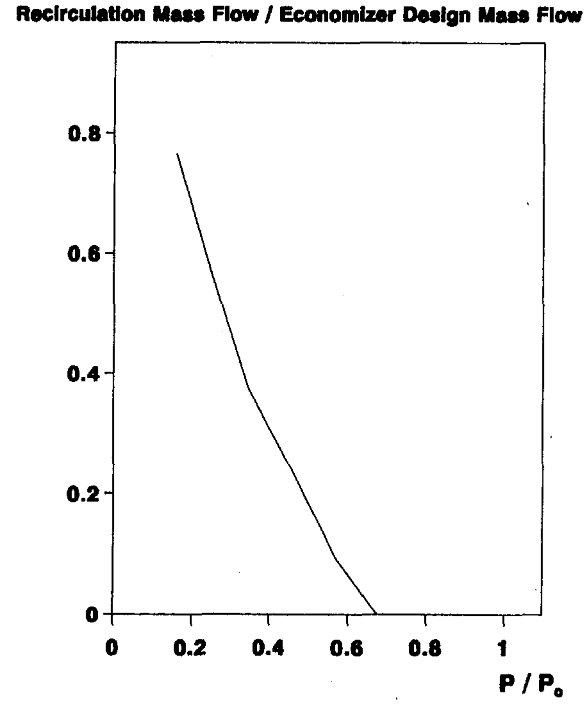

Fig. 6 Unfired single pressure level system economizer recirculation rate

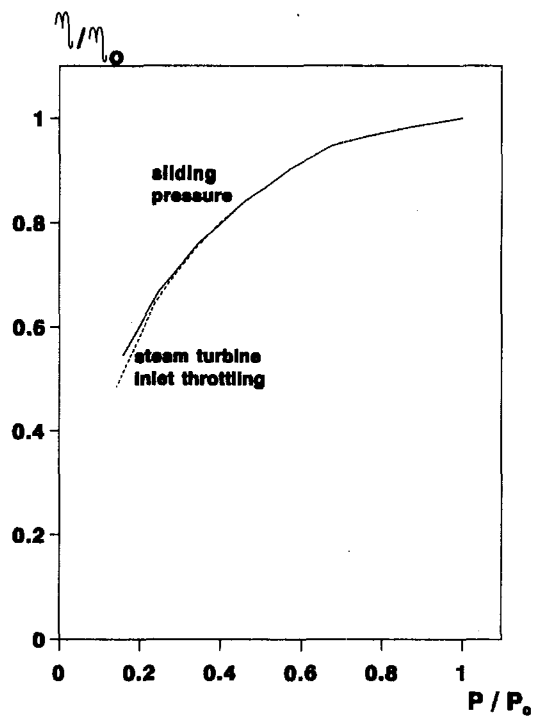

Fig. 8 Unfired single pressure level system sliding versus fixed pressure

Superheated Steam Conditions. Figure 7 gives the superheat steam temperature and pressure at reduced loads. The influence of the VIGV control is clear on the temperature, giving a slightly increasing steam temperature, corresponding to the constant gas turbine exhaust temperature.

The steam pressure is found to decrease continuously when reducing the output, although the drop appears more rapid when the TET becomes the controlling parameter. The corresponding steam mass flow is easily deduced from the temperature and the pressure using the Stodola ellipse relation at the steam turbine inlet.

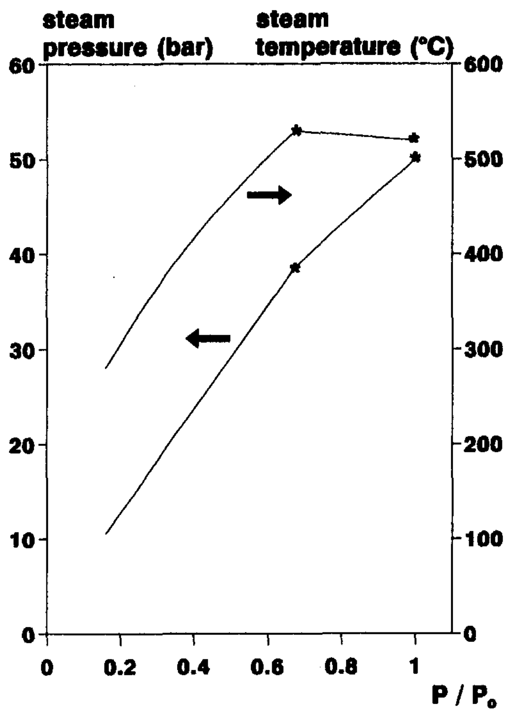

Fig. 7 Unfired single pressure level system steam conditions

Sliding Steam Pressure Versus Throttling. To prevent the steam pressure from dropping continuously when reducing the output, it can be envisaged to throttle the steam turbine inlet. One such action which is commonly used consists in maintaining the steam pressure at 50 percent of its design value when it would naturally fall further. Figure 8 shows that this turns into an efficiency penalty for the combined cycle. Moreover, maintaining the steam pressure at an artificially high value provokes a swift decrease in steam turbine outlet quality. Hence, steam turbine inlet throttling appears to be justified only if it is required by a minimum steam pressure set-point.

Supplementary Fired Single Pressure Combined Cycle

Introduction. A system similar to the previously described one, but comprising supplemental firing, is used to point out the specific characteristics of supplementary fired combined cycles.

Assumptions and Design Point Performance. The assumptions used for this cycle are similar to those mentioned in Table 1, with the addition of the supplemental firing and a higher superheated steam temperature:

- natural gas fuel (LHV = 47.5 kJ/kg)
- supplemental firing temperature of 650°C
- superheated steam temperature: 540°C

The supplemental firing temperature of 650°C was selected considering that it is about the limiting temperature requiring no design modification to the HRSG as compared to unfired plants. Above that limit, inside refractory linings would have to be used.

Table 3 presents the main design point performance figures of this combined cycle plant.

Table 3 Supplementary fired single pressure combined cycle design performance

Gas Turbine

net power output : 144.94 MWe
net efficiency : 32.49 %
heat input : 446.03 MW
fuel : natural gas - LHV = 47.5 MJ/kg
exhaust temperature : 551.4 °C
exhaust mass flow : 506.91 kg/s

Supplemental Firing

fuel mass flow : 1.34 kg/s
heat input : 63.11 MW
fuel : natural gas - LHV = 47.5 MJ/kg
flue gas mass flow : 508.25 kg/s
suppl. firing heat input / gas turbine heat input : 0.141

HRSG

steam production : 91.21 kg/s
stack temperature : 104.69 °C
overall effectiveness : 0.859 %
total heat transfer surface : 87000 m²

Steam Cycle

net output : 103 MWe
outlet quality : 91.99 %
Rankine cycle efficiency : 32.9 %

Overall

net plant power output : 247.94 MWe
net plant efficiency : 48.67 %

Performance Analysis

Part-Load Efficiency. Three variables can be used as control parameters to reduce the plant output:

- the gas turbine TET (or exhaust temperature)
- the gas turbine VIGVs
- the supplemental firing temperature

Therefore, six strategies can be used to reduce the load starting at the design point, with the following order in which these three parameters are used:

1 TET—VIGVs—supplemental firing
2 TET—supplemental firing—VIGVs
3 VIGVs—TET—supplemental firing
4 VIGVs—supplemental firing—TET
5 supplemental firing—TET—VIGVs
6 supplemental firing—VIGVs—TET

According to the results of the unfired combined cycle plant, it can be concluded that all the strategies involving a reduction of the gas turbine TET before the VIGVs are closed are not worth looking at. Strategies 3, 4, and 6 remain to be examined.

Figure 9 presents the part-load efficiencies associated with these three possibilities: Solution (6) [supplemental firing—VIGVs—TET] appears to be the best solution. In the first instance, when the supplemental firing is reduced with the gas turbine running at its design point, the efficiency actually increases as the load decreases. Such behavior was already described (Dechamps and Mathieu, 1991, 1992) in repowered cycles and observed in practice in such arrangements (Linnemeijer and Van Buijtenen, 1988). Because of this unique feature, the design point performance is maintained down to 80 percent of the design point output.

The fact that the supplemental firing has to be reduced first is beneficial for the gas turbine: It is running in all this output range at its design point, without any temperature variations in the hot sections that could decrease the availability of modern gas turbines.

LP Steam Turbine Outlet Quality. Figure 10 illustrates the evaluation of this parameter when the best strategy is used to reduce the output. The outlet quality is only slightly reduced when the supplemental firing is shut off, then increased when closing the VIGVs, and drops continuously when further reducing the gas turbine fuel flow. Because of the rise in the VIGV-controlled region, the value always remains acceptable, even at very low loads.

Unfired Versus Fired Configurations. Figure 11 compares the absolute reduced load efficiencies for the unfired case studied before and for the present supplementary fired case. It should, however, be noted that the design point refers to different absolute values in terms of output.

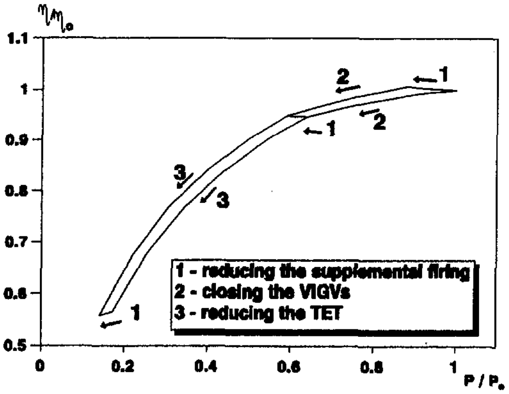

Fig. 9 Fired single pressure level system—part-load efficiencies

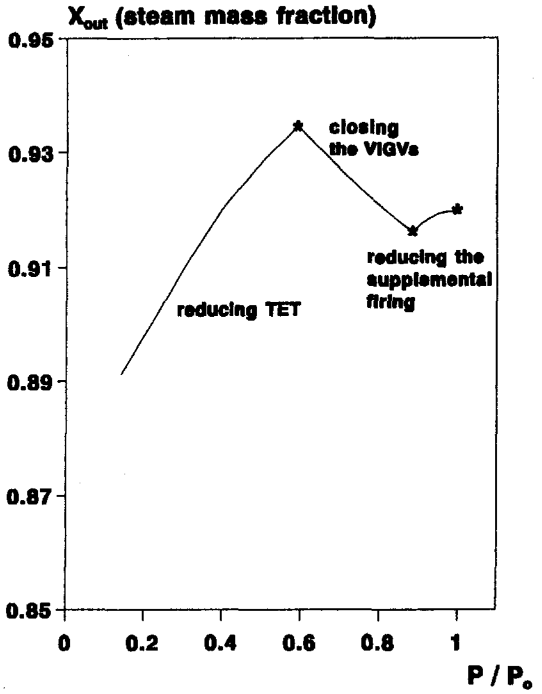

Fig. 10 Fired single pressure level system: steam turbine outlet quality

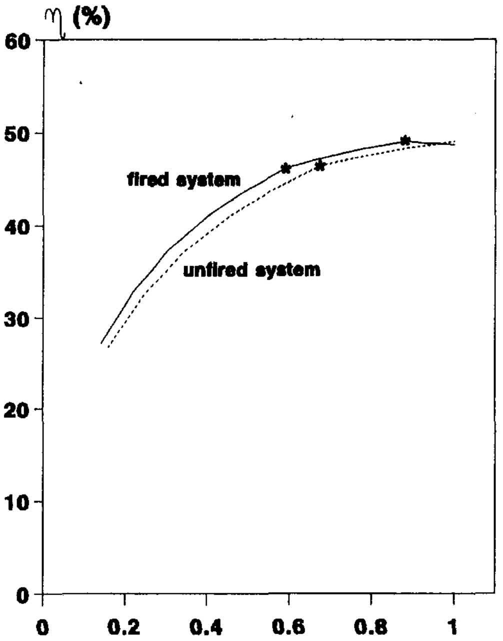

Fig. 11 Single pressure level systems: part-load efficiencies with and without supplemental firing

The supplementary fired plant clearly appears as substantially less penalized when going to reduced loads. It can therefore be said that the use of supplemental firing is a decisive advantage for single pressure combined cycles when the plant has to run often at reduced loads.

Dual-Pressure Combined Cycle in 2-2-1 Configuration

Introduction. A state-of-the-art dual pressure combined cycle in a 2-2-1 configuration (2 gas turbines–2 HRSGs–1 steam turbine) has been studied with the same method. Two cycles have indeed been studied, one without supplemental firing, and one with supplemental firing up to 650°C.

The objective is twofold:

- evaluate the flexibility at part load of the 2-2-1 arrangement.
- assess whether the use of supplemental firing has the same advantages as in the simpler single pressure system previously studied.

Assumptions and Design Point Performances. Table 4 summarizes most of the design assumptions and design point performance of the two considered cycles.

Performance Analysis

Unfired Case. Figure 12 presents the part-load efficiencies of the dual pressure combined cycle without supplemental firing.

Several strategies can be envisaged to decrease the output of such a plant. Based on the previously described systems, only the strategies when the VIGVs are closed before the TET is reduced for a given gas turbine are considered.

Three routes can be identified on Fig. 12:

- The path denoted by ABEFHI involves:
  - AB: close the VIGVs of one gas turbine,
  - BE: reduce the TET of that gas turbine,
  - EF: operate on the other gas turbine only,
  - FH: close the VIGVs of the second gas turbine,
  - HI: reduce the TET of the second gas turbine.

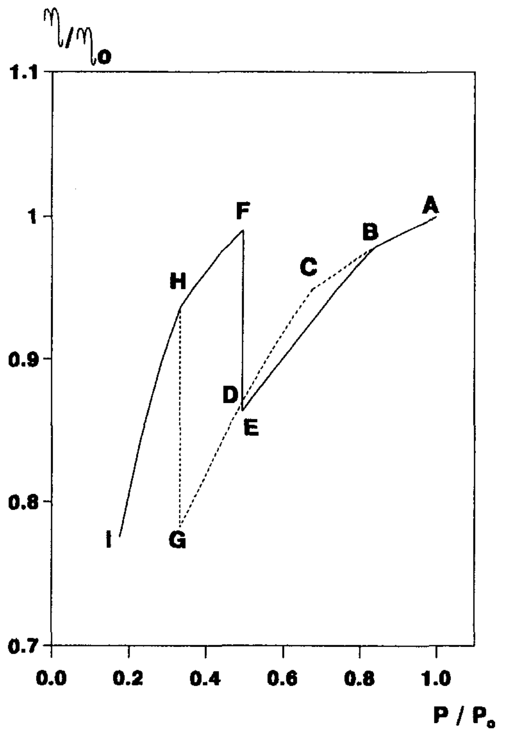

Fig. 12 Unfired dual pressure system: 2-2-1 configuration; part-load efficiencies

- The path denoted by ABCDGHI involves closing the VIGVs of both gas turbines before reducing the TET on the first one. This solution exhibits a better efficiency in the upper load range region, but the operation with two gas turbines running between points E and G is inefficient.
- The path denoted by ABCDFHI is a combination of the previous two strategies: The first gas turbine is stopped at point D, while the system comes back to point F by re-opening the VIGVs of the second gas turbine, which had been closed between B and C.

It should be said that closing the VIGVs on both gas turbines simultaneously, rather than on one before the other, does not give any significant departure from the path ABC, because these three points are nearly on a strait line. Therefore, the best way to reduce the load on this system appears to be the following, starting with the design point:

- close the VIGVs on gas turbine number 1,
- close the VIGVs on gas turbine number 2,
- reduce the TET on gas turbine number 1,
- switch to the operation with one gas turbine only as soon as it is possible, with gas turbine number 2 running at its design point (F on Fig. 12),
- close the VIGVs of gas turbine number 2,
- reduce the TET of gas turbine number 2.

Supplementary Fired Cycle. Figure 13 compares the part-load efficiencies of the two systems for which the assumptions and the design point performances are quoted in Table 4.

At the design point, the supplementary fired case produces 11.6 percent more power with a 1 %pt efficiency penalty compared to the unfired case, and requires a 40 percent increase of the heat transfer surface (see Table 4).

The dotted line represents the unfired system, when the best possible strategy is used to reduce the output, i.e., the path denoted ABCDFHI on Fig. 12. The solid line is the part-load efficiency of the supplementary fired system used in the most efficient way: The supplemental firing is reduced first, then the

Table 4 Dual pressure combined cycle design and performance

Gas Turbine

inlet pressure loss : 10 mbar
HRSG back pressure : 25 mbar
ambient temperature : 15°C
net power output / efficiency : 144.94 MWe / 32.49 %
heat input : 446.03 MW
fuel : natural gas - LHV = 47.5 MJ/kg
exhaust temperature : 551.4 °C
exhaust mass flow : 506.91 kg/s

Supplemental Firing (when applicable - in GT exhaust)

fuel mass flow : 1.34 kg/s per HRSG
heat input : 63.11 MW per HRSG
flue gas mass flow : 508.25 kg/s per HRSG
suppl. firing heat input / gas turbine heat input : 0.141
fuel : natural gas - LHV = 47.5 MJ/kg
supplemental firing temperature : 650°C

	Unfired Cycle	Fired Cycle
HRSG		
pinch point temperature differences (°C)	10	10
approach point temperature differences (°C)	2	2
HP drum pressure (bar)	60	60
LP drum pressure (bar)	6	6
HP superheat temperature (°C)	520	540
LP superheat temperature (°C)	187	160
HP steam mass flow (kg/s)	66.53	91.12
LP steam mass flow (kg/s)	9.67	2.68
deaerator pressure (bar)	3	3
stack temperature (°C)	109.7	98.3
total transfer surface (m^2)	99000	140000
overall effectiveness (%)	82.3	86.9
Steam Cycle		
steam turbine isentropic effectiveness (%)	85	85
condenser pressure (mbar)	50	50
generator efficiency (%)	99	99
auxiliary power consumption (% of gross output)	1	1
net output (MWe)	163.55	216.16
Rankine cycle efficiency (%)	33.0	34.4
outlet steam quality (-)	0.8838	0.8943
Overall		
net output (MWe)	453.43	506.04
net efficiency (%)	50.83	49.83

VIGVs are closed, and the TET is eventually reduced on one gas turbine.

The low output range is not represented for the supplementary fired case, because it is essentially similar to the unfired case.

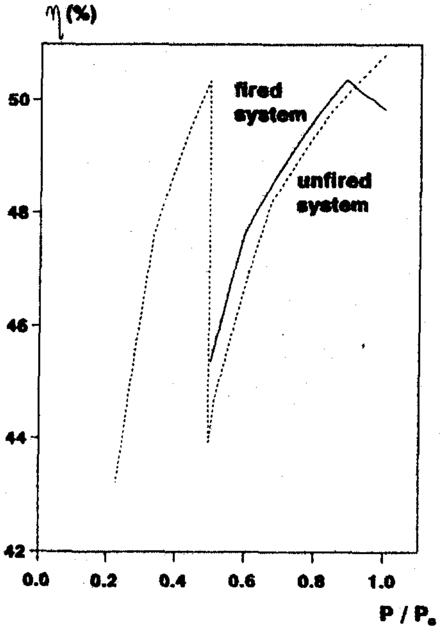

Fig. 13 Dual pressure level systems: 2-2-1 configuration with and without supplemental firing

The conclusion here is similar to that in the single pressure level system: At 60 percent load, the supplementary fired plant has a 2.5 %pt efficiency advantage over the unfired one, and this advantage is maintained further down the output-efficiency curve.

Conclusions

A methodology to appraise the performance of combined cycle plants at reduced loads has been presented and applied to single as well as multiple pressure systems, in supplementary fired or unfired configurations. It has been applied to reheat configurations as well with only minor improvements compared to those presented here.

In all cases, it was clear that the best strategy to reduce the output was to reduce the supplementary firing, if any, then close the gas turbine VIGVs and eventually reduce the gas turbine TET.

Whatever the combined cycle arrangement may be, the use of supplemental firing provides more operational flexibility and increases the plant efficiency at part load over most of the load range.

For single pressure level systems, it was demonstrated that the use of supplemental firing, although it decreases the design point efficiency by 0.33 %pt allows more flexibility at reduced loads. Moreover, the efficiency of the supplementary fired system exceeds that of the unfired one by 1 %pt over most of the load range.

A similar conclusion can be drawn for the dual pressure system, for which the additional flexibility of the supplementary firing produces the same effects, with a 2.5 %pt efficiency advantage below 60 percent load.

Acknowledgments

Mr. L. Harmel, R&D Manager of Cockerill Mechanical Industries (CMI Energy), is gratefully acknowledged for the informal discussions held during the course of this work.

References

Dechamps, P. J., and Mathieu, Ph., 1991, "Repowering Options for the Electricity Generation Mix in Belgium," ASME IGTI-Vol. 6, p. 43.

Dechamps, P. J., and Mathieu, Ph., 1992, "Modelling of a Steam Power Plant Repowering Option: Replacement of the Conventional Boiler With a New HRSG," ASME IGTI-Vol. 7, p. 331.

Dechamps, P. J., Mathieu, Ph., and Magain, D., 1993, "Advanced Combined Cycle Alternative With Advanced Gas Turbines," ASME IGTI-Vol. 8, p. 387.

Desideri, U., and Fibbi, A., 1993, "A Simplified Approach of Off-Design Performance Evaluation of Combined Cycle Power Plants With Single Pressure Steam Cycles," ASME IGTI-Vol. 8, p. 199.

Facchini, B., 1993, "A Simplified Approach to the Off-Design Performance Evaluation of Single Shaft Heavy Duty Gas Turbines," ASME IGTI-Vol. 8, p. 189.

Gyarmathy, G., 1989, "On Load Control Methods for Combined Cycle Plants," ASME IGTI-Vol. 4, p. 39.

Gyarmathy, G., and Ortmann, P., 1991, "The Off-Design of Single and Dual Pressure Steam Cycle in CC Plants," ASME IGTI-Vol. 6, p. 217.

Harmel, L., 1989, "The Combined Cycle—an Economical System for Production of Electricity," ASME IGTI-Vol. 4, p. 357.

Kehlhofer, R., 1979, "Calcul du comportement à charge partielle des centrales combinées à turbines à gaz et à vapeur," publication BBC CH-T 040 103 F.

Linnemeijer, M. J. J., and Van Buijtenen, J. P., 1988, "Design Possibilities and Performance of Combined Cycle Operation of Converted Steam Power Plants," ASME Paper No. 88-GT-178.

Laser Vibrometry Measurements of Rotating Blade Vibrations

A. K. Reinhardt

J. R. Kadambi

R. D. Quinn

Department of Mechanical and Aerospace Engineering,
Case Western Reserve University,
Cleveland, OH 44106

One of the most important design factors in modern turbomachinery is the vibration of turbomachinery blading. There is a need for developing an in-service, noncontacting, noninterfering method for the measurement and monitoring of gas turbine, jet engine, and steam turbine blade vibrations and stresses. Such a technique would also be useful for monitoring rotating helicopter blades. In the power generation industry, blade failures can result in millions of dollars of downtime. The measurement of blade vibrations and dynamic stresses is an important guide for preventive maintenance, which can be a major contributor to the availability of steam turbine, gas turbine, and helicopter operations. An experiment is designed to verify the feasibility of such a vibration monitoring system using the reference beam on-axis laser-Doppler technique. The experimental setup consists of two flat, cantilever blades mounted on a hub attached to the shaft of a dc motor. The motor rests on a linear bearing permitting motion only in the direction of the motor shaft. The motor and blade assembly is then excited via an electrodynamic shaker at the first natural frequency of the blades. The resulting blade vibration is then detected using a laser vibrometer. The vibration frequencies and amplitudes of the two rotating blades are successfully measured.

Introduction

In the power generation and aeropropulsion industries, the continuing trend in the past 30 or so years has been to generate more power or thrust per pound of equipment. This has led to the building of larger gas turbines, jet engines, and steam turbines that operate with closer tolerances at high speeds. This is also true for blades of helicopters, which perform under heavy load and sometimes in nonideal situations.

Three-fourths of all steam turbine blade failures occur in the low-pressure section with about 75 percent of these failures occurring in the L-0 and L-1 rows. These failures seem to be the chief factor in defining the useful life of fossil fuel power plants. Turbine blade failures, many of which are caused by vibration-related fatigue stresses, alone are the leading cause of steam turbine downtime costing U.S. utilities more than $235 million annually (McCloskey, 1990).

However, the availability and service life of such equipment is of significant economic importance. A consequence of such criteria is more stringent requirements for the operational safety and availability of such machinery.

Blade vibration can be described as either forced or self-excited. Forced vibration results from disturbances either upstream or downstream from the blades and can be synchronous with engine speed multiples. Flutter is an example of self-excited vibration and is caused by an interaction between the vibration response of the blade and the aerodynamic forces resulting from these blade motions. Self-excited vibrations are generally nonsynchronous with engine speed, since they are related to blade and rotor natural frequencies. Typical design practices for steam turbines call for rotor and blade natural frequencies to be at least eight times the turbine running speed (Scalzo et al., 1986).

Blade vibration monitoring can play an important role in preventing blade failure from fatigue. On-line monitoring of blade vibrations can also be used in assessing whether the turbine should be shut down for scheduled maintenance or if inspections can be postponed. Alternatively, vibration monitoring can also be used in the validation of analytical models of blade performance during the design of turbine blading. It is desirable that a blade vibration monitoring system provide information for all blades in a particular group. In helicopter applications, it can warn the pilot of dangerous rotor blade operating conditions, which then could be avoided.

This paper demonstrates the feasibility of using the reference beam laser-Doppler technique for detecting rotating blade vibration. The laser-Doppler method appears very promising. A survey of available techniques to measure blade vibration reported by Kadambi et al. (1989) shows that this technique is very promising for synchronous vibration detection. The laser-Doppler technique would allow for all the blades of a particular group to be monitored. An experimental setup is developed, which serves as the basis for the evaluation of the laser-Doppler technique. The processing of the Doppler burst is an important step in the data collection stage. The Doppler signal processor must be able to detect the intermittent signals resulting from blades rotating through the laser beam. Data analysis of the intermittent signal is the final stage of the test system. The characteristics of the blade vibration must be estimated from the data. In dealing with short time records, classical signal processing has some shortcomings; therefore other methods of signal processing need to be explored.

Experimental Setup

The main components of the experimental setup are reference beam laser-Doppler vibrometer, signal processor, electrodynamic shaker and function generator, hub and blade assembly, DC motor, and data acquisition system. The setup is shown in Fig. 1. The motor and blade assembly and shaker are mounted on a heavy steel C-channel section.

There are two basic ways of implementing the laser-Doppler method for velocity measurement: the dual beam and reference beam techniques. The dual beam method measures velocity transverse to the direction of the laser light, whereas the reference beam method measures velocity in the direction of the laser light. Only the reference beam technique is used in the present study.

The reference beam laser-Doppler technique was used to measure the vibration of rotating blades by Kulczyk and Davis

---

Contributed by the International Gas Turbine Institute and presented at ASME Cogen Turbo Power '94, Portland, Oregon, October 25–27, 1994. Manuscript received by the International Gas Turbine Institute July 20, 1994. Associate Technical Editor: E. M. Greitzer.

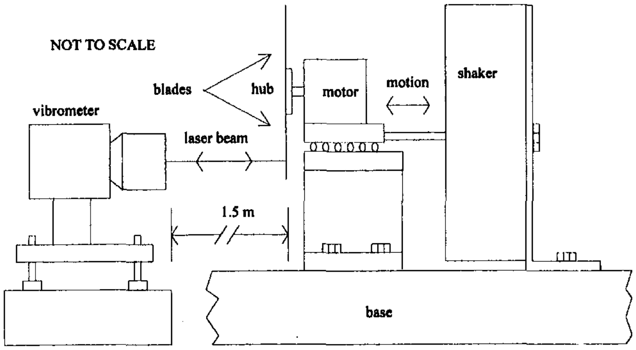

Fig. 1 Experimental setup

(1973). Later, Cookson and Bandyopadhyay (1980) incorporated fiber optics and Bragg cells into the laser-Doppler probe and measured the blade vibrations. Availability of equipment (during the 1970 to 1980 period) to detect, collect, and process the Doppler shifted signal was the limiting factor in both of these attempts to measure vibration of rotating blades.

The reference beam mode laser-Doppler vibrometer used in our tests is a Dantec Modular 55X Vibrometer. The vibrometer uses a 10 mW He-Ne laser. The reference beam mode of operation is shown in Fig. 2. Light from one laser is split into a scattering beam and a reference beam. The reference beam is directed to the detector. The scattering beam is first frequency shifted by a Bragg cell. This frequency shift allows alternating velocities with zero mean (typical of vibrating surfaces) to be detected. The scattering beam is then transmitted in the direction of unit vector $\mathbf{l}_1$ to a moving surface with velocity $\mathbf{U}$. The scattering beam is then reradiated from the moving surface to the detector located in the direction of unit vector $\mathbf{k}$ away from the surface. The Doppler-shifted scattering beam is heterodyned with the unshifted reference beam. The frequency difference between the two beams is the Doppler frequency and is proportional to the velocity. The ratio of the Doppler frequency to the laser's frequency is given by

$$\frac{\nu' - \nu}{\nu} = \frac{c - \mathbf{U}\cdot\mathbf{k}}{c - \mathbf{U}\cdot\mathbf{l}_1} - 1 \qquad (1)$$

where $\nu' - \nu$ is the Doppler frequency and ν is the frequency of the laser light. Assuming that the velocity of light c is much greater than $\mathbf{U}$, the velocity of the surface, and that the directions of $\mathbf{k}$ and $\mathbf{l}_1$ are rotated 180 deg relative to each other, then this equation can be approximated by

$$\frac{\nu' - \nu}{\nu} = \frac{2U_y}{c} \qquad (2)$$

where U_y is the on-axis (relative to the laser path) velocity of the surface (DANTEC, 1999; Reinhardt, 1994).

The heterodyned signals are then processed by a Doppler signal processor to obtain the blade vibration velocity. Normally two types of signal processor, frequency tracker and counter-type, are used for signal analysis. In our experiment, both frequency tracker and counter are used. A frequency tracker is suitable for measurements of continuous signals, and a DANTEC Model 55N20 Tracker is used for nonrotating blade vibration tests. The counter-type processor is suitable for determining vibration information from rotating blades, since it is capable of handling intermittent signals. A TSI Model 1990C Counter is used for the rotating blade vibration tests.

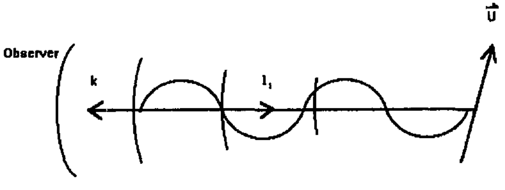

Fig. 2 Reference beam method

Table 1 Blade dimensions

	Blade A	Blade B
length (l)	7.526	7.493
width (w)	1.270	1.270
thickness (t)	0.102	0.102

(all dimensions in cm)

A 10 lbf shaker is used with its excitation axis horizontal. A rigid coupling connects the shaker's armature to the motor assembly. The shaker is driven by the amplified output of a function generator. Only sine waves of constant amplitude and frequency are used in the tests. A brushless DC motor is used to rotate the blades. The maximum speed of the motor is 7000 rpm. The speed is controlled by varying the input to the motor from the DC power supply. Motor speed is monitored via an optical tachometer, which has a resolution of 1 rpm.

The motor is mounted on a wheeled cart guided by a track. The cart and track arrangement allows the motor to slide back and forth and the assembly can be vibrated using the shaker. The bearings of the motor do not allow the shaft to slide axially. Thus, the vibration input is transferred directly to the hub and blade assembly.

The blades are two flat steel cantilever beams mounted on a small aluminum hub, rotated 180 deg relative to each other. The dimensions of the two blades are given in Table 1. The hub is fastened to the shaft with set screws. A strain gage is mounted to each blade. The center of each gage is located 0.952 cm from the clamped edge.

The blades are bolted to the hub to give a clamped boundary condition at one end. The thin edge of the blade is tangential to the direction of rotation. This minimizes the air resistance during rotation and also allows the blades to be excited via base motion to vibrate in the first bending mode.

The blades are flat and are assumed to behave as beams. The effects of rotary inertia and shear deformation are neglected, since the cross-sectional dimensions are small compared to the length. The calculated natural frequencies are given in Table 2. The calculated mode shapes are shown in Fig. 3.

A 486-66 MHz PC-based data acquisition system is used for collecting data. The test data are collected using a 16 bit data acquisition board. The sample interval is set at 192×10^{-6} s and a total of 4096 samples are collected for the nonrotating forced vibration tests of the blades. The sample interval for the free vibration tests of the blades is set to 1.536×10^{-3} s and 2048 samples are collected. The rotating blade vibration test data is collected with a sample interval of 192×10^{-6} s. Data for only one revolution are collected due to the limitation of memory on the data acquisition board to 4096 samples. The data collection is synchronized with the rotation by using a digital trigger to start the data acquisition. The digital trigger

Table 2 Calculated blade natural frequencies

	Blade A	Blade B
mode 1	146 Hz	147 Hz
mode 2	916 Hz	924 Hz
mode 3	2560 Hz	2590 Hz

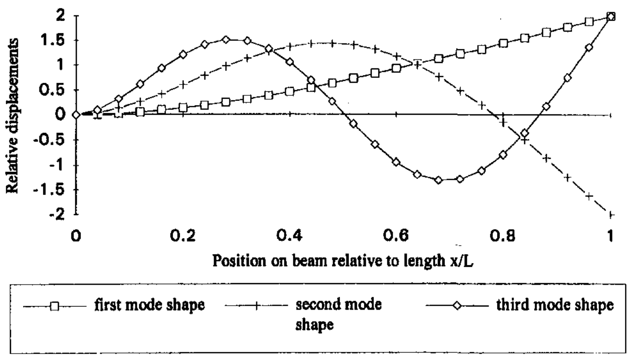

Fig. 3 Plot of theoretical blade mode shapes

is TTL compatible and is generated from an infrared reflective assembly. The assembly only produces a pulse when blade B is present (resulting in a once per revolution signal). The data collection begins after blade B has passed by the reflective assembly.

Data Processing

The short vibration records are analyzed individually. Both amplitude and frequency information are required. If the records for a given blade are appended to achieve a longer time record, then discontinuities are introduced due to phase differences between the individual records. These phase differences can be accounted for in the present analysis, but then the generality is lost. Conventional spectrum analysis using an FFT approach is limited in frequency resolution as a result of the short capture lengths. The frequency resolution for an FFT is $1/T = (1/N\Delta t)$ Hz, where T is the capture length, N is the record length, and Δt is the sample interval. Also, the calculated frequency spectrum is equal to the correct spectrum, only if an integer multiple of periods of the vibration signal is measured. Otherwise, energy of the original spectrum lines (or frequency bins) "leaks" into the other lines. Instead, a time domain least-squares curve-fitting approach is used, because of these limitations. The vibration data is $x_k = x(t_k)$, where $k = 0, 1, 2, \ldots, N - 1$. The fitting procedure is based on fitting the analytical function, $y(t_k)$, given by Eq. (3), to the data (Bevington and Robinson, 1992)

$$y_k = y(t_k) = A_1 + A_2 \sin (A_3 t_k + A_4) \qquad (3)$$

where A_1, A_2, A_3, and A_4 are the DC offset, amplitude of vibration, frequency of vibration (in radians), and phase angle (in radians), respectively. The limiting factor in any data analysis method is the short data records that are a result of the blades rotating through the vibration measuring point. The capture time for collecting vibration data from rotating blades is limited to the transit time of the blade through the laser beam. This time is approximately the width of the blade divided by the blade's velocity at the point of the measurement. As the blade's rotational speed is increased, this implies that the minimum detectable frequency increases for curve-fitting and spectral analysis methods, since both require at least two vibrational periods to be captured.

Experimental Results and Discussion

For all the tests, data are collected from a point on the blade located 5.923 cm from the clamped edge of the blade. This point is chosen because it is the location of the node of the second mode as calculated from the analytical model of the blade. By choosing this point, any mode 2 participation is negated. Also, by exciting the blades at their first natural frequencies, the effects of higher modes are minimized, due to modal orthogonality.

Table 3 Measured first natural frequency of blades

	Blade A	Blade B
strain gage	144.3 Hz	144.0 Hz
laser vibrometer	144.3 Hz	144.0 Hz

Nonrotating Blade Vibration Tests. Nonrotating tests are performed to (1) evaluate the blades' first natural frequency, (2) compare the strain gage measurement with the laser vibrometer measurement, and (3) provide a measurement of the vibration level before rotation. These tests are done with the rotor and blade assembly attached to the motor.

The first natural frequencies of the blades are determined from free vibration. Each blade is excited by "plucking" it and allowing the blade to vibrate freely in the first bending mode. Data are collected from the strain gage and the laser vibrometer. The data are then processed using an FFT algorithm. The results are given in Table 3. The gage and vibrometer both give the same frequency for a given blade. The calculated first natural frequencies of the blades agree well (<2 percent difference) with the measured values (see Tables 2 and 3).

The next nonrotating test is a verification of the vibrometer's ability to predict strain. The two cases are: (1) forced excitation at blade A's first natural frequency and (2) forced excitation at blade B's first natural frequency.

The vibrometer output is converted to strain by first integrating the velocity signal to get displacement. First, the modal participation factor is calculated from

$$u(x, t) = \phi_1 q_1(x, t) \qquad (4)$$

where u, ϕ_1, and q_1 are the displacement (from integration of velocity measurement), first mode shape and modal participation factor, respectively. The strain can now be found from

$$\epsilon = h \frac{\partial^2 u}{\partial x^2} = h \frac{\partial^2 \phi_1}{\partial x^2} q_1 \qquad (5)$$

where ϵ and h are the strain and distance from the neutral axis of the blade, respectively. This technique for determining strain from a laser vibrometer measurement is discussed later in more detail. Figure 4 shows the results of this test. The maximum absolute relative error between the laser vibrometer strain prediction and the strain gage measurement is 7 microstrain. The laser vibrometer prediction is generally higher than the gage measurement. The difference may be from the fact that the gage is not a point measurement, but represents an average over the gage's length. Also, some error may result from approximating the first mode shape of the blade with the analytical solution for the first mode shape of a cantilever beam.

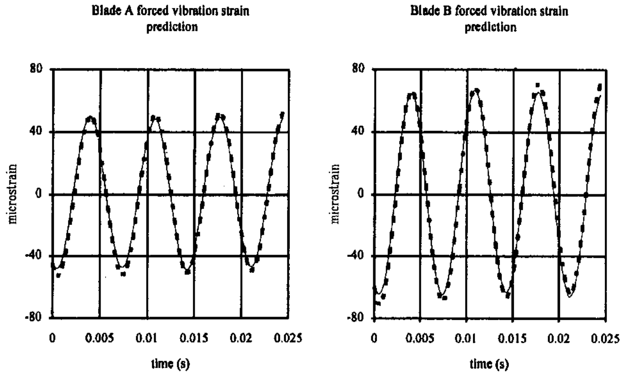

Fig. 4 Comparison of strain measured from gage to strain estimated from laser vibrometer measurement

Table 4 Results of curve-fitting stationary forced vibration tests

	Blade A		Blade B	
	mean value	2*σ	mean value	2*σ
dc level (volts)	4.90	0.04	4.94	0.02
amplitude (mm/s)	45.1	0.8	65.6	0.6
frequency (Hz)	144.0	0.6	144.0	0.1

The last nonrotating test is the measurement of the forced vibration response of the blades when excited at blade B's first natural frequency, 144.0 Hz. This provides a baseline for comparing the results from the rotating forced vibration blade tests. Data from five runs are curve-fitted using the model defined by Eq. (3). These results are averaged together and the 95 percent confidence intervals ($2*\sigma$) are calculated (see Table 4). The DC values listed in Table 4 represent the Bragg cell shift of the scattering beams frequency. The DC values do not affect the measurement of the blade vibrations. Phase is not important for the present analysis, since only a single excitation frequency is used.

Rotating Blade Vibration Tests. The rotating tests are divided into two cases: (1) rotating and not excited by shaker and (2) rotating and excited by shaker. The blades rotate through the laser beam, which results in an intermittent (blade vibration) signal. Data collection is started when blade B has passed the infrared reflective assembly. The sequence of data consists of: (1) a constant value, followed by (2) the blade A vibration signal, then (3) another constant signal gap, followed by (4) the blade B signal. A sample raw data plot is shown in Fig. 5. Data are also collected from the digital trigger. This provides a once per revolution pulse used to determine the average rotational speed of a particular test.

The speed of rotation is selected to give at least two vibration cycles per blade per revolution. The rotational speed of the tests is between 80 and 100 rpm.

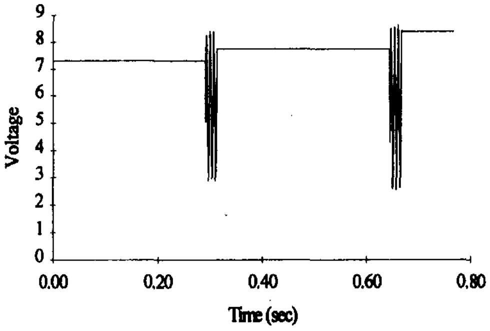

Enlargement of blade signals

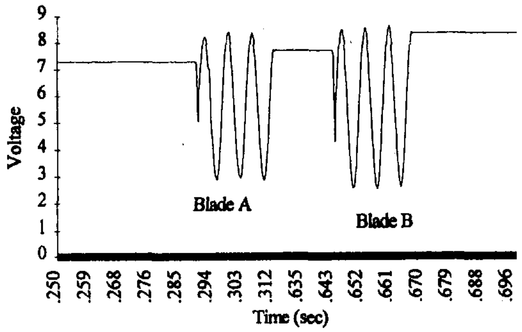

Fig. 5 Sample raw data rotating tests

Table 5 Results from rotating test of blade (not excited by shaker)

	Blade A		Blade B	
run # (RPM)	rms (mm/s)	mean value (volts)	rms (mm/s)	mean value (volts)
1 (90)	0.89	6.35	0.91	6.26
2 (90)	0.77	6.15	1.35	6.14
3 (91)	1.10	6.28	1.07	6.21
4 (90)	1.06	6.18	1.46	6.34
5 (91)	1.05	6.30	1.18	6.26
6 (91)	0.86	6.24	1.01	6.22
7 (88)	0.87	6.24	1.02	6.17

Data are collected while the blade is rotating, but not excited by the shaker in order to determine if there is any vibration attributable to rotation (i.e., unbalance or interaction with the air).

The rms average of the blade signals from the first rotating test case (not excited by shaker) is calculated. The rms average is taken due to the random fluctuation in the data values. The results from seven runs are given in Table 5.

From Table 5, it can be seen that the rotation of the blades does not excite the blades. The low-level blade signals that are observed while the blades are rotating (but not excited by the shaker) can be obtained from the rotational motion of the blade. A speckle pattern is produced when the laser beam is "dephased" on scattering from a surface whose roughness is on the order of the laser's wavelength (most materials fall in this category). The reflected component wavelets of the laser beam then interfere constructively and destructively and produce a chaotic distribution of light intensities known as the "speckle pattern" (Dainty, 1975). The blades' rotation through the laser causes spatial changes of the speckle pattern on the photodetector. This causes the detector output to vary in amplitude and phase. Therefore, the blades' rotation creates a signal, even if the blade's motion (and surface) is perpendicular to the incident laser beam. The signals that were observed are negligible when compared to the amplitude of the blade's motion in the second rotating case where the blades are excited via the shaker.

The average speed for the second rotating case (shaker turned on) is 85 rpm. The data from five runs are curve-fitted using Eq. (3) as the model. These results are averaged together and 95 percent confidence intervals ($2*\sigma$) are calculated (see Table 6). The residuals (difference between the fitted function and the experimental data) do not exhibit any periodicity and are distributed about zero. This implies that no other vibration frequencies are present in the data.

The difference in vibration amplitude between the rotating and stationary cases (both excited by shaker) may be due to stress stiffening of the blade while rotating (see Tables 4 and 6). This causes the blade natural frequencies to shift. Also, for lightly damped systems, such as the blades, the resonances are very sharp. This implies that there is a sharp roll-off in response as the excitation frequency moves away from the natural frequency. The frequency agreement between the two cases is within the uncertainty of the least-squares estimates.

Table 6 Result from curve-fitting rotating blade tests (excited by shaker)

	Blade A		Blade B	
	mean value	2*σ	mean value	2*σ
dc level (volts)	5.62	0.07	4.94	0.05
amplitude (mm/s)	52.	1.	58	1.
frequency (Hz)	144.7	0.6	143.9	0.5

Modal Filtering

These series of tests show that the vibration amplitude and frequency of a rotating blade can be determined using laser vibrometers. However, the transit time of the blade through the laser's measuring point must be greater than the time for two vibration cycles. As the rotational speed is increased, the minimum detectable frequency also increases, since curve-fitting and spectral filtering (using an FFT) the data each require a minimum of two vibration periods. This limitation can be overcome by a new signal processing technique. A modal filter can be used to determine the blade vibration information. The modal filter does not have any speed or frequency limitations. Data collected simultaneously from several points along the blade's height are used to determine the number of actively participating modes of vibration.

A modal filter will now be developed. Only the lateral vibration of a flat blade will be considered. Let the displacement at a point x on the blade at a time t be expressed as $u(x, t)$. Using laser vibrometers, several points along the blade's height can be measured simultaneously. The expansion theorem allows the velocity to be expressed as a linear combination of the mode shapes of the blade (Meirovitch, 1980)

$$\dot{u}(x, t) = \sum_{r=1}^{n} \phi_r(x)\dot{q}_r(t) \tag{6}$$

where $\phi_r(x)$ is the eigenfunction of the rth mode and $\dot{q}_r(t)$ is the time derivative of the rth modal coordinate. In theory, the number of degrees of freedom for a continuous system is infinite, but the response can be approximated by a finite number of modes.

The mode shapes may be determined from either finite element models or analytic solutions. The velocities of the blade are measured at discrete locations along the height. Essentially modal filters involve an inversion of Eq. (6) so that the $\dot{q}_r(t)$ can be determined. With measurements taken at m points along the blade, Eq. (6) can be expressed in discrete form as

$$\dot{u}(x_i, t) = \sum_{r=1}^{n} \phi_r(x_i)\dot{q}_r(t) \quad i = 1, 2, \ldots, m \tag{7}$$

$$\dot{u}(t) = B\dot{q}(t) \tag{8}$$

$$\dot{u}^T(t) = [\dot{u}(x_1, t)\dot{u}(x_2, t) \ldots \dot{u}(x_m, t)] \tag{9}$$

$$\dot{q}^T(t) = [\dot{q}_1(t)\dot{q}_2(t) \ldots \dot{q}_n(t)] \tag{10}$$

$$B = \begin{bmatrix} \phi_1(x_1) & \phi_2(x_1) & \cdots & \phi_n(x_1) \\ \phi_1(x_2) & \phi_2(x_2) & \cdots & \phi_n(x_2) \\ \vdots & \vdots & \ddots & \vdots \\ \phi_1(x_m) & \phi_2(x_m) & \cdots & \phi_n(x_m) \end{bmatrix} \tag{11}$$

The modal speeds can be found by inverting Eq. (8)

$$\dot{q}(t) = B^{-1}\dot{u}(t) \tag{12}$$

The number of measurements, m, must be greater than or equal to the number of modes, n, of interest. If $m > n$ then B^{-1} is not the true inverse of B, but a least-square approximation known as the pseudo-inverse, and the solution to Eq. (12) is given by

$$\dot{q}(t) = (B^TB)^{-1}B^T\dot{u}(t) \tag{13}$$

The dynamic stress information must be determined to be effective in monitoring the blade's condition (i.e., if high stress occurs then warn operator of turbomachinery problem). Dynamic stress is the stress rate. Similarly, dynamic strain is the rate of strain. Only dynamic strain can be determined, since the laser vibrometers measure velocity. Considering only lateral vibration of a flat blade, the dynamic strain due to bending can be evaluated by differentiating Eq. (7) with respect to position, x, and multiplying both sides by the distance, h, from the blade's neutral axis

$$\dot{\epsilon}_{\text{dynamic}} = h \sum_{r=1}^{n} \frac{\partial^2\phi_r(x)}{\partial x^2}\dot{q}_r(t) \tag{14}$$

For spectral filtering methods only one measurement is needed to determine the modal speeds, $\dot{q}_r(t)$. For modal filtering, multiple measurements are required to determine the modal speeds (using either Eq. (12) or (13)). The dynamic stress can then be determined from the strain rate through the proper constitutive equations. For this case, assuming linear elastic isotropic material, Hooke's law for uniaxial stress is valid. Applying this to Eq. (14) results in

$$\dot{\sigma}_{\text{dynamic}} = E\dot{\epsilon}_{\text{dynamic}} \tag{15}$$

where E is modulus of elasticity of the blade material.

Summary

A test setup is developed to test the possibility of measuring rotating blade vibrations using reference beam mode laser-Doppler vibrometry. The laser-Doppler vibrometry technique was successfully used in measuring rotating blade vibrational frequencies and amplitudes. The blade vibration frequency and amplitude were estimated from a least-squares curve-fitting procedure. The curve-fitting technique limits use of the method to blade rotational speeds for which at least two complete vibration cycles are observed by the laser beam on the blade. This poses a severe limitation. Modal filtering is suggested as a new signal processing technique to overcome this limitation. The use of the modal filtering technique will allow the measurement of blade vibrations with no limitation on blade rotational speed.

References

Bevington, P. R., and Robinson, D. K., 1992, *Data Reduction and Error Analysis for the Physical Sciences,* 2nd ed., McGraw-Hill, Inc., New York.

Cookson, R. A., and Bandyopadhyay, P., 1980, "A Fibre-Optic Laser Doppler Probe for Vibration Analysis of Rotating Machines," ASME JOURNAL OF ENGINEERING FOR POWER, Vol. 102, No. 3.

Dainty, J. C., 1979, *Laser Speckle and Related Phenomena,* Springer-Verlag, Berlin.

DANTEC, 1999, 55X Laser Vibrometer Instruction and Service Manual, DANTEC Elektronik.

Kadambi, J. R., Quinn, R. D., and Adams, M. L., 1989, "Turbomachinery Blade Vibration and Dynamic Stress Measurements Utilizing Nonintrusive Techniques," ASME *Journal of Turbomachinery,* Vol. 111, pp. XX–00.

Kulczyk, W. K., and Davis, Q. V., 1973, "Laser Doppler Instrument for Measurement of Vibration of Moving Turbine Blades," *Proc. Inst. Elec. Eng.,* Vol. 120, No. 9.

Meirovitch, L., 1980, *Computational Methods in Structural Dynamics,* Sijthoff-Noordhoff Company, The Netherlands.

McCloskey, T., 1990, "Troubleshooting Rotating Machinery Vibration Problems," *Power Engineering,* Vol. 94, No. 7.

Reinhardt, A. K., 1994, "Rotating Blade Vibration Measurements Using Laser Vibrometry," M.S. Thesis, Case Western Reserve University, Cleveland, OH.

Scalzo, A. J., Allen, J. M., and Antos, R. J., 1986, "Analysis and Solution of a Nonsynchronous Vibration Problem in the Last Row Turbine Blade of a Large Industrial Combustion Turbine," ASME JOURNAL OF ENGINEERING FOR GAS TURBINES AND POWER, Vol. 108.

An Assessment of the Thermodynamic Performance of Mixed Gas–Steam Cycles: Part A—Intercooled and Steam-Injected Cycles

E. Macchi

S. Consonni

G. Lozza

P. Chiesa

Dipartimento di Energetica,
Politecnico di Milano,
Milan, Italy

This paper discusses the thermodynamics of power cycles where steam or water are mixed with air (or combustion gases) to improve the performance of stationary gas turbine cycles fired on clean fuels. In particular, we consider cycles based on modified versions of modern, high-performance, high-efficiency aeroderivative engines. The paper is divided into two parts. After a brief description of the calculation method, in Part A we review the implications of intercooling and analyze cycles with steam injection (STIG and ISTIG). In Part B we examine cycles with water injection (RWI and HAT). Due to lower coolant temperatures, intercooling enables us to reduce turbine cooling flows and/or to increase the turbine inlet temperature. Results show that this can provide significant power and efficiency improvements for both simple cycle and combined cycle systems based on aero-engines; systems based on heavy-duty machines also experience power output augmentation, but almost no efficiency improvement. Mainly due to the irreversibilities of steam/air mixing, intercooled steam injected cycles cannot achieve efficiencies beyond the 52–53 percent range even at turbine inlet temperatures of 1500°C. On the other hand, by accomplishing more reversible water–air mixing, the cycles analyzed in Part B can reach efficiencies comparable (RWI cycles) or even superior (HAT cycles) to those of conventional ''unmixed'' combined cycles.

1 Introduction

The steadily increasing performance of new ''superfan'' jet engines, in terms of both power and efficiency, is spurring increasing interest toward the use of aeroderived engines for large-scale, baseload electricity generation from natural gas (Cohn et al., 1993a; Stambler, 1993). With this regard, a first point to be emphasized is that, given the relevance of efficiency for baseload duty, no simple cycle aero-engine alone, no matter how advanced, will ever compete successfully with combined gas/steam cycles based upon modern heavy-duty turbines. Evidence for this argument comes directly from the intrinsically poor thermodynamic ''quality'' of Brayton cycles: Results presented in a previous paper (Chiesa et al., 1993) show that even with pressure ratios above 60, turbine inlet temperatures above 1500°C, and substantial advances in blade cooling techniques, materials, and turbomachinery, aerodynamics would be inadequate to reach simple cycle net electrical efficiencies of 50 percent, a value well below the potential of existing, commercial combined cycles.

The most straightforward method to increase the efficiency of an aero-engine for stationary applications is the addition of a bottoming steam cycle: Indeed, a remarkable number of aero-engine-based combined cycles with net electric efficiencies close to 50 percent and power outputs below 50 MW_{el} are successfully operating throughout the world. At such low-medium power outputs aero-engine-based systems can outperform the ones based on heavy-duties by several efficiency percentage points; however, at larger power outputs (say over 100 MW_{el}), combined cycles based upon modern, high-temperature heavy-duties exhibit both superior efficiencies and remarkably lower specific costs.

There are several distinctive features of aero-engines that suggest investigating cycles different from conventional combined cycles: The multishaft arrangement makes it simpler to insert intercoolers amid the compression phase (or reheat in the expansion phase); the pressure ratio, already higher than optimum for combined cycles, can be further increased for optimum operation with unconventional cycles; the relatively low exhaust gas temperature and flow rate give poor bottoming steam cycle efficiencies. It is therefore not surprising that most of the innovative configurations alternative to the combined cycle have been proposed for aero-engines.

Several ''complications'' of the basic Brayton cycle have been proposed in recent years: injection of water and/or steam at various points along the gas cycle; insertion of heat exchangers (recuperators, compressor precoolers, intercoolers, aftercoolers), of reheat combustors, or of more complex components such as chemical recuperators and air/water saturators.[1]

Contributed by the International Gas Turbine Institute and presented at the 39th International Gas Turbine and Aeroengine Congress and Exposition, The Hague, The Netherlands, June 13–16, 1994. Manuscript received by the International Gas Turbine Institute March 18, 1994. Paper No. 94-GT-423. Associate Technical Editor: E. M. Greitzer.

---

[1] All three major world aero-engine manufacturers are presently engaged in a research program called Collaborative Advanced Gas Turbine (CAGT) aimed at developing alternative cycle concepts for stationary high-efficiency power generation (Cohn et al., 1993a). Phase I of the program, originally organized by Pacific Gas & Electric Co. and now joined by a number of US, Canada, and European utilities, includes research on the potential of intercooled combined cycles based on the General Electric GE90, intercooled regenerative cycles based on the Rolls Royce Trent, and humid air cycles based on the Pratt & Whitney FT4000 (Stambler, 1993).

The evaluation of innovative cycles is also among the projects selected for the Advanced Turbine Systems (ATS) Program sponsored by the U.S. Department of Energy (Anon, 1993a), as well as in other programs sponsored by the Electric Power Research Institute (Cohn et al., 1993b; Ghaly et al., 1993; Tittle et al., 1993).

The effect of these complications is twofold: higher net electrical efficiency due to a more favorable "shape" of the thermodynamic cycle and larger unit power output due to an increase of both specific work and mass flow. Better cycles are realized by increasing the average combustor operating temperature and reducing the exhaust gas temperature, thus abating the two major losses of the simple cycle (introduction and release of heat to/from the cycle). Higher power outputs are accomplished by modifications that decrease compressor power (intercooling), increase turbine power (water/steam injection or higher average expansion temperature), or "supercharge" the existing turbomachinery by adding compression stages in front of the engine core.

Since none of these plants has been operated or tested so far, the assessment of their performance potential can be based only on predictions of the authors proposing these cycles, who often claim very attractive efficiencies. However, due to inconsistencies among the hypotheses adopted by the various authors, such predictions do not warrant a comparison among the different schemes. The aim of this two-part paper is to investigate the thermodynamic performances of these plants and to compare them with those of combined cycles on the basis of the same, coherent set of assumptions. The analysis includes the optimization of the plant arrangement and the cycle parameters, as well as a detailed second-law analysis. The focus is on "mixed" cycles without reheat, i.e., cycles with substantial water and/or steam injection into air or gas and only one combustor. Reheat at constant TIT has been considered in a previous paper (Macchi et al., 1991); nonetheless, the variable-TIT results presented here and the recent commercial launch of a new heavy-duty reheat turbine (Anon., 1993c) make it worthy of further future investigations.

2 Calculation Model

The calculation model used to generate the results described here has been specifically developed to predict the performance of complex gas–steam cycles, particularly "mixed" cycles (Consonni, 1992). Since the structure and the capabilities of the model have been extensively described in previous papers (Consonni et al., 1991; Lozza, 1990, 1993; Chiesa et al., 1992, 1993) we recall here only the most significant features and the modifications introduced in the framework of this paper.

2.1 Basic Outline. The system to be calculated is defined modularly as an ensemble of interconnected components, which can be of ten basic types: compressor, gas turbine expander, splitter, mixer, heat exchanger, combustor, pump, saturator, steam cycle (including all its components), and shaft (accounts for turbomachine spool interconnections, as well as electric losses). Operating characteristics and mass and energy balances of each component are calculated sequentially until the conditions (pressure, temperature, mass flow, etc.) at all interconnections converge toward a stable value. Aside from the algorithm handling the component network (it is virtually possible to analyze any cycle configuration), the most distinctive features of the model lie in the calculation of the key cycle components: turbomachines, heat recovery steam generator, and saturator.

The cooled gas turbine expansion is calculated as a sequence of small steps, each consisting of an expansion followed by gas-coolant mixing. At each step, the coolant flow required to maintain the blade temperature within an assigned value is found by the heat flux balance across the blade wall. The coolant is bled at the minimum pressure required to overcome coolant circuit pressure drops, and then discharged into the main flow; the optimistic implication of this idealized "continuous" compressor bleed (one for each expansion step) is compensated by imposing a high (40 percent) coolant-side pressure drop. The polytropic efficiency of both the cooled expansion steps and the uncooled turbine varies with a similarity size parameter to account for scale effects; exit kinetic energy is partly recovered in the diffuser.

The calculation of the steam bottoming cycle and the evaluation of the steam turbine expansion have been addressed in previous papers by Lozza (1990, 1993), while the evaluation of the saturator is extensively discussed in Part B.

2.2 New Features. Since all cycles analyzed here feature intercooling (STIG is the only exception), it is important to assess whether—and how much—lower coolant temperatures allow increasing the TIT of a given engine. This was accomplished by defining "critical" values for the ratios $V_{cl,nz}/V_g$ and $V_{cl,1r}/V_g$ between the volumetric cooling flow of the turbine nozzle ($V_{cl,nz}$) or of the first rotor ($V_{cl,1r}$) and the volumetric gas flow at the nozzle exit (V_g, see section 3). Both ratios are now calculated at each iteration, based on the coolant mass flow rate and the density at the conditions of injection of the step placed

Nomenclature

h = heat transfer coefficient, W/m^{2}K
i = enthalpy, J/kg
k = mass transfer coefficient, kg/m^{2}s
k_{bw} = blade wall thermal conductivity, W/mK
$\dot{m}$ = mass flow, kg/s
p = pressure, Pa
P = electric power output, W
S = heat transfer surface, m^2
t = blade wall thickness, m
T = temperature, K or °C
x = molal fraction
V = volumetric flow, m^3/s
Y = absolute humidity, kg$_{\text{water}}$/kg
β = overall cycle pressure ratio
β_{LPC} = low pressure compressor pressure ratio
Δi_{is} = stage isentropic enthalpy drop, J/kg
λ = vaporization heat, J/kg
η = net electric LHV efficiency
η_p = polytropic efficiency
φ = relative humidity

Subscripts and Superscripts

a = air
chrg = chargeable, i.e., for all turbine blade rows except first nozzle
cl = turbine coolant
ex = exit
g = main gas flow
i = liquid–gas interface in the saturator
in = inlet
nz = first nozzle of gas turbine
opt = optimum
w = water
$1r$ = first rotor of gas turbine
$'$ = referred to dry air
$*$ = referred to saturated air mixtures

Acronyms

ICC = intercooled combined cycle
ICR = unmixed intercooled recuperated cycle
CC = combined cycle
HAT = humid air turbine cycle
HP, IP, LP = high, intermediate, low pressure
HRSG = heat recovery steam generator
ISTIG = intercooled steam injected cycle
LHV = fuel lower heating value
LPC = low-pressure compressor
RWI = recuperated water injected cycle
ST = steam turbine
STIG = steam injected cycle
TIT = first rotor total inlet temperature
TOT = turbine outlet temperature

Table 1 Performances of "reference" state-of-the-art aeroderivative and heavy-duty engines (ISO conditions), as predicted by the calculation method used in the paper

Engine Type		Aero-derivative	Heavy-duty
TIT	°C	1250	1280
β		30	15
$\dot{m}_a$	kg/s	125	600
η	%	39.9	35.8
W	kJ/kg_a	327.2	373.1
P	MW	40.9	223.9
TOT	°C	450.7	595.8

halfway up the cascade[2]; if their "critical" values are exceeded it means that, for the stipulated technology, turbine cooling is unfeasible (see section 3.1 for further comments).

Beside this addition, two adjustments were introduced to represent more closely the situation encountered in actual engines:

1 Rather than being a fixed input datum, the blade wall Biot number $Bi = h_g \cdot t_{bw}/k_{bw}$ is now calculated on the basis of the blade material thermal conductivity k_{bw} assigned in input, the calculated gas-side heat transfer coefficient h_g, and the blade wall thickness t_{bw}, which is a constant fraction of the blade chord (2.5 percent). This allows suitable variations of blade wall thermal resistance due to different operating conditions (h_g increases with β) or size (in aeroderivatives the blade chord and thus t_{bw} are smaller).

2 The polytropic expansion efficiency of the cooled and uncooled turbine sections can be different. This allows accounting for the poorer performance of the cooled section (larger trailing edge thickness and flow disturbances due to coolant ejection).

2.3 State-of-the-Art Performances. Detailed information on the characteristics and the operating parameters of commercial gas turbines (turbomachinery efficiencies, metal temperatures, cooling flows, etc.) are considered strictly proprietary by all gas turbine manufacturers. Thus, several of the parameters needed to run the calculation model are not known, but can only be estimated based on experience, theoretical analyses, pieces of information collected from manufacturers or in the literature. Despite this handicap, Consonni and Macchi (1988) and Consonni (1992) have shown that a proper scrutiny of the data publicly available (power output, efficiency, TOT, etc.) allows calibrating the most crucial model parameters (turbomachinery efficiencies and parameters describing the cooling technology) to reproduce satisfactorily the engines belonging to the same technological "generation."

The input data used for the calculations performed here (see next paragraph) produce performances in good agreement with those of the latest, most advanced engines. Table 1 shows the performance predicted for the two "reference" engines with operating conditions (TIT, β, $\dot{m}_a$) representative of state-of-the-art large-size aeroderivatives and heavy-duties recently introduced by major world manufacturers.

2.4 Basic Assumptions. The assumptions adopted to obtain all results obtained here are summarized in Table 2. Most values equal the ones adopted in previous analyses (Macchi et al., 1991; Chiesa et al., 1993). The higher value assumed here for the film cooling parameter (r_{fc}) of aeroderivatives is meant to account for improvements in film cooling technology incorporated in latest engines; for heavy-duties, film cooling is supposed to be used only in the first nozzle. The cooling technology parameters Z and r_{fc} have been held constant throughout all calculations: Therefore, the results shown here are meant to represent the potential of current technology, even when the assumed TIT is above the state-of-the-art 1250–1280°C range. Pressure drops and temperature differences of unconventional components like the saturator, the recuperator, or the aftercooler conform to the assumptions of Day and Rao (1992), which in turn are based on calculations for reasonably sized piping and equipment as quoted by vendors (Day, 1994).

Table 2 Assumptions adopted for the calculations presented in the paper. The size parameter SP used to evaluate turbomachinery efficiencies is defined as $V^{0.5}/\Delta i_{is}^{0.25}$.

Compressors	Δi_{is}=27 kJ/kg for all stages. Leakage 0.8% of inlet $\dot{m}$, at HP exit
	$\eta_p=\eta_{p,\infty}\cdot[1-0.07108\cdot\log_{10}^2(SP)]$ for $SP<1$; $\eta_p=\eta_{p,\infty}$ for $SP\geq 1$; $\eta_{p,\infty}$: 0.905 (AD), 0.895 (HD)
	Inlet Δp (filter) = 1 kPa
Combustors	$\Delta p/p$=3%, heat losses=0.4%$\cdot\dot{m}_f\cdot$LHV
	Fuel compressor: isothermal with η=0.55, followed by fuel preheat (except CC, ICR)
Turbines	Δi_{is}: 300 kJ/kg (cooled stages) and 100 kJ/kg (uncooled stages)
	$\eta_p=\eta_{p,\infty}\cdot[1-0.02688\cdot\log_{10}^2(SP)]$ for $SP<1$; $\eta_p=\eta_{p,\infty}$ for $SP\geq 1$; $\eta_{p,\infty}$: 0.89 (cooled stages) and 0.925 (uncooled stages); $\eta_{p,nz}$=0.95; diffuser recovery =50% of exit kinetic head
	Cooling parameters: Z=100, r_{fc}=0.4 (AD) or 0.25 (HD). Maximum blade temperature: 830°C (1st nozzle), 800°C (cooled turbine)
Water-air heat exchangers	Air-side $\Delta p/p$=1%, minimum ΔT=10°C for surface HE; for evaporative intercoolers exit φ=90%
Recuperators	$\Delta p/p$=2% (both sides), minimum ΔT=25°C Heat losses 0.7% of the heat transferred
Saturators	Air-side $\Delta p/p$=0.7%
HRSG and steam cycle	Approach ΔT=25°C, Pinch point ΔT=10°C
	Gas side Δp 3 kPa, $\Delta p/p$ superheaters 8%, economizers 10%, heat losses 0.7%
	Steam turbine: η=0.7 (includes el./mech. losses) for ISTIG; for CC see Lozza (1990)
Pumps	η=0.65 (includes el./mech. losses)
Other	Ambient air (φ=60%) and water: T=15°C, p=101325 Pa; Fuel: methane at T=15°C, p=4 MPa, LHV=50.01 MJ/kg
	Electric generators: see Lozza, 1990; Organic losses 0.03% of turbomachine work

---

[2] Along the step-by-step expansion, the conditions of the spent coolant injected into the mainstream vary continuously, thus preventing us from defining an actual volumetric flow for the whole cascade. By referring to the density at the step located halfway along the cascade, the definition used here gives a value of V_{cl} corresponding to "average" (for the cascade) injection conditions.

3 Turbine Inlet Temperature: Tradeoffs and Limits

TITs adopted in commercial engines presumably represent the best compromise among a number of requirements and constraints: high efficiency, low cost, high reliability, long life, blade heat transfer and temperature distribution, coolant temperature, available coolant-side pressure drop, etc. If any of the "boundary conditions" affecting this best compromise is changed, the optimum TIT will also change. For a given engine, the prediction of this change can be effectively performed only by the manufacturer, who can master all technical and economic details of his machines.

General-purpose thermodynamic analyses must rely on a simpler approach: Given the intricacies of cost assessment and the need for criteria with the widest applicability, it is appropriate to evaluate TIT tradeoffs within the realm of thermo-fluid-dynamics. Then, given the cooling technology, the pressure ratio and the cycle configuration, the constraints to be considered are related to:

- Thermodynamic optimization. In general, there will be an optimum TIT that maximizes efficiency; for TIT > TIT_{opt} the penalties due to larger cooling flows more than offset the advantages of better cycle thermodynamics (Chiesa et al., 1993).
- Fluid dynamics. Since the coolant cross section is limited by the size (and shape) of the blade and of the channels driving the coolant to the turbine, there will be a limit on the flow rate that can be forced through the coolant circuit. In general, larger cooling flows can be obtained by increasing the bleed pressure; however, this (*i*) definitely hurts efficiency and (*ii*) may not be possible without adding a compressor for the coolant.
- Emissions. The abatement of NO_x emissions calls for adequate amounts of dilution or secondary air in the combustor hot section. Consequently, the flow available for turbine cooling is much smaller than the one left after stoichiometric combustion.

Since the prediction of NO_x formation is much beyond the scope of this work, we've neglected the third issue, thus implicitly assuming that all configurations discussed in the paper are not emission constrained. This simplifying assumption has been mitigated by introducing a ceiling of 1500°C on TIT (corresponding to combustor outlet temperatures below 1600°C); this limit should insure that problems like the exponential increase of thermal NO_x with temperature, combustor cooling, corrosion, fatigue, or thermal stress can actually be solved within the realm of current technology.

Whether emission control technology can really compensate for the changes in operating parameters stipulated here will have to be verified, although two notable circumstances give credit to our simplifying assumption: (*i*) the dramatic improvements recently achieved by dry-low-NO_x technology; (*ii*) the favorable situation of mixed cycles, where the lower adiabatic flame temperature resulting from the high moisture content in the oxidizer allows achieving low-NO_x emissions even with diffusion burners and fuel preheat.

3.1 Setting the Turbine Inlet Temperature. Based on the criteria set forth above, the gains achievable by increasing TIT without changing the cooling technology have been investigated by raising TIT until:

- efficiency reaches a maximum, or
- cooling flows reach the maximum value allowed by the cooling circuit characteristics and operating conditions, or
- TIT reaches the ceiling of 1500°C.

Table 3 Cooling flows calculated for the "reference" engines representative of state-of-the-art aeroderivative and heavy-duty technology. It is assumed that, for each engine type, the volumetric flow ratios $V_{cl,nz}/V_g$ and $V_{cl,1r}/V_g$ can be increased only by improving the cooling technology.

Engine Type	Aero-derivative	Heavy-duty
$\dot{m}_{cl,nz}/\dot{m}_a$, %	7.06	6.28
$\dot{m}_{chrg}/\dot{m}_a$, %	10.01	6.23
$V_{cl,nz}/V_g$, %	3.33	2.46
$V_{cl,1r}/V_g$, %	2.75	2.37

The maximum cooling flow allowed by the cooling circuit depends on a number of factors: available pressure drop, Mach number inside blade cooling channels, Mach number of spent coolant ejected from film cooling holes, etc. In this work we have assumed that:

(*a*) The "critical" condition corresponding to the maximum flow allowable through the coolant circuit is identified by a limiting value of the ratio V_{cl}/V_g between the spent coolant volume flow rate and the volumetric flow at the first nozzle exit.

(*b*) The limiting value of V_{cl}/V_g for both the nozzle and the first rotor is the one calculated for the two reference state-of-the-art engines of Table 1. These "critical" values are listed in Table 3.

The choice of the volumetric rather than the mass flow ratio is closer to the physical basis of the problem, because the quoted limits on pressure drops, Mach numbers, and flow cross section are mainly related to the coolant volume flow.

It is worth noting that, by defining state-of-the-art simple cycle engines as "critical," assumption (*b*) implies that their TIT can be increased only by (*i*) improving the cooling technology, (*ii*) improving materials, or (*iii*) reducing the coolant temperature. The first two options have been analyzed in a previous paper (Chiesa et al., 1993); in this paper we discuss the potential of the last option.

4 Intercooling in Simple and Combined Cycles

Thermodynamic textbooks show that for an ideal Brayton cycle intercooling increases specific work but definitely impairs efficiency. However, this situation changes substantially for real cycles, not only because there is a positive influence of intercooling on the efficiency penalties due to fluid-dynamic losses in turbomachines, but especially due to the presence of relevant coolant flows. In this case, intercooling brings about lower coolant temperatures, which in turn allow reducing the coolant flow required to keep the blades below a given temperature. Since cooling flows constitute a source of relevant efficiency penalties (coolant throttling, heat transfer, mixing, etc., see Consonni, 1992), their reduction is definitely beneficial. Therefore, for a heavily cooled gas turbine the overall impact of intercooling on efficiency can be highly positive, especially when considering the possibility to take advantage of lower coolant temperatures to increase TIT, rather than to decrease cooling flows.

4.1 Intercooling in Modified Modern Aero-engines. Let us discuss the effects of intercooling by referring to a cycle with $\beta = 46$, approximately corresponding to the intercooled version of current aeroderivatives under study by some manufacturers (Stambler, 1993). Gas turbine power output has been evaluated by assuming that the flow cross section at the nozzle exit is the same as the "reference" aero-engine reported in Table 1 (TIT = 1250°C, $\beta = 30$) and operates in chocked conditions. Consequently, the predictions discussed in this chapter approximately represent what could be achieved by implementing intercooling to actual commercial engines without modifying the hot section of the turbine.[3] Besides the simple cycle, let's also consider the performances of a combined cycle where (i) the heat available in the exhaust gases is recovered in a three-pressure-level bottoming cycle condensing at 32.9°C (0.05 bar); (ii) the heat discharged by the intercooler and/or the aftercooler above 100°C (heat below 100°C is wasted to ambient) is used to produce power at 50 percent second-law efficiency, i.e., producing half the power of a reversible cycle driven by the intercooler heat and discharging heat to ambient. The work output resulting from the latter hypothesis may be produced by a separate heat recovery cycle (e.g., an organic Rankine cycle) or, more plausibly, by "recycling" the heat to other parts of the cycle by preheating the fuel, preheating the make-up water, or generating LP steam.

The situation is depicted in the diagrams of efficiency, power, and cooling flows reported in Fig. 1, which shows three types of curve:

- "allowed" conditions (continuous lines), for which the ratio V_{cl}/V_g is below its critical value;
- "not allowed" conditions (dashed lines), for which such ratio is above its critical value, thus representing unfeasible situations;
- "critical" conditions (dashed-dotted lines), for which the ratio V_{cl}/V_g at either the nozzle or the first rotor equals its upper bound, i.e., the values listed in Table 3.

With no intercooling ($\beta_{LPC} = 1$) the cycle is unfeasible because for $\beta = 46$ the coolant temperature is higher than that encountered in the reference engine with $\beta = 30$, thus requiring a V_{cl}/V_g well above the critical value. Moving toward higher β_{LPC} there is, at first, a beneficial effect on η, implying that the "technological" benefits brought about by lower cooling flows overcome the thermodynamic drawbacks. At high β_{LPC} thermodynamics eventually prevails, thus decreasing the cycle efficiency. At optimum β_{LPC} efficiency approaches 45 percent, a significant improvement over the reference case. As for power output, there is a very large increase even without increasing TIT (at 1250°C P = 70–90 MW$_e$ versus $\simeq$ 40 MW$_e$ of the base case in Table 1), partly due to the increase of specific work and partly due to higher β, which, for the same turbine nozzle area, increases the mass flow and thus power output. The figure also shows that:

- While higher TITs are always beneficial to power output, they produce significant efficiency benefits only for combined cycles, which can take advantage of higher TOT. As a matter of fact, the intercooled gas turbine with no heat recovery achieves maximum efficiency at the moderate TIT of 1280°C (and $\beta \simeq 80$, see Fig. 15 of Part B).
- At TIT = 1500°C and optimum $\beta_{LPC} \simeq 3.5$, the combined cycle efficiency reaches values ($\simeq$55 percent) fully comparable with those of large heavy-duty-based systems.
- The range spanned by efficiency and power output covers the performances projected for the intercooled version of the GE LM6000, which, as indicated in Stambler (1993), should reach a power output of 90 MW with an efficiency close to 45–46 percent, going up to 110 MW and 54 percent in combined cycle.
- "Not allowed" cooling flow situations occur only at low intercooler pressures ($\beta_{LPC} < 1.8$ for TIT = 1250°C, $\beta_{LPC} < 3.4$ for TIT = 1500°C), while critical conditions are always very close to those giving the highest efficiency. Although critical cooling flows are first established in the nozzle, they occur almost simultaneously also in the first rotor.

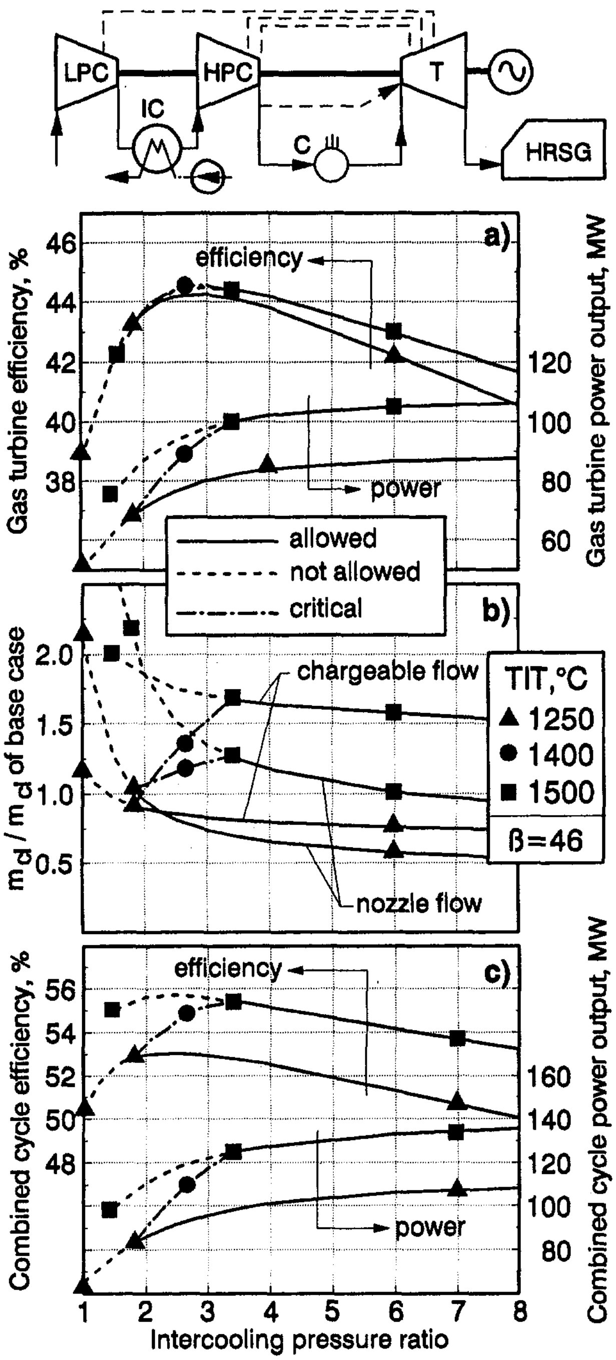

Fig. 1 Efficiency and power output of an intercooled unmixed cycle based on a modified aero-engine. The upper figure refers to the simple cycle, the lower one to the combined cycle. The middle diagram shows the ratio between the cooling flows of this case and the ones of the "reference" aero-engine quoted in Tables 1 and 3. The air mass flow is varied so as to preserve the same turbine nozzle cross section of the reference engine.

- At TIT = 1500°C, the chargeable mass flow is always much higher, although not critical, than in the "reference" engine, basically because the number of stages—and thus the area—to be cooled is much higher.

Since critical cooling conditions first occur in the nozzle, we investigated the possibility of removing this barrier by "aftercooling" the coolant bled at the compressor exit before using it in the nozzle, a practice often adopted in heavy-duties; similarly to the intercooler heat, the heat made available by

---

[3] In order to accommodate the larger enthalpy drop, the LP section of the turbine must be modified by adding one or more stages. More substantial changes are required for the compressor: a new LP section ahead of the intercooler and an adjustment of the HP cross sections to warrant the desired turbine nozzle area.

aftercooling at $T > 100°C$ was assumed to be converted to power with 50 percent second-law efficiency.

As for intercooling, the outcome of aftercooling depends on the tradeoff between lower coolant flow and the related thermodynamic penalties: irreversible aftercooler heat recovery and larger ΔT between the coolant and the blade wall. The plant scheme now includes a heat exchanger cooling the nozzle coolant down to 25°C (as at the intercooler exit), while the coolant for the turbine is bled at variable pressure as in the "reference" engine. The final temperature of 25°C has been assumed to emphasize the influence of coolant aftercooling; in practice higher final temperatures may provide slightly better performance. As shown in Fig. 2, results are very similar to the ones with intercooling only, with these minor differences:

- the lower allowable β_{LPC} corresponds now to critical cooling conditions in the first rotor rather than in the nozzle, because aftercooling cuts the nozzle cooling flow by more than 50 percent (see diagram of cooling flows);
- there is a slight increase in power output and a slight decrease in efficiency.

In conclusion, the addition of heat exchangers on the coolant flow path does not offer substantial advantages. Intercooling appears the most efficient way to limit cooling flows and increase TIT without penalizing efficiency, for both simple and combined cycles.

To confirm this statement, we also considered the option of simply lowering the coolant temperature of the "reference" engine of Table 1 ($\beta = 30$). Since cooling only the nozzle coolant would be ineffective (it would simply shift the problem to the first rotor) and since it is unrealistic to assume that each coolant bleed would have its own heat exchanger, we assumed that the entire coolant flow is bled at the compressor exit and then cooled. As before, for the combined cycle it is assumed that the heat released in the aftercooler above 100°C is recovered with 50 percent second-law efficiency.

Figure 3 shows that the severe throttling losses incurred by the chargeable flow override the gain brought about by lower coolant flows. Despite the approximate 50 percent reduction of cooling flows, at TIT = 1250°C the efficiency of both the simple and the combined cycle is more than 1 percentage point lower than that attainable with the reference engine. At TIT = 1500°C the simple cycle suffers dramatic penalties due to large cooling flows, and thus large throttling losses; the combined cycle makes up for such losses with heat recovery, although efficiency never goes above the one achieved with the reference engine. The only benefit of higher TIT is therefore a substantial increase of power output. It is worth mentioning that these results are particularly unfavorable because the reference engine of Table 1 makes best use of the coolant by bleeding it at many points along the compressor; if the configuration considered for Fig. 3 were compared with a reference engine with only 2 or 3 coolant bleeds, the outlook of aftercooling would be somewhat less grim. In any case, the relevance of throttling losses unquestionably hinders the idea of using high-pressure, low-temperature coolant for the turbine section downstream of the nozzle.

The results discussed in this chapter can be summarized by saying that, for a given cooling technology, intercooling is definitely the most convenient practice to raise the performance of aeroderived engines.

Aftercooling is generally detrimental, except when applied solely to the nozzle coolant (as in Fig. 2). The effect of aftercooling the nozzle coolant depends on how efficiently the aftercooler heat is recovered: In the more complex cycles investigated in Part B (RWI and HAT), the heat recovery mechanism is efficient enough to produce small performance gains when bleeding the nozzle coolant at the lower available temperature of the HP air circuit. However, since the gain is always very small, all cases considered hereafter do not include aftercooling of nozzle coolant; whenever possible they simply take advantage of the enhanced cooling capabilities of air/vapor mixtures by bleeding the coolant downstream water or steam injection.

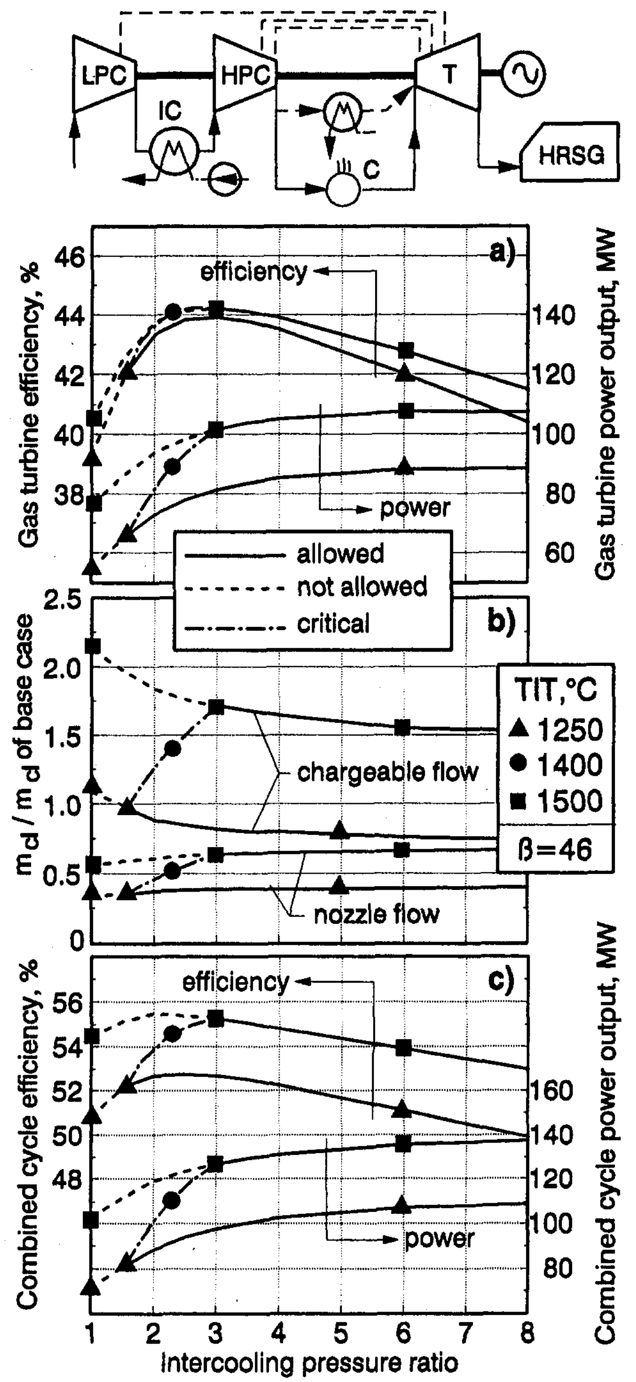

Fig. 2 Efficiency and power output of an intercooled unmixed cycle based on a modified aero-engine with aftercooling of the first nozzle coolant. The upper figure refers to the simple cycle, the lower one to the combined cycle. The middle diagram shows the ratio between the cooling flows of this case and the ones of the reference aero-engine quoted in Tables 1 and 3.

4.2 Intercooling in Combined Cycles With Heavy-Duty Gas Turbines. The question may arise whether intercooling and the related TIT enhancements can also improve the efficiency of combined cycles based on large heavy-duties. This case is inherently different from that of aero-engines, which are characterized by high pressure ratios and poor steam cycle efficiencies (due to small size). In contrast to aero-engines, in heavy-duties intercooling faces several unfavorable circum-

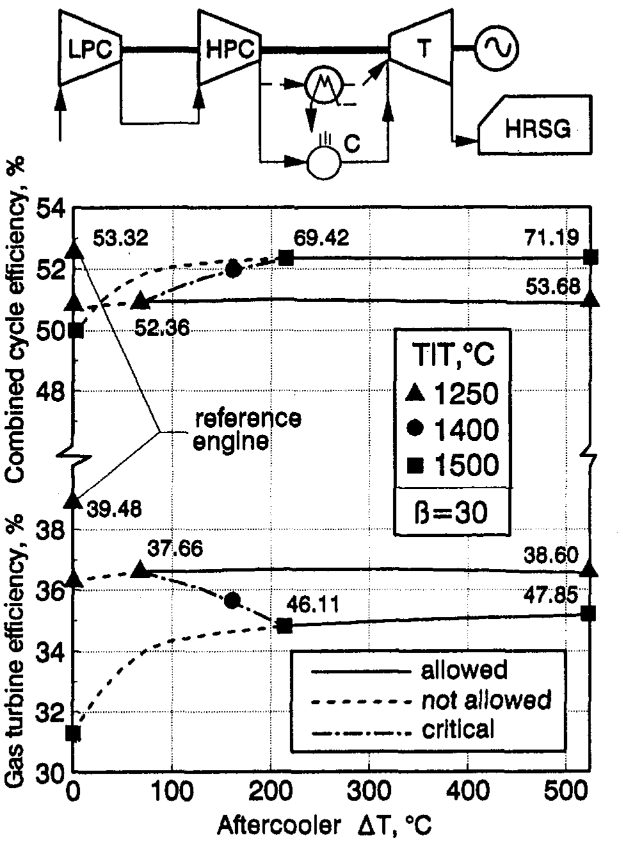

Fig. 3 Efficiency of simple and combined cycles with external cooling of the air for turbine cooling, as a function of the coolant temperature drop. *The entire cooling flow is extracted at the discharge of the HP compressor.* Numbers on top of markers represent the cycle power output [MW].

stances: (*i*) Lower β produce lower initial coolant temperature and thus higher ΔT between the coolant and the blade ($\simeq$480°C versus $\simeq$260°C for aeroderivatives); the relative increase of this ΔT brought about by intercooling is much smaller, and so are the benefits; (*ii*) at the low β of heavy-duties the increase of combustion irreversibilities caused by intercooling (in the combustor dilution air is heated under larger ΔT) is more severe; (*iii*) specific work augmentation is small, because at low β compression work is a much smaller fraction of net work; for combined cycles based on the reference engines in Table 1 the ratio between compression work and net work is $\simeq$66 percent for the heavy-duty, versus $\simeq$128 percent for the aeroderivative.

Let us discuss these issues by considering the results of calculations performed for the "reference" heavy-duty machine of Table 1. The bottoming steam cycle is a three-pressure reheat cycle, condensing at 0.05 bar with a maximum steam temperature of 565°C; the maximum pressure has been optimized in the range 100–300 bar (the optimum value depends on the gas turbine outlet temperature; see Lozza, 1993). The intercooling pressure ratio β_{LPC} has been set to the minimum value that meets the volumetric flow ratios of Table 3, with the constraint $\beta_{\mathrm{LPC}} \geq 2$. As usual, intercooling heat above 100°C is recovered with 50 percent second-law efficiency. The results summarized in Fig. 4 show that:

- The nonintercooled cycle efficiency of 55.8 percent adequately portrays the performance of large plants based on latest gas turbine and steam cycle technology. 54–55 percent *CC* efficiencies are now quoted by several manufacturers (e.g., Tomlinson et al., 1993) and have been measured on an ABB plant based on an older generation gas turbine (Werner et al., 1993).
- At constant TIT = 1280°C and β = 15, intercooling at the minimum allowed $\beta_{\mathrm{LPC}} = 2$ decreases efficiency by about 0.7 percentage points. Such a gap can be eliminated by increasing TIT to about 1350°C.
- Higher TITs give marginal efficiency gains, mostly because they require higher β_{LPC} (e.g., 2.8 at TIT = 1500°C) to lower the coolant temperature and thus meet the limit on V_{cl}/V_g: This overcomes the benefits of higher TIT even when recovering the intercooler heat (continuous line).
- At pressure ratios much higher than usually adopted in heavy-duties (the figure shows β = 30) the outcome is worse, because the higher β_{LPC} required to meet the limits on V_{cl} amplify the negative effect on the cycle thermodynamics—even with intercooling heat recovery. This means that the handicap ensuing from nonoptimal β (for current combined cycle technology $\beta_{\mathrm{opt}} \simeq 15$) cannot be fully neutralized even by TIT = 1500°C.[4]

The only benefit of intercooling is therefore an augmentation of power output: For the same inlet air flow of 600 kg/s, the intercooled cycles with TIT = 1500°C provide an electric power of about 480 MW, versus 350 MW of the reference case.

5 Steam-Injected Cycles

Injecting the steam generated in the Heat Recovery Steam Generator into the gas turbine rather than using it in a closed-loop bottoming cycle is a well-established practice. The cycle has been extensively discussed in the technical literature since its appearance (Cheng, 1978) and still recently (Rice, 1993, 1995). Fully steam injected (STIG) versions of few gas turbine engines (slight modifications to turbine bladings may be required to accommodate larger flow rates) have been commer-

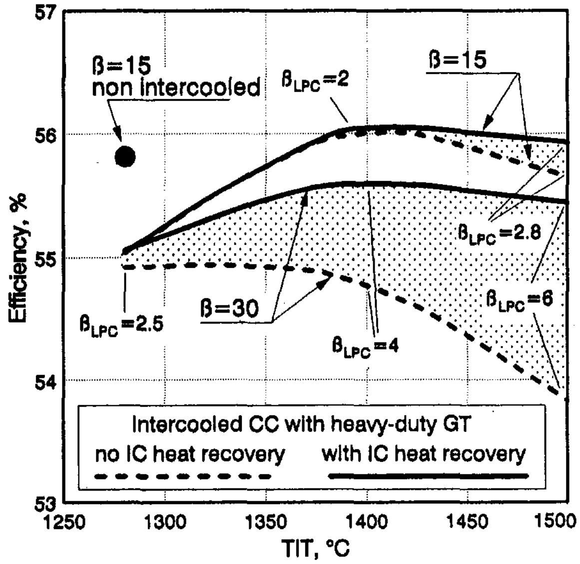

Fig. 4 Influence of intercooling on the efficiency of combined cycles based on heavy-duty gas turbines with β = 15 and β = 30. Dashed lines refer to cases where the intercooling heat is wasted to ambient; continuous lines refer to cases where the fraction of intercooling heat available at $T > 100$°C is converted to power with 50 percent second-law efficiency.

---

[4] Given the superiority of cycles with moderate pressure ratios, one might think of improving the performance of aero-engine-based combined cycles simply by reducing the pressure ratio. Although this would increase the combined cycle efficiency, it would also dramatically decrease power output due to much lower air mass flow. The consequent strong increase of specific costs makes this proposition highly unrealistic.

cially available for several years (Oganowski, 1987). Rather than high electrical efficiency alone, the rationale behind this scheme is based on considerations like operational flexibility in cogeneration applications, investment cost (lower than for combined cycles), effective NO$_x$ abatement due to massive steam injection into the combustor, etc. As an example of the tradeoffs involved, let's mention the most efficient commercial STIG package based on the large aeroderivative GE LM5000, which features a power output of 49.6 MW, with a net electric efficiency of 43.8 percent (Anon., 1993b); the combined cycle version of the same engine exhibits an 8 percent lower power output (45.9 MW) and much higher investment cost, but achieves an efficiency of 49 percent.

Efficiencies and power output of steam injected cycles can be enhanced by a more radical redesign of the engine. General Electric has been proposing the intercooled LM8000 ISTIG version for several years (Horner, 1989), but the project never reached the commercial phase.

5.1 Plant Arrangement. Figure 5 depicts the plant arrangement considered for steam injected cycles where intercooling is carried out by a surface heat exchanger. In most cases makeup water and fuel preheat in the intercooler do not improve overall heat recovery, because the same heat can be transferred to water and the fuel in the HRSG by reducing the exhaust gas temperature (except for extremely high steam injection rates). However, makeup preheat in the intercooler allows some savings in the heat transfer devices of the whole plant: (*i*) Water heaters are removed from the HRSG; (*ii*) only part of the intercooling heat is rejected to ambient, therefore reducing the size and cost of cooling towers (or air coolers), as well as their consumptions (power, water). Additionally, fresh makeup water may help in achieving the lowest possible compressed air temperature.

The arrangement assumed for the calculation of cycles with intercooling by direct-contact evaporative heat exchangers is almost the same: The only difference is a water–air mixer that substitutes the surface intercooler, with no makeup water and fuel preheat ahead of the HRSG.

The rather sophisticated HRSG arrangement shown in the figure gives the highest efficiencies:

- three-pressure-level steam generation for injection of HP steam into the combustor and IP and LP steam into the gas turbine accomplishes thorough heat recovery (even if it entails the highest water consumption);
- at each pressure, maximum superheating is accomplished by parallel heat transfer banks: This is beneficial to efficiency, minimizing the temperature gap between steam and gas;
- whenever possible, a steam turbine (ST) expands steam between the highest drum pressure and the injection pressure (after the expansion steam is reheated before being injected). This allows full optimization of all steam generation pressures, thus reducing HRSG heat transfer irreversibilities.

Turbine cooling flows (dotted lines in the figure) are bled from the compressor as in a simple cycle, while the flow for nozzle cooling is bled after HP steam injection to take advantage of the increased moisture content.[5]

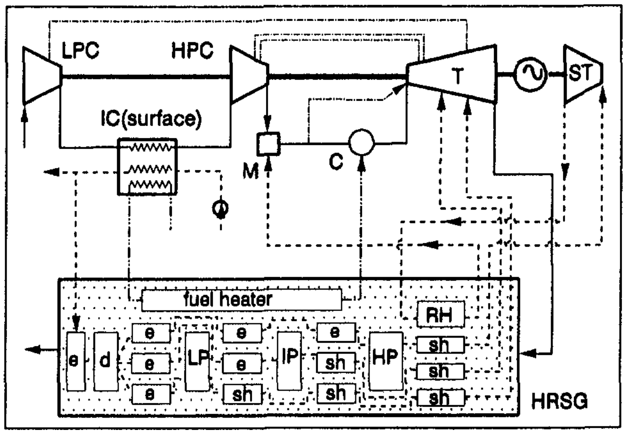

Fig. 5 Conceptual plant scheme of intercooled steam injected cycles with surface intercooler (the HRSG banks are: "e" economizers, "sh" superheaters, "d" deaerator)

As for other mixed cycle configurations considered in Part B, the scheme of Fig. 5 includes full fuel preheat up to the temperature made possible by the gas turbine discharge conditions. Fuel preheat is always beneficial to efficiency, because it substantially reduces combustion irreversibilities without significant drawbacks on other processes (heat transfer entails minor irreversibilities, while the small decrease of steam production yields only marginal reductions of specific work): For the configurations considered in the paper it generally gives a 1 percentage point efficiency increase. Despite this appealing benefit, emission concerns would presumably prevent from adopting fuel preheat in simple and combined cycles, as well as in ICRs, because without steam or water injection the achievement of low-NO$_x$ emissions most likely requires premixed burners; to avoid preignition, such burners would be fed with fuel at ambient temperature. For these reasons, we have considered fuel preheat only for mixed cycles.

5.2 Variables to Be Optimized. The cycle parameters to be optimized are (*i*) overall pressure ratio, (*ii*) intercooling pressure, and (*iii*) steam evaporation pressures. On the contrary, steam injection rates are determined by the HRSG energy balance and the imposed pinch-point ΔTs.

Let us first discuss the influence on efficiency of the intercooling pressure. Figure 6 depicts the situation for the two options of mixing and surface intercooling. Calculations were performed at fixed β and optimized steam pressures: 39.3/13.2/4.3 bar at TIT = 1250°C, $\beta = 30$; 58.9/15.9/5.6 bar at TIT = 1500°C, $\beta = 45$; both cases do not require the HP steam turbine. With surface intercooling and TIT = 1250°C the highest efficiency is reached for very low LPC pressure ratios (about 2). For β_{LPC} above optimum, the efficiency benefits brought about by intercooling are offset by the higher losses in the combustor (lower inlet temperature) and in the intercooler (heat discharge). Compared to the simple STIG cycle intercooling improves efficiency by about one percentage point. The gain reaches 3 percentage points only by taking full advantage of lower coolant temperatures to increase TIT up to 1500°C. In this case the optimum β_{LPC} is about 4, enough to meet the limits on V_{cl} (Table 3) but much lower than the value that minimizes compression work.

5.3 Surface Versus Evaporative Intercoolers. At the optimum β_{LPC} spray intercoolers do not produce any efficiency advantage over surface heat exchangers. This is not surprising because, although the former do not waste heat to ambient, in both cases the heat released by air is transferred to a sink at low temperature, with large ΔT and thus large irreversibilities. In spray intercoolers the heat sink is low-pressure water evaporating at approximately the intercooler exit temperature (it would be the exit temperature if the exit flow were saturated).

---

[5] Due to its higher heat capacity and superior heat transfer properties, steam is a more effective coolant than air. The implications of steam cooling in nonintercooled cycles have been discussed by Chiesa et al. (1992): For a STIG cycle with TIT = 1250°C the use of saturated steam for cooling would boost specific work by 12 percent, while efficiency would increase by only 0.1 percentage points. Due to the complications brought about by steam cooling (steam bleedings from HRSG drums to the turbine, more complex startup and operation, erosion/corrosion problems, etc.) such a possibility will not be considered here.

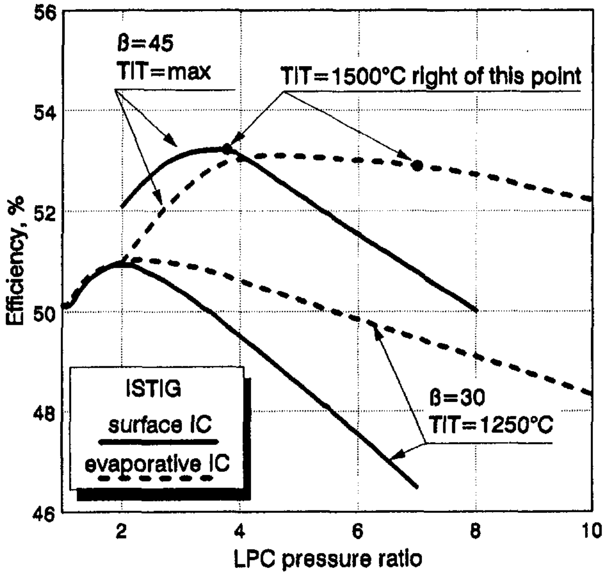

Fig. 6 Efficiency of ISTIG cycles at β = 30, TIT = 1250°C and β = 45, TIT = max as a function of β_{LPC}. Continuous lines refer to intercooling by surface heat exchangers; dashed lines refer to spray intercoolers. The points with β_{LPC} = 1 represent the nonintercooled STIG cycle; due to the coolant flow limitations discussed in section 3, in this case TIT cannot be increased.

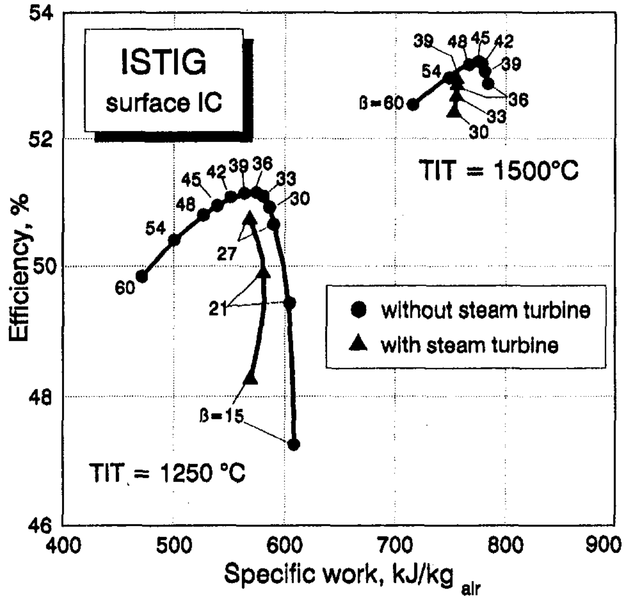

Fig. 7 Efficiency and specific work of ISTIG cycles with surface intercoolers and optimum β_{LPC}. For β higher than the ones indicated by the triangular markers the addition of an HP steam turbine (component ST of Fig. 5) has no beneficial effect.

In surface intercoolers the heat sink is the ambient; notice that in this case reducing the intercooler heat transfer irreversibilities by increasing the heat transfer area (and thus the water exit temperature) doesn't help, because the gain in the intercooler would be completely lost by discharging water at higher temperature.

At large β_{LPC} evaporative intercooling becomes more efficient because, while the heat sink of surface intercoolers remains the same, the temperature after the spray—and thus the temperature of the evaporating water—increases significantly. For example, at β_{LPC} = 6 the temperature at the outlet of the evaporative intercooler is 86.8°C: Transferring the heat released by air to water evaporating at such temperature is much less irreversible than discharging it to ambient at 15°C.

Even if spray intercoolers suffer lower heat transfer losses due to water evaporating above the ambient temperature, there are additional losses not present in surface intercooling: (*i*) water/air mixing; (*ii*) higher compression losses due to higher temperatures at the inlet of the HP compressor; (*iii*) higher stack losses, due to higher exhaust moisture content. At optimum β_{LPC} these additional losses generally produce performances slightly worse than with surface heat exchangers. For these reasons all parametric calculations have been referred to surface heat exchangers.

As for power output, the larger mass flow rate ensuing from evaporative intercooling always gives more power per kg of air entering the LP compressor. However, if one refers power output to the mass flow in the HP compressor (or the turbine), he would obtain approximately the same specific work produced with surface heat exchangers. This means that for a given size of HP turbomachinery evaporative intercooling gives no power output increase.

5.4 Results for Optimized Cycles. The results of the overall cycle optimization are summarized in the efficiency-specific work plane reported in Fig. 7. At TIT = 1250°C and 30 < β < 45 efficiency is slightly above 51 percent; at these high pressure ratios the HP steam turbine gives no benefits, because the optimum HP steam evaporating pressure does not exceed the one necessary for injection into the combustor. The adoption of higher TITs made possible by intercooling increases efficiency by about 2 percentage points, while the corresponding optimum pressure ratio increases from about 36 to 45. The results of Fig. 7 fully agree with General Electric predictions of 52 percent efficiency at TIT = 1371°C and β = 34 (Horner, 1989): For the same cycle parameters our model gives η = 52.2 percent. It is interesting to note that the thermodynamic "quality" of the two ISTIG cycles optimized for TIT = 1250 and 1500°C is almost the same (slightly better for the latter): The ratios between ISTIG and Carnot efficiencies are 51.16/81.08 = 63.1 percent at 1250°C and 53.23/83.74 = 63.6 percent at 1500°C.

The operating conditions for the optimized cycle (β = 45, TIT = 1500°C) are given in Fig. 8: With reference to a simple cycle operating at a nearly optimum pressure ratio (β = 30) and TIT = 1250°C, the increase of specific work (referred to the inlet air flow) is as large as 138 percent. Moreover, if we stipulate that the flow area of the HP turbine remains unchanged, the engine is "supercharged" with an increase of inlet air flow

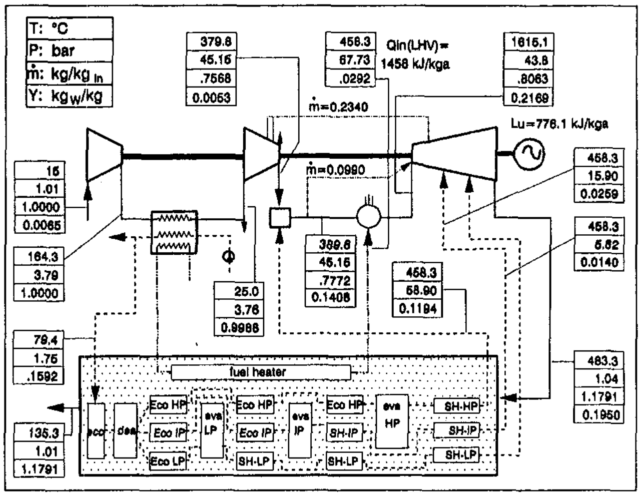

Fig. 8 Mass flow, pressure, temperature, and water content at the most relevant points of an optimized ISTIG cycle with β = 45 and TIT = 1500°C

of 31.6 percent: The cumulative result is a net power output increase of over 215 percent, which means that a "modified" ISTIG version of a 40 MW simple cycle machine would generate a power output of about 128 MW. For constant HP compressor exit flow areas (as assumed by Day and Rao, 1992), the increase in power output is even larger: about 435 percent, giving a power output of 217 MW_{el}.

Previous calculations (Macchi et al., 1991) demonstrated that the introduction of a reheat turbine would further improve the ISTIG cycle efficiency by about 3 percentage points, and almost double its specific work.

Conclusions

The analysis performed in this Part A points out that intercooling, coupled with the higher pressure ratios and the higher TITs made possible by the lower compressor temperature, can substantially enhance the efficiency and the power output of both simple and combined cycles based on current aeroderivative engines. On the contrary, intercooling does not lead to any efficiency improvement of heavy-duty-based combined cycles, although it still gives higher power outputs.

When the bottoming closed-loop steam cycle is replaced by steam injection, the cycle suffers an efficiency loss of 3–4 percentage points. Part B investigates other mixed cycle concepts able to reduce, or even reverse, this efficiency gap.

References

Anon., 1993a, "Comprehensive Program Plan for Advanced Turbine Systems," US Dept. of Energy, Office of Fossil Energy and Office of Energy Efficiency and Renewable Energy, Report to Congress, May.

Anon., 1993b, "1993 Performance Specs," *Gas Turbine World,* Vol. 13.

Anon., 1993c, "The New GT-24 ABB 240 MW Gas Turbine," ABB Company Publication, Baden, Switzerland.

Cheng, D. Y., 1978, "Regenerative Parallel Compound Dual-Fluid Heat Engine," US Patent No. 4.128.994

Chiesa, P., Consonni, S., and Lozza, G., 1992, "Gas/Steam Cycles With Open-Circuit Steam Cooling of Gas Turbines Blades," *Proc. FLOWERS 92. Energy for the Transition Age,* Firenze, Italy, pp. 303–323.

Chiesa, P., Consonni, S., Lozza, G., and Macchi, E., 1993, "Predicting the Ultimate Performance of Advanced Power Cycles Based on Very High Temperature Gas Turbine Engines," ASME Paper No. 93-GT-223.

Cohn, A., Hay, G. A., and Hollenbacher, R. H., 1993a, "The Collaborative Advanced Gas Turbine Program—A Phase I Project Status Report," *Proc. 12th EPRI Gasification Conference,* San Francisco, Oct. 27–29.

Cohn, A., Nakhamkin, M., Swensen, E., and Patel, M., 1993b, "Engineering Studies of the CASH and CASHING Cycles," *Proc. 12th EPRI Gasification Conference,* San Francisco, Oct. 27–29.

Consonni, S., and Macchi, E., 1988, "Gas Turbine Cycles Performance Evaluation," *Proc. 2nd ASME Cogen-Turbo,* Montreaux, Switzerland, pp. 67–77.

Consonni, S., et al., 1991, "Gas-Turbine-Based Advanced Cycles for Power Generation. Part A: Calculation Model," *Proc. 1991 Yokohama Int'l Gas Turbine Congress,* pp. III-201–210.

Consonni, S., 1992, "Performance Prediction of Gas/Steam Cycles for Power Generation," MAE Dept. Ph.D. Thesis No. 1893-T, Princeton University, Princeton, NJ.

Day, W. H., 1994, Turbo Power & Marine Systems (Connecticut, USA), personal communication.

Day, W. H., and Rao, A. D., 1992, "FT4000 HAT With Natural Gas Fuel," *Proc. 6th ASME Cogen-Turbo,* Houston, TX, pp. 239–245.

Ghaly, O. F., McCone, A. I., and Nakhamkin, 1993, "Engineering and Economic Evaluation of the IGCASH Cycle," *Proc. 12th EPRI Gasification Conference,* Houston, TX, pp. XX–00.

Horner, M., 1989, "LM8000 ISTIG Power Plant," presentation given by the GE Marine and Industrial Engine Division, Cincinnati, OH.

Lozza, G., 1990, "Bottoming Steam Cycles for Combined Gas–Steam Power Plants: a Theoretical Estimation of Steam Turbine Performance and Cycle Analysis," *Proc. 4th ASME Cogen-Turbo,* New Orleans, LA, pp. 83–92.

Lozza, G., 1993, "Steam Cycles for Large-Size High-Gas-Temperature Combined Cycles," *Proc. 7th ASME Cogen-Turbo Power,* Bournemouth, UK, pp. 435–444.

Macchi, E., et al., 1991, "Gas-Turbine-Based Advanced Cycles for Power Generation. Part B: Performance Analysis of Selected Configurations," *Proc. 1991 Yokohama International Gas Turbine Congress,* pp. III-211–219.

Oganowski, G., 1987, "LM5000 and LM2500 Steam Injection Gas Turbines," *Proc. 2nd Tokyo Int'l Gas Turbine Congress,* pp. III-393–397.

Rice, I. G., 1993, "Steam Injected Gas Turbine Analysis: Part II—Steam Cycle Efficiency; Part III—Steam Regenerated Heat," ASME Papers No. 93-GT-420, 93-GT-421.

Rice, I. G., 1995, "Steam-Injected Gas Turbine Analysis: Steam Rates," ASME JOURNAL OF ENGINEERING FOR GAS TURBINES AND POWER, Vol. 117, pp. 347–353.

Stambler, I., 1993, "Next Generation 'Superfans' Could Plug Electric Utility Capacity Gaps," *Gas Turbine World,* May–June, pp. 46–54.

Tittle, L. B., Van Laar, J. A., and Cohn, A., 1993, "Advanced Aeroderivative Gas Turbine: A Preliminary Study," *Proc. 12th EPRI Gasification Conference,* San Francisco, Oct. 27–29.

Tomlinson, L. O., et al., 1993, "GE Combined Cycle Product Line and Performance," General Electric rep. GER-3574D.

Werner, K. H., et al., 1993, "Deeside: an Advanced Combined Cycle Power Plant With ABB GT13E2 Gas Turbine for National Power PLC," *Proc. 7th ASME Cogen-Turbo Power,* pp. 487–498.

An Assessment of the Thermodynamic Performance of Mixed Gas–Steam Cycles: Part B—Water-Injected and HAT Cycles

P. Chiesa

G. Lozza

E. Macchi

S. Consonni

Dipartimento di Energetica,
Politecnico di Milano,
Milan, Italy

Part B of this paper[1] focuses on intercooled recuperated cycles where water is injected to improve both efficiency and power output. This concept is investigated for two basic cycle configurations: a Recuperated Water Injected (RWI) cycle, where water is simply injected downstream of the HP compressor, and a Humid Air Turbine (HAT) cycle, where air/water mixing is accomplished in a countercurrent heat/mass transfer column called "saturator." For both configurations we discuss the selection and the optimization of the main cycle parameters, and track the variations of efficiency and specific work with overall gas turbine pressure ratio and turbine inlet temperature (TIT). TIT can vary to take advantage of lower gas turbine coolant temperatures, but only within the capabilities of current technology. For HAT cycles we also address the modelization of the saturator and the sensitivity to the most crucial characteristics of novel components (temperature differences and pressure drops in heat/mass transfer equipment). The efficiency penalties associated with each process are evaluated by a second-law analysis, which also includes the cycles considered in Part A. For any given TIT in the range considered (1250 to 1500°C), the more reversible air/water mixing mechanism realized in the saturator allows HAT cycles to achieve efficiencies about 2 percentage points higher than those of RWI cycles: At the TIT of 1500°C made possible by intercooling, state-of-the-art aero-engines embodying the above-mentioned cycle modifications can reach net electrical efficiencies of about 57 and 55 percent, respectively. This compares to efficiencies slightly below 56 percent achievable by combined cycles based upon large-scale heavy-duty machines with TIT = 1280°C.

1 Introduction

This two-part paper discusses the thermodynamic performance of gas cycles whereby steam or water is injected into the gas turbine working fluid to increase both power output and conversion efficiency, with particular emphasis toward large-scale, baseload stationary power plants built around modern aero-engines. Following the analysis of steam-injected cycles in Part A, Part B focuses on intercooled recuperated water injected cycles. These include the so-called HAT (Humid Air Turbine) cycle, probably the most appealing novel gas/steam mixed cycle recently proposed in the technical literature (Rao et al., 1991; Day and Rao, 1992). As in Part A, the analysis is restricted to "premium" fuels (natural gas or clean liquid fuels). The calculation method and all the assumptions described in Part A have been maintained here.

2 Recuperated Water Injected Cycles

Recently, great interest has been paid to the intercooled recuperated (ICR) cycle selected by the US Navy to reduce the annual fuel consumption of its fleet by over 30 percent (Crisalli and Parker, 1993). However, this cycle lacks the thermodynamic "quality" necessary to reach efficiencies above 50 percent, nor can it produce a dramatic power output augmentation of the basic engine (Roberts, 1993). These limits can be overcome by water injection, which, as pointed out by El Masri (1988), can remarkably improve both efficiency and power output of intercooled recuperated cycles.

2.1 Plant Arrangement and Variables to Be Optimized.

The plant arrangement considered in the paper is shown in Fig. 1: As for ISTIG cycles, intercooling can be alternatively obtained by an evaporative or a surface heat exchanger. For the latter, the opportunity of preheating the makeup water and the fuel in the intercooler is subjected to the same considerations illustrated in section 5.1 of Part A: Also in this case preheat helps in reducing the heat transfer equipment of the plant but does not improve efficiency, because the heat recovered in the intercooler can be alternatively recovered by cooling the exhaust gases to lower temperatures.

Air exiting the HP compressor is cooled in the evaporative direct-contact aftercooler *M*: The amount of water to be injected to achieve maximum efficiency is so large that the outlet relative humidity exceeds 100 percent, resulting in an air–water spray. Spray droplets are evaporated in the first part of the recuperator to produce an air/vapor mixture that is heated and sent to the combustor. Besides the recuperator, heat recovery takes place in the economizer (ECO), which preheats the water to be injected into the aftercooler and, if present, in the evaporative intercooler. Fuel preheat is carried out first in the economizer, then in the recuperator.

---

[1] Nomenclature is the same as in Part A.

Contributed by the International Gas Turbine Institute and presented at the 39th International Gas Turbine and Aeroengine Congress and Exposition, The Hague, The Netherlands, June 13–16, 1994. Manuscript received by the International Gas Turbine Institute March 18, 1994. Paper No. 94-GT-424. Associate Technical Editor: E. M. Greitzer.

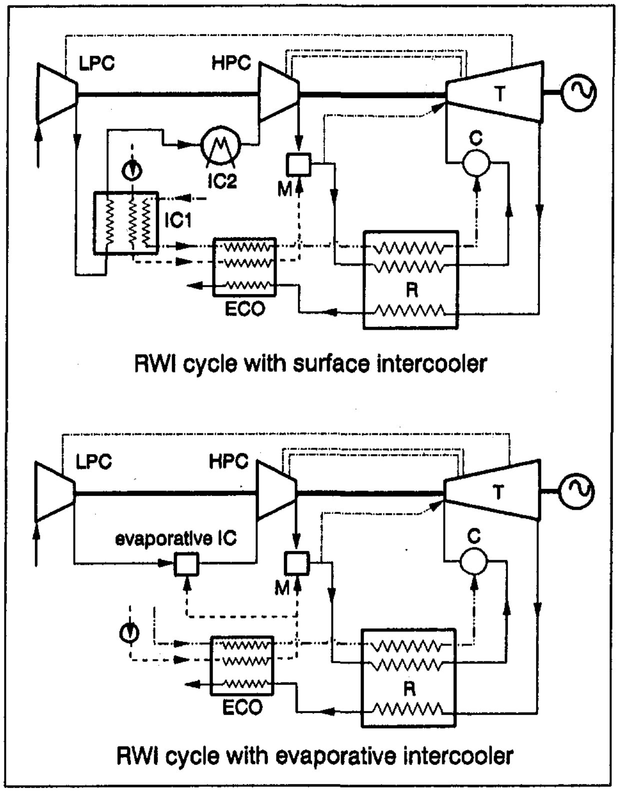

Fig. 1 **Conceptual plant scheme of intercooled water injected recuperated cycles (RWI). The plant can alternatively include intercooling by a surface heat exchanger (upper figure) or by a direct-contact spray heat exchanger (lower figure). LPC = low pressure compressor; HPC = high-pressure compressor; IC1, IC2 = intercoolers; *M* = water/air mixer; *R* = recuperator; ECO = economizer; *C* = combustor; *T* = turbine.**

The intercooler duty is set by imposing an outlet air temperature of 25°C for the surface, heat exchanger, and an outlet relative humidity of 90 percent (to insure that no water droplets enter the HP compressor) for the spray intercooler. Under these hypotheses, for a given overall pressure ratio β there are only two variables that must be optimized: (*i*) the flow rate of water injected into the aftercooler and (*ii*) the intercooling pressure.

Figure 2 shows the influence of the water injection rate on the efficiency of a cycle with TIT = 1250°C and $\beta = 30$; the intercooling pressure ratios β_{LPC} of 3.3 (surface IC) and 5.7 (evaporative IC) are those that give maximum efficiency. Zero injection represents the ICR cycle: In this case the optimum pressure ratio would be 16 (with $\beta_{\mathrm{LPC}} = 4$), with efficiencies in the neighborhood of 48 percent; the adoption of $\beta = 30$ would give a penalty of about 1 percentage point. In the RWI cycle efficiency increases with the injection rate due to the enhanced heat recovery made possible by lower temperatures at the recuperator cold end. For instance, in the case with surface IC the temperature of the gas leaving the recuperator drops from 294°C of the ICR cycle ($\beta = 30$, $\beta_{\mathrm{LPC}} = 5.5$) to 161°C of the RWI cycle with the optimum injection rate of 10.4 percent. At the same time specific work increases from 452 to 589 kJ/kg$_{\mathrm{air}}$ as a consequence of the larger turbine mass flow and specific heat produced by water injection.

It is interesting to notice that maximum efficiency is achieved when the minimum ΔT of 25°C is realized at both ends of the recuperator. The heat–temperature diagrams of this optimum situation are represented in Fig. 3, which compares the RWI cycle with an optimized ICR cycle with $\beta = 16$. In the ICR cycle the ΔT at the cold end of the recuperator is much larger than that at the hot end due to lower air heat capacity (aside from lower specific heat, the air flow is significantly lower due to cooling flows bypassing the recuperator).

Even at the low β adopted in the ICR cycle exhaust gases are discharged at temperatures close to 300°C. In the RWI cycle with optimum injection rate the presence of liquid water in the air entering the recuperator increases the heat capacity of the cold stream and balances the ΔT at the recuperator ends. Injection rates larger than optimum produce a hot-end ΔT larger than that at the cold end, with lower air preheat and thus lower efficiency. The peak of the curves in Fig. 2 results from the intersection of two lines: one corresponding to $\Delta T = 25$°C at the hot end (left branch), the other corresponding to $\Delta T = 25$°C at the cold end (right branch).

The qualitative trend of efficiency versus injection rate is the same for both surface and spray intercoolers. However, with spray IC, maximum efficiency is reached at higher injection rates (12.15 versus 10.41 percent) and higher β_{LPC} (5.7 versus 3.3); the injection rate in the intercooler (7.14 percent) is such that total water consumption is almost twice the one with surface IC.

Figure 4 shows the influence of the intercooling pressure for cycles with $\beta = 30$. Intercooling increases efficiency for two main reasons: lower compressor work and lower cooling air flow. Unlike ISTIG the cycle is recuperated, and therefore the thermodynamic drawback of intercooling (lower air temperature at the combustor inlet) is negligible. Due to the limitations on coolant flow (section 3.1 of Part A), the maximum TIT of 1500°C can be achieved only for $\beta_{\mathrm{LPC}} \gtrsim 2.8$ for surface IC and $\beta_{\mathrm{LPC}} \gtrsim 4$ for spray IC (where the HP compressor and thus the turbine coolant are at higher temperatures). As in ISTIGs, the maximum efficiency of systems with surface IC is achieved at rather low β_{LPC}, due to the importance of limiting the intercooler heat transfer irreversibilities. With evaporative IC, the very similar process accomplished in the intercooler and the aftercooler makes the efficiency curve very flat over a wide range of β_{LPC}. At low β_{LPC} (consider for instance $\beta_{\mathrm{LPC}} = 3$) surface intercooling is more efficient because air is cooled down to a lower temperature (25°C versus 63.1°C), thus reducing HP compression work (−12 percent) and the coolant temperature; these advantages, together with the reduction of exhaust losses (see discussion at section 5.3 of Part A), overcome the larger heat transfer losses in the intercooler. At higher TIT surface IC is even better be-

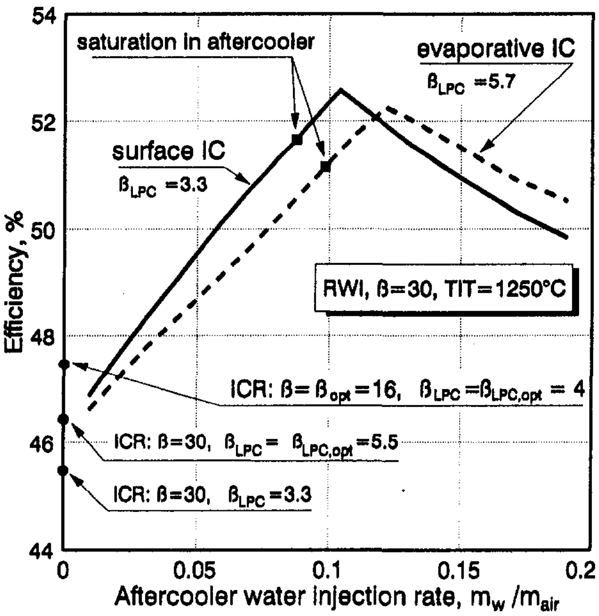

Fig. 2 **Influence of the amount of water injected in the aftercooler (*M* of Fig. 1) on the efficiency of a RWI cycle at TIT = 1250°C, β = 30, and optimum β_{LPC}. The water injection rate is referred to the air flow at the LP compressor inlet. In the scheme with evaporative IC an additional 7.14 percent of the air flow is injected in the intercooler.**

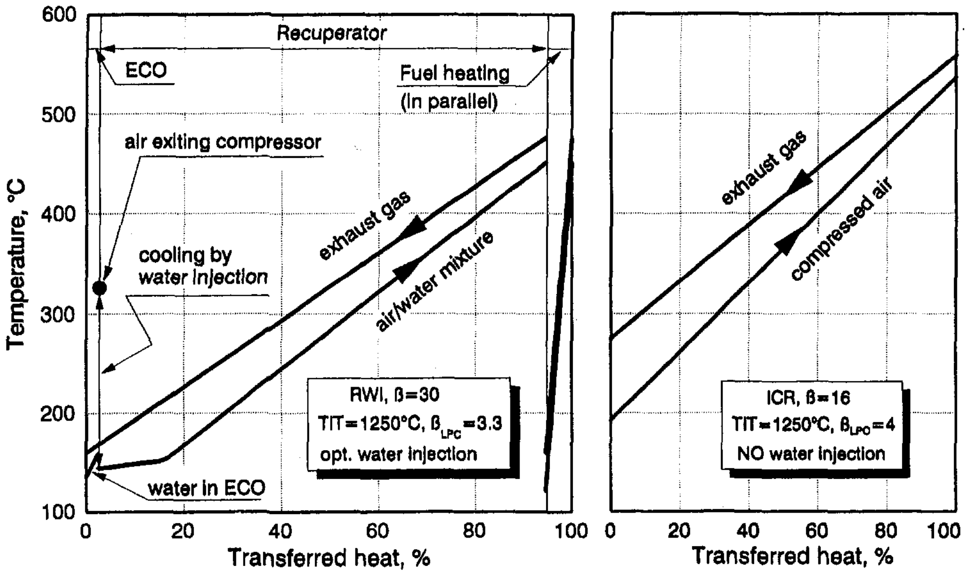

Fig. 3 Heat transfer diagrams of exhaust gas heat recovery for an optimized RWI cycle (left diagram, including the recuperator, the economizer, and the fuel heater) and for an optimized ICR cycle (right diagram, including the recuperator)

cause for $\beta_{LPC} = 3$ it allows a TIT of 1500°C, while spray IC allows at most TIT = 1395°C.

2.2 Results for Optimized Cycles. Figure 5 shows the performances of fully optimized RWI cycles at various pressure ratios. At TIT = 1250°C efficiency peaks at the rather low pressure ratio of 21, but remains very close to its maximum over a wide range of β (for $15 < \beta < 33$ efficiency varies by less than 0.5 percentage points); instead, the increase of specific work with β is substantial. Due to the reasons outlined above, surface IC gives a slight efficiency advantage (0.2–0.4 percentage points). Evaporative IC gives higher specific work; however, as pointed out in section 5.3 of Part A, such increase is obtained by increasing the flow through the HP compressor and the turbine, so that specific work, being referred to the inlet air flow, loses part of its significance as "power for a given hardware."

When taking advantage of the lower coolant temperature to increase TIT (up to the limits discussed in Part A) β_{opt} raises from 21 to about 33, the maximum efficiency achievable with surface IC raises from 52.9 to over 55 percent, and specific work increases by 35 percent. In this case efficiency is substantially more sensitive to β.

Figure 6 reports the operating parameters of the optimized cycle with surface IC, $\beta = 33$, and TIT = 1500°C. Specific work and water consumption are quite similar to the optimized

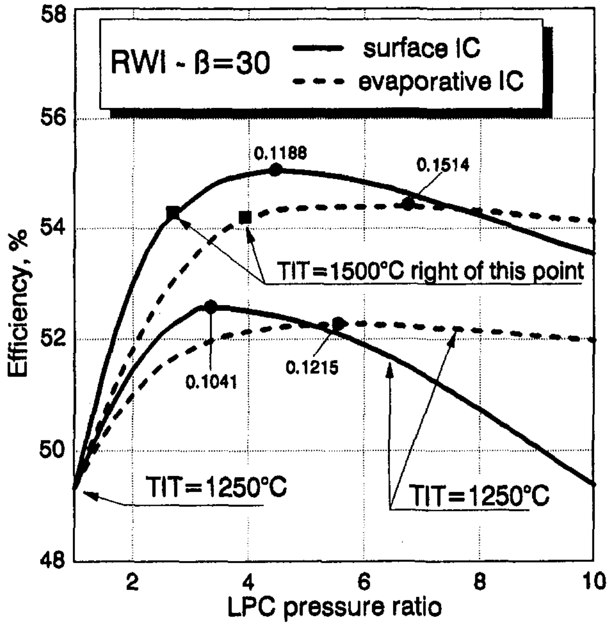

Fig. 4 Efficiency of RWI cycles at $\beta = 30$ as a function of the LP compressor pressure ratio. The numbers on top of the points at maximum efficiency indicate the water injected in the aftercooler as a fraction of the air entering the LP compressor. The portion of the two upper curves with TIT < 1500°C is characterized by "critical" turbine cooling conditions.

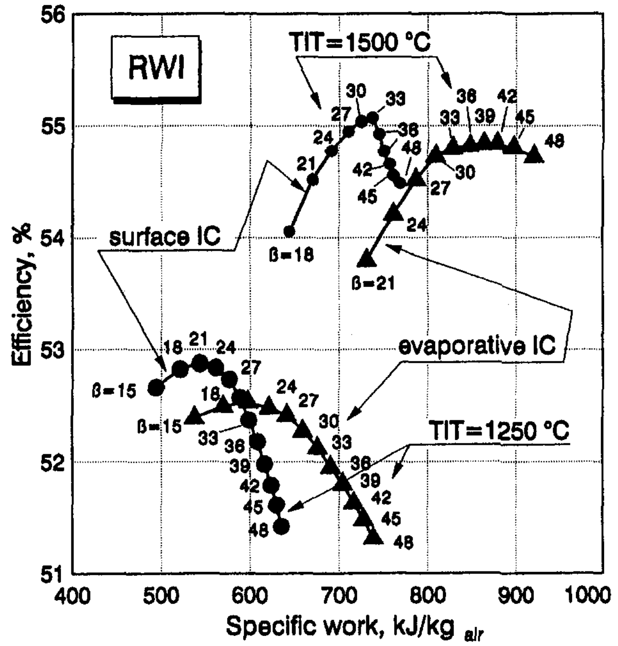

Fig. 5 Efficiency and specific work of RWI cycles with optimum β_{LPC} and water injection rate, for surface and evaporative intercoolers. For the upper curves, the low coolant temperature allows reaching TIT = 1500°C for all β represented in the figure.

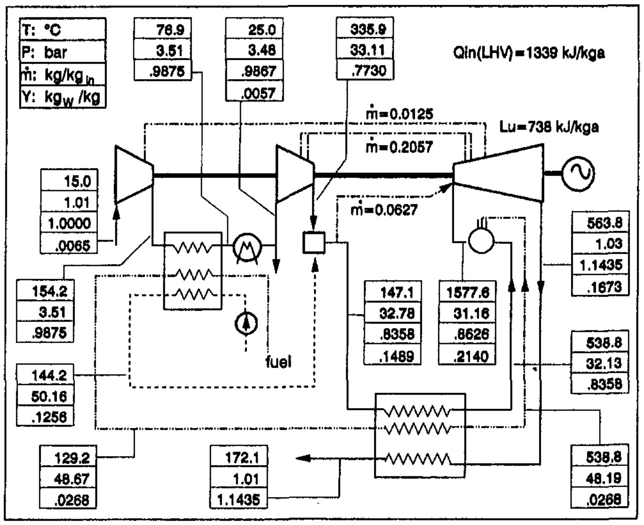

Fig. 6 Temperature, pressure, mass flow (referred to the LPC inlet flow), and water content at the most relevant points of an optimized RWI cycle with surface intercooling, $\beta = 33$ and TIT = 1500°C. Differently from Fig. 1, the scheme does not include the economizer, since the water temperature rise would be negligible in the present cycle conditions.

ISTIG case depicted in Fig. 8 of Part A, while an efficiency gain of almost two percentage points is achieved.

Compared to predictions previously published in Macchi et al. (1991), obtained at a constant TIT of 1250°C, the present estimates are more appealing: Efficiency is higher by about 2 percentage points for RWIs at the same TIT (while for ISTIGs the results of the quoted previous paper are basically confirmed). This is mainly due to less conservative hypotheses on the heat transfer equipment (minimum ΔT, pressure loss) and to the adoption of surface intercooler and of fuel heating.

3 HAT Cycles

Since the first proposal of the HAT cycle advanced by Rao (1989), several authors have carried out general studies aiming at finding the optimum plant configuration and operating parameters of this innovative and rather complex cycle. As summarized in Table 1, operating conditions and predictions reported by various authors cover a rather wide range. Although there is a consensus on the superiority of HAT over combined cycles, performance projections are somewhat controversial: Predicted HAT efficiencies vary between 53.5 and 57.4 percent, while the efficiency gain over combined cycles based on comparable technology ranges between 0.9 and 4 percentage points.

Table 1 Performances of gas-fired HAT cycles reported in the literature. Day and Rao (1992) refer to an advanced aeroderivative gas turbine (P& W FT4000) adapted to HAT conditions. Rao (1991) considers two cases (second and third column) respectively based on ABB and GE gas turbines with unspecified characteristics. Lindgren et al. (1992) refer to a heavy-duty 100 MW class gas turbine. All the plant schemes are very similar to the one in Fig. 7 (lower part). Stecco et al. (1993) do not consider a specific unit and include a heat exchanger lowering the temperature of water exiting the saturator.

Authors	Day and Rao (1992)	Rao et al. (1991)	Rao et al. (1991)	Lindgren et al. (1992)	Stecco et al. (1993)
LHV efficiency, %	55.8	57.4	53.5	55.3	54.0
Specific work, kJ/kg$_a$	735	718	638	503	370
TIT, °C	1320	n.d.	n.d.	1163	1000
Pressure ratio β	40.2	24.3	23.3	12.5	9
Reference combined cycle efficiency, %	52.9	53.4	49.5	54.4	-

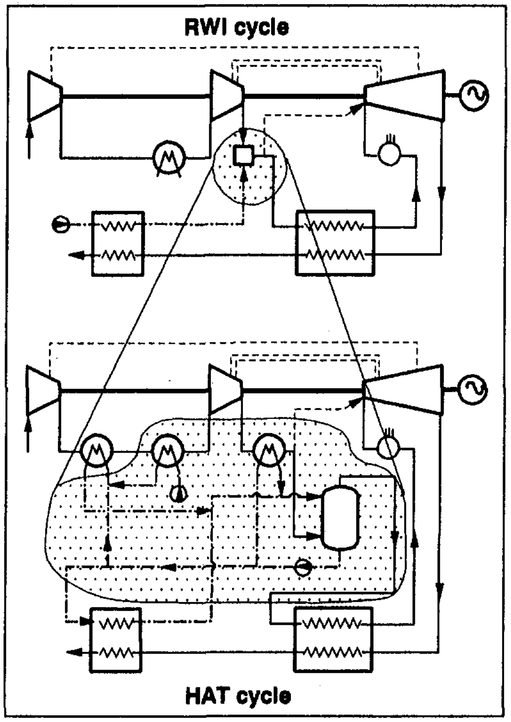

Fig. 7 Simplified plant scheme of the HAT cycle, showing the similarities with the RWI cycle

The parametric analysis developed in the following section aims at (*i*) identifying the best plant arrangement and (*ii*) predicting the influence of the operating parameters and the technological scenario on plant performance.

3.1 Improvements of HAT Cycles Versus RWI Cycles.

The HAT cycle shares several features already present in the RWI cycle discussed in the previous section:

1 Both are intercooled, recuperated gas turbine cycles, whereby water injection is used to improve efficiency and specific power;
2 in both cases, the exhaust gases leaving the recuperator enter an economizer, where they are further cooled by transferring heat to the water to be injected;
3 air coming out of the HP compressor is aftercooled.

The two basic plant schemes shown in Fig. 7 point out analogies and differences between the two concepts. In the HAT cycle the water loop is by far more complex: It includes heat recovery from three sources (intercooler, aftercooler, and economizer) and a specific device (the saturator) for air/water mixing. Air aftercooling and air/water mixing are accomplished in the RWI cycle by a single, highly irreversible process, i.e., by injecting hot water into a relatively high-temperature air stream: Evaporation takes place at a temperature much lower than those of the two streams being mixed, thus generating a significant efficiency loss (for the optimized RWI cycle considered in section 2, about 2 percentage points).

The basic idea behind the HAT cycle is to reduce this loss by separating aftercooling from water injection: First, air exiting the HP compressor is cooled by means of surface heat exchangers; then hot water produced in various heat recovery processes is injected into air much more reversibly. This is accomplished in a counterflow heat/mass transfer column (the saturator), which gradually heats and humidifies the air stream. One further advantage of HAT versus RWI cycles is the capability of recovering a significant (yet the most valuable) fraction of the heat released in the intercooler and by the low temperature exhaust gases. In the RWI cycle the heat made available by these sources is more than enough for heating the optimum water injection flow; thus, the extra heat must be wasted to the ambient, with an additional efficiency loss of about 1.5 percentage point.

3.2 The Saturator Model. The saturator is the innovative power cycle component of the HAT cycle. It consists of a countercurrent heat/mass transfer column for which the following enthalpy and mass global balances apply:

$$\dot{m}_{w,in} - \dot{m}_{w,ex} = \dot{m}_a' \cdot (Y_{a,ex} - Y_{a,in}) \quad (1)$$

$$\dot{m}_{w,in} \cdot i_{w,in} - \dot{m}_{w,ex} \cdot i_{w,ex} = \dot{m}_a' \cdot (i'_{a,ex} - i'_{a,in}) \quad (2)$$

Even if respectful of Eqs. (1)–(2), if a process to be accomplished in the saturator does not meet additional constraints, it may be considered infeasible. A comparison with a more familiar heat exchanger like the HRSG may help understand the problem: The stipulated heat transfer process is feasible when the temperature difference between hot gases and water or steam (i.e., the driving force of heat transfer) is positive at every location; a positive ΔT at the hot and cold end cannot guarantee a positive ΔT at the pinch point, even if the overall heat balance is respected. The same holds for the saturator, with the difference that we must consider both heat and mass transfer. The concept of heat flux may still hold if we consider it as the sum of sensible and latent heat.

For an infinitesimal interface surface dS the heat transfer between the two countercurrent streams is ruled by the following equation:

$$h_w(T_w - T_i) \cdot dS = h_a(T_i - T_a) \cdot dS + d\dot{m}_w \cdot \lambda(T_i) \quad (3)$$

where the left-hand side (LHS) is the sensible heat released by the liquid, and the two terms on the right-hand side (RHS) are the sensible and the latent heat received by the air, respectively. In Eq. (3):

$$d\dot{m}_w = k \cdot \ln\,[(1 - x_{w,a})/(1 - x_{w,i})] \cdot dS \quad (4)$$

is the water transferred to the gas phase through the surface dS. The molal fraction difference and the temperature difference between interface and air bulk phase can be seen as the forces that drive the transfer of mass and heat, respectively. The two driving forces can act in the same ($T_a < T_i$ and $x_{w,a} < x_{w,i}$) or in opposite directions; however, to ensure that the process in the saturator is feasible the overall energy flux (sum of sensible and latent heat) must go from water to air over the whole length of the saturator. According to our sign assumption, this means that both sides of Eq. (3) must be positive. If the limit condition (LHS = RHS = 0) is reached at any point of the saturator, the surface (i.e., the height) of the saturator tends to infinity, as an infinite surface is needed in a HRSG where the pinch point ΔT tends to zero. When the limit condition occurs, it means that the $i^* = i'_a$, where i^* is the enthalpy of saturated air at temperature T_w and i'_a is the enthalpy of air (in bulk phase) exchanging heat with water at the temperature T_w. Therefore, imposing a minimum enthalpy difference between i^* and i'_a is equivalent to setting a minimum ΔT at the pinch point of a HRSG.

Unfortunately, even under one-dimensional hypotheses the computation of i'_a along the saturator calls for the solution of a nonlinear differential system with five equations; mass balance, mass transfer, heat transfer from water to interface and from interface to gas, enthalpy balance (Chiesa, 1993). Solving this system would be too time-consuming for general parametric analyses like those carried out in this paper, whereby hundreds of cycles have to be computed during the optimization procedure. Thus, the feasibility of the process taking place in the saturator has been verified by a simplified method: The real i'_a curve in the i–T diagram is substituted by the straight line connecting its two extremes; since this line is always above the real i'_a curve (Fig. 8), checking heat/mass transfer feasibility by referring to such line is conservative, and provides a Δi margin to the real process.

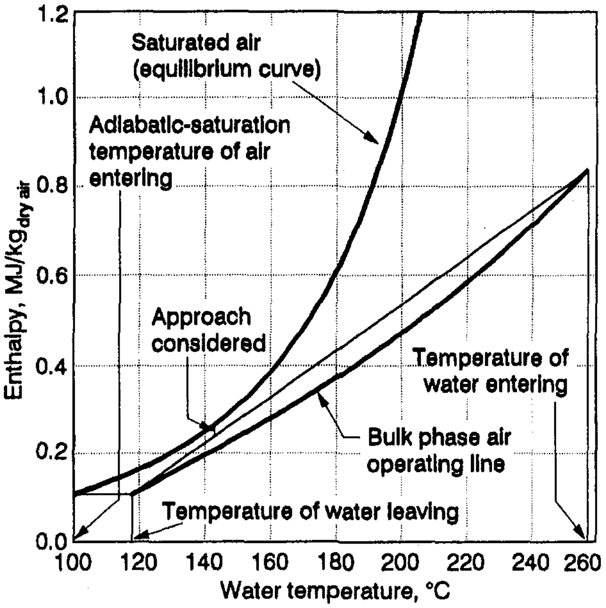

Fig. 8 Temperature–enthalpy diagram of a saturator. The saturation line represents the enthalpy of saturated air; the operating line represents the enthalpy of the bulk phase air stream in contact with water at the temperature indicated on the abscissa. To insure that heat–mass transfer effectively takes place from water to air, it is necessary that a positive Δi exist between the saturation and the operating line. The simplified approach adopted in this paper verifies Δi by approximating the operating line with the straight line shown in the figure.

In practice, the calculation of the saturator is performed as follows:

- After guessing the temperature and the humidity of air at the saturator exit (for our calculations the latter is always 100 percent), the temperature and the mass flow of water at the cold end are found by Eqs. (1) and (2).
- The straight line connecting the extremes of i'_a is compared with the saturation curve.
- If the minimum difference between the line and the saturation curve is different from the desired value, the temperature assumed for the air at the hot end is revised, and the calculation goes back to the first step.

Figure 9 depicts the saturator operating conditions typically corresponding to optimal HAT configurations. Diagrams are based on a one-dimensional differential model developed by Chiesa (1993). Two distinct processes can be individuated:

- In the lower section, the air relative humidity increases from almost dry inlet conditions to saturation: Its temperature first decreases (implying that the two terms in the RHS of Eq. (3) have opposite sign), then increases. Due to the small temperature difference between water and the interface ($T_w - T_i$, governing the heat transfer as from the LHS of Eq. (3), is typically less than 10°C), this process is characterized by relatively low heat fluxes, thus requiring a large portion of the saturator (according to Fig. 9, about 50 percent of the total saturator height, even if less than 20 percent of the total heat has been transferred).
- In the upper section saturated air gradually increases its temperature and water content up to the outlet conditions. Heat fluxes increase drastically as a consequence of vigorous mass transfer on the air side: The latent heat transfer (second term of the RHS of Eq. (3)) becomes predominant, sus-

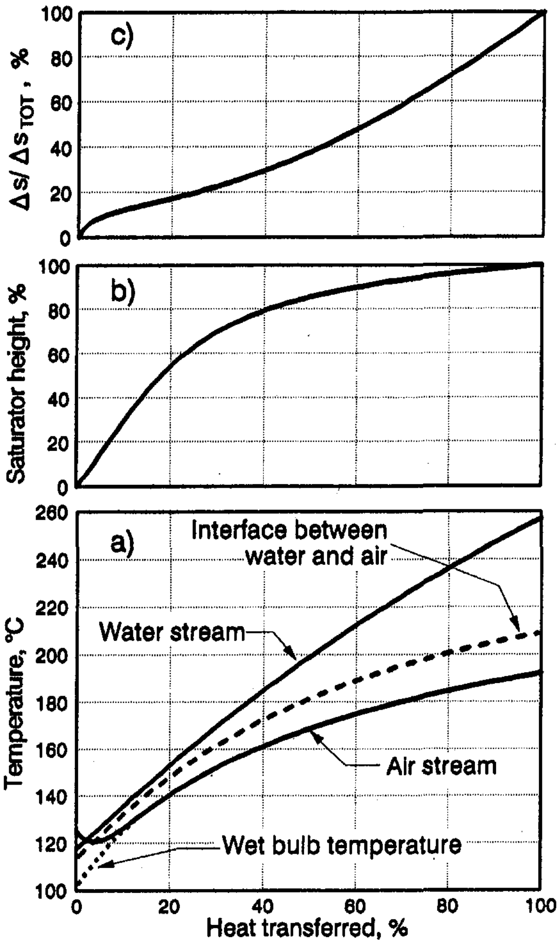

Fig. 9 Entropy generation, height, and temperature versus heat exchanged for the saturator of a HAT cycle. The lower diagram shows the temperatures of the bulk phase water, of the water-air interface, and of the air stream. Except in the lower portion, the latter coincides with the wet bulb temperature (saturated conditions). The middle diagram shows the saturator height necessary to transfer the heat quantity indicated along the abscissa.

taining a large temperature difference between water and interface ($T_w - T_i$), thus enhancing heat flux, while ($T_i - T_a$) remains relatively small.

The rate of entropy generation (a quantity proportional to the cycle efficiency loss) is highest at the two extremities: At the cold end this is due to water mixing into a nonsaturated mixture, at the hot end to the large temperature difference occurring between water and air (it is helpful to remember that injecting water into saturated air is a reversible process, since water no longer evaporates, only if the two streams are at the same temperature).

3.3 Plant Arrangement. As already mentioned, several plant arrangements have been proposed for HAT cycles. Differences among the various proposals concern the number and the location of air/water exchangers cooling the air at the exit of the LP and HP compressor, as well as the distribution of water among the various heat exchangers. In the attempt to include all possible schemes, we have selected the complex configuration represented in Fig. 10:

- Air exiting the LP compressor LPC is sequentially cooled by: (*i*) water recirculated from the saturator bottom (heat exchanger IC1); (*ii*) make-up water (heat exchanger IC2), which is then mixed with saturator water ahead of IC1; (*iii*) a cooler IC3 dissipating heat to ambient. IC3 allows minimizing the HP compressor work also when the makeup water flow in IC2 is insufficient to accomplish maximum air cooling.
- A similar sequence is arranged downstream of the HP compressor HPC, where heat exchangers AC1, AC2, and AC3 serve like IC1, IC2, and IC3 (in a real plant the three heat exchangers of each line can be arranged in a single shell).
- The heat exchanger ACf further heats the mixture of the two streams of water used for inter- and after-cooling. ACf can be placed immediately after the HP compressor (as indicated in Fig. 10) or immediately after the LP compressor, depending upon the temperatures at their discharge.
- Water exiting from ACf is mixed with water coming from the economizer (*E*) and the whole stream is finally routed to the top of the saturator.
- The ''nonchargeable'' turbine cooling flow is taken from the saturator exit (to take advantage of the superior cooling properties of humid air), while the ''chargeable'' flow is bled, as usual, from the HP compressor.
- Fuel preheat is accomplished sequentially in (*i*) a countercurrent heat exchanger cooling the water exiting the bottom of the saturator and (*ii*) the recuperator.
- The plant scheme is completed by the saturator *S*, the recuperator *R*, the combustor *C*, and the turbine *T*, which are present in all schemes.

The configurations considered in the papers quoted in Table 1 are somewhat less general than the one depicted in Fig. 10 because: (*i*) Day and Rao (1992) do not include heat exchangers IC2, IC3, ACf, AC2, and AC3, while the former, more detailed report from Rao et al. (1991) omits only AC2 and AC3; (*ii*) Lindgren et al. (1992) do not include IC3, ACf, AC2, and AC3; (*iii*) Stecco et al. (1993) do not consider IC2, IC3, ACf, AC2, and AC3, but add a cooler for the water exiting the saturator playing a role conceptually equivalent to IC3 and AC3.

All these schemes can be reproduced by setting to zero the duty of one or more of the heat exchangers in Fig. 10, i.e., by properly setting one or more of the variables defining the cycle. Thus, whether the general scheme considered here or some of the variations considered by other authors gives the highest efficiency can be assessed by optimizing the comprehensive configuration of Fig. 10.

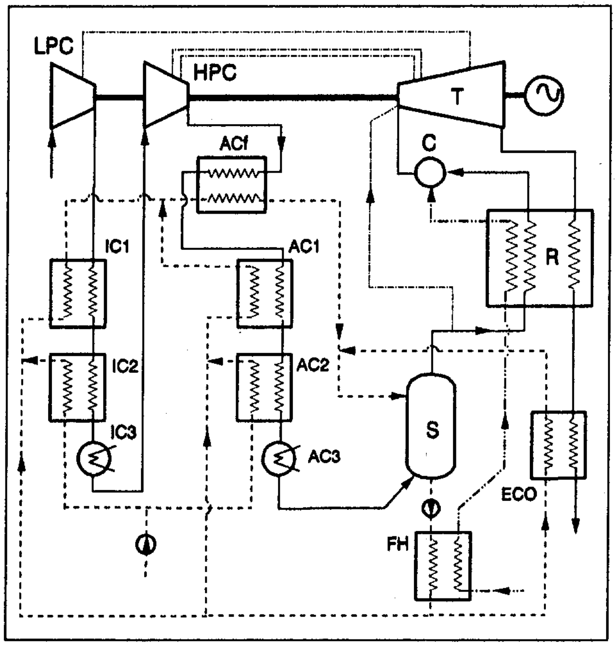

Fig. 10 Complete plant scheme of the HAT cycle considered in this paper

3.4 Plant Optimization. Given the overall pressure ratio, the seven variables that could be arbitrarily selected and therefore must be optimized are:

- intercooling pressure;
- water/air flow ratio in the saturator;
- heat dissipated to ambient, i.e., air temperatures at exit of IC3 and AC3 (two variables);
- flow split at the bottom of the saturator, where water is sent to the economizer, the intercoolers, and the aftercoolers (two variables);
- flow split of the makeup water, which can be sent either to the intercooler or the aftercooler (one variable).

In carrying out preliminary optimizations, it became apparent that three of these variables always reached their limit value:

- It is always more efficient to use the entire flow rate of makeup water for intercooling, i.e., the optimum duty of heat exchanger AC2 is zero. If only 10 percent of makeup water goes to AC2, efficiency drops by about 0.15 points.
- It is always more efficient to reach the lowest intercooling temperature at the exit of heat exchanger IC3. If air exits from IC3 at 35°C, instead of 25°C as assumed here, efficiency drops by about 0.1 points.
- It is better not to waste heat along the HP line (aftercoolers), i.e., the optimum duty of heat exchanger AC3 is zero. An air temperature drop of 10°C in AC3 (instead of 0°C) causes an efficiency drop of about 0.1 points.

These conclusions have a thermodynamic rationale. The cycle benefits from low intercooling temperatures for various reasons (lower temperature of cooling flows, lower irreversibilities of air–water heat transfer, lower compression work); hence, it is preferable to use the available cold source (makeup water) in the intercooler and then, since its thermal capacity is inadequate to reach the minimum temperature, discharge heat to ambient from the LP rather than from the HP line. Conversely, along the HP line aftercooling must be limited, because the loss due to heat discharge in AC3 cannot be compensated by enhanced heat recovery made possible by colder water at the saturator bottom. Following these considerations, all final calculations have been carried out without heat exchangers AC2 and AC3 (thus resuming the scheme of Rao et al., 1991), while the temperature at the entrance of the HP compressor has been kept to its minimum value of 25°C.

The influence of the other four variables to be optimized is not so straightforward, so that a proper optimization must be performed for each set of cycle parameters (β and TIT).

First, let us consider the effect of β_{LPC} at constant pressure ratio ($\beta = 30$) depicted in Fig. 11: Maximum efficiency is reached for values slightly higher than the one giving minimum compressor work. The optimum β_{LPC} yields the best combination among (*i*) advantages of lower turbine coolant temperature; (*ii*) minimization of the temperature difference between water exiting the intercooler (LP line) and water exiting the aftercooler (HP line); (*iii*) minimization of heat dissipated in IC3.

Figure 12 shows the sensitivity of the efficiency of a cycle with $\beta = 30$ and TIT = 1250°C to the water/air mass flow ratio at the saturator entrance. For values of this ratio lower than optimum, air/gas cooling in IC1, AC1, and ECO is incomplete, resulting in a quite sharp efficiency drop due to: (*i*) irreversibilities occurring in the lower part of the saturator, fed by air much warmer than the exiting water, (*ii*) more heat dissipated in heat exchanger IC3, (*iii*) large temperature differences in the air coolers, and (*iv*) larger exhaust losses. For water/air ratios higher than optimum the efficiency curve is quite flat: There is only a slight decrease of air outlet temperature (and therefore of the amount of water evaporated) due to the lower water temperature exiting from the various heat exchangers. As may be expected, the optimum value of the overall water flow corresponds to the situation for which the heat capacities of water and air/gas streams are balanced in all three exchangers IC1, AC1, and ECO, thereby minimizing heat transfer irreversibilities.[2]

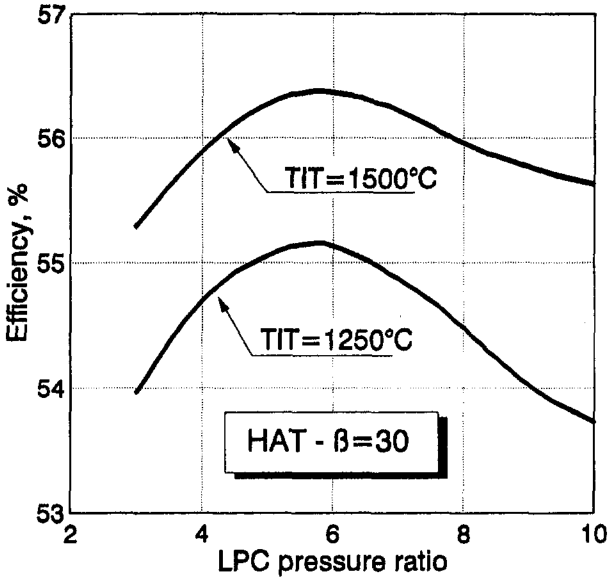

Fig. 11 Efficiency versus intercooling pressure for HAT cycles with $\beta = 30$

This statement also solves the problem of the optimum split of the water coming out of the saturator: Unbalanced heat capacities in either IC1 or AC1 would provide less heat recovery or would decrease the hot water temperature, thus penalizing the saturator and the cycle performance.

3.5 Results of Parametric Analysis. Figure 13 summarizes the results of the parametric analysis in the specific work-efficiency plane. As for the other cycles we have considered two cases: a curve for TIT = 1250°C, consistent with the conservative assumption of maintaining the same TIT of a nonintercooled machine, and a curve for which, owing to lower turbine coolant temperatures, TIT can be increased up to the limits discussed in Part A, section 3. At optimum β the efficiency gain brought about by higher TIT is about 2 percentage points, a result similar to that already found for ISTIG and RWI cycles. HAT cycles give significantly better performance than all other air/steam mixed cycles: The gain is over 2 percentage points in efficiency and about 100 kJ/kg in specific work. Figure 13 clearly shows the influence of the overall pressure ratio: Values usually adopted in modern simple-cycle aero-engines (20–30) are optimum at TIT = 1250°C, but larger β are necessary to exploit the benefits of higher TITs: At 1500°C the optimum β is 48.

As in all thermodynamic analyses of power cycles, results depend strongly on the assumptions concerning the "quality" of the cycle components. As discussed in Part A, all calculations performed in this paper refer to "state-of-the-art" components, i.e., turbomachines with excellent aerodynamic design, heat exchangers with low pressure drops and low ΔTs. For most components (gas turbines, steam turbines, HRSGs, etc.), these assumptions are derived from well-established engineering standards and reproduce the situation occurring in a real plant. Since the HAT cycle makes use of some "unconventional" components (inter/aftercooler, recuperator, saturator), with characteristics not predictable with the same degree of accuracy, it is worth investigating the sensitivity of the cycle performance

---

[2] In the economizer (ECO) this balance cannot always be maintained, because at the highest TIT considered in Fig. 14 it would require exceedingly high water temperature and pressure. This is avoided by increasing the water flow, which, as shown in Fig. 12, does not significantly penalize efficiency.

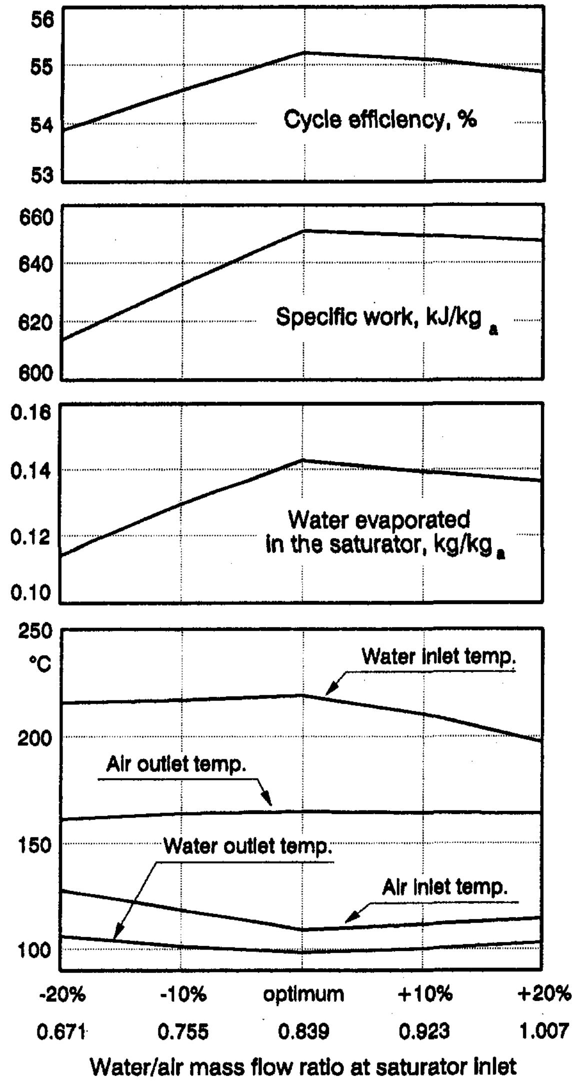

Fig. 12 Influence of the water/air mass flow ratio at saturator inlet for a HAT cycle with β = 30 and TIT = 1250°C. It is assumed that the percentage flow split among IC1, AC1, and ECO (see Fig. 10) is the same as the optimized case.

to the assumptions regarding their characteristics. The results of this analysis are shown in Table 2, showing the variations of efficiency and specific work for the cycle with β = 48 and TIT = 1500°C. The most conservative combination (the rather pessimistic situation of the last row in the table) gives an efficiency penalty of about 2 percentage points. The corresponding cycle efficiency is still about 55 percent (versus 57 percent of the cycle using the general assumptions of Table 2, Part A), confirming the excellent thermodynamic quality of the HAT cycle. Since the efficiency range spanned by the HAT sensitivity analysis covers the 55.8 percent efficiency predicted for the combined cycle (Fig. 4 of Part A), the two systems appear as very close competitors, with their relative standing crucially depending on the characteristics of heat transfer equipment.

Eventually, Fig. 14 reports the main cycle parameters of the fully optimized HAT plant achieving the highest efficiency.

4 Comparison of Mixed Air/Steam Cycles According to Second-Law Analysis

It is well known that the so-called second law (or exergy) analysis, i.e., the calculation of the efficiency loss generated by the irreversibilities occurring in each component, is a powerful tool to gain a better understanding of the thermodynamic merits of complex cycles. Table 3 summarizes the results obtained by applying this approach to the cycles considered in both parts of the paper.

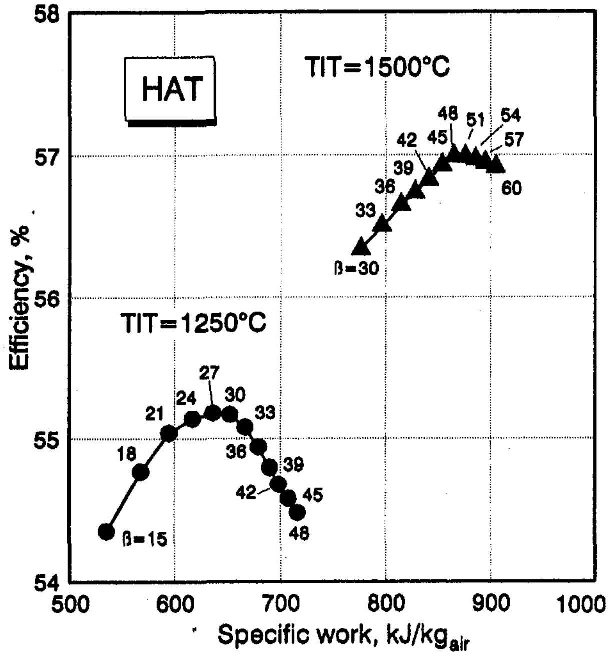

Fig. 13 Efficiency versus specific work of optimized HAT cycles. For the upper curve, the low coolant temperature allows reaching TIT = 1500°C for all β represented in the figure.

By far, the two largest irreversibilities of the simple cycle (the "reference" aeroderivative engine) are due to combustion and to the discharge of hot gases to ambient, which altogether cause an efficiency loss of about 50 percentage points. All complex cycles succeed in achieving dramatic reductions of the discharge loss (16–17 points out of 22.6 in mixed cycles, more than 20 points in the combined cycle), but no one really eliminates a significant fraction of combustion losses: gains are limited to 3–4 efficiency points, mostly due to fuel preheat and to the higher TIT made possible by intercooling. Apart from the increase of TIT, the only way to decrease combustion irreversibilities would be to increase the air temperature at the combustor inlet. With this regard the adoption of a reheat turbine (a further "complication" of the plant not considered here) together with larger recuperator loads can produce some improvement: The results presented in Macchi et al. (1991, with assumptions slightly different from those considered here) show that for ISTIG and RWI cycles the gain is about 2 percentage points.

Coming to a more specific analysis of the various terms in Table 3, the following points, common to all cycles, can be made:

Table 2 Sensitivity of efficiency and specific work of a HAT cycle (β = 48, TIT = 1500°C) to the assumptions concerning the heat/mass transfer equipment. The variation of the saturator driving force corresponds to a 20 percent reduction of the column height.

Variable subject to sensitivity analysis	Assumed value	Modified value	Loss of efficiency	Loss of specific work, %
Water-air heat exchangers ΔTmin	10°C	20°C	-0.61	-1.81
Water-air heat exchangers Δp/p	1%	2%	-0.24	-0.53
Recuperator ΔTmin	25°C	50°C	-0.36	+4.07
Recuperator Δp/p (both sides)	2%	4%	-0.35	-1.08
Saturator gas-side Δp/p	0.7%	1.4%	-0.06	-0.17
Saturator minimum driving force	27 kJ/kg	54 kJ/kg	-0.23	-0.93
All together	-	-	-2.11	-2.03

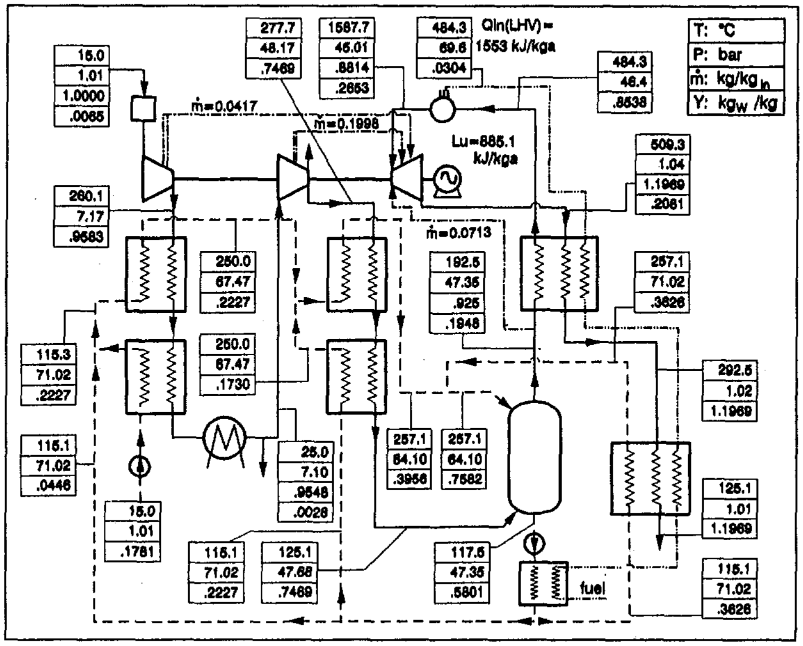

Fig. 14 Temperature, pressure, mass flow (referred to the LPC inlet flow), and water content at the most relevant points of an optimized HAT cycle with $\beta = 48$ and TIT = 1500°C

- In spite of the larger β required by efficiency optimization, intercooling produces a decrease of about 1.3 percentage points of compressor fluid-dynamic losses; however, in ICC, ISTIG, and RWI cycles this benefit is counterbalanced by the heat-exchange loss of the intercooler. Only HAT cycles accomplish intercooling in a quasi-reversible mode.

Table 3 Second-law analysis of various optimized mixed cycles

Cycle Loss source β TIT,°C	Simple 30 1250	ICC(i) 46 1500	ISTIG 45 1500	RWI 33 1500	HAT 48 1500
Combustion	27.318	26.504	24.531	23.122	23.483
Compression	4.070	3.252	2.770	2.744	2.645
Expansion	6.367	6.632	7.237	7.850	8.032
Intercooling	-	1.316	1.465	0.995	0.499
Recuperation	-	-	-	2.499	1.036
Saturator	-	-	-	-	1.232
Air/steam mixing	-	-	3.387	-	-
Aftercooling	-	-	-	1.796	0.134
Heat recovery	-	5.220 (ii)	1.860 (HRSG)	-	0.392 (ECO)
Pressure losses (iii)	-	0.292	0.319	0.378	0.384
Exhaust discharge	22.645	1.472	5.941	6.257	5.965
Others (iv)	1.249	1.660	0.980	1.066	1.066
2nd law efficiency	38.351	53.652	51.503	53.293	55.132
1st law efficiency	39.67	55.51	53.23	55.08	56.98

Notes:

(i) Intercooled Combined Cycle, based on an aero-derivative engine (see Part A, section 4) with $\beta_{LPC} = 3.5$. The steam cycle is a three-pressure nonreheat cycle (85/15/3 bar). Intercooling heat is recovered by producing steam at 1.4 bar, used in the steam turbine.

(ii) Includes all losses of the bottoming cycle (1.861 HRSG heat transfer, 1.570 steam turbine, 1.615 condenser, 0.174 steam pressure losses and mixing).

(iii) In components not present in the simple cycle.

(iv) Mainly due to electric/mechanical losses, auxiliaries consumption, fuel heating, and compression losses.

- The "indirect" effect of intercooling, i.e., the availability of low-temperature coolant for the turbine, allows higher TITs and therefore lower combustion losses (2–3 points).
- Water/steam injection in the air stream increases turbine losses of about 1–1.5 percentage points, mainly because of the larger turbine work.
- Compared to the simple cycle, mixed cycles do drastically reduce the loss due to exhaust discharge, but not as thoroughly as the combined cycle: The discharge loss drops to 5–6 points versus 1.3 points of the combined cycle. The difference is due to the large amount of water vapor discharged with the gas; even if its "thermodynamic value" is low (it can be condensed only at low temperature), its huge heat of evaporation makes the related loss significant.
- The penalty produced by pressure losses in heat transfer equipment is rather small: only 0.3–0.4 percentage points.

Although all mixed cycles have a somewhat similar loss distribution, some comments can be drawn about the specific merits (and drawbacks) of the various solutions:

- ISTIG cycles are significantly penalized by steam mixing losses (almost 3.5 points), while the complex arrangement selected for the HRSG allows limiting heat recovery losses below 2 percentage points, lower than those of the recuperator of RWIs, or of the combination recuperator-saturator of HATs.
- The higher efficiency of the RWI versus the ISTIG cycle (2 percentage points) is mainly due to: (*i*) more efficient mixing and heat transfer (recuperator + aftercooler losses in RWI are about 1 percentage point lower than mixing + HRSG losses in ISTIG); (*ii*) lower combustion losses, which benefit from the higher air temperature at the combustor inlet (537 versus 483°C).
- The superiority of HAT cycles over other mixed cycles (for the same TIT about 2 points versus RWI, 4 points versus ISTIG) is mainly due to the more efficient heat transfer and mixing mechanism accomplished in the saturator, and to the capability of efficiently recovering the intercooling heat.
- The intercooled combined cycle is also a very efficient solution, but not as good as HAT. Very efficient heat transfer and mixing

allows HAT cycles to compensate fully for the exhaust loss (almost 6 percentage points, versus 1.5 points in ICC), thus achieving the highest efficiencies of all cycles considered.

5 Conclusions

The essence of the analysis developed in this two-part paper can be captured by considering Fig. 15, which reports efficiency and power output of all cycle configurations considered in the paper under conditions giving maximum efficiency. Unlike Figs. 1 and 2 of Part A, in this figure the power output of all configurations based on modified versions of the "reference" aero-engine (simple cycle giving about 40 MW with 40 percent efficiency, see Table 1 of Part A) is calculated by imposing that the cross-sectional area at the exit of the HP compressor is always the same of the reference engine; this is consistent with the assumption made by Day and Rao (1992), and implies that modified versions can operate with essentially the same HP compressor of the reference engine. The figure also reports the performance of single-shaft combined cycles based on the "reference" heavy-duty machine (about 220 MW with 36 percent efficiency, see again Table 1 of Part A).

The comprehensive representation of Fig. 15 suggests the wide range of possibilities opened by mixed cycles and emphasizes two points:

- Intercooling remarkably enhances efficiency and power output of simple and combined cycles based on aero-engines. Notice that simple cycle achieves its maximum efficiency at a pressure ratio as high as 82. For the range of TIT considered (1250 to 1500°C), a combined cycle with an intercooled machine reaches efficiencies ranging between 53.5 and 55.5 percent. With respect to other solutions, this probably requires a minimum amount of modifications to the base engine.
- HAT provides the best performance. For the same TIT, its efficiency is about 1.5 percentage points higher than that of ICCs based on aero-engines; besides, by taking full advantage of low coolant temperatures to increase TIT, HAT efficiencies are also higher than those of the best combined cycles based on large-scale heavy-frame.

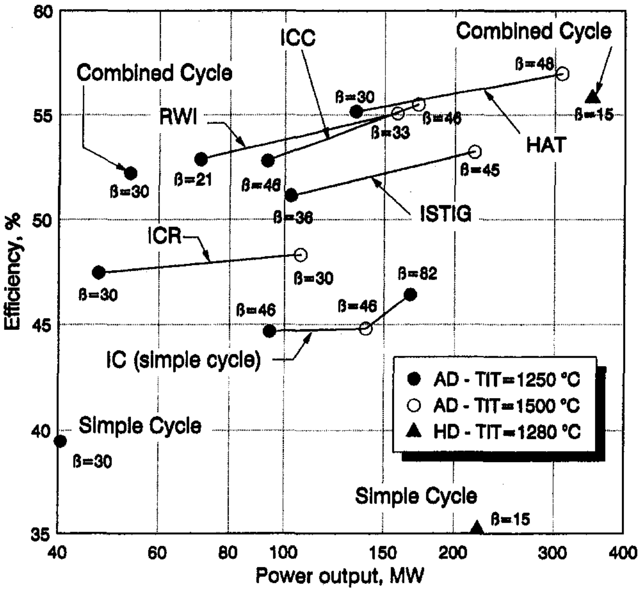

Fig. 15 Performance achievable by the various cycles considered in this two-part paper under conditions giving maximum efficiency. The power output of cycles based on aero-engines is calculated by assuming the same HP compressor outlet volume flow of the "reference" engine of Table 1, Part A.

Table 4 Water consumption for cycles considered in the paper

Cycle type	Water use, kg/kWh
CC (heavy-duty GT)	0.892
ICC (aero-deriv. GT)	0.735
ISTIG (fig.8, Part A)	0.738
RWI (fig.6, Part B)	0.613
HAT (fig.14, Part B)	0.724

Obviously, all mixed-cycle solutions require substantial R&D resources for the development of modified versions of current simple cycle aero-engines. In addition, it is difficult to anticipate their economic feasibility, even if all major aero-engine manufacturers agree in claiming that intercooled machines, ISTIG, and HAT are low-specific-cost systems (Horner, 1988; Day and Rao, 1992; Roberts, 1993).

Another important aspect is that all mixed cycles require large amounts of makeup water. However, Table 4 shows that makeup water requirements are approximately the same as combined cycles using wet cooling towers (due to the smaller power fraction produced by the steam cycle, the heat discharged by the condenser of a combined cycle based on an intercooled aero-engine is smaller than for a heavy-duty). Notice that the figures in Table 4 do not account for the blowdown necessary to keep a constant quality of the cooling tower water: Since its amount is generally 40–80 percent of the water evaporated (depending on the makeup water quality) the actual consumption of CCs equipped with wet cooling towers becomes significantly higher than other cycles.

For ISTIG, RWI, and HAT cycles, it should be also considered that: (*i*) the water treatment cost is definitely low when compared to the overall operating costs; (*ii*) water can be recovered from exhaust gas condensation, either by a direct-contact (Day and Rao, 1992) or by a low-cost surface heat exchanger (Macchi and Poggio, 1994).

References

Chiesa, P., 1993, "Thermodynamic Analysis of Humid Air Gas Turbine Cycles (HAT)," *Proc. of VII Italian National Congress on Combined Cycles*, Milan, Italy, Oct. [in Italian], pp. 169–188.

Crisalli, A. J., and Parker, M. L., 1993, "Overview of the WR-21 Intercooled Recuperated Gas Turbine Engine System—A Modern Engine for a Modern Fleet," ASME Paper No. 93-GT-231.

Day, W. H., and Rao, A. D., 1992, "FT4000 HAT With Natural Gas Fuel," *Proc. of ASME Cogen-Turbo Congress*, Houston, TX, pp. 239–245.

El-Masri, M. A., 1988, "A Modified, High-Efficiency, Recuperated Gas Turbine Cycle," ASME JOURNAL OF ENGINEERING FOR GAS TURBINES AND POWER, Vol. 110, pp. 233–242.

Horner, M., 1989, "LM8000 ISTIG Power Plant," presentation given by the GE Marine and Industrial Engine Division, Cincinnati, OH.

Lindgren, G., et al., 1992, "The HAT Cycle, a Possible Future for Power and Cogeneration," *Proc. of the 1992 FLOWERS Congress*, Florence, Italy, pp. 125–141.

Macchi, E., Bombarda, P., Chiesa, P., Consonni, S., and Lozza, G., 1991, "Gas-Turbine-Based Advanced Cycles for Power Generation. Part B: Performance Analysis of Selected Configurations," *Proc. of the 1991 Yokohama International Gas Turbine Congress*, Yokohama, Japan, Paper 72, Vol. III, pp. 211–219.

Macchi, E., and Poggio, A., 1994, "A Cogeneration Plant Based on a Steam-Injected Gas Turbine With Recovery of the Water Injected—Design Criteria and Initial Operating Experience," ASME Paper No. 94-GT-XXX.

Rao, A. D., 1989, "Process for Producing Power," US Patent No. 4,829,763, May.

Rao, A. D., et al., 1991, "A Comparison of Humid Air Turbine (HAT) and Combined-Cycle Power Plants," EPRI Report IE-7300, Project 2999-7, Final Report.

Roberts, J. A., 1993, "Current and Potential Development in the Use of Aero Derivative Gas Turbines for Power Generations Duties," CCGT-3 Seminar on Combined Cycle Gas Turbines, held at the Inst. of Mech. Eng., London, Oct.

Stecco, S. S., Desideri, U., and Bettagli, N., 1993, "The Humid Air Cycle: Some Thermodynamic Considerations; Humid Air Gas Turbine Cycle: A Possible Optimization," ASME Papers No. 93-GT-77 and 93-GT-178.

K. W. Ragland

M. K. Misra[1]

D. J. Aerts

C. A. Palmer[2]

Department of Mechanical Engineering,
University of Wisconsin—Madison,
Madison, WI 53706

Ash Deposition in a Wood-Fired Gas Turbine

A small four-stage gas turbine was directly fired with woodchips using a novel downdraft, gravel-bed combustor for a total 250 hours of tests. The average turbine blockage due to deposits was 0.19 percent per hour. The composition of deposits was studied using plasma emission spectroscopy and x-ray diffraction. The main constituents of the deposits were CaO, MgO, and K_2SO_4. The deposits contained 5 to 15 percent potassium and 0.5 to 3 percent sulfur.

Introduction

Biomass fuels are a significant energy option because they are renewable and do not contribute to the net carbon dioxide burden in the atmosphere. A combined gas turbine–steam turbine cycle is thermodynamically more efficient than the steam turbine alone as a source of electricity and heat. Direct firing of a gas turbine with biomass is potentially more cost effective than indirect firing using a heat exchanger, or gasification of biomass prior to combustion. Although considerable work has been done on deposits from coal-fired gas turbine combustors (Logan et al., 1990; Spiro et al., 1987, 1990; Wenglarz and Fox, 1990), little work has been reported on deposits from wood-fired gas turbine combustors.

Mineral matter in wood is present either in an organically bound state or as ions in solutions (Sutcliffe and Baker, 1978; Parham and Gray, 1984). For instance, potassium is present in wood primarily as ions in solution in cell vacuoles, calcium is present as pectate in cell walls and as crystalline calcium oxalate in cytoplasm, magnesium in combined form in organic molecules such as chlorophylls and proteins, and silicon as silica deposits on cell walls. The key to using wood as a turbine fuel is to manage the combustion in such a way as to minimize the mineral particulate growth.

A novel gravel-bed, downdraft combustor for a direct-fired biomass gas turbine cycle is being developed (Ragland and Aerts, 1992, 1989; Ragland et al., 1991). The combustor is designed to promote intense combustion in a thin zone and to control particulate growth by using high excess air. This paper presents the results obtained from analyses of the ash deposits taken from different stages of the woodchip-fired gas turbine.

The Combustor–Turbine System

A schematic of the test setup is shown in Fig. 1. An Allison model 250-C20B gas turbine was coupled to an L-shaped, refractory-lined, downdraft combustor. The elbow region of the combustor contains a gravel bed of magnesia chips and alumina spheres. Alumina rods near the inlet of the horizontal section of the combustor form a grid to hold the bed in place. Woodchips, approximately 2 cm in size, are fed from a lock hopper into the combustor from the top by means of a screw feeder. Pressurized, preheated air, which is supplied to the top of the combustor, dries the woodchips in the top layer of the pile and combusts the wood in a relatively thin layer at the wood–gravel interface. The bed helps in capturing and completely burning any unburned char particles entrained by the air. The hot gases from the combustor flow through a flexible stainless steel coupling to the gas turbine, which is loaded by a water brake. The exhaust from the turbine is used to preheat the air for the combustor. Ash particles are blown through the gravel bed and the turbine without hot gas cleanup. The combustor outlet temperature was held to 900°C by means of excess air to minimize ash deposition in the gravel bed.

The gas turbine is rated at a full net power of 400 hp at a combustor outlet pressure 5 atm. The gas generator turbine has two stages with a full power speed of 51,000 rpm, and the power turbine has two stages with a full power speed of 33,000 rpm. Our tests were run at about 80 percent speed and a net power of 75 hp or less. Due to a number of operational problems, the power output was highly variable during the tests. Over time some ash is deposited on the turbine blades, which is the subject of this paper. In the tests the compressor air was dumped to the test room, and the combustor supplied with house air. Further description of the test setup and performance is given elsewhere (Ragland and Aerts, 1992).

The first set of ash samples was obtained when the turbine was overhauled after 131 hours of operation. The second set of deposit samples was obtained after operating for 122 hours. Turbine failure due to bearing failure occurred at this time due to partial blockage of the turbine inlet by refractory

Table 1 Wood properties

	Poplar	Aspen
Heating value (Btu/lb, dry)	8236	8496
Elemental analysis (wt%, dry)		
Carbon	50.72	51.57
Hydrogen	6.25	6.24
Nitrogen	0.16	0.47
Sulfur	0.02	0.02
Ash	0.79	0.72
Oxygen (by difference)	42.06	40.98
Mineral analysis of ash formed at 800°C (wt % of ash)		
Phosphorous	1.01	1.76
Potassium	9.86	15.17
Calcium	31.28	30.34
Magnesium	8.36	4.83
Sulfur	1.18	0.98
Zinc	0.04	0.48
Boron	0.06	0.07
Manganese	0.59	0.20
Iron	0.46	0.56
Copper	0.04	0.04
Aluminum	0.55	0.46
Sodium	2.91	0.22
Silicon	n.d	2.30

n.d. - not determined

---

[1] Currently with Corning, Inc., Corning, NY.

[2] Currently with ENTER Software, Menlo Park, CA.

Contributed by the International Gas Turbine Institute for publication in the JOURNAL OF ENGINEERING FOR GAS TURBINES AND POWER. Manuscript received at ASME Headquarters December 1994. Associate Technical Editor: H. Lukas.

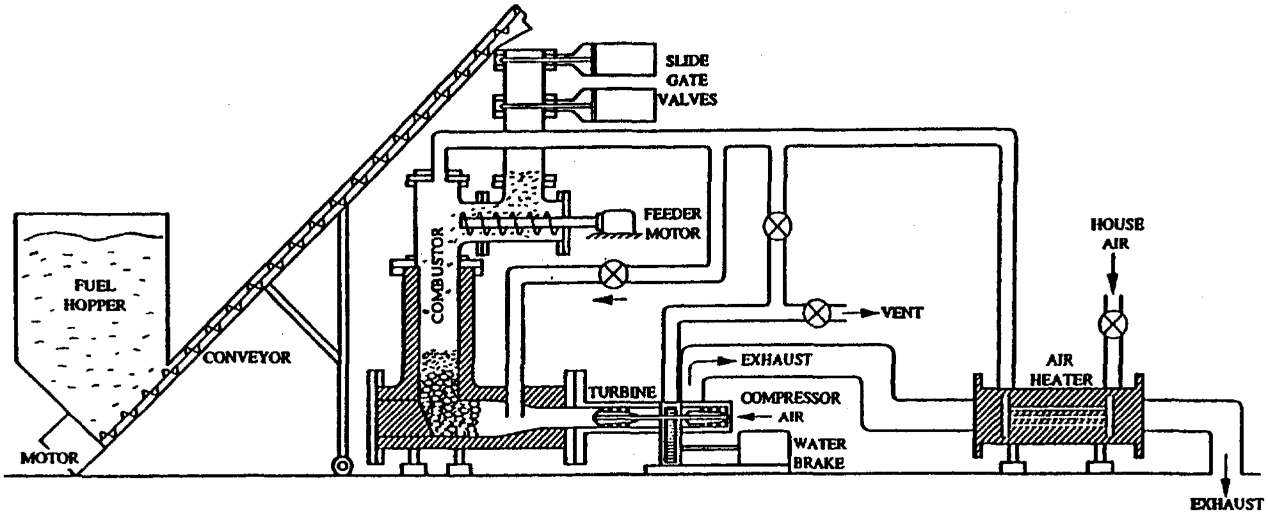

Fig. 1 Schematic of downdraft combustor/gas turbine system

Table 2 Thickness of wood ash deposits in different stages of turbine

1st Stage Rotor		~0.1 mm
2nd Stage Nozzle	Leading Edge	1.0 mm
	Trailing Edge	0.5 mm
2nd Stage Rotor	Front	~0.1 mm
	Back	< 0.1 mm
3rd Stage Nozzle		1.5 mm
3rd Stage Rotor	Front	0.15 mm
	Outer Rim	0.5 mm
4th Stage Nozzle	Leading Edge	1.6 mm
	Trailing Edge	0.2 mm
4th Stage Rotor	Back	~0.2 mm
	Front	~0.1 mm

gravel and erosion of the first stage rotor due to injested gravel. The turbine failure was not due to wood ash effects. During the first period of operation yellow poplar was used as the fuel, and during the second aspen woodchips were used (Table 1). Prior to the first overhaul approximately 3600 kg of poplar were burned, and between the first and second overhaul 1800 kg of poplar and 3700 kg of aspen were burned.

Thickness of Turbine Deposits and Blockage

The first inspection showed that the deposits were heavier on the nozzles than on the rotors. The color of the deposits ranged from light green and gray in the upstream (gas generator) stages to dark green and brown in the downstream (power turbine) stages. Both the nozzles and rotors cleaned up well with walnut shelling and did not show signs of erosion.

The thickness of the second set of turbine deposits was measured (Table 2). Due to the complex contour of the turbine blades and the brittleness of the deposits, it was difficult to measure the thickness using calipers. For deposits that chipped off in flakes, the thickness was measured using an optical microscope. The rest of the thicknesses reported in Table 2 were estimated using a feeler thickness gage. The deposits on the nozzles were 1 mm to 1.6 mm thick and deposits on the rotors were 0.1 mm to 0.5 mm thick.

A measure of turbine flow area blockage from the deposits can be given by the normalized nozzle area index number, NAIN (Kimura et al., 1987),

$$\text{NAIN} = \frac{\left.\dfrac{\dot{m}\sqrt{T}}{P}\right|_{\text{turbine}}}{\left.\dfrac{\dot{m}\sqrt{T}}{P}\right|_{\text{cleanturbine}}}$$

where $\dot{m}$ is the mass flow rate through the turbine, and P and T are the turbine inlet pressure and temperature. This equation assumes that the nozzles operate aerodynamically choked. This

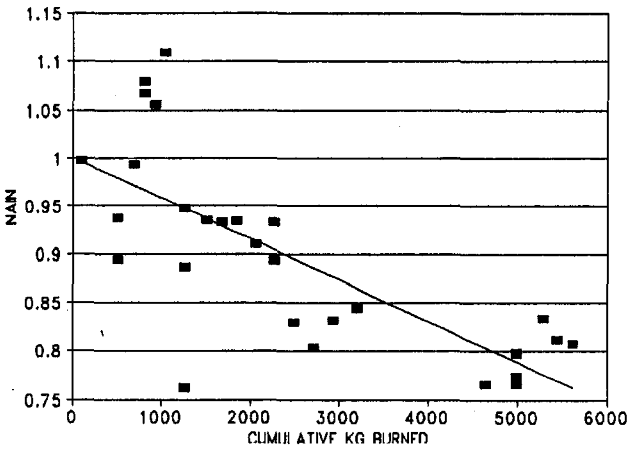

Fig. 2 Variation of normalized nozzle area index number (NAIN) with cumulative weight of fuel burned

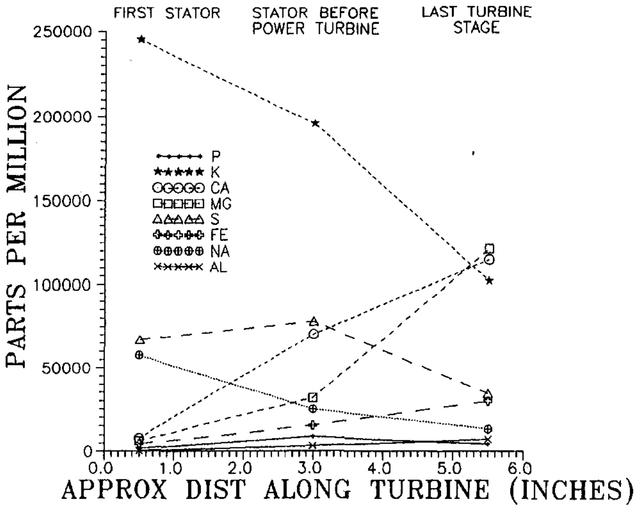

Fig. 3 Elemental composition of poplar ash deposits in different sections of the gas turbine

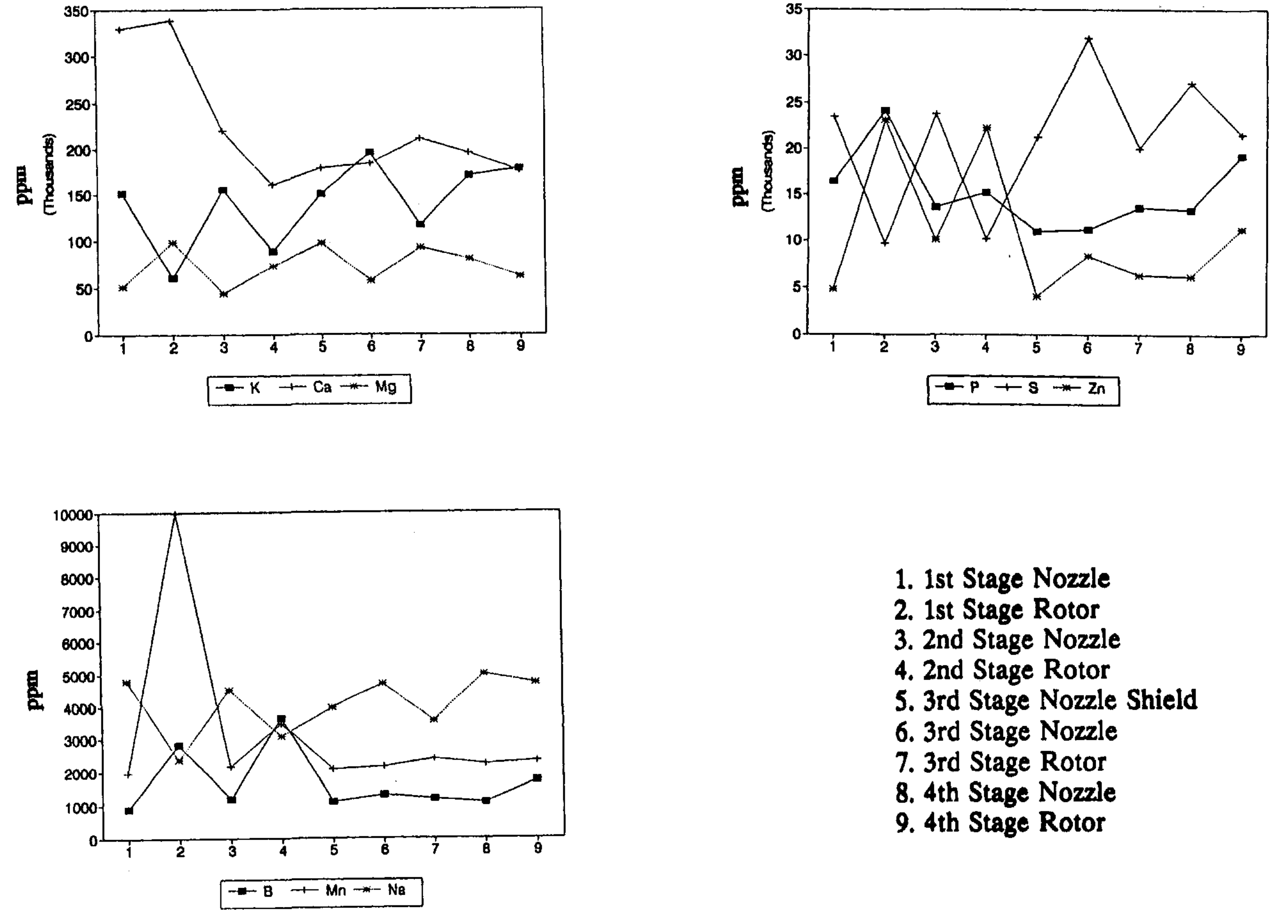

1. 1st Stage Nozzle
2. 1st Stage Rotor
3. 2nd Stage Nozzle
4. 2nd Stage Rotor
5. 3rd Stage Nozzle Shield
6. 3rd Stage Nozzle
7. 3rd Stage Rotor
8. 4th Stage Nozzle
9. 4th Stage Rotor

Fig. 4 Elemental composition of aspen ash deposits in different sections of the gas turbine

index was used to study coal combustion in a test stand, which had only a first-stage turbine nozzle for studying deposition. In our tests with a four-stage turbine each nozzle and rotor stage was not choked so that the index is approximate. Since the operating conditions used to evaluate the numerator and denominator were similar, the use of this index is reasonable.

The NAIN was evaluated for test data following the first overhaul of the turbine, and the results are shown in Fig. 2. The best-fit line ($r^2 = 0.56$) gives an area reduction rate of 4.2 percent per 1000 kg of wood burned. The results are presented as a function of cumulative wood burned because the tests were run at a variety of conditions, some at low load, and some at higher load. In terms of total hours, the NAIN decrease was 0.19 percent per hour. This reduction rate includes area reduction of all the stator and rotor stages, but is not at full load. By way of comparison, Kimura found NAIN reduction rates of 0.35 percent per hour for residual oil and 0.17–0.50 percent per hour for Otisca coal–water mixture (50 percent solids, 0.8 percent ash, 4 percent sulfur, dry) at full load, but with only a single-stage cascade of blades.

Chemical Analysis of Turbine Deposits

The turbine deposits were studied by inductively coupled plasma emission spectroscopy to determine the elemental composition, and x-ray diffraction for the identification of compounds present in the samples. Elemental analysis of deposits on the turbine stages at the time of the first turbine overhaul (Fig. 3) show that the deposits consists primarily of potassium, calcium, magnesium, and sulfur. Deposits on the first-stage nozzle (stator) are richer in alkali metals (potassium and sodium) and sulfur, whereas those in the downstream stages show decreasing concentrations of both potassium and sodium, and increasing proportions of calcium and magnesium. Small amounts of iron and aluminum were also observed. X-ray diffraction patterns of the deposits from the third-stage nozzle showed five strong peaks due to potassium sulfate (K_2SO_4) thus indicating a positive identification. Single calcium oxide and magnesium oxide peaks were also evident and possibly magnesium phosphate. Sodium, iron, and aluminum compounds were not identified either because the concentration was too low or because they were not crystalline compounds.

Chemical analyses of deposits obtained during the second turbine overhaul (Fig. 4) show that deposits on the upstream stages were richer in calcium compared to those in the downstream stages, and that the relative amounts of potassium, sodium, and sulfur were higher in the deposits on stationary nozzles compared to those on the rotating blades. The relative amount of potassium increased in the downstream stages. X-Ray Diffraction of the first-stage nozzle deposits (Fig. 5*a*) shows that the most intense peaks are calcium oxide followed by magnesium oxide, potassium sulfate, and calcium hydroxide. Weaker peaks may indicate the possible presence of K_2O, K_3AlO_3, and $Ca_3(PO_4)_2$. Deposits on the first-stage rotor (Fig. 5*b*) show strong peaks of MgO followed CaO, K_2SO_4, and $Ca(OH)_2$. Weak signals in Fig. 5(*b*) may possibly be $CaFe_3O_5$ and $KCaPO_4$. Deposits on the fourth-stage nozzle (Fig. 5*c*) were also CaO, MgO, K_2SO_4, and $Ca(OH)_2$ with probable amounts of potassium magnesium phosphate ($KMg(PO_3)_3$). Deposits on the intermediate stages were similar to those on the first stages.

Discussion

Calcium is the greatest inorganic compound in wood and is present in the turbine deposits as calcium oxide and calcium

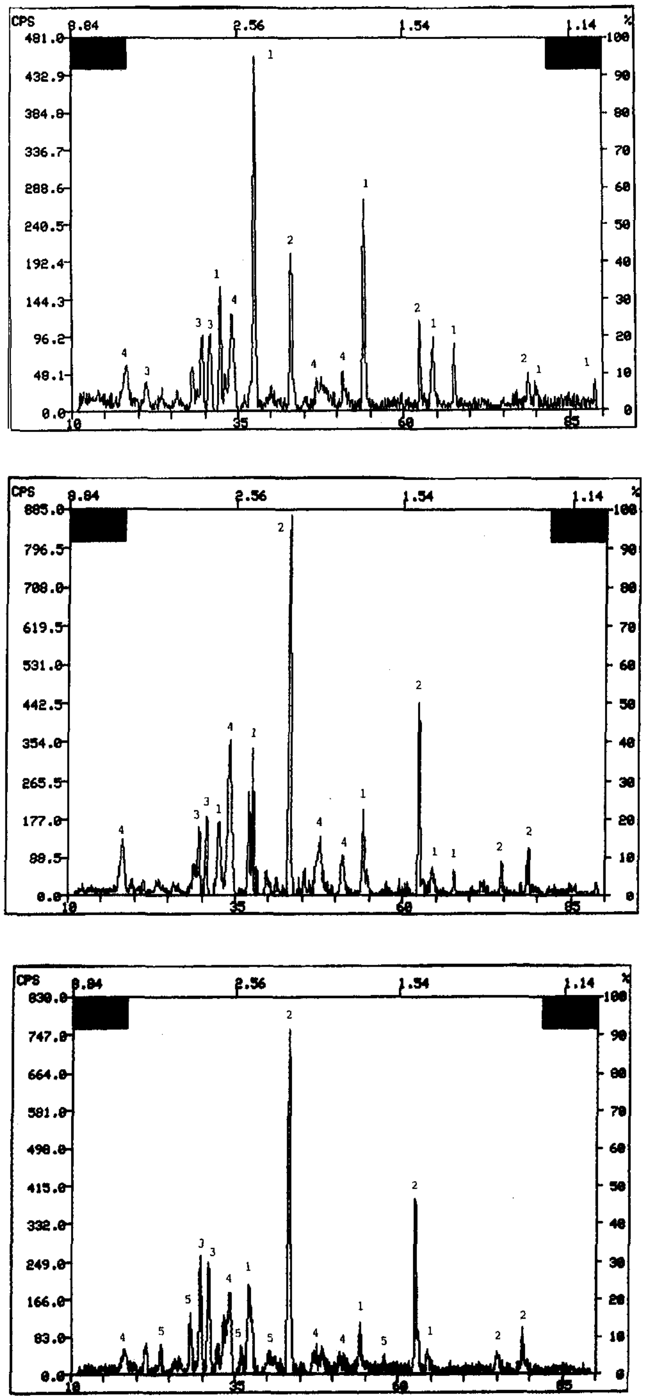

Fig. 5 X-ray diffraction pattern of wood ash deposits on stages of gas turbine: (*a*) first-stage nozzle, (*b*) first-stage rotor, (*c*) fourth-stage nozzle. Labels on the peaks correspond to: (1) CaO, (2) MgO, (3) K_2SO_4, (4) $Ca(OH)_2$, (5) $KMg(PO_3)_3$.

hydroxide. Since the calcium hydroxide has a melting point of 580°C, it was probably formed after shutdown. Potassium is the second greatest inorganic compound in wood and the identified form is potassium sulfate, which has a melting point of 1069°C. However, there is not enough sulfur in wood to react with all of the potassium. K_2O is the likely form of potassium in the deposits. It melts at 350°C, and thus would not be crystalline and would not be observed by x-ray diffraction. The magnesium is present in the deposits as MgO. There are many possibilities for other compounds in the deposits at lower levels, for example the possibility of potassium magnesium phosphate. Alumina was not observed in the deposits and thus indicates that the bed was not eroding. Very little aluminum is present in wood. The magnesia could have come from the wood or the bed. Sodium, which is a major contributor to coal ash deposits, is much less significant in wood ash deposits. Sodium levels were an order of magnitude lower than potassium in the poplar and two orders lower than potassium in the aspen. Sodium was not observed by the x-ray diffraction measurements.

After the first stage, the potassium to calcium ratio was greater in the deposits than in the wood, indicating a preferential deposition of potassium compared to calcium. Similarly, the sulfur is preferentially deposited. The deposited potassium and sulfur compounds, K_2SO_4 and probably K_2O, have a higher relative concentration on the rotors than on the nozzles (Fig. 3).

Conclusions

A four-stage Allison 250-C20B gas turbine was run at low power on woodchips for 130 hours of tests, inspected and cleaned, and run for another 122 hours using a direct fired gravel bed combustor. The deposits were 1 mm to 1.6 mm thick on the nozzles and 0.1 mm to 0.5 mm thick on the rotors. The average turbine blockage was 0.19 percent per hour. The main deposits were calcium oxide, magnesium oxide, and potassium sulfate. Although the potassium content of the wood was 0.1 percent and sulfur content was only 0.007 percent, potassium and sulfur play an important role in formation of deposits on the turbine nozzles and rotors. Further work is needed to determine the extent to which hot gas cleanup may be required between the combustor and turbine when using woodchips.

Acknowledgments

The work on the combustor-gas turbine system was supported by US DOE under grant No. DE-FG02-85CE40735. Woodchips were provided by the U.S. D.A. Forest Products Laboratory. Turbine ash analysis was carried out under grant No. CBT-8805868 from the National Science Foundation. The support of Steve Waslo at DOE, Duane Burley at NSF, and Andy Baker at FPL is gratefully acknowledged. Dave Reinholt and Craig Hoerning assisted with the combustor-turbine testing.

References

Kimura, S. G., Spiro, C. L., and Chen, C. C., 1987, "Combustion and Deposition in Coal-Fired Turbines," ASME JOURNAL OF ENGINEERING FOR GAS TURBINES AND POWER, Vol. 109(3), pp. 319–324.

Logan, R. G., Richards, G. A., Meyers, C. T., and Anderson, R. J., 1990, "A Study of Techniques for Reducing Ash Deposition in Coal-Fired Gas Turbines," *Prog. Energy & Combust. Sci.*, Vol. 16, pp. 221–233.

Parham, R. A., and Gray, R. L., 1984, "Formation and Structure of Wood," in: *The Chemistry of Solid Wood,* Roger Rowell, ed., ACS, Washington, DC, Chap. 1.

Ragland, K. W., and Aerts, D. J., 1989, "Development of a Gravel Bed Combustor for a Solid Fueled Gas Turbine—Phase I," US DOE report DE/CE40735-1.

Ragland, K. W., Aerts, D. J., and Palmer, C. A., 1991, "Evaluation of a Woodchip Fired Cogeneration System Using a Gravel Bed Combustor," presented at the IECE Conference, Boston, MA, Aug.

Ragland, K. W., and Aerts, D. J., 1992, "Development of a Gravel Bed Combustor for a Solid Fueled Gas Turbine—Phase II," US DOE report DE/CE40735-2.

Spiro, C. L., Kimura, S. G., and Chen, C. C., 1987, "Ash Behavior During Combustion and Deposition in Coal Fueled Gas Turbines," ASME JOURNAL OF ENGINEERING FOR GAS TURBINES AND POWER, Vol. 109(3), pp. 325–330.

Spiro, C. L., Chen, C. C., Kimura, S. G., Lavigne, R. G., and Schields, P. W., 1990, "Deposit Remediation in Coal-Fired Gas Turbines Through the Use of Additives," *Prog. Energy & Combust. Sci.*, Vol. 16, pp. 213–220.

Sutcliffe, J. F., and Baker, D. A., 1987, "Plants and Mineral Salts," The Institute of Biology's Studies in Biology No. 48, Edward Arnold, ed.

Wenglarz, R. A., and Fox, R. G., Jr., 1990, "Chemical Aspects of Deposition/Corrosion From Coal-Water Fuels Under Gas Turbine Conditions," ASME JOURNAL OF ENGINEERING FOR GAS TURBINES AND POWER, Vol. 112(1), pp. 1–8.

Advantages of Air Conditioning and Supercharging an LM6000 Gas Turbine Inlet

D. A. Kolp
Kolp Engineering,
Avon, CT 06001

W. M. Flye
Stewart & Stevenson
Houston, TX 77003

H. A. Guidotti
Energy Services, Inc.
Farmington, CT 06032

Of all the external factors affecting a gas turbine, inlet pressure and temperature have the greatest impact on performance. The effect of inlet temperature variations is especially pronounced in the new generation of high-efficiency gas turbines typified by the 40 MW GE LM6000. A reduction of 50°F (28°C) in inlet temperature can result in a 30 percent increase in power and a 4.5 percent improvement in heat rate. An elevation increase to 5000 ft (1524 m) above sea level decreases turbine output 17 percent; conversely supercharging can increase output more than 20 percent. This paper addresses various means of heating, cooling and supercharging LM6000 inlet air. An economic model is developed and sample cases are cited to illustrate the optimization of gas turbine inlet systems, taking into account site conditions, incremental equipment cost and subsequent performance enhancement.

Effect of Inlet Conditioning

Selection of the proper inlet/air conditioning system for a gas turbine is key to optimizing plant performance. The LM6000 (Fig. 1), GE's latest aeroderivative industrial gas turbine, is no exception.

Simple Cycle. Electric power production for the dry low-NO_x version of the LM6000 is illustrated in Fig. 2. These curves demonstrate the influence of inlet temperature and inlet pressure on the output of this engine. The effect of supercharging on engine performance in this analysis is based on a modified version of the manufacturer's cycle deck (computer model). A decrease in temperature from 100°F (38°C) to 50°F (10°C) alone raises output over 13 MW. Increased inlet pressure from sea level (101 kPa) to 16.9 psia (116 kPa) can increase the output as much as 7 MW, although below 50°F (10°C), supercharging the inlet is less effective. Note that the LM6000 power peaks at 50°F (10°C); thus, it is beneficial to heat the inlet when ambient temperature is below 50°F (10°C) and cool it at higher temperatures. GE has imposed a 45,000 kW upper limit on the engine, which translates to 44,099 kW on the new dry NO_x version, hence the flat output profile between 10°F (−12°C) and 50°F (10°C) in the highly supercharged regions. Simple cycle performance assumes 4 in. (100 mm) and 1 in. (25 mm) of water inlet and exhaust losses, respectively, as well as 60 percent relative humidity.

As expected, the increased power resulting from supercharging and cooling the inlet also improves the gross (i.e., neglecting supercharger auxiliary load) heat rate of the turbine, particularly in the higher temperature ranges. Figure 3 shows the resulting lower heat rates.

While exhaust gas temperature and flow do not impact simple cycle performance, they do affect waste heat recovery schemes such as those used in cogeneration and combined cycle plants. Figures 4 and 5 indicate that while supercharging reduces exhaust gas temperature less than 1 percent at the optimum inlet temperature of 50°F (10°C), exhaust gas flow is increased some 7 percent. Thus the overall effect of supercharging is to increase waste heat energy by 6 percent. Turbine inlet cooling can add another 20 percent to the thermal energy in the waste heat stream.

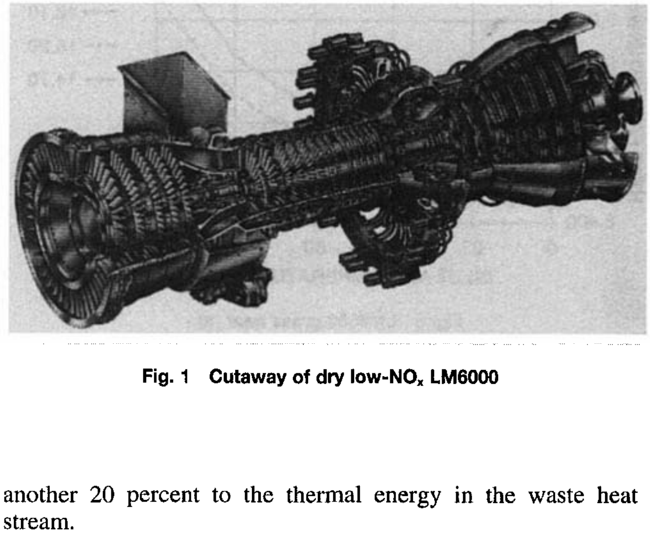

Fig. 1 Cutaway of dry low-NO_x LM6000

The auxiliary power required to operate a supercharger motor varies from zero to 2400 kW, as illustrated by Fig. 6.

The resulting net simple cycle power and heat rates are depicted in Figs. 7 and 8. Note that while there is considerable net power increase with supercharging, net gas turbine efficiency decreases, i.e., net heat rate increases with increased supercharging, due to the auxiliary load of the supercharger fan motor.

The net increase in simple cycle power is shown in Fig. 9.

Combined Cycle. The flow diagram in Fig. 12 provides a means of quantifying the effect of inlet air conditioning and pressurization on waste heat applications. For the purposes of this analysis, this combined cycle plant efficiently converts the additional exhaust gas energy into electricity by means of a three-pressure HRSG and a controlled admission, condensing steam turbine.

The net combined cycle generating capability of the LM6000 is increased more with inlet conditioning than is the simple cycle capability. Supercharging increases output over 7 MW if the inlet is pressurized to 16.9 psia (116 kPa) as shown in Fig. 10. This compares with 5 MW in the simple cycle case. Cooling the inlet from 100°F (38°C) to 50°F (10°C) results in over 15 MW of additional power versus 13 MW in the simple cycle case. The capacity increase of capital equipment in the combined cycle plant that is necessary to accommodate supercharging is more expensive than in the simple cycle case. However,

---

Contributed by the International Gas Turbine Institute and presented at the 39th International Gas Turbine and Aeroengine Congress and Exposition, The Hague, The Netherlands, June 13–16, 1994. Manuscript received by the International Gas Turbine Institute February 11, 1994. Paper No. 94-GT-425. Associate Technical Editor: E. M. Greitzer.

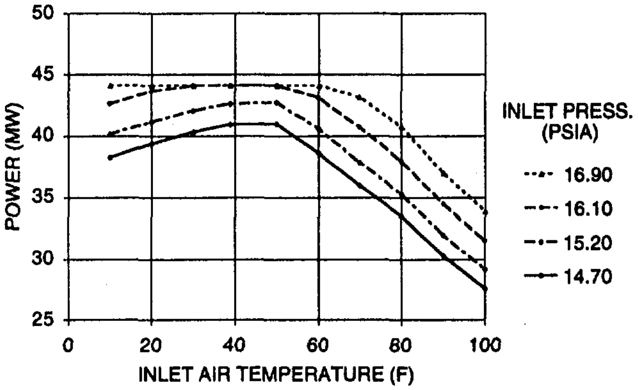

Fig. 2 LM6000 power

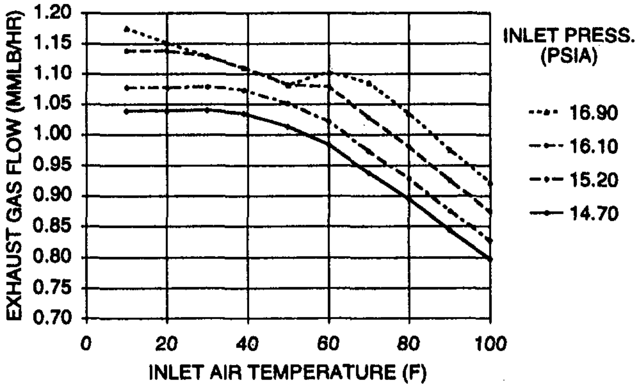

Fig. 5 LM6000 exhaust gas flow

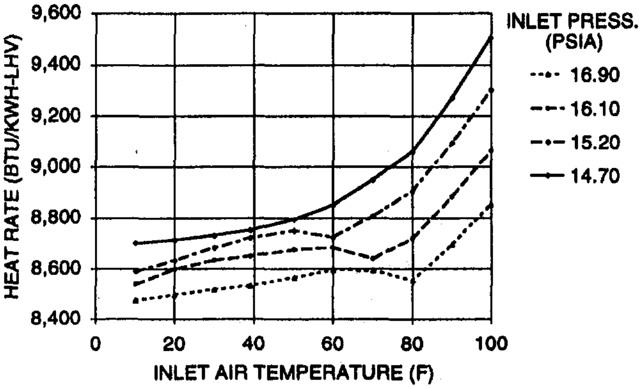

Fig. 3 LM6000 gross heat rate

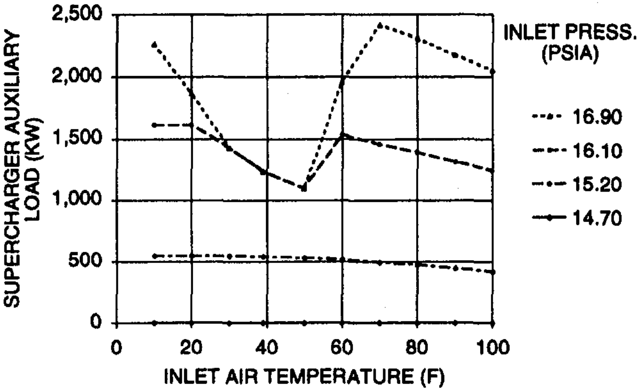

Fig. 6 Supercharger auxiliary load

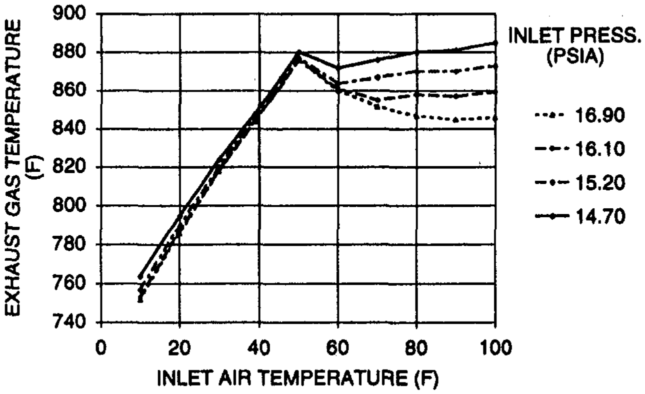

Fig. 4 LM6000 exhaust gas temperature

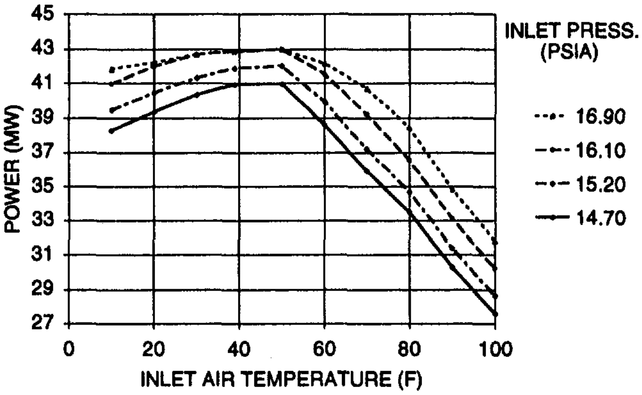

Fig. 7 Supercharged net simple cycle power

this added capital expense is more than offset since no additional fuel is required to realize the improved output from the steam side.

As in the simple cycle case, the more highly supercharged unit suffers increased heat rates (Fig. 11), but combined cycle heat rates are still under 7000 Btu/kWh-LHV (7385 kJ/kWh) at 50°F (10°C) inlet temperature. Exhaust losses are 10 in (254 mm) of water for all combined cycle performance in this analysis.

Economics

To evaluate the economic impact of inlet air conditioning, it is necessary to simulate the distribution of atmospheric conditions as a function of time. Figure 13 is based on typical hourly

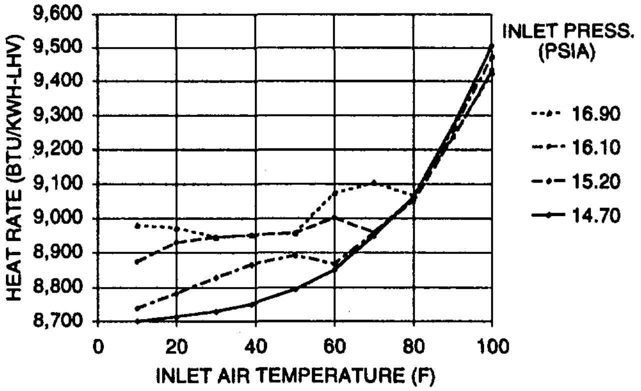

Fig. 8 Supercharged net simple cycle heat rate

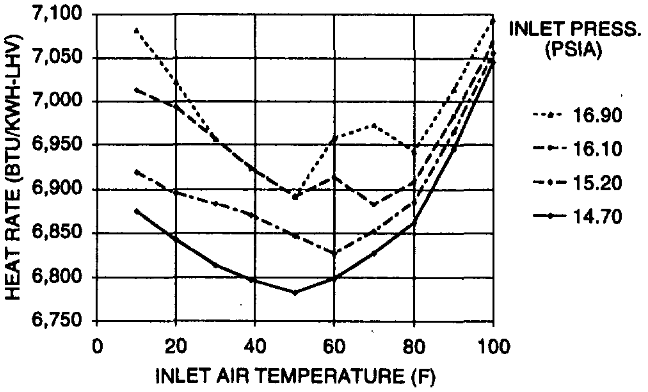

Fig. 11 Net combined cycle heat rate with supercharging

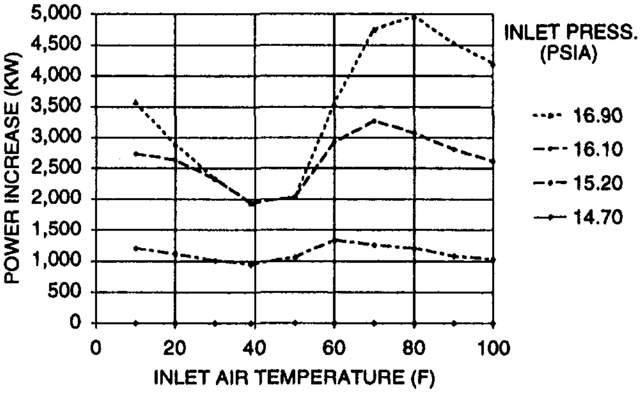

Fig. 9 Net power increase from supercharging

data gathered at a northeastern U.S. site during the course of a year. Equations developed to fit these curves enable us to determine the number of hours per year that the wet bulb and dry bulb temperatures fall below a given value. Meteorological records ascribe a discrete wet bulb temperature to each hourly dry bulb temperature recorded; the curves in Fig. 13 closely approximate these actual conditions by correlating average dry bulb and wet bulb temperatures for a given hour. These curves and the corresponding equations for the curves are utilized in determining the number of hours the atmospheric conditions at this typical site will be in a given temperature range and how much duty will be required of the heater, chiller, or evaporative cooler to achieve a particular inlet temperature during that increment of time; in the case of the LM6000, this target temperature is about 50°F (10°C) for optimum performance as illustrated in Fig. 2.

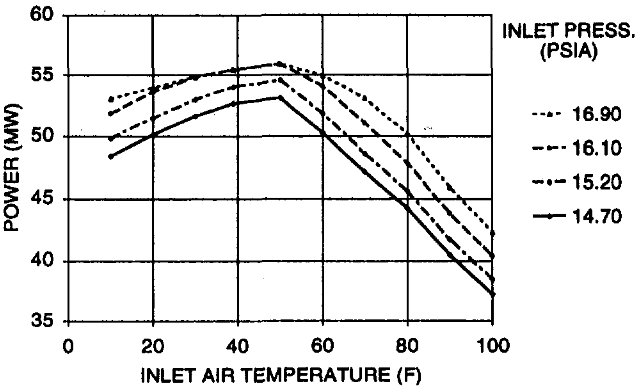

Fig. 10 Net combined cycle output

Once the equations (curves) are devised to describe the temperature duration for this site, a similar method is used to establish the turbine performance as a function of inlet temperature. An example of the curves that match the net power output of a supercharged LM6000 is given in Fig. 14.

The equations corresponding to the curves in Fig. 14 are:

For inlet pressure = 16.9 psia:

$$P = 40{,}753 + 167.48\,T - 8.1252\,T^2 + 0.2355\,T^3 - 0.00312\,T^4 + 0.00001\,T^5$$

For 16.1 psia:

$$P = 40{,}212 + 70.13\,T + 1.0314\,T^2 - 0.00073\,T^3 - 0.00084\,T^4 + 0.00001\,T^5$$

For 15.2 psia:

$$P = 40{,}870 - 320.41\,T + 22.971\,T^2 - 0.49486\,T^3 + 0.00393\,T^4 - 0.00001\,T^5$$

For 14.7 psia (sea level):

$$P = 40{,}054 - 404.17\,T + 28.844\,T^2 - 0.64725\,T^3 + 0.00556\,T^4 - 0.00002\,T^5$$

where P = Power (kW) and T = temperature (°F).

Similar equations are used to determine simple cycle heat rate as well as combined cycle power and heat rate over the full range of site temperatures from 5°F (−15°C) to 100°F (38°C).

Using the hours that the inlet temperature falls within each temperature range as defined by Fig. 13 and the power corresponding to those temperatures as defined by the respective equations for temperature and supercharging, it is possible to generate a tabulation of the kWh of power produced annually at the site under consideration. A tabulation may also be produced of fuel consumption using weather data and the equations corresponding to heat rate; see Table 1.

While supercharging increases turbine output by raising inlet pressure, the fan also raises inlet temperature as much as 30°F (17°C) when pressurizing ambient air to 16.9 psia (116 kPa); the elevated temperature can actually reduce turbine output below that of the nonsupercharged condition. To compensate for this loss, it is necessary to cool the air after supercharging. This is economically feasible with an evaporative cooler regardless

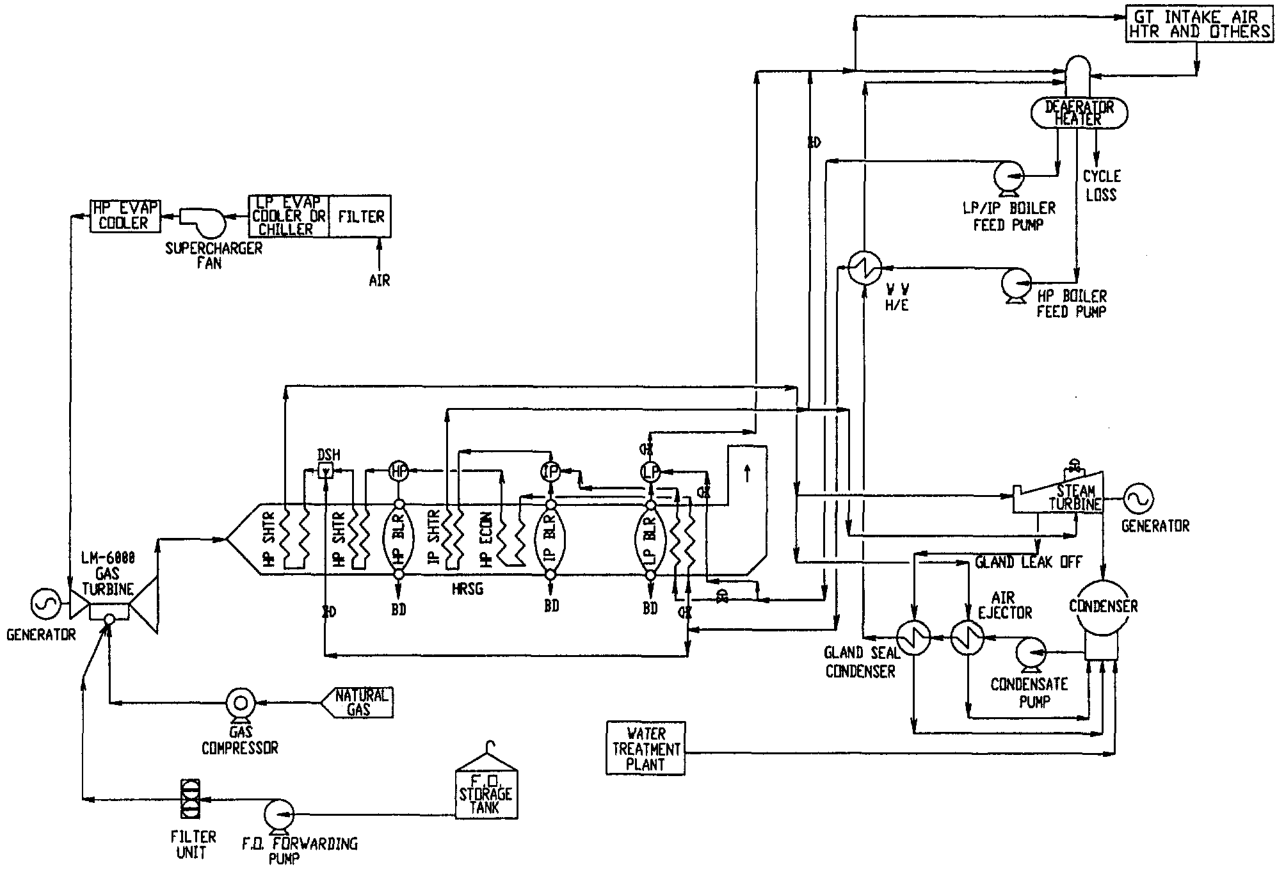

Fig. 12 Typical combined cycle

of whether chilling or evaporative cooling is used to control ambient temperatures at the supercharger inlet. For this reason, all superchargers discussed henceforth include downstream evaporative coolers to remove the heat of compression.

Evaporative Cooling and Supercharging

Simple Cycle. The addition of evaporative cooling to a turbine inlet is one of the most cost-effective means of improving performance. This is not only true in dry climates such as southwestern U.S. but is even practical in base-loaded plants operating in humid environments such as Florida. The economic benefit for the northeastern U.S. locale cited in this example is shown in Table 2.

Two electrical rates are assumed in analyzing the impact of inlet air conditioning on plant economics: $0.03 and $0.04/kWh. Capacity credit is $100/kW-yr. Cost of fuel is $3.00/

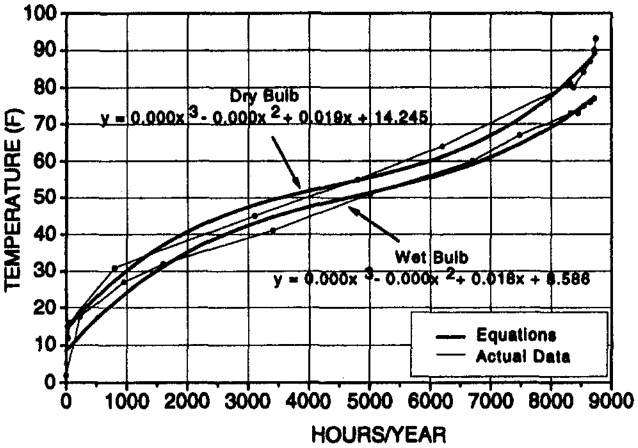

Fig. 13 Dry bulb and wet bulb temperature duration curves

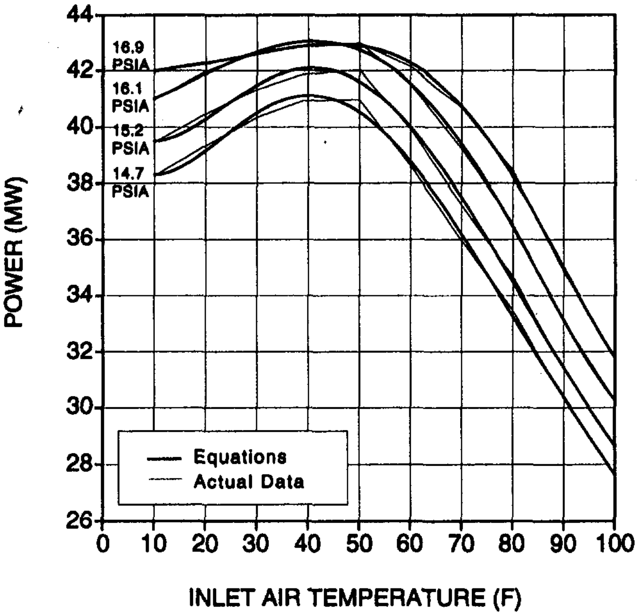

Fig. 14 Simulated net simple cycle power with supercharging

Table 1 Base plant performance and economics without inlet conditioning

Simple Cycle Performance (Dry Bulb)						
Temp. (F)	Dry Bulb Duration (Hours)	Duration in Temp. Range (Hours)	Power (KW)	Annual Power Production (KWH)	Heat Rate BTU/KWH (LHV)	Annual Fuel Consumption (MMBTU)
5	0	17	38,695	657,809	8,700	5,723
10	17	80	38,305	3,064,423	8,701	26,663
15	97	122	38,561	4,692,543	8,706	40,851
20	219	262	39,160	10,247,959	8,713	89,289
25	480	404	39,868	16,124,749	8,722	140,636
30	885	543	40,507	21,996,098	8,732	192,067
35	1,428	671	40,953	27,466,476	8,743	240,151
40	2,099	781	41,127	32,109,470	8,757	281,181
45	2,879	866	40,989	35,516,753	8,773	311,598
50	3,746	921	40,533	37,340,337	8,793	328,352
55	4,667	938	39,777	37,322,495	8,819	329,144
60	5,605	911	38,764	35,310,117	8,851	312,529
65	6,516	832	37,544	31,252,710	8,891	277,872
70	7,349	696	36,180	25,185,653	8,941	225,181
75	8,045	340	34,732	11,817,929	9,002	106,380
80	8,385	265	33,256	8,812,742	9,075	79,971
85	8,650	84	31,794	2,670,712	9,161	24,466
90	8,734	22	30,372	668,187	9,261	6,188
95	8,756	4	28,989	115,956	9,376	1,087
100	8,760		**Total**	342,373,118	9,506	
	Total	8,760				
		Average Capacity (KW)		39,084	**Total**	3,019,328

Combined Cycle Performance (Dry Bulb)						
Temp. (F)	Dry Bulb Duration (Hours)	Duration in Temp. Range (Hours)	Power (KW)	Annual Power Production (KWH)	Heat Rate BTU/KWH (LHV)	Annual Fuel Consumption (MMBTU)
5	0	17	48,871	830,814	6,892	5,726
10	17	80	48,477	3,878,162	6,875	26,662
15	97	122	48,942	5,970,920	6,858	40,948
20	219	262	49,866	13,064,794	6,842	89,388
25	480	404	50,935	20,577,619	6,827	140,485
30	885	543	51,914	28,189,570	6,814	192,086
35	1,428	671	52,640	35,321,583	6,803	240,299
40	2,099	781	53,008	41,399,437	6,795	281,303
45	2,879	866	52,967	45,869,798	6,789	311,432
50	3,746	921	52,510	48,362,070	6,788	328,258
55	4,667	938	51,665	48,461,535	6,789	329,022
60	5,605	911	50,484	45,991,348	6,795	312,529
65	6,516	832	49,041	40,802,194	6,806	277,702
70	7,349	696	47,415	33,000,909	6,822	225,124
75	8,045	340	45,687	15,533,609	6,843	106,295
80	8,385	265	43,929	11,641,223	6,870	79,975
85	8,650	84	42,196	3,544,471	6,903	24,468
90	8,734	22	40,517	891,369	6,943	6,189
95	8,756	4	38,885	155,541	6,990	1,087
100	8,760		**Total**	443,486,965	7,045	0
	Total	8,760				
		Average Capacity (KW)		50,626	**Total**	3,018,979

Simple Cycle Economics		
Value of Electricity ($/KWH)	0.03	0.04
Value of Electical Capacity ($/KW-YR)	100.00	100.00
Unit Cost of Fuel ($/MMBTU)	3.00	3.00
Simple Cycle Plant Cost @ $700/KW X 41,127 KW	28,788,900	28,788,900
Elevation	*0*	*0*
Power Generation (KWH)	342,373,118	342,373,118
Average Capacity (KW)	39,084	39,084
Fuel Consumption (MMBTU/YR)	3,019,328	3,019,328
Energy Revenue ($)	10,271,194	13,694,925
Electrical Capacity Credit ($)	3,908,369	3,908,369
Cost of Fuel ($)	9,057,985	9,057,985
Net Power Generating Revenue ($/Year)	5,121,577	8,545,308
Payback	**5.62**	**3.37**

Combined Cycle Economics		
Value of Electricity ($/KWH)	0.03	0.04
Value of Electical Capacity ($/KW-YR)	100.00	100.00
Unit Cost of Fuel ($/MMBTU)	3.00	3.00
Combined Cycle Plant Cost @ $1000/KW X 53,008 KW	53,008,000	53,008,000
Elevation	*0*	*0*
Power Generation (KWH)	443,486,965	443,486,965
Average Capacity (KW)	50,626	50,626
Fuel Consumption (MMBTU/YR)	3,018,979	3,018,979
Energy Revenue ($)	13,304,609	17,739,479
Electrical Capacity Credit ($)	5,062,637	5,062,637
Cost of Fuel ($)	9,056,936	9,056,936
Net Power Generating Revenue ($/Year)	9,310,310	13,745,179
Payback	**5.69**	**3.86**

Table 2 Simple cycle performance and economics with evaporative cooler and supercharger

Simple Cycle Performance (Wet Bulb)																		
Temp. (F)	Wet Bulb Duration (Hours)	Temp. Range (Hours)	Power (KW)				Annual Power Production (KWH)				Heat Rate (BTU/KWH-LHV)				Annual Fuel Consumption (MMBTU)			
Inlet Pressure (PSIA)			16.90	16.10	15.20	14.70	16.90	16.10	15.20	14.70	16.90	16.10	15.20	14.70	16.90	16.10	15.20	14.70
40	30	30	42,906	43,062	42,103	41,127	1,287,175	1,291,869	1,263,088	1,233,814	8,950	8,965	8,868	8,757	11,520	11,581	11,201	10,804
40	127	97	42,906	43,062	42,103	41,127	4,164,706	4,179,893	4,086,771	3,992,053	8,950	8,965	8,868	8,757	37,274	37,472	36,241	34,958
40	407	280	42,906	43,062	42,103	41,127	12,030,939	12,074,810	11,805,803	11,532,184	8,950	8,965	8,868	8,757	107,676	108,249	104,693	100,987
40	674	266	42,906	43,062	42,103	41,127	11,424,291	11,465,950	11,210,508	10,950,685	8,950	8,965	8,868	8,757	102,247	102,790	99,414	95,895
40	997	323	42,906	43,062	42,103	41,127	13,878,684	13,929,294	13,618,972	13,303,329	8,950	8,965	8,868	8,757	124,214	124,874	120,772	116,496
40	1,429	432	42,906	43,062	42,103	41,127	18,531,796	18,599,373	18,185,010	17,763,541	8,950	8,965	8,868	8,757	165,859	166,740	161,263	155,554
40	2,001	572	42,683	43,062	42,103	41,127	24,393,902	24,610,720	24,062,434	23,504,745	8,950	8,965	8,868	8,757	218,324	220,631	213,384	205,830
40	2,723	722	42,942	43,062	42,103	41,127	31,011,008	31,097,866	30,405,057	29,700,367	8,950	8,965	8,868	8,757	277,547	278,788	269,630	260,084
45	3,587	864	43,062	43,062	42,103	41,127	37,195,343	37,195,343	36,366,692	35,523,831	8,950	8,965	8,868	8,757	332,897	333,450	322,497	311,080
50	4,563	976	43,009	43,009	42,011	40,989	41,985,776	41,985,776	41,011,859	40,013,799	8,966	8,965	8,874	8,773	376,453	376,385	363,935	351,052
55	5,602	1,039	42,900	42,753	41,624	40,533	44,590,483	44,437,813	43,264,508	42,130,018	8,989	8,962	8,876	8,793	400,805	398,250	384,034	370,470
60	6,435	833	42,686	42,271	40,947	39,777	35,557,412	35,211,777	34,108,479	33,134,636	9,014	8,960	8,880	8,819	320,516	315,485	302,874	292,212
65	7,173	738	42,276	41,550	40,003	38,764	31,199,920	30,664,047	29,522,460	28,607,495	9,040	8,961	8,889	8,851	282,037	274,772	262,415	253,204
70	7,906	733	41,638	40,588	38,833	37,544	30,520,341	29,751,145	28,464,761	27,519,893	9,063	8,969	8,908	8,891	276,611	266,826	253,565	244,683
75	8,560	654	40,749	39,396	37,485	36,180	26,649,801	25,765,079	24,515,391	23,661,674	9,084	8,987	8,942	8,941	242,076	231,540	219,218	211,555
80	8,760	200	39,607	38,001	36,015	34,732	7,914,709	7,593,726	7,196,881	6,940,552	9,102	9,018	8,994	9,002	72,041	68,479	64,727	62,476
	Total	8,760				Total	372,336,286	369,854,481	359,088,673	349,512,616				Total	3,348,097	3,316,313	3,189,862	3,077,340
						Average Capacity=	42,504	42,221	40,992	39,899								

Economics of Supercharging (Simple Cycle)								
Value of Electricity ($/KWH)	0.03				0.04			
Value of Electical Capacity ($/KW-YR)	100.00				100.00			
Unit Cost of Fuel ($/MMBTU)	3.00				3.00			
Pressure (PSIA)	16.90	16.10	15.20	14.70	16.90	16.10	15.20	14.70
Capital Costs								
Add. Cost of Evap. Cooler & Inlet Heating,$	220,000	220,000	220,000	220,000	220,000	220,000	220,000	220,000
Supercharger, $	1,386,000	926,000	313,000	0	1,386,000	926,000	313,000	0
Additional Aux. Cap. Resulting from Supercharging, $	580,550	580,550	292,742	0	580,550	580,550	292,742	0
Additional Costs for Supercharging, $	1,966,550	1,506,550	605,742	0	1,966,550	1,506,550	605,742	0
Total	2,186,550	1,726,550	825,742	220,000	2,186,550	1,726,550	825,742	220,000
Revenues								
Power Generation (KWH)	372,336,286	369,854,481	359,088,673	349,512,616	372,336,286	369,854,481	359,088,673	349,512,616
Average Capacity (KW)	42,504	42,221	40,992	39,899	42,504	42,221	40,992	39,899
Fuel Consumption (BTU/YR)	3,348,097	3,316,313	3,189,862	3,077,340	3,348,097	3,316,313	3,189,862	3,077,340
Energy Revenue ($)	11,170,089	11,095,634	10,772,660	10,485,378	14,893,451	14,794,179	14,363,547	13,980,505
Electrical Capacity Credit ($)	4,250,414	4,222,083	4,099,186	3,989,870	4,250,414	4,222,083	4,099,186	3,989,870
Cost of Fuel ($)	10,044,291	9,948,938	9,569,587	9,232,021	10,044,291	9,948,938	9,569,587	9,232,021
Net Power Generating Revenue ($/Year)	5,376,212	5,368,780	5,302,259	5,243,227	9,099,575	9,067,325	8,893,146	8,738,354
Supercharging Advantage ($/Year)	132,984	125,553	59,032	0	361,221	328,971	154,792	0
Net Revenue w/ Evap. Clr. & Superchrg. ($/Year)	5,376,212	5,368,780	5,302,259	5,243,227	9,099,575	9,067,325	8,893,146	8,738,354
Net Revenue of Base Plant ($/Year)	5,121,577	5,121,577	5,121,577	5,121,577	8,545,308	8,545,308	8,545,308	8,545,308
Evap. Cool.+Supercharg. Advantage, ($/Year)	254,635	247,203	180,682	121,650	554,266	522,017	347,837	193,045
Evaporative Cooler Component of Payback	1.81	1.81	1.81	1.81	1.14	1.14	1.14	1.14
Supercharger Component of Payback	14.79	12.00	10.26		5.44	4.58	3.91	
Comb. Superchrg. & Evap. Cooler Payback	8.59	6.98	4.57	1.81	3.94	3.31	2.37	1.14

Table 3 Combined cycle performance and economics with evaporative cooler and supercharger

Combined Cycle Performance (Wet Bulb)																		
Temp. (F)	Wet Bulb Duration (Hours)	Temp. Range (Hours)	Power (KW)				Annual Power Production (KWH)				Heat Rate (BTU/KWH-LHV)				Annual Fuel Consumption (MMBTU)			
Inlet Pressure (PSIA)			16.90	16.10	15.20	14.70	16.90	16.10	15.20	14.70	16.90	16.10	15.20	14.70	16.90	16.10	15.20	14.70
40	30	30	55,531	55,747	54,379	53,008	1,665,920	1,672,412	1,631,363	1,590,247	6,915	6,925	6,866	6,795	11,520	11,581	11,201	10,805
40	127	97	55,531	55,747	54,379	53,008	5,390,149	5,411,156	5,278,339	5,145,307	6,915	6,925	6,866	6,795	37,274	37,470	36,242	34,962
40	407	280	55,531	55,747	54,379	53,008	15,570,981	15,631,665	15,247,987	14,863,686	6,915	6,925	6,866	6,795	107,676	108,242	104,696	100,996
40	674	266	55,531	55,747	54,379	53,008	14,785,830	14,843,454	14,479,123	14,114,200	6,915	6,925	6,866	6,795	102,247	102,784	99,417	95,904
40	997	323	55,531	55,747	54,379	53,008	17,962,416	18,032,421	17,589,816	17,146,493	6,915	6,925	6,866	6,795	124,213	124,866	120,776	116,508
40	1,429	432	55,531	55,747	54,379	53,008	23,984,682	24,078,157	23,487,160	22,895,204	6,915	6,925	6,866	6,795	165,859	166,730	161,268	155,569
40	2,001	572	55,921	55,747	54,379	53,008	31,959,654	31,860,255	31,078,247	30,294,971	6,915	6,925	6,866	6,795	221,007	220,618	213,390	205,850
40	2,723	722	55,444	55,747	54,379	53,008	40,039,437	40,258,308	39,270,171	38,280,430	6,940	6,925	6,866	6,795	277,874	278,771	269,638	260,110
45	3,587	864	55,747	55,747	54,379	53,008	48,151,908	48,151,908	46,970,023	45,786,220	6,925	6,925	6,866	6,795	333,452	333,430	322,507	311,110
50	4,563	976	55,784	55,784	54,379	52,967	54,457,032	54,457,032	53,085,283	51,707,141	6,911	6,911	6,856	6,789	376,373	376,375	363,948	351,065
55	5,602	1,039	55,756	55,524	53,973	52,510	57,953,553	57,712,516	56,100,225	54,579,869	6,916	6,901	6,846	6,788	400,793	398,263	384,057	370,462
60	6,435	833	55,557	54,948	53,178	51,665	46,278,775	45,772,032	44,297,008	43,036,736	6,926	6,893	6,838	6,789	320,513	315,516	302,900	292,191
65	7,173	738	55,083	54,053	52,036	50,484	40,651,052	39,891,053	38,402,415	37,257,535	6,938	6,889	6,834	6,795	282,044	274,811	262,436	253,179
70	7,906	733	54,298	52,849	50,609	49,041	39,800,128	38,738,447	37,096,394	35,947,125	6,950	6,889	6,835	6,806	276,628	266,860	253,572	244,658
75	8,560	654	53,183	51,365	48,970	47,415	34,781,434	33,592,595	32,026,660	31,009,475	6,960	6,893	6,844	6,822	242,095	231,553	219,206	211,539
80	8,760	200	51,743	49,645	47,198	45,687	10,339,874	9,920,571	9,431,614	9,129,741	6,968	6,902	6,862	6,843	72,044	68,475	64,719	62,474
	Total	8,760	50,013	47,751	45,366	43,929	483,772,825	480,023,982	465,471,827	452,784,380				Total	3,351,610	3,316,346	3,189,975	3,077,382
						Average Capacity (KW)	55,225	54,797	53,136	51,688								

Economics of Supercharging (Combined Cycle)								
Value of Electricity ($/KWH)				0.03				0.04
Value of Electical Capacity ($/KW-YR)				100.00				100.00
Unit Cost of Fuel ($/MMBTU)				3.00				3.00
Pressure (PSIA)	16.90	16.10	15.20	14.70	16.90	16.10	15.20	14.70
Capital Costs								
Evaporative Cooler (Incl. Inlet Heating),$	220000	220000	220000	220000	220000	220000	220000	220000
Supercharger, $	1,386,000	926,000	313,000	0	1,386,000	926,000	313,000	0
Additional Aux. Cap. Resulting from Supercharging, $	1,796,238	1,796,238	860,315	0	1,796,238	1,796,238	860,315	0
Additional Costs for Supercharging, $	3,182,238	2,722,238	1,173,315	0	3,182,238	2,722,238	1,173,315	0
Total	3,402,238	2,942,238	1,393,315	220,000	3,402,238	2,942,238	1,393,315	220,000
Revenues								
Power Generation (KWH)	483,772,825	480,023,982	465,471,827	452,784,380	483,772,825	480,023,982	465,471,827	452,784,380
Average Capacity (KW)	55,225	54,797	53,136	51,688	55,225	54,797	53,136	51,688
Fuel Consumption (BTU/YR)	3,351,610	3,316,346	3,189,975	3,077,382	3,351,610	3,316,346	3,189,975	3,077,382
Energy Revenue ($)	14,513,185	14,400,719	13,964,155	13,583,531	19,350,913	19,200,959	18,618,873	18,111,375
Electrical Capacity Credit ($)	5,522,521	5,479,726	5,313,605	5,168,771	5,522,521	5,479,726	5,313,605	5,168,771
Cost of Fuel ($)	10,054,831	9,949,038	9,569,926	9,232,145	10,054,831	9,949,038	9,569,926	9,232,145
Net Power Generating Revenue ($/Year)	9,980,874	9,931,407	9,707,834	9,520,158	14,818,602	14,731,647	14,362,552	14,048,001
Supercharging Advantage ($/Year)	460,717	411,250	187,676	0	770,601	712,761	319,658	0
Net Revenue w/ Evap. Clr. & Superchrg. ($/Year)	9,980,874	9,931,407	9,707,834	9,520,158	14,818,602	14,731,647	14,362,552	14,048,001
Net Power Gen. Rev. w/o Evap. Clr. ($/Year)	9,310,310	9,310,310	9,310,310	9,310,310	13,745,179	13,745,179	13,745,179	13,745,179
Evap. Cool.+Supercharg. Advantage, ($/Year)	670,564	621,098	397,524	209,848	1,073,423	986,468	617,373	302,822
Evaporative Cooler Component of Payback	1.05	1.05	1.05	1.05	0.73	0.73	0.73	0.73
Supercharger Component of Payback	6.91	6.62	6.25		4.13	3.82	3.67	
Comb. Superchrg. & Evap. Cooler Payback	5.07	4.74	3.50	1.05	3.17	2.98	2.26	0.73

Table 4 300-ton chiller duty

Cumulative Hours	Duration in Temp. Range (Hrs.)	Average Wet Bulb Temp. (F)	Average Dry Bulb Temp. (F)	Enthalpy (BTU/LB)	Temp. after Chlr/Htr Coils (F)	Enthalpy after Chlr/Htr (BTU/LB)	Delta Enthalpy (BTU/LB)	Inlet Air Flow (LB/HR) Pressure (PSIA)				Q* (BTU/HR) Pressure (PSIA)				Chiller Auxiliary Load (KW) Pressure (PSIA)			
								16.90	16.10	15.20	14.70	16.90	16.10	15.20	14.70	16.90	16.10	15.20	14.70
0	0																		
100	100	8	14																
200	100	10	16		50														
300	100	12	18		50														
400	100	14	19		50							No Chiller In This Region							
500	100	15	21		50														
1000	500	17	23	6.00	50														
2000	1000	24	30	8.70	50														
3000	1000	35	41	13.00	50														
4000	1000	43	47	16.70	50														
5000	1000	48	52	19.20	50	18.70	0.50	1,060,560	1,060,560	1,031,100	1,001,640	530,280	530,280	515,550	500,820	49	49	47	46
6000	1000	52	56	21.40	50	19.90	1.50	1,060,560	1,060,560	1,031,100	1,001,640	1,590,840	1,590,840	1,546,650	1,502,460	146	146	142	138
7000	1000	56	60	23.80	50	20.30	3.50	1,060,560	1,060,560	1,031,100	1,001,640	3,711,960	3,711,960	3,608,850	3,505,740	340	340	331	321
7500	500	61	67	27.10	56	23.60	3.50	1,075,290	1,060,560	1,014,406	977,090	3,763,515	3,711,960	3,550,421	3,419,815	345	340	325	313
8000	500	65	72	30.00	60	26.50	3.50	1,082,164	1,060,560	1,002,622	966,288	3,787,574	3,711,960	3,509,177	3,382,008	347	340	322	310
8600	600	69	78	33.00	64	29.50	3.50	1,076,272	1,040,920	983,964	948,612	3,766,952	3,643,220	3,443,874	3,320,142	345	334	316	304
8700	100	76	86	39.40	72	35.90	3.50	1,055,650	999,676	946,648	911,296	3,694,775	3,498,866	3,313,268	3,189,536	339	321	304	292
8760	60	77	88	40.30	73	36.80	3.50	1,050,740	994,766	941,738	907,368	3,677,590	3,481,681	3,296,083	3,175,788	337	319	302	291
Total	8760							0	0	0	0								

mmBtu ($2.84/mmkj). The capital cost of the base simple cycle plant is set at $700/kW installed. Incremental cost of enlarged peripheral equipment to handle additional capacity is only $300/kW since the basic LM6000 package is capable of generating the added power due to supercharging without increasing the size of the turbine package itself. Capital cost of the supercharger including fan, motor, fan house, transformer capacity, ductwork, downstream evaporative cooler, controls, foundations, design, and installation is $450/hp ($600/kW) of fan auxiliary load based on escalated cost for an existing unit. Since different organizations employ different methods of accounting for operations and maintenance, O&M have been omitted from this analysis.

At this site, a simple cycle LM6000 produces 342 × 10^6 kWh/year (see Table 1). With full evaporative cooling and a small amount of inlet heating when the temperature drops below 40°F (4°C), the same gas turbine package produces 349 × 10^6 kWh/year at a slightly better heat rate (see Table 2). The only incremental capital cost involved is that of the heating system and the evaporative coolers, approximately $220,000 depending on the type of inlet heating and evaporative cooling systems utilized. Evaporative cooling does not increase the turbine capacity; it simply enables it to operate closer to its limit more of the time. In contrast to supercharging, it is not necessary to increase the size of gas turbine plant equipment when adding evaporative cooling.

Table 1 indicates that annual net revenue of $5,121,577 is generated on an investment of $28,788,900, which is paid back in 5.62 years without evaporative cooling for the base simple cycle plant. On the other hand, Table 2 shows that evaporative cooling alone increases annual revenue $121,650 to $5,243,227 and has a payback of 1.81 years on the additional $220,000 investment at this typical northeastern U.S. site. Because the evaporative cooler has already boosted power considerably for little additional capital cost, the remaining gain realized from the addition of supercharging is reduced over the nonevaporative-cooled case in Table 1. As Table 2 indicates, payback on the capital invested in supercharging ranges from 10.26 to 14.79 years for 15.2 psia (105 kPa) to 16.9 psia (116 kPa) supercharging, respectively; supercharging paybacks are poorer than 5.62 years, the baseline for the simple cycle plant itself, and far exceed those for evaporative cooling even at this relatively humid site.

Combined Cycle. A single-engine, LM6000 combined cycle plant produces 53,008 kW without duct firing the HRSG. At an estimated $1000/kW the total installed plant costs $53,008,000. The power increase resulting from a supercharged inlet does not add to the cost of the gas turbine package per se. It does, however, require enlarged gas turbine peripheral equipment, i.e., gas compressor, switchgear, etc. and enlarged steam-side equipment, i.e., HRSG, steam turbine, etc. It is estimated that the resulting incremental equipment cost for supercharging a combined cycle plant is $684/kW. The cost of the supercharger itself is the same as in the simple cycle case, i.e., $450/hp ($600/kW).

The base combined cycle plant (Table 1), without supercharging, produces revenues, excluding O&M, of $9,310,310 per year at the $0.03/kW electrical rate. This results in a payback of 5.69 years. When an evaporative cooler is added, not only does the cooler have an extremely short payback, 1.05 years (Table 3), but combined with the supercharger, the payback ranges from 3.50 years to 5.07 years on total investments of $1,393,315 to $3,402,230 as the supercharger raises inlet pressure from sea level (101 kPa) to 16.9 psia (116 kPa), respectively. All paybacks are well below the combined cycle plant baseline of 5.69 years.

Inlet Chilling and Heating Plus Supercharging. Using an absorption chiller powered by waste-heat-generated steam or a motor-driven centrifugal chiller in conjunction with inlet heating, it is possible to maintain the LM6000 inlet at the opti-

Table 5 Simple cycle performance andeconomics with a 300-ton chiller

Simple Cycle Performance (300-Ton Chiller)

Pressure (PSIA)	16.90	16.10	15.20	14.70
Power (KW) @ 50 F	42,900	42,753	41,624	40,533
Heat Rate (BTU/KWH-LHV) @50 F	8,989	8,962	8,876	8,793

Net Power (KW)**				Annual Power Production (KWH/Year)				Annual Fuel Consumption (MMBTU)			
Pressure (PSIA)				Pressure (PSIA)				Pressure (PSIA)			
16.90	16.10	15.20	14.70	16.90	16.10	15.20	14.70	16.90	16.10	15.20	14.70
42,900	42,753	41,624	40,533	0	0	0	0	0	0	0	0
42,900	42,753	41,624	40,533	4,289,977	4,275,289	4,162,407	4,053,259	38,561	38,315	36,947	35,642
42,900	42,753	41,624	40,533	4,289,977	4,275,289	4,162,407	4,053,259	38,561	38,315	36,947	35,642
42,900	42,753	41,624	40,533	4,289,977	4,275,289	4,162,407	4,053,259	38,561	38,315	36,947	35,642
42,900	42,753	41,624	40,533	4,289,977	4,275,289	4,162,407	4,053,259	38,561	38,315	36,947	35,642
42,900	42,753	41,624	40,533	4,289,977	4,275,289	4,162,407	4,053,259	38,561	38,315	36,947	35,642
42,900	42,753	41,624	40,533	21,449,884	21,376,443	20,812,034	20,266,297	192,804	191,575	184,736	178,212
42,900	42,753	41,624	40,533	42,899,767	42,752,886	41,624,068	40,532,594	385,608	383,150	369,473	356,423
42,900	42,753	41,624	40,533	42,899,767	42,752,886	41,624,068	40,532,594	385,608	383,150	369,473	356,423
42,900	42,753	41,624	40,533	42,899,767	42,752,886	41,624,068	40,532,594	385,608	383,150	369,473	356,423
42,851	42,704	41,577	40,487	42,851,391	42,704,277	41,576,810	40,486,686	385,608	383,150	369,473	356,423
42,754	42,607	41,482	40,395	42,754,173	42,607,059	41,482,292	40,394,869	385,608	383,150	369,473	356,423
42,560	42,413	41,293	40,211	42,559,737	42,412,623	41,293,257	40,211,235	385,608	383,150	369,473	356,423
42,276	41,806	40,453	39,280	21,137,960	20,902,987	20,226,324	19,640,178	192,204	188,804	181,073	174,703
41,929	41,210	39,682	38,454	20,964,560	20,604,968	19,840,830	19,226,763	191,082	186,160	177,788	171,548
41,440	40,466	38,767	37,497	24,863,737	24,279,359	23,260,485	22,498,378	227,110	219,493	208,777	201,461
39,983	38,540	36,605	35,315	3,998,332	3,853,956	3,660,486	3,531,511	36,657	34,964	33,072	31,918
39,756	38,262	36,312	35,026	2,385,380	2,295,700	2,178,711	2,101,579	21,878	20,842	19,707	19,020
			Total	373,114,338	370,672,472	360,015,469	350,221,574	3,368,185	3,332,310	3,206,726	3,093,611

Economics of Supercharging (Simple Cycle with 300-Ton Chiller)

Value of Electricity ($/KWH)				0.03				0.04
Value of Electical Capacity ($/KW-YR)				100				100
Unit Cost of Fuel ($/MMBTU)				3.00				3.00
Pressure (PSIA)	***16.90***	***16.10***	***15.20***	***14.70***	***16.90***	***16.10***	***15.20***	***14.70***
Capital Costs								
Chiller & Coils (Incl. Heating), $	510,000	510,000	510,000	510,000	510,000	510,000	510,000	510,000
Supercharger, $	1,386,000	926,000	313,000	0	1,386,000	926,000	313,000	0
Increased Plant Size Resulting from Supercharging, $	577,430	533,366	194,721	0	577,430	533,366	194,721	0
Total Cost to Suprchrg. & Chill	2,473,430	1,969,366	1,017,721	510,000	2,473,430	1,969,366	1,017,721	510,000
Revenues								
Power Generation (KWH)	373,114,338	370,672,472	360,015,469	350,221,574	373,114,338	370,672,472	360,015,469	350,221,574
Average Capacity (KW)	42,593	42,314	41,098	39,980	42,593	42,314	41,098	39,980
Fuel Consumption (MMBTU/YR)	3,368,185	3,332,310	3,206,726	3,093,611	3,368,185	3,332,310	3,206,726	3,093,611
Energy Revenue ($)	11,193,430	11,120,174	10,800,464	10,506,647	14,924,574	14,826,899	14,400,619	14,008,863
Electrical Capacity Credit ($)	4,259,296	4,231,421	4,109,766	3,997,963	4,259,296	4,231,421	4,109,766	3,997,963
Cost of Fuel ($)	10,104,555	9,996,931	9,620,179	9,280,834	10,104,555	9,996,931	9,620,179	9,280,834
Net Revenue ($/Year)	5,348,171	5,354,664	5,290,051	5,223,776	9,079,315	9,061,389	8,890,205	8,725,992
Payback								
Net Revenue w/ Chiller & Superchrg. ($/Year)	5,348,171	5,354,664	5,290,051	5,223,776	9,079,315	9,061,389	8,890,205	8,725,992
Net Revenue of Base Plant ($/Year)	5,121,577	5,121,577	5,121,577	5,121,577	8,545,308	8,545,308	8,545,308	8,545,308
Chiller + Supercharger Advantage, $	**226,594**	**233,087**	**168,473**	**102,199**	**534,006**	**516,081**	**344,897**	**180,684**
Comb. Superchrg. & Chiller Payback	**10.92**	**8.45**	**6.04**	**4.99**	**4.63**	**3.82**	**2.95**	**2.82**

Table 6 Economics of supercharging and chilling a combined cycle

Value of Electricity ($/KWH)	0.03				0.04			
Value of Electical Capacity ($/KW-YR)	100				100			
Unit Cost of Fuel ($/MMBTU)	3				3			
Pressure (PSIA)	*16.90*	*16.10*	*15.20*	*14.70*	*16.90*	*16.10*	*15.20*	*14.70*

Combined Cycle with 300-Ton Chiller and Supercharging

Capital Costs								
Chiller & Coils (Incl. Heating), $	510,000	510,000	510,000	510,000	510,000	510,000	510,000	510,000
Supercharger (Incl. Downstream Evap. Clr.), $	1,386,000	926,000	313,000	0	1,386,000	926,000	313,000	0
Increased Plant Size Resulting from Supercharging, $	1,802,340	1,643,652	582,768	0	1,802,340	1,643,652	582,768	0
Total Cost to Suprcharge & Chill, $	3,698,340	3,079,652	1,405,768	510,000	3,698,340	3,079,652	1,405,768	510,000
Revenues								
Power Generation (KWH)	485,583,401	481,978,814	467,536,889	454,606,578	485,583,401	481,978,814	467,536,889	454,606,578
Average Capacity (KW)	55,432	55,020	53,372	51,896	55,432	55,020	53,372	51,896
Fuel Consumption (MMBTU/YR)	3,368,185	3,332,310	3,206,726	3,093,611	3,368,185	3,332,310	3,206,726	3,093,611
Energy Revenue ($)	14,567,502	14,459,364	14,026,107	13,638,197	19,423,336	19,279,153	18,701,476	18,184,263
Electrical Capacity Credit ($)	5,543,190	5,502,041	5,337,179	5,189,573	5,543,190	5,502,041	5,337,179	5,189,573
Cost of Fuel ($)	10,104,555	9,996,931	9,620,179	9,280,834	10,104,555	9,996,931	9,620,179	9,280,834
Net Revenue ($/Year)	10,006,137	9,964,475	9,743,107	9,546,936	14,861,971	14,784,263	14,418,475	14,093,002
Payback								
Net Revenue w/ Chiller & Superchrg. ($/Year)	10,006,137	9,964,475	9,743,107	9,546,936	14,861,971	14,784,263	14,418,475	14,093,002
Net Revenue of Base Plant ($/Year)	9,310,310	9,310,310	9,310,310	9,310,310	13,745,179	13,745,179	13,745,179	13,745,179
Chiller + Supercharger Advantage, $	**695,827**	**654,165**	**432,797**	**236,626**	**1,116,791**	**1,039,084**	**673,296**	**347,822**
Combined Supercharger & Chiller Payback (Years)	**5.32**	**4.71**	**3.25**	**2.16**	**3.31**	**2.96**	**2.09**	**1.47**

Combined Cycle with 850-Ton Chiller and Supercharging

Capital Costs								
Chiller & Coils (Incl. Heating), $	1,225,000	1,225,000	1,225,000	1,225,000	1,225,000	1,225,000	1,225,000	1,225,000
Supercharger (Incl. Downstream Evap. Clr.), $	1,386,000	926,000	313,000	0	1,386,000	926,000	313,000	0
Increased Plant Size Resulting from Supercharging, $	1,802,340	1,643,652	582,768	0	1,802,340	1,643,652	582,768	0
Total Cost to Suprcharge & Chill, $	4,413,340	3,794,652	2,120,768	1,225,000	4,413,340	3,794,652	2,120,768	1,225,000
Revenues								
Power Generation (KWH)	486,022,436	483,580,812	469,806,938	456,990,017	486,022,436	483,580,812	469,806,938	456,990,017
Average Capacity (KW)	55,482	55,203	53,631	52,168	55,482	55,203	53,631	52,168
Fuel Consumption (MMBTU/YR)	3,376,024	3,350,748	3,229,365	3,115,347	3,376,024	3,350,748	3,229,365	3,115,347
Energy Revenue ($)	14,580,673	14,507,424	14,094,208	13,709,701	19,440,897	19,343,232	18,792,278	18,279,601
Electrical Capacity Credit ($)	5,548,201	5,520,329	5,363,093	5,216,781	5,548,201	5,520,329	5,363,093	5,216,781
Cost of Fuel ($)	10,128,073	10,052,245	9,688,095	9,346,042	10,128,073	10,052,245	9,688,095	9,346,042
Net Revenue ($/Year)	10,000,801	9,975,509	9,769,206	9,580,439	14,861,026	14,811,317	14,467,275	14,150,340
Payback								
Net Revenue w/ Chiller & Superchrg. ($/Year)	10,000,801	9,975,509	9,769,206	9,580,439	14,861,026	14,811,317	14,467,275	14,150,340
Net Revenue of Base Plant ($/Year)	9,310,310	9,310,310	9,310,310	9,310,310	13,745,179	13,745,179	13,745,179	13,745,179
Chiller + Supercharger Advantage, ($/Year)	**690,491**	**665,199**	**458,896**	**270,130**	**1,115,846**	**1,066,137**	**722,096**	**405,160**
Combined Supercharger & Chiller Payback (Years)	**6.39**	**5.70**	**4.62**	**4.53**	**3.96**	**3.56**	**2.94**	**3.02**

Combined Cycle with 1700-Ton Chiller and Supercharging

Capital Costs								
Chiller & Coils (Incl. Heating), $	2,330,000	2,330,000	2,330,000	2,330,000	2,330,000	2,330,000	2,330,000	2,330,000
Supercharger (Incl. Downstream Evap. Clr.), $	1,386,000	926,000	313,000	0	1,386,000	926,000	313,000	0
Increased Plant Size Resulting from Supercharging, $	1,802,340	1,643,652	582,768	0	1,802,340	1,643,652	582,768	0
Total Cost to Suprcharge & Chill, $	5,518,340	4,899,652	3,225,768	2,330,000	5,518,340	4,899,652	3,225,768	2,330,000
Revenues								
Power Generation (KWH)	486,037,549	484,005,229	470,487,528	457,755,673	486,037,549	484,005,229	470,487,528	457,755,673
Average Capacity (KW)	55,484	55,252	53,709	52,255	55,484	55,252	53,709	52,255
Fuel Consumption (MMBTU/YR)	3,377,923	3,356,391	3,236,580	3,122,267	3,377,923	3,356,391	3,236,580	3,122,267
Energy Revenue ($)	14,581,126	14,520,157	14,114,626	13,732,670	19,441,502	19,360,209	18,819,501	18,310,227
Electrical Capacity Credit ($)	5,548,374	5,525,174	5,370,862	5,225,521	5,548,374	5,525,174	5,370,862	5,225,521
Cost of Fuel ($)	10,133,768	10,069,173	9,709,741	9,366,801	10,133,768	10,069,173	9,709,741	9,366,801
Net Revenue ($/Year)	9,995,732	9,976,158	9,775,747	9,591,391	14,856,108	14,816,210	14,480,622	14,168,948
Payback								
Net Revenue w/ Chiller & Superchrg. ($/Year)	9,995,732	9,976,158	9,775,747	9,591,391	14,856,108	14,816,210	14,480,622	14,168,948
Net Revenue of Base Plant ($/Year)	9,310,310	9,310,310	9,310,310	9,310,310	13,745,179	13,745,179	13,745,179	13,745,179
Chiller + Supercharger Advantage, ($/Year)	**685,422**	**665,848**	**465,437**	**281,081**	**1,110,928**	**1,071,031**	**735,443**	**423,768**
Combined Supercharger & Chiller Payback (Years)	**8.05**	**7.36**	**6.93**	**8.29**	**4.97**	**4.57**	**4.39**	**5.50**

mum 50°F (10°C) over the full range of ambient temperatures at the site in question. To determine the duty on the chiller and the subsequent power requirement, the wet bulb/dry bulb temperature duration curves in Fig. 13 and corresponding equations are used. The data in Table 4 illustrate the use of these equations to model the performance of a 300-ton (1055 kW) chiller.

Once the average wet bulb and dry bulb temperatures for a given period of time are established from the equations in Fig. 13, the change in enthalpy can be determined from each of these average points to the optimum 50°F (10°C) dry bulb on a psychometric chart. Conversely if the chiller does not have the capacity to cool the air to 50°F (10°C), the enthalpy change it can effect is used to determine the resulting inlet temperature on the psychometric chart.

Simple Cycle. The turbine capacity displayed in Table 5 reflects the net power produced by an LM6000 with supercharged and chilled inlet after deducting the auxiliary power of the supercharger fan motor and chiller drive motor. Annual power production is calculated using the number of hours of operation in each temperature range times the power output at that temperature. Note that power production with a 300-ton (1055 kW) chiller cooling the inlet is not much greater than the evaporative-cooled case, but the fuel consumption is greater because of the increased auxiliary load of the chilled system.

The equipment employed in this analysis consists of a centrifugal chiller and steam heater plus heating and cooling coils located in the turbine air inlet as well as the supercharger used in the evaporative-cooled cases. An evaporative cooler downstream of the supercharger removes the heat of compression introduced by the fan. The cost assigned to the chiller system is $1200 per kW of centrifugal chiller load. As in the case of the evaporative cooler, the plant capacity does not change, so none of the plant equipment must be enlarged as it is with supercharging. The 300-ton (1055 kW) chiller payback of 4.99 years on earnings of $102,199/year for a $510,000 investment is attractive for the simple cycle case; however, as supercharging is added, the payback period increases rapidly. A rigorous analysis addresses the optimum mix of supercharging and chilling in the summary.

Combined Cycle. Referring to Table 6, in conjunction with chillers, the plant generates more net power and produces more revenue than the fully evaporative-cooled, similarly supercharged combined cycle plant. However, a larger investment is also required to employ chilling rather than evaporative cooling to reduce inlet air temperature. Full evaporative cooling plus

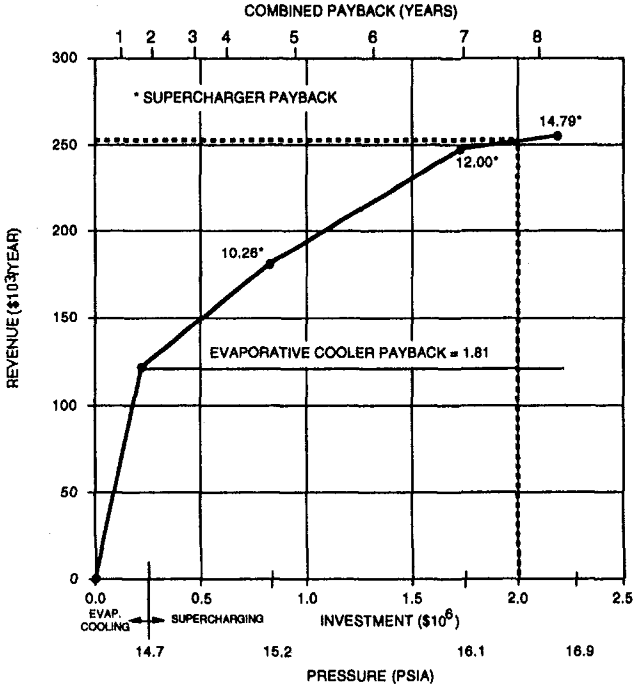

Fig. 15 Annual revenue from simple cycle, evaporative-cooled, supercharged plant

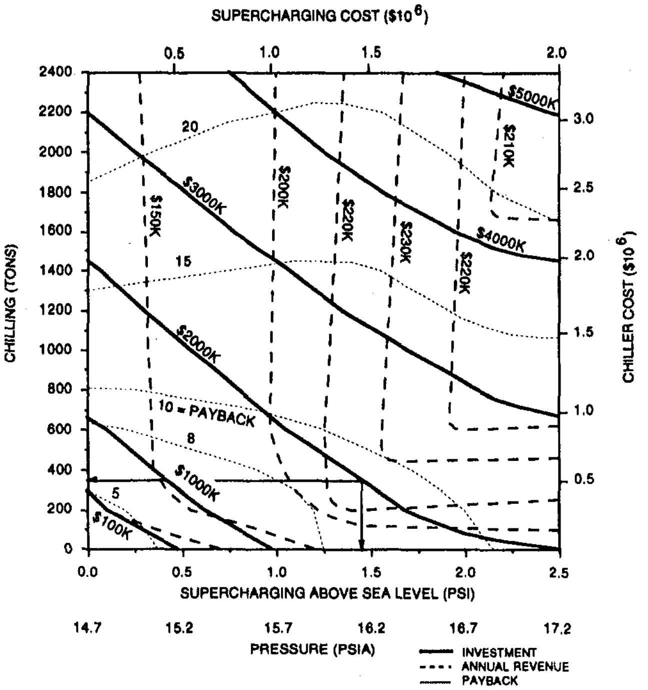

Fig. 17 Chilling and supercharging simple cycle R.O.I.

inlet heating requires a $220,000 investment. An investment ranging from $510,000 to $2,330,000 is necessary to add from 300 to 1700 tons (1055–6000 kW) of chilling. However, as Table 6 indicates, many combinations of supercharging and chilling yield paybacks less than the base combined cycle plant payback of 5.69 years using $.03/kWh electricity. The optimum combination of cooling and/or supercharging is addressed in the summary.

Summary

Evaporative Cooling. Because evaporative cooling is so cost effective, it is advisable to incorporate it before implementing supercharging, i.e., if limited capital is available it should be spent to achieve full evaporative cooling before any supercharging is introduced.

Evaporative Cooling in Conjunction With Supercharging. To demonstrate the economic impact of inlet air conditioning, assume that the plant has a capital budget of $2

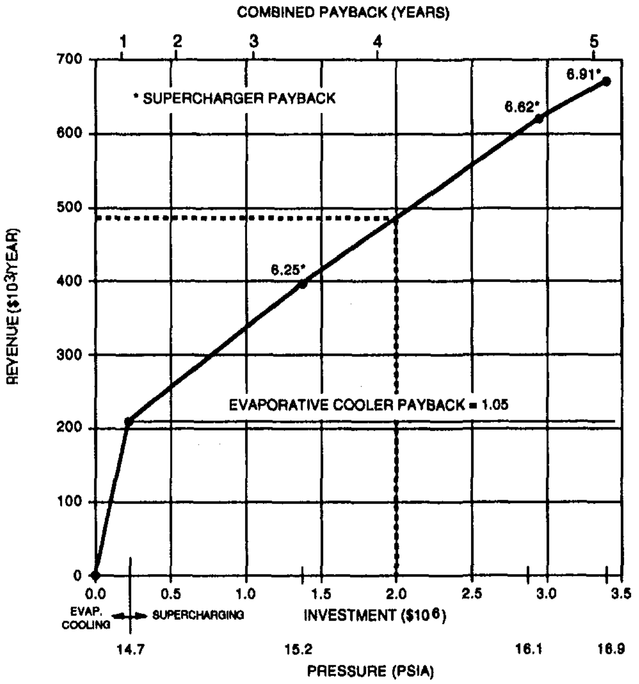

Fig. 16 Annual revenue from combined cycle, evaporative-cooled, supercharged plant

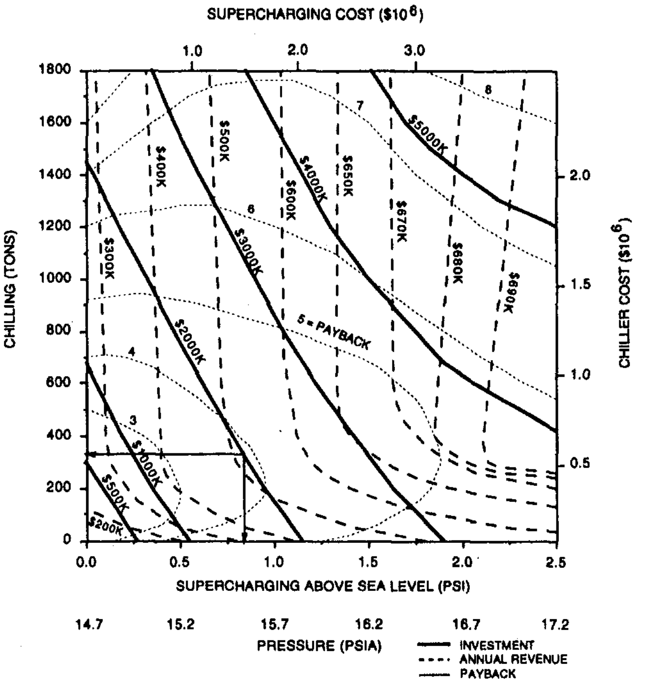

Fig. 18 Chilling and supercharging combined cycle R.O.I.

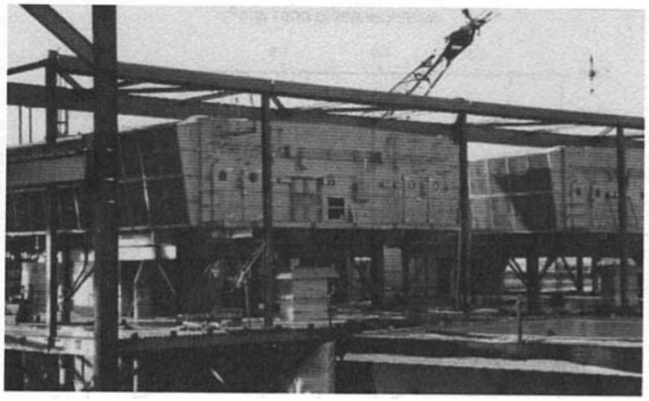

Fig. 19 Photo of inlet system

million, and its objective is to achieve a simple payback on that capital in 5.62 years (the baseline for the simple cycle case). Using the data compiled in Tables 2 and 3, plots of investment in evaporative cooler and supercharger may be made along with their corresponding annual revenues.

Figure 15 shows that while evaporative cooling can easily be justified, the combination of evaporative cooling and supercharging commensurate with a $2-million investment only returns $250,000/year, yielding a simple payback of 8 years, which is well over the 5.62-year requirement.

Investing the same $2 million in an evaporative-cooled, supercharged, combined cycle plant on the other hand does seem to satisfy the revenue requirement. Referring to Fig. 16, a $2-million system supercharged to approximately 15.5 psia (107 kPa) would produce $480,000 of annual revenues based on $.03/kWh electricity. The corresponding simple payback of 4.2 years is considerably better than the 5.69-year payback on the base combined cycle plant.

While the combination of evaporative cooling and supercharging has a very attractive payback, the plant manager will note that this is primarily the result of an overwhelmingly short payback (1 year) for the $220,000 investment in the evaporative cooler. Payback on the supercharger portion of the system runs between 6 and 7 years. The discriminating plant manager may opt to install the evaporative cooler at the higher rate of return and direct the remaining funds elsewhere, to improvements that have a shorter payback period than 6 to 7 years.

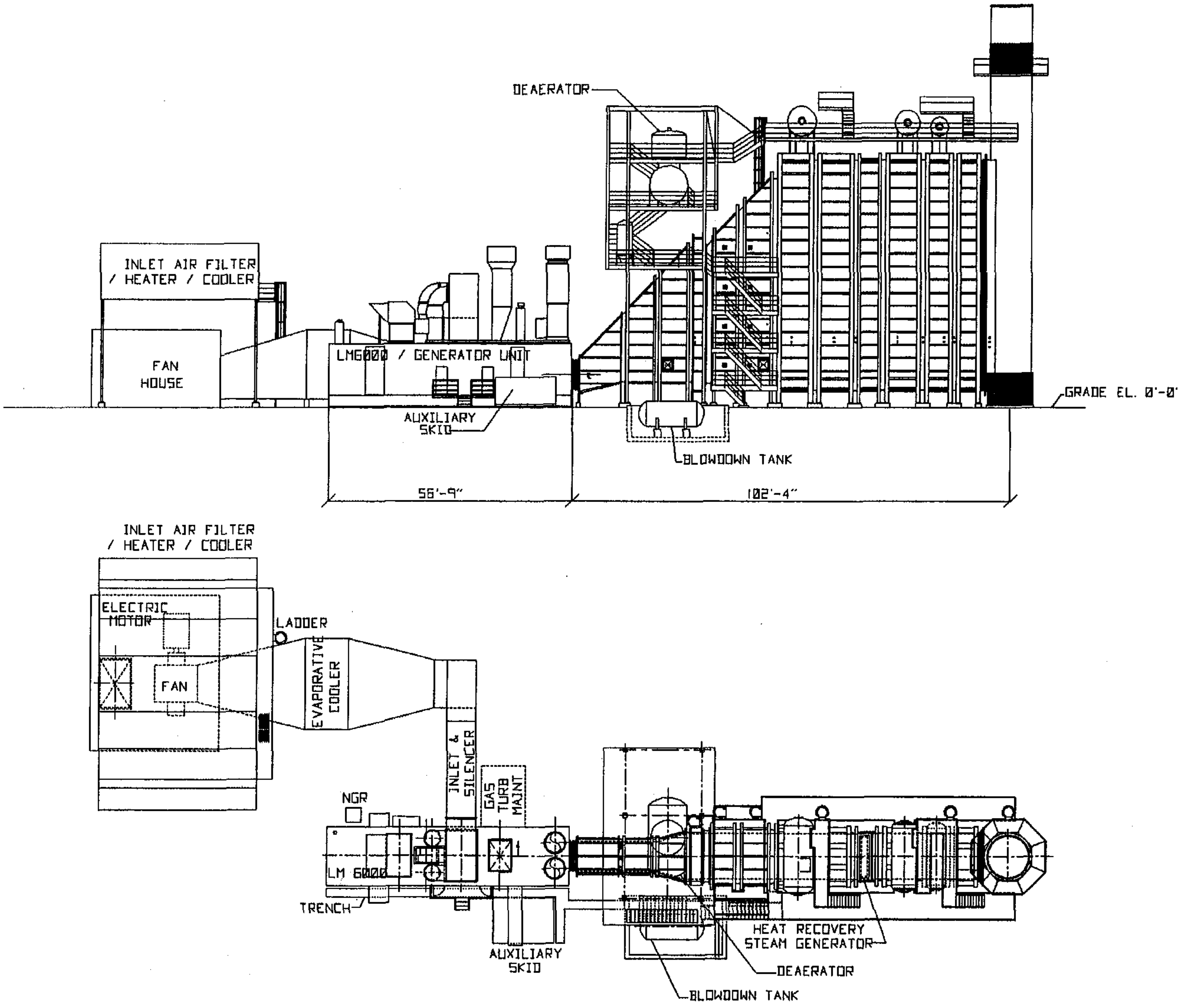

Fig. 20 Plant layout

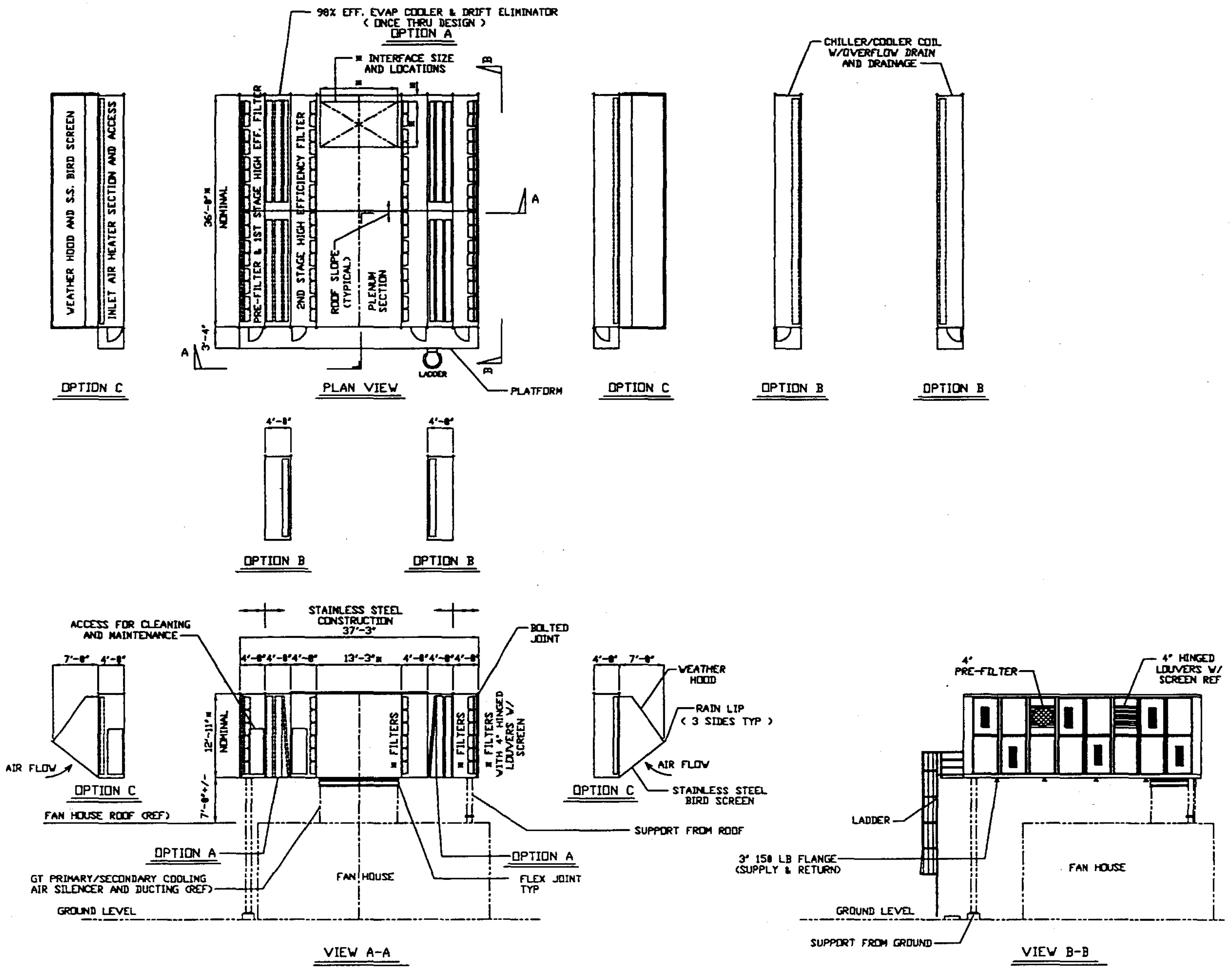

Fig. 21 Inlet air conditioning module

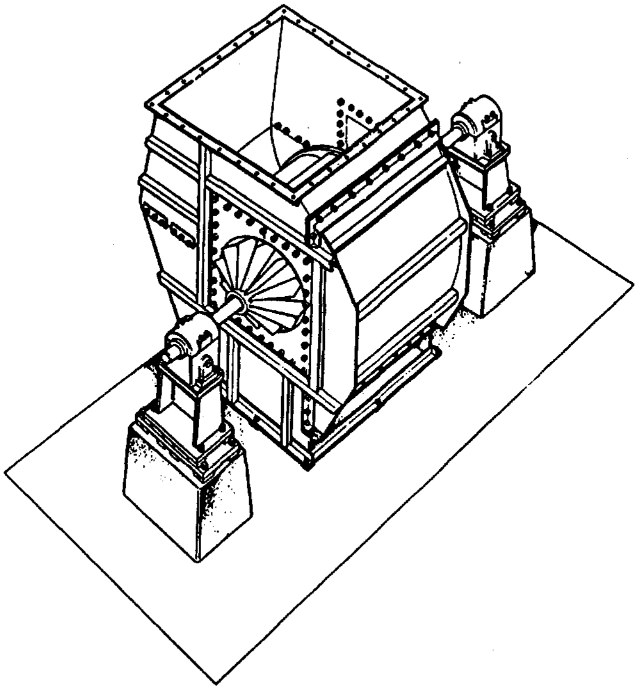

Fig. 22 Typical supercharging fan

Combining Supercharging With Inlet Chilling. As noted in the economics section, the effects of supercharging and of inlet chilling on LM6000 performance are extremely interdependent. As supercharging increases, the impact of chilling on gas turbine output is reduced, and conversely more chilling cuts into the amount of added power that can be attributed to supercharging. The following analysis enables the planner to determine the optimum mix of inlet chilling and supercharging.

Figure 17 shows a range of possible combinations of supercharging and chilling along with the investment required to achieve the respective levels of chilling and supercharging. The figure also gives the revenues and paybacks generated by each combination of chilling and supercharging. This plot enables the user to select the most cost-beneficial combination of supercharging and chilling for a given investment. For example, at the northeastern U.S. site analyzed in this study with $0.03/kWh electricity, the optimum combination for a $2-million investment calls for pressurizing the inlet to 16.1 psia (111 kPa) and 300 tons (1055 kW) of chilling. As the graph shows, this point results in annual revenues of approximately $225,000; the subsequent payback is 9 years. Nine years is well over the 5.62-year hurdle rate required by the base simple cycle plant, and also somewhat greater than the 8-year payback provided by supercharging and evaporative cooling. Figure 17 indicates that only small amounts of chilling, less than 400 tons (1407 kW), and very little supercharging, less than 0.3 psi (2.1 kPa), are feasible in simple cycle applications. In fact, comparing Fig. 17 with Fig. 15, it is clear that the only sensible choice for economically improving the LM6000 simple cycle performance is evaporative cooling.

Figure 18 indicates that the prospects for chilling and supercharging are much better on a combined cycle plant. In this instance if $2 million is available for inlet air conditioning, the figure indicates that the optimum combination of chilling and supercharging is 300 tons (1055 kW) and 15.5 psia (107 kPa), respectively. The net revenues generated by this combination of chilling and supercharging are over $500,000/year, which results in a simple payback of 4 years—slightly better than the 4.2-year payback resulting from the combination of evaporative cooling and supercharging (Fig. 16). Interestingly, the combination of evaporative cooler and supercharger produces annual revenues similar to the chiller and supercharger over the entire investment range for the combined cycle plant.

Equipment

Plant Layout. A plot plan for an LM6000 with inlet cooling and supercharging in conjunction with an HRSG is shown in Fig. 20. The air enters the inlet house where it passes a combination of heating/cooling coils, or evaporative coolers, as well as prefilters and high performance filters before entering the fan house. The options analyzed earlier in this paper are illustrated in Fig. 21. Option A is a 98 percent efficient evaporative cooler, meaning that the temperature will be reduced at least 98 percent of the difference between the wet bulb and dry bulb temperature. The Option A module can be replaced with the Option B module consisting of cooling coils capable of reducing the temperature to the optimum for the given site conditions—50°F (10°C) in this study. Option C may be added if additional chilling and/or inlet heating or deicing are required.

Figure 19 shows the inlets of two LM6000's with high-performance inlet filtration, inlet chilling, and heating.

A fan similar to one used on a supercharged gas turbine in Boron, California, is shown in Fig. 22.

Conclusions

In analyzing the effect of various forms of inlet air heating, cooling, and supercharging on an LM6000 at a typical northeastern U.S. site, evaporative cooling is clearly beneficial in both simple and combined cycle, base-loaded gas turbine plants, particularly if limited funds are available to improve turbine performance. Payback on evaporative cooling ranges from 1 year for combined cycle to 2 years on a simple cycle plant assuming $0.03/kWh electricity, $3/mmBtu ($2.84/mmkJ) fuel, and a $100/kW capacity credit.

Because supercharging adds heat of compression to inlet air, it is necessary to cool the air downstream of the supercharger evaporatively to improve performance. This supercharged system is marginal in simple cycle plants (6–10 years payback) but consistently provides a 6-year payback in a combined cycle or cogeneration facility using the values of electricity and fuel given above. Payback is shorter if the cost of energy is raised to $0.04/kWh.

When inlet air entering as well as leaving the supercharger is evaporatively by cooled, payback drops to between 1 and 5 years for the combined cycle plant on investments up to $3.5 million. In the simple cycle case, supercharging combined with inlet evaporative cooling is not practical because the payback on the supercharger component runs between 10 and 15 years. Figures 15 and 16 summarize the economic impact of evaporative cooling and supercharging.

Supercharging combined with chilling can be cost effective at low levels, i.e., below 0.4 PSI (2.7 kPa) and 300 tons (1055 kW), but beyond these points the payback quickly begins to exceed 5 years in a simple cycle plant. In the combined cycle case, the combination of chilling and supercharging may be more beneficial than evaporative cooling and supercharging. Up to $4 million may be invested in this system resulting in over $690,000 in additional annual revenues for a single gas turbine. It is important to select the proper mix of chilling and supercharging to obtain these returns, however; too much chilling and too little supercharging can cut these revenues by half. The methods described in this paper are useful in identifying the optimum combination of inlet treatment for a specific situation.

Figures 15 and 16 in conjunction with Figs. 17 and 18 enable the user to identify precisely the optimum mix of LM6000 inlet heating, cooling, and supercharging for a given incremental investment at a typical northeastern U.S. site. These same figures may be used as a guideline in selecting inlet air conditioning systems for any gas turbine installation.

References

1 DeBiasi, V., "Total Cost of 46-MW Borax Cogen System Put at $30 Million," *Gas Turbine World,* Mar.–Apr. 1983.

2 Kolp, D. A., Roberts, R., and Kim, S. Y., "100MW Combined Cycle Achieves 7000 Btu/kWh Heat Rate at JFK International Airport," ASME Paper No. 92-GT-40.

3 Oganowski, G., "GE LM6000 Development of the First 40% Thermal Efficiency Gas Turbine," *G.E. Marine & Industrial Engine Bulletin,* 1990.

4 Leonard, G., and Stegmaier, J., "Development of an Aeroderivative Gas Turbine Dry Low Emissions Combustion System," ASME JOURNAL OF ENGINEERING FOR GAS TURBINES AND POWER, Vol. 116, 1994, pp. 542–546.

Forging of Compressor Blades: Temperature and Ram Velocity Effects

A. Saigal

K. Zhen

Department of Mechanical Engineering,
Tufts University,
Medford, MA 02155

T. S. Chan

Manufacturing Technical Resources,
General Electric Company,
Lynn, MA 01910

*Forging is one of the most widely used manufacturing process for making high-strength, structurally integrated, impact and creep-resistant Ti-6A1-4V compressor blades for jet engines. In addition, in modern metal forming technology, finite element analysis method and computer modeling are being extensively employed for initial evaluation and optimization of various processes, including forging. In this study, DEFORM, a rigid viscoplastic two-dimensional finite element code was used to study the effects of initial die temperature and initial ram velocity on the forging process. For a given billet, die temperature and ram velocity influence the strain rate, temperature distribution, and thus the flow stress of the material. The die temperature and the ram velocity were varied over the range 300 to 700°F and 15–25 in./sec, respectively, to estimate the maximum forging load and the total energy required to forge compressor blades. The ram velocity was assumed to vary linearly as a function of stroke. Based on the analysis, it was found that increasing the die temperature from 300 to 700°F decreases the forging loads by 19.9 percent and increases the average temperature of the workpiece by 43°F. Similarly, increasing the initial ram velocity from 15 to 25 in./sec decreases the forging loads by 25.2 percent and increases the average temperature of the workpiece by 36°F. The nodal temperature distribution is bimodal in each case. The forging energy required to forge the blades is approximately 18 kips *in./in.*

Introduction

In order to select the proper forging equipment and make quality forging products, it is necessary to estimate the required forging load and energy. To investigate the effects of various process variables on the forging process, it is better to consider the process as a system. The major interactions between the process variables in the metal forging process are shown in Fig. 1. For a given billet or a preformed workpiece, the rate of deformation and die temperature influence the flow stress, strain rate, and temperature distribution in the workpiece. Finally, flow stress, friction, and geometry determine the forging load and energy.

DEFORM, a FEM analysis software package, is used to investigate the effects of rate of deformation and die temperature on the forging loads. The main purpose here is to predict the forging loads and energies as a function of (*a*) initial die temperature and (*b*) initial ram velocity.

Application of the Finite Element Method for Forging Simulation

For the analysis of forging process and to predict stress and strain fields and metal flow, many numerical methods are available. In comparison with the other methods, the finite element method has many advantages in dealing with solutions of problems with complex shapes, treatment of non-steady-state processes, and in obtaining detailed stress and strain fields. Finite element analysis and computer modeling are being extensively used for analysis of simple to complex forging processes [1].

A general purpose FEM analysis program called DEFORM has been used in this study. The main features of the program include (*i*) use of higher-order elements, (*ii*) general description of dies and of the automation of die boundary condition, which enable the user to use any number of arbitrarily shaped dies with different friction types and coefficients, and (*iii*) automatic initial mesh generation and re-mesh generation during the simulation process. DEFORM is capable of handling both rigid-plastic and rigid-viscoplastic materials, and can account for both constant friction shear stress or Coulomb type friction at the die–workpiece interface. In addition to linear elements, the program uses higher-order elements [2].

The basis of this program is the variational principle functional for rigid-viscoplastic material. The constitutive equation for the rigid-viscoplastic finite element formulation used may be represented by [3]:

$$\sigma'_{ij} = \frac{2}{3}\frac{\bar{\sigma}}{\dot{\bar{\epsilon}}}\dot{\epsilon}_{ij} \tag{1}$$

The variational principle functional for rigid-viscoplastic material can be written as [3]:

$$\Phi = \int_{\nu} E(\dot{\epsilon}^*)dV - \int_{S_F} F\cdot\upsilon^* dS + \int_V \tfrac{1}{2} k_1 (\dot{\epsilon}_{KK})^2 dV \tag{2}$$

where the starred quantities are kinematically admissible ones.

The first term on the right-hand side of Eq. (2) represents the distortional strain energy, the second term represents the rate of work due to the external tractions (force), and the third term represents the rate of strain energy.

The effective stress $\bar{\sigma}$, which is a function of the total effective strain and effective strain rate, is given by:

$$\bar{\sigma} = \tfrac{2}{3}\sigma_Y(\bar{\epsilon})\,[1 + (\dot{\epsilon}/\gamma)^{m_1}] \tag{3}$$

where $\sigma_Y(\bar{\epsilon})$ is the static yield stress, γ and m_1 are material constants.

Contributed by the International Gas Turbine Institute and presented at the 39th International Gas Turbine and Aeroengine Congress and Exposition, The Hague, The Netherlands, June 13–16, 1994. Manuscript received by the International Gas Turbine Institute March 30, 1994. Paper No. 94-GT-428. Associate Technical Editor: E. M. Greitzer.

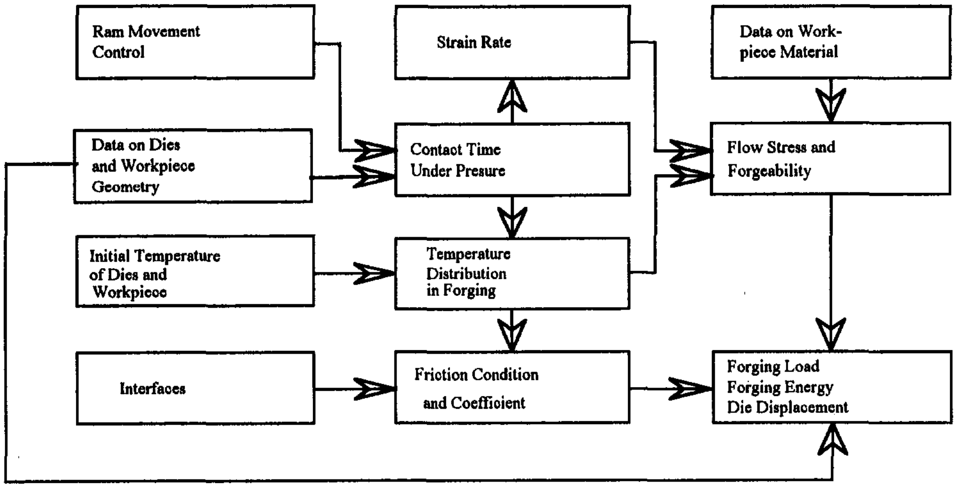

Fig. 1 Major interactions between the process variables in the forging process

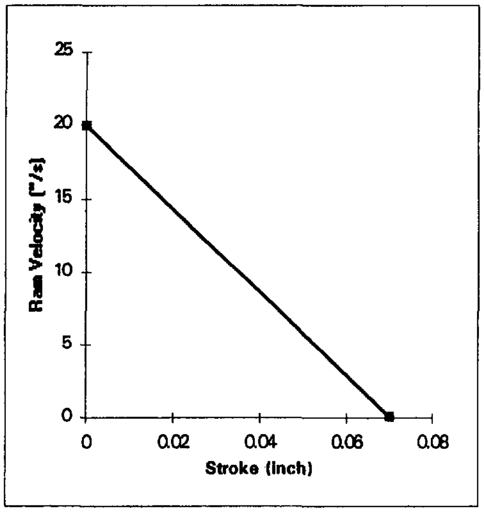

Fig. 2 Ram velocity—stroke curve

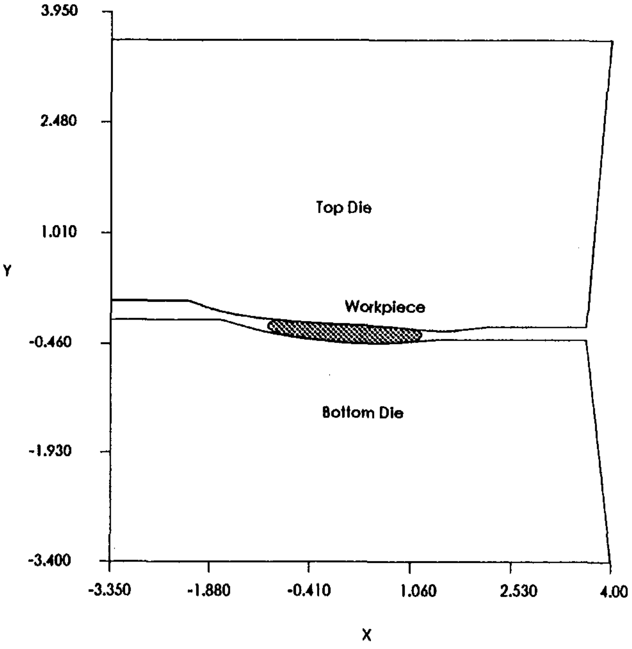

Fig. 3 The workpiece and the dies at the start of the simulation

The work function $E(\dot{\epsilon})$ can be expressed as:

$$E(\dot{\epsilon}) = \int_0^{\dot{\epsilon}} \bar{\sigma}\, d\dot{\bar{\epsilon}} \qquad (4)$$

The discretization of this functional follows the standard procedure of the finite element method. If one substitutes the distribution functions and the strain rate expression into Eq. (2), the variational functional Φ becomes a set of nonlinear algebraic simultaneous equations, which can be solved iteratively by the Newton–Raphson method [3].

Im et al. have used the finite element method to analyze the effect of flash dimensions and billet size in a closed die forging

Nomenclature

γ = material constant
$\bar{\epsilon}$ = effective strain
$\dot{\epsilon}^*$ = strain rate tensor
$\dot{\bar{\epsilon}}$ = effective strain rate
$\dot{\epsilon}_{ij}$ = strain rate component = $\frac{1}{2}(v_{i,j} + v_{j,i})$
v^* = kinematically admissible velocity vector of a surface point
dS = area increment of the external surface of the body
$d\mathbf{V}$ = volume increment undergoing plastic deformation
$\sigma_Y(\bar{\epsilon})$ = static yield stress
$\bar{\sigma}$ = effective stress; flow stress
σ'_{ij} = deviatoric stress component
v_i = velocity component, (,) in $(v_{i,j} + v_{j,i})$ denotes differentiation
Φ = variational functional related to the total potential energy
$E(\dot{\epsilon})$ = work function
$\mathbf{F}$ = external force vector acting on the surface of the body
fs = shear stress
k_1 = a large positive constant that penalizes the dilational strain rate
k_2 = shear strength of the deforming material
m_1 = material constant
m_2 = constant in the function of shear stress, $fs = m_2 k_2$, and $0 \le m_2 \le 1$
S_F = surface area of the body on which the surface force vector F acts
T = temperature

Table 1 Forging simulation results as a function of initial ram velocity

Initial Ram Velocity ("/s)	15	20	25
Average Temperature of the Workpiece (°F)	1587	1607	1623
Maximum Forging Load (Kips/in)	1123	960	840
Change in Forging Load (%)	0	-14.5	-25.2

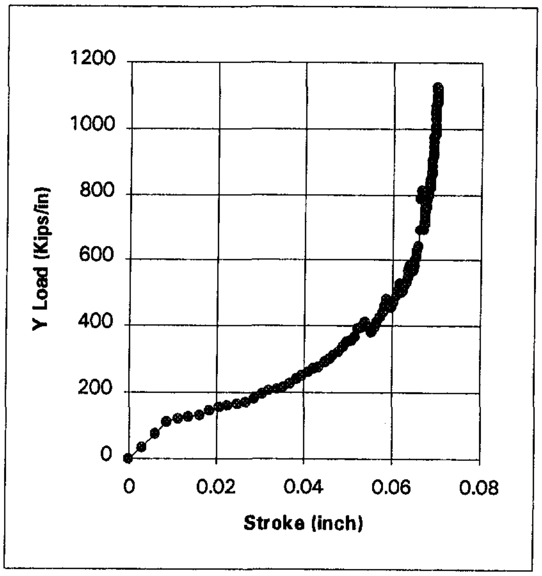

Fig. 4 Forging load as a function of stroke for initial ram velocity of 15 in./s

of an Al 6061 part with a flange and a shaft [4]. Frater et al. have simulated the ability of a particular preform to fill the die using specific flash geometry [5]. Ficke and Oh have analyzed the isothermal closed die compressor disk forging process [6]. Oh et al. have analyzed the capabilities of the code and applied it on example solutions [7]. Gleykin et al. have used DEFORM to study the effects of initial temperature distributions in the dies on the forging process [8].

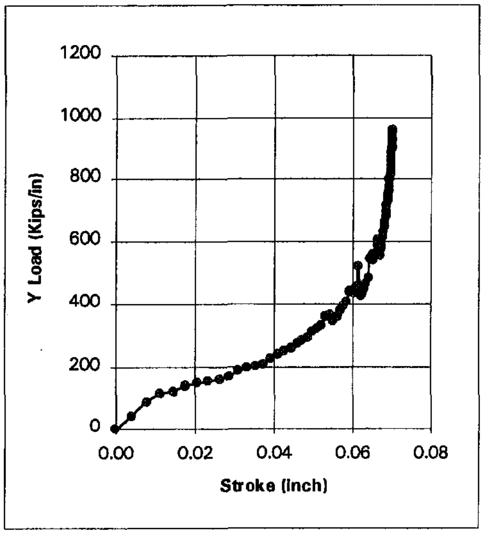

Fig. 5 Forging load as a function of stroke for initial ram velocity of 20 in./s

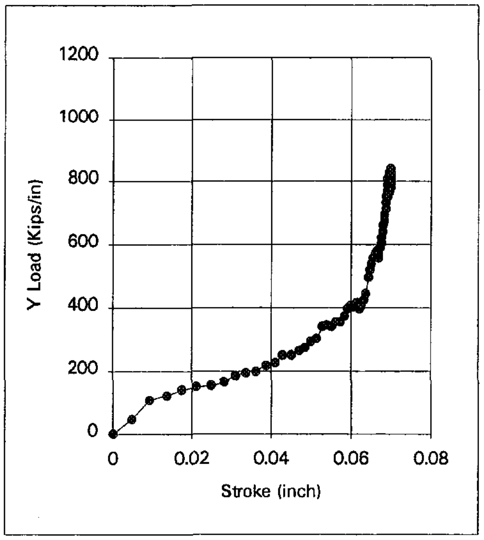

Fig. 6 Forging load as a function of stroke for initial ram velocity of 25 in./s

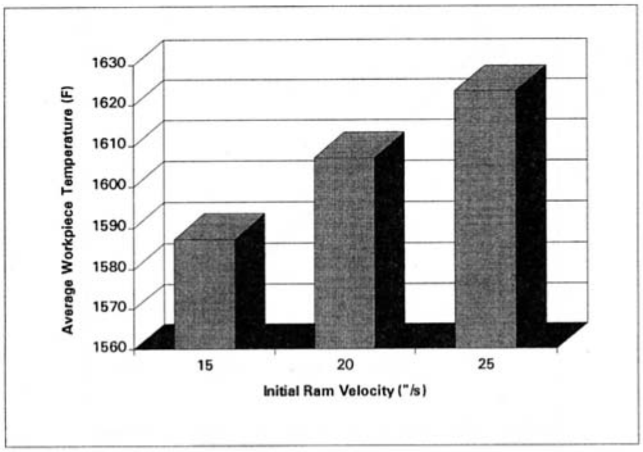

Fig. 7 Average workpiece temperature as a function of initial ram velocity

Flow Stress of the Material

Forging loads and energy in a forging operation are directly influenced by the instantaneous flow stress of the material being forged. For a given composition and microstructure, the flow stress of a metal depends on (*a*) the part geometry, (*b*) the type of metal flow, (*c*) the flow stress of the deforming material under forging conditions, and (*d*) the friction at the die–workpiece interface. During forging, different portions of the workpiece undergo different amounts of deformation depending on the preform configuration and the finish forging. The effect of strain in hot forging of most common metallic materials on the flow stress can be neglected and only enters into the calculations

Table 2 Forging simulation results as a function of initial die temperature

Initial Die Temperature (°F)	300	500	700
Average Temperature of the Workpiece (°F)	1607	1631	1650
Maximum Forging Load (Kips/in)	960	824	769
Change in Forging Load (%)	0	-14.2	-19.9

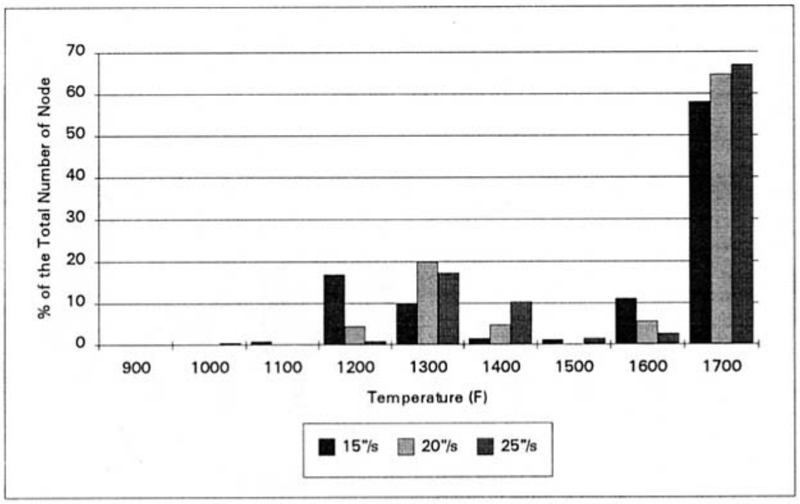

Fig. 8 Final nodal temperature distribution as a function of the initial ram velocity

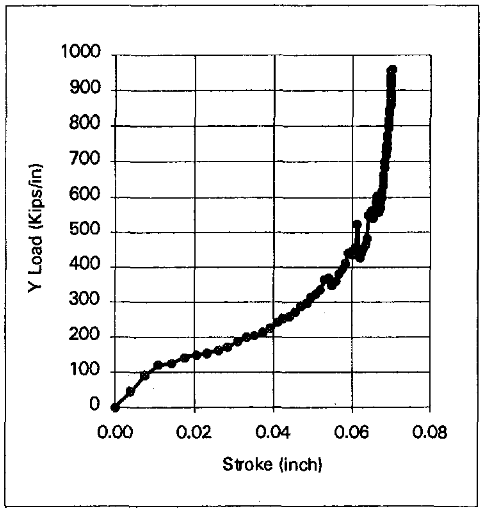

Fig. 9 Forging load as a function of stroke for initial die temperature of 300°F

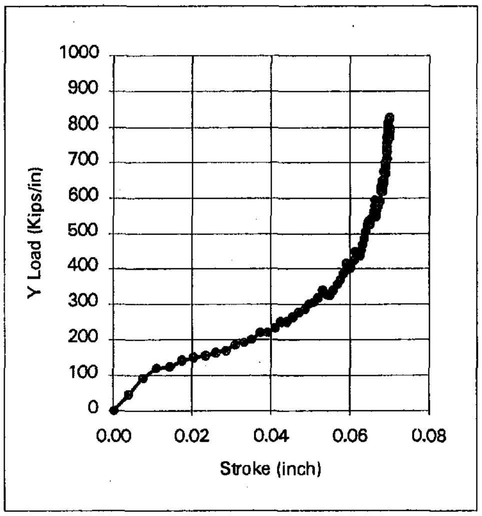

Fig. 10 Forging load as a function of stroke for initial die temperature of 500°F

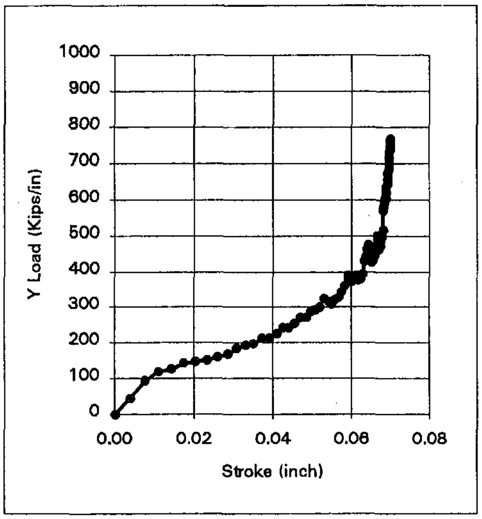

Fig. 11 Forging load as a function of stroke for initial die temperature of 700°F

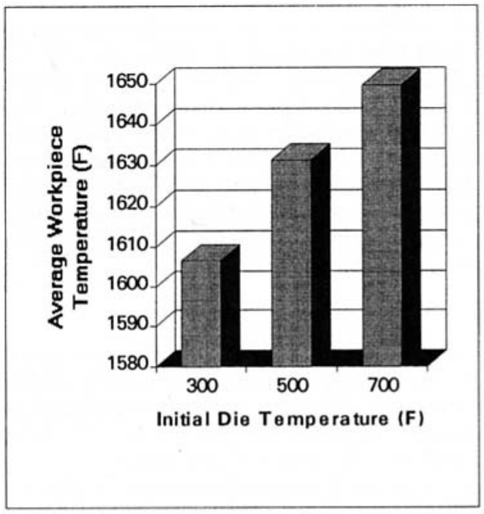

Fig. 12 Average workpiece temperature as a function of initial die temperature

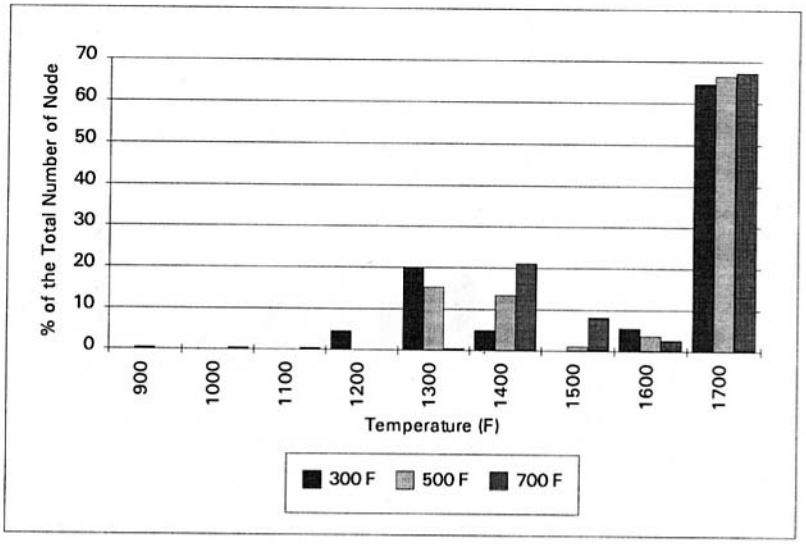

Fig. 13 Final nodal temperature distribution as a function of the initial die temperature

indirectly. The rate of deformation or strain rate is determined by (*i*) the speed of the ram and (*ii*) the initial and final thickness of the forging. The temperature of the forging at the end of the forging stroke depends on (1) initial billet temperature, (2) initial die temperature, (3) rate of deformation, and (4) frictional conditions. The temperature varies across the forging due to die chilling and also due to heat generation by friction and deformation.

The flow stress $\bar{\sigma}$ is a function of strain $\bar{\epsilon}$, strain rate $\dot{\bar{\epsilon}}$, and temperature T, and can be represented by [2]:

$$\bar{\sigma} = \bar{\sigma}\,(\bar{\epsilon}, \dot{\bar{\epsilon}}, T) \qquad (5)$$

In hot forming of metals at temperatures above the recrystallization temperature, the influence of strain on the flow stress of nearly all metals is very much strain-rate dependent, and as such, the influence of strain-rate becomes increasingly important.

For forging process simulations, DEFORM provides several methods for controlling the ram movement. The method used here is ''speed-stroke,'' i.e., ram speed is a function of stroke. Mechanical presses with crank-driven rams are rated in tons of force exerted at or near the end of the stroke [9]. For simplification, the ram velocity is assumed to be a linear function of stroke as shown in Fig. 2.

Friction conditions at the die–material interface greatly influence metal flow, formation of surface and internal defects, stresses acting on the dies, and the load and energy requirements. In most forming applications, the lubricity of a lubricant is the single most significant factor, since it directly determines the interface friction. In order to evaluate the performances of various lubricants and to be able to predict forming pressures, it is necessary to express the interface friction quantitatively, in terms of a factor or a coefficient. The friction shear stress, fs, is most commonly expressed as

$$fs = m_2 k_2 \qquad (6)$$

where k_2 is the shear strength of the deforming material and $0 \le m_2 \le 1$. The value of m_2 varies as the forging condition varies [1]. In hot forging of titanium and high-temperature alloys with glass lubricants, m_2 varies between 0.1 and 0.3. In this study, a constant friction factor of 0.3 is assumed.

In addition, in metal-forming processes both plastic deformation and friction contribute to heat generation. Approximately 90 percent of the mechanical energy involved in the process is assumed to be transformed into heat.

Workpiece and Dies

Figure 3 shows a typical cross section of the workpiece and the dies at the start of the simulation. In order to obtain insight into three-dimensional forging, a number of simulations were performed at different cross sections.

The simulations were performed on a VAX 4000/300 machine. The simulations involved placing the preform between the dies and reducing its height by 0.070 in. by compressing it. The bottom die was held stationary while the top die impacts the workpiece with a certain initial velocity.

Compressor blades are typically made of titanium Ti-6A1-4V alpha-beta alloy. Hot forging of this alloy is typically performed over the temperature range 1400–1800°F. The workpiece was assumed to be initially at 1700°F. The forging dies are typically made of H-13 chromium hot worked tool steel. The dies are often preheated to minimize local chilling, which can result in cracking. The dies are assumed to be rigid.

For this study, the variables of interest are the forging load per unit length (maximum vertical *Y* load value) and the nodal temperature distribution in the workpiece at the end of the stroke. Energy was calculated as the area under the *Y* load curve.

Results and Discussion

(a) Effect of Initial Ram Velocity. Table 1 summarizes the simulation results dealing with the effect of the initial ram velocity on the forging process. Figures 4–6 show the forging load as function of stroke for initial ram velocity of 15, 20, and 25 in./s, respectively. The initial die temperature is set at 300°F. Increasing the initial ram velocity from 15 to 25 in./s decreases the forging load by 25.2 percent. Figure 7 shows that the average workpiece temperature increases by 36°F from 1587 to 1623°F as the ram velocity increases from 15 to 25 in./s. This can be attributed to the die chilling effect, which is more extensive at lower initial ram velocities since it takes more time to perform the forging operation. Figure 8 shows the final nodal temperature distribution as a function of the initial ram velocity. The nodal temperature distribution is bimodal with a significant fraction of nodes having temperatures between 1200 and 1500°F and between 1700 and 1800°F. In addition, as the initial ram velocity increases, the fraction of nodes with temperatures greater than 1700°F increases.

(b) Effect of Initial Die Temperature. Table 2 summarizes the simulation results dealing with the effect of the initial die temperature on the forging process. Figures 9–11 show the forging load as a function of stroke for initial die temperature of 300, 500, and 700°F, respectively. The initial ram velocity is set at 20 in./s. Increasing the initial die temperature from 300 to 700°F decreases the forging load by 19.9 percent. Figure 12 shows that the average workpiece temperature increases by 43°F from 1607 to 1650°F as the initial die temperature increases from 300 to 700°F. This can once again be attributed to the die chilling effect. Figure 13 shows the final nodal temperature distribution as a function of the initial die temperature. As the initial die temperature increases, the fraction of nodes with temperature greater than 1700°F increases. Integrating the area under the load curve in Fig. 9, the total net energy required to deform the workpiece by 0.070 in. is approximately 18 kips *in./in.

Conclusions

Finite element analysis was used to study the effects of initial ram velocity and initial die temperature on the forging process. Based on the analysis, it was found that increasing the die temperature from 300 to 700°F decreases the forging loads by 19.9 percent and increases the average temperature of the workpiece by 43°F. Similarly, increasing the initial ram velocity from 15 to 25 in./sec decreases the forging loads by 25.2 percent and increases the average temperature of the workpiece by 36°F. The nodal temperature distribution is bimodal in each case. The forging energy required to forge the blades is approximately 18 kips *in./in.

References

1 Kobayashi, S., Oh, S. I., and Altan, T., *Metal Forming and Finite-Element Method,* Oxford University Press, 1989.

2 DEFORM User's Manual, Scientific Forming Technology Corp., Columbus, OH, 1991.

3 Mielnik, E. M., *Metal Working Science and Engineering,* McGraw-Hill, New York, 1991.

4 Im, Y. T., Altan, T., and Shen, G., ''Investigation of the Effects of Flash Dimensions and Billet Size in Closed-Die Forging,'' Report No. ERC/NSM-88-12, Ohio State University, Columbus, OH, 1988.

5 Frater, J., Tadros, W., and Zinolabedini, R., ''Forging Preform Synthesis,'' Report No. ERC/NSM-88-22, Ohio State University, Columbus, OH, 1988.

6 Ficke, J. A., and Oh, S. I., ''FEM Simulation of Closed Die Forging of Isothermal Titanium Disk Forging Using ALPID,'' *Proceedings of NAMRC XII,* Michigan Technological University, Houghton, MI, 1984.

7 Oh, S. I., Wu, W. T., Tang, J. P., and Vedhanayagam, A., ''Capabilities and Applications of FEM Code DEFORM: The Perspective of the Developer,'' *Journal of Materials Processing Technology,* Vol. 27, 1991, pp. 25–42.

8 Gleykin, S. F., Saigal, A., and Chan, T. S., ''Effects of Initial Temperature Distributions in the Dies on the Forging Process,'' *Computer Applications in Shaping & Forming of Materials,* M. Y. Demeri, ed., TMS Annual Meeting, Denver, CO, 1993, pp. 107–116.

9 Jenson, J. E., Forging Industry Handbook, Forging Industry Association, Cleveland, OH, 1966.

Arbitrary Surface Flank Milling of Fan, Compressor, and Impeller Blades

C. Y. Wu
Design Engineering,
Pratt & Whitney Canada Incorporated,
Longueuil, Quebec, Canada

It is generally conceived that a blade surface is flank millable if it can be closely approximated by a ruled surface; otherwise the slow machining process of point milling has to be employed. However, we have now demonstrated that the ruled surface criterion for flank milling is neither necessary nor sufficient. Furthermore, many complex arbitrary surfaces typical of our blades in fans, axial compressors, and centrifugal impellers in aviation gas turbines are actually closely flank millable and can be rendered exactly flank millable with one or more passes per surface often without sacrificing, indeed usually with gain, in performance.

Introduction

Point milling and flank milling are the two common metal cutting methods for compressor blades in aviation gas turbines. The former is a well-known technique whereby a blade surface is cut by the ball-nose of a cutter following a dense set of isoparametric curves on the mathematical surface interpolating the blade design curves. While the implementation of a point milling software package may be complex, from a conceptual point of view, it is a simple, well-defined problem. Its major advantage to the airfoil designer is that almost any smooth surface can be point milled, offering total freedom to the design process. From the manufacturing point of view, however, the main disadvantage of point milling is that it is a very time-consuming process; each passage of the cutter removes only a small amount of material. Another disadvantage is that by its very nature, point milling produces a scalloped surface finish; the height of the scalloped ridges is directly related to the ball-nose radius and the number of cuts over the surface.

Compared with point milling, flank milling is a much less well-known technique. In conventional flank milling, the entire blade surface is obtained after one single passage of the cutter through the blank material, engaging every point of the cutting edges on the conical as well as the ball-nose surface of the cutter. This is illustrated in Fig. 1. Thus conceptually, flank milling is not as easy to understand as point milling. It is generally conceived that a surface is flank millable if it can be closely approximated by a ruled surface. To complicate the problem further, the milled surface may deviate from the ruled surface, sometimes quite significantly, owing to the twist of the surface along a straight line element. To our knowledge, previously such deviations have either been ignored, or minimized by compromising the design or slightly modifying the cutter orientation. Then finally there are the hardware difficulties such as blade and cutter deflection arising from the severe force from large volume metal removal.

In spite of all these difficulties, considerable effort has been invested to understand and apply flank milling whenever possible. This is mainly because flank milling, when applicable, offers significant cost reduction over point milling. In particular, flank milling has been extensively employed in the manufacture of centrifugal impellers for aviation turbomachinery (Brown and Plucinski, 1979; Pratt, 1981; Willis, 1975; Wu et al., 1982). Another advantage is that it gives a good clean surface finish, which is an additional productivity improvement factor because it reduces the time required for surface polishing.

At Pratt & Whitney Canada Inc., for more than a decade we have been striving to expand the domain of applicability of flank milling to cover axial compressors in the form of integrally bladed rotors (IBRs). Axial compressor rotor blades are generally considered to be not flank millable, owing to the severe twist of the blade surfaces as well as other complexities. However, by imposing three design curves to lie on a highly twisted but nevertheless ruled surface, and then reducing the deviation between the ruled surface and the machined surface by introducing the technique of multiple pass flank milling (Wu et al., 1983), we were able to flank mill two moderately complex rotors. This exercise clearly demonstrates that the ruled surface

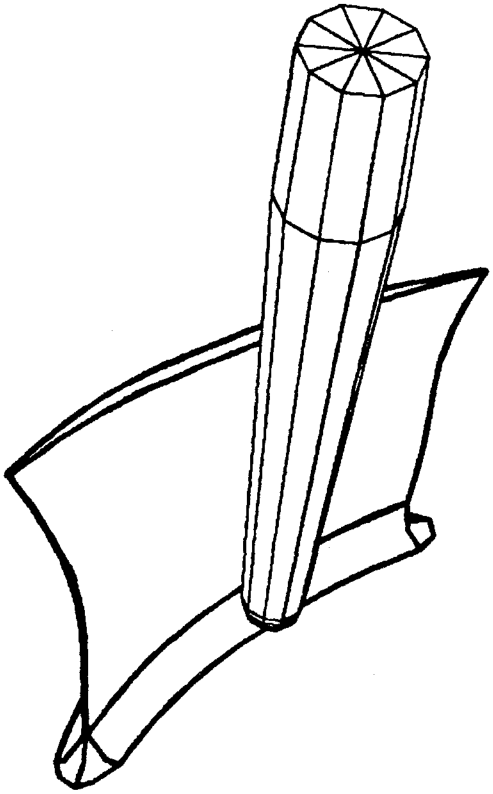

Fig. 1 Schematic illustration of flank milling

Contributed by the International Gas Turbine Institute and presented at the 39th International Gas Turbine and Aeroengine Congress and Exposition, The Hague, The Netherlands, June 13–16, 1994. Manuscript received by the International Gas Turbine Institute March 10, 1994. Paper No. 94-GT-426. Associate Technical Editor: E. M. Greitzer.

criterion is not sufficient to guarantee that a surface is flank millable in the conventional single-pass manner.

Encouraged by our initial success with multiple pass, we attempted to flank mill more complex surfaces defined by four or more curves by dividing them into two or more overlapping ruled surfaces stacking one on top of the other. However, hardware-wise we were unable to blend in smoothly two adjacent passes. One cannot realistically resolve this challenge without first having a far more flexible and powerful software to facilitate the design of a flank millable blade and generating tool paths efficiently before resolving the hardware problems. This, in fact, was the motivation behind our drive to develop what we now call Arbitrary Surface Flank Milling (ASFM) system, which is conceptually a quantum jump from the conventional ruled surface flank milling approach.

In the ASFM system, a surface can be defined with a lot more than three curves, which the designer specifies, without the constraint that they should be lying even approximately on a ruled surface; it is therefore an arbitrary surface. Given such a surface, the ASFM system rapidly generates a set of flank milling tool paths to closely match the cutter surface to the design curves in a weighted manner. The matching is done by choosing one among the infinitely many curves on the conical surface of the cutter to match one point each on every design curve. Since one of the infinite number of curves on the cutter surface is a straight line, we have included the ruled surface constraint as a particular member of a much larger family of flank millable surfaces. The matching process is necessarily complex, requiring highly flexible, powerful, and user-friendly software to facilitate the efficient convergence between design intent and flank millability and will be discussed further in the next section.

If the flank milled surface thus produced does not yield satisfactory performance, we would opt for two or more flank milling passes, stacking the passes one on top of the other. We have also solved the problem of blending the adjacent passes to yield a smooth surface.

We have applied the ASFM system to flank mill a large number of axial IBRs, fan IBRs as well as centrifugal impellers of high complexity inducer design, which would not be flank millable in the conventional approach.

In what follows, let us first discuss the basic concept of arbitrary surface flank milling in some depth.

Concepts and Challenges

Figure 2 shows a blade surface designed with six curves together with a conical cutter. The actual number of design curves can vary widely between a minimum of 3 and a maximum of any number; we have had cases of 15 to 20 curves. Referring to Fig. 2, one may imagine an arbitrary surface *Sb* interpolating the six design curves C_1 to C_6, then *Cp* is a curve on the cutter surface *Sc*, which is closest to the blade surface Sb for the particular cutter position and orientation depicted in the figure; and *Cb* is a curve on *Sb*, which is closest to *Sc*. If *Cb* is "sufficiently" close to *Cp* for the entire blade surface from the leading to the trailing edge then we have a flank millable surface that approximates the design intent surface.

However, it is a subtle but important point to realize that the family of the proximity curves *Cp* does not generate the exact flank milled surface. The exact flank milled surface is the enveloping surface swept out by the cutter surface. It is composed of individual enveloping curve, shown as *Ce* in Fig. 2, associated with each cutter position. The computation of each enveloping curve, however, depends not only on the particular cutter position but also on its immediate preceding and immediate following cutter positions. Such "nearest-neighbor coupling" can have very strong effects on the machined surface, especially when the cutter orientations are varying dramatically, usually near the leading and trailing edge.

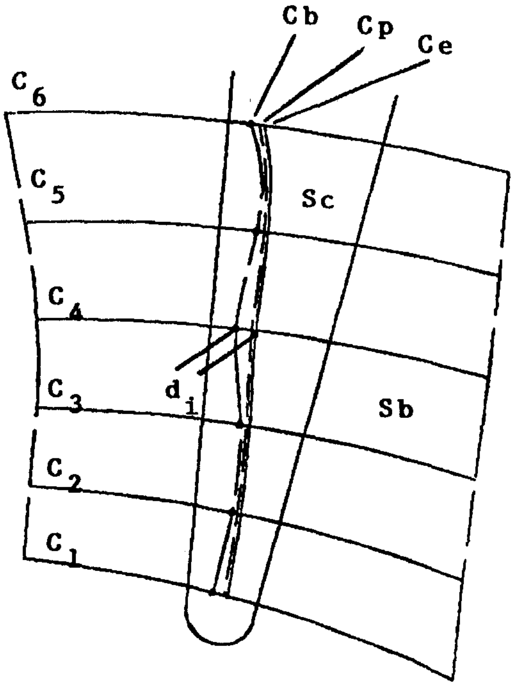

Fig. 2 Schematic illustrating the relationships between the proximity curve and the enveloping curve on the cutter surface with the blade

Since the exact flank milled surface cannot be obtained before we have a complete trajectory, but a complete trajectory is known only after individual cutter position is determined approximately via proximity curve calculation, one has to arrive at the cutter trajectory iteratively. We start out using a proximity curve calculation to determine the approximate cutter positions individually, then change over to compute the enveloping curves in subsequent refinement, which involves variation of individual cutter position or groups of cutter positions simultaneously.

When there are three or more design curves, there is no guarantee that the flank milled surface could match all the curves exactly. Thus, in Fig. 2, *Ce* deviates from *Cb* by d_i with respect to each curve C_i. Typically in the design of the blade, some curves have tighter tolerance than some other curves; thus $\sigma_i = d_i/t_i$ is a measure of the significance of the deviation between the flank milled surface and the design curve C_i, where t_i is the tolerance assigned to curve C_i. So far we have been focusing on one particular cutter position. To generalize our discussion, we may use $\sigma_{ij} = d_{ij}/t_{ij}$ where i denotes the C_i curve and j denotes the jth cutter position or equivalently, the path length along curve C_i. If σ_{ij} is less than 1.0 for all (i, j), then the flank milled surface is acceptably close to the design intent. Theoretically at least then, our problem is to find a set of cutter positions such that $\sigma_{ij} \leq 1$, if we can very reliably define t_{ij}.

However, we cannot very reliably define t_{ij}. While there are many rules as to how to design a blade for targeted performance, such rules do not always yield a unique blade geometry. Indeed, given some performance requirements, there may be many possible blade designs that yield satisfactory results. Differences between two blades along some design curves may be compensated by differences along some other curves such that they give similar performance. One eventually has to rely on aerodynamics and structural analysis, and ultimately on experimental tests on hardware sometimes, to really decide whether seemingly different designs give equivalent performances.

With such understanding, we may view the challenge of finding a flank milled blade that gives equivalent performance as a "freely" designed blade in a bolder and broader perspective.

For each design intent blade surface, we initialize a complete set of values for t_{ij}, based on our experience and/or best guess.

A scheme would then try to optimize the cutter positions and orientations by minimizing σ_{ij}. This is done for some 30 to 50 noncrossing cutter positions covering the entire blade surface. The resultant σ_{ij} will help in adjusting the t_{ij}s more realistically. The new t_{ij}s may now be defined with respect to the new nominal blade geometry obtained from the previous iteration or they may stay with the original design intent. How fast the iteration $t_{ij} \leftrightarrow \sigma_{ij}$ would converge to some meaningful values for highly complex blades is the major challenge to our design methodology and software capabilities.

How are the t_{ij}s set? They are set to alter and control the general as well as the details of all the blade section profiles so that the curvatures, the inlet metal angles, the exit metal angles, the leading edge radii, the trailing edge radii, the chord lengths, the chord angles, the blade thicknesses and the location of maximum thickness along each blade section, etc., all combine to give the targeted performance as achieved in the original design intent blade. In this context, the original design intent blade acts as a seed to start off the design of the flank millable blade. Highly efficient and reliable aerodynamics and structural analysis programs facilitate our setting of the $t_{ij}s$, alongside with the guidance provided by the ASFM system, which sets the realistic manufacturing constraint on the $t_{ij}s$ imposed by flank milling.

Ideally, the convergence of the $t_{ij} \leftrightarrow \sigma_{ij}$ iteration process should be carried out in a completely automated way and indeed, we have made great strides toward this goal. However, the problems are so immense and complex that much more effort will be needed. The next section outlines our systematic approach toward meeting the challenges.

The ASFM System

Our software system comprises of close to 30 batch programs; each one performs some special function that belongs to one or more of the following three logical phases of the system:

Phase I—Test for Flank Millability. The mission of this phase is: given a blade design in the form of a number of curves on its suction surface and pressure surface, the user may rapidly generate the *probable* flank milled blade profile with the associated tool paths. The important points here are the speed and the reliability of the results so that in a small fraction of the time added to the regular design cycle, we know whether or not we should go ahead with flank milling, and if we do, the designer should have the means to generate new design blades in the vicinity of the original design so that the new iterations will stay closely flank millable.

Starting with three or more design curves on each surface, cutter size specifications, and a set of user supplied initial t_{ij} values, which could be just the best guesses only at this point, the main program DESIGN in Phase I will first define a set of cutter positions extending from the leading edge to the trailing edge of the surface, each cutter surface touching two of the design curves tangentially (e.g., C_1 and C_6 in Fig. 2) with the axis perpendicular to the curve that is closest to the hub (e.g., C_1 in Fig. 2). Next, the program begins an optimization of each cutter position by minimizing $\Sigma_i \sigma_{ij}$. Since the process involves one cutter position at a time, the distances between the cutter surface and the design curves are based on proximity curve concept as discussed in the previous section.

Now optimization is a tricky mathematical exercise that may not always converge to the best possible solution for each cutter position. However, if the process is carried out for a sufficiently large number of cutter positions, one may observe how flank millable the design surface is and adjust the t_{ij} value accordingly. For simple and moderately complex blades this is not too difficult to do, especially after one has acquired some experience. Thus one may repeat the optimization process a few times rapidly and within a few hours, decide whether the blade has a good chance to be flank millable.

Phase II—Detail Matching. The results of Phase I become the starting point in this phase. In Phase I we obtain some cutter trajectories that give a probable flank milled surface, here we want to fine tune each enveloping curve associated with the cutter trajectories to yield a flank milled blade that gives equivalent performances aerodynamically and structurally to the design intent. In this phase there are over a dozen programs. We will only outline some key programs below:

(*i*) BKGEN: back-generate accurately the flank milled surface from a cutter trajectory using enveloping curve calculation. This is possible here because in this phase, we always have a complete cutter trajectory.
(*ii*) RENDN: rendering of the cutter vectors in directions normal to a chosen design curve.
(*iii*) RENDP: rendering of the cutter vectors in a sliding (parallel) manner along a chosen design curve.
(*iv*) SMTH: smooth out the cutter vectors along any section.
(*v*) CHKADJ: check whether or not there are interferences between the cutter and the adjacent blade.
(*vi*) TLCHG: tool change program. This program allows one to change tool and generate new tool paths based on the old one. Slight rematching will be necessary.
(*vii*) LETE: construct leading and trailing edge circular or elliptical arcs from the back-generated flank milled blade sections.
(*viii*) GEOM: analyses the geometries of the flank milled blade profiles such as inlet and exit metal angles, leading and trailing edge radii, throat areas, thicknesses, etc.

The greatest challenge in Phase II is automation. In theory one should be able to complete the job in one batch run but in practice this is far from being easy, in spite of the fact that we have made great progress in this direction. Typically, we will first run SMTH and then RENDN to obtain good matching for one or more of the most critical design curves. Then RENDP is run to minimize the deviations from the other curves. Most likely then one needs to run RENDN again to depart from the most critical curve in certain areas to achieve better matching for the other curves; then we rerun RENDP again. This cycle is repeated a number of times for both the suction and the pressure surfaces. A good starting set of tool positions from Phase I is very important so that one always searches in a small neighborhood for the best solution. SMTH, CHKADJ, TLCHG, etc., are run every now and then. BKGEN is run back to back with every program that changes any cutter orientations. The programs are very user-friendly and fast; although run in batch mode, they give the feeling of interactive execution. LETE is run to create a complete blade geometry to be analyzed by GEOM and then detailed aerodynamics and structural analysis to check the performance. Depending on the complexity of the blade, it typically takes a few days, performing several to a dozen iterations between flank milling definition and performance analysis, to reach a flank milled blade of equivalent performance to design intent.

Figure 3 shows the results of detail matching tool path for the suction surface of an axial compressor. The solid curves are the design intent curves, the dots are points on the back-generated flank milled surface, while the straight lines are the associated *CL* vectors.

In Fig. 4, we compare the blade sections for both surfaces of the design intent(solid) and flank milled(dashed) blade. While one may see significant differences in individual section, overall the performances of the two are quite close.

Phase III—Manufacturing Concerns. The tool path generation in Phases I and II are solely concerned with the finishing cut. When we come to actual metal removal, we need to generate roughing cut, semi-finishing cuts, and very important, we

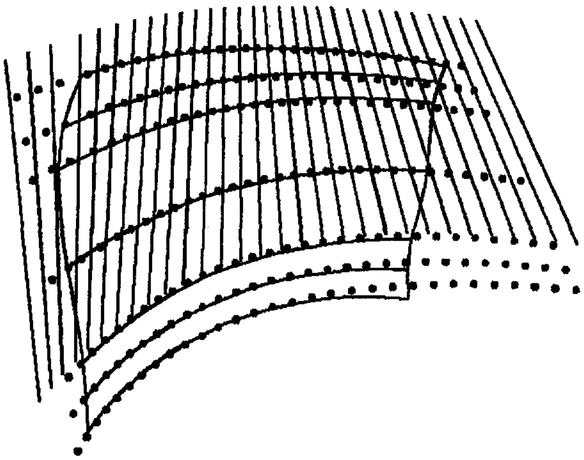

Fig. 3 Results of detail matching for the suction surface of an axial compressor

have to have a way to cope with blade and cutter deflections. Phase III addresses these problems with a number of programs:

(*i*) OPEN: this program generates cutter location vectors for a flat-end or ball-end cutter right between two adjacent blades with a user-specified lead angle of the cutter for efficient opening cut between two blades.

(*ii*) SEMROU generates semi-finishing and roughing pass from the finishing pass by offsetting the finishing pass away from the blade.

(*iii*) TLCHG: tool change, same program as in Phase II, to allow rapid change to different size roughing or semi-finishing cuts, but not finishing cuts at this stage.

(*iv*) CHECK: checks tool-blade interference after OPEN, TLCHG, or SEMROU has been run.

(*v*) DEFL: adjusts the cutter vectors to compensate for blade thickening due to blade deflection and cutter deflection.

(*vi*) INTERP: interpolates a dense set of *CL* vectors from a spare set to facilitate smooth metal cutting.

The circular or elliptical leading and trailing edges of the blade are usually not flank milled. They are point milled to blend in smoothly with the flank milled surfaces.

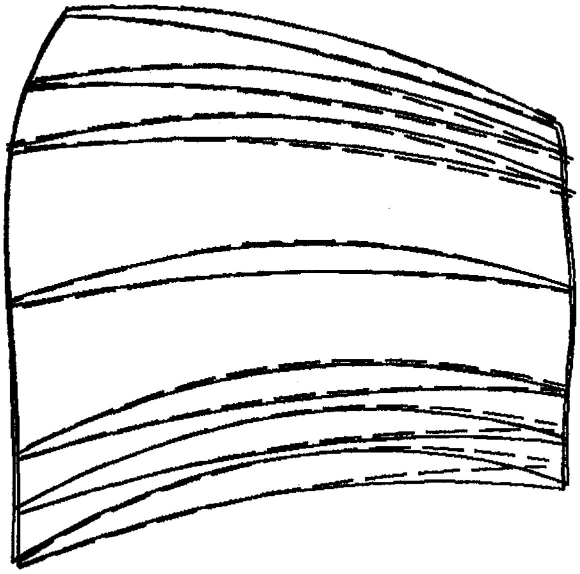

Fig. 4 Comparison between blade sections of flank milled blade (dashed) and design intent curves (solid)

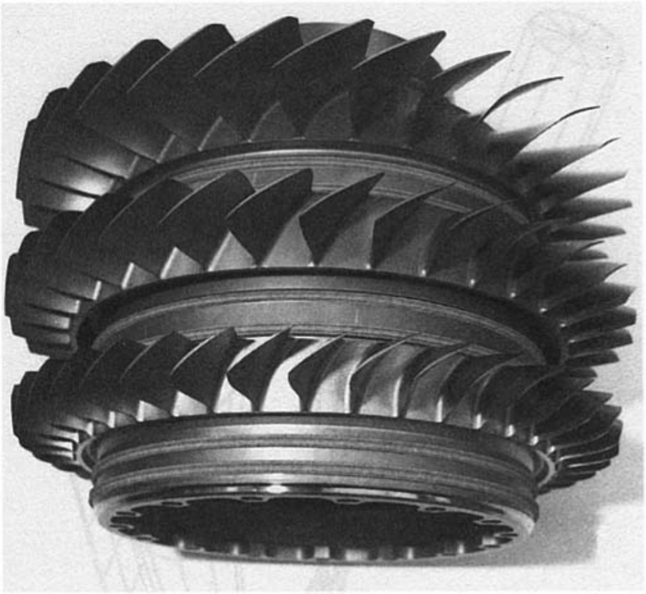

Fig. 5 Three flank milled IBRs welded together

We conclude this section with photographs of some of the rotors we have actually fabricated.

Figure 5 shows three axial IBRs welded together to form a drum rotor. The diameters of the rotors are approximately 12 in. The first rotor (the one on top in the photo) has relatively simple blade geometry, while the second and the third have increasingly complex blade shapes.

In Fig. 6 we show an experimental impeller. The main blade is 10 in. long while the splitter blade is 6 in. long. The main blade leading edge is 3 in. tall. Note the very complex blade geometries.

Multiple Pass Flank Milling. If a blade is too complex to be flank milled in the manner outlined above we may want to flank mill each surface with two or more passes, one stacked on top of the other. Owing to the complexities, both software-wise and hardware-wise, multiple pass is only employed with large rotors, typically our fan IBRs. So far we have not gone beyond two passes, but the techniques are the same for more passes.

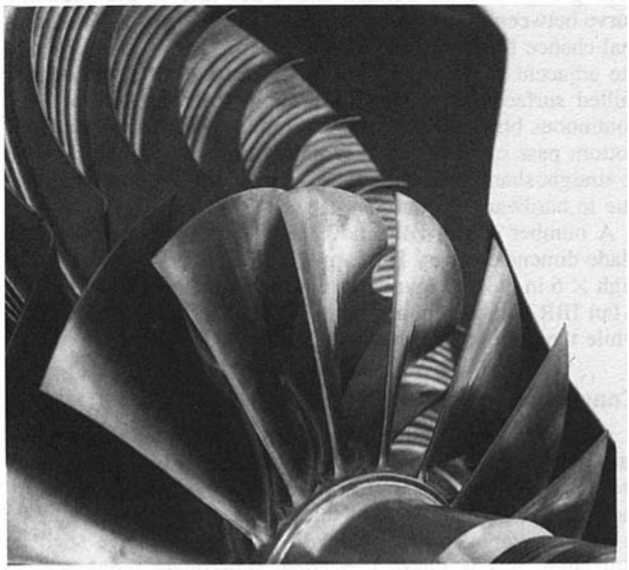

Fig. 6 An impeller with highly complex blades

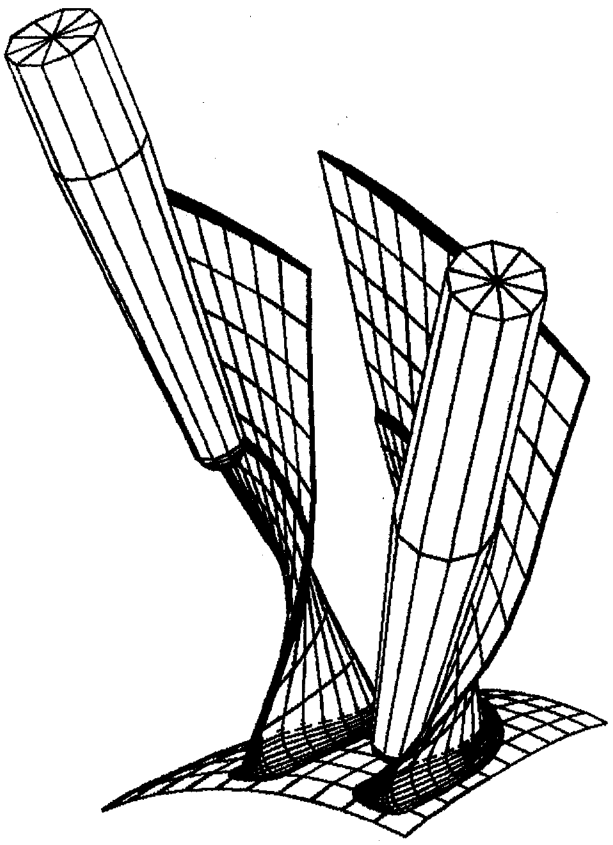

Fig. 7 Computer simulation of two-pass flank milling of highly twisted fan blades

Figure 7 shows the computer simulation of two pass flank milling of a fan blade. The top pass resembles the regular single pass, with a standard tapered ball-end cutter. The tangency point between the tapered cutting edge and the ball end follows a curve on the blade surface, which is the boundary curve between the two passes. The length of the cutting edge is not important as long as it is long enough to cover the entire top part of the blade. The length of the tapered cutting edge of the bottom pass, however, is important: That entire length is engaged in metal removal so that the transition point between the tapered cutting edge and the straight shank lies just on the boundary curve between the two passes. Such an arrangement gives optimal chance for the cutter to clear the top part of the blade and the adjacent blade. Along the boundary curve, the two flank milled surfaces are tangential radially to ensure smooth and continuous blade profiles. A small radial profile is given to the bottom pass cutter in the transition from tapered cutting edge to straight shank to avoid a sharp step along the boundary curve due to hardware discontinuity.

A number of fan IBRs have been fabricated this way; the blade dimensions vary between 7 in. high × 5 in. wide to 9 in. high × 6 in. wide. Figure 8 shows the two photographs of such a fan IBR. The top photographs shows the leading edge view while the bottom one shows the trailing edge view.

Conclusion

We have presented the concepts, the structure, and the applications of our Arbitrary Surface Flank Milling system. There are two central themes to bear in mind throughout the development and implementation of this system. First, if any surface is flank millable, our system will very rapidly give such an indication; this is Phase I. Second, subsequent refinement to give a high-quality flank millable blade with optimal performance has to be rapidly convergent; this is Phase II. Speed is absolutely important here because we cannot afford to add significant lead time to an already complex and lengthy blade design process involving critical compromise between aerodynamics, structure, and dynamics.

From a different perspective, one wonders whether there is a way of completely incorporating flank millability in the blade design process from the very beginning so that when the design is finished, one automatically has a blade that is guaranteed flank millable. In theory this is a good approach and our ASFM system is in fact quite capable of doing so. As soon as there are three design curves, one obtains the tool paths, interpolates more design curves in-between to more fully cover the blade, then renders the tool paths only to produce different designs. This will guarantee every blade as designed would be flank

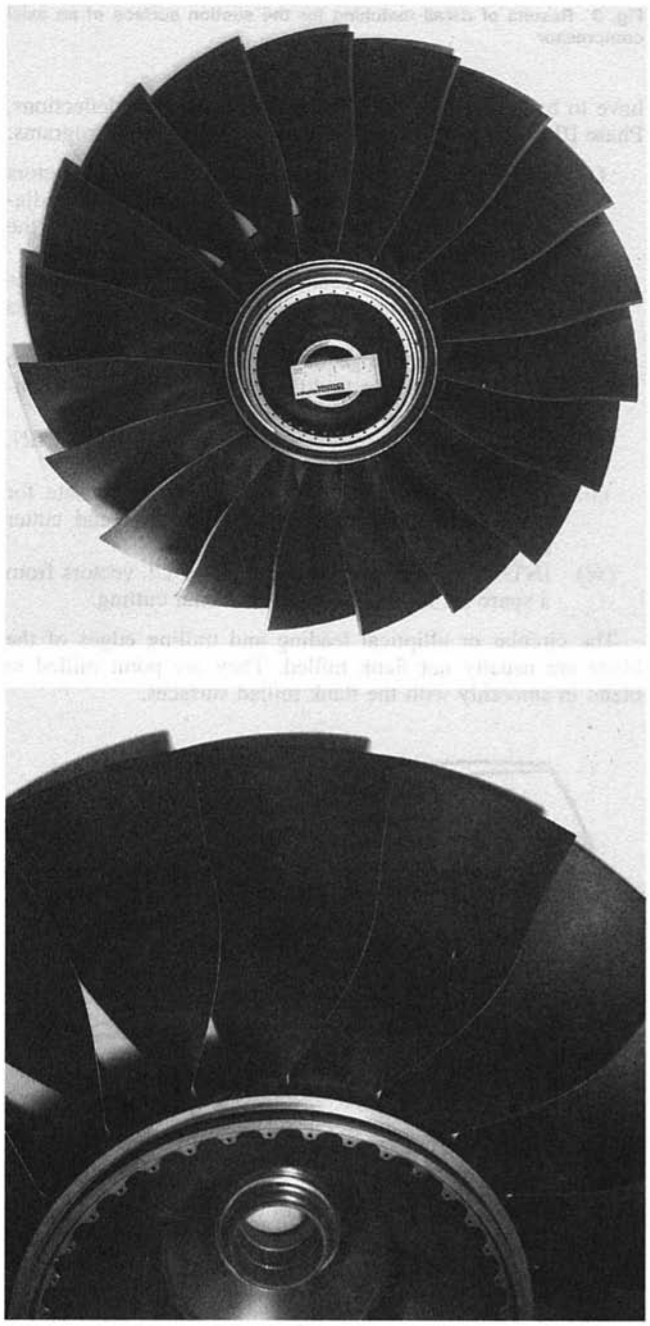

Fig. 8 A two-pass flank milled fan IBR as viewed from the leading edge (top), and from the trailing edge (bottom)

millable. However, in practice, such an approach has not yet been tried.

This is because there is advantage to first designing a blade without any flank milling constraint, obtaining the best results possible, and then modifying it to be flank millable. In this way we know exactly what is being compromised or gained. We have up to now worked on 25 different fans, axial compressors, and centrifugal impellers that are not flank millable in the conventional ruled surface approach. Analysis of the back-generated ASFM blades shows results that analytically are sometimes slightly better, sometimes slightly worse in performance and structural integrity. However, for all of the 13 parts that have actually been fabricated and tested up to now, the performances were always slightly better than the original design intent. This is especially so for the structural properties and life of the rotor. One cannot help wondering, maybe there is something intrinsic in the flank milling process in that it imposes a very uniform variation of geometric parameters such as curvature and blade thickness in a radial direction, thus reducing stress concentrations and may also be beneficial to the aerodynamics. These may be interesting topics for further studies.

As of now, the greatest benefit we reap from ASFM is cost reduction. This is especially true for our large IBRs and impellers.

Acknowledgments

I would like to thank the many people in the following departments in P&WC who have supported and actively participated in the work reported here: Component Engineering, Manufacturing Engineering Development, Production Engineering, and Project Engineering.

Special thanks are to D. Fong who has been very helpful in our development work and applications, and to T. Luong who closely participated in the Phase III development and applications. I am deeply indebted to A. Vasiljevic, who has been most ingenious in many applications, and has contributed various ideas of fundamental importance in our drive toward total automation.

Finally, I would like to thank P&WC for permission to publish this work.

References

Brown, L., and Plucinski, J., 1979, "A Modern Method for Productivity and Profit—The Application of CAD/CAM at Pratt & Whitney Aircraft of Canada Ltd.," CSME Conference, University of Sherbrooke.

Pratt, M., 1981, "Computerized Compressor Design," *Turbomachinery International,* May–June.

Willis, F. F., 1975, "Graphic Design and Numerical Control Programming for Turbo-Rotor Manufacturing," ASME 75-GT-56.

Wu, C. Y., Altintas, Y., and Thompson, R. A., 1982, "Tool Positioning and Feedrate Problems in Impeller Flank Milling," *Proceedings of the 1982 Canadian Conference on Industrial Computer System,* McMaster University, Hamilton, Ontario, Canada.

Wu, C. Y., Raw, J. A., Thompson, R. A., Townsend, P. R., and Wilford, A. P., 1983, "A CAD/CAM System for Flank Milling an Axial Compressor Blisk," *2nd Canadian CAD/CAM & Robotics Conference Proceedings,* Toronto, Canada.

Laser Guidance for Repairing Gas Turbine Parts

Z. Galel
SeamX, Inc.,
Mountain View, CA

J. L. Hunt

T. H. Unger

Kennametal, Inc.,
Raleigh, NC

As a result of normal operating conditions, jet engine parts tend to distort. During repair, many of these parts require some form of selective cutting. Due to the differences between each individual part, automation such as CNC machining becomes complex. The need to map each individual part prior to machining has prohibited repair facilities from introducing sophisticated automation. This paper presents for the first time a novel method that addresses many problems related to selective material removal in jet engine repairs. Similar to a terrain-following cruise missile, a laser-guided cutter is used to follow a selected datum surface. For example, in the case of Honeycomb Airseals, the thin laser beam penetrates the honeycomb cell structure to follow the base metal. The method minimizes parent metal removal and under-minimum-wall condition. As a result, life potential of parts is extended, and repair costs are reduced. The ability to track a moving part and modify the cutting path automatically produces one more significant advantage: Accurate setup of a part on a machine is no longer critical. The method has applications in the repair of airseals, frames and cases, and airfoils.

Introduction

Due to normal operating temperature, stress, and pressure, jet engine parts tend to distort during service. During repair, those parts that are considered to be thin wall shells will typically require some form of material removal. Examples include: removal of worn honeycomb from airseals, removal of worn plasma spray from cases, and removal of weld buildup from cases and airfoil tips. Whether repairing cases, airseals, or airfoils, the process can be defined as selective cutting. The need to maintain as much base metal as possible regardless of part distortion is fundamental to the jet engine repair business.

A new approach to address this classic problem in jet engine repair is described below. As described in Fig. 1(*a, b*) the approach constitutes the use of a sensor, a cutter, signal processing electronics, computer-based pattern recognition, and an actuating mechanism.

Sensor signals are processed initially by the appropriate electronic components. Data are evaluated by algorithms mimicking the human thought process. These algorithms evaluate and recognize important patterns in the data. The system is autonomous. It has the authority to decide and execute a cutting path, or trajectory, without giving the operator a quantitative, mathematical description of the trajectory. The trajectory is executed by the system using a motion control system to modify the position of the cutting tool by means of a servomotor system coupled to a linear slide. The linear slide carries the cutter mechanism including a quick-disconnect tool holder with a carbide insert, or a grinder or a milling system. Figure 2 shows the slide in the retracted position. Figure 3 shows the slide in the extended position with approximately 12 mm (0.5 in.) of travel. The system in its entirety is an accessory to existing manual machine tools. Mounted in place of a standard cutter, the system is easy to attach or detach from any manual machine tool.

The system has three main components: the cutter head, which is mounted on the machine tool and connected with an umbilical chord to the electronics cabinet. Figure 4 describes the electronics cabinet, which contains computers, electronics, and power management modules and is connected to a hand-held console, which is used by the operator to control the system. The hand-held console and the cutter are shown in Fig. 4 on top of the cabinet.

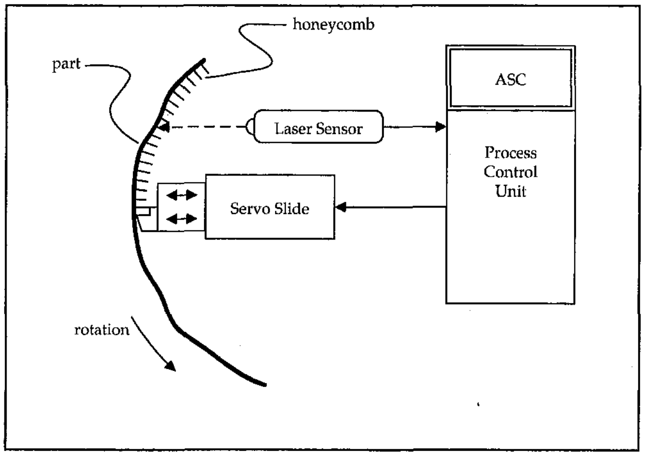

Fig. 1(*a*) Autonomous selective cutter operating principle

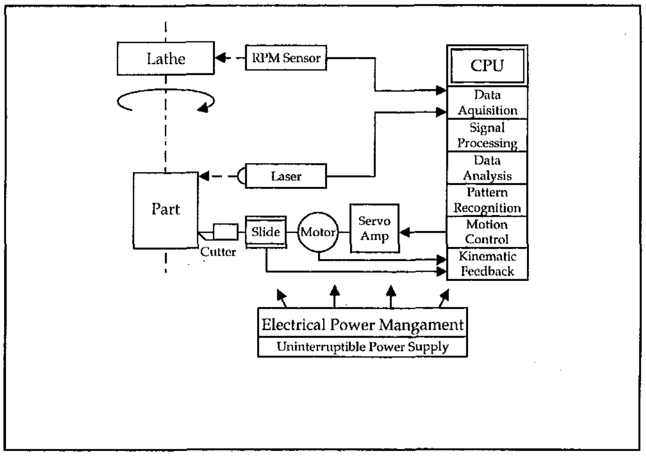

Fig. 1(*b*) Autonomous selective cutter system schematic

Contributed by the International Gas Turbine Institute and presented at the 39th International Gas Turbine and Aeroengine Congress and Exposition, The Hague, The Netherlands, June 13–16, 1994. Manuscript received by the International Gas Turbine Institute February 7, 1994. Paper No. 94-GT-6. Associate Technical Editor: E. M. Greitzer.

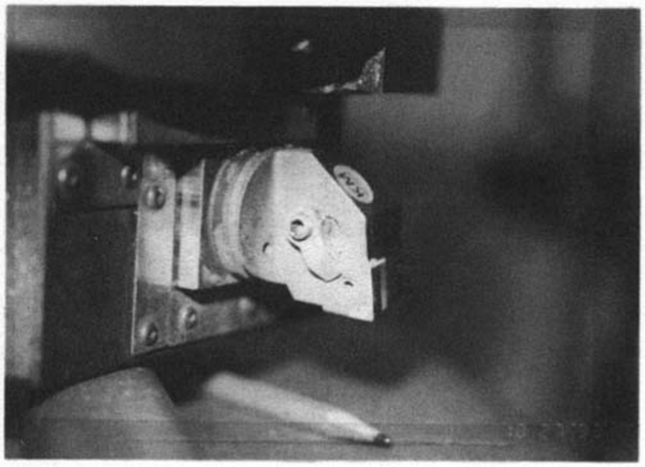

Fig. 2

Design Philosophy and Considerations

Described below are considerations that were used in the overall approach to system design. It may be useful to consider these points in the design of other systems, in particular where high levels of automation are proposed.

During the development effort, significant emphasis was given to user input, resulting in a simple operator interface. The complexity of the system was to be transparent to the user, who would operate the system by pressing a ''GO'' or ''STOP'' button. The specification for the system design mandated that the system does not require the user to program the system or to use a keyboard.

To the operator of a standard machine tool, a typical jet engine part appears to have ''high spots'' and ''low spots'' where the part distortion is convex or concave. The purpose of using the laser-guided cutter is to compensate and adjust the cutter position to follow part distortions. As a result, to the operator, all parts appear to machine as if they were perfectly round.

In some shops, user acceptance of sophisticated equipment was known to be a potential problem, in particular when significant productivity gains are claimed. In consideration of this potential problem, the approach of ''moderate automation'' was used.

What is the basic philosophy of moderate automation? The operator remains as an essential part of the process. He carries on one hand a set of reduced responsibilities regarding the accuracy of the cut, and on the other hand, a set of new responsibilities regarding the operation of a sophisticated machining system. Above all, the operator is given an ''enabling technology,'' or a better tool to do a better job. Consequently, the operator's role is enhanced, not diminished. This is in complete contrast with CNC machine tools and other forms of robotics, where eliminating the hands-on operator is a key goal.

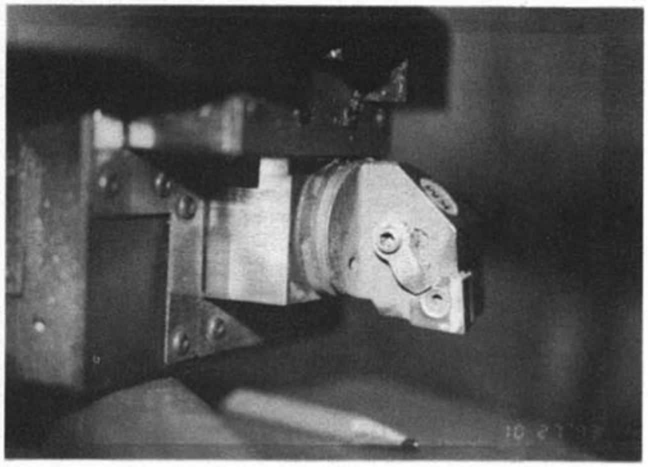

Fig. 3

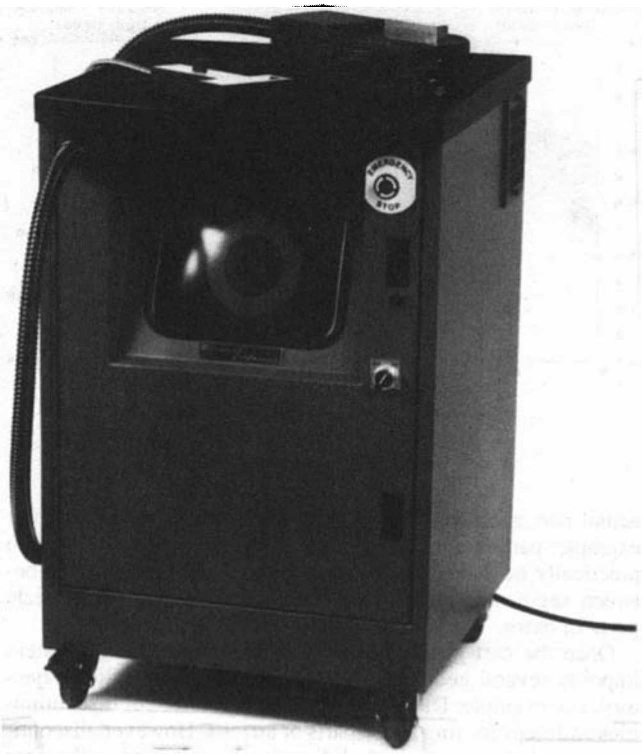

Fig. 4

A fundamental design consideration was to allow the operator to continue to work in his familiar work environment, with familiar equipment. By designing the system to be self-contained, and specifically by keeping the existing cutting technology, operators require little time to understand the system and its operation.

From an appearance point of view, the design consideration was to make the system blend in with other shop equipment and accessories in regard to external shape and color.

Schematic System Description

While it is possible to detect distance to a metallic body in several ways, the key to a practical system is accuracy and robustness. The requirement for a robust system comes both from the physical operating conditions such as vibration and shock, and from the classic causes of measurement errors inherent to noncontact sensors. These measurement errors are typically associated with the physics of secondary reflections from corners, six of which exist in each honeycomb cell, as well as presence of airborne metal chips and dust generated by the cutting process. Measurement errors will also occur due to varying levels of surface reflectivity resulting from differences in material, part condition, and service-related deposits. To address these operating limitations, a laser displacement sensor was selected in conjunction with digital signal processing, and various software and logic filters.

As a result of the actual shop environment and operating conditions, only a small fraction of the sensor data is admitted as reliable data, which are then used for further analysis. The purpose of the analysis is to reconstruct the data to identify the

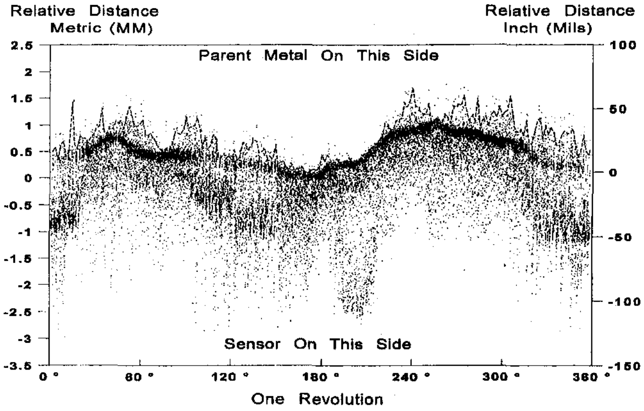

Plot #1

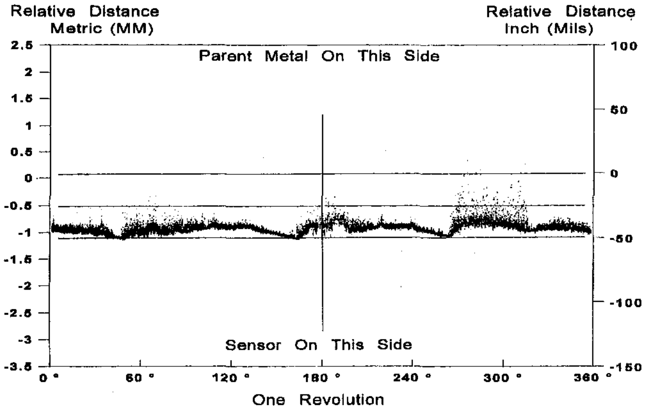

Plot #3

actual part geometry including several geometric features, for example: part distortion, part off-center setup, and regions with practically no data due to plugged honeycomb cells, gaps between segmented airseals, or boroscope holes or fuel nozzle ports in cases.

Once the part geometry has been reconstructed, the system imposes several geometric rules in regard to the cutter trajectory. For example: Data must be smooth and free of discontinuities and steps for ring shape parts or airfoils. However, discontinuities and steps in the radial direction are allowed in the case of segmented parts. Furthermore, during the ''flight'' between one segment and the next, the cutter trajectory must be optimized to minimize acceleration and deceleration.

Finally, a real-time motion control system is constantly updated with new position requirements by the computer logic. Feedback of actual cutter position versus cutter command position is routed back to the computer.

Surface Tracking Verification

Data plots were used during system development to evaluate system performance against precalibrated parts. Each data plot represents a 360 deg scan consistent with one revolution of a part. The data plots reveal several operating parameters.

Data spread is a term used to describe range in which 90 percent of the data resides at each point on the circumference of the part. Plot #1 shows a spread of 3.5 mm (0.14 in.) at the 120 deg position, where the circumference is divided into 360 deg. If the desired accuracy is defined as a 0.02 mm (0.0008 in.) envelope, the corresponding signal-to-noise ratio can be approximated to be 1:175. Using pattern recognition algorithms and rule sets corresponding to the expected mechanical behavior of the part, the actual part location can be defined. Naturally, when signal-to-noise ratio is more favorable, such as in Plot #2, accuracy can be further enhanced. The effect of the third dimension, or *Z* axis, is noticed in Plot #3. In this case a near-perfect circular part with an approximate diameter of 450 mm (18 in.) was centered on a lathe within 0.025 mm (0.001 in.). The part was clamped directly to the faceplate using a three-jaw-chucking system. The resulting distortion to the part, caused by the clamping forces, is noticeable from the three lobes described in Plots #2 and #3.

The approximate distortion is 0.25 mm (0.010 in.) per lobe as seen in Plot #2. This distortion is further compounded by a secondary distortion coupled with a varying surface condition as described in Plot #3. Data spread was not as favorable due to a surface condition, which changed the reflectivity and hence the laser sensor's ability to ''find'' the part.

To compensate for the inability of the laser sensor to determine the part position precisely, signal analysis and logic filters are employed, resulting in the two parallel lines described in plot #4. Special attention is given to the ''window'' between the solid line and the broken line. In the case of brazed honeycomb, these varying signal levels correspond with varying levels of braze alloy including partially plugged cells and cells with minimal levels of braze alloy.

Plot #4 is typical of a distorted part with an off-center condition, which resulted from its position on the lathe, in addition to the basic part distortion. Plot #4 is typical for a part with a basic distortion of approximately 0.5 mm (0.02 in.), which is further compounded by the part's wobble motion on the lathe of approximately the same magnitude.

During system development, tracking errors resulting from a phase shift related to servo performance occurred when the

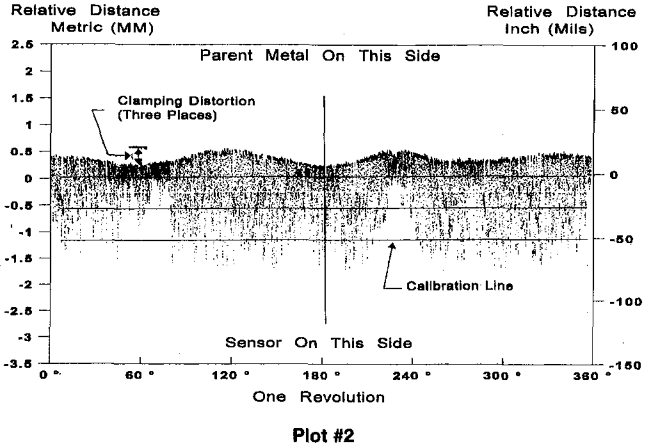

Plot #2

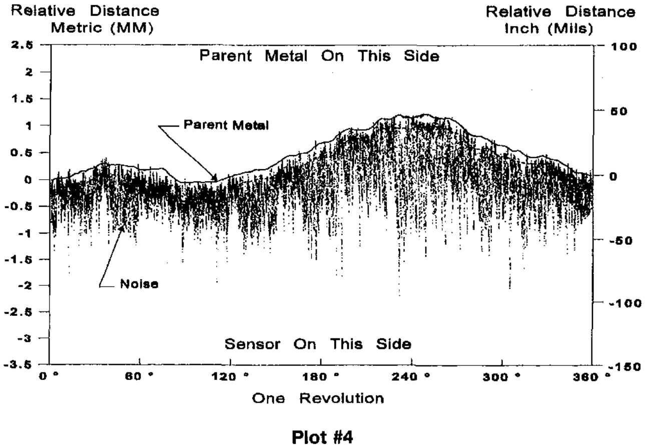

Plot #4

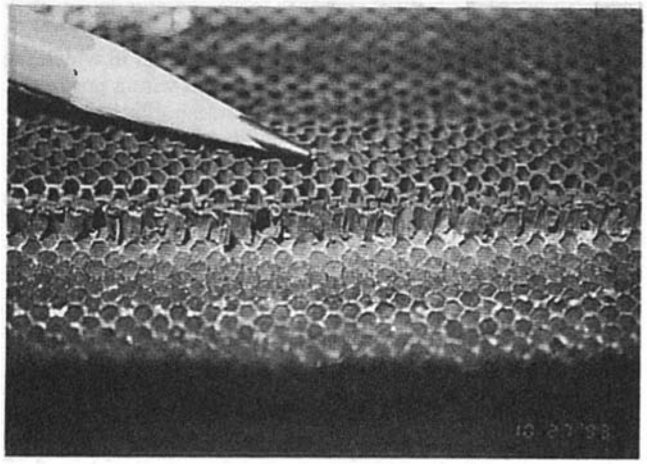

Fig. 5

servo was not tuned to optimize system performance. Servo optimization takes into consideration not only the trivial and traditional servo characteristics but also specific requirements and operating parameters related to the specific system configuration.

As part of system development a comparison was made to ascertain the benefit of using the system in relation to alternative technologies as follows:

Manual machining, hand blending, and chiseling: Parts were brought to pre-braze surface condition of approximately 125 rms surface finish with typical saving of 2 to 4 hours in labor per part resulting from reduced setup time and reduced in-process time. Loss of wall thickness during the repair was reduced from approximately 0.25 mm (0.010 in.) per repair cycle to approximately 0.10 mm (0.004 in.) per repair cycle. This difference in wall thickness may translate into two additional repair cycles. These numbers were difficult to measure scientifically and represent our best estimates.

Chemical stripping: The growing regulatory pressures are making it difficult in many countries to continue with compliance while maintaining chemical stripping facilities.

Inserts

During the development effort of the laser-guided cutter it was found that carbide inserts were failing at a rate estimated to be 50 percent faster than in traditional manual machining. Typically an insert was consumed during a 12 mm (0.5 in.) wide cut of a 760 mm (30 in.) diameter part, rotating at 16 rpm with a feed of 0.13 mm/rev (0.005 in./rev). Several possible causes such as suboptimal system rigidity, part flexing, and servo system backlash were investigated. When these and other possible causes for premature insert failure were eliminated, attention was directed to insert workload cycle.

Traditional machining of distorted parts, in particular during lathe operations, engages the carbide insert with the part only in the areas that are not concave relative to the machined surface. Typical circular parts may engage the inserts down to 80 percent of the time. When machining segments such as airseal segments, the typical engagement can be as low as 10 percent of the time as a result of some segments ''closing up'' during service while others tend to ''open up.'' When these segments are fixtured in a ring form to be machined as a set, operators will notice that one or two segments ''clean up'' first, while other segments lag behind. All this means that the demand on the actual cutting tip is reduced to part-time engagement.

By its inherent ability to follow the part contours, the laser guidance causes the carbide insert to engage the metal continuously, imposing a much more severe workload for the insert. As a result, a separate effort was launched to develop an improved carbide insert with the appropriate PVD and CVD coating technology to provide the wear resistance and the dry lubricity characteristics and thus accommodate the higher workload.

Airseals

As a group, airseals may be defined as static structures lined with a sacrificial surface. Figure 5 describes a typical worn honeycomb surface from a large commercial engine with approximately 3500 hours since the previous repair. The purpose of the sacrificial surface is to provide a controlled gap relative to a rotating blade or knife-edge seal. By the nature of its sacrificial surface, the part must be refurbished frequently to restore the nominal gap and as a result, engine fuel efficiency and performance. With typical cost of a new airseal of US $15,000 to 80,000, extension of life expectancy has a significant financial impact. Current generation engines contain approximately 20 to 30 components with honeycomb airseals per engine, including high-pressure compressor, high-pressure turbine, low-pressure turbine, and secondary flow areas such as bearing housings.

The specific problem with machining of airseals is the accumulated distortion present in each part. This distortion is evident in Fig. 6 as a nonuniform removal by traditional machining of the honeycomb described previously in Fig. 5. This distortion is a result of nonuniform wall thickness due to original manufacturing and previous repairs, distortion caused by the last service cycle, and distortion due to part clamping in the machining fixture. Machining of segments is more problematic since two segments, each with a different repair history, may be clamped in a fixture next to each other, with a difference in parent metal wall thickness up to 0.5 mm (0.02 in.).

Market research indicated that the problem with machining distorted parts is asking repair shops to consider alternative repair technologies (see below), where process efficiency is sacrificed in return for minimized parent metal removal. These processes include hand blending, chiseling, EDM, chemical stripping, and shearing.

The advantage of a guidance system in the repair of airseals is the ability to extend the life cycle of the parts beyond the typical two to four repairs.

Cases

Also known as frames, cases are fundamentally structural parts, having a thin-walled shell with front and rear flanges. Due to their size, with diameters up to 1500 mm (60 in.), setup

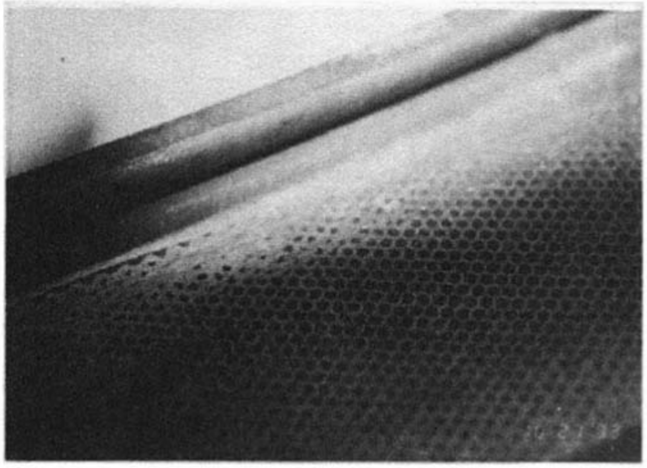

Fig. 6

of cases on a machine tool can take 8 hours or more. Typical reasons for machining cases are to remove fretting from a flange surface, to remove excess weld buildup, or to remove a worn plasma spray (also known as flame-spray and metallizing) buildup used for previous dimensional restoration. In these applications, the ability to guide a cutter in parallel to the base metal may alleviate the need for setup altogether. The primary requirement in these operations is to cut parallel to the existing parent metal. For selective cutting of plasma spray, where the goal is to eliminate an existing layer of plasma spray, sensors other than lasers can be used to accomplish this task.

Alternative Technologies

The purpose of developing a new technology is usually to provide the user with a means to do a job ''better, faster, and cheaper,'' with the baseline or reference point being the alternative technologies afforded to the user. This case is no exception. A brief description is provided below for reference only.

Chemical stripping is a means to dissolve the braze alloy, or plasma spray, selectively, without affecting the parent metal. This method is effective particularly in situations where the chemical composition of the parent metal is significantly different from that of the braze alloy or plasma spray.

Water jet stripping is a means to selectively chisel or blast a layer or coating such as plasma spray or silicone rubber away from the parent metal by means of a high-energy water jet, approximately 1 mm (0.04 in.) in diameter. This method is limited by the requirement to set up a dedicated shop floor area to accommodate the water supply system, sound attenuation, and the related robotic manipulator.

Manual machining should be counted as an important alternative since it is widely used throughout the repair industry. The shortcoming of the manual approach is the operator dependency and long setup time, in particular for case repair.

Chisel and blend is a form of manual operation in which the bulk of the honeycomb or rubber is removed with a pneumatic chisel. Typically, the balance of the undesirable layer is removed by hand blending using a hand-held power tool.

Electro Discharge Machining (EDM) is used in limited situations. While EDM is a high-precision method of material removal, it is a very slow process requiring several hours per part.

Conclusion

The introduction of an autonomous, laser-guided tooling for jet engine component repair was based on the principal of moderate automation. Its design considerations and principles were developed with the machine operator in mind. Similar principles can be applied to new areas of automated equipment. The difficulties in introducing this new technology to the shop floor included not only issues related to user interface, but also to the technical difficulties of collecting reliable data at high rates. Simple electronic, mathematical, and statistical algorithms proved to be insufficient for accurate trajectory generation. However, the use of pattern recognition methods raised the accuracy to acceptable levels.

The use of machining equipment with the authority to decide upon and execute a cutting trajectory independently has potential for many other applications requiring selective cutting.

Acknowledgments

The authors wish to extend their thanks to the teams at SeamX and Kennametal who supported the development of this new technology.

Comparison Between EBW and GTAW for Turmo IV C Compressor Blade Repairs

W. Miglietti
MATTEK-CSIR,
Pretoria, South Africa

A research study was undertaken to evaluate whether electron beam welding (EBW) or gas tungsten arc welding (GTAW) could be utilized for repairs to the leading edges of the Turmo IV C compressor blades. These blades are manufactured from Ti-6Al-4V. The study entailed performing a series of welding trials. For the GTAW process a matching filler metal to the parent metal was used, whereas for the EBW process, the welds were made autogenously. After metallographic examination of the weld microstructure, mechanical property assessments were undertaken, namely tensile and fatigue tests, the latter being a stringent test to evaluate the performance of the welded joint. The results demonstrated that the EB welds had equivalent properties to the parent metal, whereas the GTA welds had poorer fatigue properties due to undesirable microstructure that resulted in the weld zone. The results achieved herein showed that the EBW process would be an appropriate technique for the restoration of these compressor blades.

Introduction

Turmo compressor blades from the Puma helicopter suffer from severe sand erosion, resulting in degradation of the leading edge of this aerofoil. Due to the fact that EBW and GTAW are two joining processes that have been extensively used in the manufacture and repair of gas turbine components (Yonesawa, 1987; Becker et al., 1980; Brene, 1980; Broomfield, 1986; Farthing, 1984) a study was initiated to investigate the feasibility of undertaking a weld repair to restore the leading edge back to its original dimension. The definition of a successful weld repair applied by the customer was that the final weld repair should have equivalent mechanical properties to that of the parent metal. This was most relevant for the fatigue properties. These blades are manufactured from Ti-6Al-4V material, which is regarded by the aviation industry as the ''work-horse'' of the Ti alloys. Receiving approximately 75 of these blades it was found that in the worst case the erosion occurred 30 mm along the tip of the blade and 10 mm away from the hub of the blade along the leading edge as indicated in Fig. 1(*a*) and schematically in Fig. 1(*b*).

Proposed Repair Scheme in General Principles

(*a*) Inspection of eroded area.
(*b*) Machining of eroded area.
(*c*) Preparation of surfaces to be welded.
(*d*) Cleaning of prepared surfaces.
(*e*) EB weld preformed or forged section onto the eroded blade or GTA weld up the eroded area.
(*f*) Inspection for cracks.
(*g*) Restoration of the welded blade to its original profile.
(*h*) NDE evaluation by X-ray and fluorescent dye penetrant inspection.
(*i*) Postweld heat treatment if necessary.
(*j*) QA inspection and over check.

Experimental Procedure

As these blades are manufactured from Ti-6Al-4V, some 1.6 mm IMI 318 alloy in sheet form was purchased from IMI Titanium in the United Kingdom to match the thickness of the blades where erosion occurred.

For metallographic investigation, two sheets of dimensions 50 × 50 × 1.6 mm were butt welded together in a square groove configuration, as shown schematically in Fig. 2. Prior to welding the mating surfaces for both the GTA and EB welds were sheared with a guillotine, then ground and the edges deburred with no chamfering necessary. After machining all sheet samples were soaked in an aqueous solution of 2 → 4 percent HF and 30 → 40 percent HNO_3 acid, followed by an appropriate water rinse and drying. After chemical cleaning the samples were cleaned with toluene as preweld cleaning is critical to weld quality, since any foreign matter (solvents, dirt, or oil) on the mating surface would be detrimental, both metallurgically and mechanically, to the weld properties. For EBW the two sheets were welded autogenously at a voltage of 120 kV, beam current of 7.5 mA, welding speed of 40 mm/s, and focus current of 1.823 mA. The maximum joint gap stipulated when welding was 0.1 mm. However, in most cases the joint gap was less than 0.05 mm.

For GTAW, the same joint configuration as shown in Fig. 2 was utilized and welding was performed using a 1.6-mm-dia filler metal of Ti-6Al-4V in an argon dome. Essentially all GTA welds were performed at a voltage of 12 V and current of 100 A.

For the mechanical properties evaluation, specimens were cut out from the annealed welded sheet as shown schematically in Fig. 3. The tensile and fatigue strength test configurations for the welded joints are shown in Figs. 4(*a*) and (*b*), respectively.

All fatigue testing was axial tension–tension using a minimum-to-maximum stress ratio *R*

$$\left(R \text{ factor} = \frac{\bar{\sigma}\,\text{MIN}}{\bar{\sigma}\,\text{MAX}}\right)$$

of 0.1 at a testing frequency of 10 Hz. All welded specimens had the crown of the weld and any undercutting ground flat prior to fatigue testing.

It is well known (Rabelotto, 1968) that residual welding stresses affect the mechanical properties of welds. It has been

---

Contributed by the International Gas Turbine Institute and presented at the 39th International Gas Turbine and Aeroengine Congress and Exposition, The Hague, The Netherlands, June 13–16, 1994. Manuscript received by the International Gas Turbine Institute February 16, 1994. Paper No. 94-GT-50. Associate Technical Editor: E. M. Greitzer.

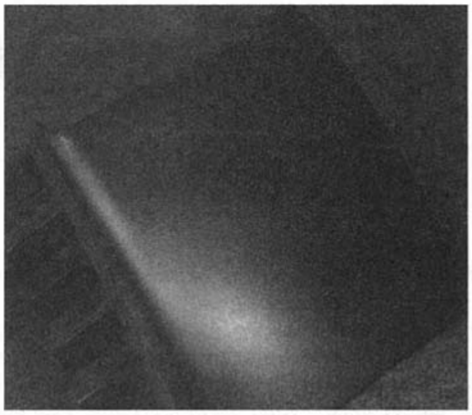

Fig. 1(*a*) Erosion along the leading edge of the compressor blade

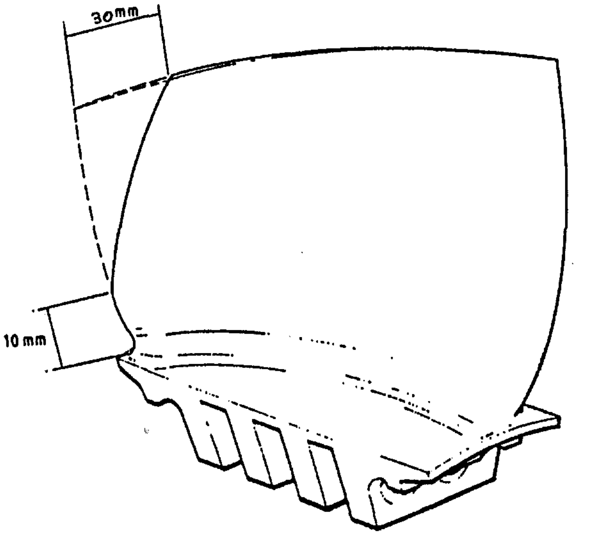

Fig. 1(*b*) Schematic representation of erosion along the leading edge of the blade

reported that the highest values of residual stress in Ti-6Al-4V welds occur when the EBW process is used; values up to 49 percent of the UTS have been encountered (Rabelotto, 1968). This strongly influences the fatigue behavior of the weld.

For this reason, two heat treatments were investigated to reduce the levels of residual stress, namely:

- annealing at 700°C for 1 hour in vacuum then slow cool to room temperature
- stress relieving at 550°C for 4 hours in vacuum then slow cool to room temperature

It so happens that the temperature at which stress relief occurs is also 30°C above the aging temperature for Ti-6Al-4V and hence an increase in hardness is expected to occur in the base metal with some loss in ductility.

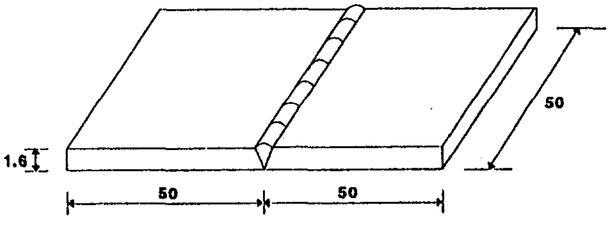

Fig. 2 Weld joint to be used for metallurgical investigation (all dimensions in mm)

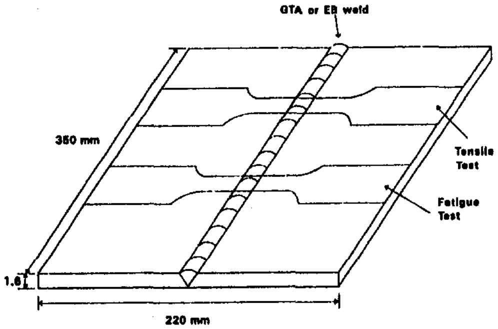

Fig. 3 Weld joint showing areas for tensile and fatigue investigation

After the last weld heat treatment all welded samples were NDE examined for cracks and porosity via X-rays.

Metallographic Results and Discussion

EBW. Figure 5 shows the fusion zone to consist of acicular martensitic α' needles dispersed in prior β grains. The α' needles can be more clearly seen in Fig. 5(*b*). The HAZ as seen in Fig. 6 consists of a mixture of martensitic α' and primary α. The parent metal as seen in Fig. 7 consists of almost (bright) equiaxed α with (dark) β around the α grain boundaries. Figure 8 is a macrograph of the EB weld, where columnar grains bigger than those of the parent metal can be seen.

As there is a lack of α phase on the prior β grain boundaries in Fig. 5(*a*) and Fig. 8, this implies that the cooling rate was fast (Mazumder and Steen, 1982). These microstructures are similar to those found in a study by Banas (1974) on EBW, LBW, and PAW. The fusion zone, which consists of α' as the principal phase, would be expected to lack ductility as Bartlo (1961) showed in a detailed study of individual structures. He also noted that this structure had good fatigue strength.

GTAW. Figure 9(*a*) shows the fusion zone to consist of a Widmanstätten α arrangement and the serrated α. Figure 9(*b*) shows α at the large prior β grain boundaries, which is an indication of the slow cooling rate with GTAW. Part of the HAZ as seen in Fig. 10(*a*) consists of a mixture of acicular α and martensitic α'. The part of the HAZ close to the parent metal as seen in Fig. 10(*b*) consists of α' needles and primary α. The HAZ experiences the fastest cooling rate and this is the

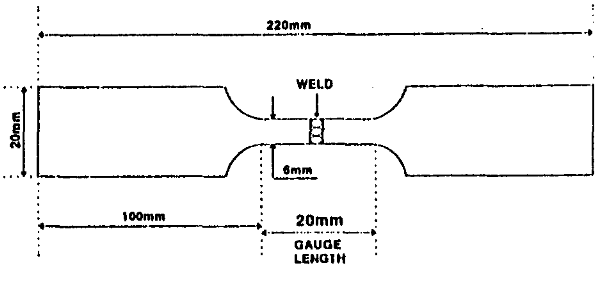

Fig. 4(*a*) Transverse tensile test configuration for welded joints

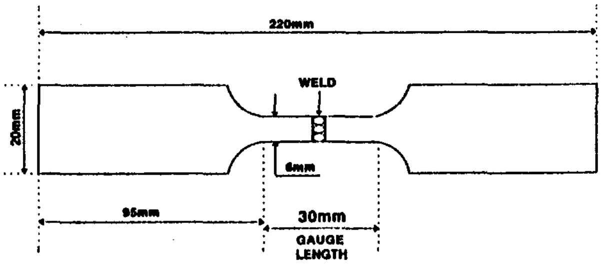

Fig. 4(*b*) Transverse fatigue test configuration for welded joints

Fig. 5(*a*) Micrograph of the fusion zone showing acicular martensitic α' needles dispersed in prior β grains, magnification 100×

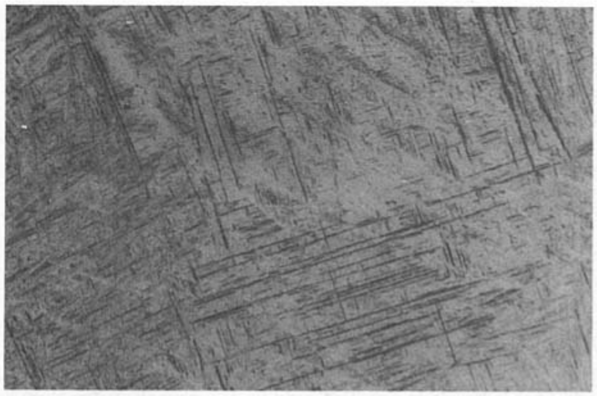

Fig. 5(*b*) Micrograph showing the α' needles present in the fusion zone, magnification 200×

reason why α' needles formed. The parent metal as seen in Fig. 11 consist of bright equiaxed α with dark β around the α grain boundaries. Figure 12 is a macrograph of the GTA weld and clearly the fusion zone area can be distinguished from the parent metal by the very large grain size in the fusion zone area. The grains in the fusion zone are 100 times bigger than those present in the parent metal.

The Widmanstätten microstructure in the fusion zone is undesirable for welds that have to endure fatigue conditions according to Bergmann et al. (1991).

The reason for the difference in the fusion zone microstructures of the GTA and EB welds can be explained as follows. When the weld cools from above 990°C (the $\beta/(\alpha + \beta)$ transus), the transformed β structure varies from martensitic to Widmanstätten as the cooling rate decreases from water quench speeds to those characteristics of air cooling (Collings, 1983). As the cooling rate is much faster with EBW (note the welding speed is very fast at 40 mm/s, which results in a low heat input) than GTAW (which is a high heat input process resulting in slow cooling rate), the EB welds should show a martensitic structure whereas the GTA welds should be a Widmanstätten structure. This was the case as found in the study.

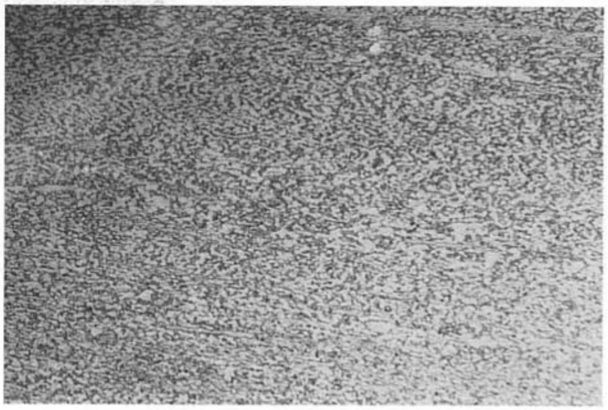

Fig. 7 Micrograph of the parent metal consisting of almost equiaxed α with β around the α grain boundaries, magnification 200×

Also the α phase on the prior β grains indicates a slow cooling rate typical of GTAW, whereas the absence of this phase in Fig. 5 indicated a fast cooling rate typical of EBW.

Hardness Surveys and Discussion

Figure 13 shows the hardness variation across the EB weld in the as-welded condition. There is an increase in hardness from 315 Hv in the parent metal to 358 Hv in the HAZ, to 365 Hv in the fusion zone. The maximum difference in hardness between the parent metal and fusion zone is therefore 50 Hv.

Figure 14 shows the hardness survey variation across the EB weld in the welded + annealed condition. There is an increase in hardness from 315 Hv in the parent metal to 355 in the HAZ, to 358 Hv in the fusion zone. The maximum difference in hardness between the parent metal and fusion zone is therefore 43 Hv.

Figure 15 shows the hardness variation across the EB weld in the welded + stress relieved condition. There is an increase in hardness from 329 Hv in the parent metal to 343 Hv in the HAZ to 350 Hv in the fusion zone. The maximum difference in hardness between the parent metal and fusion zone is therefore 21 Hv.

Figure 16 shows the hardness variation across the as-welded GTA weld. As can be seen, the maximum hardness occurred

Fig. 6 Micrograph of the HAZ consisting of a mixture of martensitic α' and primary α, magnification 200×

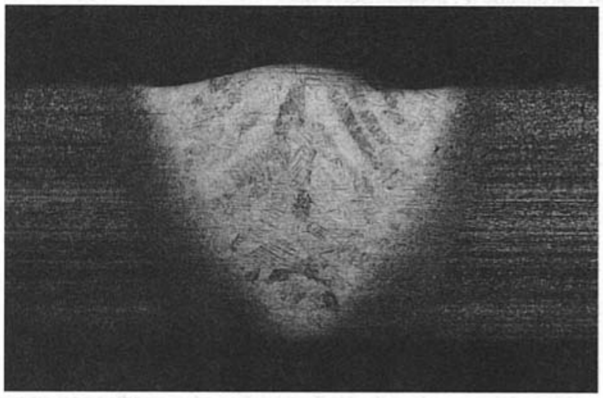

Fig. 8 Macrograph of an EB weld, magnification 30×

Fig. 9(*a*) Micrograph of the fusion zone consisting of Widmanstätten α and serrated α, magnification 200×

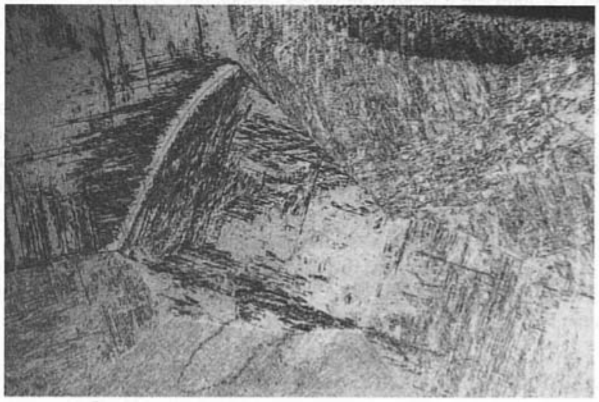

Fig. 9(*b*) Micrograph showing α at the large prior β grain boundaries indicative of slow cooling, magnification 100×

Fig. 10(*a*) Micrograph of the HAZ consisting of a mixture of acicular α and martensitic α', magnification 100×

Fig. 10(*b*) Micrograph of the HAZ consisting of α' needles and primary α, magnification 100×

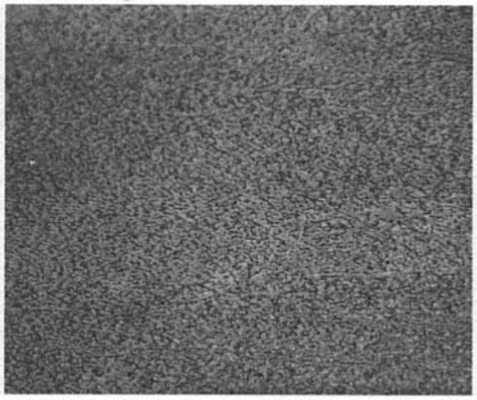

Fig. 11 Micrograph of the parent metal consisting of almost equiaxed α with β around the α grain boundaries, magnification 200×

Fig. 12 Macrograph of a GTA weld, magnification 12×

in the HAZ. This is the area where the fastest cooling rate occurred. The fusion zone is softer than the parent metal, proving that the Widmanstatten structure is softer than the martensitic structure. The difference in hardness between the parent metal and the HAZ is 130 Hv. Figure 17 shows the hardness variation across the GTA weld in the welded and annealed condition. As can be seen, the hardness in the HAZ has decreased significantly due to this annealing. The fusion zone is still the softest area. The difference in hardness between the parent metal and HAZ is 42 Hv. Figure 18 shows the hardness variation across the GTA weld in the welded and stress relieved condition. The hardness in the parent metal has now increased. The maximum hardness and softness occurred in the HAZ and fusion zone, respectively.

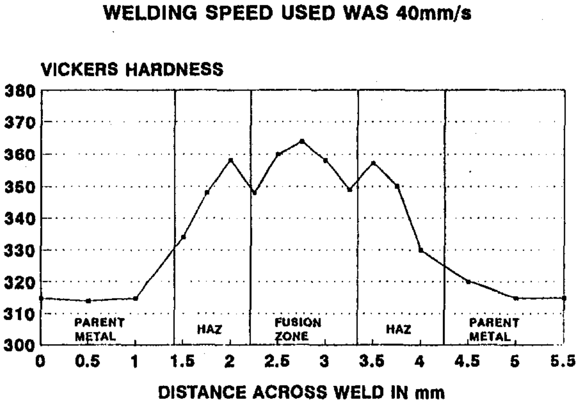

Fig. 13 Hardness survey across as-EB welded Ti-6Al-4V sheet

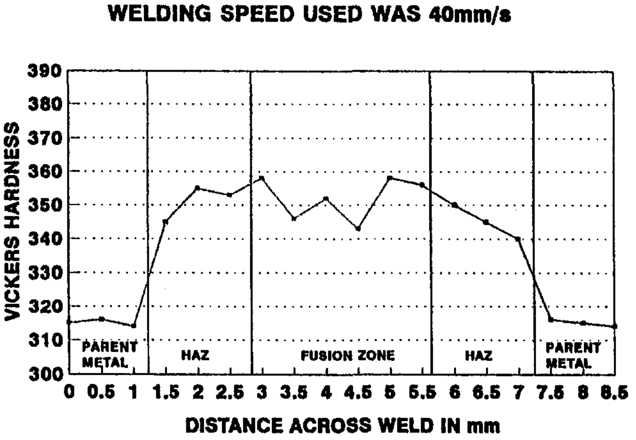

Fig. 14 Hardness survey across EB welded and annealed Ti-6Al-4V sheet

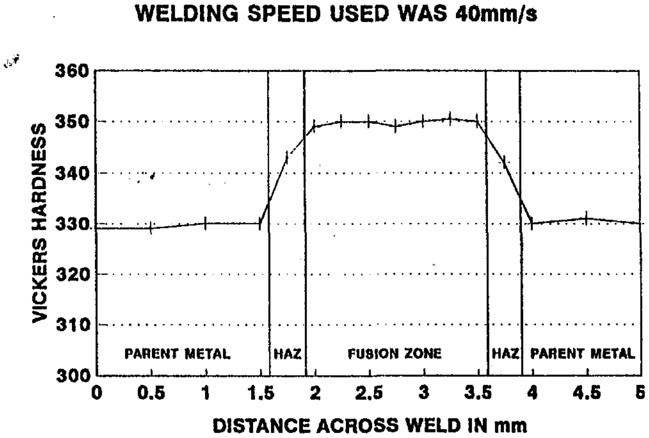

Fig. 15 Hardness survey across EB welded and stress relieved Ti-6Al-4V sheet

For EBW, as can be seen from Fig. 13, the maximum hardness occurred in the fusion zone. After postweld annealing (Fig. 14) the hardness in the fusion zone drops, implying that the annealing heat treatment partially annealed the weld. More surprising after postweld stress relieving (Figure 15), the hardness in the fusion zone dropped further and as was expected the hardness in the parent metal increased.

Postweld annealing had not reduced the microhardness variation across the fusion zone, whereas stress relieving reduced the microhardness variation, such that the microhardness is constant for the entire width of the fusion zone.

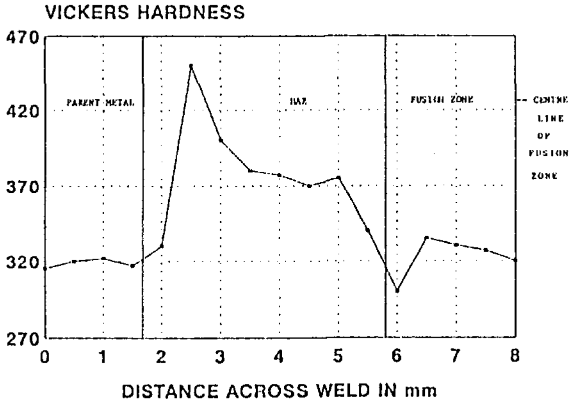

Fig. 16 Hardness survey across as-GTA welded Ti-6Al-4V sheet

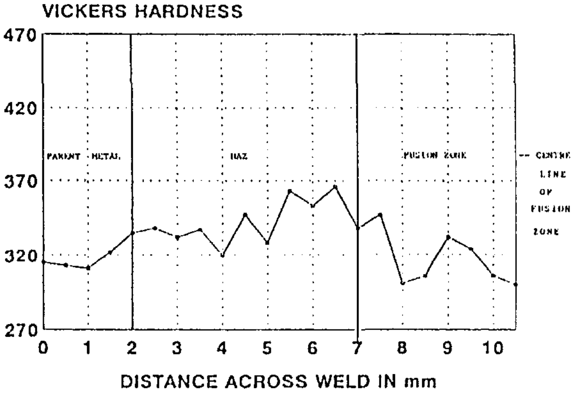

Fig. 17 Hardness survey across GTA welded and annealed Ti-6Al-4V sheet

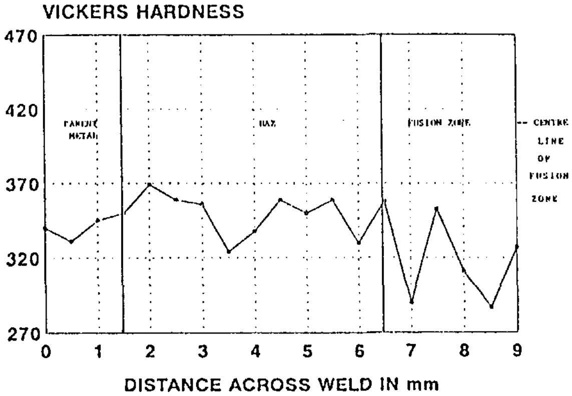

Fig. 18 Hardness survey across GTA welded and stress relieved Ti-6Al-4V sheet

Mechanical Property Results and Discussion

Tensile Strengths. Tensile strengths can be found in Tables 1 and 2. The results are an average of four samples.

All the EB welded tensile specimens in their various conditions failed in the parent metal. Due to the fine acicular martensitic α' needles in the fusion zone, the weld often exhibits higher tensile strengths than the base metal and for this reason failure occurred in the parent metal.

As can be seen in Table 1, the tensile and yield strengths of the EB welds are elevated by stress relieving. The percentage elongation, however, does decrease significantly. Also the tensile and yield strengths of the EB welds decreased slightly

Table 1 Summary of the tensile properties of the EB welds

Condition of Specimen	Tensile Strength (MPa)	Yield Strength (MPa)	Elongation *%
Parent Metal	1035	954	17
As-Welded	1050	962	12,5
Welded + Annealed	1020	937	13,5
Welded + Stress Relieved	1078	1001	10,5

Table 2 Summary of the tensile properties of the GTA welds

Condition of Specimen	Tensile Strength (MPa)	Yield Strength (MPa)	Elongation %
Parent Metal	1035	954	17
As-Welded	1047	971	8,5
Welded + Annealed	996	927	10,5
Welded + Stress Relieved	1014	910	7,5

Table 3 Fatigue strength of EB welded specimens

Condition of Specimen	Endurance Limit in MPa at 10^7 cycles	Percentage of Parent Metal Endurance Limit
Parent Metal	550	-
As-Welded	400	73
Welded + Annealed	500	90
Welded + Stress Relieved	545	99

by postweld annealing; however, the percentage elongation is slightly improved compared to the as-welded and welded + stress relieved condition.

All the GTA welded tensile specimens in their various conditions failed in the parent metal. Due to the acicular Widmanstätten α arrangement and serrated α microstructure in the fusion zone, the weld exhibited higher tensile strengths than the base metal except for the welded and annealed specimens where the annealing reduced the tensile strength to lower than the base metal.

Except for the welds on the annealed specimens, all welded specimens including the stress relieved specimens had very low elongations, which are on the order of 50 percent of the parent metal. The elongation of the welded and annealed specimens was slightly higher at about 62 percent of the parent metal. This decrease in elongation is probably due to the Widmanstätten and serrated α microstructure.

Fatigue Data. The fatigue properties and *S-N* fatigue curves (i.e., stress versus number of cycles to failure) of the EB and GTA welded specimens can be found in Tables 3 and 4 and Figs. 19 and 20, respectively.

Table 4 Fatigue strength of GTA welded specimens

Condition of Specimen	Endurance Limit in MPa at 10^7 cycles	Percentage of Parent Metal Endurance Limit
Parent Metal	550	-
As-Welded	410	75
Welded + Annealed	400	73
Welded + Stress Relieved	400	73

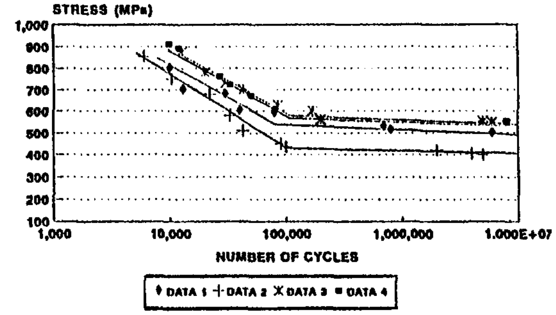

DATA 1 : WELDED AND ANNEALED AT 700°C FOR 1hr
DATA 2 : AS WELDED DATA 3 : PARENT METAL
DATA 4 : WELDED AND STRESS RELIEF AT 550°C FOR 4hr

Fig. 19 Fatigue properties of EB welded 1.6 mm Ti-6Al-4V sheet

For the EB welded specimens, the fatigue strength/endurance limit of the as-welded specimens is 73 percent of the parent metal fatigue strength. This is due to the weld microstructure and the high residual welding stresses that result after EBW. Annealing is not a completely effective means of reducing the residual stresses and for this reason, annealed specimens failed at 90 percent of the parent metal fatigue strength. Stress relief at 550°C for 4 hours seems to be an effective means of greatly reducing the residual stresses. This is seen by the equivalent fatigue strength of the stress-relieved welds compared to those of the parent metal.

For the GTA welded specimens, the fatigue strength/endurance limit of the as-welded specimens is 75 percent of the parent metal fatigue strength. The welded + annealed and welded + stress-relieved welds had a fatigue strength/endurance limit of 73 percent of the parent metal. Therefore the postweld heat treatment did not play a role in increasing the fatigue properties of the welded specimens. Thus the comment by Bergmann et al. (1991) seems correct that the Widmanstätten and serrated α microstructures are associated with low high cycle fatigue properties. The extremely interesting result achieved when fatigue testing the GTA welds was that the low cycle fatigue properties were better than those of the parent metal. No reason for this phenomenon was found.

The reason for the EB welds having better fatigue properties than that of the GTA welds is because the EB welds have a finer microstructure and smaller grains in the fusion zone whereas the GTA welds have a Widmanstätten microstructure and large grains in the fusion zone.

Fracture Characteristics

Fracture surfaces of the fatigue test specimens of the EB welds, regardless of the condition, revealed dimpled fracture surfaces as seen in Fig. 21.

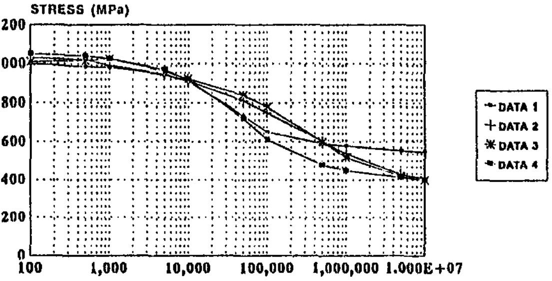

DATA 1: PARENT METAL DATA 2 : AS-WELDED
DATA 3: WELDED AND ANNEALED AT 700°C FOR 1hr
DATA 4: WELDED AND STRESS RELIEF AT 550°C FOR 1hr

Fig. 20 Fatigue properties of GTA welded 1.6 mm Ti-6Al-4V sheet

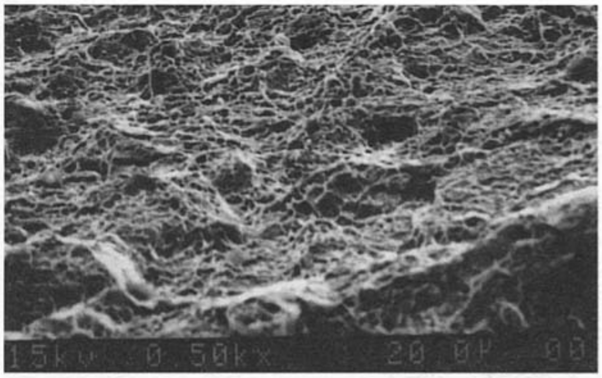

Fig. 21 Dimpled fracture surface of fatigue test specimen

NDE Examination

All welds were X-ray examined using Sauerwein real time microfocus X-ray system with full computer image enhancement at a voltage of 110 kV, a current of 0.7 mA, and filament current of 0.34A. No significant defects such as porosity or cracking were observed for either the EB weld or GTA weld as seen in Figs. 22 and 23, respectively.

Conclusions

From this study the following conclusions were made for EBW of 1.6 mm Ti-6Al-4V sheet:

(*a*) For the EB welds, regardless of the postweld treatment used, the microstructure of the fusion zone consisted of acicular martensitic α' needles dispersed in prior β grains. The HAZ consisted of a mixture of α' and primary α. The parent metal consisted of almost equiaxed α with β around the α grain boundaries.

(*b*) The fusion zone consisted of small columnar grains that were larger in size than the equiaxed grains in the parent metal.

(*c*) The width of the fusion zone was on the order of 2.3 mm.

(*d*) For all welded specimens, whether postweld heat treated or not, the maximum hardness occurred in the fusion zone. Postweld annealing tended to soften the weld partially as seen by the decrease in hardness in the fusion zone. Postweld stress relief tended to increase the hardness partially in the parent metal. Postweld annealing had not reduced the microhardness variation in the fusion zone, whereas stress relief reduced the microhardness variation, such that the microhardness was constant for the entire width of the fusion zone.

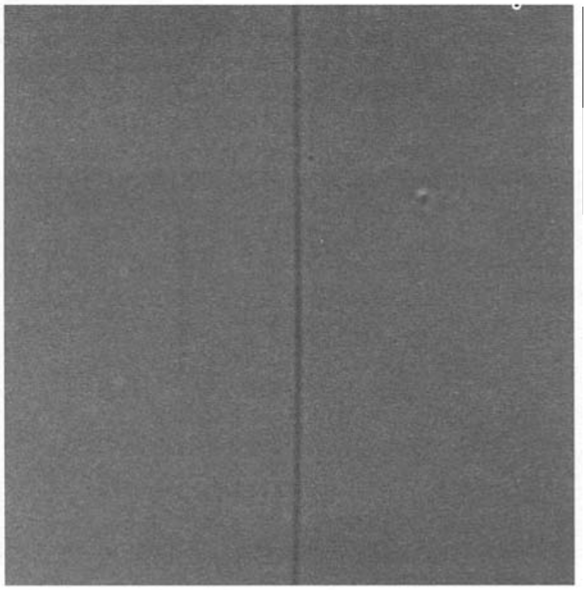

Fig. 22 X-ray analysis of an EB weld in 1.6 mm Ti-6Al-4V sheet

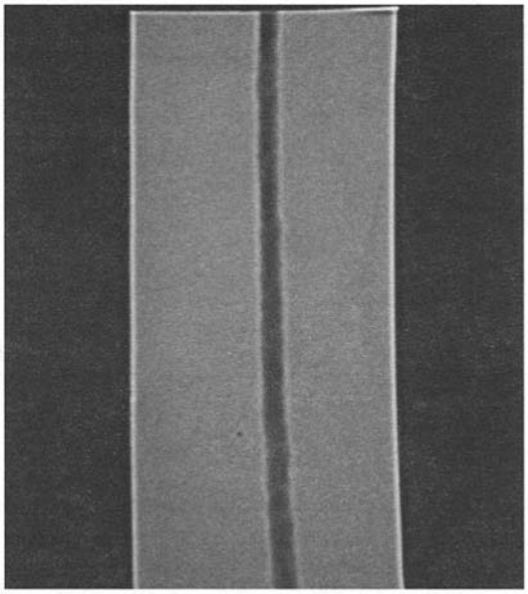

Fig. 23 X-ray analysis of a GTA weld in 1.6 mm Ti-6Al-4V sheet

(*e*) The tensile strengths of the as-welded, annealed, and stress-relieved specimens were greater than that of the parent metal. Due to the fine acicular martensitic α' in the fusion zone, the weld exhibited higher tensile strengths than that of the parent metal.

(*f*) The presence of larger grains in the fusion zone and residual welding stresses affected the fatigue properties of the as-welded specimens, such that it took approximately 2.5 times as many cycles to fail the stress-relieved welded specimens as the as-welded specimens. Thus residual welding stresses have a detrimental effect on the fatigue properties of the welds. Stress relief at 550°C/4 hours raised the endurance limit to that of the parent metal (i.e., 550 MPa), whereas postweld annealing at 700°C/1 hour raised the endurance limit to 90 percent (500 MPa) of the parent metal's endurance limit. Therefore by stress relief, EB weld fatigue properties are made equivalent to that of the parent metal.

(*g*) Nondestructive examination using X-ray techniques revealed welds free of porosity and cracking.

From the study the following conclusions were made for GTAW of 1.6 mm Ti-6Al-4V sheet:

(*h*) For the GTA welds, the microstructure of the fusion zone consisted of a Widmanstätten α arrangement and serrated α microstructure with the HAZ consisting of these structures and primary α. The parent metal consisted of equiaxed α with β around the α grain boundaries.

(*i*) The fusion zone consisted of very large grains due to the slow cooling after GTAW.

(*j*) The width of the fusion zone was on the order of 5.5 mm.

(*k*) For all welded specimens, whether postweld heat

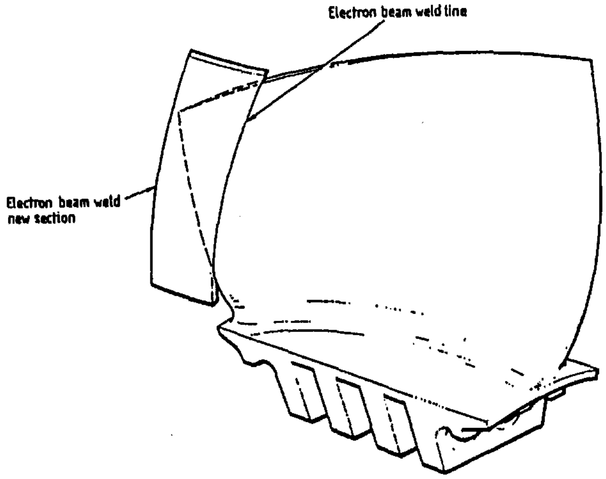

Fig. 24 EBW of new section onto the area where the erosion took place

treated or not, the maximum hardness occurred in the HAZ. Postweld annealing tended to soften the HAZ partially as seen by the decrease in hardness in this area. Postweld stress relief tended to increase the hardness in the parent metal partially. Neither postweld annealing or stress relief reduced the microhardness variation in the fusion zone.

(*l*) The tensile strengths of the as-welded and welded + stress-relieved specimens were greater than those of the parent metal. Due to the presence of the Widmanstätten α and serrated α in the fusion zone, the GTA welds exhibited higher tensile strengths than the base metal.

(*m*) The presence of the Widmanstätten and serrated α reduced the fatigue strength/endurance limit of all the welded specimens. The postweld heat treatment did not increase the high-cycle fatigue properties. However, rather surprisingly the low-cycle fatigue properties of the welded + annealed and welded + stress-relieved specimens were better than those of the parent metal. No reason was found for this phenomenon.

(*n*) Nondestructive examination using X-ray techniques revealed welds free of porosity and cracking.

From both studies on EBW and GTAW of Ti-6Al-4V, it was concluded that although the tensile properties of the GTA welds were better than those of the parent metal, the fatigue strength was only 73 percent of the parent metal's fatigue strength. Thus from a repair point of view the GTA welds would not have equivalent fatigue properties to those of the parent metal. However, the EBW results certainly looked promising as both the tensile strength and fatigue strength of welds were equivalent to those of the parent metal, once the welded samples were given a stress relief heat treatment of 550°C/4 hours. As the customer had a well-maintained EB facility, the customer felt that the advantages of the EBW process (e.g., fast travel speed, high production rates, little distortion, small fusion and heat-affected zone, etc.) in combination with the results achieved in this study would make the EBW repair of Turmo IV C compressor blades a viable proposition. Thus a repair scheme using EBW was developed accordingly. Figure 24 shows schematically how a new preformed section was welded onto the eroded blade. Figure 25 shows schematically how the leading edge must be restored to its original profile via CNC milling. Figure 26 shows an actual blade fully EB welded where the leading edge has been restored to its original profile. The repaired blade was subsequently etched and the EB weld can be clearly seen. Figure 27 shows a macrograph of the EB weld joining a 2.6 mm sheet section onto the 1.6 mm blade.

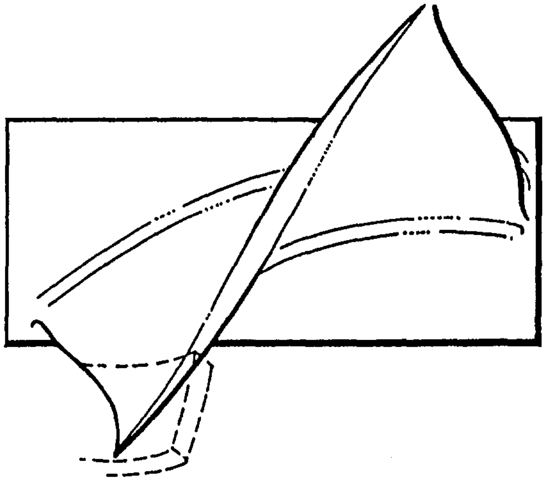

Fig. 25 Restore leading edge profile, CNC machine, and blend to existing profile

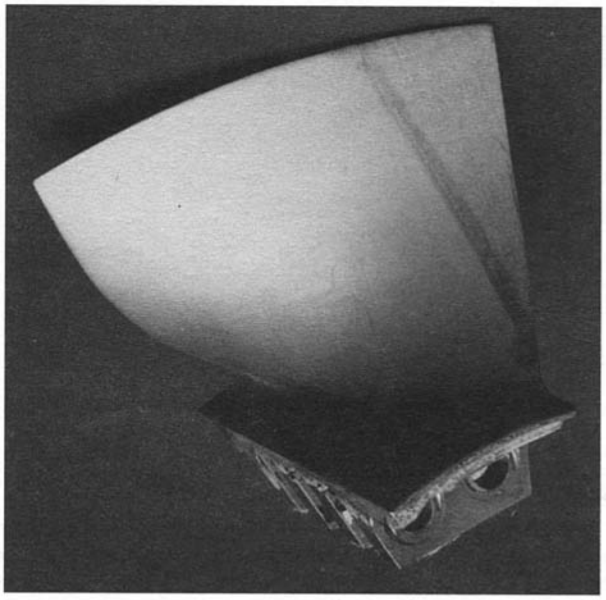

Fig. 26 EB welded repaired blade fully machined and re-contoured: EB weld seam can be seen due to macroetching

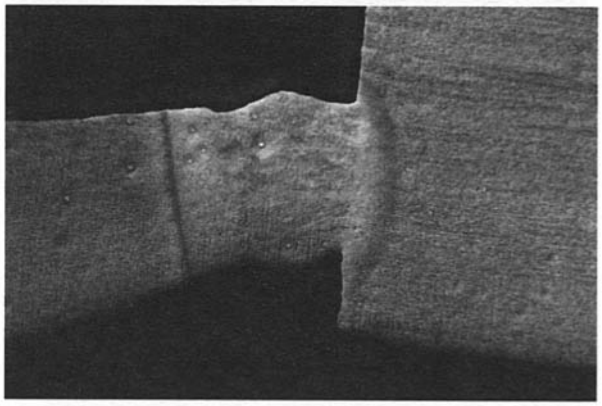

Fig. 27 Macrograph showing the new section, which was EB welded to the blade, magnification 20×

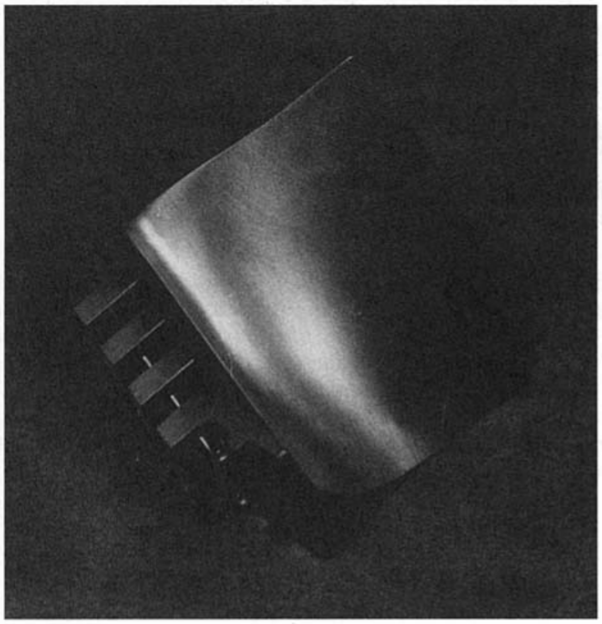

Fig. 28 TiN coated compressor blade

For demonstration purposes a TiN coating was placed on the repaired blade, Fig. 28, to slow the rate of future erosion. This, however, was not evaluated and hence will form part of a study in a future program.

Based on the results attained in this study the following repair scheme was deemed viable for the repair of sand-eroded Turmo compressor blades:

(*a*) Inspection of eroded area.
(*b*) Machining of eroded area.
(*c*) Preparation of surfaces to be welded.
(*d*) Cleaning of prepared surfaces.
(*e*) EB weld preformed or forged section onto the eroded blade.
(*f*) Inspection for cracks.
(*g*) Restoration of the welded blade to its original profile.
(*h*) NDE evaluation by X-ray and fluorescent dye penetrant inspection.
(*i*) Postweld heat treat at 550°C for four hours.
(*j*) QA inspection and overcheck.

Acknowledgments

The author would like to thank the Specialty Metals Programme of MATTEK, in particular, Mr. J. Benson, Mr. D. de Wet, Dr. N. R. Comins, Mr. P. Nkgomba, Mr. J. Davies, Miss E. Erasmus, Mrs. H. Snyders, Mrs. C. Stearn, and Mr. S. Yates for their help in this project.

References

Banas, C. M., 1974, "Electron Beam, Laser Beam and Plasma Arc Welding Studies," NASA Contractor Report No. NASA CR 132 386, Mar.

Bartlo, J., 1961, ASTM STP 459, pp. 144–154.

Becker, D. W., Nessler, R. W., and Baeslack, W. A., 1980, *Titanium 80,* Kyoto, p. 255.

Bergmann, H. W., Brene, J., Cantello, M., and Juckenath, B., 1991, *Laser Welding of Titanium and Titanium Alloys.*

Brene, J., 1980, *Titanium 80,* Kyoto, p. 2369.

Broomfield, R. W., 1986, "Application of Advanced Joining Techniques to Titanium Alloys," *Proceedings of the International Conference on Titanium,* p. 69.

Collings, E. W., 1983, "The Physical Metallurgy of Titanium Alloys," *American Society for Metal,* H. L. Gegel, ed.

Farthing, T. W., 1984, "Application of Titanium and Titanium Alloys," *Proceedings of the 5th International Conference on Titanium,* Munich, Germany.

Mazumder, J., and Steen, W. M., 1982, "Microstructure and Mechanical Properties of Laser Welded Titanium 6Al-4V," *Metallurgical Transactions A,* Vol. 13A, p. 865.

Rabelotto, R., Lambase, J. M., and Toy, A., 1968, "Residual Welding Stresses in Titanium and Their Effects on Mechanical Behaviour," *Welding Research Supplement,* July.

Yonesawa, K., 1987, *Welding International,* Vol. 12, p. 1131.

Gas Turbine Acoustic Enclosure Design by the Statistical Energy Analysis Method

L. K. H. Lu

M. Mitchell

Marine Division,
Westinghouse Electric Corporation,
Sunnyvale, CA 94088

Acoustic enclosure design is a complex problem that involves the interaction of multiple components. Yet the present conventional approach uses a two-dimensional closed-form solution to evaluate transmission loss of acoustic wall. In this paper, Statistical Energy Analysis (SEA) was first studied for simple cases of radiation efficiency, transmission loss, and flanking path calculations. The effectiveness of the SEA method for complex systems was then demonstrated through a practical design application to gas turbine enclosure. It was found that SEA was a useful tool for gas turbine acoustic enclosure design.

1 Introduction

The effectiveness of the acoustic design for an enclosure depends on many factors, such as the transmission loss of the enclosure wall, the absorption of wall surfaces, the interaction between acoustic spaces, and the transmission of energy among structural components. The two-dimensional closed-form solution of a plate-type structure [1] has been used to evaluate only the transmission loss across the enclosure walls. Other factors such as effects of structure-borne noise transmission, etc., are generally neglected or estimated by empirical equations in this approach. Statistical Energy Analysis (SEA) [2], on the other hand, maintains energy balance among the components. Hence, noise transmission between acoustic spaces, acoustic space to structure, and structure to structure are accounted for simultaneously.

Crocker et al. [3] have applied SEA to calculate transmission loss of single and double wall panels. DeJong [4] applied SEA to single composite material panel transmission loss predictions. Recently, SEA has been applied to double wall with bridges [5]. Although SEA is most suitable for complex system noise evaluation such as aircraft, automobile cabin noise, marine machinery noise transmission [6], etc., it has not been applied to the acoustic insulation design of multiple component systems. The purpose of this paper is to demonstrate the applicability of the SEA method to complex system noise evaluation of gas turbine acoustic enclosures.

2 Statistical Energy Analysis

SEA is a procedure to calculate vibrational energy balance in a system. As vibrational energy inside the enclosure builds up, it is transmitted to the least resistant paths. The amount of energy each panel receives from the source depends on the wall thickness, the air gap size for double wall, the damping treatment, etc. The acoustic panels not only receive or radiate energy to the acoustic spaces, but also interact with other structural components such as supporting subbase beams, etc.

Parameters commonly used in acoustic evaluations by closed-form solutions are directly or indirectly related to the SEA equations. For example, radiation efficiency of a plate into a half-space is related to coupling loss factor by

$$\eta_{12} = \frac{\sigma_{\text{rad}} S \rho_0 c_0}{\omega \rho_p h_p}$$

where S = surface area, p = density, c_0 = wave speed air, and h_p = plate thickness.

Figure 1 shows the radiation efficiency of a simple plate calculated by the SEA approach as compared with test data obtained from open literature [7, 8]. The plate (baffled or unbaffled) was modeled by one transverse element with the appropriated surface area and thickness. A single acoustic space was used for the fluid (water or air) media. The results indicated that SEA predictions were within the test data scattering band.

Transmission loss is related to coupling loss factor for a panel inserted between two acoustic spaces by

$$\eta_{12} = \frac{c_0 S}{8\pi f v} \tau$$

or

$$TL = -10 \log \eta_{12} + 10 \log \frac{c_0 S}{4 v_0 \omega}$$

where v = volume. The sound absorption coefficient is considered in SEA by the dissipation loss factor of an air cavity:

$$\eta_{\text{air}} = \frac{c_0 S}{4\pi v} \frac{\alpha}{f}$$

Gas turbine acoustic enclosures are often insulated by dou-

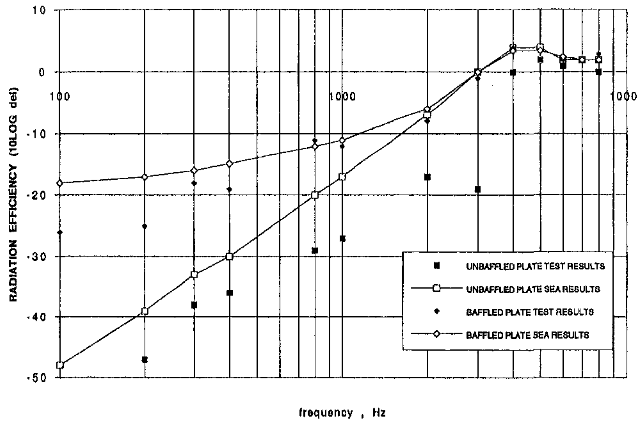

Fig. 1 Radiation efficiency calculated by the SEA

Contributed by the International Gas Turbine Institute and presented at the 39th International Gas Turbine and Aeroengine Congress and Exposition, The Hague, The Netherlands, June 13–16, 1994. Manuscript received by the International Gas Turbine Institute February 9, 1994. Paper No. 94-GT-354. Associate Technical Editor: E. M. Greitzer.

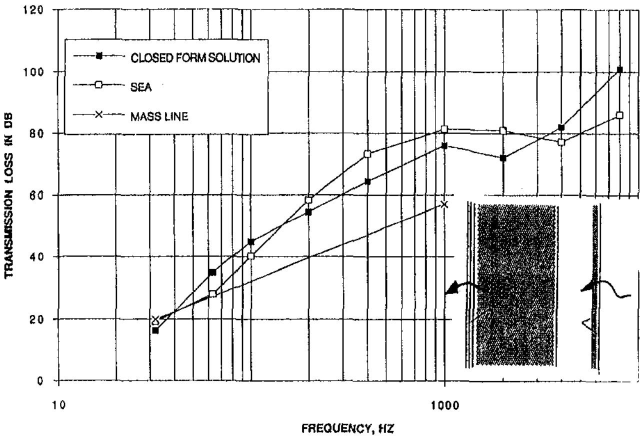

2a. No Flanking Path

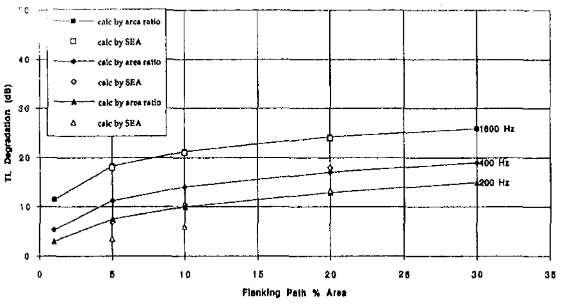

2b. 1/8" Steel Plate Flanking Path

Fig. 2 Comparison of TL calculated by the closed-form solution and by SEA

ble wall panels. Generally, a four "energy block" multijunction subsystem is required to model this wall at high frequencies. Direct coupling between acoustic spaces, which follows mass law, is considered by mass-spring-mass junctions at low frequencies. Figure 2(*a*) shows the transmission loss and noise reduction calculated by a closed-form solution [1] and the SEAM [9] computer code for a double wall inserted in between two rooms. Agreement of results by these two approaches for this simple system is quite satisfactory. The effect of flanking path is important in system noise design. For example, a small area of untreated expansion joint may degrade the enclosure noise performance substantially. Using the configuration in Fig. 2(*a*), the effect of opening is predicted for cases with a second panel made of $\frac{1}{8}$ in. untreated single steel plate. Figure 2(*b*) shows the results of SEA calculated transmission loss degradation, as compared with those calculated by transmission coefficient and area ratio [10]. The results predicted by the SEA agree well with the calculation for most of the frequency ranges.

3 SEA Model of Gas Turbine Enclosure

The SEA model of a marine gas turbine and its enclosure consists of approximately 80 energy blocks and 150 junctions, as shown in Fig. 3. Double wall panels are installed at the inlet and exhaust ends. Single wall with mineral wool insulation is used in the middle turbine casing area. Inlet and exhaust stacks are modeled by pipe energy blocks. Excitation in the form of sound pressure levels is applied at the inlet plenum, outlet plenum, and outside the turbine casing. Sound power radiation to the engine room is considered by including near-field and far-field three-dimensional acoustic energy blocks.

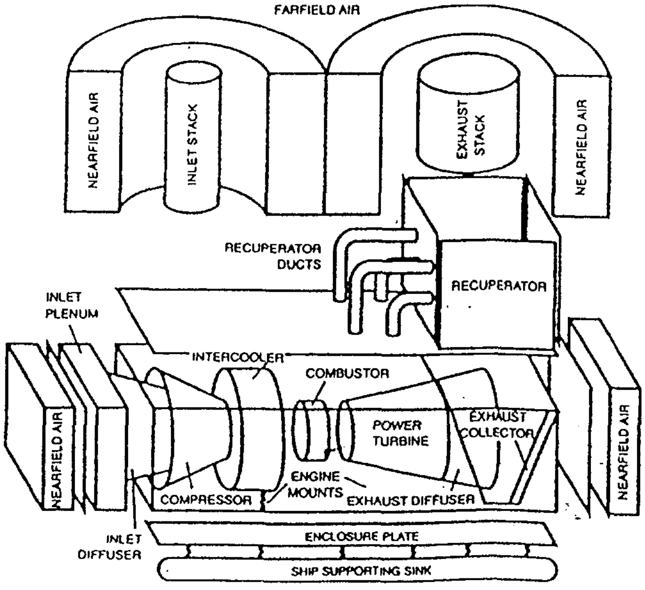

Fig. 3 SEA model of a marine gas turbine with enclosure

Responses at typical critical locations are plotted and compared with those obtained by two-dimensional closed-form solutions, as shown in Fig. 4. Due to the differences in assumptions in modeling approaches, it is expected that acoustic responses predicted from a two-dimensional simple model would be different from that of a three-dimensional system model at some locations. Discrepancies depend on, among other factors, the amount of interaction between components. If energy flow to an acoustic space is solely from a single panel, two-dimensional closed-form solutions will usually produce a decent prediction. However, more often than not, responses at an acoustic space are results of multiple paths of sound transmission, reflection, and absorption of other acoustic spaces and structural components. The impact of three-dimensional characteristics can not be ignored.

To illustrate this point of view, the effects of untreated bottom acoustic enclosure wall on near-field sound pressure levels were calculate by the SEA method. Three cases were compared

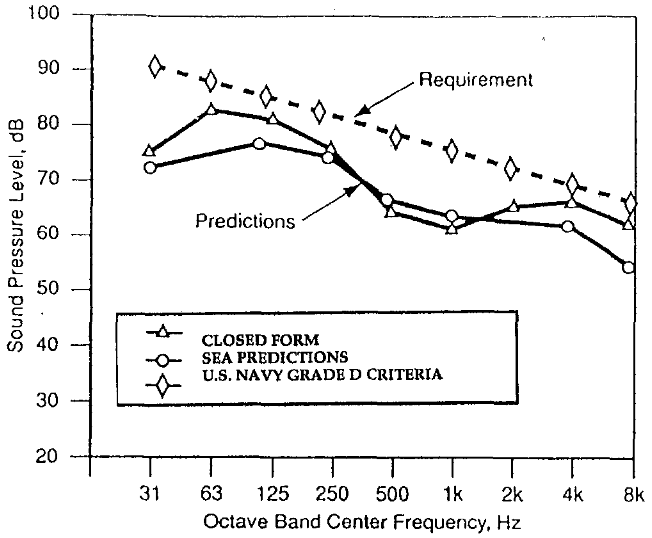

Fig. 4 Comparison of TL calculated by the closed-form solution and SEA

Table 1

	bottom wall	inside insulation	outside insulation	relative SPL at one meter
case 1	1/4" steel plate damped	4" fiberglass	none	0 dB (baseline)
case 2	1/4" steel plate undamped	none	none	5 to 10 db increase
case 3	1/4" steel plate undamped	none	3 " fiberglass	approx. 3 dB increase

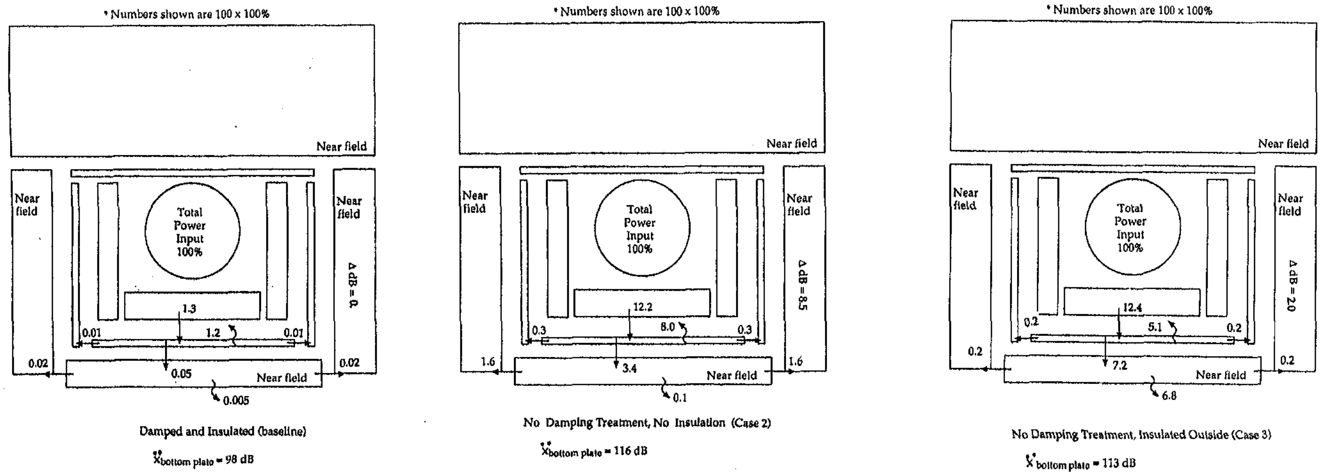

Fig. 5 Comparison of percentage of energy flow at 1600 Hz for treated and untreated bottom enclosure panel

on relative sound pressure level base as shown in Table 1 and Fig. 5.

The most efficient design of the bottom panels is not only to insulate the wall but also to damped out the structural responses (baseline case). However, two alternatives are desirable from practical design considerations. When the bottom wall is totally untreated (case 2), the plate surface becomes a significant noise flanking path. 3.4 percent of the total energy "leaks" through the untreated, undamped plate to the bottom acoustic space and transmitted to the near-field side resulting in a 5 to 10 dB SPL increase. If insulation is provided outside the enclosure wall (case 3), between the bottom plate and the foundation, most of the energy (6.8 out of 7.2 percent) is absorbed by the insulation material. Other parts of structural and acoustic paths could only contribute to the SPL increase of 3 dB. These analytical results are consistent with industrial experiences.

References

1 Sharp, B. H., "Predictions Methods for Sound Transmission of Building Elements," *Noise Control Engineering* Vol. 11, 1978, pp. 53–63.

2 Lyon, R. H., *Statistical Energy Analysis of Dynamics*, The MIT Press, 1975.

3 Crocker, M. J., Battacharya, M. C., and Price, A. J., "Sound and Vibration Transmission Through Branch and Tie Beams Using Statistical Energy Analysis," *Journal of Engineering for Industry*, Vol. 93, Aug. 1971.

4 Quartara, L. R., and DeJong, R. G., "Acoustic Analysis of Composite Materials," presented at the Earthmoving Industry Conference, IL, 1987.

5 Sullivan, R. P., and Gibbs, B. M., "Sound Insulation of Wide Cavity Bridged Heavyweight Construction," presented at the Internoise Conference, 1992, Ontario, Canada.

6 Rockwood, W. B., Lu, L. K. H., Warner, P. C., and DeJong, R. G., "Statistical Energy Analysis Applied to Structure Noise in Marine Structure," presented at the ASME Winter Annual Meeting, Boston, 1987.

7 Maidanik, G., "Response of Ribbed Panels to Reverberate Acoustic Fields," *JASA*, 1962.

8 Blake, W. K., "The Acoustic Radiation from Unbaffled Strips With Application to a Class of Radiation Panels," *Journal of Sound and Vibration*, 1975.

9 *SEAM Users Manual*, Cambridge Collaborative, Cambridge, MA, 1989.

10 Beranek, L., *Noise Reduction*, McGraw-Hill, New York, 1960.

S. B. Shepard
Naval Sea Systems Command,
Washington, DC 20362

T. L. Bowen
Naval Surface Warfare Center,
Annapolis Detachment, Carderock Division,
Annapolis, MD 21802

J. M. Chiprich
Westinghouse Electric Corporation,
Marine Division,
Sunnyvale, CA 94088

Design and Development of the WR-21 Intercooled Recuperated (ICR) Marine Gas Turbine

The U.S. Navy is developing an Intercooled Recuperated (ICR) marine gas turbine, designated the WR-21, for propulsion of future surface ships. The objectives of this development program and the key technical requirements are summarized. The design of the WR-21 is described in considerable detail. Meeting all the design requirements for performance, space, weight, reliability, maintainability, and life has been challenging. Numerous design tradeoffs and iterations have been performed to optimize the design within the constraints imposed in the ICR technical specification. Integration of the WR-21 engine into the DDG51 Flight IIA ship, which is the U.S. Navy's first application, has influenced the WR-21 design. This paper discusses the aspects of the DDG-51 application that were factored into the design of the ICR engine in order to reduce installation costs.

Introduction

The objectives of this development program are to reduce propulsion fuel consumption by 30 percent, increase maintenance flexibility, enable meeting future emissions standards, and enhance ship mobility. The advanced development of the WR-21 began in late December 1991 with the competitive award of the contract to Westinghouse Marine Division in Sunnyvale, CA. This engine is based on the Rolls-Royce RB211 family of commercial airline engines. The parent aero-engine components are modified to incorporate an intercooler and recuperator into the existing simple-cycle engine configuration. System integration, performance, and package design are Westinghouse responsibilities, and gas generator and power turbine development is performed by Rolls-Royce. The intercooler and recuperator are being developed by Allied Signal Aerospace Systems and Equipment in Torrance, CA. Since the majority of the ship operating time is spent at low power and low speed, variable area nozzles are incorporated into the power turbine to maintain high thermal efficiency at off-design conditions. The development of a digital control system for the WR-21 is subcontracted to CAE in Montreal, Canada.

Requirements

The ICR technical specification [1] defines all the performance, design, operation, physical and installation, environmental, ship interface, and qualification requirements in detail. A previous paper on the WR-21 engine [2] summarized the major ICR requirements; hence the discussion here will be intentionally brief. During the detailed design of the ICR, conflicts between two or more requirements frequently arose. In order to resolve such conflicts and to guide the contractor team in optimizing the ICR design, the U.S. Navy specified the following relative ranking of ICR design attributes in order of descending importance:

(*a*) ICR unit production cost:
  - $6.5 million (FY91) 100th unit based on production rate of 20 per year

(*b*) Fuel usage:
  - maximum allowable specific fuel consumption is specified at eight operating points from 2.5 to 110 percent rated power as shown in Table 1.

(*c*) Logistic support cost:
  - minimize modifications to maintain commonality with the aircraft core engine, and maximize use of standard parts, materials, and processes already in the Government inventory;

(*d*) Reliability and maintainability:
  - minimum mean time between failure (MTBF) of 1000 h for the ICR system, 20,000 h for the recuperator, 14,000 h for the intercooler, 4500 h for the control system including sensors, and 2200 h for all internal and external shipboard repairs;
  - minimum mean time between removal (MTBR) of 10,000 h each for the gas generator and power turbine;
  - maximum mean time to restore system (MTRS) of 24 h for all ICR O-level and I-level maintenance actions combined;
  - maximum time to remove and replace a gas generator, 48 h; power turbine, 72 h; intercooler, 24 h; and recuperator, 120 h;
  - maximum mean time to repair (MTTR) controls, 2 h, and lube oil module and other components, 9.75 h;
  - maximum O-level preventive maintenance of 4.5 man-hours per week and preventive plus corrective maintenance of 6.75 man-hours per week.

(*e*) Survivability:
  - MIL-S-901 shock, external free field blast overpressure, nuclear-biological-chemical contamination, and MIL-STD-461 and -462 electromagnetic compatibility requirements as tailored in the ICR technical specification.

(*f*) Dimensions:
  - Limited to 8 m (315 in.) length, 2.64 m (104 in.) width, and 4.83 m (190 in.) height

(*g*) Power rating:
  - 21.6 MW (29,000 hp) based on U.S. Navy standard rating conditions of MIL-E-17341.

(*h*) Weight:
  - limited to 54,431 kg (120,000 lb) total dry weight.

Contributed by the International Gas Turbine Institute and presented at the 39th International Gas Turbine and Aeroengine Congress and Exposition, The Hague, The Netherlands, June 13–16, 1994. Manuscript received by the International Gas Turbine Institute, February 9, 1994. Paper No. 94-GT-79. Associate Technical Editor: E. M. Greitzer.

(*i*) Noise:
- MIL-STD-740 airborne and structureborne requirements as tailored in the ICR technical specification.

(*j*) Exhaust temperature:
- limited to 387.8°C (730°F) when operating from idle to 110 percent power in the normal (non-bypass) operating mode.

As evidenced by the list above, affordability in terms of acquisition and operating and support costs has become the highest priority of the ICR program. This reflects the post–Cold War reality of shrinking defence budgets and the need to do more with less. When the ICR development program began more than a decade ago, the priority was on increased performance and military capability, and increased cost was acceptable due to the higher threat level.

Design and Development

ICR design, development, and model and component rig testing have been on going since contract award on December 26, 1991. The vast majority of the design work was completed by the December 1993 time frame. Meeting all design requirements for performance, space, weight, reliability, maintainability, and life has been challenging and has required design tradeoffs within technical specification constraints. The biggest challenges were meeting fuel consumption, power, and envelope requirements while providing adequate access within the enclosure for maintenance and change out of engine modules. The ICR design is discussed in the following paragraphs and consists of enclosure, intermediate-pressure compressor (IPC), high-pressure compressor (HPC), combustor and combustor manifold, high-pressure turbine (HPT), intermediate pressure turbine (IPT), power turbine (PT), intercooler system, recuperator, and lube oil module (LOM), as shown in Figs. 1 and 2. The electronic control unit (ECU) and control system is described by Carlson [3].

Enclosure

The enclosure, Fig. 3, houses the engine, recuperator core, recuperator ducting and valves, fire protection system, fresh water and glycol-cooled intercooler, intake bellmouth, exhaust collector, turbine to gear high-speed coupling shaft (HSCS), accessory gearbox (with fuel and lube oil pumps, air breather, and starter), enclosure heating and lighting system, enclosure cooling system, fuel system and other components such as IPC and HPC bleed air piping, igniter boxes, junction boxes and cabling. The enclosure and subbase are required to fit within the footprint (i.e., length and width) of the LM2500 that is installed on U.S. Navy surface combatants.

Table 1

MAXIMUM ALLOWABLE SPECIFIC FUEL CONSUMPTION

PERCENT POWER	MAXIMUM ALLOWABLE SFC g/kW-hr (lb/hp-hr)	POWER TURBINE OUTPUT SPEED rad/s (rpm)
2.5	520.9 (0.856)	110 (1053)
5.0	404.4 (0.664)	139 (1326)
10.0	322.5 (0.530)	175 (1671)
20.0	258.6 (0.425)	220 (2105)
30.0	230.0 (0.378)	252 (2410)
50.0	208.1 (0.342)	299 (2857)
75.0	206.3 (0.339)	343 (3271)
100.0	219.1 (0.360)	377 (3600)

CONDITIONS FOR MAX ALLOWABLE SFC
Power turbine speed based on cubic propeller load,
100% power equals 19.7 MW (26,400 bhp)
37.78 C (100 F), 101.33 kPa absolute (14.696 psia) ambient air
101.6 mm (4 inches water) intake loss
152.4 mm (6 inches water) exhaust loss
29.44 C (85 F) seawater temperature
40% relative humidity
42.566 MJ/kg (18,300 btu/lb) fuel lower heating value

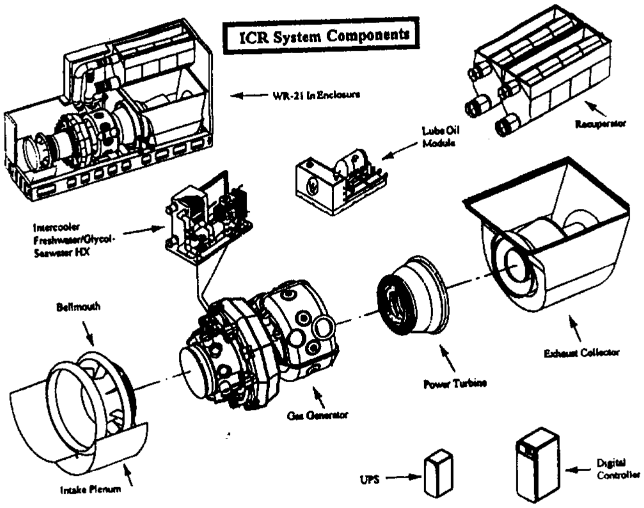

Fig. 1

The enclosure panels consist of encapsulated insulation material, lead sheet acoustic septum, steel face with damping treatment, 304L perforated steel, steel structure and viton acoustic seals to meet thermal attenuation, fire resistance, blast over pressure, shock, air tightness, and noise requirements. All panels are bolted on and removable except for panels that are welded on the sides and rear of the recuperator housing to provide strength. Removable panels of the same size are interchangeable. Vertical frame members in the forward half of the enclosure are removable. Two panels on each side have integral doors. Enclosure access for maintenance is gained through the doors or by removing panels. Composite panels are not used since they have less low-frequency acoustic attenuation, require qualification for toxicity in fires, show no production cost benefit, and have low weight savings. For improved maintenance access, the enclosure floor is 12 cm (5 in.) lower than the subbase box beams, a small access panel is provided in the floor for access to the accessory gearbox, and the insides of each of the two subbase box beams are scalloped to allow removal of the accessory gearbox out the enclosure side.

An aft shear wall provides enclosure torsional stiffness. The ICR has a weight limitation of 54,431 kg (120,000 lb). Approximately 50,348 kg (111,000 lb) is supported by the enclosure and subbase foundation, which excludes the weights of the off-engine intercooler heat exchanger module, lube oil module, and electronic control unit. Twenty-six standard Navy 5B 5000 pound mounts, equally loaded, support the enclosure and subbase. An additional two of these mounts are installed, preloaded, on the subbase to reduce vertical mount shear loads due to the

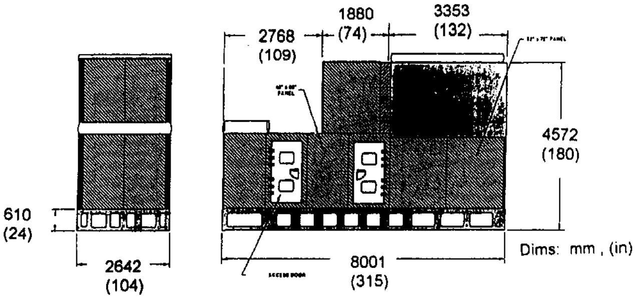

Fig. 2

rake angle of the ICR installed in the ship. Auxiliary shock snubbers are not used. To reduce the frequency of taking H and J readings for the high-speed coupling shaft (HSCS) a pin and ring alignment fixture is installed at each corner to monitor changes in enclosure position relative to the foundation.

The enclosure connects to the cooling air duct via a connection at the top of the recuperator duct house. The cooling air fan is provided by the ship. The current DDG51 fan has adequate flow capacity but requires changes to the blade angles to increase exit pressure (cooling air pressure drop through the enclosure and around the recuperator is higher than the pressure drop for the LM2500 module). A flow guide is installed just aft of the combustor manifold to provide adequate cooling flow to the power turbine casing and cold ring. An exhaust gas deflector is installed to shield the exhaust boot from hot exhaust gasses. The cooling air and exhaust boots accommodate lateral shock movements of approximately 15.2 cm (6 in.) to 16.5 cm (6.5 in.). System testing will be conducted to verify enclosure surface temperatures, and to determine the adequacy of localized temperatures inside the enclosure and the need for additional heat shields. Areas that need cooling are instrumentation, wiring, sensors, power turbine VAN actuator, exhaust boot, HSCS, turbine casings, gearbox, and walls of enclosure and recuperator. Pneumatically actuated cooling air inlet vent dampers supplied with the ICR are designed to close upon loss of ship's low pressure air. These dampers are installed in the cooling air duct to the enclosure to make more space available within the recuperator duct house for maintenance and routing of high-pressure compressor bleed air piping.

The 35.6 cm (14 in.) IPC and 15.2 cm (6 in.) HPC aluminum bleed air pipes are routed to the exhaust uptakes through boots in the enclosure top. The 10.2 cm (4 in.) CRES customer bleed pipe is routed through the floor.

The radial air intake is a composite structure. The intake plenum is shaped to maintain uniform circumferential velocity and to increase the velocity from the intake through the plenum into the radial intake flare. The exhaust collector outer surfaces are insulated to reduce heat rejected to the enclosure. The HSCS tunnel is insulated on the inside to keep the HSCS temperatures below 171°C (340°F). Access to the collector is provided by removing a side panel. The collector provides access to the HSCS via panels in the collector side and the HSCS tunnel. The engine is vertically supported at four locations using linkages and clevis mounts bolted to the subbase beams. The aft supports also provide fore and aft restraint. Lateral shock restraint is provided by a key beneath the power turbine and by a lateral stop system attached to the front supports. Liners on the clevis mounts are used for alignment.

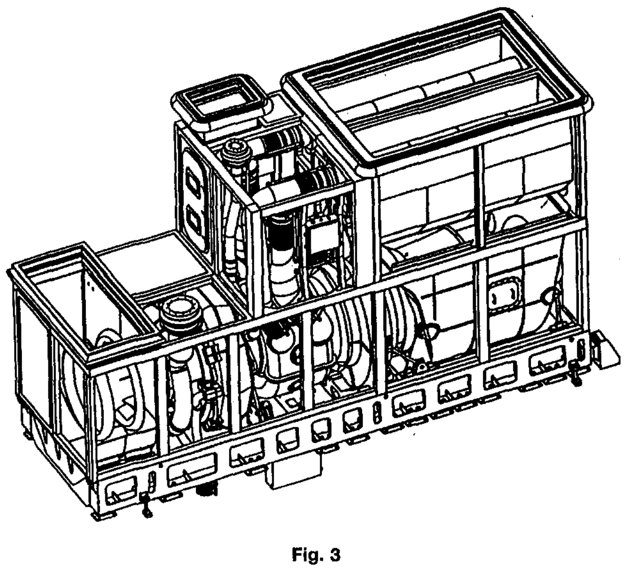
Fig. 3

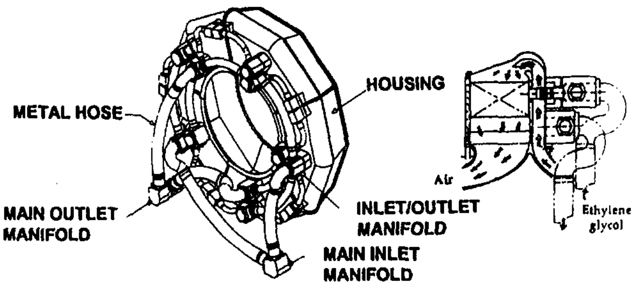

Fig. 4 On-engine intercooler configuration

Engine modules are removed horizontally through the ship air intake ducts. The two recuperator core modules are each removed through the intake ducts after removing the recuperator ducting and duct house panels. Horizontal rails, turning rails, and soft patches in the front and rear sides of the intake duct are required for removal.

A CO_2 fire extinguishing system is used. Eight optical flame detectors that respond to flame flicker and CO_2 emissions from hydrocarbon fires are provided. The fire detection scheme is a single zone nonvoting system. Continuous coaxial thermistor cables are provided for heat detection in the power turbine and combustor manifold areas. One manual CO_2 inhibit switch is located on each side of the enclosure.

Recuperator

The recuperator system consists of two cores, two lines of air ducting from the combustor manifold to the recuperator and back, ducting valves and pneumatic valve actuators. Each core module has four core sections fabricated from 14Cr4MO stainless steel. Compared to Incoloy 800, 14Cr4MO is less expensive, has better coefficient of thermal expansion characteristics and is about equal in overall corrosion resistance. INCO 625, a much more expensive material, has superior corrosion resistance and has good mechanical properties, and is considered an alternate core material if needed. Burner rig tests of core material are being conducted by the Navy. The two 30.5 cm (12 in.) supply valves and two 30.5 cm (12 in.) bypass valves in the recuperator ducting operate in unison and off the same pneumatically operated actuator. A hydraulic pump is provided for emergency manual operation. Two 40.6 cm (16 in.) return air check valves are provided to isolate the recuperator completely to prevent flow and temperature distortions to the combustor cans and turbine during a recuperator battle damage failure. Short-term cleaning will be accomplished through recuperator bypass operation to heat the core up to 482°C (900°F) minimum. Steam lance from the top of the recuperator will be used for long-term cleaning. For operating at low ambient temperatures and low power, provisions are made in the control system to partially or fully bypass the intercooler to prevent H_2SO_4 condensation and associated corrosion in the recuperator by automatically maintaining HPC discharge temperatures above 149°C (300°F).

Intercooler

The intercooler system comprises the on-engine intercooler subassembly and the sea water heat exchanger module. The on-engine intercooler assembly, Figs. 4 and 5, cools the IPC discharge air prior to entering the HPC and consists of 90–100 CuNi core, core housings, metal hoses, inlet and outlet manifolds, and valves. The air flow from the IPC is radially outward and is turned 180 deg inward by the intercooler housing in combination with two turning vanes to give acceptable uni-

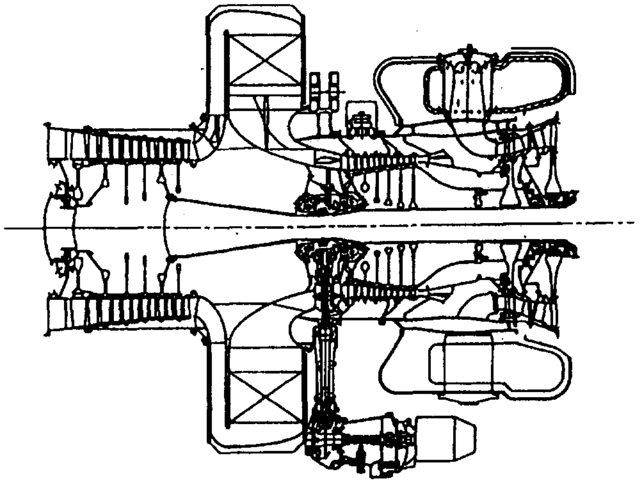

Fig. 5 Gas generator layout

form flow into the core. The sea water heat exchanger module cools the fresh water coolant (50/50 mixture of water and glycol) and is comprised of a titanium plate frame heat exchanger, Navy standard titanium fresh water pump and motor, fresh water bypass valves, air purge, holding tank, and a skid. An additional 88.3 L/s (1400 gpm) sea water pump and associated sea water system components are provided by the ship for each ICR.

During normal operation the fresh water bypass valves are modulated by the control system based on relative humidity and IPC discharge pressure to prevent cooled IPC discharge air from condensing. The on-engine system is provided with isolation valves and a relief valve set at 758 kPa gage (110 psig) to prevent boiling of the fresh water/glycol mixture during intercooler inoperative conditions. The ICR is capable of producing 9843 kW (13,200 hp) when the intercooler is inoperative without exceeding established engine operating limits. The fresh water coolant flow rate is 56.8 L/s (900 gpm). If a two-speed sea water pump is used, the sea water flow is 88.3 L/s (1400 gpm) at full power down to approximately 10,400 kW (14,000 hp); below 10,440 kW (14,000 hp) the flow is 59.9 L/s (950 gpm). Intercooler water nozzles are located between the IPC discharge and the intercooler core. There are five intercooler core and housing segments that can each be removed through the escape trunk or intake.

Lube Oil Module

For the DDG51 application, the lube oil module (LOM) is a self-contained unit with oil reservoir, 5 μm duplex filters, deaerator, and shell and tube oil cooler sized to remove 8440 kilojoules (8000 btu) per minute with an engine oil inlet temperature of 73.8°C (165°F). The oil is cooled by the ship's main reduction gear lube oil. However, the first LOM that will be tested with the ICR during advanced development will have a plate frame heat exchanger and will be water cooled due to the nonavailability of a lube oil coolant source. Plate frame heat exchangers take less space than shell and tube, but require fire safety modifications and qualification testing to make the unit acceptable for use with flammable fluids. During ICR development consideration will also be given to fuel-cooled plate frame heat exchangers for use in the absence of a lube oil coolant source.

Intermediate and High-Pressure Compressors

The six-stage fixed geometry IPC is a derivative of the RB211-535 and has a pressure ratio of 2.90. Parts that are common to the 535 are stages two through six rotor blades and stator vanes, stages two through six (except stage five) disks, roller bearings, and bleed valves. The stage one airfoils have been modified to increase flow capacity approximately 4 percent over the 535. Rotor blades and rotor drum are titanium. Vanes are 12 percent chrome steel except for the stage four vanes, which are aluminum alloy. The IPC split case is steel protected by Sermetel W and has borescope ports at ten and two o'clock for each stage. The sixth stage handling bleed air valves provide multiple steps of bleed for surge protection. Bleed air valve hysteresis is incorporated to reduce valve cycling for small power changes. Freeman Moritz slots are also provided in the casing to resist stall.

The ten strut stainless steel intermediate casing provides a bridge between the IPC and HPC to transmit structural loads and to accept mounting of the intercooler segments. It allows for a 25.4 cm (10 in.) extension of the IPT stub shaft, houses the internal gearbox and right angle gearbox for accessory takeoff, and provides the air flow path from the IPC exit radially to the intercooler housing and from the intercooler core axially to the HPC.

The six-stage fixed geometry HPC is a derivative of the 535 with essentially the same aerodynamic flow path and a pressure ratio of 4.90. The rotor blades, disks, stator, and rear shaft assembly are common to the 535. Disks and rotor blades for stages one through four are titanium. Stage five and six rotor blades are nickel base alloy. Stator vanes are chromium steel, except for stages five and six, which are nickel base. HPC third stage has three handling bleed air valves. Customer bleed air is taken from the HPC discharge. Borescope ports are provided at two and ten o'clock positions for each stage.

The accessory gearbox is mounted from the HPC casing and the intercooler cover. The lube oil and fuel pumps, starter, and breather are mounted on the gearbox, which houses bevel gears for transmitting torque from the HPC shaft via a radial drive shaft to the accessory gearbox drive train. The starter is near common to the Rolls-Royce Trent 800, but alternate starter system designs that require less air flow are being investigated. The lube oil pump provides servo pressure for actuating the off engine electronically controlled fuel metering valve and the power turbine VANs.

Combustor and Combustor Manifold

The ICR has nine combustor cans with swept discharge nozzles radially mounted in a combustor manifold, Figs. 2 and 5. The combustor design is based on the SM1C marine axial can annular and RB211 industrial radial can annular designs. The radially mounted combustor can arrangement has two advantages. First, it allows the combustor system to be arranged within the same length as the RB211 annular combustor, which is a significant contribution to enabling the ICR to be fitted within the LM2500 footprint lengthwise. It also has the added advantage of keeping the same RB211 HPT and IPT bearing spacing, which helps preserve the RB211 rotor dynamics characteristics. Secondly, it is compatible with the industrial RB211 dry low emissions (DLE) combustor development, which forms a common technology base for future ICR DLE combustor development to meet future NO_x and other exhaust emission requirements.

Space is reserved for the ICR DLE combustor once developed. The DLE is a premixed, lean burn design using series fuel staging. The design will be based on the industrial RB211 DLE combustor being developed for natural gas applications [4, 5]. For the Navy application additional development will be needed.

The design of the manifold system and inner casing has to accommodate thermal and pressure stresses, thermal growth, rigidity, sealing, fretting, low cycle fatigue, flow distribution, loads from the recuperator ducting, producability, and maintainability of combustor and surrounding components such as the HPT. The combustor manifolds are a delivery air manifold (DAM) and a return air manifold (RAM). The DAM takes HPC discharge air and supplies it via ducting to the recuperator. The RAM evenly distributes the return air to the combustors. The inner casing is the backbone of the engine that has to take high bending and shear loads due to shock. Seals are necessary to prevent leakage from the DAM to the RAM. The combustor is effusion cooled and is coated on the inside with a thermal barrier coating on a corrosion resistent bond coat. Each can has two ignitors, which are not cross connected with flame tubes. There are two ignition exciter units, each one controlling and having a separate high tension lead to one igniter in each combustor can. Combustor cans are removable within the enclosure.

There is an aggressive combustor development and test program ongoing to address cooling and metal temperatures, flow uniformity to all cans, ignition, igniter position, stability, fuel injection, temperature profile to HPT vanes and blades, smoke and emissions measurements.

High-Pressure and Intermediate-Pressure Turbines

The single-stage HPT is a derivative of the RB211-524 with modified vane and blade angles and increased turbine capacity. The vane and blade airfoils are film cooled and have a cooled interlock shroud. The HPT airfoils are INCO 738 coated with a silicon aluminide coating. The single stage IPT is a derivative of the RB211-535 with a new blade profile and increased turbine capacity. The IPT cooled vane is INCO 738 with a silicon aluminide coating. The IPT blade alloy is single crystal CMSX-4 to provide increased creep life that matches that of the other turbine airfoils. It is coated with a silicon aluminide or platinum aluminide pending further testing. The IPT blade has an interlocking integral shroud. The use of silicon aluminide coatings is a departure from U.S. Navy experience but consistent with Rolls-Royce practice; however, coatings planned for the ICR along with a CoCrAIY coating will be burner rig tested on IN 738 and CMSX-4 substrate alloys. Peak blade metal temperatures are being maintained below 950°C (1742°F) for oxidation resistance.

Power Turbine

The PT is a new five-stage design based on the Rolls-Royce Trent 700 and 800 designs. The first stage has variable area nozzles (VANs) and stages 2 through 5 are closely modeled after the Trent. The VANs are hydraulically actuated with lube oil via a ring gear arrangement to insure constant throat areas of all VANs. Each VAN is individually removable. One (as opposed to two) stage of VANs was chosen for several reasons. The PT counterrotation relative to the IPT results in a low deflection high-efficiency first stage VAN; a second-stage VAN would produce high flow deflection angle resulting in high loss for a small return in inlet capacity at maximum power; high end wall leakages would occur due to annulus slope in way of the stage two VANs; and last, two stages of VANs would result in two highly compromised low reaction stages instead of one. The VAN is fully closed (minimum area ratio) at 40 percent power and below and fully open at 100 percent power and above. The first stage operates as an impulse turbine at 40 percent power and as a 100 percent reaction turbine at full power. The PT design point was selected at 67 percent full power to optimize low power fuel efficiency and full power requirements. Optimizing at a lower power would result in lower stage two through five efficiencies and less power capability for the full power condition.

Turbine disk rim cooling is accomplished by incorporating a modulating system that is integral with the VANs. Turbine blades are welded in pairs and do not have interlocking shrouds due to low blade torsional stiffness and face loadings. Vanes for stages two through five are cast in segments of six.

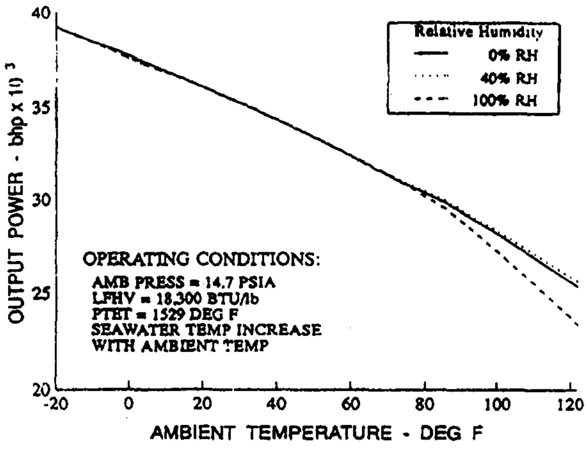

Fig. 6

PT airfoils are IN 738 with a silicon aluminide coating. Peak blade metal temperatures are maintained below oxidation temperatures. Disks are INCO 718 slabs for reduced cost. Carbon versus labyrinth seals are used in the power turbine bearing area due to low sealing pressures at low powers, and the performance penalty from parasitic air flow required with conventional labyrinth seals is avoided.

Performance

Requirements for specific fuel consumption (sfc) and power have been met. The design was optimized for low power sfc since the sfc margin was the smallest in the 20 to 30 percent power range and since more than adequate life margins exists at 110 percent power, 21,625 kW (29,040 hp). ICR design life is based on meeting either the 3000 hour endurance test or a 40 year ship life (85,000 engine hours and 15,000 start cycles after allowing for ship restricted availabilities), whichever is most severe. Generally, these two criteria have not conflicted. Figure 6 shows the variation in output power as a function of ambient temperature, relative humidity, and ambient seawater temperature, which affects intercooler system performance.

Maintenance Flexibility

The IPC, HPC, HPT, IPT, and PT are prebalanced as individual modules, which allows replacement of these modules without the need to rebalance the engine onboard the ship. Full advantage of this capability may not be realized on the DDG-51 due to engine room space constraints; however, for new ship designs this advantage can be fully exploited.

Ship Integration Influences

The WR-21 is designed as a marine gas turbine, taking into consideration the operating environment, physical space constraints, and duty cycles unique to marine applications. The engine can operate in ambient temperatures ranging from −40°C (−40°F) to 52°C (125°F). The intercooler system incorporates a bypass system to maintain intercooler exit temperatures above dew point regardless of seawater temperature. The materials and coatings, outlined earlier, were chosen for their proven effectiveness in marine environments, drawing from millions of hours of marine gas turbine experience in Naval and industrial applications.

The design of the gas turbine enclosure was strongly influenced by ship integration considerations. Temperature limits were imposed on the exterior walls of the enclosure, 52°C (125°F) max for the engine portion and 56°C (133°F) max at the recuperator.

To maintain the temperature limit at the recuperator, the walls of the enclosure are cooled. The heat load imposed on the engine room in a DDG-51 is not changed as a result. The gas turbine base plate and enclosure also support both the gas turbine and the recuperator. This arrangement minimizes thermal and shock load movements between the two components and does not require any reinforcing of decks or structures beyond the gas turbine foundations.

The intercooler system utilizes seawater to cool the freshwater/glycol mixture, which in turn cools the IPC discharge air. On the DDG-51, the existing seawater system requires the addition of two standard Navy pumps for a two-ICR, two simple-cycle engined ship, and four standard navy pumps for an all-ICR engined ship.

The IPC, HPC, HPT, IPT, and PT are prebalanced as individual modules, which allows replacement of each without the need to rebalance the engine on board ship.

The intercooler system saltwater heat exchanger module has been configured to fit in existing DDG-51 engine room space and minimize engine room rearrangement.

Summary

This paper has described the objectives of the ICR development program and the resulting design. The ICR engine, designated the WR-21, is a purpose designed gas turbine that provides high efficiencies over a very broad power range and is a compact, self-contained package. The fuel savings and package design make the WR-21 intercooled recuperated gas turbine both technically possible and economically attractive for integration into the DDG-51 and other ship applications.

References

1 Naval Sea Systems Command, "Technical Specification for the Intercooled Recuperated Gas Turbine Engine System (ICR)," N00024-91-PR-52146, 17 May 1991, with subsequent revisions.

2 Crisalli, A. J., and Parker, M. L., "Overview of the WR-21 Intercooled Recuperated Gas Turbine Engine System—A Modern Engine for a Modern Fleet," ASME Paper No. 93-GT-231, 1993.

3 Carlson, R. J., West, P. M., and Azouz, D. E., "Digital Control System Development for an Intercooled Recuperated Gas Turbine," ASME Journal of Engineering for Gas Turbines and Power, Vol. 117, 1995, pp. 172–175.

4 Willis, J. D., Toon, I. J., Schweiger, T., and Owen, D. A., "Industrial RB211 Dry Low Emission Combustion," ASME Paper No. 93-GT-391, 1993.

5 Corbett, N. C., and Lines, N. P., "Control Requirements for the RB 211 Low-Emission Combustion System," ASME Journal of Engineering for Gas Turbines and Power, Vol. 116, 1994, pp. 527–533.

J. M. Vaught
Vaught Engineering Inc.,
Mesa, AZ 85208

Updating the ANSI Standard on Measurement of Exhaust Emissions

The American National Standards Institute (ANSI) required that the source testing Standard on Measurement of Exhaust Emissions from Stationary Gas Turbine Engines, B133.9, be brought up to date with today's regulatory requirements and best measurement technology. The criteria for the design of the Standard along with its content and format are discussed. The selection of measurement methods for gaseous components, smoke, and particulates emitted by present-day emission-controlled industrial gas turbine engines is presented.

Introduction

A competitive program was initiated by an ASME Research Task Force on Gas Turbine Emissions Standards to provide for the development of a new ANSI Standard for measuring, analyzing, and reporting exhaust emissions from stationary gas turbine engines. Applications were sought from individuals and organizations wishing to participate in a research project to clarify and document the best measurement procedures and standards that were either in use or being reduced to practice. Competitive bids were obtained and a contract issued for the project.

This new source testing Standard, ''Measurement of Exhaust Emissions from Stationary Gas Turbine Engines,'' was needed because:

- Procedures and techniques had continued to evolve since the publication of the last Standard [1].
- Measurement and reporting requirements were unclear, were obsolete, and varied from agency to agency.
- Method 20(2), the USEPA measurement procedure for gas turbines, was limited as it covered only oxides of nitrogen (NO_X) and sulfur (SO_X).

These obsolete and limited methods left many measurement and reporting problems unsolved or incorrectly solved. Significant funding and technical resources were being spent unnecessarily in conducting source testing for stationary gas turbines.

> Note: The term ''Standard'' is used by ANSI to connote a practice or measurement method, *not the regulation of emission levels* as used by regulatory authorities in the United States.

Design of the Standard

A program to develop the Standard was begun in February 1992. This work included research on measurement methods and emissions regulations as well as standards development. A coordinated final draft of the Standard was submitted to ANSI for approval on June 1, 1993.

Steering Committee. Representatives from ASME Research, the gas turbine industry, EPRI, and USEPA and the contractor formed a committee to provide technical direction and review progress during the development of the Standard. Meetings were held to monitor progress of the program and to review and comment on the criteria, the content of the Standard, technical findings of the research, and on the draft Standard. The membership of the Committee is listed at the end of this paper.

Program Objectives. The Standard is written to provide guidelines for the emissions measurement of stationary gas turbine engines. It is designed to simplify, standardize, and reduce the cost of the measurement process wherever possible. The expected users are engineers and measurement technicians who require information on the measurement of emissions from gas turbines. The Standard also is written to inform project managers, contract and procurement staff, and engineers not directly involved with emissions of the measurement control and compliance of gas turbines.

Specific criteria for the Standard were established by the Steering Committee early in the program. These criteria were:

1 To standardize measurement techniques, analysis procedures, and reporting criteria.
2 To follow ANSI format and the ASME *Guide to Writing Codes and Standards.*
3 To be applicable to all industrial gas turbine engines operating on natural gas and distillate fuel oil.
4 To be applicable to engines with emission controls such as water injection and selected catalytic reduction (SCR).
5 To provide reference to other turbine regulations and measurement procedures.
6 To have general approval of industry and the USEPA.
7 To set no regulatory limits or control regulations.
8 To incorporate the International Standards Organization (ISO) gas turbine emissions measurement specification to the extent feasible.

Since there are many different sizes and applications of stationary gas turbines throughout the world, it was an objective of the program that these differences be considered in the development of the new Standard. Emissions measurement of turbines using heat recovery after firing and steam and water injection for NO_X controls was included. The very low concentration of pollutants typical of turbines using dry low NO_X combustion and SCR after treatment also was considered.

Current measurement methods were researched to find the best methods, reduced to commercial practice, to include in the Standard. Where applicable, the measurement methods are referenced to EPA protocols. Since the development of measurement instrumentation is ongoing, future improvements will require periodic updating of the Standard.

It also was necessary to incorporate methods to measure each of the exhaust components controlled by the various regulatory

---

Contributed by the International Gas Turbine Institute and presented at the 39th International Gas Turbine and Aeroengine Congress and Exposition, The Hague, The Netherlands, June 13–16, 1994. Manuscript received by the International Gas Turbine Institute March 12, 1994. Paper No. 94-GT-427. Associate Technical Editor: E. M. Greitzer.

agencies and emission regulations. Laws and rules were researched, and the results became one of the bases for the Standard.

Concurrently, the specification "Gas Turbines—Exhaust Gas Measurement" was being developed by ISO [3, 4]. While this specification did not provide for use of USEPA protocols and was not acceptable for use in the United States, considerable effort by an international working group had been expended in its development. It was an objective of the program that the new Standard incorporate as much of the ISO document as was practical.

Other measurement specifications such as those used for aircraft gas turbines [5] and for reciprocating engines [6] were reviewed for methods and content. These specifications were found to be only indirectly applicable to the testing of stationary gas turbines in the United States.

Content

The Standard contains information that will guide the user in the technologies of emissions compliance and control as well as measurement. During their review of requirements, the Steering Committee found that many agency staffs had little experience with most of the gas turbines used in the United States that are operated on clean fuels, natural gas, and distillate oil. Also, they found that agency personnel were unfamiliar with the practical aspects of engine operation, the formation, identity, and concentration of the various components in the exhaust of turbines, the measurement of these components, and methods of emission control. As a result, the Standard was designed to provide information and references on these subjects as well as to establish the best measurement practices. The subjects covered in the Standard are as follows:

Definitions. Terms most likely to be encountered in emissions measurement, compliance, and control.

Exhaust Components. Description of each of the chemical components in the gas turbine exhaust.

Responsibilities. Gas turbine manufacturer and user environmental responsibilities.

Operating and Test Conditions. Specification of system operating and test conditions.

Measurements. Recommended methods of measurement of gaseous components, smoke, particulates, and fuel. Definition of the measurement system, sampling, instrumentation, and quality provisions.

Calculations and Conversions. Specification of methods of calculating emissions.

General References. Information on reference conditions, physical properties, air laws, regulations, air toxics, and emission control methods.

Measurement of Gaseous Components

The Standard specifies the gaseous components in the exhaust and the methods to be used to measure them. These components are listed in Table 1. This listing was determined by the Steering Committee based on the regulatory requirements of the EPA, the state agencies, and the collective experience of the members. It is recognized that measurement technology is advancing rapidly, and this listing deserves regular updating.

Measurement System. The three basic elements of the measurement system are: (1) the sampling probe, (2) transfer and conditioning, and (3) analytical instruments and data acquisition. These elements are described in detail in the Standard and refer to EPA protocols. A schematic of the measurement system is shown in Fig. 1.

With the exception of sulfur dioxide, sulfuric acid mist, and water vapor, the gaseous measurements are to be made by continuous flow sampling instruments. These instruments are combined into a measurement system.

Table 1 Gaseous exhaust components

Component	Recommended Method
Oxides of nitrogen (NO_x)	Chemiluminescence
Carbon monoxide (CO)	Nondispersive infrared
Carbon dioxide (CO_2)	Nondispersive infrared
Sulfur dioxide (SO_2)	Fuel analysis
Sulfuric acid mist (H_2SO_4)	Impinger train
Total hydrocarbons	Flame ionization detector
NMHC and VOC	Gas chromatograph
Ammonia (NH_3)	Chemiluminescence difference
Oxygen (O_2)	Electrochemical or paramagnetic
Water vapor (H_2O)	Impinger train

Sampling. The approach taken for sampling gaseous components is designed to save test time and effort. It differs from the multipoint traverse usually required by the USEPA in Method 2 [7], which requires at least eight and normally many more sampling locations in two planes.

The Standard recommends that the sample be proven to be representative using a carbon balance. Once that is done, sampling may be achieved using a three-holed sampling probe tube or a single probe located at 16.7, 50, and 83.3 percent of a measurement line taken through the centroid of the duct area. Ducts larger than 2.4 m can be sampled at 0.4, 1.2, and 2.0 m from the wall to reduce probe overhang. The use of three sampling points is based on the EPA Continuous Emission Monitoring Specification 2 [8] and is illustrated in Fig. 2.

The number of sampling points is reduced because, in the majority of industrial turbine installations, the exhaust gas stream is well mixed and the concentration of the individual components is, from a practical standpoint, uniform across the entire exhaust duct. This uniformity is due to the length of exhaust ducting, the changes in direction and cross section required for the installation of boilers and silencers, and the requirement for stack heights. As a result, the number of sample points required for sampling gas turbine gaseous components is far less than that required for most industrial plants. The EPA CEM Specification provides substantiation that a representative gas sample can be obtained with three sampling points.

Sample Transfer and Conditioning. Long lines are often unavoidable in the measurement of large turbine systems; however, the sample transfer time should be kept as short as possible. It is important to avoid condensation of the various constituents, particularly water vapor, hydrocarbons, and sulfates. It is recommended that the entire sample line be heated above the condensation temperature of each constituent, considering its concentration. The sample is to be conditioned in a manner compatible with the various analyzers.

Instrumentation. Descriptions, general requirements, and performance specifications are given for each of the instruments and measurement methods recommended. These are listed in Table 1. For additional detailed information, specific USEPA methods and ISO standards are given as references.

These measurement methods, listed in Table 1, will not be covered in this summary paper. Some of the findings and recommendations on measurement methods that were formulated during the development of the Standard are discussed below.

Hydrocarbons and VOC. In most instances in the United States, a measurement of the volatile organic compounds (VOC) emitted by the engine is required. VOC are usually defined as the total of all hydrocarbons (HC) emitted minus the methane and ethane components. In many instances the term non-methane hydrocarbons (NMHC) is used synonymously with VOC. In modern engines, emissions of VOC

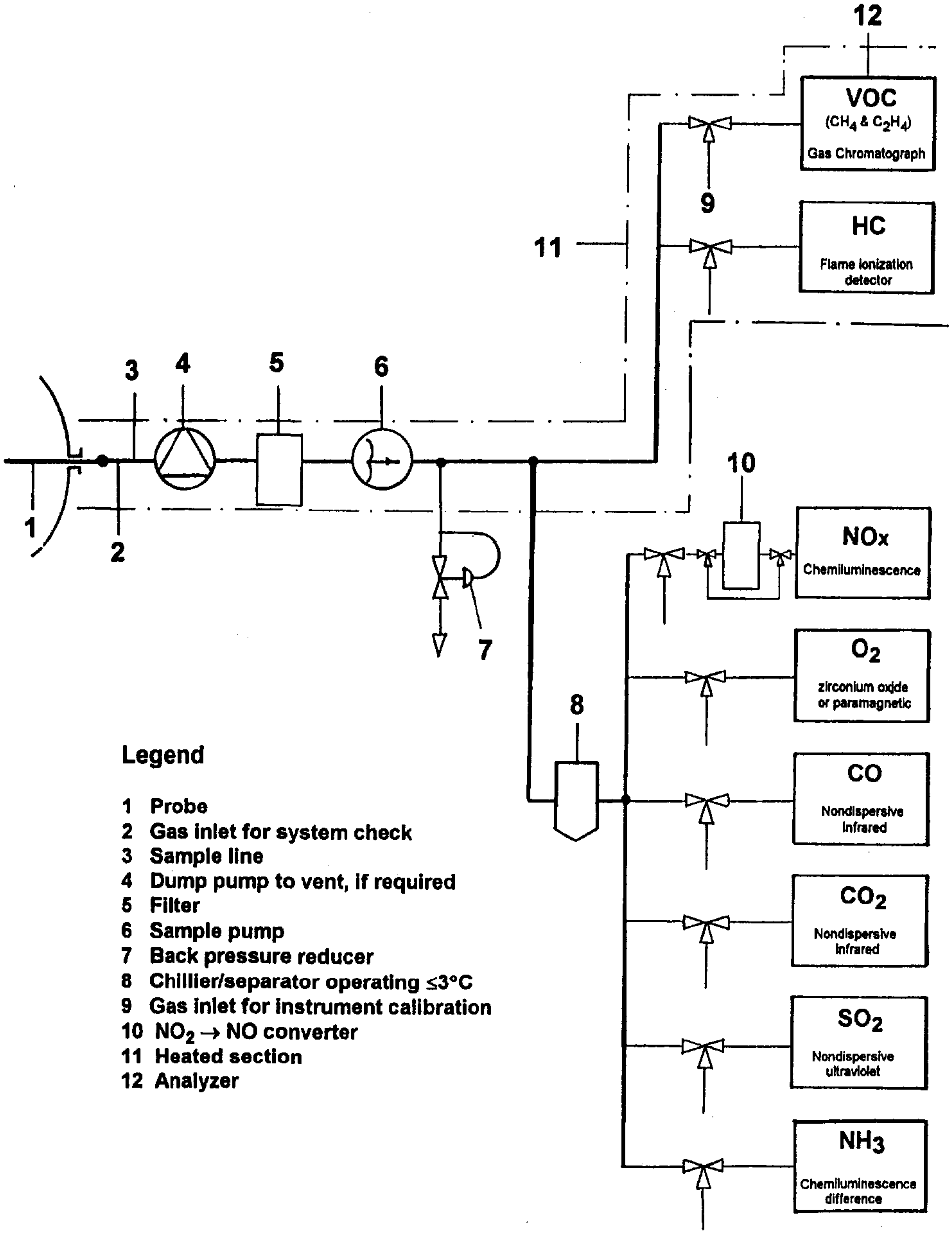

Fig. 1 Measurement system for gaseous components

are often at a very low concentration, less than 1 to 10 ppmC (methane equivalent). Their measurement requires the accurate determination of concentrations of both the total and methane exhaust components. This determination is accomplished by measuring total HC and subtracting measured methane.

It is recommended that the measurement of total hydrocarbons be made using a flame ionization analyzer and volatile organic compounds by gas chromatograph (GC). Direct analyzers combine the features of both these instruments to obtain VOC concentrations.

Separate analyzers can also be used to obtain VOC emissions. To improve accuracy, it is recommended that the ratio of VOC to total HC be obtained using the GC, and this ratio be applied to the total HC obtained by flame ionization detector (FID) to obtain the concentration of VOC in the exhaust.

Ammonia. Ammonia in the exhaust of a turbine resulting from NO_X emission control equipment, such as SCR, must be controlled to low concentration level, typically 10 ppm. The chemiluminescence difference method was listed as the best method then available. However, none of the methods commercially available was considered accurate enough. It was recognized that considerable research on ammonia measurement is in progress, and the Standard will require subsequent updating.

Water Vapor. The exhaust from a gas turbine can contain varying quantities of water vapor, approximately 2 to 15 percent by volume. The absolute amount depends on the products of combustion that are fuel related, the absolute humidity of the air ingested into the engine, and the amount of water injected into the engine for emission control or power augmentation. Water entering the engine from evaporative inlet coolers and water fuel emulsions also must be considered.

The water vapor content of the exhaust is used in making emission calculations, and determining this value accurately is important. The quantity of water in the exhaust can be determined either by direct measurement or by measurement and summation of all sources. In the case where direct measurement

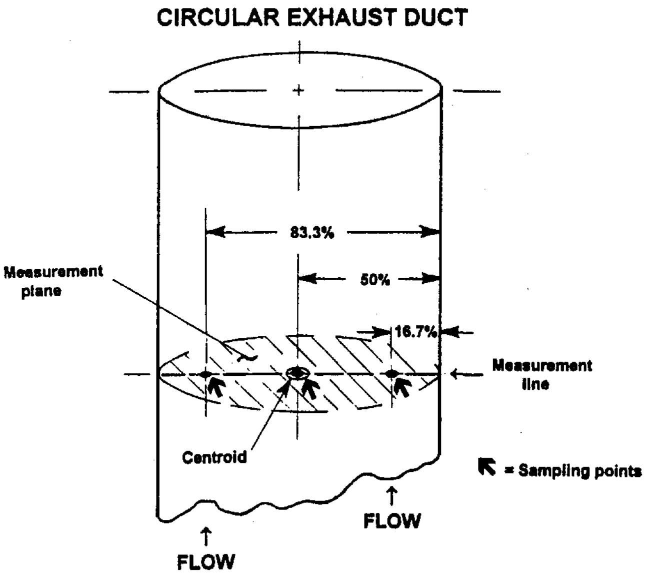

Measurement line established normal to flow through the centroid of exhaust duct measurement plane and in direction of expected stratification.

Fig. 2 Sampling points

is required, the reference method cited in EPA Method 4 [9] is recommended.

Instrument Calibration Gases. The calibration of instruments through the use of calibrating gases is described in the Standard. These gases, introduced at the sampling probe, are to have certificates of compliance per ISO standards or USEPA protocols. Accuracy requirements for a number of calibration gases, including zero gas, are recommended in the Standard.

Smoke Measurement

Smoke emitted from gas turbines is measured in two general ways: (1) visible plume opacity, and (2) smoke density that measures soot in the exhaust. Smoke measurements are made from engines operating on liquid fuels. Engines operating on natural gas will normally have no visible exhaust plume.

Visual Opacity. Currently, visual determination using USEPA Method 9 [10] is the only accepted and practical method of determining the visual opacity of the exhaust plume of a gas turbine. However, this method does not produce results of acceptable accuracy.

Other methods were examined and found deficient. LIDAR measurements [11] were found to be too expensive for routine source testing. Transmissometers [12] measure the light obscuration caused by smoke in the exhaust duct but do not take into account plume behavior or plume illumination.

Method 9 requires that a trained observer, holding a valid USEPA certificate, make and record one or more sets of observations. The positive error of Method 9 for black plumes is cited as less than 5 percent. Evaluations of Method 9 during certification training [13] show that at the opacity values of 10 and 20 percent, which are the usual compliance levels for gas turbines, the standard deviation of measurement was 3.16 percent and 5.25 percent opacity, respectively.

When the standard deviation is as high as 25 to 33 percent of the measured value, compliance difficulties can be expected, particularly in cases where compliance is marginal. When this deviation occurs, referee measurements of smoke density are recommended. These measurements would be made using a *smokemeter* or *in-stack transmissometer* that was correlated with visual opacity tests made during source testing. In order to be effective, this procedure must be agreed to by the cognizant regulatory agency so that when questioned by an inspector, compliance during routine operation of the engine can be demonstrated using the referee method.

Smoke Density. In the United States regulations do not require smokemeter readings. Since these readings are required in Europe and other regions, smoke density measurement was included in the Standard.

Two different methodologies are available: smoke spot and optical. In the smoke spot procedure, a metered quantity of exhaust is passed through a filter paper and the density of the smoke stain on the paper is graded optically. In the optical procedure, a continuous flow of exhaust is extracted, metered, and passed through a cell that measures its light obscuration. Three of the most common methods of measuring smoke from gas turbines were evaluated for inclusion in the Standard. These are described below.

ICAO/SAE Aircraft Method. The SAE Aircraft Method is a spot filtration procedure that is designed and used to measure the smoke density of aircraft gas turbine exhaust. In this method, the mass of exhaust collected and the optical grading of the stain are closely controlled. This method is specified by the International Civil Aviation Organization (ICAO) and aviation agencies throughout the world [14].

Bacharach/ASTM. Bacharach is the spot filtration method specified by ISO [3] and used throughout Europe to measure both turbine and diesel engines. It is not as precise as the aircraft method and employs a different scale for smoke density. The method, also identified as ASTM D2156, was designed for use with oil heating equipment [15].

Rolls-Royce Optical Smokemeter. The Rolls-Royce optical smokemeter was designed to measure smoke from gas turbines and component rigs on a continuous basis. It provides a measurement of the carbon density based on a standard cell that can be calibrated in units of carbon mass (milligrams per cubic meter) or in terms of Bacharach or SAE Smoke Numbers [16].

Comparison of Methods. These methods were compared for accuracy for the range of low smoke density typical of modern gas turbine engines. This evaluation, based on the accuracy stated in the description of each method, was to determine if a difference in accuracy that could be easily discernible and lead to a recommended method existed.

Figure 3 shows the results of the accuracy evaluation. In order to obtain a direct comparison between the methods, the smoke number values from the SAE and Bacharach methods were converted to carbon mass per unit of exhaust gas using published conversion data.

Recommendations. In reviewing the commercially available methods of measuring smoke, the Steering Committee decided not to recommend a specific method at this time. While

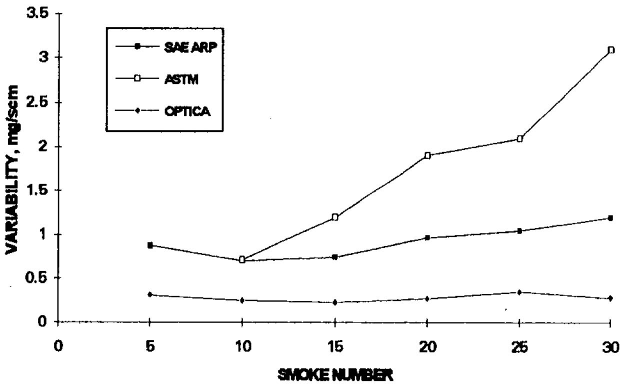

Fig. 3 Variability of smoke measurement

the optical smokemeter is the most accurate, it could not be recommended for use in the Standard because there were no commercially developed competitive methods.

The spot filtration methods were found to be of insufficient accuracy in the low smoke density ranges required by industrial gas turbines. The Steering Committee determined that *no method would be recommended* in the Standard, but that the most commonly used methods would be described for the convenience of the user.

Particulate Measurement

The measurement of particulate material (PM) is frequently required in the United States by state and local agencies if the gas turbine is run on liquid fuel. In some instances PM measurement has been directed by local agencies even when the engine is run on natural gas.

Present Method 5. The method of measurement mandated by these agencies is USEPA Method 5 [17], a method that uses filtration and collection of the particulates in the exhaust by traversing the exhaust duct over a large number of specified sampling points. It requires long sampling times because of low mass loading of particulates in the exhaust stream. It also requires the determination of the velocity profile of the exhaust at these same points using a pitotstatic probe. From this profile, the mass flow rate of the engine exhaust is computed. While this method may be acceptable for use in measuring various industrial sources such as cement kilns and coal fired boilers, it is misapplied to gas turbine engines. This application is expensive and time consuming and has high variability resulting in inaccurate data.

Alternate Methods. Because of these difficulties, an alternate method was sought to determine PM emissions from turbines. Various procedures were examined, including correlation of particulate mass with the optical density of the exhaust [18] and the use of full-sized and miniature dilution tunnels similar to diesel testing [19]. It was found that while research was continuing on optical correlation, this method had not yet been brought to commercial practice. Dilution tunnels, commonly used in automotive testing, would extend, not shorten, the sampling times and would not give real time test results.

Recommended Modifications to Method 5. The possibility of modification of Method 5 was examined to see if it could be simplified and made more practical and less costly. It was determined that a number of changes should be made when Method 5 is used to measure gas turbine PM. These changes, described below, were incorporated in the Standard.

Eliminate Isokinetic Sampling. The particulate material in the exhaust of a gas turbine operating on distillate fuel is composed primarily of submicronic carbon particles and condensable hydrocarbons and sulfates. With low-sulfur distillate fuels all of the particles present in the exhaust are submicronic and will follow streamlines. Isokinetic sampling, to assure that the velocity into the probe and the stream velocity are equal, is unnecessary.

Increase Sample Flow. With the elimination of isokinetic sampling, the sample flow rate may be increased, reducing collection times to obtain the required sample mass of 20 mg.

Reduce the Number of Sampling Points. As was previously discussed, the gas stream exiting from an industrial gas turbine is well mixed. The number of sampling points was reduced to the same three recommended for gas sampling. Verification that the gas sample is representative serves to determine that particulate sampling will also be representative.

Eliminate Velocity Profiling. The determination of mass flow from a gas turbine using the velocity profile measured in the exhaust duct is not recommended due to inaccuracy in measuring the true average flow velocity. Instead, the flow through the system should be determined using fuel flow measurements and a carbon balance. This determination should be verified by the computed exhaust flow using the engine manufacturer's engine performance model (performance deck) corrected to the source test conditions.

Eliminate PM Measurement From Gas Fired Engines. The Standard states that the measurement of particulates from natural gas fuels engines is *not recommended.* The level of material in the exhaust resulting from the combustion of natural gas is extremely low and is below the practical threshold of measurement using Method 5. In some instances, agencies have required sampling times as long as 24 hours in order to obtain a viable sample.

Air Toxics

As a result of the 1990 Clean Air Act Amendments, numerous compounds have been listed as air toxics [20]. The emission of these compounds is regulated at the levels of 10 tons per year, or 25 tons in combination.

Occurrence in Gas Turbine Exhaust. At these regulated levels, the emissions of these quantities of air toxic compounds from gas turbine engines operating on natural gas and high quality distillate fuels are unlikely due to the cleanliness of the fuels and the design and installation characteristics of industrial turbine engines. Some air toxic compounds cannot be generated by gas turbines. More specific reasons are as follows:

1. High fuel quality is required to extend engine endurance life and maintain performance. The level of contaminants in the fuel must be closely controlled in order to prevent erosion and corrosion of the engine gas path. ASTM specifications require that trace metal concentrations of vanadium, sodium and potassium (in combination), calcium, and lead be held to 0.5 ppm by weight [21].
2. High combustion efficiency and large dilution ratios are design characteristics of stationary gas turbine engines. Typical combustion efficiencies are 99.99 percent and air-to-fuel ratios are approximately 50:1. In combination, these characteristics along with careful design control of combustors have resulted in total HC emission levels in the exhaust gas of 1 to 10 ppm, measured as methane. As a result, only minute fractions (ppb or less) of unburned fuel components will be present in the exhaust.
3. Good fuel filtration is required to prevent finely divided solids containing earth compounds and metals from entering the fuel system and fouling and eroding control orifices and fuel injectors.
4. High quality inlet air filtration is used to prevent airborne particles from entering the engine and causing deterioration of engine performance and life. These particles also are prevented from subsequently being oxidized and reinjected into the atmosphere.
5. Close specification control of other fluids such as water, steam, and lubricating oil used in gas turbines is maintained. These fluids have specifications that stipulate allowable levels of contaminants to prevent deposition, corrosion, and erosion in the engine. Particularly rigid control is required to minimize the induction of halogen compounds to prevent them from entering the gas path. This class of compounds is particularly corrosive and greatly reduces engine life.

Determination of Air Toxic Compounds. Air toxic compounds emitted by the engine must come from the fluids introduced into the engine during its operation. These fluids are fuel, air, lubricating oil, water, steam, and engine washing compounds. Each installation should be considered specific. If determinations of the presence and quantity of emissions of air toxic compounds must be obtained, it is recommended that an analysis of each of the fluids used by the engine be made to determine the presence and expected concentrations of compounds that can form air toxic compounds.

Because of very low concentrations, direct measurement of these compounds in the exhaust is not recommended. If exhaust measurement is mandated, the prior identification of each air toxic compound, its source, and probability of occurrence is recommended.

Summary and Conclusions

B133.9 New Standard. The revised ANSI Standard B133.9 has been completed and is available from the American National Standards Institute. Its use will provide the following:

1 The guidance and criteria for the measurement of exhaust emissions from stationary gas turbines.
2 Standardized measurement techniques, analysis, and reporting in the United States and internationally.
3 Reduced labor and cost of source testing by simplified sampling, exhaust flow measurement, and measurement of particulates.
4 Improved understanding of the character and measurement of gas turbine emissions by industry and government staff involved in the permitting process.

Contract Versus Committee Methods. In the past most standards, including ANSI B133 Gas Turbine Procurement Standards, have been written by volunteer committee members whose membership and time were sponsored by their various employers. Because this committee activity was secondary to their main work, standards development was a slow and limited process. Recent reductions in technical staffs have made voluntary committee work even less productive.

Changing this procedure to one in which research, development, and drafting of the standard are performed by a contractor under the technical direction of a steering committee has proven to be advantageous to the sponsoring groups. Our experience in writing the new B133 Exhaust Emissions Standard has shown the following advantages of using the committee method:

- *Defined scope.* The specific work requirements are defined by contract that can be monitored and administered.
- *Reduced manpower.* The technical man-hours and involvement required of the sponsors' technical staff are greatly reduced.
- *Shortened time.* The time to complete the Standard is shortened to less than half the usual development time.
- *Cost and time are controlled.* The cost and time required of each sponsor are known at the onset of the contract and can be budgeted.
- *Defined responsibility.* It is the responsibility of the contractor to produce a superior specification.

Acknowledgments

The author thanks the following for their assistance during the development of this specification:

Steering Committee

R. P. Allen, General Electric Company, Schenectady, NY (now Clemson University, Clemson SC)
R. J. Art, ASME Research, Washington, DC
W. Gray, Special Consultant, Radian Corporation, Research Triangle Park, NC
W. S. Y. Hung, Solar Turbines Inc., San Diego, CA
R. Huntley, Emission Measurement Branch, USEPA, Research Triangle Park, NC
J. J. Macak, Westinghouse Electric Corporation, Orlando, FL
G. Opdyke, Dykewood Enterprises, Stratford, CT
H. Schreiber, Electric Power Research Institute, Palo Alto, CA
W. H. von Klein Smid, Engineering Consultant, Corona del Mar, CA
P. Westlin, Emission Measurement Branch, USEPA, Research Triangle Park, NC

Other Contributors

Allison Gas Turbine Division, General Motors Corporation, Indianapolis, IN
Cook & Associates, Inc., Indianapolis, IN
Rolls Royce plc, Derby, United Kingdom
U.S. Naval Air Warfare Center, Trenton, NJ

References

1 Procurement Standard for Gas Turbine Environmental Requirements and Responsibilities, ANSI B133.9, ASME, New York, Apr. 1979.

2 Standards of Performance for New Stationary Sources, Subpart GG—Standards of Performance for Stationary Gas Turbines, US Federal Register Title 40, Part 60, 1979.

3 Gas Turbines—Exhaust Gas Emission—Measurement and Evaluation," Draft International Standard 11042-1, ISO/TC 192, International Standards Organization, Geneva, Switzerland, 1992.

4 Herrmann, B., and Opdyke, G., "ISO Standard for Gas Turbine Measurements," IGTI Cogen-Turbo, Budapest, Hungary, Sept. 1991.

5 "International Standards and Recommended Practices, Environmental Protection," Annex 16, Vol. II, Aircraft Engine Emissions, International Civil Aviation Organization, Montreal, Canada, Nov. 1993.

6 "Exhaust Emissions Measurement Recommendations for Reciprocating Engines and Gas Turbines," CIMAC Number 12, International Council on Combustion Engines, Apr. 1991.

7 "Method 2—Determination of Stack Gas Velocity and Volumetric Flow Rate (Type S Pitot Tube)," 40 CFR, Part 60, Appendix A, Method 2, Aug. 1993.

8 "Performance Specification 2—Specifications and Test Procedures for SO_2 and NO_X Continuous Emission Monitoring Systems in Stationary Sources," Par. 3.2 Reference Method, US Federal Register, Title 40, Part 60, Appendix B, Performance Specification 2, Aug. 1993.

9 "Method 4—Determination of Moisture Content in Stack Gases," US Federal Register, Title 40, Part 60, Appendix A, Method 4, Aug. 1993.

10 "Method 9—Visual Determination of the Opacity of Emissions From Stationary Sources," 40 CFR, Part 60, Appendix A, Method 9, Aug. 1993.

11 "Alternate Method 1—Determination of the Opacity of Emissions From Stationary Sources Remotely by LIDAR," 40 CFR, Part 60, Appendix A, Method 9, AMI, Aug. 1993.

12 "Performance Specification 1—Specifications and Test Procedures for Opacity Continuous Emissions Monitoring Systems in Stationary Sources," 40 CFR, Part 60, Appendix B, Spec. 1, Aug. 1993.

13 Heinsohn, R. J., Davis, J. W., and Anderson, G. W., "Individual Accuracy in Estimating Plume Opacity," *Journal of Air and Waste Management,* Vol. 42:443, Apr. Aug. 1993.

14 "Aircraft Gas Turbine Exhaust Smoke Measurement," Aerospace Recommended Practice ARP1179, Rev. B, Society of Automotive Engineers, Warrendale, PA, Apr. 1991.

15 "Standard Test Method for Smoke Density in Flue Gases From Burning Distillate Fuels," ASTM Designation: D2156, ASTM, Philadelphia, PA, Oct. 1980.

16 "Rolls-Royce Optical Smokemeter Performance Specification," Rolls-Royce plc, Derby, United Kingdom, Jan. 1993.

17 "Method 5—Determination of Particulate Emissions From Stationary Sources," US Federal Register, Title 40, Part 60, Appendix A, Method 5, Aug. 1993.

18 Few, J., Lewis, J., and Hornkohl, J., "Optical Measurements of Turbine Engine Exhaust Particulates," US Naval Air Propulsion Center Report No. NAPC-PE-221C, University of Tennessee Space Institute, Tullahoma, TN, July 1991.

19 "Subpart N—Emission Regulations for New Otto-Cycle and Diesel Heavy-Duty Engines; Gaseous and Particulate Exhaust Test Procedures," US Federal Register, Title 40, Part 86 Subpart N, Jan. 1993.

20 "National Emission Standards for Hazardous Air Pollutants," Title 1, Section 112, US Clean Air Act Amendments 1990; PL 101-549, Nov. 15, 1990.

21 "Gas Turbine Fuels," ANSI/ASME B133.7M, ASME, New York, 1985.

M. A. Niemotka
formerly of Pratt & Whitney Aircraft Engines,
West Palm Beach, FL 33417

J. C. Ziegert
Department of Mechanical Engineering,
University of Florida,
Gainesville, FL 32611

Optimal Design of Split Ring Dampers for Gas Turbine Engines

Vibration analysis techniques used for labyrinth air seals are presented, along with a derivation of the methods used to calculate the dissipation capability of split ring dampers. After defining the problem in classical optimization format, the methods used to automate the process are presented, along with the results for a particular test case. For the case considered, the optimal designs were found to lie at or near the design space boundaries.

Introduction

The annular air seal is commonly used in gas turbine engines to prevent gas flow from one section of the engine to another. The rotating part of the seal is designed to maintain clearances on the order of 0.125–0.25 mm with the mating static structure, thus producing an effective seal (Fig. 1).

The seal is a full hoop structure, which can vibrate with both axial and circumferential nodal patterns. If the natural frequency of any of these modes is near a driving frequency present in the system, vibrations of excessive magnitude may develop, leading to premature failure. For this reason, it is common to provide additional damping to the system in the form of a split ring damper. The damper is a wire formed into a ring containing a gap which rides in a groove provided for it on the seal (Fig. 2). It may have a circular, rectangular, or other cross section. Centripetal forces generated by engine rotation cause the ring to be forced against the seal surface. Vibrational modes of the system result in relative motion between the ring and the seal surface, which causes energy to be dissipated, thus lowering the amplitude of vibration to an acceptable level.

Current design methods for split-ring dampers are based largely on past experience. In this paper we will present a method for automatically determining the optimal damper design for circular or rectangular cross sections.

Split Damper Analysis

The vibrational modes of an annular air seal have two identifying indices. The first is "m," which is the number of axial nodes in the vibration pattern. The second is "N," which is the number of full wavelengths that are present around the circumference of the seal. Each combination of m and N defines a unique vibrating shape or mode (Fig. 3). Since the axial length of the seal is normally much less than the circumferential length, it is customary to restrict consideration to axial modes of $m = 1$, while circumferential modes up to $N = 12$ are normally considered. Assuming negligible damping for now, the natural frequency associated with each of these modes may be obtained by solving the generalized eigenvalue problem:

$$[M]\ddot{x} + [K]x = 0 \tag{1}$$

These frequencies are then compared with the driving frequencies from the rotor and also with the natural frequencies of the mating static structure. The damper is designed to maximize dissipation at the natural frequency that comes closest to one of the potential drivers in the structure surrounding it.

The rotating seal will vibrate and assume a nodal pattern corresponding to the design frequency. This involves a bending of the ring around the circumference. Since the damper ring is split, and thus can carry no hoop load, it will not assume its own nodal pattern, but will instead be forced by centripetal loading to follow the seal's shape. Figure 4 shows the damper ring and seal at the interface surface. When the seal bends in the direction shown, the seal is loaded in tension on the outer fibers and compression in the inner fibers. The opposite is true for the damper, which will bend with tension on the top fibers. Due to compressive frictional forces at the interface, however, the damper will shrink in length. Because of this mismatch at the damper/seal interface, a slipping motion may occur.

Assumptions

Figure 5 shows a typical damper ring configuration with the nomenclature to be used in this paper. The underlying assumptions for the system are:

1 Seal thickness and sectional properties are constant.
2 Coefficient of friction, μ, is constant.
3 The seal radial thickness is small compared to its radius.
4 Hooke's Law applies: Only elastic deformation is considered.
5 The assumed radial displacement of the seal nodal pattern is $w = B^* \cos(N\theta)$.
6 The seal body will undergo only inextensible flexural vibration (neutral axis length remains constant).
7 Due to the surface friction force, the damper ring may experience a significant extension of its neutral axis.

Strains in the Seal and Damper

The following analysis is based on work presented by Alford [1–4]. For in-plane bending of a circular ring:

$$\frac{M}{EI} = \frac{1}{R^2}\left[w + \frac{d^2w}{d\theta^2}\right] \tag{2}$$

Using Eq. (2), the bending strain on the surface is:

$$\epsilon_{\text{bend}} = \frac{c}{R^2}\left[w + \frac{d^2w}{d\theta^2}\right] \tag{3}$$

For the seal, the bending strain is compressive at the interface, while it is tensile for the damper ring. Therefore,

---

Contributed by the International Gas Turbine Institute and presented at the 38th International Gas Turbine and Aeroengine Congress and Exposition, Cincinnati, Ohio, May 24–27, 1993. Manuscript received at ASME Headquarters March 1, 1993. Paper No. 93-GT-116. Associate Technical Editor: H. Lukas.

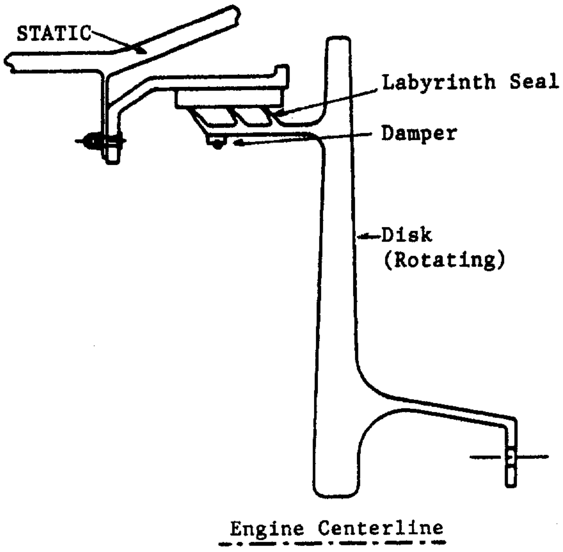

Fig. 1 Annular air seal

$$\epsilon_{s,\text{bend}} = -\frac{c_s B}{R_s^2}[N^2 - 1]\cos(N\theta)$$

$$\epsilon_{d,\text{bend}} = \frac{c_d B}{R_d^2}[N^2 - 1]\cos(N\theta) \qquad (4)$$

The opposing strains at the interface cause friction forces in the circumferential direction, which will cause the ring to undergo elongation or contraction. Over some portion of the region, the friction forces may be sufficient to prevent slipping. For now it will be assumed that no slipping occurs at the interface over the region, $0 < \theta < \theta_0$, where θ_0 is to be determined. For a θ that is greater than θ_0, slipping will occur, and the friction force over the region will be maximum and will cause the damper ring to contract in compression. Therefore, the total strain in the damper ring at the interface is the sum of the bending strain and the frictional strain.

To determine θ_0, the point where the slipping motion ceases, consider the seal with a deflected shape of amplitude B_i where slippage is impending at $\theta = \pi/2N$, but friction forces are just high enough to prevent it. The strain in the seal is equal to the strain on the damper ring for a no-slip condition. $\epsilon_{d,\text{friction}}$ is compressive because the seal elongation strain is zero (inextensible) and its bending strain is compressive at the interface, while the damper ring surface bending strain is tensile.

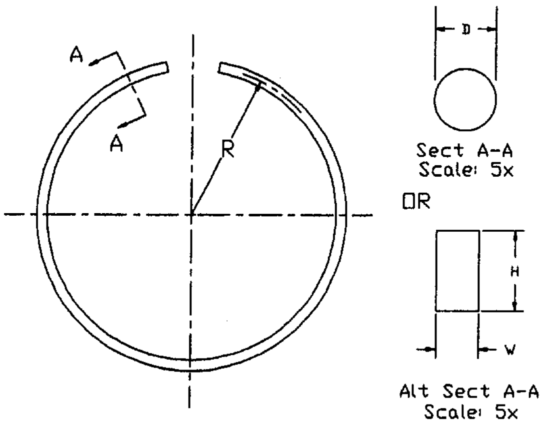

Fig. 2 Split ring damper

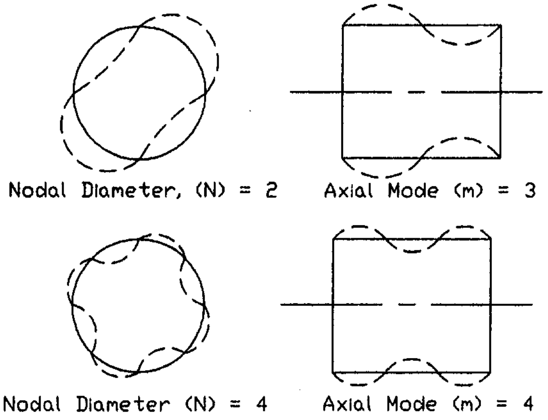

Fig. 3 Vibrational patterns for shell structures

$$\epsilon_d = \epsilon_s$$

$$\epsilon_{d,\text{bend}} + \epsilon_{d,\text{friction}} = \epsilon_{s,\text{bend}}$$

$$\epsilon_{d,\text{friction}} = \epsilon_{s,\text{bend}} - \epsilon_{d,\text{bend}}$$

$$= -\left[\frac{c_d B}{R_d^2} + \frac{c_s B}{R_s^2}\right](N^2 - 1)\cos(N\theta) \qquad (5)$$

We may alternately calculate the strain caused by friction at any point in the ring by dividing the frictional force at that point by the product of the damper area and its modulus of elasticity. The frictional force at any point is obtained by integrating the force per unit length over the length of application. Let F be the frictional force per unit length at the interface prior to the onset of slipping, where F is a function of θ. Then,

$$\epsilon_{d,\text{friction}} = \frac{R_d}{A_d E}\int F d\theta \qquad (6)$$

Therefore,

$$d\epsilon_{d,\text{friction}} = \frac{F R_d}{A_d E}d\theta$$

$$F = \frac{A_d E}{R_d}\frac{d\epsilon_{d,\text{friction}}}{d\theta} \qquad (7)$$

Substituting the expression for $\epsilon_{d,\text{friction}}$ from Eq. (5) yields:

$$F = \frac{N A_d E c_d B}{R_d^3}\left[\frac{c_s}{c_d}\left(\frac{R_d}{R_s}\right)^2 + 1\right](N^2 - 1)\sin(N\theta) \qquad (8)$$

Thus, when there is no slipping $F_{\max}$ will occur at the nodes, when $\theta = \pi/2N$ ($\sin(N\theta) = 1$). When slipping is impending at the nodes, $F = F_{\max} = \mu P$, $\sin(N\theta) = 1$, and $B = B_i$, which is the modal amplitude corresponding to no slippage for a given

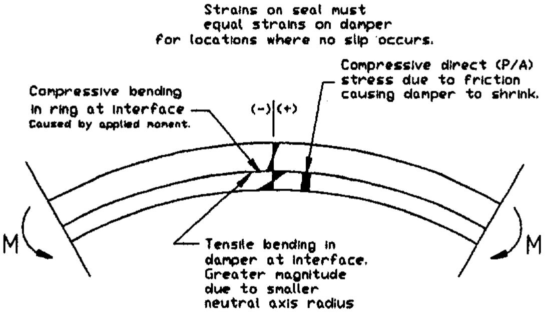

Fig. 4 Stress at damper/seal interface

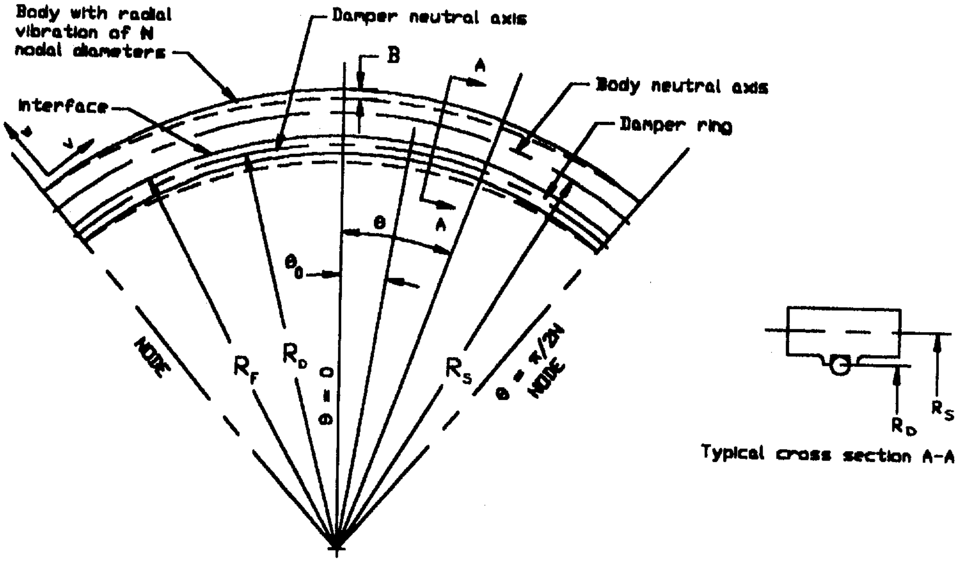

Fig. 5 Damper nomenclature

radial load per unit length, P. Equation (8) may then be solved for B_i:

$$B_i = \frac{\mu P R_d^3}{N A_d E c_d} \frac{1}{\left[\frac{c_s}{c_d}\left(\frac{R_d}{R_s}\right)^2 + 1\right](N^2 - 1)} \quad (9)$$

The "lock-up" load P_i required to stop all slipping for a given amplitude B may also be obtained:

$$P_i = \frac{N A_d E c_d B}{\mu R_d^3}\left[\frac{c_s}{c_d}\left(\frac{R_d}{R_s}\right)^2 + 1\right](N^2 + 1) \quad (10)$$

If $B > B_i$ for some P, slipping will proceed over the region $\theta_0 \le \theta \le \pi/2N$. At the point, $\theta = \theta_0$, F is equal to μP. Combining Eqs. (9) and (10), we obtain:

$$F = \mu P_i \sin(N\theta) = \mu P \frac{B}{B_i} \sin(N\theta) \quad (11)$$

At $\theta = \theta_0$,

$$\sin(N\theta_0) = \frac{P}{P_i} = \frac{B_i}{B} \quad (12)$$

Calculation of Slip Between Damper and Seal

To find the slip, the tangential displacement of the damper ring surface, v_d, must be calculated over the region where slip is occurring, and compared to the tangential displacement of the seal. In this region, the friction force per unit length is at a maximum and therefore,

$$\epsilon_{d,\text{friction}} = -\frac{\mu P R_d}{A_d E}\left(\frac{\pi}{2N} - \theta\right) \quad (13)$$

Since the ring is assumed to be extensible,

$$\epsilon_{d,\text{friction}} = \frac{w}{R_d} + \frac{1}{R_d}\frac{dv_d}{d\theta} \quad (14)$$

and,

$$\frac{dv_d}{d\theta} = -\frac{\mu P R_d^2}{A_d E}\left(\frac{\pi}{2N} - \theta\right) - B\cos(N\theta) \quad (15)$$

Equation (15) can be integrated to yield:

$$v_d = -\frac{B}{N}\sin(N\theta) - \frac{\mu P R_d^2}{2A_d E}\left(\frac{\pi}{2N} - \theta\right)^2 + C \quad (16)$$

The tangential displacement of the damper ring, v_r, at the interface radius, R_f, can be obtained by adding the bending component and the tensile component of the ring's displacement.

$$v_r = -\frac{B}{N}\sin(N\theta) - \frac{\mu P R_d^2}{2A_d E}\left(\frac{\pi}{2N} - \theta\right)^2 + \frac{c_d B R_f}{N R_d^2}(N^2 - 1)\sin(N\theta) + C \quad (17)$$

For the seal body at the interface, the technique is similar. However, the bending strain displacement has the opposite sign and the "stretching" term is equal to zero since inextensibility is assumed. Let v_0 = the displacement of the seal at the interface and s = slip. Then $s = v_0 - v_r$ = relative displacement. Using the equations above and combining the integration constants, and noting that at $\theta = \theta_0$, $s = 0$, the expression for slip is:

$$s = \frac{\mu P R_d^2}{E A_d}\left[-\frac{1}{N^2}\frac{R_f}{R_d}\left(\frac{\sin N\theta}{\sin N\theta_0} - 1\right) + \frac{1}{2}\left[\left(\frac{\pi}{2N} - \theta\right)^2 - \left(\frac{\pi}{2N} - \theta_0\right)^2\right]\right] \quad (18)$$

for $\theta_0 \le \theta \le \pi/2N$. For all other locations, $s = 0$.

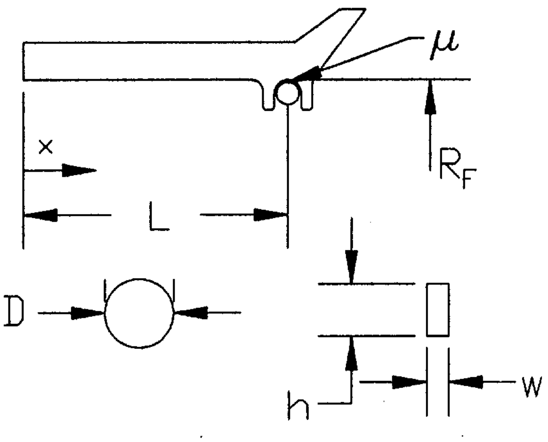

Fig. 6 Design variables

Table 1 Results of circular cross section optimization

Trial	Initial				Final				Constraints			
#	x1(mm)	x2(mm)	x3	x4	x1(mm)	x2(mm)	x3	x4	C1	C2	C3	Q
1	2.0	223	1	0.55	3.75	200	1	0.7	0.81	0.10	0.83	9.40
2	1.0	223	1	0.55	2.28	201	1	0.7	0.81	0.32	0.83	7.36
3	0.5	223	1	0.55	2.28	201	1	0.7	0.81	0.32	0.83	7.36
4	3.0	223	1	0.55	3.75	200	1	0.7	0.81	0.10	0.83	7.36
5	4.0	223	1	0.55	3.75	200	1	0.7	0.81	0.10	0.83	9.40
6	5.0	223	1	0.55	3.75	200	1	0.7	0.81	0.10	0.83	7.36
7	2.0	218	1	0.55	3.75	201	1	0.7	0.81	0.10	0.83	7.37
8	2.0	214	1	0.55	3.75	200	1	0.7	0.81	0.10	0.83	7.36
9	2.0	209	1	0.55	3.75	200	1	0.7	0.81	0.10	0.83	7.36
10	2.0	200	1	0.55	3.75	200	1	0.7	0.81	0.10	0.83	7.36
11	2.0	223	1	0.55	3.75	200	1	0.7	0.81	0.10	0.83	7.36
12	2.0	223	0.92	0.55	3.75	200	1	0.7	0.81	0.10	0.83	7.36
13	2.0	223	0.84	0.55	3.75	200	1	0.7	0.81	0.10	0.83	7.36
14	2.0	223	0.76	0.55	3.75	200	1	0.7	0.81	0.10	0.83	7.36
15	2.0	223	0.68	0.55	3.75	200	1	0.7	0.81	0.10	0.83	7.36
16	2.0	223	0.59	0.55	3.75	200	1	0.7	0.81	0.10	0.83	7.36
17	2.0	223	1	0.70	3.75	200	1	0.7	0.81	0.10	0.83	7.36
18	2.0	223	1	0.60	3.75	200	1	0.7	0.81	0.10	0.83	7.37
19	2.0	223	1	0.50	2.28	201	1	0.7	0.79	0.32	0.83	7.36
20	2.0	223	1	0.40	3.75	200	1	0.7	0.81	0.10	0.83	7.36
21	2.0	223	1	0.30	2.28	201	1	0.7	0.81	0.32	0.83	7.36

Work Calculation

The work, W, done by the friction force in a full cycle may be obtained by multiplying the friction force by the relative displacement and integrating over the slip region:

$$W = 16\,\frac{(\mu P)^2 R_d^3}{N^2 E A_d}\left[\frac{-R_f}{R_d}\left(\cot N\theta_0 + N\theta_0 - \frac{\pi}{2}\right) - \frac{1}{3}\left(\frac{\pi}{2} - N\theta_0\right)^3\right] \quad (19)$$

The power, D, dissipated by the damper ring is obtained by multiplying the work per cycle by the frequency of vibration, f. The absolute value is necessary since slip is defined as a negative in Eq. (19):

$$D = \left|16 f\,\frac{(\mu P)^2 R_d^3}{N^2 E A_d}\left[\frac{-R_f}{R_d}\left(\cot N\theta_0 + N\theta_0 - \frac{\pi}{2}\right) - \frac{1}{3}\left(\frac{\pi}{2} - N\theta_0\right)^3\right]\right| \quad (20)$$

Note that the energy dissipated is a function of θ_0, the angle where slippage starts. As shown in Eq. (12), this angle is a nonlinear function of the modal amplitude, B. Therefore, the damping is a nonlinear function of the modal amplitude, B. In particular, a finite modal amplitude, B_i, exists where no slipping occurs, and no energy is dissipated by the damper.

Damper Performance Metric

The nonlinear dependence of the dissipation on the amplitude of vibration, which is unknown at the design stage, makes it difficult to compare the performance of various damper designs. Therefore, it was decided to base the comparison on an assumed vibrational amplitude, which results in a vibratory hoop stress in the seal equal to the allowable vibratory stress obtained from a Goodman Diagram analysis. A relative dissipation ratio, Q, can then be formed, which is the ratio between the total system energy and the energy dissipated by the damper.

$$Q = \frac{\text{Seal vibrational energy} + \text{energy dissipated by damper}}{\text{Energy dissipated by damper}} \quad (21)$$

Note that the vibrational energy of the seal is a function of the modal amplitude, B, which is measured at the free end of the seal, while the energy dissipated by the damper is calculated based on the radial amplitude at the particular axial location of the seal.

For design purposes Q may be used to measure the merits of one damper design versus another. As Q becomes smaller, the percentage of total system energy that is dissipated by the damper increases. For the assumed B_{damped}, the damper with the smaller Q value would provide the largest dissipation, and thus the greatest reduction in actual response amplitude. The optimal damper design is then that design which minimizes the value of Q.

Design Variable Definition

Q is a function of four or five design variables, depending on the damper cross section desired. They are: (1) (x_1): damper diameter (or width for rectangular cross section); (2) (x_2): interface radius, R_f; (3) (x_3): axial location along the seal; (4) (x_4): the coefficient of friction between the seal and damper; and (5) (x_5): damper aspect ratio = height/width if a rectangular cross section is desired (Fig. 6). The interface radius and axial location design variables were normalized by dividing by the maximum interface radius, and the seal length, respectively.

Constraints

The problem will be constrained by two strength and one stability criteria. First, the additional damper load must not increase the total hoop stress at the knife edge tip, $\sigma_{\text{total}} = \sigma_{\text{vib}} + \sigma_{\text{steady}}$, to greater than 80 percent of $\sigma_{.2\%YS}$. Second, the total bending stress at the seal base must not exceed $\sigma_{.2\%YS}$. Finally, damper separation is not allowed. If the damper's inertia is

Table 2 Results of rectangular cross section optimization

Trial	Initial					Final					Constraints			
#	x1(mm)	x2(mm)	x3	x4	x5	x1(mm)	x2(mm)	x3	x4	x5	C1	C2	C3	Q
22	2.0	223	1	0.55	1	3.38	223	1	0.64	0.80	0.74	0.0	0.83	1.15
23	1.0	223	1	0.55	1	3.43	223	1	0.7	0.82	0.74	0.0	0.83	1.13
24	0.5	223	1	0.55	1	3.60	223	1	0.7	0.91	0.74	0.0	0.83	1.13
25	3.0	223	1	0.55	1	3.40	223	1	0.7	0.81	0.74	0.0	0.83	1.14
26	4.0	223	1	0.55	1	3.70	223	1	0.7	0.97	0.74	0.0	0.83	1.13
27	5.0	223	1	0.55	1	3.50	223	1	0.64	0.85	0.74	0.0	0.83	1.15
28	2.0	218	1	0.55	1	3.38	223	1	0.7	0.80	0.74	0.0	0.83	1.14
29	2.0	214	1	0.55	1	3.38	223	1	0.7	0.80	0.74	0.0	0.83	1.14
30	2.0	209	1	0.55	1	3.45	223	1	0.7	0.82	0.74	0.0	0.83	1.13
31	2.0	200	1	0.55	1	3.55	223	1	0.7	0.88	0.74	0.0	0.83	1.13
32	2.0	223	1	0.55	1	3.38	223	1	0.7	0.80	0.74	0.0	0.83	1.14
33	2.0	223	0.92	0.55	1	3.75	223	0.94	0.7	0.80	0.74	0.0	0.83	1.11
34	2.0	223	0.84	0.55	1	3.75	223	0.94	0.7	0.80	0.71	0.002	0.83	1.12
35	2.0	223	0.76	0.55	1	3.75	223	0.96	0.7	0.85	0.71	0.005	0.83	1.12
36	2.0	223	0.68	0.55	1	3.75	223	0.95	0.7	0.81	0.71	0.0	0.83	1.12
37	2.0	223	0.59	0.55	1	3.75	223	0.94	0.7	0.80	0.72	0.0	0.83	1.11
38	2.0	223	1	0.70	1	3.75	223	1	0.7	0.97	0.71	0.003	0.83	1.13
39	2.0	223	1	0.60	1	3.38	223	1	0.7	0.80	0.71	0.0	0.83	1.13
40	2.0	223	1	0.50	1	3.38	223	1	0.62	0.80	0.74	0.0	0.83	1.14
41	2.0	223	1	0.40	1	3.38	223	1	0.7	0.80	0.74	0.0	0.83	1.13
42	2.0	223	1	0.30	1	3.75	223	1	0.7	0.98	0.74	0.0	0.83	1.13
43	2.0	223	1	0.70	0.7	3.38	223	1	0.7	0.80	0.74	0.003	0.83	1.14
44	1.0	250	1	0.90	0.9	3.38	200	1	0.62	0.80	0.74	0.0	0.83	1.15
45	1.0	250	1	1.10	1.1	3.75	201	1	0.7	0.98	0.74	0.002	0.83	1.13
46	1.0	250	1	1.20	1.2	3.40	200	1	0.7	0.82	0.74	0.004	0.83	1.14
47	1.0	250	1	1.25	1.3	3.38	200	1	0.7	0.81	0.74	0.004	0.83	1.14

greater than the force per unit length applied to the damper, i.e., the radial load is insufficient to cause the ring to maintain contact with the seal, separation will occur. Since the damper radial load is caused strictly by centrifugal forces, the equation for separation may be written as:

$$\rho A_d q^2 B < \rho A_d R_d \omega^2$$

$$\rho A_d (2\pi f)^2 B < \rho A_d R_d \left(\frac{\text{rpm}*2\pi}{60} \right)^2$$

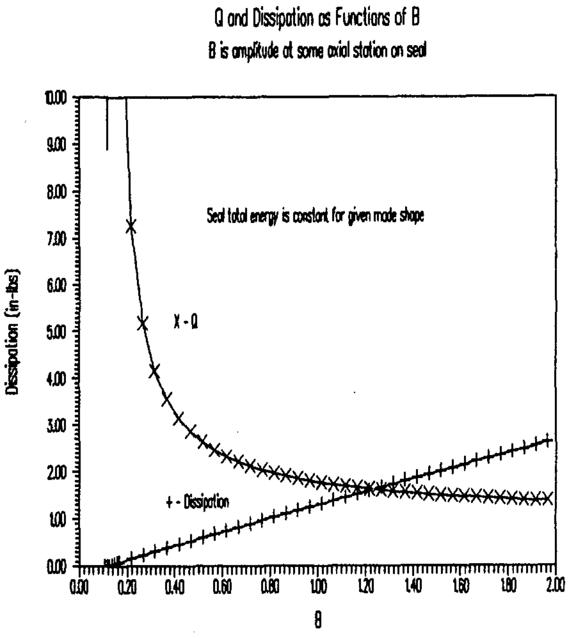

Fig. 7 Q and dissipation as functions of amplitude

or

$$3600 \frac{B}{R_d} \left(\frac{f}{\text{rpm}} \right)^2 - 1.0 < 0 \qquad (22)$$

In addition, a series of side constraints are used. The damper diameter will be limited such that 1.0 mm $\leq x_1 \leq$ 7.5 mm. This is based on size limitations of the seal, and the need for attachment material. The normalized interface radius will be limited to $0.95 \leq x_2 \leq 1.0$. For values smaller than 0.95, the material added to the seal to house the damper increases in radial height to a point where additional stiffness is added to the seal, and the neutral axis of the seal may also shift. The normalized axial location will be limited such that $0 \leq x_3 \leq 1.0$. The coefficient of friction will be limited such that $0.4 \leq x_4 \leq 0.7$. Finally, if a rectangular cross section is used, the aspect ratio will be limited to $0.8 \leq x_5 \leq 1.25$. These limits are used so that the damper will not have a tendency to "roll" over, or be too long axially to fit on the seal. With the objective function, design variables, and constraints defined, the problem can now be summarized in classical optimization format:

$$\text{minimize } Q(x); \quad x = (x_1, x_2, x_3, x_4, \{x_5\})$$

subject to:

$$g_1(x) = 0.8\sigma_{.2\%YS} - \sigma_{\text{hoop}} \geq 0\text{—Hoop Stress}$$

$$g_2(x) = \sigma_{.2\%YS} - \sigma_{\text{bending}} \geq 0\text{—Bending Stress}$$

$$g_3(x) = 1 - 3600 \frac{B}{R_d} \left(\frac{f}{\text{rpm}} \right)^2 \geq 0\text{—Separation}$$

$$g_4(x) \text{ thru } g_{13 \text{ or } 15}(x) \geq 0\text{—Side Constraints} \qquad (23)$$

The minimization of Q was accomplished using the Keefer and Gottfried exterior penalty function method as described in Vanderplaats [5], based on its robustness and ability to handle

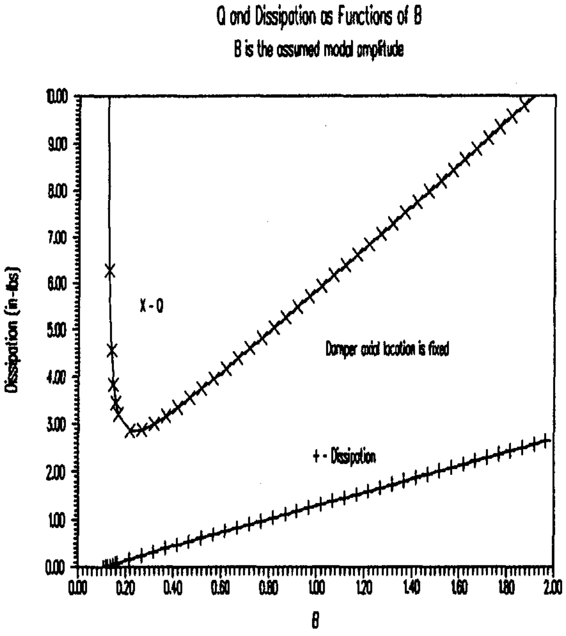

Fig. 8 *Q* **and dissipation as functions of modal amplitude**

starting points outside the feasible region. A pseudo-objective function, Q', is defined as:

$$Q'(x) = Q(x) - r_p \times \sum_{i=1}^{n} \{\min [0, g_i(x)]\}^2 \qquad (24)$$

The penalty multiplier, r_p, is a positive variable, which serves to increase (penalize) the pseudo-objective function for any violated constraints. Low values of r_p will typically result in solutions in the infeasible region. Therefore the penalty multiplier is increased as the search progresses to force convergence on the constrained optimum. Normalization of the design variables and constraints so that all values fall in the region $0.0 \le x_i \le 1.0$ ensures that all constraint violations are given equal weight.

OPTLIB [6], an optimization code library produced by the University of Missouri, which contains a menu of general optimization algorithms, was used to perform the search for the optimum damper design. For this study, Powell's method was selected to generate successive search directions through the design space. The one-dimensional searches were performed using the Golden Section algorithm.

The program starts with an initial damper design, as defined by assigned values of x_1, x_2, x_3, x_4, $\{x_5\}$. Each starting vector lies in the basin of attraction of some local minimum. Ten different starting vectors were used for both the circular and rectangular damper to attempt to find the best local minimum.

With the initial damper geometry known, the additional load on the seal caused by the damper mass can be calculated. The change in steady-state stress is found by using the method of superposition. Since the problem is purely linear, for a given damper load at a known axial station, the new stress in the seal can be calculated using Eq. (25), where $(\sigma/\delta)_{\text{static}}$ is known from a static F.E. analysis:

$$(\sigma_{ss})_{\text{new}} = (\sigma_{ss})_{\text{old}} + \frac{\text{damper load}}{\left(\dfrac{\text{load}}{\delta}\right)_{\text{static}}} * \left(\frac{\sigma}{\delta}\right)_{\text{static}} \qquad (25)$$

The OPTLIB code, which performs the search, calls a FORTRAN subroutine to evaluate the objective function and constraints. The axial location is sent to the interpolation subroutine to update the ratios and find the amplitude of vibration at the current axial location from the mode shape data. Finally, Q and the constraints are calculated and returned to the optimization program. The program generates new values of the design variables according to the strategy outlined above. The process is repeated until the lowest value of Q is found. The final values of the design variables are output, along with the values of the constraints.

Results

The optimization code was run on the test case shown in Fig. 1. In order to test for local minima of the objective function, various starting points for the design variables were chosen. The results from the program are summarized in Table 1 for circular dampers and Table 2 for rectangular cross sections, with the optimum designs highlighted.

As can be seen, for the test case studied, both the optimum circular and rectangular dampers were found to have the minimum interface radius, and the maximum coefficient of friction.

The circular damper had the largest diameter allowed, located at the far end of the seal, and showed no local minima within the design space. Even at the boundaries, where the optimum was found, the constraints of stress magnitude and damper separation tended to be well within the allowable bounds.

For the different starting points, the rectangular cross section exhibits local minima with damper heights of approximately 6.75 mm and 7.5 mm.

Discussion

Figure 7 is a plot of total energy dissipation and Q, as functions of B, the amplitude of radial motion of the damper axial station along the seal. For any given mode shape and the assumed response amplitude, the seal's total energy is fixed. Therefore, the numerator of Q becomes a constant plus the dissipation produced by the damper. The damper dissipation is a function of the amplitude at the axial location chosen. Since seal energy is constant for the mode shape, moving to the far end of the seal has the effect of increasing B, which will decrease Q.

A larger diameter wire would also produce similar results by providing additional pressure load, which also increases dissipation, but is limited by the stress constraints. Finally, a larger

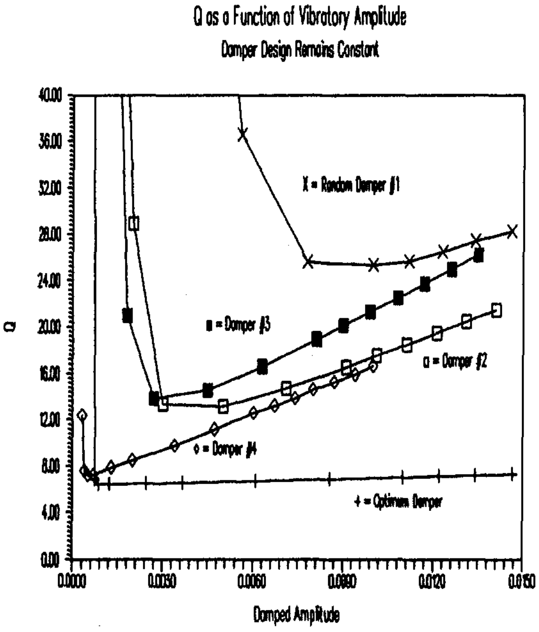

Fig. 9 *Q* **as a function of modal amplitude**

coefficient of friction will provide a larger amount of work for a given displacement.

From Eq. (17), it can be seen that with all other variables being held constant, slip increases linearly with respect to c_d, the distance between the seal's neutral axis and the interface surface. In addition, for a given damper, reducing R_f and R_d by the same amount causes R_f/R_d to become larger, which increases dissipation.

The test case tended to validate these observations for the circular cross section. For the rectangular cross section, however, the optimum damper was located only 95 percent of the distance from the base to the end, and the hoop stress constraint was active. This move in location indicates that for optimum dissipation, the pressure produced by the damper is a stronger contributor than the axial location. For this case it is more advantageous to move the seal toward the base, even though the local amplitude is lower, in order to satisfy the stress constraints, rather than sacrifice pressure load by making the damper cross section smaller.

For the rectangular cross section tested, an aspect ratio greater than 1 would add additional distance between the neutral axes, but the optimum damper was found to have an aspect ratio less than one. For this particular test case then, we may conclude that damper load is a stronger influence on overall effectiveness than the distance between neutral axes.

Evaluation of Q as a Design Metric

The relative dissipation ratio, Q, is computed using an assumed modal amplitude, which may not actually occur. For this amplitude, the lowest value of Q corresponds to the largest amount of dissipation by the damper. For a given seal, larger values of dissipation (smaller Q) will result in larger reductions of vibratory amplitude.

When the seal system is in the design stage, it is difficult to determine the actual vibratory amplitude. Modal analysis can be used to approximate the response only if the internal damping and forcing function are assumed. Figure 8 is a plot of dissipation and Q as functions of the modal amplitude. Note that a different definition of B is used than in Fig. 9. Here, B is the assumed amplitude, which is used to calculate seal energy for a given axial location of the damper. As can be seen, as B decreases and approaches B_l, the lock-up amplitude, Q tends to increase in a quadratic fashion. As B increases above B_l in value, Q tends to be linearly related. Therefore, if $B_{\text{damped,actual}}$ is less than the assumed B, Q will be higher, but infinite life will be achieved. If $B_{\text{damped,actual}}$ is greater than the assumed B, the design does not meet design requirements, and must be redesigned.

For the given circular optimum damper design, $x_1 = 7.5$ mm, $x_2 = 200.3$ mm, $x_3 = 1.0$, $x_4 = 0.700$, various damped amplitudes were assumed, and the corresponding Q values calculated. The results are presented in Fig. 9. Also shown are four randomly generated damper designs. The design variables chosen are summarized in Table 3. The results are similar for the rectangular damper. As can be seen, over the range of amplitudes shown, the optimum damper design still provides the lowest Q value.

Table 3 Random dampers

Trial	x_1 (mm)	x_2 (mm)	x_3	x_4
1	2.5	222.5	0.92	0.550
2	2.0	215.9	0.84	0.580
3	1.5	211.4	0.60	0.700
4	2.8	200.3	0.90	0.300

Only random damper #4 comes close to the optimum, but this is due to the fact that the optimum damper would be near lock-up for lower B values in this regime. If in fact, the locked-up amplitude for the optimum damper is converted back to a vibratory stress, it is seen that infinite life would result.

The important thing to note from the graph is that although the Q value for the optimal damper design is not expected to be attained when the hardware is manufactured, the optimum design will provide the maximum amount of dissipation possible for the given constraints. When hardware is produced, vibration tests can be performed to evaluate the actual reduction in vibratory amplitude.

Conclusions

It has been demonstrated that by using standard optimization techniques, it is possible to design an optimum split ring damper. For the test case presented, the optimum damper existed on the bounds of the design space for the circular damper, and near the boundary for the rectangular cross section. It is shown that the relative dissipation ratio, Q, is a valid metric for comparison of candidate designs, since the damper selected based on Q evaluated for some assumed amplitude would also be the optimum for any other reasonable amplitude of response. Using the optimization technique increases the likelihood that the vibrational amplitude will be reduced to an acceptable level, since no other damper design, subject to these constraints, can provide greater dissipation than the optimum design.

References

1 Alford, J. S., "Nature, Causes, and Prevention of Labyrinth Air Seal Failures," *Journal of Aircraft*, Vol. 12, No. 4, 1975, pp. 313–318.

2 Alford, J. S., "Protection of Labyrinth Seals From Flexural Vibration," ASME JOURNAL OF ENGINEERING FOR POWER, Vol. 86, 1964, pp. 141–148.

3 Alford, J. S., "Protecting Turbomachinery From Unstable and Oscillatory Flows," ASME JOURNAL OF ENGINEERING FOR POWER, Vol. 89, 1967, pp. 513–528.

4 Alford, J. S., "Dimensional Stability and Structural Integrity of Labyrinth Seals," Paper No. 660048, *SAE Transactions*, Vol. 75, 1966.

5 Vanderplaats, G. N., *Numerical Optimization Techniques for Engineering Design With Applications*, Chaps. 3, 5, McGraw-Hill, New York, 1984.

6 Gabriele, G. A., and Ragsdelle, K. M., *OPTLIB: An Optimization Program Library User's Manual*, University of Missouri—Columbia, Design Productivity Center, Columbia, MO, 1984.

Lyapunov's Stability of Nonlinear Misaligned Journal Bearings

P. G. Nikolakopoulos

C. A. Papadopoulos

Department of Mechanical Engineering,
University of Patras,
Patras, Greece

In this paper the stability of nonlinear misaligned rotor-bearing systems is investigated, using the Lyapunov direct method. A finite element formulation is used to determine the journal bearing pressure distribution. Then the linear and nonlinear stiffness, damping, and hybrid (depending on both displacement and velocity) coefficients are calculated. A general method of analysis based on Lyapunov's stability criteria is used to investigate the stability of nonlinear misaligned rotor bearing systems. The equations of motion of the rigid rotor on the nonlinear bearings are used to find a Lyapunov function using some of these coefficients, which depend on L/D ratio and the misalignment angles ψ_x, ψ_y. *The analytical conditions for the stability or instability of some examined cases are given and some examples for the orbital stability are also demonstrated.*

1 Introduction

It is well known that in the rotor-bearing dynamic phenomena, the fluid film of the journal bearing under large-amplitude vibrations introduces nonlinear forces. Neglecting these forces introduces significant error. In such cases linear theory typically predicts vibration amplitudes larger than the bearing clearances. Furthermore, important vibration phenomena, such as subharmonic resonance and instability limit cycles, are ''filtered out'' of the linear differential equations of the problem, thus giving fault predictions. On the other hand, in the nonlinear models, the problems of stability and instability are better posed.

An investigation of stability behavior of rigid rotors supported on plain cylindrical bearings is important for a reliable bearing design. The dynamic stability of a rotor bearing system, including nonlinearities, is a problem that has attracted attention for some time. Many theoretical and experimental investigations have been done in which the stability of rotor bearing systems is examined. Dimarogonas [1] presented a general method for stability analysis of rotating shafts using a continuous rotor with any number of discontinuities and linear and nonlinear forces. Some stability charts from experimental investigations of linear stiffness and damping coefficients are given by Glienicke [2]. The stability of a rigid rotor in oil journal bearings including the effect of elastic distortion in the bearing liner is investigated by Majumdar et al. [3]. Crosby [4] investigated the stability of a rigid rotor in rapture finite journal bearings, using numerical methods and solving the nonlinear equations of motion. The stability of oil whirl and whip in rotor-bearing systems is investigated by Muszynska [5, 6], using experimental and analytical techniques. Parszewski and Krynicki [7] presented the method for rotor bearing system stability using the bearing shape function presentation. Ogrodnik et al. [8] examined the stability of a rigid rotor with varying degrees of static journal-bush misalignment. They gave orbits in which the effect of static and dynamic misalignment in the system stability is presented. A general method of analysis based on Lyapunov's direct method for studying the dynamic stability of elastic rotor linear bearing systems was proposed by El-Marhomy and Schlack [9].

The stability of nonlinear bearing system, solving numerically the equations of motion, is presented by Hashish et al. [10]. Some orbits with different initial conditions are plotted and stability diagrams are also presented. Adams [11] developed a general analysis to simulate steady-state and transient vibration phenomena of complex rotor-bearing support systems. Orbits for some nonlinear cases are presented. Crooijmans et al. [12] presented an analysis of the self-excited vibrations of a rotor carried in cylindrical bearings.

As for aligned linear journal bearing, eight dynamic coefficients (four stiffness and four damping) are used. When misalignment occurs, 32 linear coefficients are introduced, which relate the force or moment with displacement or rotation. These 32 linear coefficients were calculated by Pafelias [16] where the effect of the journal misalignment on the journal-bearing dynamics was examined. The present paper is extended to nonlinear cases, where the dynamic coefficients, as it will be seen, are much larger. In detail one could follow this extension in [13].

Bannister [17] investigated the nonlinearities into a partial journal bearing using experimental and numerical techniques. In his analysis the misalignment effects are also included.

The purpose of this paper is to present the effects of misalignment on both the dynamic coefficients and the stability of nonlinear journal-bearing systems, giving analytical conditions for this stability. This is done by modeling the system as a continuous rigid rotor mounted on misaligned bearing with various nonlinear coefficients using the sense of Lyapunov that defines the stability of stationary equilibrium position. With the method presented one could conclude for the stability of an analogue system without solving the equations of motion. These stability criteria are tested by comparing with stability regions found in the sense of Poincaré, which defines the orbital stability. In this paper also the stability is examined using the hybrid coefficients introduced and defined in [13].

2 Reynolds Equation

Let us consider a journal bearing with geometric characteristics as shown in Fig. 1, with laminar flow incompressible oil film and constant viscosity of the lubricant. Neglecting the body forces, and the variation of the pressure across the film thickness, and considering a no-slip condition at the Newtonian fluid and the solid interface, the Reynolds equation takes the form,

$$\nabla \cdot \left(\frac{h^3}{12\mu} \nabla P \right) = \nabla \cdot [h\bar{U}] - V \qquad (1)$$

where μ is the lubricant viscosity, $P = P(\theta, z)$ is the unknown pressure distribution, and $h = h(\theta, z)$ is the oil film thickness, given by the following expression for a misaligned journal:

Contributed by the International Gas Turbine Institute and presented at the 39th International Gas Turbine and Aeroengine Congress and Exposition, The Hague, The Netherlands, June 13–16, 1994. Manuscript received by the International Gas Turbine Institute February 4, 1994. Paper No. 94-GT-72. Associate Technical Editor: E. M. Greitzer.

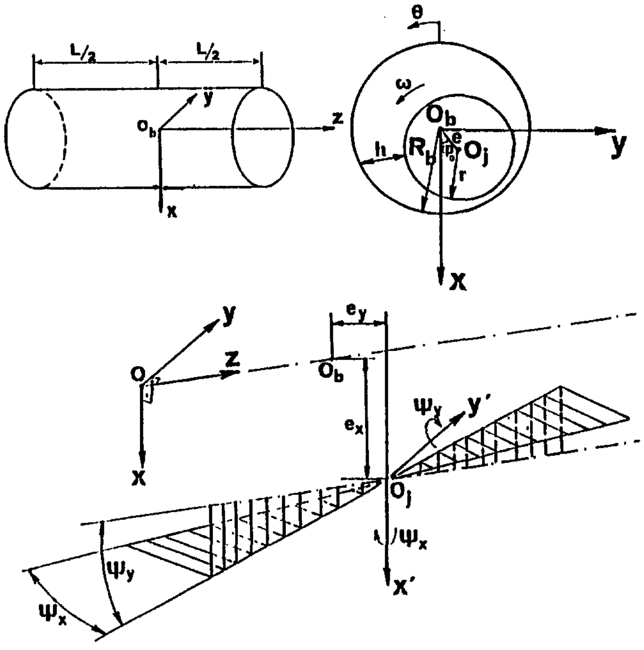

Fig. 1 Geometry of the journal bearing

$$h(\theta, z) = c + e_0 \cos \theta + z[\psi_y \cos(\theta + \varphi_0) + \psi_x \sin(\theta + \varphi_0)] \quad (2)$$

where ψ_x and ψ_y are the misalignment angles (Fig. 1).

In Eq. (1) in the case of an immobile bearing, $2\bar{U} = U\hat{\imath} + V\hat{\jmath}$. For steady-state bearing operation the velocities have the values $V = 0$ and $U = \omega r$ (where ω is the angular velocity) and for dynamic loading V and U are given by the equations:

$$V = \dot{x} \cos(\theta + \varphi_0) + \dot{y} \sin(\theta + \varphi_0) + z[\dot{\psi}_y \cos(\theta + \varphi_0) + \dot{\psi}_x \sin(\theta + \varphi_0)]$$

$$U = \omega r - \dot{x} \sin(\theta + \varphi_0) + \dot{y} \cos(\theta + \varphi_0) + z[-\dot{\psi}_y \sin(\theta + \varphi_0) + \dot{\psi}_x \cos(\theta + \varphi_0)] \quad (3)$$

where $\dot{x}$ and $\dot{y}$ are the velocities of the journal center. For an aligned bearing, the rotational velocities $\dot{\psi}_x$ and $\dot{\psi}_y$ are equal to zero. For the expression of U in Eq. (3) the velocities $\dot{x}$, $\dot{y}$, $\dot{\psi}_x$, $\dot{\psi}_y$ are very small compared with ωr and could be neglected.

Thus a finite element algorithm, using linear triangular elements, was programmed to solve the Reynolds equation based on Huebner formulation [14]. In this formulation the true pressure distribution in an incompressible lubricant film minimizes the discretized power functional,

$$I(P) = \int_A \left[\left(\frac{h^3}{24\mu} \nabla P - h\bar{U} \right) \cdot \nabla P \right] dA + \int_{s_q} Qpds \quad (4)$$

where $Q = h(\bar{U} - (h^2/12\mu)\Delta P) \cdot \hat{m}$.

In its discretized form, the problem is solved by minimizing the system functional (4) with respect to the unknown (generally interior) nodal pressures subjected to the no-negativity constraint(s),

$$p \geq 0 \quad (5)$$

This is a simple cavitation algorithm suitable for the simple linear triangular finite element used. Other cavitation algorithms require other finite elements, like four or eight-node quadrilateral elements. But a major disadvantage with elements other than the triangle is that closed integration over the element may not be possible. Thus numerical integration by Gaussian quadrature or some other algorithms becomes necessary. This entails extra computation time, and the resulting improvement in accuracy may not always warrant the more elaborate procedure. Clearly, for coarser meshes the solution becomes too inaccurate, and for finer meshes there is little change in the results obtained.

For a given external loading condition, the static equilibrium position of the journal center can be found by equating the hydrodynamic forces with externally applied load. A two-dimensional Newton–Raphson search technique is applied for the calculation of the equilibrium position of the journal center when the sum of the hydrodynamic forces F_{hydr} and the external loads F_{ext} equals to zero.

$$\sum (F_{\text{hydr}} + F_{\text{ext}}) = 0 \quad (6)$$

A 27 × 9 finite element grid with linear triangular elements was used for the solution. The model consists of a rotor with diameter $D = 0.0254$ m, radial clearance $c = 63.5$ μm, angular velocity $\omega = 1256$ rad/s, and viscosity $\mu = 0.012$ Pa·s.

3 Dynamic Coefficients

The hydrodynamic forces, in the general case that biplanar misalignment occurred, in the two main directions depend on the displacements, the rotations, and the respective velocities:

$$F_x = F_x(x, y, \psi_x, \psi_y, \dot{x}, \dot{y}, \dot{\psi}_x, \dot{\psi}_y)$$
$$F_y = F_y(x, y, \psi_x, \psi_y, \dot{x}, \dot{y}, \dot{\psi}_x, \dot{\psi}_y) \quad (7)$$

Analogue expressions are used for the moments produced by the misalignment. It is obvious that in the linear case there are 16 elastic and 16 damping coefficients. The expansion of the expressions (7) and those of moments applying Taylor series gives 32 linear and many more nonlinear coefficients, which depend on displacements, linear rotations, and angular velocities, and their combinations. These coefficients could be calculated doing linear and rotational perturbations on a steady running condition simultaneously. In small perturbations the equivalent (sum of linear and nonlinear) coefficients K^{eq}, C^{eq}, and A^{eq} converge in the linear coefficient values and for bigger perturbations these coefficients have a variance that depends on the geometry and the operation conditions of the problem.

In Fig. 2 the calculated linear dimensionless stiffness and damping coefficients are compared with those of Bannister [17] for 120 deg partial journal bearing. As one could observe there is good agreement. To test the nonlinear coefficients it is more informative to examine the orbits produced.

Eight linear coefficients relating the force displacement and velocity are produced by expression (7). Their aligned values differ from misaligned values as the misalignment angles are changed in one plane $\psi_x \neq 0$ or $\psi_y \neq 0$, or in two planes $\psi_x \neq 0$ and $\psi_y \neq 0$.

A hybrid term is defined as the partial derivative of the force in respect with both displacement and velocity. The importance of all stiffness, damping, and hybrid coefficients is not the same. Some of them give substantial contribution to the force (as the relating force displacement) but some other do not (as the relating force rotation). The number of nonlinear coefficients produced by these expressions is very large. These coefficients could be calculated using this analysis but could not be presented in this paper due to their large number so some of the most important are selected and presented.

Applying third-order Taylor's series to force expressions, keeping the above-mentioned important terms and neglecting those with sum of superscripts bigger or equal to four, Eq. (8) is obtained, for the forces in the x and y directions, respectively,

$$F = K^{eq}_{Fx} \Delta x + K^{eq}_{Fxy} \Delta x \Delta y + K^{eq}_{Fy} \Delta y + C^{eq}_{F\dot{x}} \Delta \dot{x} + C^{eq}_{F\dot{x}\dot{y}} \Delta \dot{x} \Delta \dot{y} + C^{eq}_{F\dot{y}} \Delta \dot{y} + A^{eq}_{Fx\dot{x}} \Delta x \Delta \dot{x} + A^{eq}_{Fx\dot{y}} \Delta x \Delta \dot{y} + A^{eq}_{Fy\dot{y}} \Delta y \Delta \dot{y} + A^{eq}_{Fy\dot{x}} \Delta y \Delta \dot{x} \quad (8)$$

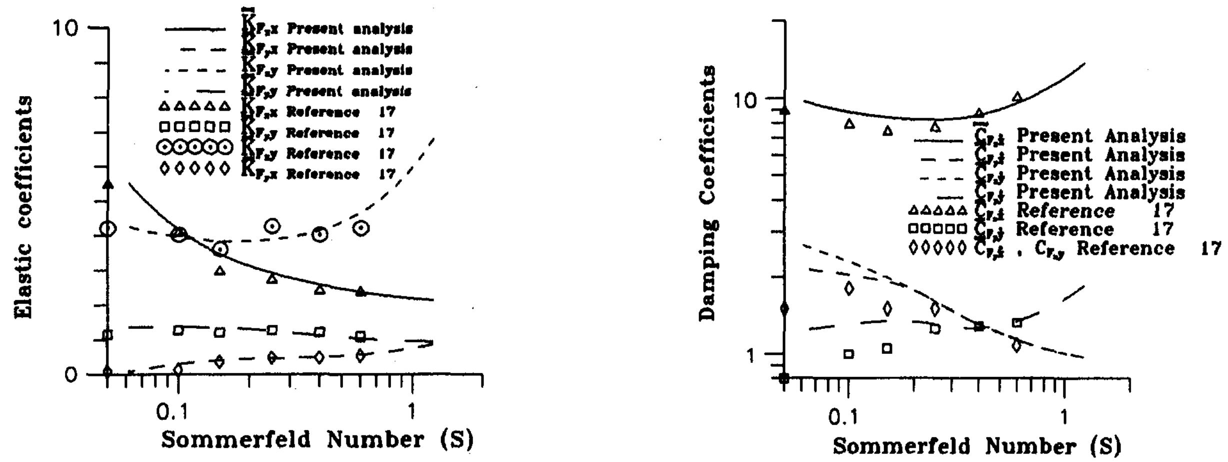

Fig. 2 **Comparison of the stiffness and damping coefficients calculated using the described algorithm with the corresponding results of the sited reference**

where F stands for F_x or F_y, K, C, and A are the stiffness, damping, and hybrid coefficients, and

$$K^{eq}_{Fx} = K_{Fx} + K_{Fx^2}\Delta x + K_{Fx^3}\Delta x^2$$

$$K^{eq}_{Fxy} = K_{Fxy} + K_{Fx^2y}\Delta x + K_{Fxy^2}\Delta y$$

$$K^{eq}_{Fy} = K_{Fy} + K_{Fy^2}\Delta y + K_{Fy^3}\Delta y^2$$

$$C^{eq}_{F\dot{x}} = C_{F\dot{x}} + C_{F\dot{x}^2}\Delta\dot{x} + C_{F\dot{x}^3}\Delta\dot{x}^2$$

$$C^{eq}_{F\dot{x}\dot{y}} = C_{F\dot{x}\dot{y}} + C_{F\dot{x}^2\dot{y}}\Delta\dot{x} + C_{F\dot{x}\dot{y}^2}\Delta\dot{y}$$

$$C^{eq}_{F\dot{y}} = C_{F\dot{y}} + C_{F\dot{y}^2}\Delta\dot{y} + C_{F\dot{y}^3}\Delta\dot{y}^2$$

$$A^{eq}_{Fx\dot{x}} = A_{Fx\dot{x}} + A_{Fx^2\dot{x}}\Delta x + A_{Fxy\dot{x}}\Delta y + A_{Fx\dot{x}^2}\Delta\dot{x} + A_{Fx\dot{x}\dot{y}}\Delta\dot{y}$$

$$A^{eq}_{Fx\dot{y}} = A_{Fx\dot{y}} + A_{Fx^2\dot{y}}\Delta x + A_{Fxy\dot{y}}\Delta y + A_{Fx\dot{x}\dot{y}}\Delta\dot{x} + A_{Fx\dot{y}^2}\Delta\dot{y}$$

$$A^{eq}_{Fy\dot{y}} = A_{Fy\dot{y}} + A_{Fxy\dot{y}}\Delta x + A_{Fy^2\dot{y}}\Delta y + A_{Fy\dot{x}\dot{y}}\Delta\dot{x} + A_{Fy\dot{y}^2}\Delta\dot{y}$$

$$A^{eq}_{Fy\dot{x}} = A_{Fy\dot{x}} + A_{Fxy\dot{x}}\Delta x + A_{Fy^2\dot{x}}\Delta y + A_{Fy\dot{x}^2}\Delta\dot{x} + A_{Fy\dot{x}\dot{y}}\Delta\dot{y}$$

The subscript of the coefficients means differentiation of F_x or F_y by the rest of the subscript. Some of the nonlinear coefficients are calculated and presented in Fig. 3 versus the misalignment angles. In Figs. 2 and 3 all coefficients are in dimensionless form (with bar), where,

$$\bar{k}_{F_ix_j} = k_{F_ix_j}\frac{c}{W} \quad \bar{C}_{F_i\dot{x}_j} = C_{F_i\dot{x}_j}\frac{c\omega}{W} \quad \bar{A}_{F_ix_j\dot{x}_j} = A_{F_ix_j\dot{x}_j}\frac{c^2\omega}{W}$$

$$\bar{k}_{F_ix_j^2} = k_{F_ix_j^2}\frac{c^2}{W} \quad \bar{C}_{F_i\dot{x}_j^2} = C_{F_i\dot{x}_j^2}\frac{c\omega^2}{W} \quad \bar{A}_{F_ix_j^2\dot{x}_j} = A_{F_ix_j^2\dot{x}_j}\frac{c^3\omega}{W}$$

$$\bar{k}_{F_ix_j^3} = k_{F_ix_j^3}\frac{c^3}{W} \quad \bar{C}_{F_i\dot{x}_j^3} = C_{F_i\dot{x}_j^3}\frac{c\omega^3}{W} \quad \bar{A}_{F_ix_j\dot{x}_j^2} = A_{F_ix_j\dot{x}_j^2}\frac{c^3\omega^2}{W}$$

and c is radial clearance, W is the external load, and ω the angular velocity. The misalignment angles are also in the form.

In Fig. 3 some dimensionless second and third-order nonlinear terms versus misalignment angles $\bar{\psi}_x = \psi_x L/c$ and $\bar{\psi}_y = \psi_y L/c$, for Sommerfeld numbers $S = 0.0929$ and $S = 0.639$, are presented. These coefficients are used for the Lyapunov stability. The signs play an important role in the state of stability.

4 Stability in the Sense of Lyapunov

The model consists of a rigid rotor of mass m supported by a nonlinear misaligned bearing. As it was mentioned by Nikolakopoulos and Papadopoulos [13] there are many nonlinear terms in the case of misaligned rotor bearing systems. A general Lyapunov function should include all these coefficients, which appear in equations for F_x and F_y. To find such a general function is a very difficult task, if not impossible. Lyapunov in his book [15] deals with special cases, named critical cases. So this method can be applied in this problem for critical cases. Each critical case includes some nonlinear terms. Which nonlinear term is to be used depends on the importance of the term on the specific problem and the limitations to find a suitable Lyapunov function. In this paper only the terms of odd order with hybrid terms are used in order to investigate the stability in the large using the second method of Lyapunov.

First Case. Let us consider the nonlinear bearing model, which after naming $x_1 = x$, $x_2 = \dot{x}$, $x_3 = y$, $x_4 = \dot{y}$ can be described by the matrix equation,

$$\begin{Bmatrix} \dot{x}_1 \\ \dot{x}_2 \\ \dot{x}_3 \\ \dot{x}_4 \end{Bmatrix} = \begin{bmatrix} 0 & 1 & 0 & 0 \\ -\dfrac{k_{F_xx}}{m} & -\dfrac{c_{F_x\dot{x}}}{m} & 0 & 0 \\ 0 & 0 & 0 & 1 \\ 0 & 0 & -\dfrac{k_{F_yy}}{m} & -\dfrac{c_{F_y\dot{y}}}{m} \end{bmatrix} \begin{Bmatrix} x_1 \\ x_2 \\ x_3 \\ x_4 \end{Bmatrix} + \frac{1}{m}\begin{Bmatrix} 0 \\ -k_{F_xx^3}x_1^3 \\ 0 \\ -k_{F_yy^3}x_3^3 \end{Bmatrix} \tag{9}$$

Let consider also the Lyapunov function V and his time derivative in the form,

$$V = ax_1^4 + bx_1^2 + c'x_2^2 + dx_3^4 + ex_3^2 + fx_4^3$$

$$\dot{V} = 4ax_1^3\dot{x}_1 + 2bx_1\dot{x}_1 + 2c'\dot{x}_2x_2 + 4dx_3^3\dot{x}_3 + 2ex_3\dot{x}_3 + 2fx_4\dot{x}_4 \tag{10}$$

where a, b, c', d, e, and f are all positive numbers.

From Eqs. (9) and (10) the final expressions of V and $\dot{V}$ are obtained,

$$V = \frac{c'}{2}\frac{k_{F_xx^3}}{m}x_1^4 + c'\frac{k_{F_xx}}{m}x_1^2 + c'x_2^2 + \frac{f}{2}\frac{k_{F_yy^3}}{m}x_3^4 + f\frac{k_{F_yy}}{m}x_3^2 + fx_4^2$$

$$\dot{V} = -2\left(c'\frac{c_{F_x\dot{x}}}{m}x_2^2 + f\frac{c_{F_y\dot{y}}}{m}x_4^2\right) \tag{11}$$

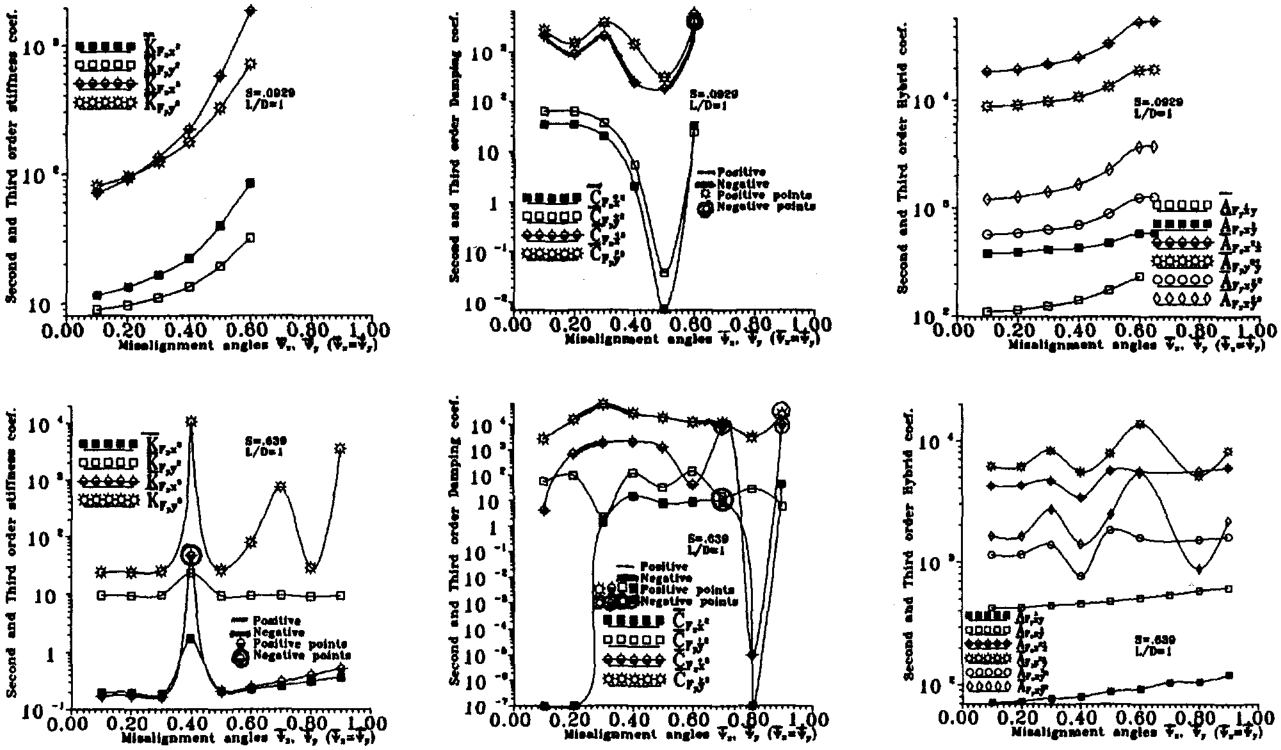

Fig. 3 Nonlinear stiffness, damping and hybrid coefficients, of a misaligned journal bearing for $S = 0.0929$ and $S = 0.639$, with $L/D = 1$

The function V could be taken as a Lyapunov function because it is a real continuous function $V(\bar{x})$, $\bar{x} = \{x_1, x_2, x_3, x_4\}$ possessing continuous first partial derivatives with respect to the variables $\bar{x}$ and $V(\bar{x}) > 0$ if $K_{F_x x}$, $K_{F_x x^3}$, $K_{F_y y}$, $K_{F_y y^3}$ are positive in a domain of interest $\forall(\bar{x}) \neq 0$ and $V(\bar{0}) = 0$. Also the time derivative of V could be written as $\dot{V} = dV/dt = \sum_{i=1}^{m} (dV/dx_i)(dx_i/dt) = \nabla V \cdot \dot{X}$, where ∇V is the gradient of the scalar function V and X could be displacement or velocity. The stability of the system depends on positive or negative definiteness of the function $\dot{V}$. If the function V is positive definite ($V > 0$) and $\dot{V} < 0$ because $c', f, c_{F_x \dot{x}}, c_{F_y \dot{y}}$ are positive constants, the nonlinear system (9) is asymptotically stable. If the definiteness of V and $\dot{V}$ cannot be found then the method with Lyapunov functions cannot give an answer for the stability of the system. In this case the stability for the nonlinear system could be examined in the sense of Poincaré or orbital stability, by solving the equations.

Second Case. Let consider the nonlinear model:

$$\begin{Bmatrix} \dot{x}_1 \\ \dot{x}_2 \\ \dot{x}_3 \\ \dot{x}_4 \end{Bmatrix} = \begin{bmatrix} 0 & 1 & 0 & 0 \\ -\dfrac{k_{F_x x}}{m} & -\dfrac{c_{F_x \dot{x}}}{m} & 0 & 0 \\ 0 & 0 & 0 & 1 \\ 0 & 0 & -\dfrac{k_{F_y y}}{m} & -\dfrac{c_{F_y \dot{y}}}{m} \end{bmatrix} \begin{Bmatrix} x_1 \\ x_2 \\ x_3 \\ x_4 \end{Bmatrix}$$

$$+ \frac{1}{m} \begin{Bmatrix} 0 \\ -k_{F_x x^3} x_1^3 - c_{F_x \dot{x}^3} x_2^3 - A_{F_x x^2 \dot{x}} x_1^2 x_2 \\ 0 \\ -k_{F_y y^3} x_3^3 - c_{F_y \dot{y}^3} x_4^3 - A_{F_y y^2 \dot{y}} x_3^2 x_4 \end{Bmatrix} \quad (12)$$

The Lyapunov function V and his time derivative are:

$$V = \frac{c'}{2} \frac{k_{F_x x^3}}{m} x_1^4 + c' \frac{k_{F_x x}}{m} x_1^2 + c' x_2^2 + \frac{f}{2} \frac{k_{F_y y^3}}{m} x_3^4 + f \frac{k_{F_y y}}{m} x_3^2 + f x_4^2$$

$$\begin{aligned} \dot{V} &= -2c' \left(\frac{c_{F_x \dot{x}}}{m} + \frac{c_{F_x \dot{x}^3}}{m} x_2^2 + \frac{A_{F_x x^2 \dot{x}}}{m} x_1^2 \right) x_2^2 \\ &\quad - 2f \left(\frac{c_{F_y \dot{y}}}{m} + \frac{c_{F_y \dot{y}^3}}{m} x_4^2 + \frac{A_{F_y y^2 \dot{y}}}{m} x_3^2 \right) x_4^2 \\ &= -2c' \lambda_3(x_1, x_2) x_2^2 - 2f \lambda_4(x_3, x_4) x_4^2 \\ &= -2c'(\lambda_3) x_2^2 - 2f(\lambda_4) x_4^2 \end{aligned} \quad (13)$$

If $\lambda_3(x_1, x_2) > 0$ and $\lambda_4(x_3, x_4) > 0$ then the system (12) is asymptotically stable, if $\lambda_3(x_1, x_3) < 0$ and $\lambda_4(x_3, x_4) < 0$ then is unstable and if $\lambda_3(x_1, x_2) = 0$ and $\lambda_4(x_3, x_4) = 0$ then the system is stable. The sign of the quadratic $\lambda(x)$ functions is examined using Sylvester's theorem. In case the signs of the polynomials λ_2, λ_3 are opposite then the method with Lyapunov functions cannot give answer for the stability. The function given by Eq. (10) is the general Lyapunov function for nonlinear systems with odd order of nonlinear terms and without coupled terms. All these nonlinear systems are solved numerically and examined for their stability in the sense of Poincaré.

In Fig. 4(a) the orbit coming from the solution of the nonlinear system (9) is plotted. It is observed that there is a good agreement between Lyapunov and Poincaré concerning the system stability. Figure 4(c) represent stable solution for system (12).

In Fig. 4(b) an unstable solution for the system (12) is obtained. The values of the nonlinear terms in systems (9) and (12) are taken from Fig. 3.

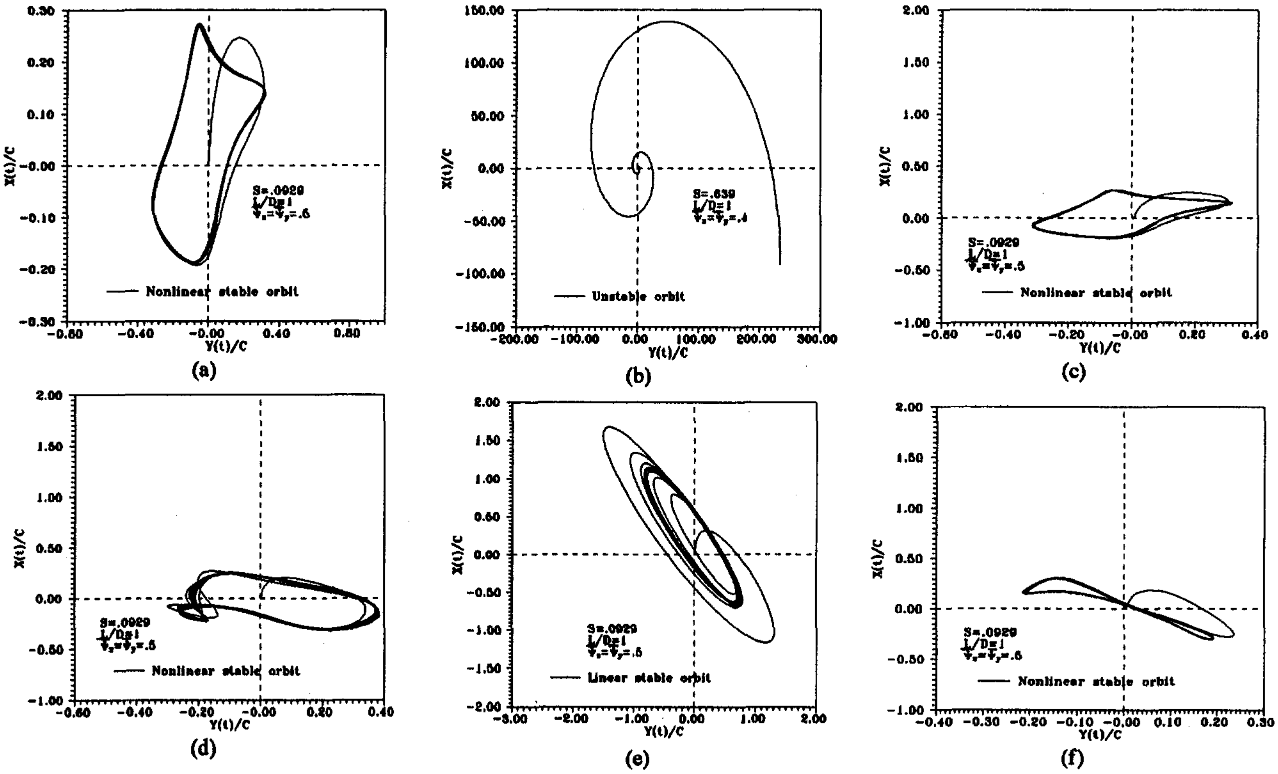

Fig. 4 Linear and nonlinear orbits

5 System Response and Orbital Stability

In this paragraph the effects of the nonlinear coefficients on the dynamic system response, using expression (8) for F_x and F_y, are investigated. In the results paragraph the journal center orbit and the response spectra are presented for some cases of misaligned rotor bearing systems. The nonlinear equations of motion are:

$$m\ddot{x} + F_x = W + F_x(t)$$

$$m\ddot{y} + F_y = F_y(t) \qquad (16)$$

where W is the static load and $F_x(t)$, $F_y(t)$ are the unbalance forces. This system of differential equations is solved numerically using the Runge–Kutta fourth order, with time step dt = 0.0001 s. This analysis is used to find the orbit of the journal center and to conclude for the stability in Poincaré sense.

The true nonlinear simulation of the orbit of the center of the shaft claims the solution of the system (16) using the equations for the oil film forces. The orbits presented in Fig. 4 are plotted using that nonlinear coefficients, which give, according to the stability conditions found, stable or not systems. The initial conditions for all the cases presented in the results paragraph have zero values for the displacements and velocities. The initial conditions could have an effect on the stability of the nonlinear systems's changing the initial conditions, not only the shape of the orbit but also the state of the stability could be changed. This is a characteristic of chaotic systems.

In Fig. 4(d–f) the difference between the linearized and nonlinear systems is demonstrated. Comparing the linear and nonlinear orbits it is obvious that the linear analysis predicts vibration bigger than the clearance but the nonlinear theory predicts smaller vibrations $X(t)/c < 1$ and $Y(t)/c < 1$. In Fig. 5 spectrums for linear and nonlinear analysis are given. It can be observed that in the nonlinear spectrum appear more harmonics of higher order appear, as was expected.

6 Conclusions

The nonlinear stiffness, damping, and hybrid coefficients of a bearing are calculated using the present finite element formulation. The second theorem of Lyapunov is used for the stability analysis of nonlinear misaligned rotor-bearing systems. Some critical cases are examined. The basic feature of Lyapunov's second method is that stability is investigated without solving the system equations, saving calculation time. The analytical conditions of the stability could also be used for vibration control. The success of the method depends on the selection of the Lyapunov function. The choice of a suitable Lyapunov function is not always obvious and there is not general procedure for its generation. A Lyapunov function suitable for a specific system of differential equations may not be suitable for another system of equations.

The stability of a nonlinear rotor bearing system using Lyapunov functions depends on the sign of the nonlinear stiffness, damping, and hybrid terms. In the case where the positive or

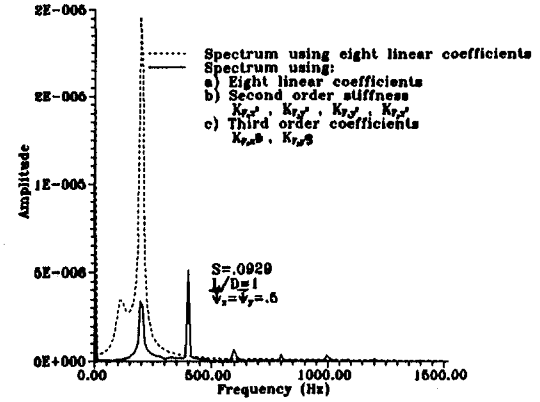

Fig. 5 Linear and nonlinear frequency-amplitude diagram

negative definiteness of the Lyapunov function and of his time derivative cannot be found, the method cannot be applied, and other stability methods have to be used.

Linear theory predicts journal to bearing vibration amplitudes larger than the bearing clearances. Nonlinear theories are more well posed for stability and instability problems.

References

1 Dimarogonas, A. D., "A General Method for Stability Analysis of Rotating Shafts," *Ingenieur-Archiv.*, Vol. 44, 1975, pp. 9–20.

2 Glienicke, J., "Experimental Investigation of the Stiffness and Damping Coefficients of Turbine Bearings and Their Application to Instability Prediction," *Proc. Inst. Mech. Eng.*, Vol. 181, Pt. 3 B, 1966–67.

3 Majumbar, B. C., Brewe, D. E., and Khonsari, M. M., "Stability of a Rigid Rotor Supported on Flexible Oil Journal Bearings," ASME *Journal of Tribology*, Vol. 110, 1988, pp. 181–187.

4 Crosby, W. A., "The Stability of Rigid Rotor in Rapture Finite Journal Bearings," *Wear*, Vol. 80, 1982, pp. 333–346.

5 Muszynska, A., "Stability of Whirl and Whip in Rotor/Bearing Systems," *Journal of Sound and Vibration*, Vol. 127(1), 1988, pp. 49–64.

6 Muszynska, A., "Whirl and Whip in Rotor/Bearing Systems Stability Problems," *Journal of Sound and Vibration*, Vol. 110(3), 1986, pp. 443–462.

7 Parszewski, Z. A., and Krynicki, K., "Rotor/Bearing Systems Stability: Composition Approach With Bearing Shape Function Presentation," *Tribology Transactions*, Vol. 32, 1989, No. 4, pp. 517–523.

8 Ogrodnik, P. J., Goodwin, M. J., and Penny, J. E. T., "The Effect of Translational and Conical Bearing Misalignment on the Response and Stability of a Non-linear Rotor Bearing System," in: *Vibration and Wear in High Speed Rotating Machinery*, 1990 Kluwer Academic Publishers, pp. 547–558.

9 El-Marhomy, Abd. Alla, and Schack, A. L., "Dynamic Stability of Elastic Rotor-Bearing System via Lyapynov's Direct Method," ASME *Journal of Applied Mechanics*, Vol. 58, 1991, pp. 1056–1063.

10 Hashish, E., Sankar, T. S., and Osman, M. O. M., "Finite Journal Bearing With Non-linear Stiffness and Damping. Part 2: Stability Analysis," ASME *Journal of Mechanical Design*, Vol. 104, 1982, pp. 406–411.

11 Adams, M. L., "Non-linear Dynamics of Flexible Multi-Bearing Rotors," *Journal of Sound and Vibration*, Vol. 71(1), 1980, pp. 129–144.

12 Crooijmans, M. T. M., Brouwers, H. J. H., Van Campen, D. H., and de Kraker, A., "Limit Cycle Predictions of Non-Linear Journal Bearing System," ASME *Journal of Engineering for Industry*, Vol. 112, 1990, pp. 168–171.

13 Nikolakopoulos, P. G., and Papadopoulos, C. A., "Nonlinearities in Misaligned Journal Bearings," *Tribology International*, Vol. 27(4), 1994, pp. 243–257.

14 Hubner, K. H., *The Finite Element Method for Engineers*, Wiley, New York, 1999.

15 Lyapunov, A. M., "Probleme General de la Stabilité du mouvement." Kharkov, 1892; Princeton University Press, Princeton, NJ, 1947.

16 Pafelias, T., "Solution of Certain Problems of Viscous Laminar Flow With Applications in Engineering Problems," PhD Thesis, Rensselaer Polytechnic Institute, Troy, NY, Jan. 1974.

17 Bannister, R. H., "Theoretical and Experimental Investigations Illustrating the Influence of Non-linearity and Misalignment on the Eight Oil Film Coefficients," *I. Mech. E*, 1976.

Nonlinear Behavior of a Magnetic Bearing System

L. N. Virgin

T. F. Walsh[1]

J. D. Knight

Department of Mechanical Engineering and
Materials Science,
Duke University,
Durham, NC 27708

This paper describes the results of a study into the dynamic behavior of a magnetic bearing system. The research focuses attention on the influence of nonlinearities on the forced response of a two-degree-of-freedom rotating mass suspended by magnetic bearings and subject to rotating unbalance and feedback control. Geometric coupling between the degrees of freedom leads to a pair of nonlinear ordinary differential equations, which are then solved using both numerical simulation and approximate analytical techniques. The system exhibits a variety of interesting and somewhat unexpected phenomena including various amplitude driven bifurcational events, sensitivity to initial conditions, and the complete loss of stability associated with the escape from the potential well in which the system can be thought to be oscillating. An approximate criterion to avoid this last possibility is developed based on concepts of limiting the response of the system. The present paper may be considered as an extension to an earlier study by the same authors, which described the practical context of the work, free vibration, control aspects, and derivation of the mathematical model.

Introduction

Magnetic bearings are under development for use in a number of practical applications (O'Connor, 1992) and offer compelling advantages in certain circumstances. However, they also present significant challenges to the designer of magnetic levitation systems for rotating shafts where rotor dynamic stability and robust vibration control are fundamental considerations (Nonami et al., 1990; Williams et al., 1991; Lee and Kim, 1992).

Hebbale (1985) illustrated several nonlinear aspects of magnetic bearings and examined the effects of coordinate coupling that arises from eddy currents during shaft rotation.

The present work examines the effects of coordinate coupling due to the geometry of the pole arrangement and the uneven flux distribution that results from nonconstant gaps when the shaft is displaced from the bearing center. These coupling forces arise even in the nonrotating case. In this work, the effects of eddy currents and other transient phenomena are neglected.

System Model

Consider the active magnetic bearing shown schematically in Fig. 1. Each magnet pair is independently subject to linear flux control, but the forces from the actuator include coordinate coupling. Experimental measurements were used to determine the relationship between principal and normal forces. Details of the form of this coupling can be found in Knight et al. (1993), together with the derivation of the equations of motion. In summary, it was found that the ratio of the attractive, on-axis force between each magnet and the shaft to the normal, off-axis force was proportional to the shaft displacement in the off-axis direction. For magnet 1, for instance,

$$F_x = \alpha x F_y \tag{1}$$

The principal force is modeled using one-dimensional magnetic circuit theory. Applying independent-axis control of flux, making the flux in each magnet equal to a steady bias flux plus a control flux

$$B_i = B_b + B_{i,c} \tag{2}$$

where the control flux is of equal magnitude but opposite sign in opposing magnets, i.e.,

$$B_{1,c} = -B_{3,c} \tag{3}$$

and is proportional to shaft displacement

$$B_{1,c} = -ky \tag{4}$$

The components of dimensionless force from all magnets acting together can be derived as

$$F_x = Kx - \frac{A}{2} x(1 + K^2 y^2) \tag{5a}$$

$$F_y = Ky - \frac{A}{2} y(1 + K^2 x^2) \tag{5b}$$

for the case of symmetric geometry and control, with no gravity loading.

It is important to note that in the absence of geometric coupling of x and y forces, this system would be entirely linear. The actual forces available from a magnet arrangement will contain additional nonlinearities, but these are neglected in the present analysis. Note also that an increase in the proportional gain does not diminish the magnitude of the coupling, but increases it.

These forces can be obtained from a potential energy function:

$$V = \left(\frac{K}{2} - \frac{A}{4}\right)(X^2 + Y^2) - \frac{A}{4} K^2 X^2 Y^2 \tag{6}$$

where the terms are given in the nomenclature section. A useful analogy is to consider the free behavior of the shaft akin to the motion of a small ball rolling on this potential energy surface as shown in Fig. 2. Three different values of the coupling parameter are used. Due to the coupling (the last term in Eq. (6)) these are *not* surfaces of revolution and it is precisely this apparently subtle feature that underlies much of the nonlinear behavior to be described later. If coupling and deflections are rela-

---

[1] Current address: Engineer, Blading Design Group, Power Generation Business Unit, Westinghouse Corp., Orlando, FL.

Contributed by the International Gas Turbine Institute and presented at the 39th International Gas Turbine and Aeroengine Congress and Exposition, The Hague, The Netherlands, June 13–16, 1994. Manuscript received by the International Gas Turbine Institute March 17, 1994. Paper No. 94-GT-341. Associate Technical Editor: E. M. Greitzer.

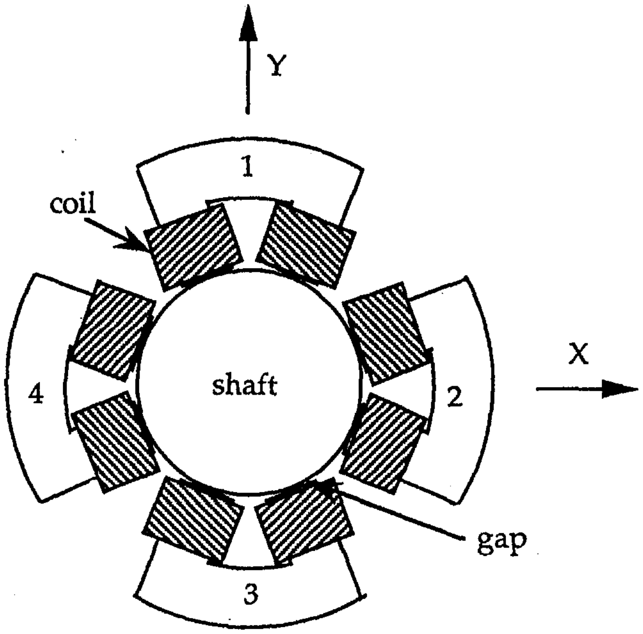

Fig. 1 Geometry of active magnetic bearing and shaft

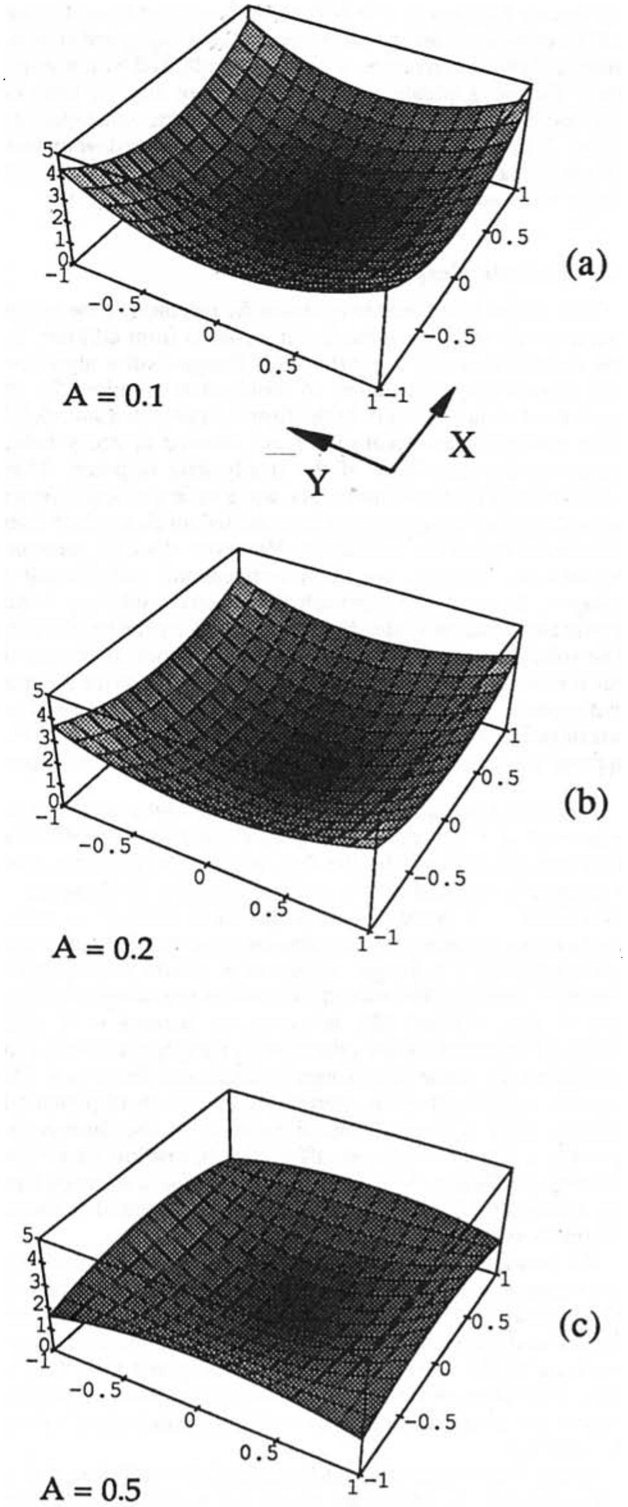

Fig. 2 Potential energy wells for different degrees of coupling A: 0.1, 0.2, 0.5 (K = 5.0)

tively strong then Fig. 2(*c*) indicates the possibility of trajectories "escaping" from the region locally surrounding the stable equilibrium (rest position). Although this "unstable in the large" type of behavior is less likely to occur for practical values of the system parameters (the shaft may hit the magnets), the potentially catastrophic nature of this event is given due consideration.

Derivative feedback control is also introduced and the subsequent actuator forces can be added to an unbalance forcing function, which finally results in dimensionless equations of motion of the form:

$$X'' = -\frac{1}{K}\left(KX + \Gamma X' - \frac{A}{2}X(1 + K^2Y^2 + 2K\Gamma YY' + \Gamma^2 Y'^2)\right) + E\Omega^2 \cos \Omega T \quad (7)$$

$$Y'' = -\frac{1}{K}\left(KY + \Gamma Y' - \frac{A}{2}Y(1 + K^2X^2 + 2K\Gamma XX' + \Gamma^2 X'^2)\right) + E\Omega^2 \sin \Omega T \quad (8)$$

where again the terms are given in the nomenclature section. The primes indicate differentiation with respect to dimensionless time T. These equations may be integrated in time after assigning values to the system parameters K, Γ, A and E, along with appropriate initial conditions for the state variables X, Y, X', and Y'. It should be noted that the forms of the forcing function in the final terms of Eqs. (7) and (8) also constitute initial conditions, in the form of an assumed phase angle for

Nomenclature

A = coupling parameter
B = flux, T
C, D, G, H = constants in the harmonic balance solution
E = eccentricity
F = force, N
K = stiffness (proportional feedback)
k = dimensional proportional feedback, T/m
V = potential energy
x, y = dimensional position, m
X, Y = nondimensional position
α = force proportionality constant, 1/m
Γ = damping (derivative feedback)
Ω = forcing frequency

the forcing function at $T = 0$. Initially, steady-state oscillations will be considered using both numerical simulation and approximate analytical techniques. This will be followed by a transient study focussing attention on initial behavior starting from the rest state. The catastrophic "escape" scenario corresponding to Fig. 2(c) with forcing is described including the development of a potentially useful approximate criterion for restricting the forces to avoid this possibility (Walsh, 1993).

Steady-State Response

Two methods are used to examine the response of the system to unbalance forcing: numerical integration from arbitrary initial conditions using a fourth-order Runge–Kutta algorithm; and approximate calculation of steady-state solutions by the harmonic balance method. In the former approach a sufficiently large number of transient cycles are allowed to decay before recording the magnitude of the steady-state response. These solutions may be considered exact, and a variety of sophisticated algorithms and fast computers have shifted much research interest toward numerical simulation. However, the data generated by such an approach are often cumbersome and difficult to interpret. In the latter approach the assumed solution is harmonic and hence only steady-state information can be obtained. The solutions are approximate (a series solution is truncated) but it is still useful to obtain a functional form for the solution that captures the essential response dependence on system parameters. Clearly it is useful to combine and compare these two approaches, and this is the path followed by the present paper.

Numerical Simulation. The effects of four parameters are examined: K, Γ, A, and E. The proportional control coefficient K determines how rapidly the flux, and thereby the force, from a magnet is reduced as the shaft approaches that magnet. A value of $K = 1$ would cause the flux to be reduced to zero at contact (not counting the contribution from the derivative control coefficient Γ). Larger values of K would correspond to "stiffer" bearings. Because of the form of non-dimensionalization of Eqs. (7) and (8), however, an increase in K while holding Γ constant causes a decrease in the effective dissipation coefficient, by virtue of a change in the natural frequency. This must be considered when interpreting the results of parametric studies, since a straightforward increase in the dimensional quantity k ($1/m$) would not affect the dissipation (derivative control) coefficient. The fact that K cannot be eliminated from the equations of motion is a result of the essential nature of nonlinear systems.

The measurements of Knight et al. (1992) indicate that 0.15 is a reasonable value for the coordinate coupling coefficient A. These measurements were made using an actuator geometry similar in size and clearance to those in present use in magnetic bearings. In the calculations below, A is varied from 0.05 to 0.25. The values of Γ were chosen to provide dissipation of the same order as in a linear system having damping ratios between 0.1 and 0.3.

Figure 3 shows the effect of increasing the coefficient K from 1.0 in part (a) to 3.0 in part (b) to 5.0 in part (c). As noted above, increasing K alone results in a smaller value of the derivative control coefficient. With this in mind, Fig. 3 indicates an important feature of the system: For some combinations of parameters, the response exhibits a split, with the motion on one axis having a much higher amplitude than that on the other axis. Associated with this split is a sudden jump in one of the amplitudes as the frequency is increased. In fact, one of the solutions of Fig. 3(c) extends beyond an eccentricity of 1.0, which in the physical case would result in solid contact. At some frequencies near the natural frequency, however, two solutions exist that are both within the physical bounds of the system. Furthermore, the solutions are dependent on the initial conditions. For the case shown, the integration begins with both shaft position and velocity equal to zero. The numerical integration proceeds until all transients have decayed and the peak amplitudes in the two directions are sampled. The forcing function, the final terms in Eqs. (7) and (8), also imposes an implicit initial condition by virtue of its assumed phase. In fact, the cosine portion of the forcing function begins with a step imposition of force at time $t = 0$, although all transients associated with this discontinuity have decayed before the amplitudes are sampled. Practically, loading of this sort might result from blade loss in a turbomachine. If, however, the cosine and sine parts of the force are exchanged, the solutions for X and Y are also found to have exchanged places. This dependence on phase or initial conditions is a characteristic of nonlinear systems.

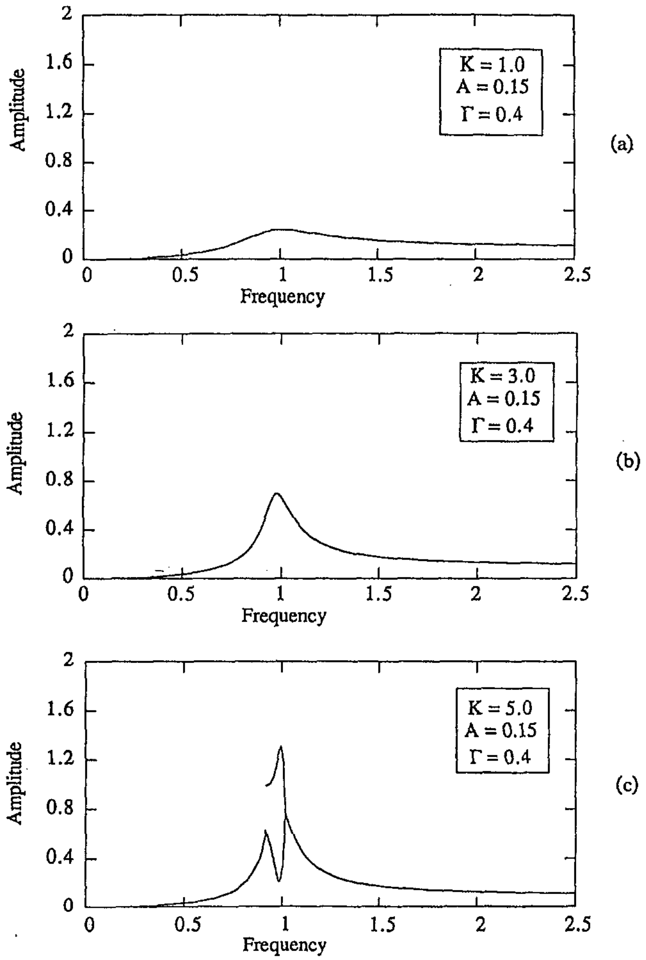

Fig. 3 Effect of variation in dimensionless proportional control coefficient K: 1.0, 3.0, 5.0 (A = 0.15, Γ = 0.4)

Figure 4(a) shows a typical time series of the X and Y displacements in the region where the symmetry of the response is broken. It is interesting to note that a linear response based on a paraboloid potential energy surface would have resulted in a phase lag of $\pi/2$ between the two responses, as well as equal amplitudes. This effect is seen more clearly in Fig. 4(b) where X and Y are plotted against each other, the phase projection of Fig. 4(c).

The effect of the coupling parameter can also be examined. Figure 5 illustrates the effect of increasing the value of A, while K is held constant at 0.3. The values of all parameters except A are equal to those of the case shown in Fig. 3(b). As A is increased beyond a threshold value, between 0.15 and 0.25, multiple solutions appear near the natural frequency. In this set of plots, the natural frequency is a constant, making this parametric variation somewhat easier to interpret than the previous one.

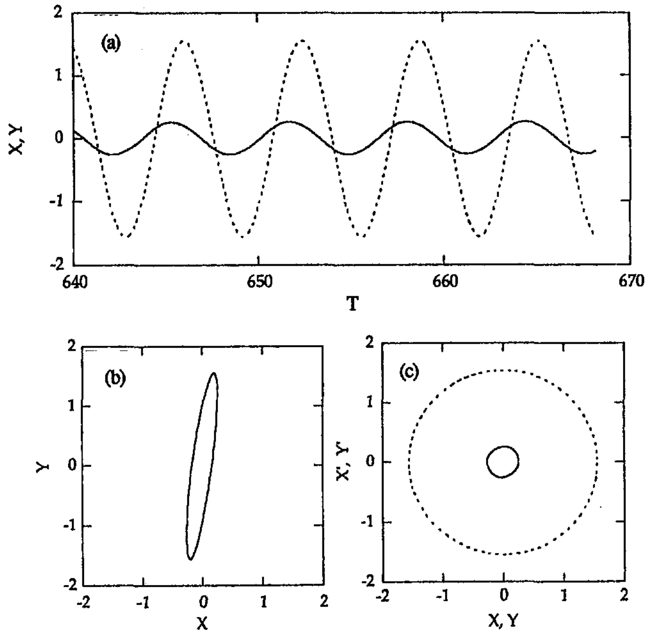

Fig. 4 Typical time series and phase projections of the coupled oscillation (K = 5.0, A = 0.15, Γ = 0.4, E = 0.1, Ω = 0.9925)

Reduction of the derivative control coefficient Γ can also bring about a situation with multiple solutions, as shown in Fig. 6, as can an increase of the unbalance eccentricity, not shown. The important practical implication of this type of loss of stability is that it may cause a sudden, discontinuous jump in the response.

Thus, the bifurcation seems mostly to be an amplitude-driven phenomenon, such that when a critical amplitude is exceeded, the solutions split. In all cases, the split is initial-condition-dependent. In some cases the split is followed by instability.

Solution by Harmonic Balance. The other approach to examining the steady-state response of a nonlinear system adopted in the present study is the harmonic balance method, which is approximate but analytical rather than numerical (Jordan and Smith, 1987; Virgin, 1988). It has the advantage that both stable and unstable solutions can be located, whereas numerical integration can locate only stable solutions.

The method consists of assuming steady solutions of the form

$$X = C \cos \Omega T + D \sin \Omega T \tag{9}$$

$$Y = G \cos \Omega T + H \sin \Omega T \tag{10}$$

where C, D, G, and H are to be determined. Equations (9) and (10) are differentiated and substituted into the equations of motion. The resulting powers of trigonometric functions are expanded using trig identities, after which the harmonics higher than 1 are neglected. Because the truncation of higher harmonics is not performed until after the powers of trig functions are expanded, the solution retains its nonlinear character, although the equations have been approximated. The resulting four algebraic equations for the constants C, D, G, and H are coupled and highly nonlinear and must themselves be solved by a numerical Newton–Raphson iteration. When the constants are found, the steady amplitudes can be calculated readily.

Figure 7 shows the amplitudes obtained by harmonic balance for the case corresponding to Fig. 6(a). These results indicate that in the neighborhood of the natural frequency, four solutions actually exist; two are identical. Two of the solutions are apparently unstable, but the harmonic balance method does not yield stability characteristics. Based on the results of numerical integration, however, it appears that the solutions corresponding to equal amplitudes for X and Y are unstable when they lie between the unequal solutions. Thus the jump in one of the amplitudes stems from a change in that solution's stability. Where the equal-amplitude solutions lie below the unequal solutions, they are the stable ones. The unequal solutions are believed to exist at all frequencies, but are difficult to locate by Newton–Raphson beyond the range that is shown.

The close correspondence between the numerical and analytical results supports the validity of both methods. Neither method alone is sufficient for a complete understanding, however, because the numerical solutions are dependent on initial conditions, and the analytical solutions provide no information on stability. Stability analyses based on Floquet theory and numerical path-following techniques will form the basis of future research.

Transient Response

In a typical linear dynamic system the natural period is a constant and steady-state amplitudes are independent of initial conditions, i.e., the response is unique. This is not necessarily the case for nonlinear systems, and Knight et al. (1993) have shown that for the system under consideration the natural period of the coupled, unforced, undamped system is a function of amplitude and interesting precession behavior is observed. For the forced nonlinear system the initial conditions determine which steady-state solution is picked up. Furthermore, in chaotic systems, this sensitivity to initial conditions is extreme with adjacent trajectories diverging exponentially (Jordan and Smith,

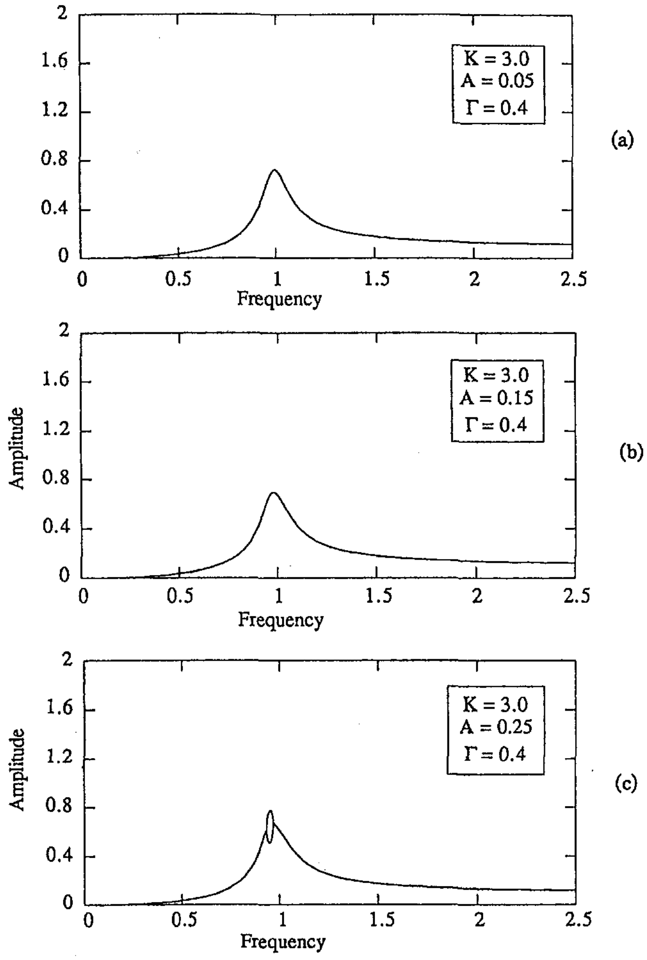

Fig. 5 Effect of variation in the coupling A: 0.05, 0.15, 0.25 (Γ = 0.4, K = 3.0)

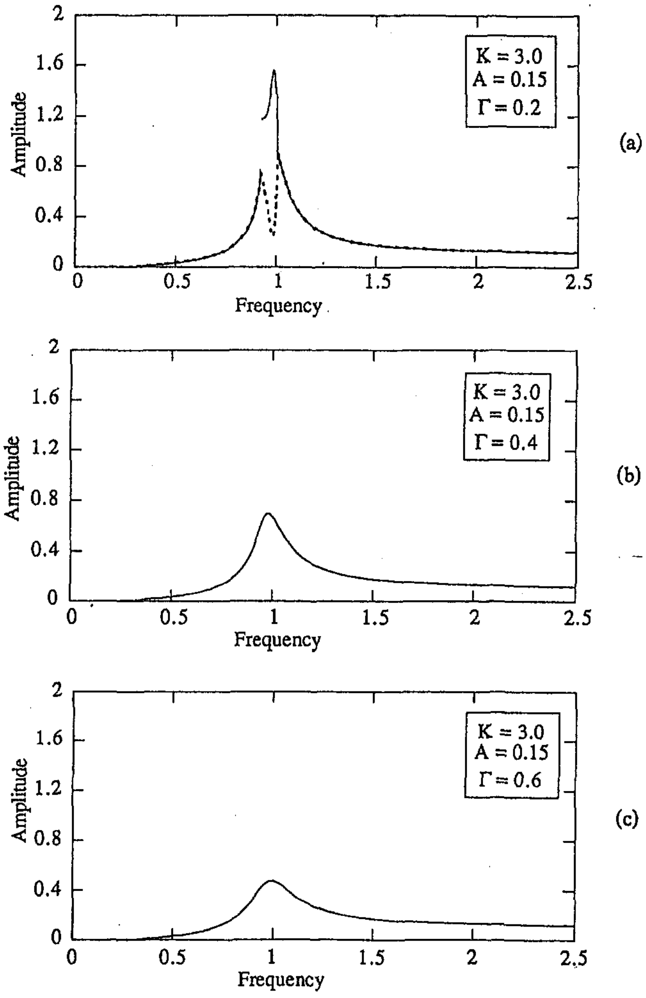

Fig. 6 Effect of variation in derivative control coefficient Γ: 0.2, 0.4, 0.6 (K = 3.0, A = 0.15)

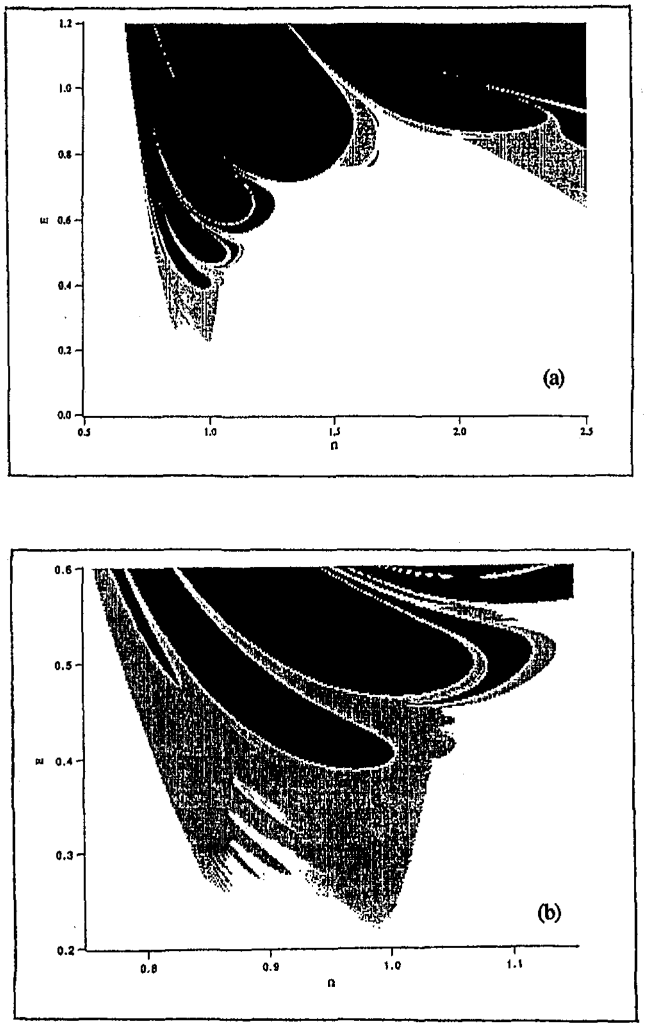

Fig. 8 Escape eccentricity versus escape frequency ratio (K = 3.0, A = 0.15, Γ = 0.2, E = 0.1); the lower figure is an enlargement

1987) even though the system is deterministic and the response bounded.

An interesting feature of this system is found for the forced case corresponding to Fig. 2(c). Suppose the system is started from rest. Applying the periodic force will result in transient behavior followed by one of two general outcomes. First, the system may settle into some kind of steady-state behavior, resulting in an oscillation of the form shown in Figs. 3–7. However, a second and more dramatic possibility occurs when the forcing is sufficiently large to cause "escape" from the potential energy well, i.e., enough energy is present in the system for the schematic ball to traverse the hilltop that surrounds the equilibrium point: The stiffness becomes negative. In a nonlinear system such as this the question of what constitutes "large" forcing is not as simple as it appears. Clearly, the greater the forcing magnitude (eccentricity E) the greater the response, and proximity to the resonant frequency is also likely to cause magnified response. The essentially nonlinear phenomenon of escape is captured by mapping the combinations of forcing parameters which lead to escape. This is shown in Fig. 8 for a grid of approximately 40,000 simulations. The initial conditions are zero displacement and velocity in both directions. The black areas indicate that starting from rest the solution escaped (to infinity) within 4 forcing cycles and the grey corresponds to escape between 4 and 100 cycles. The unshaded regions are those forcing parameter combinations that lead to steady-state behavior. The general dependence of escape on the forcing parameters is as expected; however, the boundaries between escape and no escape are fractal in nature, revealing self-similar behavior on finer and finer length scales (Walsh, 1993). A close up view of the resonance region is shown in Fig. 8(b).

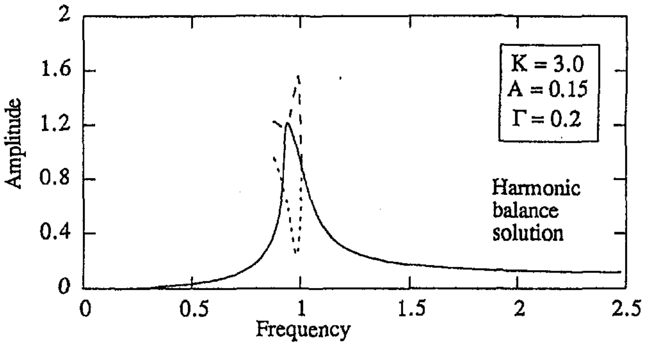

Fig. 7 Multiple coexisting solutions obtained using the harmonic balance method (K = 3.0, A = 0.15, Γ = 0.2)

An Approximate Criterion. It is tempting to try to establish a criterion such that escape is avoided. This type of behavior has been encountered in other physical systems with a softening spring nonlinearity and the following approach delineates regions of the forcing parameters as safe or unsafe according to an ad hoc analytical criterion, which can then be compared directly to the escape boundaries obtained using numerical simulation.

Returning to the approximate analytical solutions obtained using the harmonic balance method, it is relatively easy to recast the equations so that given a limiting displacement the combination of forcing parameters required to achieve this response can be identified, and plotting these boundaries in the parameter space the safe (below the boundary) and unsafe (above the boundary) regions can be obtained. This is shown in Fig. 9(*a*) where $K = 3$, $X_{\max} = 0.4$, $A = 0.15$, and Γ is varied as indicated. Figures 9(*b–d*) show similar plots where a different parameter has been varied while the others are kept fixed. In all cases the effects of the parameters on the escape characteristics are more or less as expected. Although these results are based on steady-state oscillation, by adjusting the maximum allowable displacement it is possible to ensure that the boundaries are below the exact transient results of Fig. 8. As expected the proximity to resonance has the greatest influence on the likelihood of escape. Similar approaches have also been developed based on limiting the maximum velocity or total energy of the response and various safety factors have been incorporated (Virgin, 1989; Virgin et al., 1992).

Conclusions

Equations of motion and limited parametric studies are presented for the case of a magnetic bearing subject to flux control, with geometric coordinate coupling. There are two effects of the coupling parameter on the system potential energy: a reduction of the principal stiffness, and introduction of a nonlinear normal stiffness.

The equations of motion are nonlinear and exhibit behavior that is distinctly different from that of linear systems. In forced response (rotating unbalance), the amplitudes of the system show bifurcations that are the result of changes in stability of multiple coexisting solutions. The stability seems mostly to be amplitude dependent, and the "critical" amplitude is a function of several parameters: K, Γ, E, and A. Under certain circumstances the system may lose all stability resulting in escape. An approximate criterion to avoid this possibility is introduced.

The practical consequences of the results presented here are significant to the design of magnetic bearing actuators and controllers. The bifurcations and the associated tendency to escape, which appear to be primarily amplitude-driven phenomena, are predicted to begin within the clearance of the auxiliary bearings typical of present magnetic bearing systems. The possible interaction of coordinate coupling with the additional nonlinearity involved in accidental contact with the auxiliary bearings is beyond the scope of the present work, but should be pursued further. The discontinuities are especially likely to cause difficulty when there is a sudden change in parameters, which could result from large unbalance due to blade loss or other failure, a sudden amplitude shift due to base motion or step changes in bearing force associated with temporary control interruption. It is likely that most of these effects could be removed or compensated for if the control of axes were coupled appropriately. To the authors' knowledge, this is not being done in practice because it requires more complex control algorithms and/or additional circuitry. Because the nonlinear effects explored here all arise from the geometric coupling in the bearing actuator, the design of the actuator is of extreme importance. The independent horseshoe design used in this paper is one of two widely used geometries, the other consisting of a series of pole pairs extending inward from a continuous backing ring. The second geometry may be found to be preferable, but additional measurements are needed to determine the level of coupling to be expected there. It should not be assumed to be smaller without further study.

In the long term, successful implementation of magnetic bearings where large eccentricities may be encountered will depend

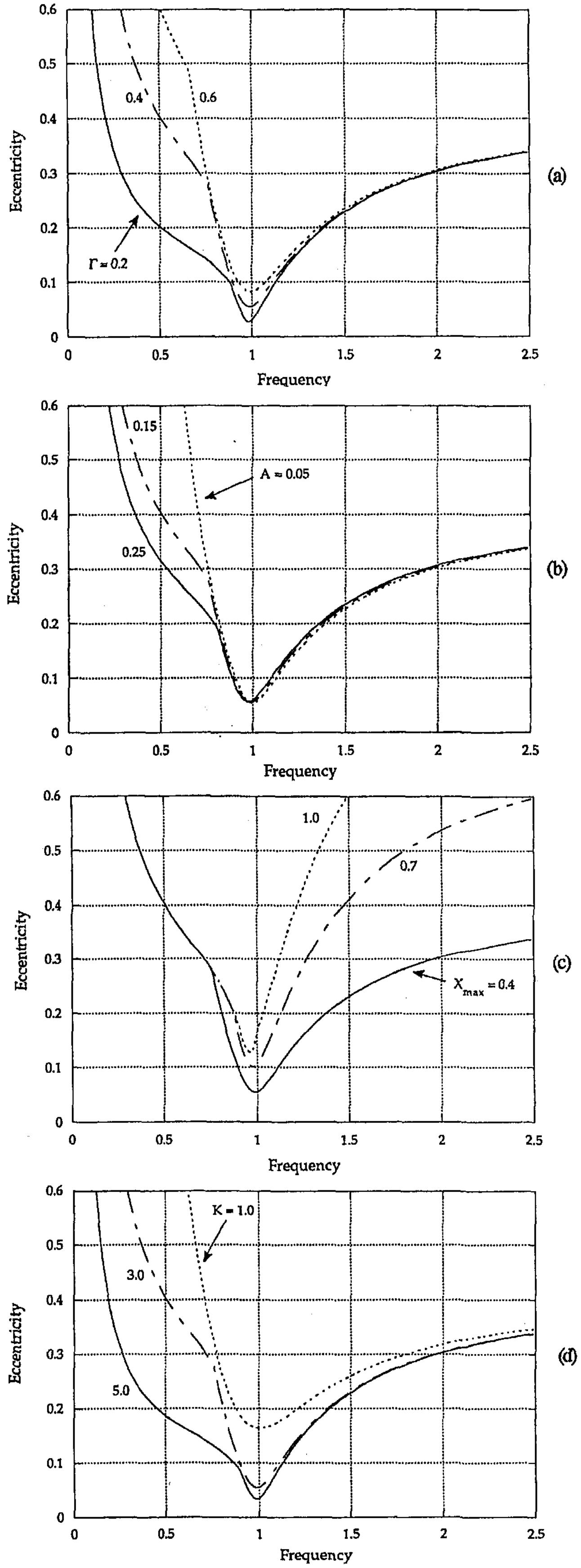

Fig. 9 Loci of the lowest eccentricity that causes a specified displacement for a given forcing ratio. Results based on harmonic balance. Base parameters: $X_{\max} = 0.4$, $A = 0.15$, $\Gamma = 0.4$, $K = 3.0$: (*a*) variation of Γ, (*b*) variation of A, (*c*) variation of $X_{\max}$, (*d*) variation of K.

on a deeper understanding of the nonlinear characteristics of the combined rotor–actuator–control system.

References

Hebbale, K. V., 1985, "A Theoretical Model for the Study of Nonlinear Dynamics of Magnetic Bearings," Ph.D. Thesis, Cornell University, Ithaca, NY.

Jordan, D. W., and Smith, D. W., 1987, *Nonlinear Ordinary Differential Equations,* Clarendon Press, Oxford, United Kingdom.

Knight, J. D., Xia, Z., and McCaul, E. B., 1992, "Forces in Magnetic Journal Bearings: Nonlinear Computation and Experimental Measurement," *Proceedings of 3rd International Symposium on Magnetic Bearings,* Alexandria, VA, July, P. E. Allaire, ed.

Knight, J. D., Walsh, T., and Virgin, L. N., 1993, "Dynamic Analysis of a Magnetic Bearing System With Flux Control," *2nd International Symposium on Magnetic Suspension Technology,* Seattle, WA.

Lee, C. W., and Kim, J. S., 1992, "Modal Testing and Suboptimal Vibration Control of Flexible Rotor Bearing System by Using a Magnetic Bearing," ASME *Journal of Dynamic Systems, Measurement, and Control,* Vol. 114, pp. 244–252.

Nonami, K., Yamanaka, T., and Tominaga, M., 1990, "Vibration and Control of a Flexible Rotor Supported by Magnetic Bearings," *JSME International Journal,* Series III, Vol. 33, No. 4, December, pp. 475–482.

O'Connor, L., 1992, "Active Magnetic Bearings Give Systems a Lift," *Mechanical Engineering,* Vol. 114, No. 7, July, pp. 52–57.

Virgin, L. N., 1988, "On the Harmonic Response of an Oscillator With Unsymmetric Restoring Force," *Journal of Sound and Vibration,* Vol. 126(1), pp. 157–165.

Virgin, L. N., 1989, "Approximate Criterion for Capsize Based on Deterministic Dynamics," *Dynamics and Stability of Systems,* Vol. 4, No. 1, pp. 55–70.

Virgin, L. N., Plaut, R. H., and Cheng, C. C., 1992, "Prediction of Escape From a Potential Well Under Harmonic Excitation," *International Journal of Nonlinear Mechanics,* Vol. 27, No. 3, pp. 357–365.

Walsh, T. F., 1993, "Nonlinear Dynamic Analysis of a Magnetic Bearing System With Flux Control: The Effects of Coordinate Coupling," M. S. Thesis, Duke University, Durham, NC.

Williams, R. D., Keith, F. J., and Allaire, P. E., 1991, "A Comparison of Analog and Digital Controls for Rotor Dynamic Vibration Reduction Through Active Magnetic Bearings," ASME JOURNAL OF ENGINEERING FOR GAS TURBINES AND POWER, Vol. 113, pp. 535–543.

Experimental Analysis of Journal Bearings

A. H. Elkholy
Department of Mechanical Engineering,
United Arab Emirates University,
Al-Ain, United Arab Emirates

A. Elshakweer
Global Engineering Technology,
Kitchener, Ontario, Canada

This study presents a comprehensive technique, which could be applied to almost any rotating equipment to identify and diagnose journal bearing problems that relate to metal-to-metal bearing surface contact. Orbital measurements that describe bearing parameters in different modes of operation were experimentally obtained and analyzed. Such parameters may include: attitude angle, minimum oil film thickness, and the possibility of metal-to-metal rubbing occurrence. The general outline of the presented experimental technique was substantiated using the Raimondi–Boyd well-documented design charts and good correlation between experimental and analytical results was obtained.

Introduction

The design of journal bearings is of considerable importance to the development of rotating machinery such as compressors, pumps, turbines, internal-combustion engines, motors, and generators. In its most basic form a journal bearing consists of a rotatable shaft (the journal) contained within a close-fitting cylindrical sleeve (the bearing). The journal and bearing surfaces are separated by a film of lubricant that is supplied to the clearance space between the surfaces in order to: permit assembly of the journal and bearing, provide space for the lubricant, accommodate unavoidable thermal expansions, and tolerate any shaft misalignment or deflection.

The fundamental purpose of a journal bearing is to provide radial support to a rotating shaft. Under load, the centers of the journal and the bearing are not coincident but are separated by a distance called the eccentricity. This eccentric arrangement establishes a converging-wedge geometry, which, in conjunction with the relative motion of the journal and the bearing, permits a pressure to be developed by viscous effects within the thin film of lubricant and thus produces a load-carrying capability. However, if the load is too large or the shaft rotation too slow, the wedgelike geometry will not form and metal-to-metal contact can occur.

In practical bearing design, a trial and error procedure is always required [1, 2]. The bearing design is usually done first, on the basis of what is reasonably practical according to bearing theory, then it is decided whether or not the bearing will carry the required load at the specified speed [3]. For these reasons, an experimental analysis technique is usually required to verify the design and diagnose its problems.

This study presents a step-by-step procedure, which utilizes a dual-channel Fast Fourier Transform (FFT) analyzer in conjunction with an electronic filtering system and two noncontacting probes, to measure shaft orbit in different modes of operation and hereby identify bearing characteristics. This will facilitate the diagnosis of any existing bearing and/or the improvement of the bearing design.

Test Setup

As shown in Fig. 1, the Kaman Multi-Vit (Multi-Purpose Variable Impedance Transducer) measuring system, model KD-2300-2S, was used due to its linear transfer characteristic and its wide frequency range. The system's noncontacting eddy current probes were installed 90 deg apart to monitor shaft vibration. The measuring system was powered by + and −12 V DC (±0.5 V DC) at 70 mA [4]. The output from each probe was connected to the dual-channel FFT analyzer. The setup is also provided with an electronic filter to filter out the AC vibration signals when required.

Testing Precautions

In order to obtain reliable and accurate results, the following precautions were imposed:

1. The probes were mounted on a rigid bracket that exhibits no resonance in the excitation range of operation.
2. As stated in [4], the gap between each probe and the shaft was fixed at 1.27 mm in order to insure linearity.
3. The probes were calibrated to provide linear output (constant sensitivity with position) in accordance with the manufacturer's procedure. The probes output voltage were set to zero while the shaft was in the stand still position.
4. Each channel of the FFT analyzer was calibrated in the time domain to give direct displacement reading.

Definitions

For the purposes of accuracy and clarity, the terms used in the analysis procedure are defined below. The first four terms are uniquely applicable to this paper while the other two are general and well-known terms [5].

Eccentricity Circle

The eccentricity circle is defined by the locus of the shaft center around the bearing center while the shaft is making a pure rolling on the bearing surface. Figure 2 shows how this circle is generated.

Steady-State Shaft Position

The steady-state shaft position is the average position of the shaft center after the hydrodynamic film has been established and the shaft vibrations have been filtered out.

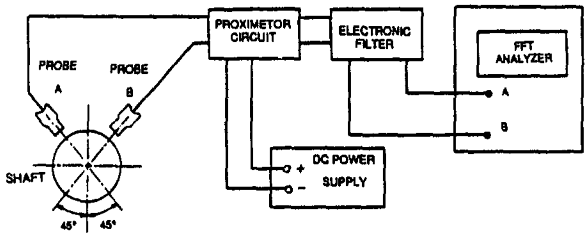

Fig. 1 Connection diagram

Contributed by the International Gas Turbine Institute and presented at ASME Cogen Turbo Power '94, Portland, Oregon, October 25–27, 1994. Manuscript received by the International Gas Turbine Institute July 20, 1994. Associate Technical Editor: E. M. Greitzer.

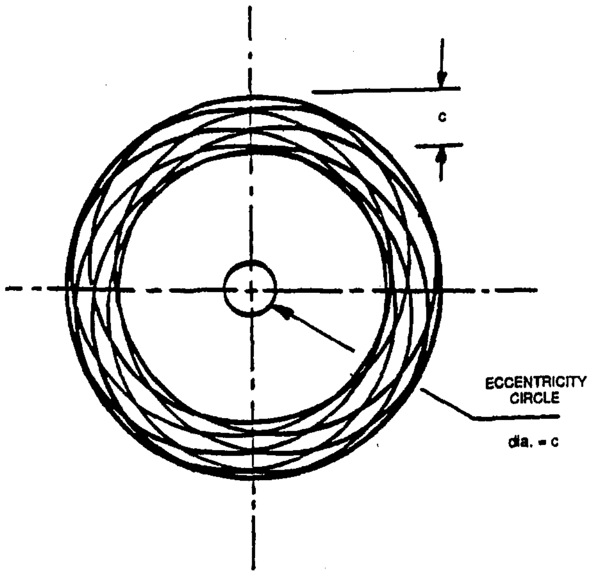

Fig. 2 Generation of eccentricity circle

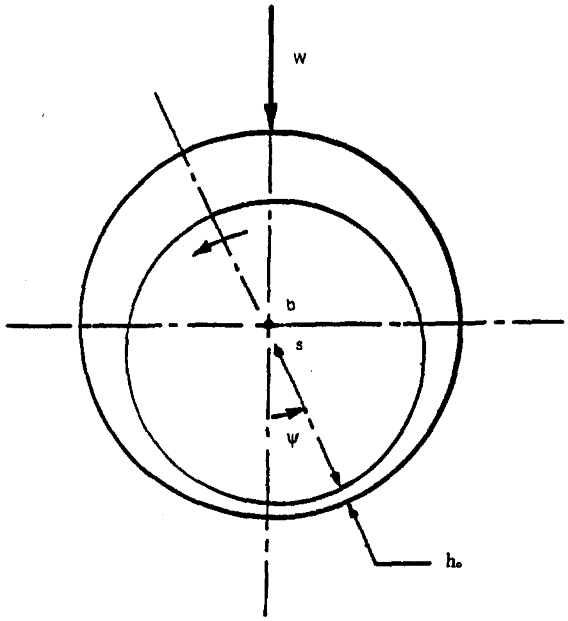

Fig. 3 Attitude angle and minimum oil film thickness

Orbital Cycle

This is the part of the probe signal, in the time domain, that repeats itself periodically and defines one complete orbit.

Rubbing Parameter (*R*)

This is the minimum oil film thickness when the shaft center deviates from the steady-state position due to any external forcing function. A zero rubbing parameter will indicate metal-to-metal contact.

Attitude Angle (Ψ)

The attitude angle is the angle included between the direction of the steady-state load W through the center of the bearing and the line connecting the geometric center of the bearing and the center of the shaft; see Fig. 3.

Minimum Oil Film Thickness (h_o)

This is the thickness of the oil film measured at the bearing attitude line when the shaft center is in its steady-state position; Fig. 3.

Determination of the Shaft Orbit

The shaft orbit describes the path of the shaft center inside the diameter of the eccentricity circle for one complete orbital cycle. In the time domain, the FFT analyzer was used to display the vibration signals from the two probes, in order to determine the orbital cycle of the bearing. As an example, see Fig. 4, for shaft speed = 15 revolutions per second the measured orbital cycle omit was found to be 0.13 second or equivalent to two shaft revolutions for this specific setting. The time window was then set at 0.2 second so that at least one orbital cycle is displayed.

The analyzer channels were then calibrated, using a sensitivity of 10 mV/0.0254 mm, to convert the voltage amplitude to displacement units. Figure 5 shows the measured signals. The analyzer was then switched to the Nyquist mode to produce the actual shaft orbits for different modes. Figure 5 shows these orbits. Using an interactive digital plotter while the analyzer was AC coupled, the shaft orbit was plotted around the origin of the graph. The analyzer was then DC coupled and the shaft orbit was plotted on the same graph. Using the electronic filter, the steady-state shaft position, DC shift, was then determined by filtering out the shaft vibration. This was also plotted on the graph and is represented by point "s."

Shaft Center Determination

With the bearing journal remaining static under the gravitation load, the oil will squeeze itself out from the portion of the bearing under the load [6], and there will be direct metal-to-metal contact over an area around point "A," shown in Fig. 6. The probe output DC signals at this condition represent the origin of the graph shown in Fig. 5, which in turn represents the center of the static shaft.

After the bearing is set in motion, and due to the hydrodynamic pressure generated by shaft rotation, stability will be achieved by the shaft moving over to its steady state position (point "s"). This position represents the DC shift obtained when the shaft vibration, AC signal, is filtered out. As indicated, Fig. 3 shows the shaft in its steady-state position.

Finding the bearing center will be the last step needed to determine the bearing parameters and/or characteristics. This is described in the following paragraphs.

Bearing Center Determination

Physically, the bearing center lies on the bearing centerline Y–Y (shown in Fig. 6), which is located exactly midway be-

Nomenclature

B = bearing diameter
c = bearing diametral clearance
d = eccentricity circle diameter
h_o = minimum oil film thickness
J = journal diameter
L = bearing effective length
N = journal rotational speed in revolutions per second
P = load per unit of projected bearing area = W/JL
R = rubbing parameter
s = steady-state shaft position
S = Sommerfeld number
W = applied external load
μ = absolute viscosity of lubricating oil
ψ = bearing attitude angle

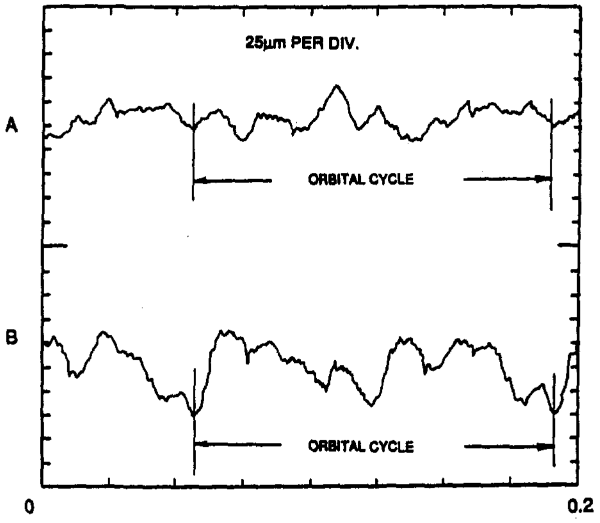

Fig. 4 Probe vibration signals

tween the two probes. Accordingly, this line can be represented by a line drawn diagonally from the origin of the graph shown in Fig. 5 midway between the two axes A and B. The center of the bearing will be the center of the eccentric circle whose circumference passes through the origin of the graph. This representation is shown in Fig. 5.

Bearing Parameters

To determine the bearing parameters from the measured orbits, the following steps were followed:

1 The actual eccentricity circle was first drawn on the orbital graph. The diameter of the eccentricity circle was calculated as follows:

$$d = B - J \tag{1}$$

where

d = eccentricity circle diameter of the actual bearing diametral clearance (c)

B = measured bearing diameter

J = measured journal diameter

2 The bearing attitude angle (ψ) was determined by joining the bearing center and the shaft steady-state position.

3 The minimum film thickness (h_o) was then measured radially from point "s" to the circumstance of the eccentricity circle.

4 The rubbing parameter (R) was also measured radially from point "M" to the circumference of the eccentricity circle.

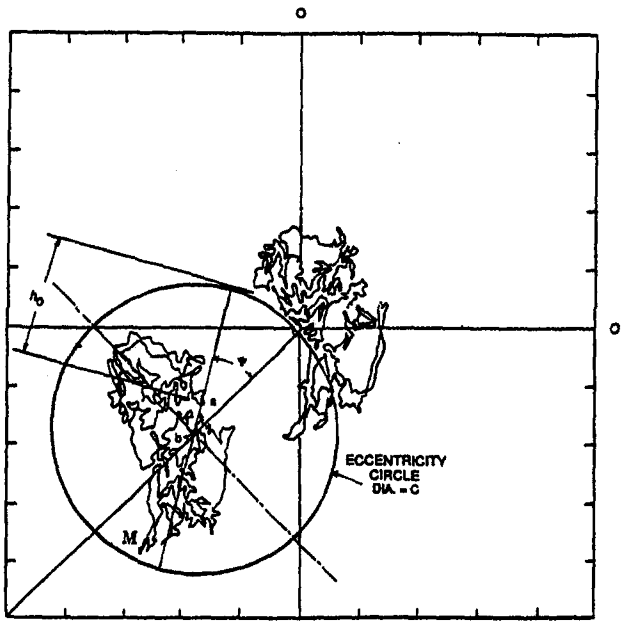

Fig. 5 Shaft orbits

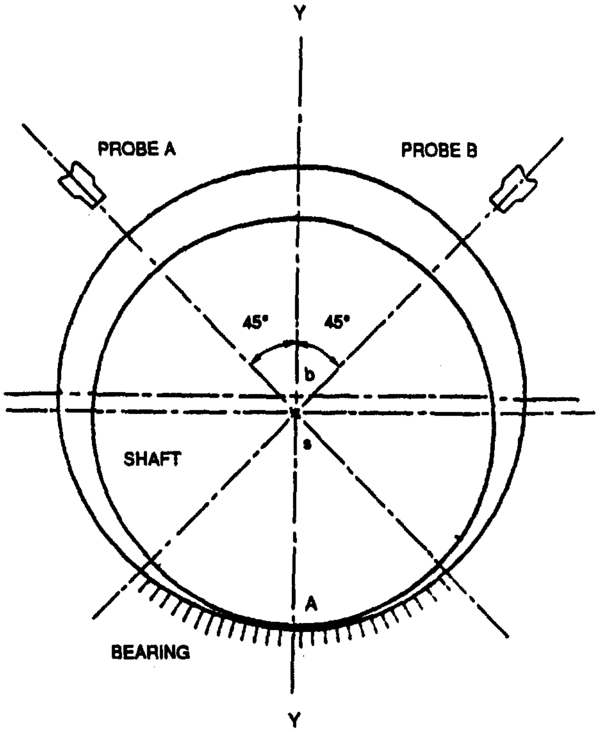

Fig. 6 Standstill shaft

Test Results and Procedure Substantiation

The bearing used for this study has a journal diameter of $J = 45$ mm, an effective length $L = 35$ mm, and a diametral clearance of 0.254 mm. This results in a slenderness ratio of $L/J = 35/45 = 0.78$. The oil used for all the experiments

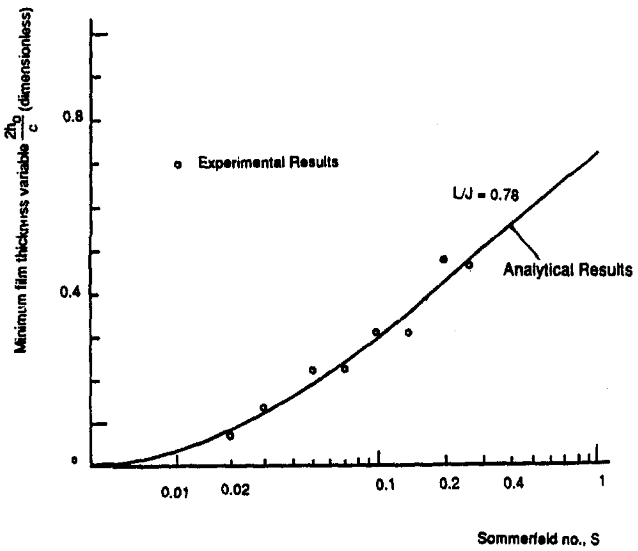

Fig. 7 Correlation between experimental and analytical results

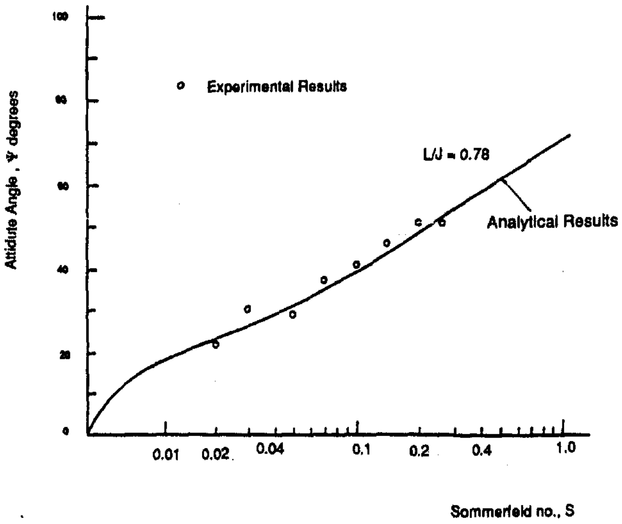

Fig. 8 Correlation between experimental and analytical results

is the multigrade oil 20 W 50 whose viscosity–temperature relationship is given in [5]. The rotational speed of the bearing as well as the applied load were varied either simultaneously or individually and accordingly the attitude angle ψ and the minimum oil film thickness h_o were obtained as demonstrated in Fig. 5. On the other hand, the temperatures of the lubricating oil as it enters and leaves the bearing were monitored during testing. The oil viscosity μ was determined at the average of these temperatures using the viscosity–temperature relationships given in [5]. The results were presented using the dimensionless bearing-characteristic number, known as Sommerfeld number. This quantity is defined by the equation:

$$S = \left(\frac{J}{c}\right)^2 \frac{\mu N}{P} \tag{2}$$

where all terms given in Eq. (2) are defined in the nomenclature.

Moreover, the Raimondi–Boyd charts obtained in the 1950s [7] represent a comprehensive solution to the Reynolds hydrodynamic lubrication equation. The charts are so complete that later on [8] and even today, they are the best approach to use in the analysis and design of full-film journal bearings. In this study, two of these charts are reconstructed based upon the work presented in [5] and [9] and are shown in Figs. 7 and 8 by solid lines at slenderness ratio = 0.78 to represent the bearing under consideration. The applied load and journal speed were monitored during testing and the Sommerfeld number was found to vary over a range from 0.02 to 0.26. The experimental results are shown on Figs. 7 and 8 for comparison with the analytical results. As indicated, the correlation between the analytical results obtained from the criteria given in [5, 9] and the results obtained using the procedure outlined in this study is very good (correlation factor = 0.92). This gives support to the procedure as a useful tool for use to examine and diagnose journal bearings.

Furthermore, analyzing the probe's vibration signals in the frequency domain can further identify the reasons due to which unsatisfactory orbital parameters may be obtained.

References

1 Rippel, H. C., "Design of Hydrostatic Bearings," *Machine Design*, Parts 1 to 10, Aug. 1 to Dec. 5, 1963.

2 O'Donoghue, J. P., and Rowe, W. B., "Hydrostatic Bearing Design," *Tribology*, Vol. 2, Feb. 1969, pp. 25–71.

3 Hirs, G. G., "The Load Capacity and Stability Characteristics of Hydrodynamic Grooved Journal Bearings," *ASLE Transactions*, Vol. 8, 1965, pp. 296–305.

4 Kaman Sciences Corporation, *Measurement Solution Handbook*, 1988, pp. 22–25.

5 Shigley, J. E., and Mitchell, L. D., *Mechanical Engineering Design*, 4th ed., McGraw-Hill Book Company, 1983, pp. 536–546.

6 Reason, B. R., and Narang, I. P., "Rapid Design and Performance Evaluation of Steady State Journal Bearings—A Technique Amendable to Programmable Hand Calculators," *ASLE Transactions*, Vol. 25, No. 4, 1982, pp. 429–449.

7 Raimondi, A. A., and Boyd, J., "A Solution for the Finite Journal Bearing and Its Applications to Analysis and Design, I, II, and III," *ASLE Transactions*, Vol. 1, 1958, pp. 159–174, 175–193, and 194–209, respectively.

8 Moes, H., and Bosma, R., "Design Charts for Optimum Bearing Configurations: 1—The Full Journal Bearing," ASME *Journal of Lubrication Technology*, Vol. 93, 1971, pp. 302–306.

9 Shigley, J. E., and Mischke, C. R., *Standard Handbook of Machine Design*, McGraw-Hill, Ch. 28, 1986.

Experimental Identification of Linearized Oil Film Coefficients of Cylindrical and Tilting Pad Bearings

P. Arumugam

S. Swarnamani

B. S. Prabhu

Department of Applied Mechanics,
Indian Institute of Technology,
Madras, India

The dynamic behavior of the rotating machinery supported by the hydrodynamic journal bearings is significantly influenced by the dynamic characteristics of the oil film. In the present work an efficient identification method is used to identify the stiffness and damping coefficients of the tilting pad and cylindrical journal bearings of a flexible rotor-bearing system. The method uses FRFs (Frequency Response Functions) obtained by the measurements and the finite element method. The accuracy and feasibility of the method were tested and demonstrated by theoretical simulation. The possible effects of oil-film inertia is also verified by the theoretical simulation. The method can be further extended to identify twelve linearized oil-film coefficients.

Introduction

The dynamic characteristics of modern turbomachines, generally operating at beyond few critical speeds, have to be predicted accurately to avoid the possibility of operating the machine at near the critical speeds or the unstable speed range and further to identify the sources of vibration of the machine during operation. The finite element modeling of dynamics of rotating machinery is more accurate and reliable compared to transfer matrix method (Firoozian and Stanway, 1989). If the machine is supported by fluid-film bearings, the dynamic behavior is significantly influenced by the stiffness and damping characteristics of the oil film of the bearing, but the exact values of stiffness and damping coefficients are not known. The stiffness and damping characteristics are greatly dependent on many physical and mechanical parameters, such as temperature, load, speed, misalignment, etc., of the system. Hence, to simulate the dynamic characteristics of the rotor-bearing system, the stiffness and damping characteristics of the fluid-film bearings have to be identified accurately.

Several different time-domain and frequency-domain techniques have been developed for determining the oil-film bearing coefficients. Burrows and Sahinkaya (1982) assessed the relative merits of each method and showed that frequency domain techniques were less susceptible to noise. Many works have dealt with identification of bearing coefficients and rotor-bearing system parameters using impulse, step change in force, and synchronous and nonsynchronous excitation techniques. Zhang et al. (1992), and Rouvas et al. (1992) have used impact excitation to identify the bearing coefficients. Impulse testing may lead to underestimation of input forces when applied to a rotating shaft as a result of the generation of friction-related tangential force components (Muszynska et al., 1993) and, further, is prone to poor signal-to-noise ratios because of the high crest factor. Also the force input phase is important as it may lead to over/underestimation of ratio of displacement to force. Different methods have been developed (Stanway, 1984; Sahinkaya and Burrows, 1984; Hong and Lee, 1992) to identify the bearing coefficients from the unbalance response of the system. A simulation study carried out by Hong and Lee (1992) shows that in the regions, except near the vicinities of the critical speeds, the errors of identified values of bearing coefficients are significant due to poor signal-to-noise ratio. Muszynska et al. (1989a, 1989b, 1993) have applied a sweep frequency rotating force perturbation method to rotating systems for dynamic stiffness identification and showed that excellent signal-to-noise ratio data can be obtained for identification of the rotor-bearing system parameters. In the present work unidirectional sweep frequency excitation using an electromagnetic exciter is applied to obtain the Frequency Response Functions (FRFs).

The method of structural joint parameter identification proposed by Wang and Liou (1991) has been extended to identify the eight linearized oil-film coefficients utilizing the experimental FRFs and the theoretical FRFs obtained by finite element modeling. This method has been used to identify the linearized oil-film coefficients of tilting pad and cylindrical journal bearings.

Theoretical Formulation

The equation of motion of a rotor-bearing system can be written as

$$[M]\{\ddot{\alpha}\} + [C + C_b]\{\dot{\alpha}\} + [K + K_b]\{\alpha\} = \{F\} \quad (1)$$

where $[M]$, $[C]$, and $[K]$ are mass, damping, and stiffness matrices of the rotor, respectively, $[C_b]$ and $[K_b]$ are damping and stiffness matrices, respectively, of the bearings for which the dynamic coefficients have to be identified, $\{F\}$ denotes external force vector and $\{\alpha\}$ represents displacement vector. The dynamic stiffness matrix of the rotor-bearing system can then be expressed as

$$[D_t] = -\omega^2[M] + i\omega[C + C_b] + [K + K_b] = [H_t]^{-1} \quad (2)$$

where $[H_t]$ represents the matrix of FRFs of the rotor-bearing system including the bearings for which the dynamic coefficients have to be identifed. $[H_t]$ should be determined experimentally. The dynamic stiffness matrix of a rotor-bearing system excluding the bearings for which the dynamic coefficients have to be identified can be expressed as

---

Contributed by the International Gas Turbine Institute and presented at the 39th International Gas Turbine and Aeroengine Congress and Exposition, The Hague, The Netherlands, June 13–16, 1994. Manuscript received by the International Gas Turbine Institute February 4, 1994. Paper No. 94-GT-81. Associate Technical Editor: E. M. Greitzer.

$$[D_r] = -\omega^2[M] + i\omega[C] + [K] = [H_r]^{-1} \tag{3}$$

where $[H_r]$ is the FRFs of the rotor excluding the bearings for which the dynamic coefficients have to be identified. $[H_r]$ can be obtained using a finite element technique without considering the bearings and taking free support conditions in place of them.

Using Eqs. (2) and (3), one can obtain the following equation:

$$[D_t] - [D_r] = [H_t]^{-1} - [H_r]^{-1} = [K_b] + i\omega[C_b] \tag{4}$$

Hence, if the FRF matrices $[H_t]$ and $[H_r]$ are known, then the bearing parameters can be obtained from Eq. (4). Note that if the values of $[H_t]$ and $[H_r]$ are exact, then theoretically one can obtain the exact dynamic coefficients of the bearings since there is no approximation in the formulation of the Eq. (4). To overcome the problem of measurement noise, it is necessary to consider the possible existence of measurement noise. To avoid the inverse operation of the FRF matrix, the following method (Wang and Liou, 1991) is applied. From Eq. (4) one can obtain the following:

$$[H_t]([H_t]^{-1} - [H_r]^{-1})[H_r] = [H_t]([K_b] + i\omega[C_b])[H_r]$$

or

$$[H_r] - [H_t] = [H_t]([K_b] + i\omega[C_b])[H_r] \tag{5}$$

Let $[H] = [H_r] - [H_t]$, r_{ij}, and b_{ij} be the coefficients of the FRF matrices $[H_r]$ and $[H_t]$ and c_{ij} and k_{ij} be the coefficients of the bearing matrices $[K_b]$ and $[C_b]$, respectively, where $i, j = 1, 2, \ldots, n$, then, $h_{ij} = r_{ij-bij}$ and $d_{ij} = k_{ij} + i\omega c_{ij}$. With these notations Eq. (5) can then be written as

$$\begin{bmatrix} h_{11} & h_{12} & \cdots & h_{1n} \\ h_{21} & h_{22} & \cdots & h_{2n} \\ \cdot & \cdot & \cdot & \cdot \\ \cdot & \cdot & \cdot & \cdot \\ h_{n1} & h_{n2} & \cdots & h_{nn} \end{bmatrix}$$

$$= \begin{bmatrix} \sum_{j=1}^{n}\sum_{i=1}^{n} b_{1i}r_{j1}d_{ij} & \sum_{j=1}^{n}\sum_{i=1}^{n} b_{2i}r_{j1}d_{ij} & \cdots & \sum_{j=1}^{n}\sum_{i=1}^{n} b_{ni}r_{j1}d_{ij} \\ \sum_{j=1}^{n}\sum_{i=1}^{n} b_{1i}r_{j2}d_{ij} & \sum_{j=1}^{n}\sum_{i=1}^{n} b_{2i}r_{j2}d_{ij} & \cdots & \sum_{j=1}^{n}\sum_{i=1}^{n} b_{ni}r_{j2}d_{ij} \\ \cdot & \cdot & \cdot & \cdot \\ \cdot & \cdot & \cdot & \cdot \\ \sum_{j=1}^{n}\sum_{i=1}^{n} b_{1i}r_{jn}d_{ij} & \sum_{j=1}^{n}\sum_{i=1}^{n} b_{2i}r_{jn}d_{ij} & \cdots & \sum_{j=1}^{n}\sum_{i=1}^{n} b_{ni}r_{jn}d_{ij} \end{bmatrix} \tag{6}$$

From Eq. (6) one can obtain $n \times n$ of equations. It can be written in matrix form as follows:

$$\{A\}_{n^2\times 1} = [D]_{n^2\times n^2}\{E\}_{n^2\times 1} \tag{7}$$

where A is

$$[h_{11}h_{21} \cdots h_{n1}h_{12}h_{22} \cdots h_{n2}h_{13}h_{23} \cdots h_{nn}]^T_{n^2\times 1}$$

D is

$$\begin{bmatrix} b_{11}r_{11} & b_{12}r_{11} & \cdots & b_{1n}r_{11} & b_{11}r_{21} & b_{12}r_{21} & \cdots & b_{11}r_{n1} & \cdots & b_{1n}r_{n1} \\ b_{11}r_{12} & b_{12}r_{12} & \cdots & b_{1n}r_{12} & b_{11}r_{22} & b_{12}r_{22} & \cdots & b_{11}r_{n2} & \cdots & b_{1n}r_{n2} \\ \cdot & \cdot & \cdot & \cdot & \cdot & \cdot & \cdot & \cdot & \cdot & \cdot \\ \cdot & \cdot & \cdot & \cdot & \cdot & \cdot & \cdot & \cdot & \cdot & \cdot \\ b_{11}r_{1n} & b_{12}r_{1n} & \cdots & b_{1n}r_{1n} & b_{11}r_{2n} & b_{12}r_{2n} & \cdots & b_{11}r_{nn} & \cdots & b_{1n}r_{nn} \\ b_{21}r_{11} & b_{22}r_{11} & \cdots & b_{2n}r_{11} & b_{21}r_{21} & b_{22}r_{21} & \cdots & b_{21}r_{n1} & \cdots & b_{2n}r_{n1} \\ b_{21}r_{12} & b_{22}r_{12} & \cdots & b_{2n}r_{12} & b_{21}r_{22} & b_{22}r_{22} & \cdots & b_{21}r_{n2} & \cdots & b_{2n}r_{n2} \\ \cdot & \cdot & \cdot & \cdot & \cdot & \cdot & \cdot & \cdot & \cdot & \cdot \\ \cdot & \cdot & \cdot & \cdot & \cdot & \cdot & \cdot & \cdot & \cdot & \cdot \\ b_{21}r_{1n} & b_{22}r_{1n} & \cdots & b_{2n}r_{1n} & b_{21}r_{2n} & b_{22}r_{2n} & \cdots & b_{21}r_{nn} & \cdots & b_{2n}r_{nn} \\ b_{31}r_{11} & b_{32}r_{11} & \cdots & b_{3n}r_{11} & b_{31}r_{21} & b_{32}r_{21} & \cdots & b_{31}r_{n1} & \cdots & b_{3n}r_{n1} \\ b_{31}r_{12} & b_{32}r_{12} & \cdots & b_{3n}r_{12} & b_{31}r_{22} & b_{32}r_{22} & \cdots & b_{31}r_{n2} & \cdots & b_{3n}r_{n2} \\ \cdot & \cdot & \cdot & \cdot & \cdot & \cdot & \cdot & \cdot & \cdot & \cdot \\ \cdot & \cdot & \cdot & \cdot & \cdot & \cdot & \cdot & \cdot & \cdot & \cdot \\ b_{n1}r_{1n} & b_{n2}r_{1n} & \cdots & b_{nn}r_{1n} & b_{n1}r_{2n} & b_{n2}r_{2n} & \cdots & b_{n1}r_{nn} & \cdots & b_{nn}r_{nn} \end{bmatrix}_{n^2\times n^2}$$

and E is

$$[d_{11}d_{21} \cdots d_{n1}d_{12}d_{22} \cdots d_{1n} \cdots d_{nn}]^T_{n^2\times 1}$$

with $d_{ij} = k_{ij} + i\omega c_{ij}$.

Note that this equation is formed directly from the elements of Eq. (6). Equation (7) contains the $n \times n$ parameters as unknowns. Hence, theoretically, this equation can be solved to get exact values of linearized dynamic coefficients provided the FRFs are exact. The bearings and seals are usually modeled as four stiffness and four damping coefficients. Hence, in actual practical cases the number of unknowns would be less; one can use those equations that have the transfer function between the same points as the coefficients. The real and imaginary part of the unknown parameter, $k + i\omega c$, can be separated and then Eq. (8) can be written as follows:

$$\{A\}_{n^2\times 1} = \{[D] + i\omega[D]\}_{n^2\times 2n^2}\begin{Bmatrix} \{K\} \\ \{C\} \end{Bmatrix}_{2n^2\times 1} \tag{8}$$

Nomenclature

C_p = machined radial clearance of the tilting pad
C_r = radial clearance of the cylindrical bearing
W = steady-state load on the test bearing
b = width of the bearing
c = bearing damping coefficient
d = diameter of the bearing
k = bearing stiffness coefficient
Ω = rotative speed
ω = perturbation frequency

Subscripts

xx = horizontal direction
yy = vertical direction

Equation (8) has $2n^2$ unknowns, but has only one set of n^2 simultaneous equations. However, the vector $\{A\}$ and matrix $[D]$ are functions of frequency ω and if the FRFs are known at m discrete frequencies, $\omega_1, \omega_2, \ldots \omega_m$, then for each frequency one can have a set of n^2 simultaneous equations. To smooth the random measurement error the FRFs at more than two frequency points can be taken and the least-squares method can be used to obtain the unknown dynamic parameters as:

$$\begin{Bmatrix}\{K\}\\ \{C\}\end{Bmatrix} = \left(\begin{bmatrix}{[D]}_{\omega_1}\\ {[D]}_{\omega_2}\\ \cdot\\ \cdot\\ {[D]}_{\omega_m}\end{bmatrix}^T \begin{bmatrix}{[D]}_{\omega_1}\\ {[D]}_{\omega_2}\\ \cdot\\ \cdot\\ {[D]}_{\omega_m}\end{bmatrix} \right)^{-1} \begin{bmatrix}{[D]}_{\omega_1}\\ {[D]}_{\omega_2}\\ \cdot\\ \cdot\\ {[D]}_{\omega_m}\end{bmatrix}^T \begin{Bmatrix}\{A\}_{\omega_1}\\ \{A\}_{\omega_2}\\ \cdot\\ \cdot\\ \{A\}_{\omega_m}\end{Bmatrix} \tag{9}$$

This equation can be used to find not only the bearing parameters but also the full stiffness and damping matrices of the system provided the complete FRFs of the system are known.

Theoretical Simulation

The identification algorithm presented here can identify the bearing coefficients exactly, if the FRFs are free from noise. However, measurement noise is unavoidable in practice. Further, the inertia coefficients of oil film, which are not being identified in the present method, may affect the accuracy of the identified coefficients. Hence the simulation studies have been carried out to know the effect of measurement noise and the inertia coefficients of the oil film.

Effect of Measurement Noise. In this simulation study, a random noise with normal distribution (zero mean, variance σ^2) was added to the FRFs to simulate the measurement noise. If the $H_{ij}(\omega)$ denotes the frequency response function between the ith and the jth points of the rotor bearing system, then the variances of the random noise σ_r^2 and σ_i^2, for real and imaginary parts of the FRFs, are defined as:

$$\sigma_r^2 = e_n^2(\mathrm{Re}H_{ij}(\omega)^2_{\max}) \quad \text{and} \quad \sigma_i^2 = e_n^2(\mathrm{Im}H_{ij}(\omega)^2_{\max}) \cdot$$

where the subscript max denotes the maximum value in the frequency range of interest and e_n represents the noise level. If the noise level is given then a set of random numbers can be generated by a computer program.

The simulated system is a rotor supported on two bearings. The length of the shaft is 1260 mm and the diameter is 50 mm. A disk of 200 mm diameter and 420 mm long is centrally mounted on the shaft. The internal viscous loss factor and hysteretic loss factor are assumed to have the values 1.0×10^{-4} s and 0.0, respectively. The stiffness and damping coefficients of the left-end bearing, assumed to be isotropic, are 1.75×10^7 N/m and 3.0×10^5 Ns/m, respectively. The characteristics of the right-end bearing are identified using the proposed algorithm. The detailed procedures of the simulation are summarized here:

- Find the equation of motion of the rotor-bearing system without the bearing for which the dynamic coefficients are to be identified using the finite element technique, i.e., considering the free-end condition at the right-end bearing location.
- Find the equation of motion of the rotor-bearing system including the right-end bearing.
- Compute the necessary FRF matrices from the equation of motion.
- Determine the frequency range of interest, $\omega_{\min}$ and $\omega_{\max}$, and the frequency resolution $\Delta\omega$.
- Determine the number N and the noise level e_n, then generate one set of N discrete random values with normal distribution to add to the real part of the discrete FRFs and another set of N random values to add to the imaginary part of the discrete FRFs. Identify the bearing coefficients from the noisy FRFs using Eq. (9).

In the present example the number N was set to be 400 and the frequency resolution is 0.125 Hz. The noise level of 3 percent is considered. The results are shown in Table 1. The identified values of coefficients are more or less accurate; the error is less than 8 percent. However, the error of the damping coefficients may increase if the values are very small compared to the values of the stiffness coefficients. This is because of the characteristics of the least-square method. In general, the smaller parameter may have larger percentage error by using the least-square method (Wang and Liou, 1991).

One can improve the accuracy of the smaller parameters by adding the identified values of the larger parameter into the equation of motion and repeating the identification algorithm to identify the smaller parameters alone.

Effect of Inertia Coefficients. The hypothetical rotor-bearing system taken in the previous simulation study is considered in this simulation study also. 10 percent (11.5 kg) of the rotor mass is taken as the value of the inertia coefficients of the oil film. The simulation procedure is as follows:

- Find the equation of motion of the rotor-bearing system without the bearing for which the dynamic coefficients are to be identified using the finite element technique, i.e., considering the free-end condition at the right-end bearing location.
- Find the equation of motion of the rotor-bearing system including the right-end bearing (with the stiffness, damping, and inertia coefficients).
- Compute the necessary FRF matrices from the equation of motion.
- Determine the frequency range of interest, $\omega_{\min}$ and $\omega_{\max}$, and the frequency resolution $\Delta\omega$ and then determine the number N.
- Identify the bearing coefficients from the FRFs using Eq. (9).

The results are shown in Table 2. From the result it is clear that the proposed method is not affected by the inertia coefficients even if their values are significant.

Table 1 Effect of measurement noise

Coefficients	Exact	Identified	Error (%)
Kxx (N/m)	1.5 10^5	1.3815 10^5	7.9
Kyy (N/m)	1.5 10^5	1.4775 10^5	1.5
Cxx (Ns/m)	5.0 10^3	4.7763 10^3	4.5
Cyy (Ns/m)	5.0 10^3	5.1973 10^3	-3.9

Table 2 Effect of inertia coefficients

Coefficients	Exact	Identified	Error (%)
Kxx (N/m)	$1.5\ 10^6$	$1.5018\ 10^6$	.0012
Kyy (N/m)	$1.5\ 10^6$	$1.5018\ 10^6$	.0012
Cxx (Ns/m)	$5.0\ 10^4$	$5.0030\ 10^4$	.0006
Cyy (Ns/m)	$5.0\ 10^4$	$5.0030\ 10^4$	.0006

Experimental System

Test Rig. The proposed method is used to identify the dynamic coefficients of bearings in a rotor-bearing test rig. The test rig (Fig. 1) is a single mass flexible rotor supported by a self-aligning ball bearing at one end and by the test bearing (hydrodynamic tilting pad/cylindrical bearing) at the other end. The rotor is coupled to the motor through an electromagnetic coupling. Three different bearings have been tested. A brief description of the parameters of the test rig is as follows:

Rotor parameters:
Shaft length between bearing centers 825 mm;
Shaft diameter 30 mm; Rotor mass 24.5 kg;
Bearing parameters of test bearings: Bearing diameter 25 mm;

(i) Tilting pad bearing; 4 pads; $b/d = 0.3$; $C_p = 54\ \mu m$
(ii) Tilting pad bearing; 4 pads; $b/d = 0.4$; $C_p = 42\ \mu m$
(iii) 360 deg cylindrical bearing; $b/d = 1$; $C_r = 65\ \mu m$

where C_p is the machined radial clearance of the tilting pad bearing and C_r is the radial clearance of the cylindrical bearing.

Instrumentation

Exciter and Transducers. A noncontact electromagnetic exciter (designed at the University of Kassel) is used for excitation. The exciter has a built-in calibrated force transducer for measuring the excitation force applied to the rotor. The displacement responses are measured using eddy current proximity probes with proximitor (eddy probe drivers).

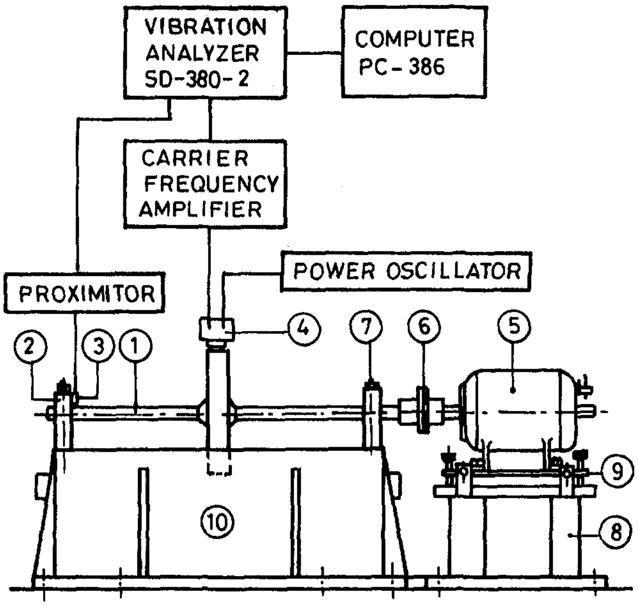

1 Flexible shaft rotor
2 Test bearing
3 Eddy probe
4 Electromagnetic Exciter
5 Motor

6 Electromagnetic coupling
7 Rolling element bearing
8 Motor base
9 Adjustable base plate
10 Main frame cum oil sump

Fig. 1 Rotor-bearing test rig (schematic)

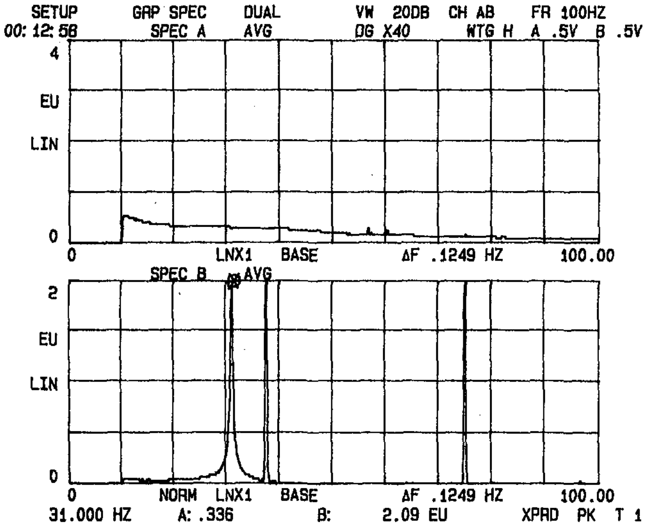

Fig. 2 Frequency spectrum of the perturbation force and the displacement response, tilting pad bearing, $b/d = 0.4$, load between pad, speed = 2250 rev/min

Analyzer. The measured input and output signals are analyzed in a two-channel signal analyzer. The analyzer has 12 bits A/D converter for each channel, channel phase match of ±1.5 deg and 800 lines of frequency baseband resolution. The frequency range used in the present analysis is 0–100 Hz and the corresponding frequency resolution is 0.125 Hz.

Measurements. The rotor mass is excited by unidirectional sine sweep perturbation force using the electromagnetic exciter and the displacement response is measured at the test bearing (3 mm away from the inside edge of the bearing) to get the transfer function (FRF). Typical values of forcing level and the associated displacement response level are shown in Fig. 2. In Fig. 2 the SPEC A shows the frequency spectrum of the sine sweep perturbation force applied to the rotor and SPEC B shows the frequency spectrum of the displacement response at the test bearing. The excitation force level varies from 0.2 N to 0.5 N in the frequency range of 10–60 Hz. In the displacement response spectrum the marked peak is the resonance peak of 2.09 μm occurring at 31.000 Hz. The other two peaks occurring at the 37.5 Hz (1ω) and 75.0 Hz (2ω, where ω is the rotating frequency of the rotor) are due to unbalance and misalignment force excitations. The amplitude ranges used in the present analysis are 0.0–4.0 N and 0.0–4.0 μm for the excitation force and the displacement response, respectively.

The analyzer directly gives the transfer function (FRF) between the excitation force and the displacement response for the chosen locations and the same can be transferred to the computer for further analysis/storage. The FRF curve of a typical case is shown in Fig. 3. In the Fig. 3 numerator of EU/EU (Engineering Unit/Engineering Unit) refers to the displacement unit μm and denominator refers to the force unit N. The displacement to force ratio at the resonance frequency of 31.124 Hz is found to be 4.67 $\mu m/N$ with the phase angle of −104.0 deg. From Fig. 3 it is clear that the FRF is more or less accurate particularly in the frequency range of 20–40 Hz. FRFs in this frequency range only are used for the indentification of bearing coefficients. A typical cross-coupled FRF, i.e., the FRF obtained by applying excitation at the rotor mass in the vertical direction and measuring the displacement response in the horizontal di-

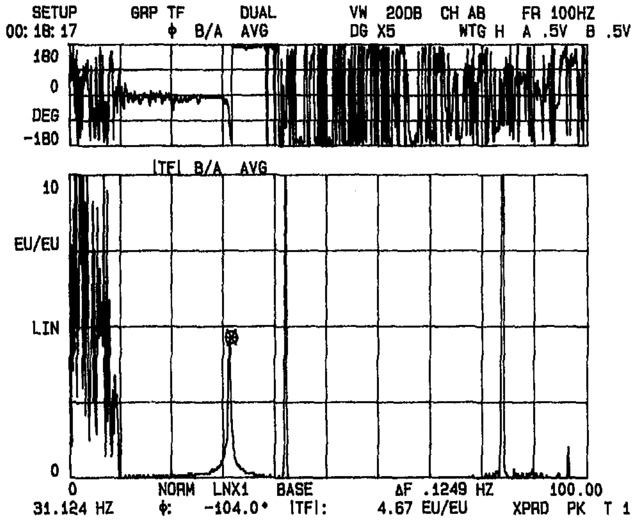

Fig. 3 The measured FRFs of the rotor-bearing system, tilting pad bearing, *b/d* = 0.4, load on pad, speed = 2500 rev/min

rection of the bearing or vice versa, is shown in Fig. 4 to illustrate the response level and the phase error in the FRF.

For the case of tilting pad bearings the FRFs are measured only in the horizontal direction for excitation in the horizontal and vertical directions for excitation in the vertical direction because the cross-coupled stiffness and damping coefficients are zero (theoretically) for the tilting pad bearings. But in the case of a cylindrical bearing the FRFs are measured in both directions (vertical and horizontal) for excitation in each direction. Thus two FRFs are measured for tilting pad bearings and four FRFs are measured for cylindrical journal bearing.

Identification. The identification algorithm presented here needs FRFs of the rotor-bearing system and also the FRFs of the rotor without those bearings for which the coefficients are to be identified, i.e., with free-end condition at that bearing location. The latter FRFs are difficult to obtain experimentally. Hence a finite element technique is used to obtain the equation of motion of the rotor considering free-end condition at the location of the test bearing in the rotor. The rotor is supported by the self-aligning ball bearing. Since the rolling element bearing is new the clearance in the bearing may not be sufficient to behave nonlinearly. Further, since the stiffness of the ball bearing is higher than the shaft as well as the hydrodynamic bearing, the bearing characteristics do not significantly influence either the first critical speed or the response of the rotor-bearing system. In the present analysis the stiffness of the rolling element bearing is estimated using the approximate relation given by Gargiulo (1980) and the same is added in finite element model of the rotor at the appropriate nodal degrees of freedom. The bearing dynamic coefficients are identified using Eq. (9).

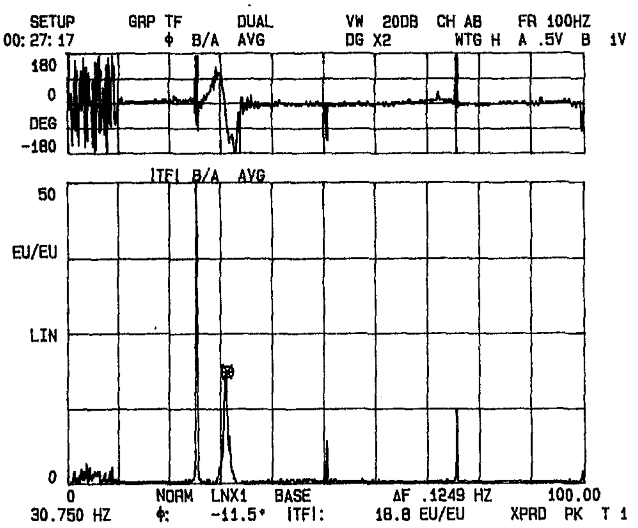

Fig. 4 The measured cross coupled FRFs of the rotor-bearing system, cylindrical journal bearing, *b/d* = 1.0, speed = 1500 rev/min

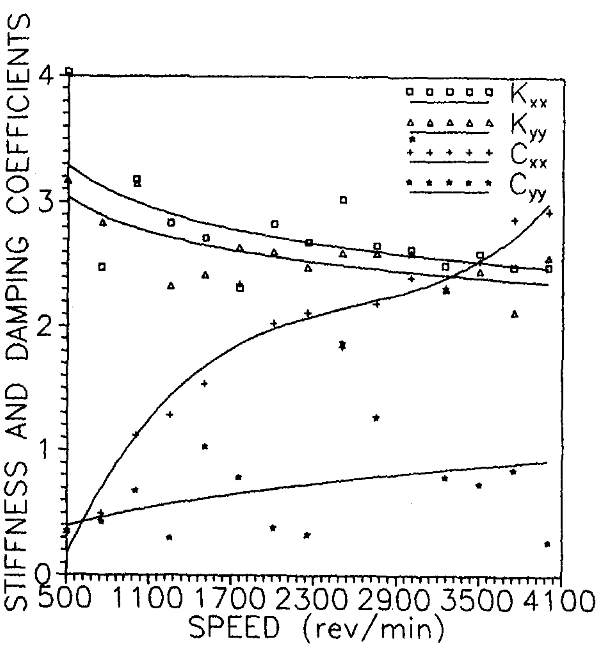

Fig. 5 Identified stiffness and damping coefficients of tilting pad bearing, load between pad configuration (No. of pads 4, *b/d* = 0.4, C_p = 42.0 μm)

Results and Discussion

The stiffness and damping coefficients are nondimensionalized as given below:

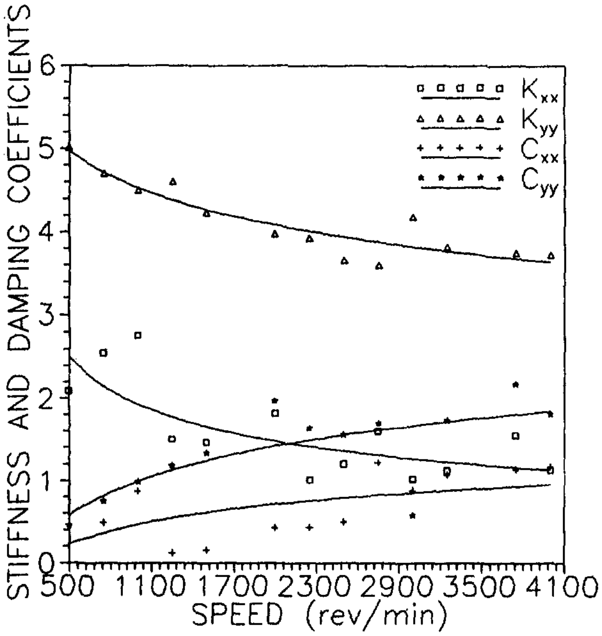

Fig. 6 Identified stiffness and damping coefficients of tilting pad bearing, load on pad configuration (No. of pads 4, *b/d* = 0.4, C_p = 42.0 μm)

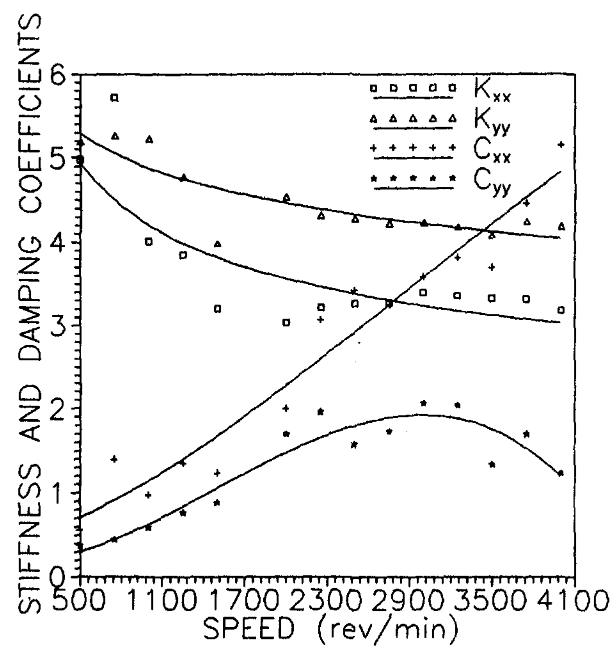

Fig. 7 Identified stiffness and damping coefficients of tilting pad bearing, load between pad configuration (No. of pads 4, b/d = 0.3, C_p = 54.0 μm)

$$K_{ij} = (C'k_{ij})/W;\; C_{ij} = (C'\Omega c_{ij})/W \text{ with } (i, j = x, y)$$

where W = 124.5 N is the steady-state load on the bearing; $C' = C_r$ for cylindrical bearings; $C' = C_p$ for tilting pad bearings.

The nondimensional coefficients of stiffness and damping versus the speed of the rotor are shown in Figs. 5–8. The estimates, with the exception of C_{yy} of tilting pad bearings of b/d = 0.4 (Figs. 5 and 6), exhibit less scattering. The estimate is scattered because not only the speed of the rotor but also the viscosity of the lubricating oil is changing. The scattering of the results may also be due to the excitation of both the forward and reverse modes simultaneously since the applied perturbation does not discriminate on direction of the applied force. The results of load between configuration of tilting pad bearings show that the bearing is not performing like an isotropic bearing. This is due to variations of pad clearance from pad to pad both in the assembled and machined clearances and the misalignment in the bearing. Further the bearing pedestals are not isotropic. The anisotropic behavior of the tilting pad bearings with load between pad configuration is also reported in the works of Someya (1989). Figure 8 shows stiffness and damping coefficients of cylindrical bearing. In this case cross-coupled damping coefficients are not shown since they are very small.

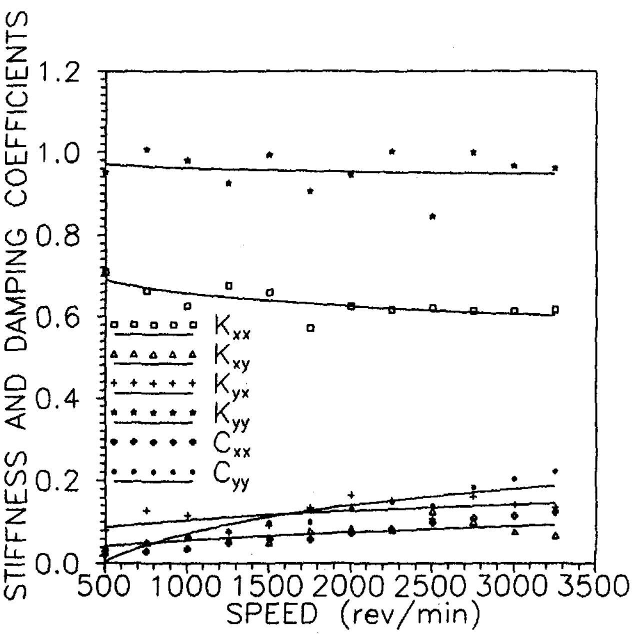

Fig. 8 Identified stiffness and damping coefficients of cylindrical journal bearing (b/d = 1.0, C_r = 65.0 μm)

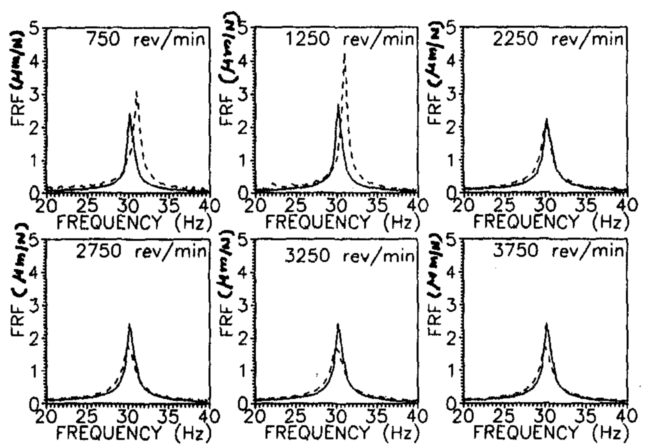

Fig. 9 Comparison of FRFs measured and predicted by finite element analysis using identified bearing coefficients; tilting pad bearing (b/d = 0.3, load between pad), —— predicted, - - - measured

The effectiveness of the identification algorithm is tested by demonstrating the ability of the identified model to predict the first natural frequency (in bending) and FRFs of the rotor-bearing system. Figure 9 shows the comparison of FRFs predicted by finite element method using the identified model and the FRFs actually measured on the rotor-bearing system. Figures 10 and 11 show the comparison of natural frequency (in bending) obtained experimentally and predicted by finite element method using the identified stiffness and damping coefficients of bearings. The comparisons are satisfactory.

Conclusions

In the present work an extended method has been utilized for the identification of linearized oil-film coefficients of cylin-

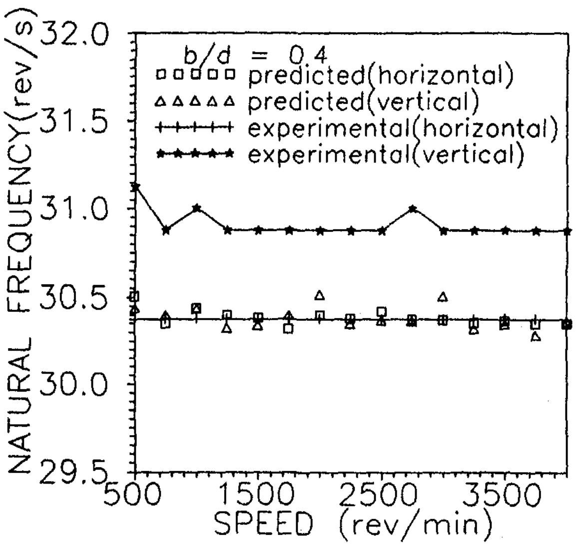

Fig. 10 Comparison of first natural frequency in bending obtained by experiment and predicted by finite element analysis using identified bearing coefficients, tilting pad bearings (load between pad)

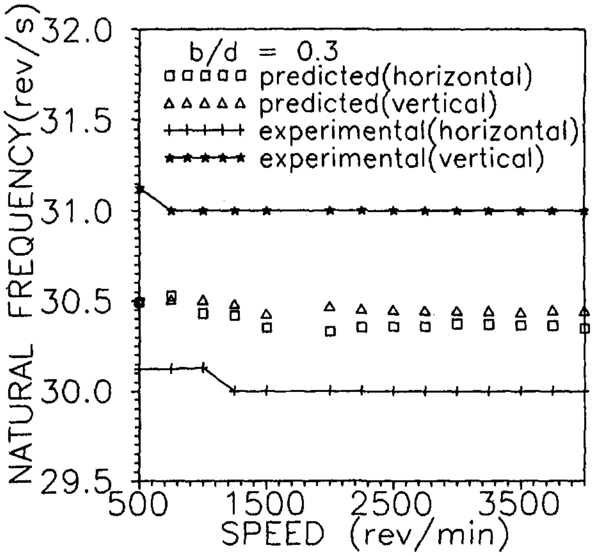

Fig. 11 Comparison of first natural frequency in bending obtained by experiment and predicted by finite element analysis using identified bearing coefficients, tilting pad bearing (load between pad)

drical and tilting pad journal bearings. This method can also be used for the identification of all the stiffness and damping coefficients of the system if the complete frequency response function of the system is known.

The effect of inertia coefficients of the oil-film on the identification method is practically nil. This is demonstrated in the simulation study.

The method presented here can be extended to find all twelve coefficients of the bearing.

Linearized oil-film coefficients of a flexible rotor-bearing system are estimated experimentally. Comparison of FRFs predicted using the finite element method with the measured FRFs shows that the identified oil-film coefficients are fairly accurate.

The number of frequency response functions needed for the estimation are only two per bearing for tilting pad bearings and four per bearing for cylindrical bearing.

This method can be easily applied to field cases since it is easy to implement for on-line identification and only a few measurements are needed at each speed.

References

Burrows, C. R., and Sahinkaya, M. N., 1982, "Frequency-Domain Estimation of Linearized Oil-Film Coefficients," ASME *Journal of Lubrication Technology,* Vol. 104, pp. 210–215.

Firoozian, R., and Stanway, R., 1989, "Design and Application of a Finite Element Package for Modeling Turbomachinary Vibrations," *Journal of Sound and Vibration,* Vol. 134, pp. 115–137.

Gargiulo, E. P., Jr., 1980, "A Simple Way to Estimate Bearing Stiffness," *Machine Design,* July 24, pp. 107–110.

Hong, S.-W., and Lee, C-W., 1992, "Identification of Bearing Dynamic Coefficients by Using Measured and Computed Unbalance Responses in Flexible Rotor-Bearing Systems," *International Conference Proceedings of Institution of Mechanical Engineers,* C432/074, pp. 183–191.

Muszynska, A., Bently, D. E., Franklin, W. D., and Hayashida, D. R., 1989a, "Identification of Modal Parameters of Rotating Systems Using Perturbation Techniques: Part 1," presented at the Twelfth Biennial ASME Conference, Mechanical Vibration and Nosie, Montreal, Canada.

Muszynska, A., Bently, D. E., Franklin, W. D., and Hayashida, D. R., 1989b, "Identification of Modal Parameters of Rotating Systems Using Perturbation Techniques: Part 2," presented at the Twelfth Biennial ASME Conference, Mechanical Vibration and Noise, Montreal, Canada.

Muszynska, A., Bently, D. E., Franklin, W. D., Grant, J. W., and Goldman, P., 1993, "Application of Sweep Frequency Rotating Force Perturbation Methodology in Rotating Machinery for Dynamic Stiffness Identification," ASME JOURNAL OF ENGINEERING FOR GAS TURBINES AND POWER, Vol. 115, pp. 266–271.

Rouvas, C., Murphy, B., and Hale, K., 1992, "Bearing Parameter Identification Using Power Spectral Density Methods," *International Conference Proceedings of Institution of Mechanical Engineers,* C432/151, pp. 297–303.

Sahinkaya, M. N., and Borrows, C. R., 1984, "Estimation of Linearized Oil-film Parameters From the Out of Balance Response," *Proceedings of Institution of Mechanical Engineers,* Vol. 198C, pp. 131–135.

Someya, T., 1989, *Journal Bearing Data Book,* Springer-Verlag, London, pp. 222–223.

Stanway, R., 1984, "Journal Bearing Identification Under Operating Conditions," ASME *Journal of Dynamic Systems, Measurement, and Control,* Vol. 106, pp. 178–182.

Wang, J. H., and Liou, C. M., 1991, "Experimental Identification of Mechanical Joint Parameters," ASME *Journal of Vibration and Acoustics,* Vol. 113, pp. 28–36.

Zhang, Y. Y., Xie, Y. B., and Qiu, D. M., 1992, "Identification of Linearized Oil-Film Coefficients in a flexible Rotor-Bearing System, Part I: Model and Simulation," *Journal of Sound and Vibration,* Vol. 153, pp. 531–547.

Zhang, Y. Y., Xie, Y. B., and Qiu, D. M., 1992, "Identification of Linearized Oil-Film Coefficients in a flexible Rotor-Bearing System, Part II: Experiment," *Journal of Sound and Vibration,* Vol. 153, No. 3, pp. 549–559.

T. B. Dewhurst

P. Tang

Department of Mechanical Engineering,
University of Maine,
Orono, ME 04469

The Use of Imposed Displacements to Determine Impact Forces in a Multiple Blade Shed Incident

Experimental data from a multiple blade shed incident are used to determine the forces exerted by the blades on a containment ring. A transient, dynamic, finite element procedure is used to model the ring during the blade shed. This work focuses on the selection of the proper numerical parameters that lead to a stable and accurate numerical solution while maintaining physical reality. Examination of the degree of implicitness and various measures of damping, as well as incorporation of large displacement algorithms, has lead to a simulation that successfully determines the forces on the ring. Accurate determination of these forces is necessary for optimal design of containment systems.

Introduction

Objectives. The long-term objective of this work is to develop numerical techniques to accurately model the response of containment rings, in aircraft gas turbine engines, to a multiple blade shed. This modeling process is extremely complicated and requires accurate representation of the ring behavior, both geometric and material, as well as a reasonable estimate of what loads the blade fragments exert on the ring. Once this is accomplished, then various ring designs may be analyzed for their effectiveness in containing the blade fragments.

The work described here addresses a preliminary aspect of the overall goals. The immediate objective is to determine the loading function exerted by the failed blades on the containment ring. Specifically, the objective is to develop a procedure for using the finite element method to determine the reaction forces when displacements from photographed experiments are imposed upon the model. When developing this procedure the sensitivity of the solution to various numerical and physical parameters will be examined.

This is a vital step in the overall process of analyzing containment ring designs. While the results of this work will only indicate the forces exerted by the blades on the ring for a particular engine design and under certain test conditions, an understanding of these forces is important for the design of future containment systems of advanced design and materials.

Relevance. The development of optimized containment systems is crucial in the effort of increasing engine performance while reducing fuel consumption and maintaining passenger safety. While increasing the bulk of the containment system would improve its capability to contain engine fragments, it would also increase engine weight, which would hamper fuel efficiency goals. Thus, accurate analysis of containment ring designs is crucial to ensure adequate safety without incurring excessive weight penalties. The objective of this work is to develop the capability to model containment system performance accurately.

Past Work. A review of the literature on the subject of containment quickly shows that the emphasis of research in this area has concentrated on the containment of burst disk fragments, whereas the research reported here concentrates on blade fragment containment. However, Federal Aviation Administration (FAA) regulations for commercial aircraft do not require containment of burst disk fragments, whereas containment of blade fragments is required. Currently, instead of requiring containment of burst disks, the FAA has stringent requirements on disk life and stress levels to prevent failure, and containment of disk fragments is being considered for the future (FAA, 1990).

Annual reports on the incidents of engine rotor fragment containment, issued jointly by the FAA and Naval Air Propulsion Center (NAPC, 1969), and substantiated by similar reports published by the Society of Automotive Engineers (SAE, 1987), indicate the extent to which blade failures occur in commercial aircraft.

While research literature on the containment of blade fragments is scarce, there is a significant amount of literature dealing with burst disk fragments. The Naval Air Propulsion Center (NAPC) conducted a Rotor Burst Protection Program (RBPP), which followed an experimental approach (1969) and then examined the use of woven materials for use in containment rings (Salvino et al., 1988), while Hagg and Sankey (1974) developed an analytical technique for evaluating ring integrity during a rotor burst. Various computational programs were evaluated for their ability to model containment of burst disks as reported in a report by the Electric Power Research Institute (EPRI, 1984). Dewhurst (1991) detailed the various types of failure mode for containment rings and noted that during blade shed incidents, field and experimental data showed that containment rings invariably suffered brittle tensile failure during a noncontained blade failure. The lack of ductility was significant. Dewhurst (1991) also outlined a procedure for determining the loads of the blades on the ring by imposing experimentally determined displacements as a function of time. The procedure was simplistic and was encumbered with numerical instabilities. As a result, a full solution to the problem was not attainable.

Approach

The immediate objective of the work reported here is to utilize the finite element method to determine the load exerted by the blades on the containment ring during a multiple blade shed. The experimental data available describe the deformation of the ring as a function of time and so the simplest technique would involve imposing the experimentally determined dis-

---

Contributed by the International Gas Turbine Institute and presented at the 38th International Gas Turbine and Aeroengine Congress and Exposition, Cincinnati, Ohio, May 24–27, 1993. Manuscript received at ASME Headquarters March 1, 1993. Paper No. 93-GT-127. Associate Technical Editor: H. Lukas.

placements upon the ring and then determining the reaction forces at these points. These reaction forces would then be indicative of the forces generated by the blades when impacting the ring. However, past experience has shown that use of imposed displacements can lead to numerically unstable solutions even when an unconditionally stable solution algorithm is used. To achieve the stated objective, while utilizing the available experimental data, requires a thorough examination of the imposed displacement approach, determination of the proper solution algorithm, and a study of the various parameters, numerical and physical, that affect the solution stability and accuracy.

Relationship Between Numerical Modeling and Physical Behavior. The basic equation of motion being solved is the dynamic equation

$$[\mathbf{M}]\{\ddot{\mathbf{u}}\} + [\mathbf{C}]\{\dot{\mathbf{u}}\} + [\mathbf{K}]\{\mathbf{u}\} = \{\mathbf{F}_{\text{app}}(t)\} \tag{1}$$

The finite element code ANSYS (1989) is used and the transient, nonlinear dynamic solution procedure is implemented. The nonlinear equation is solved using the Newton–Raphson solution procedure, and the Newmark implicit direct integration scheme is used to define the time-dependent parameters. Thus,

$$\dot{\mathbf{u}}_{t+\Delta t} = \dot{\mathbf{u}}_t + [(1-\delta)\ddot{\mathbf{u}}_t + \delta\ddot{\mathbf{u}}_{t+\Delta t}]\Delta t \tag{2}$$

$$\mathbf{u}_{t+\Delta t} = \mathbf{u}_t + \dot{\mathbf{u}}_t\Delta t + [(\tfrac{1}{2} - \eta)\ddot{\mathbf{u}}_t + \eta\ddot{\mathbf{u}}_{t+\Delta t}]\Delta t^2 \tag{3}$$

The structural damping matrix [**C**] may be approximated as a combination of the mass and stiffness matrices, or

$$[\mathbf{C}] = \alpha[\mathbf{M}] + \beta[\mathbf{K}] \tag{4}$$

In employing the Newmark methods, the parameters δ and η were introduced that govern the degree of implicitness, and in the approximation of the damping matrix, the terms α and β were introduced, which are indicative of the type of physical damping present in the simulation. In addition to these parameters, a procedure must be developed for determining an appropriate time step and concerns of large-scale rotations and deflections must also be addressed.

Newmark Parameters (Numerical Damping). Examination of Eqs. (2) and (3) shows that the Newmark parameters δ and η control the implicitness of the solution. The larger these values, the more heavily the velocity and displacement are weighted toward the values at the new time. In general, this leads to a more stable solution. However, the closer the value is weighted toward the average value of the old and new time, the more accurate the solution. According to Hughes (1987), the discretization of the ring into finite elements introduces higher modes, which are not representative of the physical object and thus, they must be damped out both to achieve numerical stability and to resemble physical reality more closely. A value of $\delta > \frac{1}{2}$ is necessary to ensure adequate dissipation of the higher frequency modes and unconditional stability is obtained when, in addition,

$$\eta \geq \tfrac{1}{4}(\tfrac{1}{2} + \delta)^2 \tag{5}$$

and

$$\tfrac{1}{2} + \delta + \eta > 0. \tag{6}$$

In the finite element code used here, ANSYS, the two weighting parameters, δ and η, are related to another factor, γ, which represents dissipation of higher frequency modes introduced by numerical discretization. The relationship between these constants is given as

$$\delta = 0.5(1 + 2\gamma) \tag{7}$$

and

$$\eta = 0.25(1 + \gamma)^2 \tag{8}$$

Thus, a single value of γ is chosen to represent the numerical dissipation to damp out high-frequency modes that do not represent physical reality. Examination of these equations shows that when $\gamma > 0$, the requirements for stability and accuracy are met. In the modeling work described here, various values of $\gamma > 0$ were used, and the effect on the results was documented.

Viscous Damping. In addition to the numerical damping of the high-frequency modes, the question of physical damping must also be addressed. As indicated by Eq. (4), Rayleigh damping is used in the solution and the parameters α and β represent the manner in which the damping matrix [**C**] is approximated as a combination of the mass and stiffness matrices. While it is difficult to describe the physical implications of these parameters, it can be said in general that as α increases in value, the damping is more indicative of rigid body damping such as a structure immersed in a viscous fluid; β represents a damping of modes due to internal dissipation and this is more indicative of normal structural damping. Alternatively, it could be said that the viscous damping is a function of the absolute velocities while the structural damping is a function of the relative, or strain, velocities within the material. Increasing the viscous damping would cause the lower frequencies to be damped more and the higher frequencies to be damped less; increasing the value of the structural damping would cause the opposite to happen. In the problem being modeled here, it must be assumed that the viscous damping is relatively trivial and the bulk of the damping must be structural.

It is difficult to determine absolute values for α and β and instead it is more common to measure damping in terms of damping ratios, ξ_i, which relate actual damping to critical damping for a particular mode of vibration. Typical damping ratios (ξ_i) vary depending upon the material in question and the manner in which it is constructed, but a value of 3–4 percent is commonly used for steel-frame type structures; for the modeling of the containment ring, values in this range will be used.

In the ANSYS formulation, the constants α and β are related to the damping ratio by the following relation:

Nomenclature

Finite Element Nomenclature

[**M**] = mass matrix
[**C**] = damping matrix
[**K**] = stiffness matrix
[**S**] = stress stiffening matrix
{**u**} = displacement
{$\dot{\mathbf{u}}$} = velocity
{$\ddot{\mathbf{u}}$} = acceleration
{$\mathbf{F}_{\text{app}}$} = applied forces

Weighting Parameters

δ, η, γ = Newmark parameters
α, β = Rayleigh damping parameters
ξ_i = damping ratio

Time Step Parameters

ω_i = natural frequency, rad/s
f_i = natural frequency (cycles/s)
ΔT = time step
N = integration points/cycle
c_d = speed of sound (dilitational)
E = Young's modulus
ρ = density
λ, μ = Lame parameters

Conservation Terms

KE = kinetic energy
SE = strain energy
n = number of blades
I = Impulse

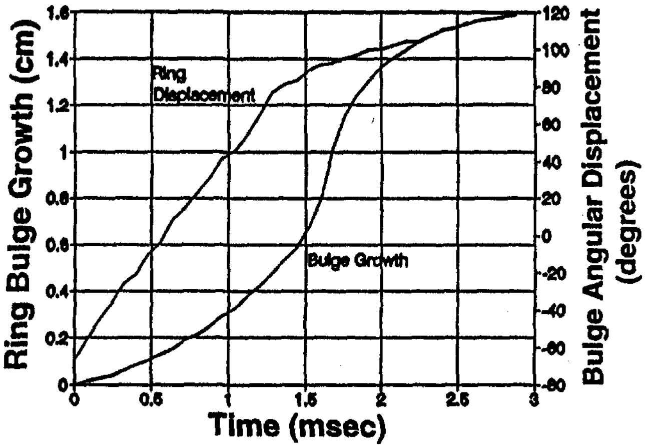

Fig. 1 Bulge growth and angular displacement as a function of time

$$\xi_i = \alpha/2\omega_i + \beta\omega_i/2 \tag{9}$$

$$\omega_i = 2\pi f_i \tag{10}$$

where ω_i is a natural frequency of interest to the problem at hand. While both damping terms on the right-hand side of Eq. (9) are strong functions of frequency, their sum is nearly constant over the frequency range where the terms intersect. For a given damping ratio (ξ) and a frequency range (f_1 to f_2), two equations can be solved simultaneously for the values of α and β. In the modeling of the containment ring, a modal analysis was performed to determine the natural frequencies of the ring, which were then used in the determination of the values of α and β.

Time Step. One of the most critical parameters in the solution of a transient dynamic solution is the choice of the integration time step (ΔT) and as it is critical, there are a number of guidelines to aid in the determination of a time step that allows accurate, stable solutions. The criteria considered applicable to the current modeling situation include:

1 Adequate resolution of the loading curve
2 Resolution of the response frequency
3 Consideration of wave propagation effects

Ultimately, the last of these criteria was the principal factor in determining the time step for the modeling of the containment ring. According to Hughes (1987) the size of the time step is defined as

$$\Delta T \leq \frac{2}{W^h_{\max}} \tag{11}$$

where $W^h_{\max}$ is defined as the maximum element frequency, which is defined as

$$W^h_{\max} \leq c_d g^{1/2} \tag{12}$$

where

$$c_d^2 = (\lambda + 2\mu)/\rho \tag{13}$$

and g is governed by the element dimensions. For the quadrilateral elements used in this analysis, substitution of Eq. (12) into Eq. (11) reduces to

$$\Delta T \leq \frac{2}{W^h_{\max}} \leq 2c_d^{-1}g^{-1/2} = c_d^{-1}(h_1^{-2} + h_2^{-2})^{-1/2} \tag{14}$$

Large Deflections With Stress Stiffening. Examination of failed containment rings and photos of a containment incident show that the ring undergoes large deflection and appears to be subjected to a large internal pressure. Therefore, the experimental data indicate that it is appropriate to include large deflection theory in the solution of this problem, and furthermore, as the ring is deformed radially, it is strengthened circumferentially, and as such, it is appropriate to include stress stiffening in the solution procedure.

Stress stiffening is an effect that causes a stiffness change in the element due to internal stress. In the containment ring, stress stiffening represents the coupling between the circumferential strength and the radial deflections within the structure. As the circumferential stress increases, the capacity to carry radial loads increases.

As the containment ring undergoes large deflection, the structure stiffness matrix based on the initial geometry does not characterize the deformed structure. Therefore, in modeling this containment incident, the large deflection algorithm in ANSYS has been used where the stiffness matrix is updated periodically. To include large deflection theory with stress stiffening, the governing equation is of the form

$$([\mathbf{K}^{up}] + [\mathbf{S}^{up}])\{\mathbf{u}\} = \{\mathbf{F}\} + [\mathbf{S}^{up}]\{\mathbf{u}^o\} \tag{15}$$

where the matrix $[\mathbf{S}]$ represents the increase in stiffness due to stress stiffening and the "*up*" superscript indicates that the matrices are updated to account for the large deflections. The vector $\{\mathbf{u}^o\}$ represents the previous displacement solution.

Imposed Displacements. In addition to numerous field data, which allow examination of failed containment rings, a containment incident was recreated experimentally, and the resulting effects were photographed. Based on the field data and the photographs, Dewhurst (1991) has developed a scenario for a "typical" multiple blade shed incident. As the blades are failing, a bulge forms in the containment ring. As the incident progresses, the bulge grows in amplitude and the peak of the bulge moves circumferentially in the same direction as the rotor spins.

To model the containment incident, the peak bulge amplitude and angular location are measured from the experimental data (Fig. 1). A finite element mesh of the ring is constructed (Fig. 2), and then the measured displacements are imposed on the mesh in a time-dependent manner. Zero displacement boundary conditions are imposed on the back flange of the ring, while near the front edge only the displacement at the peak of the bulge is imposed, and then only for one time step. As time progresses, the previous boundary condition for the bulge is released and the peak displacement is applied at the next "downstream" node. For each time step, the reaction force is calculated at the point where the bulge displacement boundary condition is imposed as this force is indicative of the force exerted by the failed blades on the containment ring. A full description of this procedure is given by Dewhurst (1991). Due

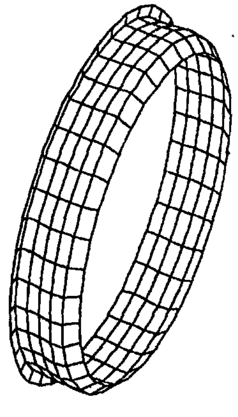

Fig. 2 The finite element mesh, 8-noded isoparametric elements

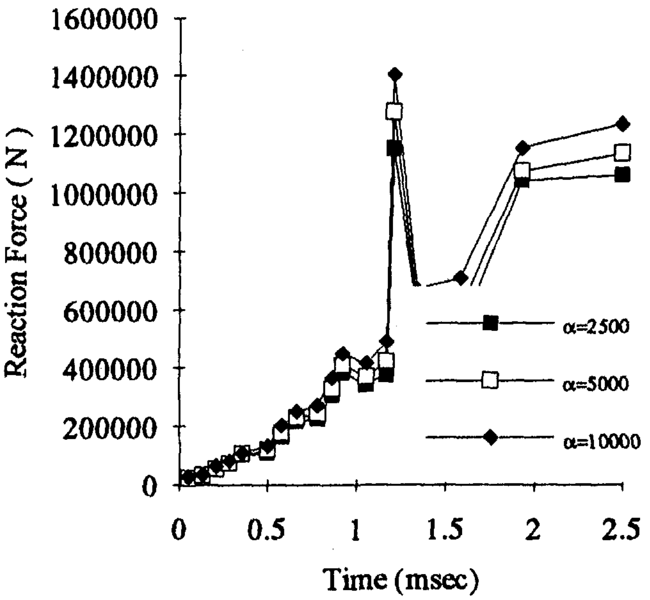

Fig. 3 **Reaction force versus time, viscous damping (α) varied, (β = 0)**

to the limitations of the photography equipment, the displacement data gleaned from the experiment cover a period of only 2.5 ms; it is believed that the entire incident did not last more than 3 ms.

Other Parameters. In addition to the Newmark parameters, damping constants, time step size, and the inclusion of large deflection with stress stiffening, there are other parameters that significantly affect the results, yet have not yet been investigated. These include nonlinear, high strain rate material properties, and more advanced techniques for applying the experimental displacements.

At this point in the analysis, the use of linear material properties was considered an important first step in the overall procedure of obtaining an accurate solution. Experimental data showed very little plastic elongation of the material, indicating the majority of the deflections occurred in the elastic regime. While high strain rate material properties would be of interest, they were not initially available. Further modeling of this incident would most naturally involve advanced material models and properties.

Results

A complete analysis of the containment ring during the multiple blade shed has been accomplished using the approach outlined above. Examination of the Newmark parameters, Rayleigh damping coefficients, time step size, and effect of large deflection with stress stiffening, has led to a feasible numerical solution that is consistent with physical reality.

Newmark Parameters. The value of γ in Eqs. (7) and (8) was manipulated subject to the constraints in Eqs. (5) and (6). The unconditional stability motion for the Newmark method is:

$$2\eta \geq \delta \geq \tfrac{1}{2} \tag{16}$$

Several simulations were run, using a simpler mesh than that shown in Fig. 2, and γ was allowed to range from 0.1 to 0.5. Examination of the displacements and reaction forces, as γ was allowed to vary, showed very little change in these measures of performance. Thus, the accuracy and stability of the solution was determined to be not sensitive to changes in the Newmark parameters, within the specified ranges. For the full-scale solution, a value of γ = 0.4 was used.

Viscous Damping. Examination of the Rayleigh damping parameters showed the solution to be extremely sensitive to these coefficients. First, an approach was taken in which the sensitivities of the results to these parameters was studied. A plot of the peak reaction force versus time, for various values of α, is shown in Fig. 3. In these plots, the structural damping is neglected, β = 0, and α is allowed to range from 2500 to 10,000. Examination of Fig. 3 shows that the rigid body damping does not significantly affect the results, which agrees with the physical problem.

On the other hand, a plot of the peak reaction force versus time for various values of structural damping (see Fig. 4), shows a high level of sensitivity. In this plot, β is allowed to vary from 0 to 0.0002, for a constant value of α. Examination of Fig. 4 shows that the results are very sensitive to changes in the structural damping, which also is consistent with the physical problem. Thus, while the value of α is not too critical, the value used for β in the analysis of the containment ring must be carefully chosen.

To determine the optimal values of α and β, a modal analysis of the ring was performed. A damping ratio of 4 percent and two of the higher natural frequencies, ω_{20} = 3146 rad/s and ω_{32} = 6205 rad/s, were used to calculate the Rayleigh damping parameters. Substituting these values into Eq. (10) and then into Eq. (9) gives

$$\alpha = 167$$

and

$$\beta = 8.56 \times 10^{-6}$$

which were the values used in the final analysis.

Time Step. A properly sized time step is critical to ensure that all pertinent behavior is accounted for, without using a step size that is so small that the CPU time used in the solution is prohibitively expensive. A study was done on the fine mesh to determine the effect of changes in the time step. For given values of α, β, and γ, a constant time step was used in the solution procedure. This was repeated for a number of different time step values ranging from 3 μs up to 25 μs. A plot of the reaction forces as a function of time is given in Fig. 5 for various time step sizes. Examination of this figure indicates that even the largest step size is sufficiently small to capture all

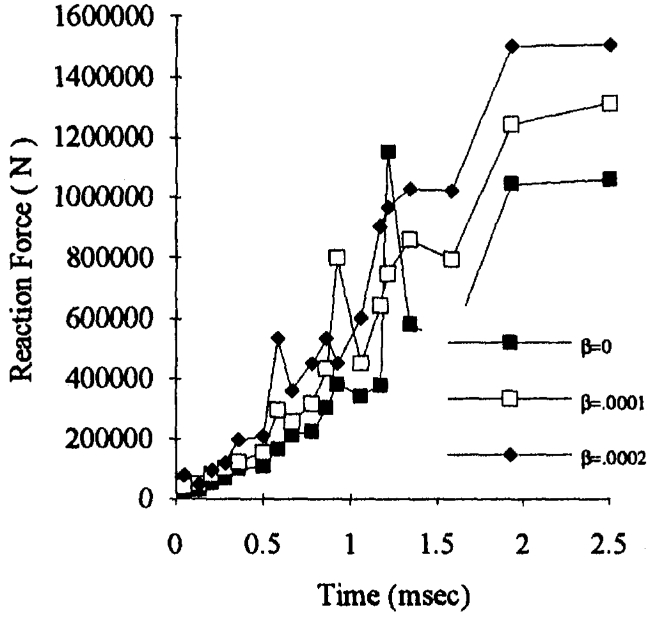

Fig. 4 **Reaction force versus time, structural damping (β) varied**

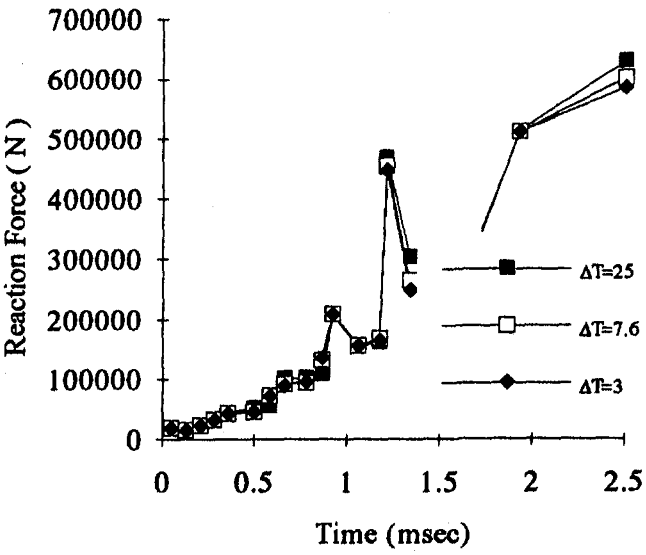

Fig. 5 Reaction force versus time, time step (ΔT, μs) varied

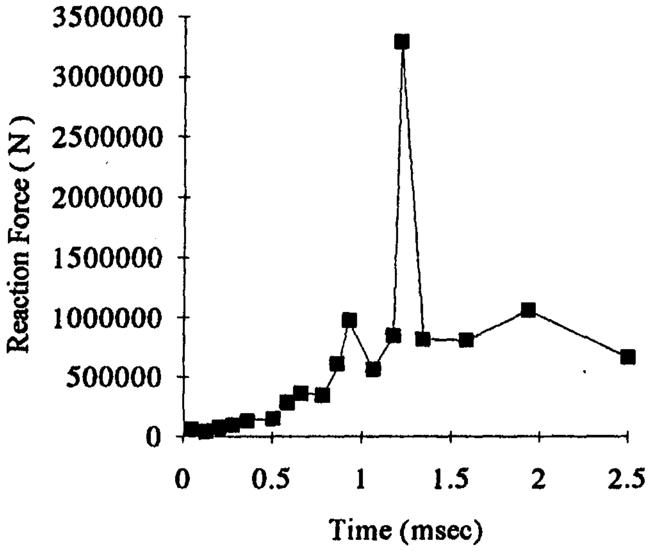

Fig. 6 Reaction forces versus time, final set of parameters

pertinent behavior. It should be noted that the reaction forces in general are significantly reduced in Fig. 5 and the following plots. The results shown in Figs. 3 and 4 are from the coarse mesh and were merely used to determine the sensitivity of the results to damping parameters. All the following results are from the refined mesh and therefore are considered more accurate.

Substituting in the appropriate values for the quadrilateral shell elements into Eq. (17) gives a value of the time step of 20.3 μs. Two simulations were done, one with a time step size of 5.7 μs, and the other with a time step size of 3 μs; in these two simulations there was very little difference in the results as shown in Fig. 5. Due to other concerns, an overly conservative value of 3 μs was used in the final analysis.

Large Deflections With Stress Stiffening. Initial studies of the blade shed incident were performed without the use of the large deflections and stress stiffening capabilities in ANSYS. In these early simulations, the solutions were quite unstable. When an imposed displacement boundary condition was removed from a node, the displacement at that node tended to rebound drastically toward the center of the ring. This type of reaction prohibited the simulation of the full blade shed incident to be completed. Inclusion of these capabilities has been judged to be the most critical factor in obtaining a complete solution to the blade shed incident.

Final Set of Parameters Used and Results. The final set of parameter values are listed in Table 1. This solution included the large deflection algorithm with stress stiffening, and the displacements shown in Fig. 1 were applied over a total of 18 load steps. The time step was held constant over the entire simulation, regardless of the size of the load step. The entire simulation required 26 hours of CPU time on an IBM 3090.

Table 1 Final set of parameters used

γ	Newmark Parameter	0.4
α	Viscous Damping	167
β	Structural Damping	$8.56\text{x}10^{-6}$
ξ	Damping Ratio	4%
ΔT	Time Step	3.0 μsec

A plot of the reaction forces for this final set of parameters is shown in Fig. 6. Examination of this figure indicates that the reaction forces generally increase with time as do the displacements, which is to be expected. The spike in the reaction forces near the middle of the simulation is largely due to the steep rise in the amplitude of the bulge as shown in Fig. 1. This indicates that a large increase in the forces exerted by the blades on the ring (recognized here as reaction forces) is responsible for this large rise in ring displacement.

Throughout this modeling procedure, many approximations have been made. As such, it is necessary to investigate the accuracy of the results obtained to determine areas of future work. First, a momentum balance can be performed where the change in momentum of the blades, assuming a final velocity of zero, can be compared to the impulse, which is approximated as the area under the reaction force versus time curve. In another check, the initial kinetic energy of the blades can be compared to the strain energy consumed in the deformation of the ring.

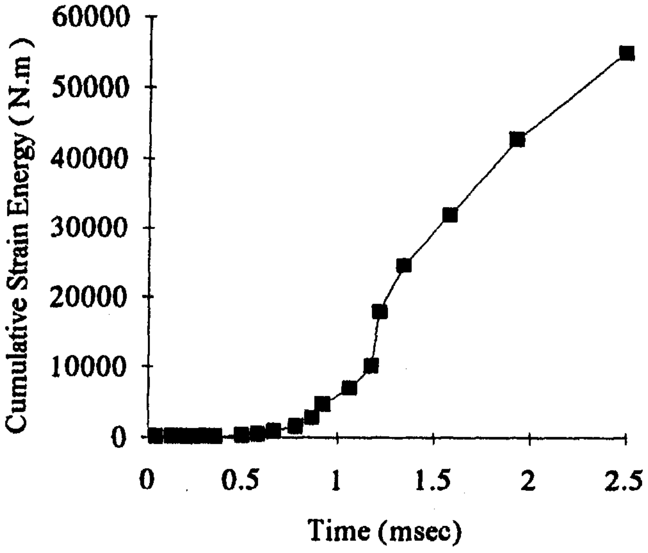

Fig. 7 Cumulative strain energy in containment ring

Impulse—Momentum Balance. The results will be valid only if the impulse, I, is less than the maximum change in momentum, or

$$I \leq (mv)_{\max} = nm_b r\omega_0 \qquad (17)$$

Examination of Fig. 6 shows that the impulse is on the order of 1620 N-s, and substituting in appropriate values into Eq. (17) gives a maximum change in momentum of 1820 N-s. Thus, the impulse calculated is within 10 percent of the maximum possible value, demonstrating that the reaction forces calculated here may be quite valid. These numbers could be closer if the final momentum of the blades were known and the final momentum could be subtracted from the right-hand side of Eq. (17).

Kinetic Energy—Strain Energy Balance. The initial kinetic energy of the blades may be calculated and compared to the strain energy calculated in the modeling of the containment ring. Again, since the final velocities of the blades are unknown, a value of zero will be used, and this number too will serve as an upper bound on the strain energy calculated in the simulation. The initial kinetic energy of the blades is given by

$$KE = n\tfrac{1}{2}m_b(r\omega_0)^2, \qquad (18)$$

the strain energy is calculated by ANSYS as

$$SE = \tfrac{1}{2}\{\mathbf{u}\}^T[\mathbf{K}]\{\mathbf{u}\}, \qquad (19)$$

and the simulation results may be valid as long as

$$SE_{\text{ring}} \leq (KE_{\text{blades}})_{\max} \qquad (20)$$

A plot of the cumulative strain energy as a function of time is given in Fig. 7. The initial kinetic energy of the blades is calculated to be 469 kN-m while the strain energy calculated by ANSYS during the simulation was 55 kN-m. This represents a significant difference in contrast to the close agreement in the momentum balance. This difference is due, in part, to the kinetic energy being a function of the second power of velocity and so the residual velocity of the blades, ignored in both balances, is more significant in the energy balance. This is not a sufficient explanation for the entire discrepancy and further investigation is required. It should be noted that this result is quite consistent with experimental observation where very little elongation of the ring occurred, less than 1 percent overall and no more than 3 percent at any location.

Stress Results. While only linear material properties have been used for the current simulation, the stresses achieved are indicative of those present in the ring. A plot of the effective stresses in the ring is shown in Fig. 8. These results are taken from near the end of the simulation and would be indicative of the stress results in the ring near the time of failure.

Discussion of Results and Conclusion. The most significant aspect of the results presented here is that the important parameters in the analysis of containment incidents have been identified, and a procedure has been presented that allows the simulation of these occurrences. Further refinement of this procedure can be a valuable tool in the design and analysis of containment systems constructed of traditional or advanced materials.

The two most important parameters are (1) implementation of the large deflection and stress stiffening algorithms and (2) the structural damping parameter. Previous results have shown that stable solutions are not possible without the large deflection and stress stiffening algorithms. The results presented here clearly show the sensitivity of the results to the amount of structural damping present. The "correct" value of structural damping was established by use of the damping ratio, but the tests conducted here only indicate the sensitivity of the results to this value without any indication of whether or not this is the best value.

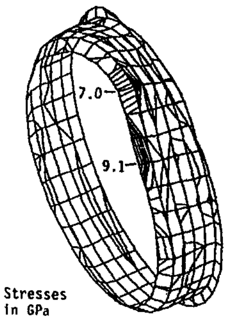

Fig. 8 Effective stress contours in the ring near time of failure

The stress results do indicate that the containment ring must be able to withstand consistent impact forces on the order of 1 MN. Since experimental data have indicated that it is not the direct impact of the blades on the ring that causes failure, but that the brittle tensile failures are due to large hoop stresses, it would be more critical to look at these stress values. The preliminary results achieved here indicate that the effective stresses are on the order of 10 GPa. which significantly exceed the ultimate strength of the material under static conditions. This would indicate that failure had already occurred by this time or that further refinement of the solution procedure is required.

Future Work

The progress chronicled here represents a significant step in the attempt to model the containment incident since a numerical procedure has been established that is not only theoretical in nature but is based upon experimental data. Two areas of immediate study await. First, nonlinear material properties must be incorporated and, second, a more advanced analysis code should be used.

While ANSYS has been adequate for modeling this incident, the use of DYNA3D (Hallquist, 1983) promises to enhance the accuracy of the modeling process further due to its ability to model high-speed impact problems, and its capabilities of incorporating more complex material models. Research into these areas will continue to improve the process of modeling containment rings during multiple blade sheds.

References

ANSYS, 1989, "Engineering Analysis Systems," Swanson Analysis, Inc., Houston, PA, May.

Dewhurst, T. B., 1991, "The Impact Load on Containment Rings During a Multiple Blade Shed in Aircraft Gas Turbine Engines," ASME Paper No. 91-GT-163.

EPRI, 1984, "Assessment of Turbine-Casing Impact Code Calculations," EPRI N-2744, May.

FAA, 1990, "Background Data and Proposed Advisory Circular, A Development Plan to Support Turboshaft Engine Rotor Burst Protection," Apr.

Hagg, A. C., and Sankey, G. O., 1973, "The Containment of Disk Burst Fragments by Cylindrical Shells," ASME JOURNAL OF ENGINEERING FOR POWER, Vol. 95, Nov.

Hallquist, J. O., 1983, "Theoretical Manual for DYNA3D," Lawrence Livermore Laboratory, UCID-19401, Mar.

Hughes, T. J. R., 1987, *The Finite Element Method,* Prentice-Hall Inc., Englewood Cliffs, NJ.

NAPC, 1969, "Rotor Burst Protection Program," NAPTC-AED-1901, May.

NAPC, 1987, "Statistics on Aircraft Gas Turbine Engine Rotor Failures That Occurred in US. Commercial Aviation During 1981," DOT/FAA/CT-86-42, Mar.

SAE, 1987, "Report on Aircraft Engine Containment," AIR 4003, Sept.

Salvino, J. T., et al., 1988, *Experimental Guidelines for the Design of Turbine Rotor Fragment Containment Rings,* DOT/FAA/CT-88/21, FAA Technical Center, Atlantic City International Airport, NJ.